

LL

Electro-Topological Analysis and Diagnostics of the Superconducting Magnet Systems for the Large Hadron Collider

by Piotr Artur Komorowski

A dissertation submitted to the Faculty of Physics
in partial fulfillment of the requirements for the degree of

Doctor of Philosophy

at the

Warsaw University of Technology



CERN LIBRARIES, GENEVA



CM-P00068853

Thesis-2000-Komorowski

Thesis Supervisor: Prof. Andrzej Sukiennicki

CERN Supervisor: Dr. Davide Tommasini

Warsaw, January 2000

2251947

Thesis - 2000 - Komorowski

God, grant me the serenity to accept the things I cannot change,
the courage to change the things I can,
and the wisdom to know the difference between the two.

Dr. Reinhold Niebuhr

Acknowledgments

The work presented in this thesis has been carried out in the Main Magnets and Superconductors group at the European Laboratory for Particle Physics (CERN) in Geneva, within the framework of the CERN Doctoral Student Program.

As any doctoral thesis boldly exploring the areas where no one has gone before, it had known its moments of blissful joy as well as its moments of utmost despair and frustration. I am most grateful to my supervisor at CERN, Dr. Davide Tommasini, director of the LHC Short Magnet Model Program, who was always there for me both in times of success and in the periods of great difficulties. I would like to thank him for taking care not only of my scientific growth throughout the last three years, but also for further development of my personality. Dr. Tommasini, who initiated this work, showed me that there are things in our lives that we cannot change, but we should always have the courage to change the things we can. We should always do our best while doing so, because even if the obstacles along the way may seem to be hard to handle, the most unexpected solutions may present themselves already behind the next turn of the road. From the perspective of time I can only say that it was indeed worth to struggle up to the very end of the road and to get to see the final results of this work.

I am exceedingly grateful to Prof. Andrzej Sukiennicki, the supervisor of this thesis at the Warsaw University of Technology, for his support and encouragement from the very beginning of my work at CERN. I wish to thank him as well for having been my teacher during five years of my undergraduate studies at the former Faculty of Applied Physics and Mathematics, because the present results of my work are most of all the fruits of knowledge that was passed to me back then.

I would like to express my gratitude to Dr. Stephan Russenschuck from the LHC-ICP group for many fruitful discussions that we had together concerning the design and

optimization of the superconducting accelerator magnets, and for patience with which he was answering all my questions. I would also like to thank him for initiating me into the undocumented features of his Routine for the Optimization of Magnet X-Sections, Inverse Field Calculation and Coil End Design (ROXIE) – the software environment used at CERN for the computer-aided design of the accelerator magnets. Thanks to ROXIE the reader will have the opportunity to enjoy throughout this thesis the state of the art illustrations of magnetic vector field patterns in the LHC magnets and more...

I would like to thank Dr. Norbert Siegel, the former head of the Short Dipole Magnet Program, Dr. Carlo Wyss, the director of the Main Magnets and Superconductors group, and Dr. Rüdiger Schmidt, the director of the Doctoral Student Program at CERN, for their constant support and personal interest in this project.

Special thanks go to Hans Kummer and the entire team of the Magnet Assembly Hall 927 for having to cope with me for the last three years, but especially for the assembly of the test magnets.

I would like to thank William Billereau and Angelo Gandi for preparing the image transfer films and bringing the design of multilayer printed circuit pick-up coils into life.

I express my gratitude to Prof. Gianfranco Coletti and Prof. Francesco Guastavino for taking care of me during my stay at the University of Genoa in Italy, and for the wonderful atmosphere of work and friendship that I had an opportunity to experience in their laboratory.

I would like to address special thanks to Dr. Stefan Kurz from the University of Stuttgart, who during one conference banquet, on the contrary to my initial impression, showed me that the contemporary techniques of numerical field calculations for the design of superconducting magnets evolve nowadays almost as fast as any other domains of modern applied physics. What is even more astonishing, during the very same banquet Dr. Kurz truly taught me to appreciate the beauty behind this evolution.

Last but not least I would like to thank my Guardian Angel, who on one midsummer night whispered to me under the shower what was wrong with my finite element transient electromagnetic model of the damaged magnet, and caused thus a major breakthrough in the entire project. This is another, although not very scientific proof, that the solutions to most difficult problems may present themselves anytime and anywhere...

Piotr Komorowski

Geneva, December 15, 1999

Contents

Acknowledgments	iv
Contents	vi
Motivation	xi
Overview of the Thesis	xiv

Chapter 1

The Large Hadron Collider Project

at the European Laboratory for Particle Physics	1-1
1.1 The Key Questions of Physics Addressed by the LHC	1-4
1.1.1 The Problem of the Origin of Mass in the Universe	1-8
1.1.2 In Search for the Theory of Everything	1-9
1.1.3 Missing Antimatter Mystery	1-11
1.2 Parameters and Performance of the LHC	1-12
1.2.1 Principles of the Synchronous Acceleration	1-12
1.2.2 Layout of the LHC Accelerator Facility	1-14
1.2.3 Multi-Staged Acceleration of the Proton Beam	1-18
1.2.4 Machine Performance Issues	1-19
1.3 Superconducting Dipole Magnets for the LHC	1-21
1.4 The Short Dipole Magnet Program	1-25
1.5 Objectives of the Electro-Topological Analysis and Diagnostics	
of the Superconducting Magnet Systems for the LHC	1-32
References	1-36

Chapter 2

Electromagnetic Principles of the Design of

Superconducting Accelerator Magnets for the LHC	2-1
--------------------------------------------------------------	------------

2.1 Magnetostatic Problems in 2-D	2-4
------------------------------------------------	------------

2.2	Multipole Expansion of the Complex Magnetic Field	2-6
2.3	Normalized Multipole Coefficient Notation	2-9
2.4	Solution of the Laplace Equation for the Vector Potential	2-12
2.5	Magnetic Field Harmonics of a Single Current Line Conductor	2-15
2.6	Pure Multipole Field Generation	2-18
2.7	Current Shell Approximation	2-24
2.8	Approximate Magnetic Field Calculations for the LHC Dipole Coils	2-30
2.8.1	Inner Layer Contribution to the Field Induction inside the Aperture	2-31
2.8.2	Outer Layer Contribution to the Field Induction inside the Aperture	2-32
2.8.3	Total Field Induction due to Both Layers	2-33
2.9	Comparison of the Current Shell Model with the ROXIE Calculations	2-34
2.10	Influence of the Nonsaturated Iron Yoke on the Magnetic Field within the Magnet	2-37
2.10.1	Cylindrical Air-Iron Boundary Problem	2-37
2.10.2	Analytical Calculations for the Nonsaturated Iron Yoke	2-44
2.10.3	Single Aperture LHC Dipole Magnet with Nonsaturated Iron Yoke	2-50
2.11	Saturated Iron Yoke	2-54
2.11.1	FEM Formulation for 2-D Numerical Analysis of the LHC Dipole Magnets with Saturated Iron Yoke	2-56
2.11.2	Reduced Vector Potential Representation	2-66
	References	2-71

Chapter 3

A Novel Method for the Inter-Turn Short-Circuit Localization

	in Superconducting Collared Coils	3-1
3.1	Static Analysis of an Inter-Turn Short Circuit at Room Temperature	3-3
3.2	Criteria for the Azimuthal Localization of the Fault-Affected Area	3-7
3.3	Limitations of DC Test and Analysis for Detection and Localization of Inter-Turn Short-Circuits	3-11
3.4	Detection of the Insulation Failures with the HV Discharge Test	3-12
3.5	Eddy Currents in Quasi-Static Time-Varying Magnetic Fields	3-16
3.5.1	Proximity Effects in the Copper Wedges and in the Coil Reinforcement Structure	3-17
3.5.2	Skin Effect in the Current-Driven Coil Conductors	3-24
3.5.3	Transient Skin Effect	3-26

3.6	FEM Formulation of the Transient Electromagnetic Problem for the Numerical Analysis of the Magnetic Field During the High Voltage Discharge Test	3-30
3.7	Modeling of the Collared Magnet Assembly	3-32
3.7.1	Evolution from the Static towards the Transient Model	3-32
3.7.2	Optimization of the Transient Model	3-34
3.8	Transient Magnetic Field in Presence of the Inter-Turn Short-Circuit	3-38
3.8.1	The Reference Field Pattern	3-38
3.8.2	Magnetic Field Distortions Induced by Short-Circuits	3-38
3.9	Detection Method	3-41
3.10	Design and Fabrication of the Pick-Up Coils	3-43
3.10.1	Evolution of the Design Process in Search for the Optimal Solution	3-43
3.10.2	Assembly of the Multilayer Printed Circuit Pick-Up Probe	3-46
3.11	Experimental Set-Up	3-49
3.12	Test Results	3-52
3.12.1	Reference Magnetic Field	3-52
3.12.2	Activation of the Inter-Turn Short Circuits and Analysis of the Damaged Magnet	3-59
3.12.3	Probe Misalignment Analysis	3-64
3.13	Appendix A. High Voltage Discharge Measurements: Test Procedures and Analysis of the Results	3-68
A.1	Description of the Experimental Set-Up	3-68
A.2	Discharge Circuit Modeling	3-71
A.3	Procedure Applied for the Analysis of the Experimental Data	3-78
	References	3-81

Chapter 4

Advanced TDR Techniques for the Signal Integrity Analysis

	in the Instrumentation of the LHC Magnets	4-1
4.1	General Remarks on the Measurement Method	4-3
4.2	Types of Electrical Faults Encountered in the Circuits	4-3
4.3	Transient Losses in the Line and the Choice of the Input Signal	4-4
4.3.1	Transient Skin Effect in a Pulse-Excited Cable	4-4
4.3.2	Distortion of the Rectangular Pulse	4-8
4.3.3	Distortion of the Haversine Pulse	4-10
4.3.4	Time Duration of the Transient Regime	4-16

4.4	TDR for the Localization of Inter-Turn Short-Circuits in the Coiled Systems Wound with Superconducting Rutherford Cable	4-18
4.4.1	Reflection Image of the Inter-Turn Short-Circuit in the System with Wound Cables	4-18
4.4.2	Pulse Reflection Measurements in the Coils Wound with Superconducting Cable	4-23
4.5	Localization of Electrical Faults in the Instrumentation Circuits of the LHC Magnets	4-30
4.5.1	Voltage Tap Circuit	4-30
	Dipole Magnet MB2	4-32
	Short Straight Section Quadrupole	4-34
4.5.2	Temperature Transducer Circuit	4-37
4.5.3	Pressure Transducer Circuit	4-45
4.5.4	Conclusions	4-47
Appendix A	Operational Calculus Approach to the Distributed Line Problem	4-49
	Distributed Line and the Laplace Transform	4-49
	Approximation of the Lossless Line	4-53
Appendix B	Calculation of the Ideal Step Response to Complex Loads and Line Transitions	4-55
	Example 1. Line matched at the input and terminated with shunt R - L load	4-55
	Example 2. A connector between two cables of the same characteristic impedance	4-59
	Example 3. Transition between the lines with different characteristic impedance	4-63
References	4-64

Chapter 5

Partial Discharge Analysis for the Overall Quality Assessment

	of the Ground Insulation in Superconducting Magnets	5-1
5.1	Partial Discharge Detection	5-4
5.2	Test Magnets for the PD Analysis of the Ground Insulation Quality	5-10
5.3	PD Measurements Performed on the Dipole Magnets	5-13
	Test No. 1 – General test of insulation between the quench heaters and the collars	5-13
	Test No. 2 – Simultaneous test of insulation between the quench heaters and the coil, and between the quench heaters and the collars	5-15

Test No. 3 – Sidewise test of the ground insulation	5-17
References	5-19
Conclusions	6-1

Motivation

The main challenge of the Large Hadron Collider project (LHC) being developed at the European Laboratory for Particle Physics (CERN) is not posed, as one might expect at the first sight, by the gigantic detectors for the particle physics experiments or by an enormous amount of civil engineering required to successfully install and maintain the entire accelerator facility. The main and most difficult challenge is presented by the 15-m long twin aperture superconducting dipole magnets operated at the temperature of superfluid helium, generating the magnetic field of 8.33 T, and responsible for guiding two counter-circulating 7-TeV proton beams on a stable orbit. More than 1200 of such magnets must be installed in the 27-km long accelerator ring in order to accomplish the task. At the same time 20 other types of superconducting magnets will take care for the beam injection, focusing, and extraction, as well as for the correction of the multipole field errors.

In view of the series production of such an impressive number of the modern superconducting magnets a complete system of sophisticated diagnostic tools and procedures must be developed to ensure the highest quality and the overall integrity of the superconducting coils, of their electrical insulation, and of the surrounding magnet structure. The necessity of the high performance insulation in the superconducting dipole magnet is not exactly driven by the same reasons that enforce the use of the insulating materials in the standard non-superconducting electromagnetic systems. For the stability reasons the superconducting Nb-Ti filaments in the cable are immersed in the copper matrix. At the temperature of 1.9 K any current traversing the cable, not exceeding the critical current value for the superconductor at the given nominal magnetic field, is transmitted via the zero-resistivity superconducting filaments. Thus one could hypothetically imagine a

superconducting coil of the magnet operating with the copper matrix acting as an insulator between the superconducting Nb-Ti. Unfortunately the problem is much more complex.

At the temperature of superfluid helium the heat capacity of metals is so small that the slightest movement of the cable, corresponding to the fractions of a single millimeter, may cause enough friction to locally increase the temperature of the cable above the critical temperature of the superconductor. In this case the imposed current density surpasses the value of the critical current density and the surplus is carried away by the copper matrix. It is clear that the complete lack of insulation under such circumstances or even the presence of some pointwise defects would lead to short-circuits, additional energy losses and, eventually, further irreversible increase of the temperature.

Prevention of any cable displacement presents another challenge since during the operation of the magnet at its nominal field, the electromagnetic Lorentz forces of some 14000 N act on each meter of the cable length trying to tear the entire magnet structure apart. To eliminate those movements the coils are confined in a fixed volume with a pre-compression sufficient to counteract the electromagnetic forces exerted on them. Moreover, the outer layer of the cable insulation is covered with an adhesive, which tightly bonds the adjacent cable windings. The adhesive polymerized during the heat treatment of the cable gives to the coil its final rigid shape and form.

If the copper matrix and the helium coolant manage to efficiently carry the heat away from the superconducting filaments the cable may recover its stability and superconducting state, and eventually a potentially dangerous problem is auto-corrected. However if the cooling is not sufficient enough, the normal zone starts propagating rapidly along the cable and the magnet quenches inevitably, i.e. it undergoes a violent resistive transition from the superconducting to the normal state. The energy stored in a twin aperture superconducting dipole magnet corresponds to about 7.4 MJ. During the quench all of this energy would be released into the magnet destroying it in a spectacular explosion. Therefore as soon as the quench is detected the stored energy is dissipated in the copper part of the cable and discharged safely into a special dump resistor. Hence comes another prerequisite for the cable insulation. Since the magnet is powered up with the high current of 11.5 kA the resistive voltage resulting from the propagation of the normal zone builds up very fast in the coil. Even in the high performance quench detection systems this voltage can raise as high as 1kV before the quench is detected and the magnet protection procedure is triggered. The cable movement is, of course, not the unique cause of the local hot spot creation in the magnet. A stray particle beam hitting the magnet will invoke the same effect.

All of those factors combined together impose very high prerequisites on the characteristics of the applied insulating material. It must not only show excellent electrical and mechanical properties in extremely low temperatures and withstand the build-up of the voltages of more than 1kV without a dielectric breakdown, but also it has to endure the high radiation doses with as little degradation as possible.

This extremely important dielectric barrier separating two adjacent cable turns of the superconducting coil can be easily damaged during one of the magnet assembly stages causing thus a possible inter-turn short-circuit. The localization of the fault in most cases evolves into a complex, expensive and time-consuming process. The possibility of any intervention on the assembled magnet is extremely restricted. After the assembly the only existing access to the magnet coils is provided via the connection terminal for the power supply. Although even in this phase the possible electrical defects are well detectable with the standard pulse propagation methods, they often disappear after the magnet is disassembled for repair due to the release of the prestress in the coils. Time-consuming methods involving local controlled pressure increase over small sections of the coils, combined with the standard high voltage discharge tests must be employed thereafter to reestablish and localize the short-circuit. Although this doctoral thesis addresses many different aspects of the analysis of the superconducting magnets and their instrumentation circuits, it is especially focused on the novel method conceived for the precise localization of the electrical insulation failures in the assembled magnet system by means of transient magnetic field analysis. The unprecedented advantage of this approach in comparison to the standard detection procedures outlined above leads to the identification and localization of the fault-affected area before the magnet is disassembled. The method can be used at any assembly stage starting from the collared coils and finishing on the fully assembled magnet enveloped by the iron yoke and clamped by the bolted stainless steel cylinder.

Overview of the Thesis

The first chapter of the thesis discusses the LHC project and its objectives. The key questions of the modern particle physics are addressed along with the reasons for which the united resources of the physicists and engineers from all over the world consider these questions to be worth answering. The challenges posed by the accelerator facility, the experiments, the particle detection, the beam dynamics and its phase stability, and of course by the dipole magnets and their cryogenic system are outlined in this part.

The second chapter underlies the scientific background necessary for the development of the ideas presented throughout the thesis. The notation conventions for the harmonic analysis of the magnetic field are introduced along with the notions of the symmetry preserved as far as the coil geometry and the current distribution in a modern accelerator dipole magnet are concerned. This chapter addresses as well the characteristic properties of the magnetic vector field decomposed into separate harmonic components, and discusses the roles attributed to different parts of the magnet system in the generation of the magnetic field. Both analytical and numerical calculations with the implications for the design of the magnet are demonstrated for a flawless single aperture LHC dipole operating under normal – steady current conditions.

In chapter three an idea for the novel method is born. It begins with the analysis of the dipole symmetry breaking imposed by a redistribution of the current due to a short-circuit between the consecutive turns of the coil. Initially the problem is studied in the static case. The effect predicted for the static case is then developed throughout this chapter by gradual elimination of the encountered problems towards the transient magnetic field analysis. The peculiarity of the localization of the electrical insulation failures presented therein is based on

the fact that the dipole magnets are operated most of the time with the steady current. The magnet system is submitted to the variable magnetic field only during the acceleration phase of the particle beam. During this phase the current is ramped in the magnet at the constant rate and the fast transient phenomena do not occur. Thus a minor interest attributed by the accelerator physics community to the transient phenomena in the dipole magnets is fully justified.

The contents of this chapter show that the test activation of a dipole magnet with a pulsed magnetic field at room temperature gives a lot of advantages as far as the diagnostics and the quality assessment of the entire magnet system are concerned. The approach leads inevitably to the analysis of the transient states of the magnetic field; the area of physics in which the exact analytical solutions exist only for a couple of simplified model problems. The sole fact that the components of the system are subject to time-varying magnetic fields implies that the eddy current effects must be calculated for all of the non-magnetic metallic materials. Also the magneto-dynamic problem of the current redistribution in the conductors due to the transient skin effect must be taken into account. All of these aspects inevitably lead to the creation and careful optimization of the transient electromagnetic Finite Element Method (FEM) model capable of predicting and reflecting the real experimental results. Finally, the application of the results leads to the design and production of necessary instrumentation for the non-destructive localization of electrical insulation failures in the accelerator magnet systems with a precision of a few millimeters. This conclusion fully justifies the somewhat exotic treatment of the transient states of the magnetic field in the magnets that are by definition not supposed to be subject to a pulsed magnetic field.

In chapter four advanced time domain reflectometry techniques (TDR) are used for the analysis of the integrity of the signal propagating in the instrumentation circuits of the magnets. The technique involves the excitation of the circuit under test with either a fast edge step function, or a well-defined voltage impulse confined in time and frequency domains, and thereafter detection of the amplitude and time of reflections along the line. Both variants of the method are successfully applied to localize electrical faults in the voltage tap, pressure transducer, and temperature sensing carbon gage circuits of the LHC string dipole and quadrupole magnets.

The last chapter of the thesis addresses the method, which has never ever been used at CERN. Partial Discharges (PDs) are pulsed shaped high frequency currents in the cable insulation, which may occur between the conductive area of the cable and its insulation or along the insulation surface. The statistical results of the method, i.e. the number, the

magnitude, and the phase angle of PDs, may lead to the detection of the possible insulation imperfections and defects, or of the ongoing degradation of the insulation even if the HV tests, e.g. the measurements of leakage current, are successfully passed. Sometimes it is required that the sensitivity of the measurements is as high as 1 pC as far as the amplitude of the detected PDs is concerned. The detection system must be designed according to the recommendations for the implementation of low level signal measurements in order to successfully recover the PD signal from noise. In addition the measurement area must be decoupled from any external electromagnetic fields. The research studies presented in this chapter were carried out at the PD facilities of the Genoa University in Italy.

Chapter 1

The Large Hadron Collider Project at the European Laboratory for Particle Physics

The motivation for building particle accelerators comes from the everlasting desire of mankind to unveil the mysteries of the surrounding world, to gain better understanding of the laws of nature and to comprehend the structure of the universe. Although with each answered question the multitude of new unknowns appears on the horizon this extraordinary quest has never ceased to advance on its way and a man has never given up the challenge of reaching into the very heart of the matter.

To understand the physical processes taking place in our world nowadays one has to understand the conditions which existed when it all began some 15 billion years ago at the very origin of the universe in an explosion commonly referred to as the Big Bang. The circumstances, which accompanied the very instance of creation of the entire universe, can be reconstructed in a micro scale by analyzing the results of collisions between counter-circulating beams of particles accelerated to extremely high energies. In fact the same laws of physics govern both the large-scale universe and the micro-world of quantum mechanics. Since we are but a speck of dust on the rim of the galaxy which contains myriads of stars similar to our Sun we cannot do much more than a humble observation of the splendor of the universe as far as the experimental exploration of the large scale macro-world is concerned. On the other hand the areas of the micro-world are far beyond the capacity of the direct human sensory experience. But the quantum universe is right there at our hand ready to be submitted not only to the passive observation but also to our experiments providing that we are clever enough to penetrate the kingdom of the subatomic scale. In this regard the particle accelerators behave like gigantic microscopes bridging the existing gap and allowing to behold the invisible, to experience what cannot be seen with a naked eye.

Apart from the difference in scale the process of looking into the subatomic structure via the particle accelerator is similar to the process of looking at our surroundings with our own eyes. In case of the human eye the light emitted by the sun or other light sources acts as a probe sensing observed objects. The photons reflected or refracted by a specific object must return to the eye where the picture of the object is formed and transmitted to the brain. In biological microscopy the focusing power of the eye becomes not sufficient for the direct observation of the test samples and therefore the optical microscopes must be used. In silicon lithography or medical microscopy, as the explored scales drop down, shorter wavelengths of light must be used in order to obtain higher resolution. Shorter wavelength is equivalent to the higher transverse momentum transfer at the moment of the contact between the probe and the observed object. At the scale where the wavelengths associated with the photons are bigger than the size of the observed objects the photons become not efficient as the probing particles and in the Scanning Electron Microscope (SEM) they are replaced with electrons. However even the most powerful SEM can only show a fuzzy picture of an atom. If we still want to go further and successfully examine the subatomic structure of matter the probing particles must be accelerated to extremely high energies. The higher the energy the greater the sensitivity to small length scales. To explore the quantum world in the range of the length scales of the order of $\Delta r = 0.1$ fm the transverse momentum transfer supplied by the probing particles must be at least of the order of $\Delta p \sim \frac{\hbar}{\Delta r} \approx 2 \text{ GeV} / c$. This prerequisite for high energies became an inseparable attribute characterizing the area of physics which tries to analyze the structure of matter on the subatomic level.

The Large Hadron Collider (LHC) is an example of a new generation of particle accelerators designed for the High Energy Physics (HEP) experiments. The facility will be installed in the existing 27-km long tunnel ring of the Large Electron Positron Collider (LEP) at the European Laboratory for Particle Physics (CERN) in Geneva (Fig. 1.1). The project was officially approved by the CERN Council in 1994. The new machine should be operational in the year 2005. It will collide two counter-circulating 7 TeV proton beams guided in the magnetic field of 8.33 T. Such a high intensity of the magnetic field, necessary for deflecting the high-energetic proton beam in the circular ring of the accelerator, can only be realized with superconducting magnets. More than 1200 of 15-m long dipole magnets [1] cooled by superfluid helium at the temperature of 1.9 K must be installed in the accelerator ring in order to achieve this goal. Apart from the dipoles, approximately 400 of 3.5 m-long superconducting quadrupole magnets generating the gradient field of 220 T/m will be

required for the magnetic focusing of the beam. Some 20 other types of insertion and corrector magnets are still necessary for the injection and extraction of the beam, for the trajectory corrections and for the elimination of the magnetic field errors generated by the main magnets. In total more than 8000 superconducting magnets are required to ensure the efficient control of the beam stability.

This chapter gives a general overview of the LHC project. It formulates the key questions of physics that will be addressed by the LHC. It touches the two major pillars of the entire project by discussing the issues of the Accelerator Physics and of the Applied Superconductivity in service of Particle Physics. Finally it points out the greatest challenges of the LHC project posed by the design and fabrication of 1232 modern twin-aperture superconducting dipole magnets and it outlines the objectives of this thesis.

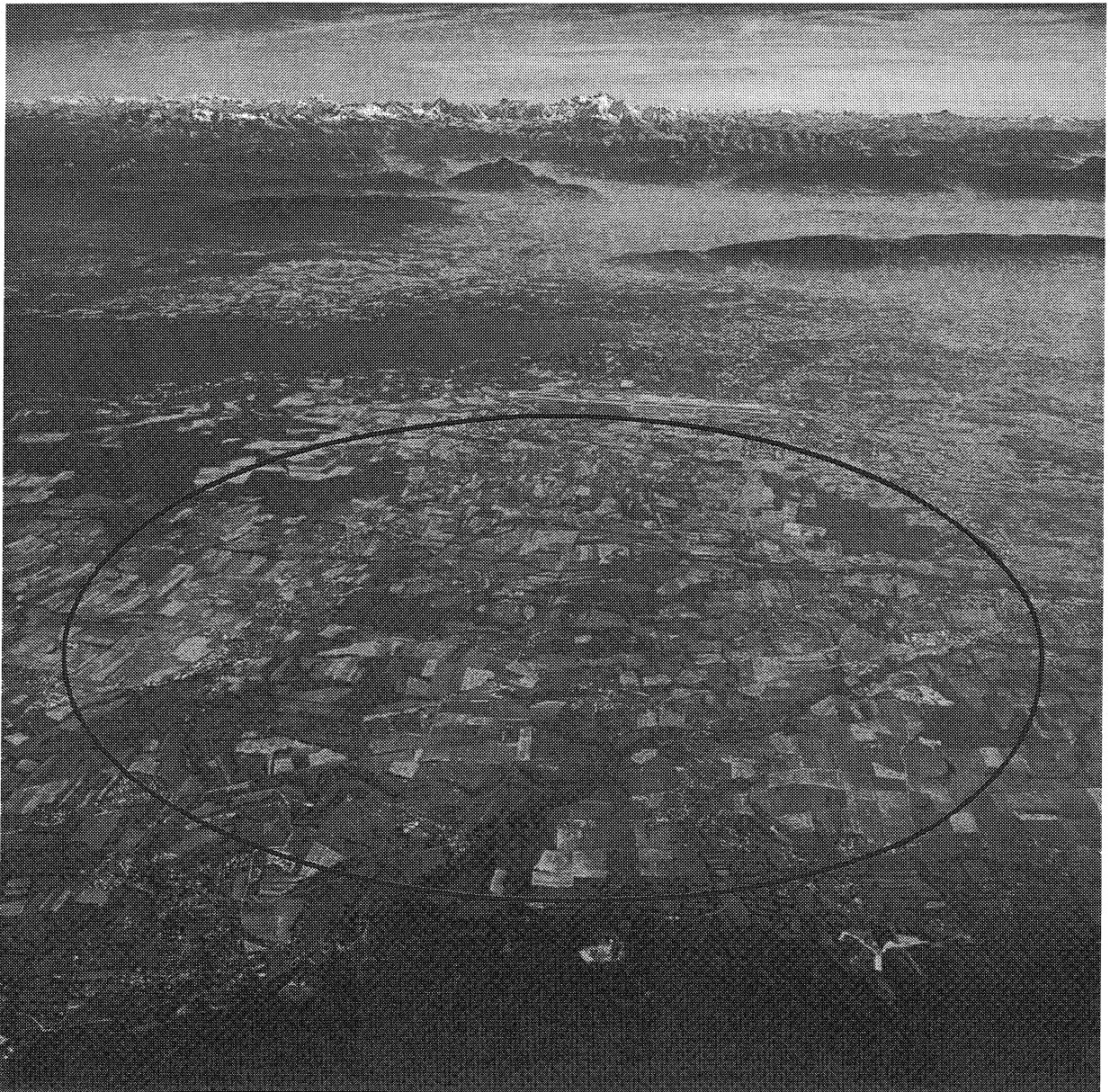


Figure 1.1 Location of the 27-km long accelerator ring at CERN

1.1 The Key Questions of Physics Addressed by the LHC

All matter in the universe is composed of two categories of fundamental particles: quarks and leptons. The representatives of both groups are classified as fermions, i.e. they all have the spin $\frac{1}{2}$ and obey the Fermi-Dirac statistics as far as the occupation of the quantized energy levels is concerned. The theory of quarks and leptons and their interactions is called the Standard Model. Although for traditional and historical reasons it has an attribute of model imprinted in its name, actually it is a fully mathematical formulation of the consistent quantum field theory. Despite the fact that some aspects of the theory are still conceptually incomplete the Standard Model does not really bear any traits of the model in the usual sense of the word.

A special class of the gauge theories describes the interactions between the particles within the framework of the quantum field theory. The fundamental pillar of any gauge theory is an existence of an invariance principle, which defines the gauge symmetry in the system of particles and imposes the presence of the interactions between them. In the quantum world the energy of any interaction is carried in form of the discrete packages called quanta, which correspond to the messenger particles transmitting the forces between the constituents of matter. Thus an interaction process among two elementary particles takes place with an exchange of another particles between them. The messenger particles responsible for the interactions between the quarks and leptons are called gauge bosons. They all have integral spin and obey the Bose-Einstein statistics as far as the occupation of the quantized energy levels is concerned. There are four fundamental forces conveyed between the particles by the gauge bosons. These are:

- gravity,
- electromagnetism,
- weak force and
- strong force.

In 1864 Maxwell showed that the electricity and magnetism have the same origin and therefore can be united into electromagnetism. One century later in 1965 Feynman, Schwinger and Tomonaga shared the Nobel Prize in Physics for the development of the quantum theory of electromagnetism called Quantum Electrodynamics (QED). QED was already a predecessor of the Standard Model. Photon is a gauge boson responsible for transmitting electromagnetic interactions.

Before the year 1970 the consistent theories of the weak and strong interactions have not existed yet. Short-ranged weak force plays an essential role in the formation of the heavy elements. It is also responsible for the generation of the energy in the sun. The interaction is called weak because its strength is minor in comparison to the electromagnetic interactions. If the relative magnitude of both forces is estimated using their effective potentials it can be demonstrated that the electromagnetic force is approximately 10^4 times stronger than the weak force. Also the typical time scales of the interactions are much longer for the weak interactions as compared to the appropriately defined time scales of the electromagnetic processes. In 1970 the theory that proposed unification of the electromagnetic and weak forces under the common dome of electroweak interactions was shown to be mathematically consistent. In 1973 the first experimental evidence for this unification saw the light of day. Finally in 1979 Weinberg, Salam and Glashow were awarded a Nobel Prize in Physics for their contribution to the development of the electroweak theory. Apart from the photon, the messenger particles of the electroweak interactions are the W^+ , W^- , and Z^0 gauge bosons. A decay of a free neutron into a proton, an electron and an electron anti-neutrino via a W^- boson acting as the mediator is an excellent example of a weak interaction (Fig. 1.2)

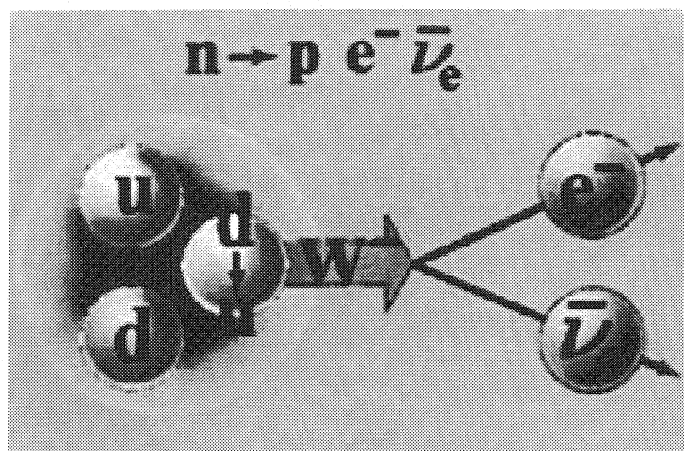


Figure 1.2 Decay of a free neutron composed of quarks (ddu) into a proton composed of quarks (uud), an electron and an electron antineutrino via the W^- gauge boson mediating the weak interaction.

The nucleus containing multiple protons carrying the same positive electric charge remains stable despite the repulsive interaction between them, therefore there must exist another attractive force stronger than the electromagnetic interaction that prevents the nucleus from falling apart. This presentiment for existence of the short-ranged strong nuclear force holding the constituents of the nucleus of an atom together accompanied

scientists since Rutherford found the first evidence for a proton in 1919. Nevertheless the quantum theory of the strong interactions called Quantum Chromodynamics (QCD) was formulated only in 1973. The gauge bosons of the strong force are eight gluons believed to be massless. They convey strong interactions between the quarks. The strong force is somewhat unusual in comparison to the other forces. It is weaker when the quarks are close together and it becomes stronger as soon as we would like to enforce their separation from each other.

There are six different kinds of quarks called quark flavors, which are grouped into three families of doublets. For historical reasons the quarks are named: up, down, charm, strange, top and bottom (see Table 1.1). There are also three doublets of leptons formed by electron, muon and tau particles and their corresponding neutrinos. For example the electron doublet is formed by the electron and its neutrino, etc. (see Table 1.2). Each of the particles in both groups has also its corresponding anti-particle with opposite charge (and all other quantum numbers). On the contrary to leptons, quarks carry the color charge defined by QCD. Each of the quark flavors comes thus in three colors referred to as: red, green, and blue. By analogy to electrically charged electrons and nuclei, which combine together to create electrically neutral atoms, the color charged quarks combine together to create colorless or color neutral hadrons. Proton composed of two up quarks and one down quark (uud), and neutron composed of two down quarks and one up quark (ddu) are representatives of baryons - the class of hadrons composed of three quarks (qqq). By analogy to residual electric field present around neutral atoms, which forces them to form molecules, the residual color force field outside the protons and neutrons generates the attractive nuclear force responsible for forming the nuclei (Fig. 1.3).

The members of the second class of hadrons called mesons are composed of one quark and one anti-quark ($q\bar{q}$), e.g. a pion π^- is composed of quarks anti-up and down ($\bar{u}d$).

Table 1.1 Quark doublets

Quark Flavor	Free Quark Mass [GeV/c ²]	Electric Charge [proton units]
u up	0.005	2/3
d down	0.01	-1/3
c charm	1.5	2/3
s strange	0.2	-1/3
t top	180	2/3
b bottom	4.7	-1/3

Table 1.2 Lepton doublets

Lepton Flavor	Lepton Mass [MeV/c ²]	Electric Charge [proton units]
e^- electron	0.511	-1
ν_e electron neutrino	$< 7 \cdot 10^{-6}$	0
μ^- muon	106	-1
ν_μ muon neutrino	< 0.3	0
τ^- tau	1777.1	-1
ν_τ tau neutrino	< 30	0

The entire universe known to us is built up only of the quarks up and down, electrons, electron neutrinos and the gauge bosons. All of the remaining particles are present either in the cosmic rays, or are generated artificially in the particle accelerators, but even then they are very-short lived, they decay almost instantaneously and the role they play in the universe is not known.

The combinations of quarks, which are not color neutral, must be bound within a specific hadron. This implies that free quarks do not exist, however their existence within the structure of the hadron can be probed for. If the probing particles have the wavelengths of the

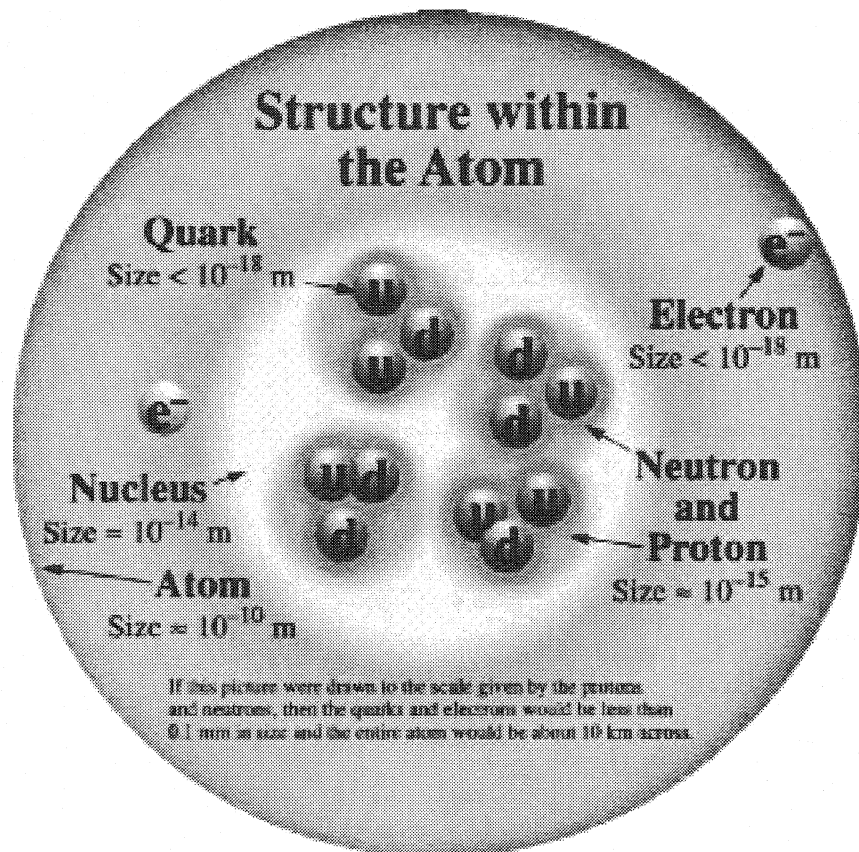


Figure 1.3 Subatomic structure of matter

order of the size of the proton the entire mass of the proton will be sensed in the course of the experiment. This mass corresponds to $938 \text{ MeV}/c^2$. On the other hand if the probing particles are accelerated to very high energies corresponding to the wavelengths much smaller than proton size they may penetrate into the subhadronic structure of the proton and scatter from its single constituents, i.e. form the quarks or gluons. By analyzing different scattering patterns the number of quarks inside the proton can be established. In this case the separate constituents of the proton are hit by the sensing particle in such a violent and powerful manner that the quarks do not have the time to recoil and sense the full magnitude of the

strong force acting between them. Therefore the probed mass corresponds to the state of the quark as if it were a free particle. Looking at the Table 1.1 it is easy to verify that the sum of the free quark masses does not add up to the total rest mass of the proton. It is due to the fact that most of the hadronic mass comes from the energy confinement resulting from the bound state of the quarks forming the proton. In this regard the constituent mass of the quarks up and down locked up in the hadron corresponds to approx. $330 \text{ MeV}/c^2$ for each of them. It cannot be calculated very precisely because the nonperturbative bound state does not allow the application of the perturbation theory.

1.1.1 The Problem of the Origin of Mass in the Universe

The masses of quarks and leptons are not very well understood. The Standard Model explains neither their relative values nor the apparent lack of regularity among them. The masses of neutrinos are not known at all. Most of the theorists agree that they are different from zero nevertheless at the current stage only the upper limits for the expected values can be set. From the astronomical observations and calculations of the rotation momentum of the galaxies it turns out that the galaxies are much heavier than what could be deduced from their visible matter constituents. Approximately nine tenth of the mass of the universe is invisible due to this effect. Could the mystery of dark matter be explained by large amounts of massive neutrinos? At this point we approach even more if not the most challenging problem of the modern physics. Despite the impressive level of complexity and refinement that physics has reached in the recent century, still it does not even explain the origin of the visible mass in the universe. We simply do not know why the matter has developed mass and we do not understand where this mass actually comes from.

The original prediction of the Standard Model clearly states that all of the gauge bosons are massless. In 1983 the Nobel Prize winning experiments UA1 and UA2 directed by Carlo Rubbia, demonstrated at CERN the direct experimental evidence for the existence of the heavy bosons of the weak interactions: Z^0 with the mass of $91 \text{ GeV}/c^2$ and W^+ , W^- with the masses of $80 \text{ GeV}/c^2$ each. The problem of mass can be technically explained within the framework of the Higgs mechanism proposed by the Scottish physicist Peter Higgs. The mechanism assumes that the vacuum state of the universe is not at all empty. Even in the ideal vacuum continuous processes of energy creation and annihilation take place constantly giving birth and causing death of transient particles. These processes contribute to the formation of a spin zero scalar Higgs field filling the entire space. The fermions and gauge

bosons can interact with this field. In this case the universal gauge symmetry present in the system is not valid for its vacuum state. Due to the interaction with the Higgs field and the spontaneous symmetry breaking of this ground state the initially massless gauge bosons of the weak interactions absorb the energy from the Higgs field, develop mass and become heavy. In a similar way the masses of fermions can be explained. The existence of another heavy particle – the zero spin scalar Higgs boson is required for the Higgs mechanism to be consistent and mathematically sound. The mass of this missing particle has been predicted within the energy range of 1 TeV. Although the solution of the problem seems satisfactory it is a little bit forced, i.e. it does not come out as the natural consequence of the Standard Model, and in this regard the question of mass is still rather poorly understood. What is the source of the Higgs field and how the Higgs boson functions remains still a mystery. The search for the Higgs particle will be the main and most important quest of the LHC aiming to shed some light on the mechanism of the mass development in the universe. Two major LHC detectors called ATLAS and CMS will be thoroughly searching for the manifestations of the Higgs boson in the expected energy range.

1.1.2 In Search for the Theory of Everything

The unprecedented success of the unification of electromagnetic and weak forces, which can be easily classified as one of the most important achievements of humanity, generated a lot of enthusiasm and instantaneously propelled the scientists towards the integration of the strong and electroweak interactions into a common Grand Unified Theory (GUT). Unfortunately the task had proven not to be trivial and since 1973 the QCD remains stubbornly separated from the electroweak theory. Both concepts coexist side by side within the common framework of the Standard Model yet there is no direct link between them. In order to successfully achieve the grand unification some of the GUTs require the transitions between the fermions and leptons to be possible at the time point close to the origin of the universe, when all of the forces should have presumably emerged from the common unity. The idea of the interchange between the leptons and quarks within the framework of Super Symmetry (SUSY) brings in the existence of the yet unseen supersymmetric particles capable of undergoing such transitions at the early stage of the unfolding universe. The transformation of leptons into fermions and vice versa implies also the decay of the most stable hadron of this universe – the proton. The lifetime of the proton is estimated to be of the order of 10^{32} years. Although

several experiments are running throughout the world aiming to find evidence of this phenomenon, the decay of the proton into leptons has not been observed yet.

The decay of any particle is a random statistical process, therefore if large amounts of particles are brought together the probability of observing a proton dying in the burst of photons is slightly increased. The LHC with its unprecedented luminosity of 10^{34} of proton collisions per second and per squared centimeter will provide an excellent opportunity for attempting such an observation.

Apart from the protons, the LHC has been designed also to collide counter-circulating heavy ion beams, e.g. lead. This kind of collisions provide extremely high center-of-mass energy available for the production of new particles, and aim to analyze the high energy nucleus-nucleus interactions as well as to find the signatures of the quark-gluon plasma state of matter characteristic for the very first instants of the newborn universe. In the quark-gluon plasma state of matter the energy of the system is so high that the quarks and gluons exist as free non-constituent entities due to the fact that the strong force does not emerge yet as the separate interaction binding them together into hadrons. Thus the LHC heavy ion experiments with their dedicated heavy ion detector called ALICE will provide an excellent ground for the investigation of the proton decay, possible existence of the supersymmetric particles and signatures of the quark-gluon plasma. Some other GUT formulations require also the existence of the magnetic monopoles predicted by the Dirac's equation. The search for the magnetic monopole will also become an additional quests of the LHC.

The uttermost dream of any particle physicist on this planet would be of course to incorporate also the gravity into the integral picture of nature and thus to unify the entire theoretical physics in the grand Theory of Everything (TOE). Unfortunately the relativistic theory of gravity seems to strongly dislike quantum mechanics. In this matter the theory gives an impression to follow exactly the spirit and the attitude of her author, Albert Einstein, who used to openly express his utmost aversion towards the quantum mechanical concepts of physics. As a result the numerous attempts of theoretical fusion between quantum mechanics and relativistic theory of gravity have ended up in enormous renormalization problems breaking up the calculations with the divergent observables stubbornly tending to infinity against all sense and reason.

In 1984 the conceptually beautiful although extremely complex Superstring Theory successfully realized the marriage between the reluctant couple of quantum mechanics and relativistic gravity. At the same time the concept of SUSY seemed to be automatically incorporated into the theory. On the other hand the heretical anomalies causing an imminent

break-down of the most sacred conservation laws of physics in previous unification attempts, this time vanished in the natural way. All of this happened at the price of formulating the theory within the framework of abstract 11-dimensional space consisting of 4 traditional space-time dimensions and 7 additional ones rolled up and folded at the scale level of 10^{-35} m and thus inaccessible from our traditional 4-dimensional world. All of this theoretical approach is still at the early stage of its development and waits for a good experimental evidence. The graviton – a presumable transmitter of the gravitational interaction has not been observed yet.

The consequences of a fully consistent TOE could have an enormous impact on our understanding of the universe. The theory could bring for example an answer if the set of what we refer to in our world, as physical constants can be different in different parts of the universe. Could it be that somewhere else in the vast stretches of the universe, under certain conditions the speed of light is expressed by a value different from the one we know?

1.1.3 Missing Antimatter Mystery

According to the GUT equations there should be a balance between matter and antimatter in the universe. Apparently it is not the case, because both the world around us as well as the vast universe seem to be composed of matter rather than of antimatter. In 1960 Sakharov showed theoretically that at the origin of the universe equal amounts of matter and antimatter were produced, however the quark asymmetry defined a unique arrow of the time flow and made the particles of antimatter more unstable than the particles of matter. Nowadays this effect can be observed uniquely via a very sophisticated and subtle process of the spontaneous symmetry breaking with respect to the charge conjugation and space inversion (CP violation resulting in breaking of the charge-parity invariance) in the systems of mesons called neutral kaons. Although right now the effect is very small it played an essential role in shaping of the early universe and the fourth LHC detector called LHC-B will be built especially for the investigation of the CP violation and the study of rare decays of mesons *B*.

1.2 Parameters and Performance of the LHC

1.2.1 Principles of the Synchronous Acceleration

The particles accelerated to very high energies move in the accelerator ring almost with the speed of light and the relativistic effects of their motion must be taken into account. The equation of motion for a relativistic proton of rest mass m_0 and charge q in a magnetic field B is

$$\frac{d\vec{p}}{dt} = q(\vec{v} \times \vec{B}) \quad (1.1)$$

where

$$\vec{p} = \frac{m_0 \vec{v}}{\sqrt{1 - \left(\frac{v}{c}\right)^2}} \quad (1.2)$$

is the relativistic momentum of the particle moving with velocity v close to the velocity of light denoted as c . The differentiation of momentum (1.2) with respect to time yields:

$$\frac{d\vec{p}}{dt} = \frac{m_0 \frac{d\vec{v}}{dt}}{\sqrt{1 - \left(\frac{v}{c}\right)^2}} + m_0 \vec{v} \cdot \frac{\frac{\vec{v}}{c^2} \frac{d\vec{v}}{dt}}{\sqrt{\left(1 - \left(\frac{v}{c}\right)^2\right)^3}} \quad (1.3)$$

Thus in the general case the force acting on the particle can have the component parallel not only to acceleration but also to the velocity vector. In the case of the proton deflected in the magnetic field perpendicular to the velocity vector the force and the velocity of the particle are orthogonal, i.e. the force acting on the particle is parallel to the centripetal acceleration pointing towards the center of the accelerator ring. Due to this only the first term is present in the formula (1.3) and the equation of motion (1.1) becomes:

$$m_0 \gamma \frac{d\vec{v}}{dt} = m_0 \gamma \vec{v} \times \vec{\omega} = q(\vec{v} \times \vec{B}) \quad (1.4)$$

where ω is the angular frequency of the circular motion and γ is defined for notational convenience as:

$$\gamma = \frac{1}{\sqrt{1 - \left(\frac{v}{c}\right)^2}} \quad (1.5)$$

Taking the orthogonality relations between the vectors in Eq. (1.4) corresponding to the situation of our high energy proton moving in the beam pipe of the accelerator ring the equation of motion is simplified to:

$$m_0 \gamma \omega = q v B \quad (1.6)$$

Hence the resonance relation follows:

$$\omega = \frac{qB}{m_0 \gamma} \quad (1.7)$$

Formula (1.7) expressed in terms of frequency at which the proton circulates in the accelerator ring is:

$$f = \frac{\omega}{2\pi} = \frac{qB}{2\pi m_0 \sqrt{1 - \left(\frac{v}{c}\right)^2}} \quad (1.8)$$

During the acceleration cycle the proton moving along the beam pipe of the accelerator absorbs energy while passing through the radio frequency (RF) section of the accelerator facility. The RF sections consist of cavities mounted around the beam pipe and resonating at a frequency corresponding to a multiple of the beam circulation frequency expressed by formula (1.8). The electrically charged beam of protons must traverse the RF section exactly when the electric field in the cavities has the right direction and phase for the acceleration of the particles. As during the acceleration process the velocity of the accelerated particles tends to the velocity of light, the relation (1.8) can be satisfied only if either the alternating frequency of the RF sections is decreased, or the intensity of the magnetic field is increased, or both actions occur simultaneously. In machines called synchrocyclotrons the magnetic field is held constant whereas only the frequency changes. The accelerators like LEP or LHC in which the magnetic field is changed irrespective of what happens to the frequency are called synchrotrons. In electron synchrotrons the frequency of the RF sections is kept constant whereas in proton synchrotrons both frequency and the intensity of the magnetic deflector field are changed during the acceleration of the particle beams.

The particles accelerated close to the speed of light traverse the entire 27-km long circumference of the accelerator ring at CERN 11240 times per second. The beam has a bunched structure, i.e. the particles are grouped in bunches.

The superconducting RF cavities of the LHC will generate the maximum voltage of 16 MV at the frequency of 400 MHz. This corresponds to the RF period of 2.5 ns. However it was decided that the bunch of protons would arrive at the RF cavity only once within the

10 consecutive RF periods giving thus the separation of 25 ns or 7.5 m between two consecutive bunches. Each of both counter-circulating proton beams will contain 2835 bunches. The population of each bunch will amount to 10^{11} particles grouped on the average length of 75 mm (root mean squared value).

The angular frequency of circular motion expressed by (1.7) is related to the proton velocity by the formula

$$\omega = \frac{v}{R} \quad (1.8)$$

where R is the radius of the orbit imposed by the accelerator ring. Taking (1.7) and (1.8) into account it follows that:

$$R = \frac{m_0 \gamma v}{qB} = \frac{m_0 v}{qB \sqrt{1 - \left(\frac{v}{c}\right)^2}} = \frac{p}{qB} \quad (1.9)$$

From (1.9) it turns out again that in order to keep the accelerated protons on the same orbit the intensity of the magnetic field must increase as the protons gain higher energy. Eq. (1.9) represented in mixed units of accelerator physics becomes

$$R = \frac{p}{0.3B} \quad (1.10)$$

where R is given in meters B in Tesla and p in GeV/c. The radius of the curvature R substituted into formula (1.10) does not correspond to the curvature of the 26.8 km-long accelerator tunnel because the bending dipole magnets do not cover completely the entire length of the tunnel. It is a consequence of the arrangement of the lattice of magnets defined by the layout of the accelerator.

1.2.2 Layout of the LHC Accelerator Facility

A layout of the LHC is based on the 8-fold symmetry presented schematically in Fig. 1.4. The accelerator ring consists of 8 arc sections interlaced by 8 long straight sections. The arc section in each octant contains twenty three 106.9-m long arc cells, which can be further decomposed into two identical 53.45-m long half cells. Each half cell contains three 14.3-m long bending dipole magnets (MB) and a short straight section comprising 3.1-m long lattice quadrupole (MQ), combined dipole and sextupole correctors (MSCB), a beam position monitor (BPM) and a place for another short corrector magnet whose type depends on the

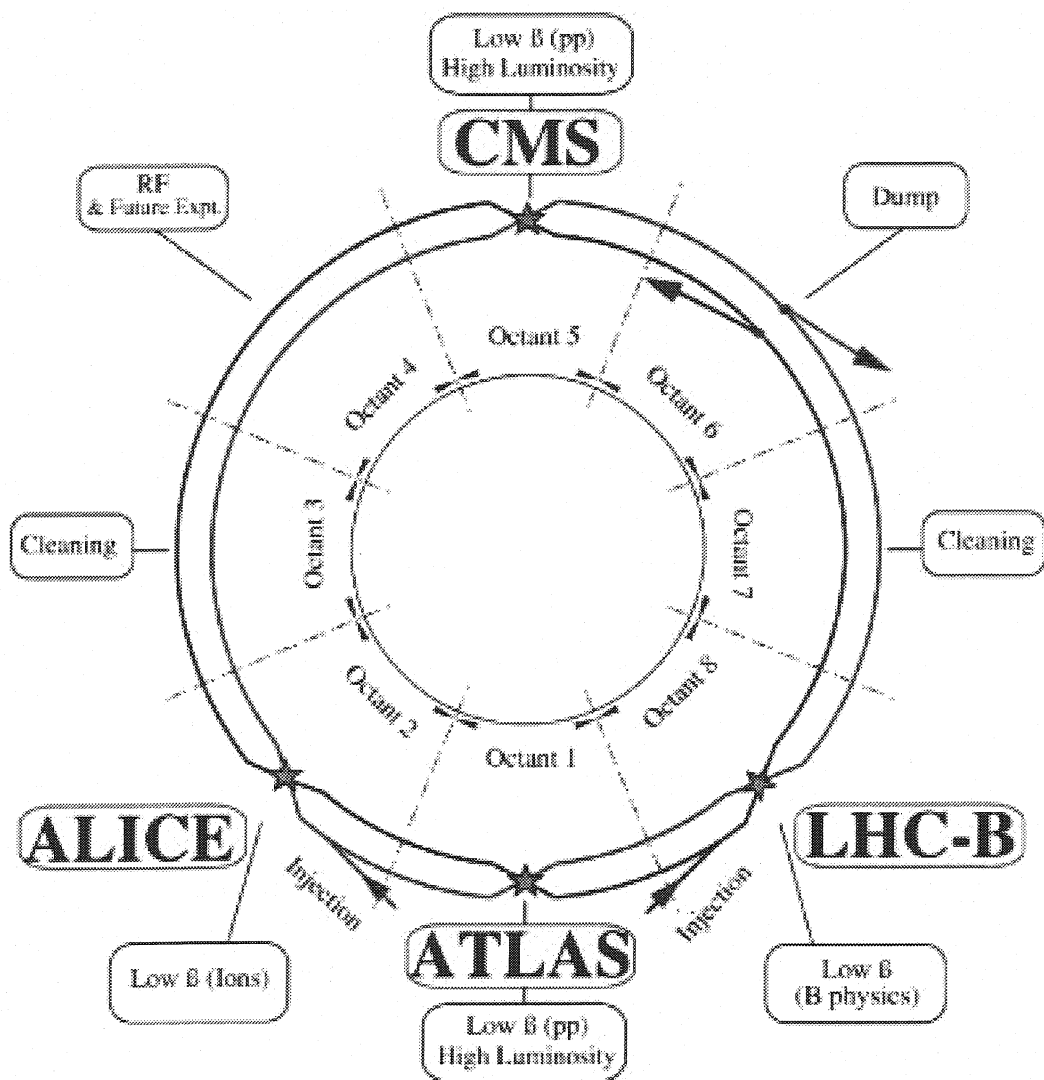
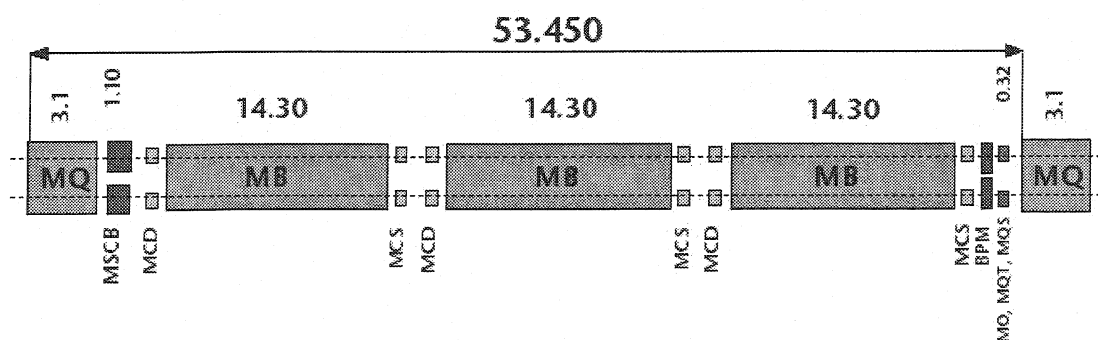


Figure 1.4 Schematic layout of the Large Hadron Collider



MQ : Lattice Quadrupoles
 MB : Dipole magnet
 MSCB : Combined Sextupole and Dipole correcteur

MO : Landau Octupole
 MQT : Tuning Quadrupole
 MQS : Skew Quadrupole

MCS : Local Sextupole corrector
 MCD : Local Decapole corrector
 BPM : Beam position monitor

Figure 1.5 Schematic layout of an arc half-cell

position of the half-cell in the lattice of the accelerator (Fig. 1.5). Each long straight section has the length of approx. 500 m available for the experiments and special utilities. Dipole magnets guide the beam in the arc sections of the collider by deflecting the trajectory of the accelerated particles towards the center of the arc curvature. Due to the intentional and inevitable presence of the straight sections in the accelerator lattice the bending power of the dipole magnets must be higher than what could be deduced from the formula (1.10) for the curvature radius of 4265 m corresponding to the 26.8 km long circumference of the LHC tunnel. The described layout of the accelerator allows to host 1232 bending dipole magnets. Each of them represents the magnetic length of 14.3 m which results in the total length of 17617.6 m. Thus with each completed turn of the accelerator ring the proton beam is not deflected by the dipole magnets on the length of almost 10 km. The total full magnetic length of the dipole magnets corresponds to the effective curvature radius of 2.8 km and such is the bending radius of the arc sections in each octant of the LHC. The dipole magnets in the arc sections are not straight but must follow this radius of curvature. As a result the deviation of the dipole magnet from the straight line in the middle of its length amounts to 9 mm. Substituting the radius $R = 2800$ m into the formula (1.10) along with the maximal $p = 7000$ GeV/ c momentum of the proton beam results in the magnetic field of 8.33 T. Such high intensity of the magnetic field can be realized at acceptable costs of production only with superconducting magnets cooled down to the temperature of superfluid helium. This presents the most challenging problems as far as the designs of the magnets and the cryogenic system are concerned.

The magnetic focusing of the beam is provided by a different (already mentioned) type of magnets – the quadrupoles. The focusing effect is illustrated in Fig. 1.6 for the cross-section of the main LHC quadrupole. The pattern of the magnetic field is represented there in form of the vector matrix. In the center of the magnet aperture the strength of the magnetic field is zero but it rises linearly with the increasing distance from the center. The quadrupole vector field symmetry imposes that the field is purely vertical in the median plane of the magnet (the plane defined by the horizontal symmetry axis) and purely horizontal in the vertical symmetry plane of the magnet. The protons (moving in the direction into the surface of the paper in Fig. (1.6)) which are defocused in the horizontal plane will be deflected towards the center of the magnet aperture. For the protons initially defocused in the vertical plane the effect is opposite. They will be deflected even more away from the center of the magnet. Thus the second kind of quadrupole magnet is necessary for focusing the protons in the vertical plane and defocusing the ones in the horizontal plane. This effect is obtained by

rotating the magnet in Fig. (1.6) by 90 degrees. Each cell in the arc section of the LHC contains one focusing and one defocusing quadrupole magnet. This configuration of alternating polarity quadrupoles called a FODO pattern has a net focusing effect on the beam in both horizontal and vertical planes. As a result of this alternating gradient magneto-optical system the path of particles within the FODO lattice describes an oscillatory trajectory contained within the envelope defined by the betatron function characterizing the peak deviation of the beam from the center of the beam pipe. For the LHC this deviation amounts to 10 mm.

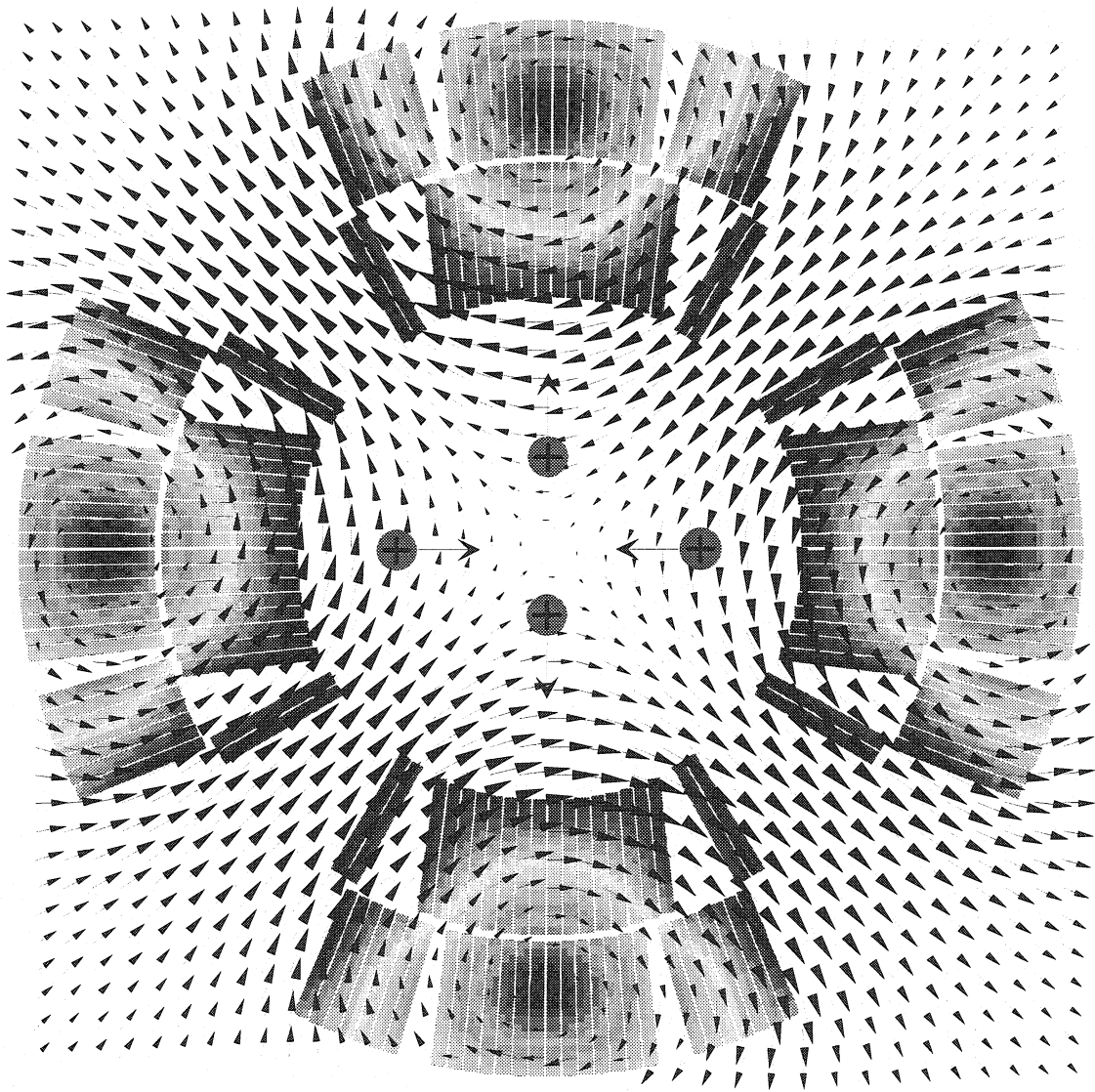


Figure 1.6 Magnetic focusing effects imposed on the proton beam by the quadrupole magnet

The detectors of the corresponding physics experiments are located in the long straight sections of the octants No. 1, 2, 5 and 8 (see Fig. 1.4). At these four locations the protons cross from one beam pipe to the other in order to enable the collisions between the counter-circulating beams. Two 450 GeV/c proton beams are injected into LHC via the

injector systems in octants No. 2 and 8. The crossing of the particle beams does not take place in the remaining four long straight sections apart from the ones occupied by the physics experiments. The long straight sections in octants No. 3 and 7 are used for the collimation of the beam. The RF sections independent for the two beams are located in the octant No. 4. Octant No. 6 contains the beam extraction systems used to dump the beams from the accelerator ring before the new injection.

1.2.3 Multi-Staged Acceleration of the Proton Beam

The injection of the proton beams into the LHC ring is preceded by a multi-staged acceleration scheme. The entire CERN accelerator complex is shown in Fig. 1.7. The LHC will take advantage of the existing particle sources and accelerators. In the first stage the protons will be accelerated in the linear accelerator (LINAC) to the energy of 50 MeV. Next, in the low energy Proton Synchrotron Booster (PSB) they will gain the energy of 1.4 GeV. Subsequent Proton Synchrotron (PS) will act as the medium energy booster accelerating the protons to the energy of 26 GeV. The correct structure of the beam will be already formed at this stage by the 40 MHz RF system.

Any unstructured beam of particles is automatically divided into bunches by adiabatic capture resulting from the phase stability principle. Some finite spread always exists in the time of arrival of individual protons into the region of the RF section. A synchronous proton

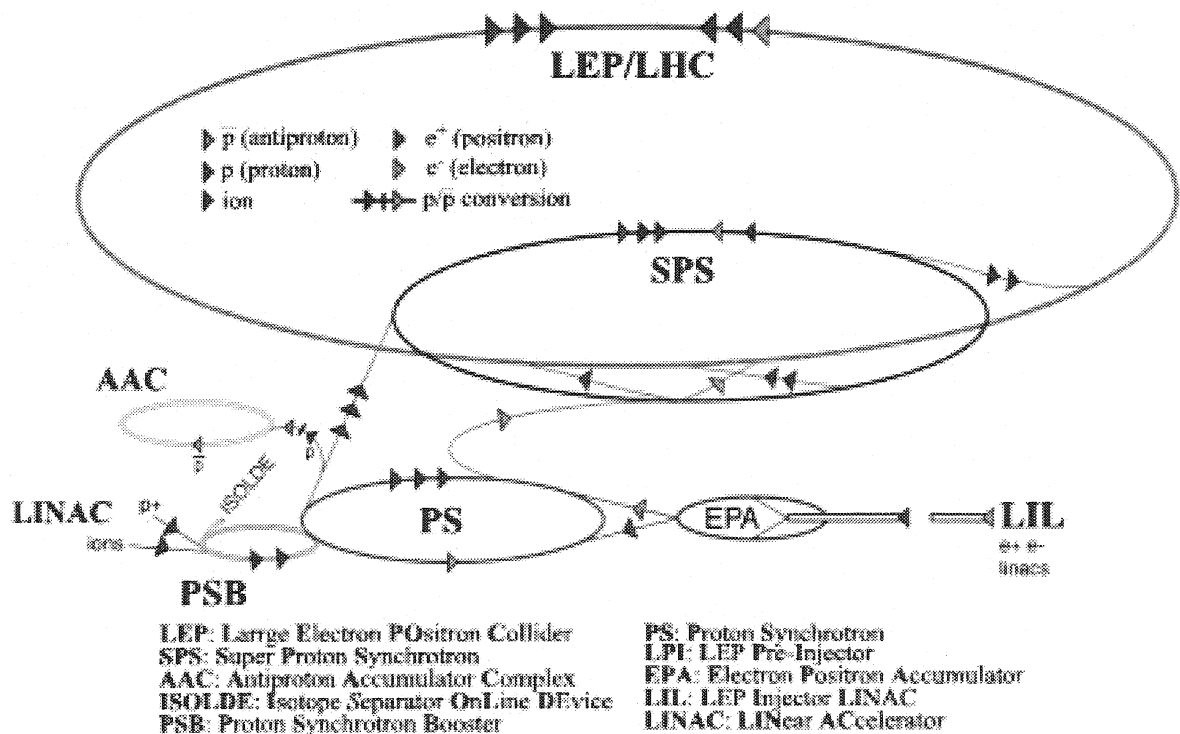


Figure 1.7 CERN accelerator complex – current and future projects

arrives at a certain time t_0 of the accelerating RF cycle and it experiences a corresponding accelerating electric field E_0 . Let us assume that at the moment of its arrival the voltage wave in the RF cavity is falling. A proton that arrives at the RF cavity earlier will experience then a larger electric field. As a result a larger force accelerating this proton will increase the radius of its orbit during the next turn in the accelerator ring. For the particles moving close to the velocity of light acceleration increases momentum but not velocity. Thus the longer path length enforced by the increased radius of the orbit will cancel out the small effect of the velocity increase and the next reentry of this proton into the RF cavity will be shifted to a later time, i.e. towards the arrival time of the synchronous proton. By analogy the proton which reaches the perimeter of the RF section later than the synchronous particle will experience lower strength of the electric field, and due to the smaller acceleration the radius of its orbit will be decreased. Thus its arrival at the next acceleration cycle will take place earlier and again it will be shifted towards the arrival time of the synchronous particle. The protons that arrive at the RF cavity at random times with respect to t_0 will experience varying accelerations or decelerations. As a consequence of the self-correcting principle of the phase stability the particles will be finally grouped into bunches with the arrival times centered on the synchronous proton in each bunch and the bunch spacing imposed by the resonance frequency of the RF cavity. Thus the 40 Mhz RF system of the PS accelerator will enforce the envisaged 25 ns spacing between the consecutive bunches.

The trains of structured bunches will be transferred from PS booster to the SPS accelerator acting as the medium energy booster for the LHC. The beam will be then accelerated in the SPS ring and injected into the LHC at the energy of 450 GeV. The dipole field generated by the magnet system of the LHC at injection will correspond to 0.54 T. The acceleration of two counter-circulating proton beams from this energy to the energy of 7 TeV will take about 22 min. At the end of acceleration the superconducting dipole magnets will be operating at the nominal field of 8.33 T. At this point the counter-circulating beams will be available for creating 14 TeV center-of-mass collisions.

1.2.4 Machine Performance Issues

The total energy of the proton is always shared between all of its constituents. Moreover, due to the subtle quantum effects the energy of constituents decreases slowly with the increasing collision energy and at the energy of 7 TeV it is virtually impossible or rather improbable that the particular quarks or gluons building up the proton carry more than 10 % of its total

energy. Due to this fact the protons need to be accelerated to the energy of 7 TeV in order for the physics experiments to explore the energy range of 1 TeV as far as the interactions between the quarks are concerned. On the contrary to protons the beams of electrons and positrons accelerated to the energy of 1 TeV would produce the collisions with the center-of-mass energy corresponding exactly to 2 TeV. Unfortunately any electrically charged particle forced to move along the circular trajectory produces synchrotron radiation – with every turn completed in the circular accelerator it loses energy by emission of photons according to the formula [2]:

$$\frac{\Delta E}{2\pi R} = \frac{1}{3\epsilon_0} \frac{e^2 E^4}{(m_0 c^2)^4 R} \quad (1.11)$$

where R is the curvature of the trajectory and E is the energy of the beam and ϵ_0 is the dielectric constant. In case of LEP with each turn the RF cavities must pump the energy of 220 MeV back to the beam of light electrons in order to keep them at the constant energy of 50 GeV. For the same beam at the doubled energy of 100 GeV the synchrotron radiation losses are 16 times higher and amount already to 3.5 GeV per turn. For the 500 GeV electron beam accelerated in a hypothetical 250-km long accelerator ring with radically increased radius of curvature the losses would amount to 220 GeV per turn. One can easily draw the conclusion that LEP is most probably the last circular electron-positron collider in the world. Since the energy loss in formula (1.11) is inversely proportional to the rest mass of the accelerated particle the synchrotron radiation is approx. 10^{13} times smaller for the protons, which are 1836 times heavier than electrons. Thus the gain in the synchrotron radiation definitely wins over the drawback of the energy repartition among the constituents in favor of the hadron colliders. Nevertheless, apart from the high energy of the beam the high rate of the collisions defined by the luminosity of the collider remains a determinant factor of the successful particle physics experiments. The luminosity L is defined as

$$L = \frac{N^2 f n}{4\pi\sigma_x\sigma_y} \quad (1.12)$$

where N is the population of a single bunch of particles, n is the total number of bunches, f is the frequency of particle revolutions in the accelerator ring, and the parameters $\sigma_{x,y}$ express the horizontal and the vertical size of the beam at the point of collision. The number of events of the particular kind taking place in time T is then

$$N_e = \sigma LT \quad (1.13)$$

where σ is the cross-section for the particular type of event to occur.

With the round beam of 16 μm size at the collision point the LHC must provide the unprecedented luminosity of $10^{34} \text{ cm}^{-2} \text{ s}^{-2}$ in order to successfully explore the 1 TeV region for the manifestations of the Higgs boson. This value of luminosity exceeds the luminosity of operating worldwide contemporary accelerators by more than one order of magnitude. From the moment when the proton beams reach their nominal energy of 7 TeV this high luminosity must be maintained for 10 hours during which the physics experiments will take place. This again imposes high requirements on the quality of the magnetic field generated by the superconducting magnets responsible for the beam stability.

1.3 Superconducting Dipole Magnets for the LHC

The acceleration of counter-circulating beams of particles and their corresponding antiparticles gives a possibility of guiding both beams in the same vacuum tube; due to the opposite charge carried by both types of particles moving in opposite directions a unique direction of the magnetic field is sufficient to deflect both beams at the same time. This is the case of the LEP collider, which accelerates the counter-circulating beams of electrons and positrons. At the points where the particle bunches are not supposed to collide the electromagnetic separators shift their trajectories with respect to each other preventing thus the unwanted collisions outside the experimental areas.

Unfortunately this concept had to be abandoned for the LHC due to the difficulties with production and storage of the extremely large number of antiprotons necessary to achieve the required high luminosity value. As a consequence two separate magnetic channels with opposite magnetic field directions are needed for acceleration of the counter-circulating proton beams. In order to reduce the production costs of large amount of superconducting magnets both beam lines have been integrated into a common yoke. In this way both magnetic channels share the same reinforcement structure and the same cryogenic system. This design solution proves to be more economical in comparison to the alternative configuration comprising two separate magnet rings for the proton beams. A fully assembled two-in-one twin aperture dipole magnet for the LHC is illustrated in Fig. 1.8.

The only way this magnet can generate the magnetic field of the order of 8 T exists within the framework of the superconducting technology. In this regard the niobium-tin (Nb_3Sn) would be an excellent choice for the winding material of the superconducting coils. In the magnetic field of 8 T at the temperature of liquid helium (4.2 K) this superconducting compound allows to convey the current densities of about 2300 A/mm^2 without transition to

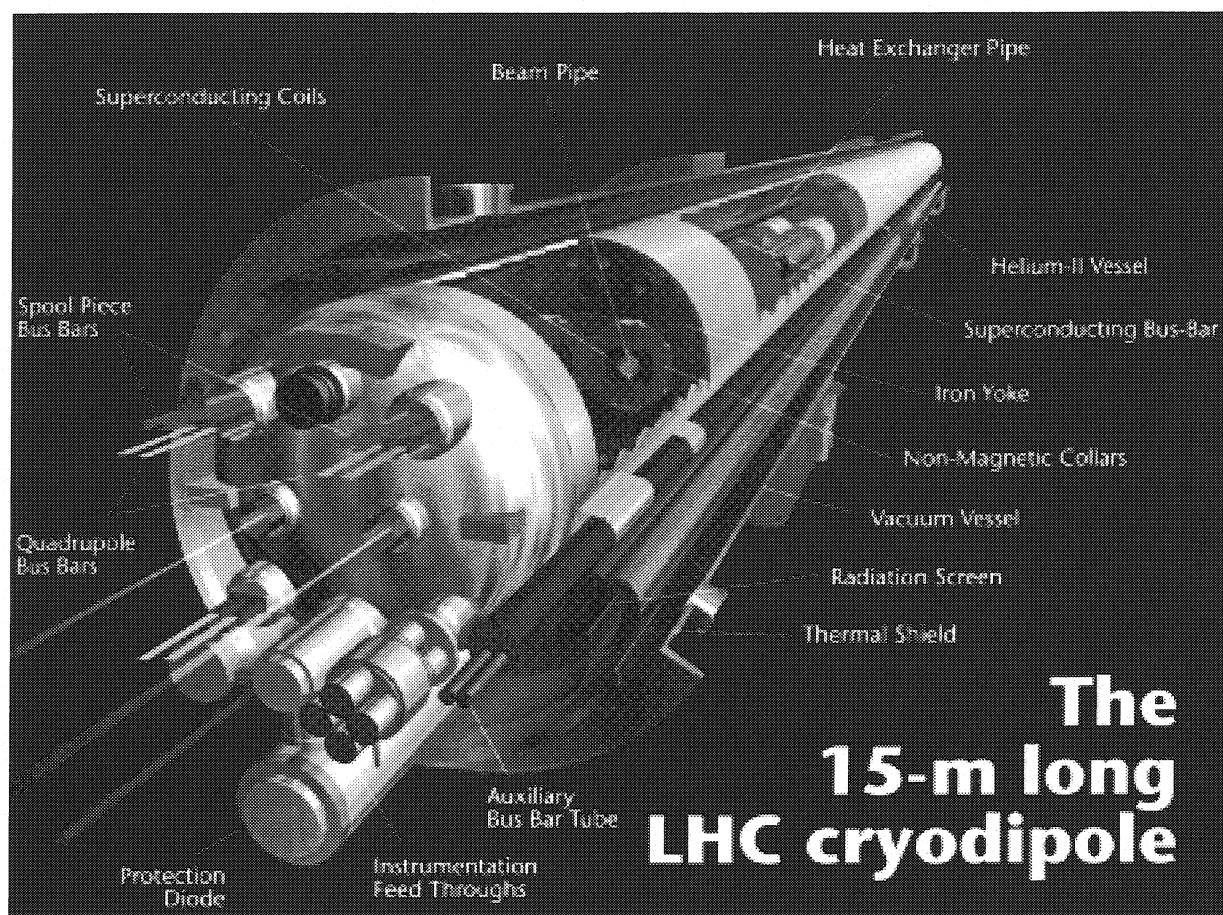


Figure 1.8 Fully assembled twin aperture dipole magnet for the LHC

the normal state. A superconducting dipole magnet built recently at the Lawrence Berkley Laboratory in United States with the Nb_3Sn wires generated the magnetic field of 13 T [3]. Unfortunately the material is brittle and very difficult to handle. As a consequence the coils of the magnet must be wound with the normal (nonsuperconducting) cable containing nonreacted niobium and tin. After winding the heat treatment of the coil at the temperature of 700°C triggers the chemical reaction and binds the niobium and tin into the Nb_3Sn superconducting type II compound. Both the material and the winding technology are too expensive for the series production of 1232 technologically challenging superconducting dipole magnets. Thus again the traditional Nb-Ti type II superconductor offers the only practical solution. However, all of the superconducting magnets built with the Nb-Ti cable operating at the temperature of liquid helium at the accelerator facilities around the world generate magnetic fields below 5 T. The only way of generating the magnetic fields higher than 8 T with this conductor requires to cool it below the lambda point of helium (2.17 K) to the temperature of about 1.9 K [4]. The critical surface of the Nb-Ti with the marked working point of the LHC is shown in Fig. 1.9. Above this surface the superconductor undergoes a

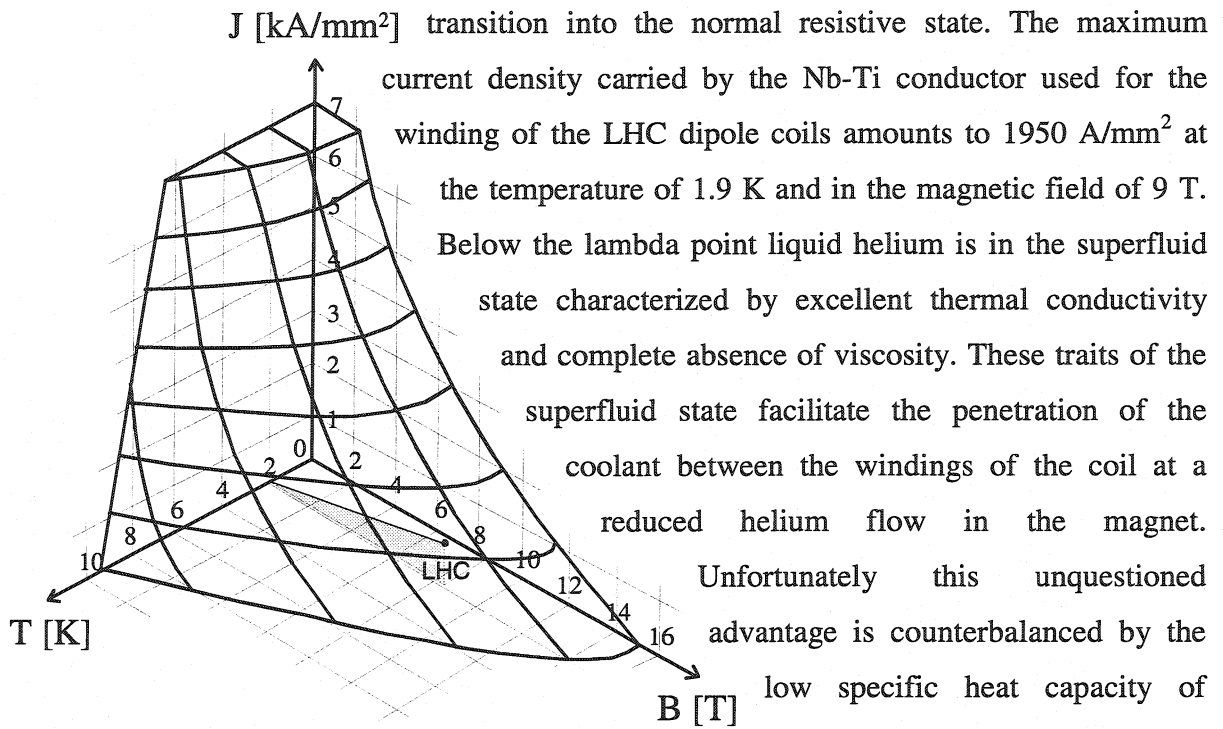


Figure 1.9 Critical surface of the Nb-Ti material with the working point of the LHC dipoles at the nominal magnetic field of 8.33 T and the temperature of 1.9 K

transition into the normal resistive state. The maximum current density carried by the Nb-Ti conductor used for the winding of the LHC dipole coils amounts to 1950 A/mm² at the temperature of 1.9 K and in the magnetic field of 9 T. Below the lambda point liquid helium is in the superfluid state characterized by excellent thermal conductivity and complete absence of viscosity. These traits of the superfluid state facilitate the penetration of the coolant between the windings of the coil at a reduced helium flow in the magnet. Unfortunately this unquestioned advantage is counterbalanced by the low specific heat capacity of metals at low temperatures. For normal metals it is given by the formula:

$$c_n(T) = \gamma T + \beta T^3 \quad (1.14)$$

The term linear in temperature expresses the electron contribution to the specific heat. The parameter γ denotes the Sommerfeld constant. The second term varying as the third power of the temperature describes within the Debye model the predominant phonon contribution to the specific heat of normal metals at the cryogenic temperatures close to absolute zero. The factor β denotes the proportionality constant. The specific heat of Nb-Ti in the normal state would be described by Eq. (1.14) but in the superconducting state it is given by

$$c_s(T, B) = \gamma T \frac{B}{B_{c2}} + \left(\beta + \frac{3\gamma}{T_c^2} \right) T^3 \quad (1.15)$$

where T_c is the critical temperature of Nb-Ti at zero magnetic field and B_{c2} is the second critical field at zero temperature [5]. As a net effect of Eq. (1.15) the specific heat capacity of Nb-Ti at the temperature of 1.9 K is approximately 10 times lower than at the temperature of 4.2 K. This implies both higher and faster temperature increase for a given deposit of energy. As a consequence, during the operation of the magnet the microscopic movement of the coil cable corresponding to the fractions of a millimeter may cause enough friction to locally overheat the superconductor above the critical temperature causing thus a local resistive transition. To a certain extent the magnet is metastable, which means that due to the

electromagnetic forces acting on the cable during the operation of the magnet. The distance between the two apertures is 194 mm. The aperture of each coil responsible for the generation of the dipole magnetic field in each of the vacuum beam pipe channels is 56 mm in diameter. A ferromagnetic yoke is clamped around the collared coil assembly by an external stainless steel shrinking cylinder. The yoke enhances the magnitude of the magnetic field induction inside the apertures of both magnetic channels, reduces the intensity of the fringe fields outside the magnet by providing convenient flux return paths, and prevents the collars from expanding when submitted to the Lorentz forces exerted on the coils. The shrinking cylinder is also an outer wall of the superfluid helium vessel. The inner wall of the helium tank is defined by the outer perimeter of both cold bore vacuum tubes used to guide the proton beams. The cold mass inside the shrinking cylinder is filled with liquid helium at a pressure slightly exceeding 1 bar and cooled to the temperature of 1.9 K by means of the heat exchanger pipe. The cryostat surrounding the cold mass contains thermal shields, cryogenic pipelines, radiation insulation and the support system of the magnet. All of these elements are enclosed within the vacuum vessel retaining the pressure inferior to 10^{-6} mbars. Two thermal shields covered with superinsulation and operating at the temperatures of 5-10 K and 55-75 K respectively, constitute two intermediate heat intercept stages minimizing any possible heat leakage into the cold mass.

1.4 The Short Dipole Magnet Program

Since 1989 a test and evaluation program of short superconducting dipole magnets (MBSMS) for the LHC is under way at CERN. It was intensified in 1995 when a production of a new series of 1-m long dipole magnets was launched [7]. So far 23 single aperture and 5 double aperture models have been made and tested in multiple assembly variants. Under superfluid helium conditions some of these magnets have reached the magnetic field intensity exceeding 9 T during the initial excitation, and the magnetic field above 10 T after several training quenches, approaching thus the 10.5 T short sample limit imposed by the applied Nb-Ti cable. The invaluable experience resulting from the MBSMS program is applied in the design optimization of the long dipole magnets for the LHC. Also most of the experiments carried out throughout this thesis were executed on short dipole magnets in view of the implementation of the results into the series production of the series production of the LHC magnets.

In order to understand the objectives of this work it will be necessary to get acquainted with the test object. This chapter aims to introduce a single aperture short dipole model by going step-by step through its assembly stages. Apart from different lengths the assembly of the short dipole model is equivalent to the assembly of the full-scale long magnets.

The superconducting coils for the LHC dipole magnets are assembled in different phases. First the inner and outer layers of the coils are wound with 15-mm wide Rutherford cable. In order to achieve an optimal current distribution in the coil, the characteristics of the cables are different for each of the two layers. In the case of the inner layer, there are 8900 superconducting Nb-Ti filaments, each of 7 μm diameter, in a single strand of the cable (Fig. 1.11). Within the strand the superconductor is immersed in a copper matrix with a copper to superconductor ratio of 1.6 : 1. Fig. 1.12 shows separate superconducting filaments arranged in clusters forming the double stacking configuration. The ensemble of the clusters immersed in the copper matrix defines the internal structure of the strand composite. Apart from the central part of the strand (Fig. 1.11) a layer of the pure matrix material surrounds also the entire bundle of filament clusters. The thickness of this layer varies from 50 – 80 μm . Twenty eight strands, each of 1.065 mm in diameter, constitute an inner layer cable (Fig. 1.13). The transversal-cross section of this cable is shown in Fig. 1.14.

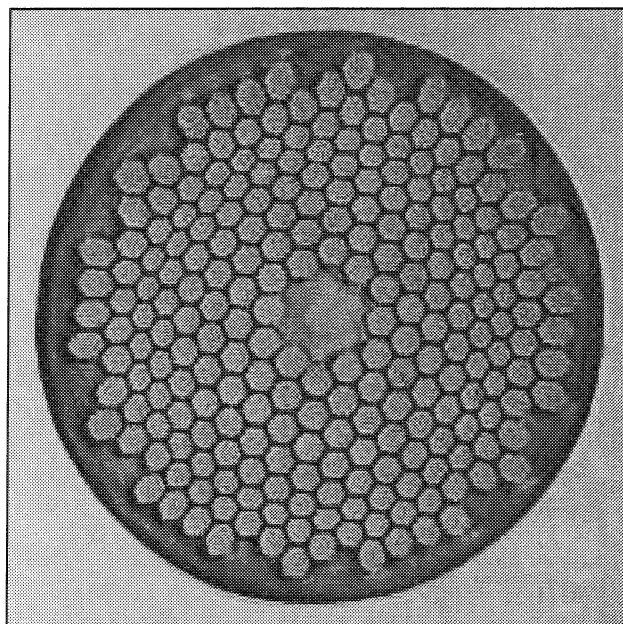


Figure 1.11 Inner layer strand

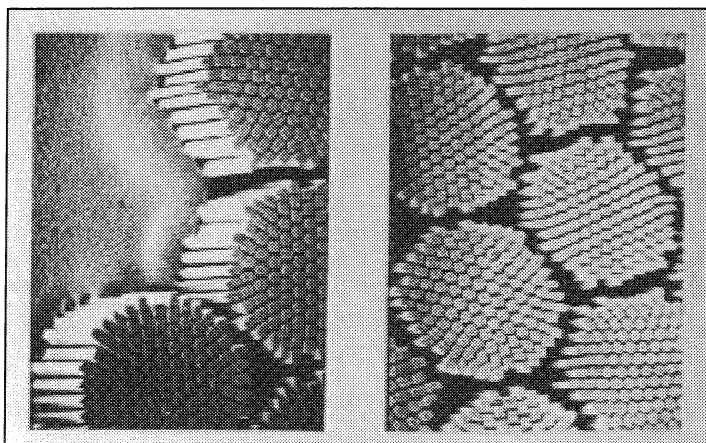


Figure 1.12 Stacking of the filaments in a strand

A single strand for the outer layer cable consists of 6500 filaments, each of 6 μm diameter (Fig. 3.5.) The copper to superconductor ratio in the strand is 1.9 : 1. An external layer cable is composed of thirty six strands, each of 0.825 mm in diameter (Fig. 3.6.). The complex

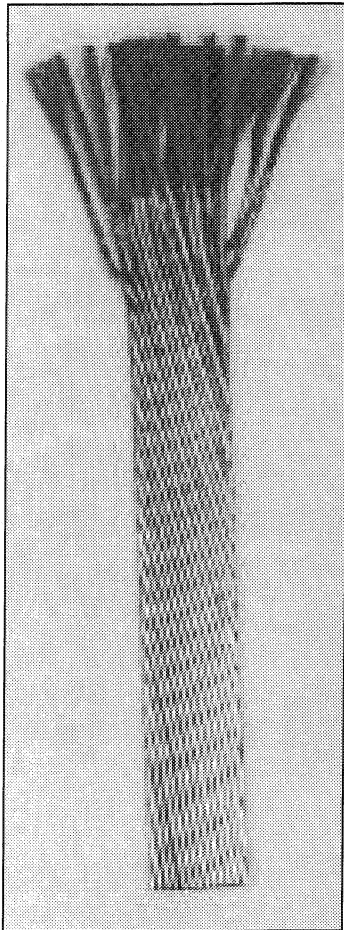


Fig. 1.13 A sample of the inner layer cable

structure of the composite cable is a consequence of the stability considerations. The titanium grains of the size of 10 nm play the role of the pinning centers in the Nb-Ti superconductor. Despite their omnipresence in the conductor material the superconducting filaments must still be small enough to be stable against the flux jumping. The copper matrix acts as a stabilizer for the tiny filaments. If due to the cable movement or the impact of the stray proton the temperature of the superconductor is locally increased the current carried by the conductor will easily exceed the maximum critical current density. In this case the surplus is automatically carried away by the copper matrix. With all the excess current transferred to copper the thermally disturbed superconductor will continue to carry its critical current density

without undergoing a violent resistive transition to the normal state. In the situation of the shared current flow divided between the superconductor and the copper matrix the heat is generated in both components of the cable. It is up to the coolant (liquid helium) to efficiently carry this excess heat away if the superconductor is to recover from the thermal distortion

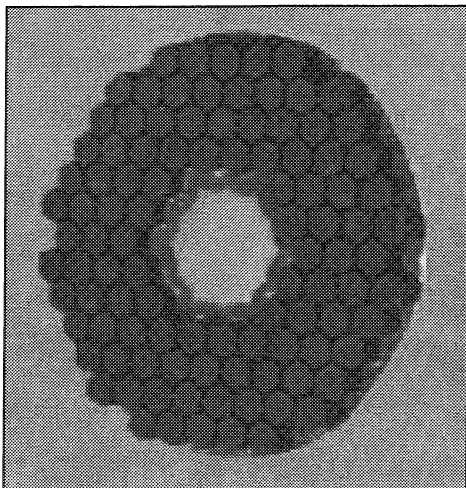


Figure 1.15 Outer layer strand

and regain its full stability. Even in the extreme case, if the situation cannot be auto-corrected and the thermal distortion of the system leads inevitably to a quench, the copper matrix plays an essential role in the protection of the coils.

Once the normal zone propagates throughout the magnet the resistivity of copper is much lower than the

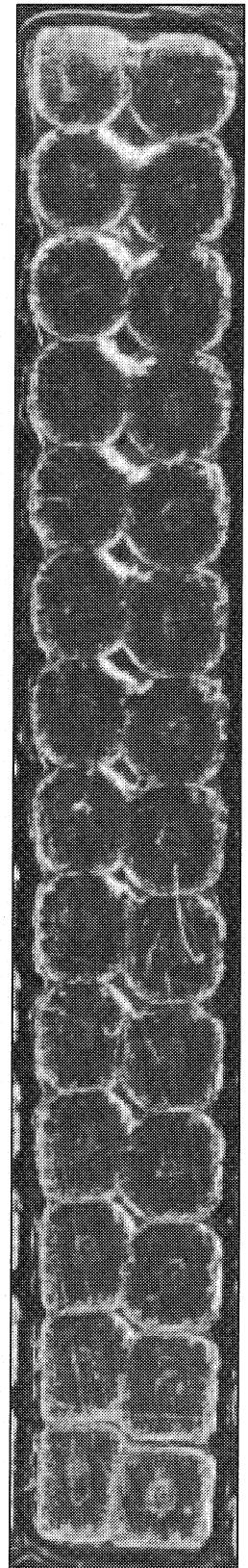


Figure 1.14

Cable cross-section

resistivity of Nb-Ti in the normal state. Thus the quench current flowing in the copper matrix will reduce the Joule heat generated in the conductor, and the copper will help to spread the energy uniformly throughout the entire magnet preventing the localized overheating of the zone around the hot spot origin of the quench. Actually, once the quench is detected the natural spread of the normal zone is sped up by a system of quench heaters running along the coils of the magnet.

The electrical insulation for both types of cable is composed of three polyimide layers. The first two layers are wrapped around the cable with 50% overlap. The last layer is wound over them with 2 mm gap between the consecutive turns as it is shown in Fig. 1.17. The width of the external insulation tape is 9 mm. The 2 mm spacing creates channels for the superfluid helium. In this way, during the operation of the magnet, the coolant can easily penetrate between the coil turns, and any excessive heat load can be efficiently conducted away from the magnet. The effective thickness of the entire insulation system is about 125 μm . The outermost insulation layer is covered with adhesive. After winding the coils are heated in a curing mold.

During this process adhesive binds the adjacent cable turns together

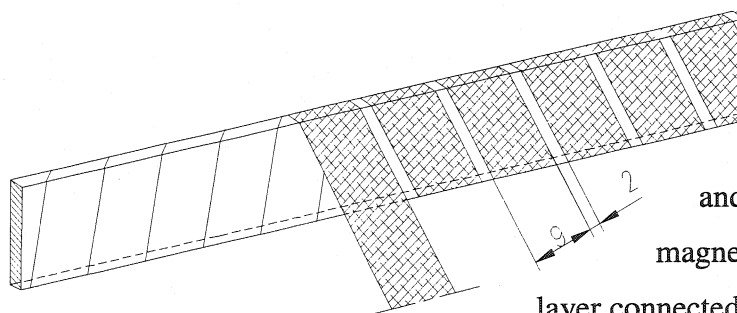


Figure 1.17 Cable insulation

both coils are shown schematically in Fig. 1.18. The uppermost part of the drawing is a side projection view of an assembled pole with the external layer placed on top of the internal one. Below, there are top projection views of the inner and outer layers separately. The layer jump section, where the two layers are connected with each other, is visible in Fig. 1.19. A special

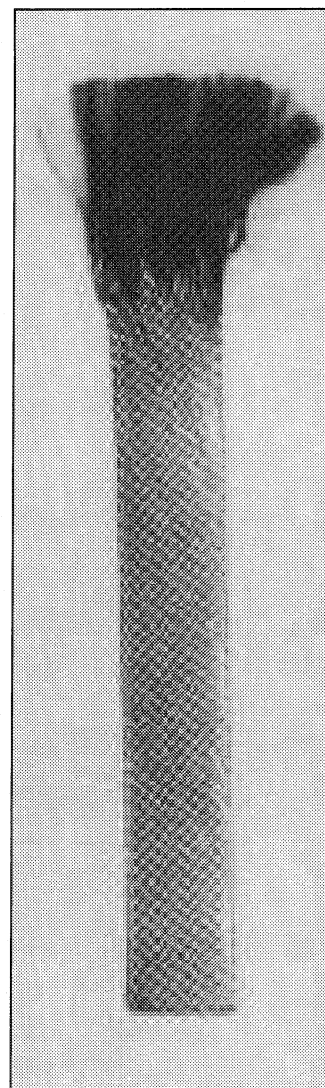


Fig. 1.16 A sample of the outer layer cable

and the final form is given to the coil. A completed inner layer coil contains 15 cable windings, and an outer one 25. A single pole of the magnet consists of one inner and one outer

layer connected together in series. Thus a single pole contains 40 cable turns. One-meter long models of



Figure 1.18 Schematic drawings of one-meter long coils

corrugated spacer is inserted between both layers during the assembly to provide an additional inter-layer helium circulation during the operation of the magnet.

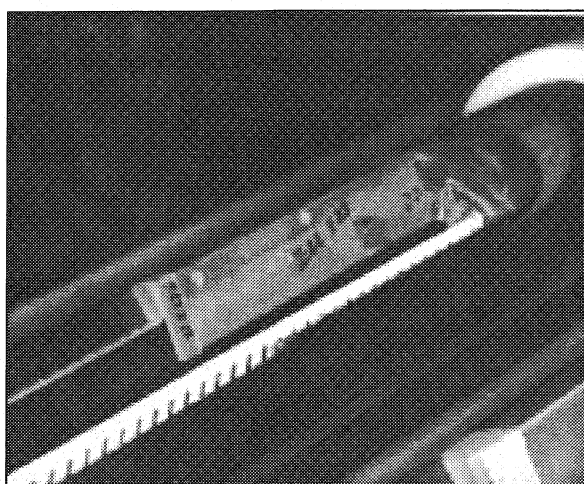


Figure 1.19 Layer jump section

conductor blocks improve the current distribution in the coil, and thus assure the envisaged quality of the magnetic field.

The coil reinforcement structure in the form of stainless steel or aluminum collars is clamped around the coils during the so-called collaring process. The entire configuration is uniformly compressed (Fig. 1.21) until the circular openings in the top pack of the collars are aligned with the openings in the bottom pack. When this

Two poles connected together in a serial sequence of layers outer-inner-inner-outer constitute a single aperture of the magnet, which is then collared. A cross-section of the collared magnet assembly is shown in Fig. 1.20. Horizontal symmetry axis indicates the border between both poles. The longitudinal wedge shaped copper spacers visible on the cross-section between the

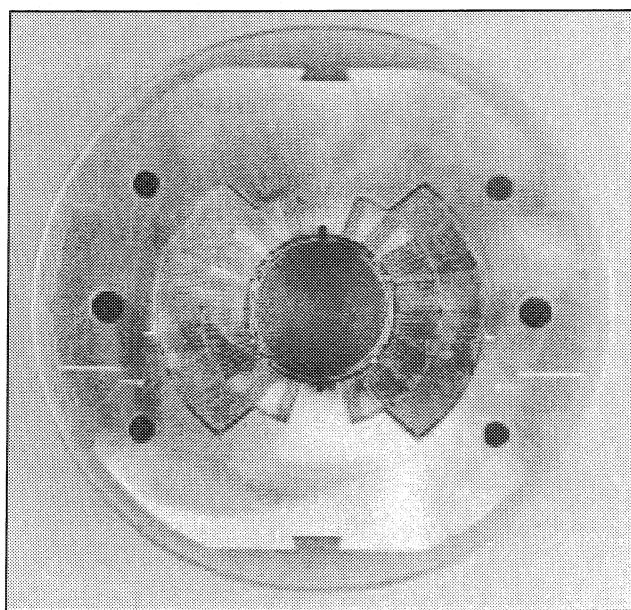


Figure 1.20 Cross-section of the collared assembly

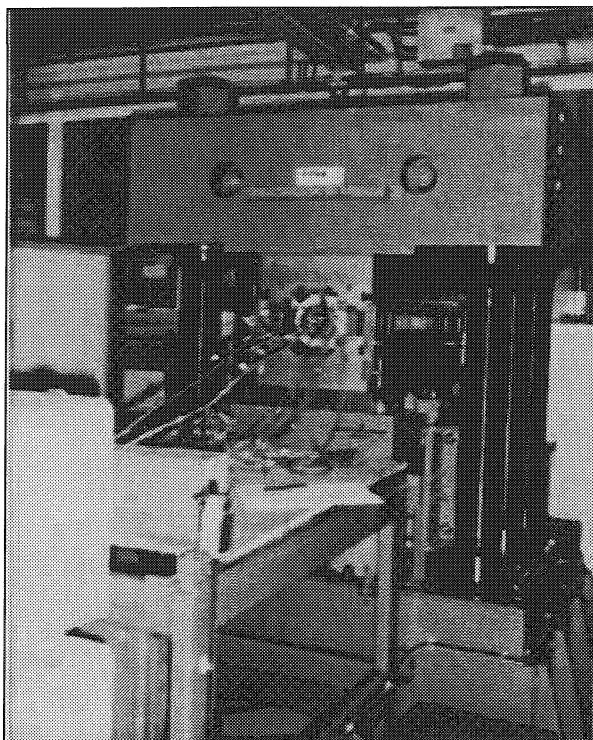


Figure 1.21 Collaring of the coil

state is achieved, the locking rods are inserted into the two holes located in the horizontal median plane of the collars along the entire length of the coils. When the external pressure is released the coils spring back and expand the collars. The residual prestress remaining in the coils prevents the motion of the cables and counteracts the stresses arising during the operation of the magnet due to the electromagnetic forces acting on the coils. In order to obtain the desired residual prestress, the elastic moduli and the size of the coils are measured before the collaring [8]. The information acquired during these measurements allows to calculate the

thickness of shimming for the assembly of the magnet, and thus to adjust the value of the stress remaining in the coils after the collaring. Fig. 1.22 shows the shims placed between the layers of the coils and the upper part of the collars.

The outer layer of the coils is separated from the collars by 0.5 mm of ground insulation and by a 0.7-mm thick austenitic steel protection sheet called collaring shoe. The aim of the collaring shoe, visible also in Fig. 1.22, is to protect the ground insulation of the coil, and to decrease the friction forces acting on the coils during

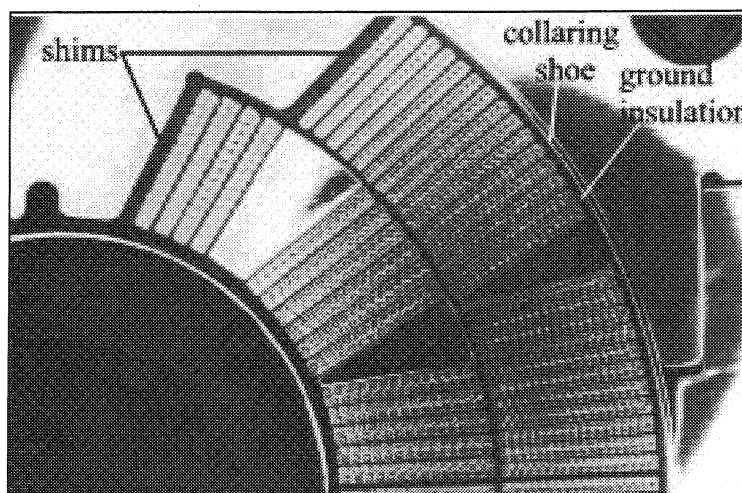


Figure 1.22 Shimming of the coil

the collaring process, and thus to prevent the coil from being damaged.

The collared assembly after yoking constitutes a single aperture magnet. The schematic drawings of the transversal cross-section and the side view of an assembled MBSMS single aperture magnet are shown in Figs 1.23 and 1.24. A photograph of the magnet without the cryostat is shown in Fig. 1.25.

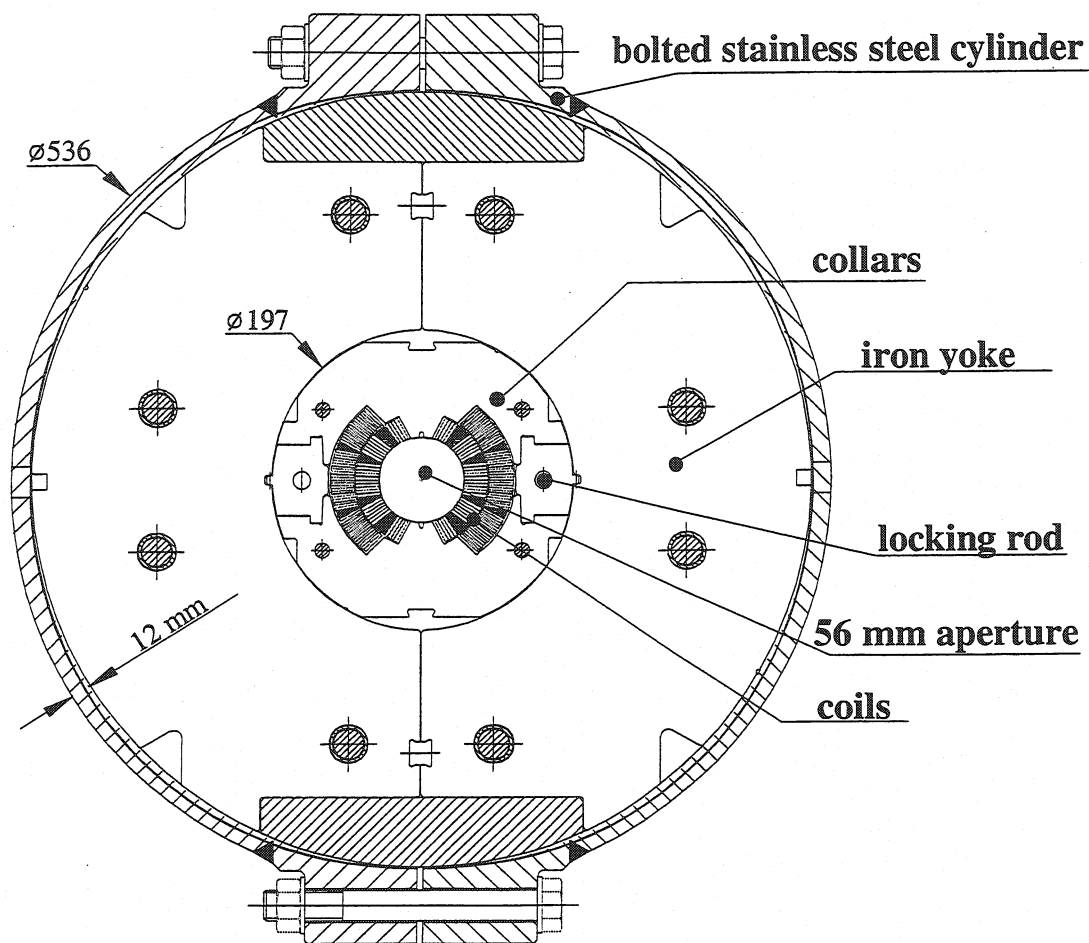


Figure 1.23 Cross section of a single-aperture dipole magnet

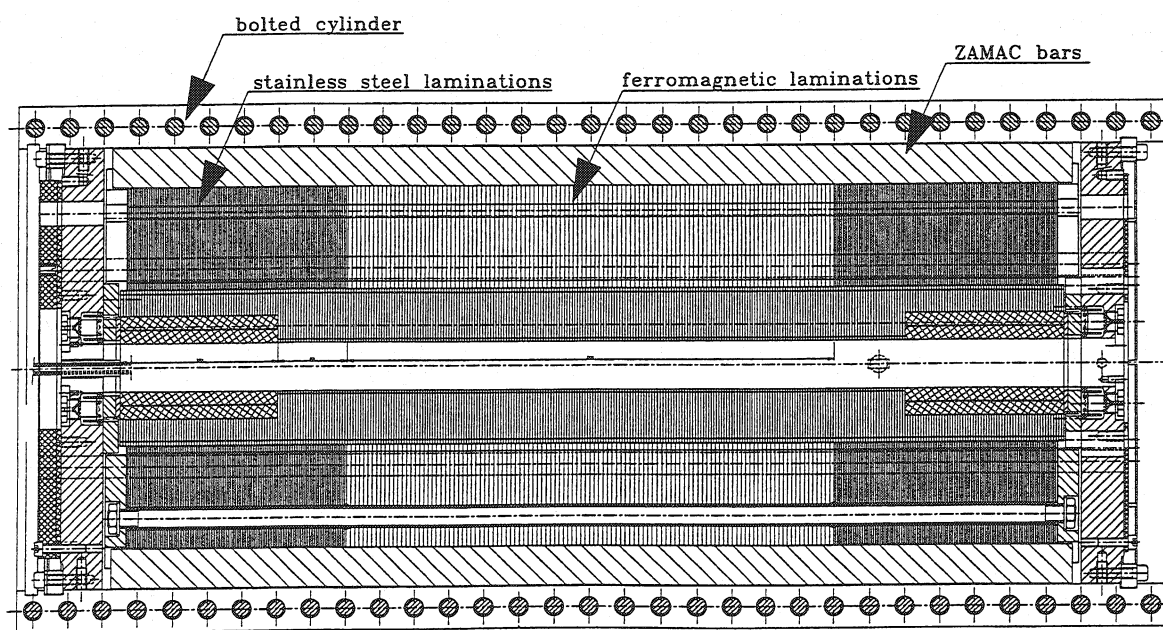


Figure 1.24 Side view of the magnet

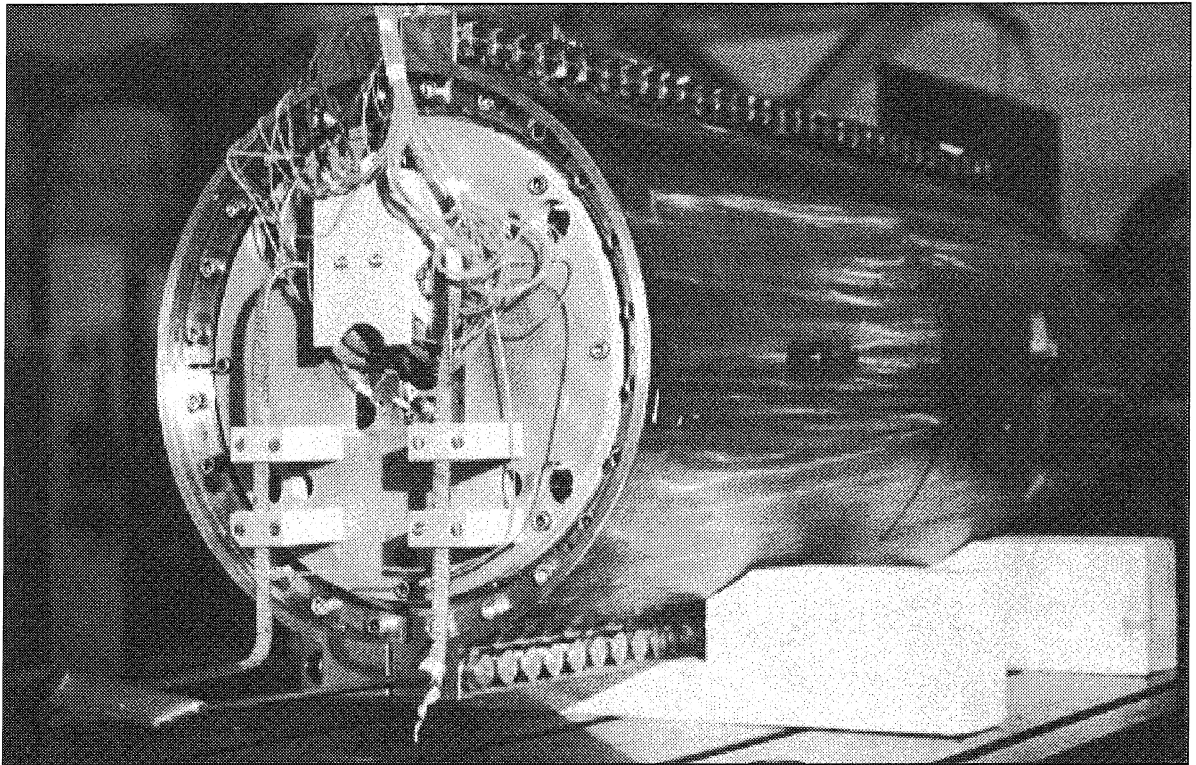


Figure 1.25 Single aperture short dipole magnet

1.5 Objectives of the Electro-Topological Analysis and Diagnostics of the Superconducting Magnet Systems for the LHC

Two consecutive cable turns of the coil winding in the superconducting dipole magnet for the LHC are separated by about $250\ \mu\text{m}$ of insulation. This dielectric barrier can be easily damaged during one of the assembly phases described in the previous paragraph leading thus to a possible inter-turn short-circuit.

As it was discussed in previous sections, thermal perturbations caused in the superconducting magnet system by microscopic cable movements or impact of the stray particles impose shared current flow characterized by the initial transport current divided between the superconductor and its stabilizing copper matrix. Any perforations present in the insulation system of the magnet under the conditions of the shared current flow regime would lead to short-circuits, additional energy losses and excessive heat generation. As a consequence the magnet would not be able to recover its stability even from minor thermal distortions and would be automatically forced to undergo a resistive transition to the normal state.

At the nominal field of 8.33 T the magnet is powered up with a direct current of 11.5 kA. The propagation of the normal zone during the quench of the magnet is accompanied by a very fast increase of the resistive voltage due to the fact that any resistance appearing in the coil windings is multiplied by the high current intensity of 11.5 kA. This voltage measured with respect to the ground can rise as high as 1.3 kV before the quench protection system is triggered and the energy stored in the magnet is safely redirected into the dump resistor. The resistance of the quenching coils causes also the decline of the current in the magnet after the power supply is switched off. This weakening current produces inductive voltage drops between the coil turns. The insulation system of the magnet must absolutely withstand the resistive and inductive voltages building up in such situation. Due to the high energy stored in the magnet any perforation of the insulator layer encountered during the resistive transition of the magnet to the normal state would lead to the local burnout of the cable and irreversible destruction of the coil.

Thus it is extremely important to assure the overall integrity of the insulation system in the magnet. If any anomalies are encountered they must be unconditionally diagnosed, localized and repaired. The work presented in this thesis was carried out in the framework of the CERN Doctoral Student Program as the research and development project associated with the MBSMS Short Dipole Model Program. The work was concentrated on the efficient detection and localization of the defects in the insulation system of the superconducting magnets in view of the series magnet production for the LHC. Since the beginning of 1997 several different areas and aspects of the problem have been addressed in the course of three consecutive years.

- The possible inter-turn short circuits encountered in the coils are well detectable when the magnet is collared. The presence of the insulation failure can be diagnosed by means of high voltage discharge test performed on the magnet. At the first stage of the project a complete experimental set-up integrated with the data acquisition and analysis system for this kind of test has been developed, tested and implemented as the preliminary diagnostic tool for the series production of the LHC magnets. The complete system has been assembled in five units and delivered to the external companies charged with the performance of the impulse tests on the coils for the LHC magnets. So far three companies are equipped with the system: Noell in Germany, Ansaldo in Italy, and

Jeumont in France. The test procedures and the experimental set-up are described in paragraph 4 and appendix A of chapter 3.

The high voltage discharge test allows to diagnose the presence of the insulation defect but the localization of the fault-affected area remains beyond the capabilities of this approach. When a defective magnet is disassembled for repair the collars are removed and the internal prestress in the coils is inevitably released. As a consequence the diagnosed inter-turn short-circuit disappears. Time consuming methods involving local controlled pressure increase over small sections of the coil must be employed thereafter to reestablish the position of the defect. In the case of 15-m long coils this procedure may take 1-2 weeks before successful localization of the problem is achieved. Chapter 3 introduces a novel method of the precise short-circuit localization in the assembled magnet system by analysis of the distortion of a pulsed magnetic field generated in the aperture of the magnet during a high voltage discharge test. The method has been recently presented on the 16th International Conference on Magnet Technology in USA where it has been met with great interest. The résumé of the concepts presented in chapter 3 of this thesis has been accepted for the publication in IEEE Transactions on Applied Superconductivity early in the year 2000. At the moment this thesis is being submitted for official examination, the adaptation of the approach for the long LHC dipole magnets is in course. The understanding of the novel method requires a thorough knowledge of mutual implications between the magnet design, topology of the coil winding, geometry of the conductor distribution in the transversal cross-section of the coil, symmetry conservation and symmetry breaking as far as the current distribution in the coil conductors is concerned, and the quality of the magnetic field in the magnet. All of these aspects are discussed in details in chapter 2.

- The second part of the project addressed the auxiliary instrumentation circuits of the LHC magnet systems. Chapter 4 describes a successful adaptation of the advanced Time Domain Reflectometry (TDR) techniques for the analysis of the signal integrity in these circuits of the magnet, which are responsible for monitoring and transmitting the vital status information concerning the magnet system and its cryogenic environment. The tests presented in this chapter were carried out on the voltage tap, temperature and pressure transducer circuits of the string of full-scale LHC magnets simulating the behavior of the standard half-cell of the LHC arc section.

- The third and last part of the project concerned partial discharges, and aimed at the detection of the hidden defects in the ground insulation of the magnets. The phenomenon of partial discharges is not yet fully understood at the current stage of its theoretical description. The measurement technique is rather difficult to implement, it has never been used at CERN, and never in the world in the context of superconducting accelerator magnets. Due to these factors the contents of the partial discharge studies was not at first intended to be incorporated as an integral part of this thesis. The situation has been changed after a very promising measurement session carried out in the laboratories of Components, Materials and Electrical Technologies at the University of Genoa in Italy. Very interesting results obtained from the examination of the partial discharge patterns unveiled a powerful potential of this method for the analysis of the ground insulation integrity in the LHC dipole magnets. The possibility of successful detection of hidden human error type of manufacturing defects has been welcomed at CERN with great enthusiasm. As a result a thorough investigation of the method has been scheduled for the year 2000. Chapter 5, the smallest one of the entire thesis, discusses the results of the experiments carried out in Italy at the beginning of October 1999.

References for Chapter 1

- [1] M. Bona et al., The LHC Magnet System and its Status of Development, Proceedings of the 4th International Congress on Superconductivity, Orlando, FL, USA, 1994, NASA Conf. Publ. NASA-CP-3290, 1996, pp. 65-74
- [2] E. J. N. Wilson, Introduction to Particle Accelerators, 1996-1997 CERN Academic Training Programme, Lecture Series for Postgraduate Students
- [3] R. Scanlan et al., Preliminary Test Results of a 13 T Niobium Tin Dipole, Applied Superconductivity 1997, Netherlands, June 30 – July 3, 1997, pp. 1503-6
- [4] L. Evans, LHC Accelerator Physics and Technology Challenges, Proceedings of EPAC'98, Stockholm, June 22-26, 1998
- [5] S. A. Elrod et al., The Specific Heat of Nb-Ti from 0 to 7 T between 4.2 and 20 K, Advanced Cryogenic Engineering, Vol. 20
- [6] K. Dahlerup-Petersen et al., The Protection System for the Superconducting Elements of the Large Hadron Collider at CERN, Proceedings of the 1999 Particle Accelerator Conference – PAC'99, New York City, NY, USA, March 29 – April 2, 1999
- [7] N. Andreev et al., State of the Short Dipole Model Program for the LHC, Proceedings of EPAC'98, Stockholm, June 22-26, 1998
- [8] P. Komorowski, User's and Developer's Guide to the Application Specific LabVIEW Support for the Elastic Modulus Machine, Internal Note 97-07, CERN, Geneva, September 1997

Chapter 2

Electromagnetic Principles of the Design of Superconducting Accelerator Magnets for the Large Hadron Collider

The pattern of the magnetic field in modern superconducting accelerator magnets is mainly determined by the geometry of the coils and the distribution of the current in the conductors. In chapter 3 the analysis of the distortion of a pulsed magnetic field generated in the magnet during a high voltage discharge will be applied for the precise localization of inter-turn short circuits in the superconducting coils. Before we come to the analysis of transient magnetic fields it is essential to introduce the principles of the design of the accelerator magnets and to explain the physics behind the magnetic field calculations under normal operation conditions, i.e. when the magnet is powered up with a direct current. The main emphasis of this chapter is put on dipole magnets; nevertheless, the general principles of the magnetic field analysis and magnet design introduced here can be easily applied for different types of magnets, e.g. quadrupoles, sextupoles, etc. Only the topics essential for the ideas developed later on in chapter 3 are discussed in details. Of course this constitutes but a small subset of many complex factors that have to be taken into account during the design and manufacturing process of the magnet. Other important topics e.g. the cryogenics and the stability of the superconducting magnet systems, quench protection, deformations of mechanical structure due to the electromagnetic forces, mechanical accuracy for the manufacturing of the magnets, etc., can be found in many excellent books given in references [1], [2], [3].

A schematic view of a superconducting dipole coil is shown in Fig. 2.1. In the straight section of the coil all conductors are parallel to the beam axis OZ. In reality an accelerator dipole magnet cannot be straight. It has to follow the curvature of the orbit of the particles circulating in the accelerator. Nevertheless the deviation of the magnet from an ideal straight line in a 27-km long tunnel of the LHC accelerator ring is very small. As the diameter of the

aperture is much smaller (56 mm) than the total length of the magnet (15 m), the conductors in the straight section of the coil can be considered as infinitely long. If the above-mentioned assumptions

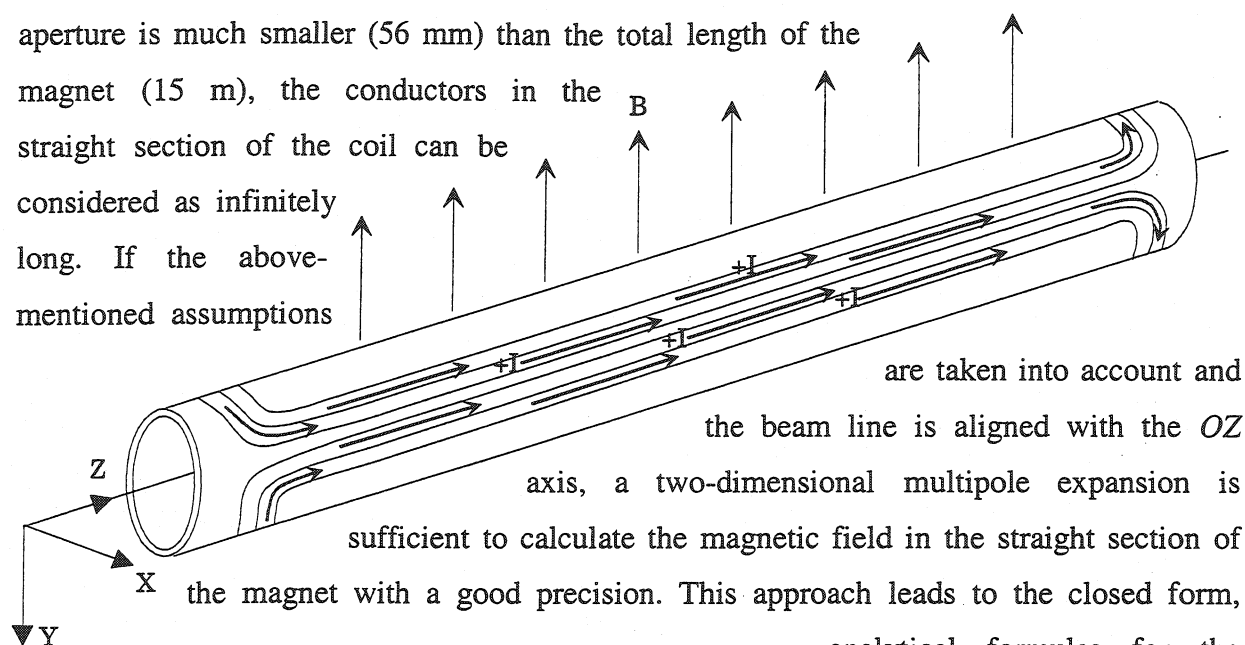


Figure 2.1 Schematic representation of a superconducting dipole coil

are taken into account and the beam line is aligned with the OZ axis, a two-dimensional multipole expansion is sufficient to calculate the magnetic field in the straight section of the magnet with a good precision. This approach leads to the closed form, analytical formulas for the evaluation of the magnetic field components. A schematic pattern of the magnetic field in the coupled LHC dipole coils designed to guide two counter-circulating particle beams at the same time is shown in Fig. 2.2. Not the entire coil can be analyzed using 2-D expansion of the magnetic field. The magnetic field pattern in the head region – the end area of the coil where the superconducting

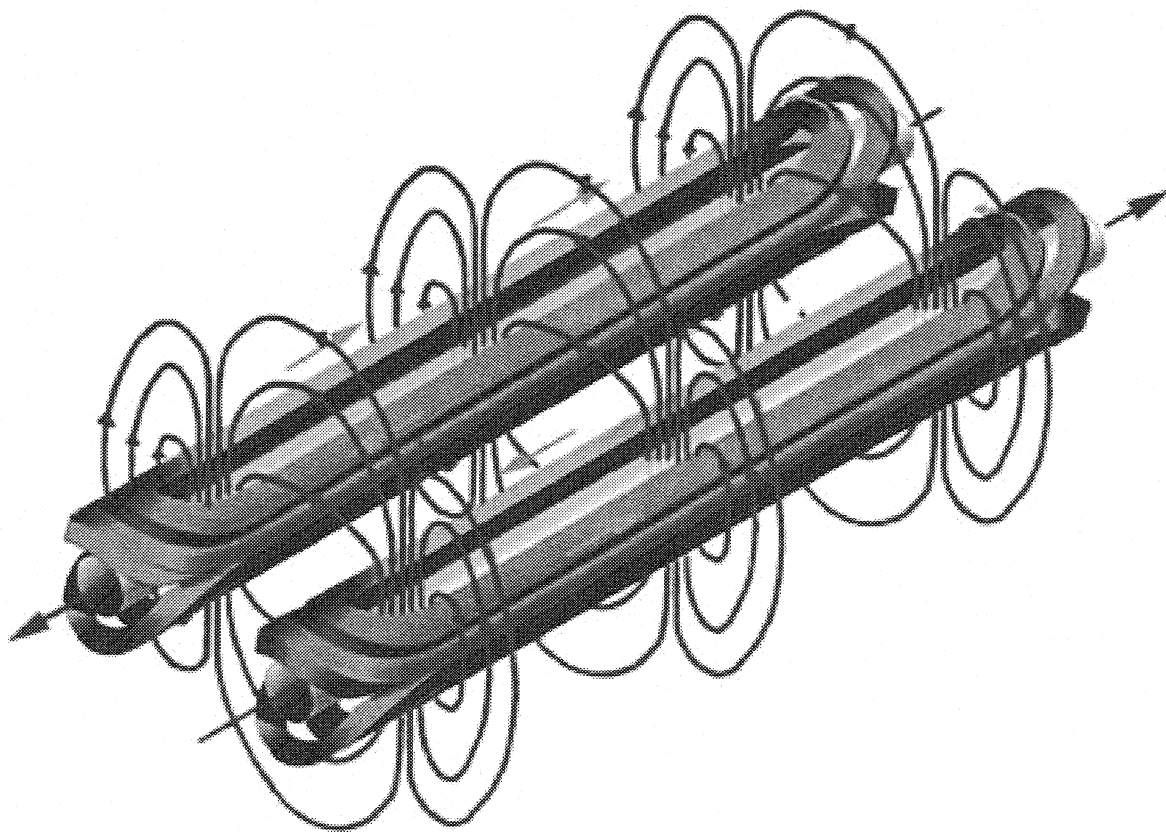


Figure 2.2. Magnetic field flux lines in the coupled LHC dipole coils

cables run across the beam pipe, requires a separate 3-D treatment based on the Finite Element Method (FEM) [4]. The complex topology of the head of the coil imposes a complicated current distribution and as a consequence no analytical solution exists for the problem. The influence of the ends on the overall magnetic field quality in the 15-m long magnet is minor. Nevertheless the perturbations introduced by the head may require further corrections or compensations as far as the trajectory of the accelerated proton beam is concerned. An example of the end region of the single dipole coil with the calculated 3-D vector field matrix is shown in Fig. 2.3. The modeling and the calculation was done with the Routine for the Optimization of Magnet X-Sections, Inverse Problem Solving and End Region Design program package (ROXIE) developed at CERN and used for the integrated design of the superconducting accelerator magnets [5].

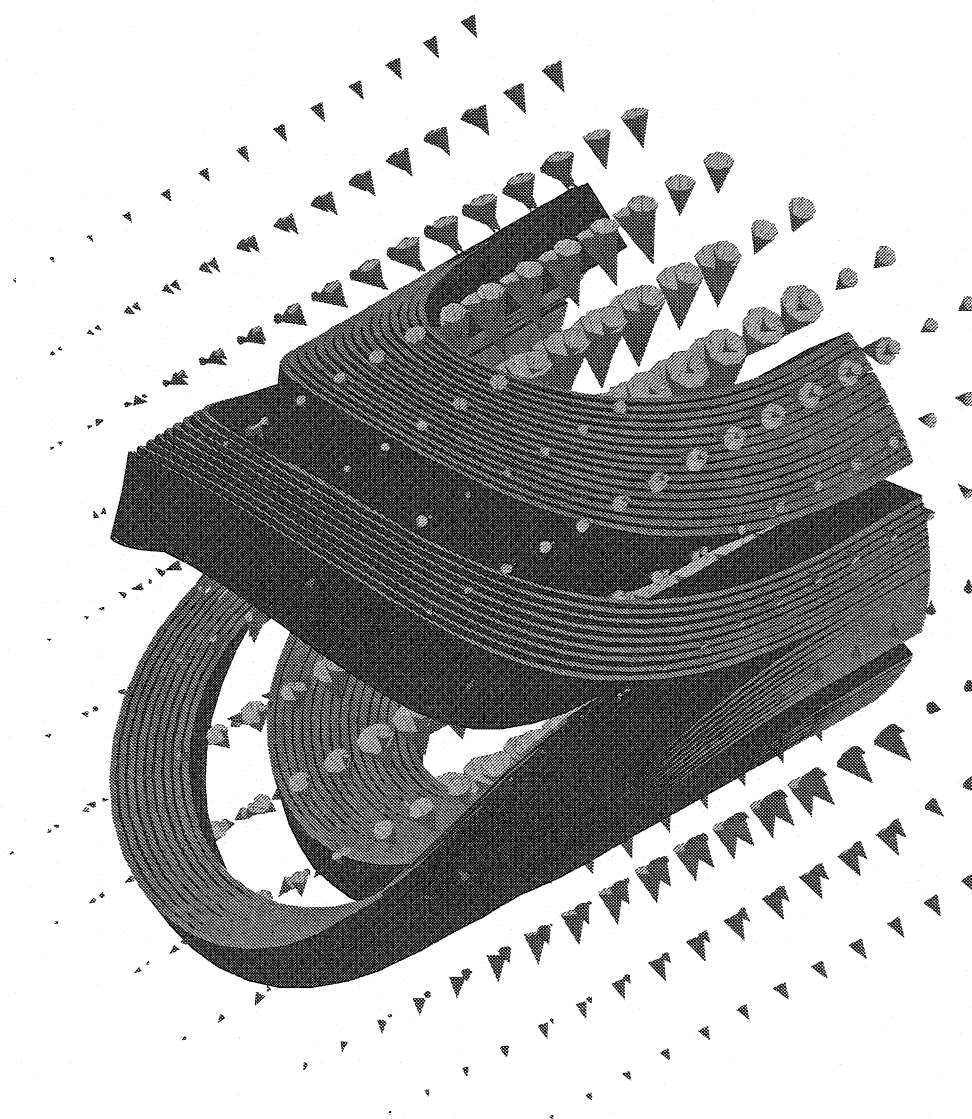


Figure 2.3 Magnetic vector field in the end region of a dipole coil

2.1 Magnetostatic Problems in 2-D

Magnetostatic problems are described by the following, reduced system of Maxwell equations:

$$\nabla \times \vec{H} = \vec{j}_s \quad (2.1)$$

$$\nabla \cdot \vec{B} = 0 \quad (2.2)$$

$$\vec{B} = \mu_0(\vec{H} + \vec{M}) \quad (2.3)$$

where H is the magnetic field intensity, j_s is the density of the imposed source currents, B the magnetic field induction (magnetic flux density) and M the magnetization. Magnetic induction B can be expressed in terms of the vector potential A in the following manner:

$$\vec{B} = \nabla \times \vec{A} = \begin{vmatrix} \vec{e}_x & \vec{e}_y & \vec{e}_z \\ \frac{\partial}{\partial x} & \frac{\partial}{\partial y} & \frac{\partial}{\partial z} \\ A_x & A_y & A_z \end{vmatrix} = \vec{e}_x \left(\frac{\partial A_z}{\partial y} - \frac{\partial A_y}{\partial z} \right) + \vec{e}_y \left(\frac{\partial A_x}{\partial z} - \frac{\partial A_z}{\partial x} \right) + \vec{e}_z \left(\frac{\partial A_y}{\partial x} - \frac{\partial A_x}{\partial y} \right) \quad (2.4)$$

where

$$B_x = \frac{\partial A_z}{\partial y} - \frac{\partial A_y}{\partial z} \quad B_y = \frac{\partial A_x}{\partial z} - \frac{\partial A_z}{\partial x} \quad B_z = \frac{\partial A_y}{\partial x} - \frac{\partial A_x}{\partial y} \quad (2.5)$$

In two-dimensional magnetic field the axial component does not exist, i.e. $B_z = 0$, therefore only A_z component of the vector potential is necessary and entirely sufficient to describe the field. Thus in Cartesian coordinates,

$$B_x = \frac{\partial A_z}{\partial y} \quad B_y = -\frac{\partial A_z}{\partial x} \quad B_z = 0 \quad (2.6)$$

and in cylindrical coordinates

$$B_r = \frac{1}{r} \frac{\partial A_z}{\partial \theta} \quad B_\theta = -\frac{\partial A_z}{\partial r} \quad B_z = 0 \quad (2.7)$$

In general a curl of the vector potential in Eq. (2.4) is not unique. A curl of a gradient of any scalar potential is always zero, and thus a curl of a vector potential defined as $\vec{A}' = \vec{A} + \nabla \psi$, where ψ denotes an arbitrary scalar field, produces the same result, i.e.: $\nabla \times \vec{A}' = \nabla \times \vec{A}$, which does not affect the physical quantity of the magnetic field induction. To remove this ambiguity the Coulomb gauge condition can be used:

$$\nabla \cdot \vec{A} = 0 \quad (2.8)$$

Since all of the excitation currents in the 2-D model flow in the z direction, the vector potential is dependent only on the x and y coordinates: $\vec{A} = A_z(x, y)\vec{e}_z$.

Thus the Coulomb gauge (2.8) often used in 3-D problems to remove the ambiguity of the solution is automatically imposed in a 2-D problem. The solution of such a problem using vector potential approach is unique providing that the correct boundary conditions are applied. Taking Eq. (2.8) into account the curl of the magnetic field induction yields:

$$\nabla \times \vec{B} = \nabla \times (\nabla \times \vec{A}) = \nabla(\nabla \cdot \vec{A}) - \nabla^2 \vec{A} = -\nabla^2 \vec{A} \quad (2.9)$$

On the other hand taking Eqs. (2.1) and (2.3) into account

$$\nabla \times \vec{B} = \mu_0 \nabla \times (\vec{H} + \vec{M}) = \mu_0 \vec{j}_s + \mu_0 \nabla \times \vec{M} \quad (2.10)$$

Comparing Eqs. (2.9) and (2.10) one obtains

$$\nabla^2 \vec{A} = -\mu_0 \vec{j}_s - \mu_0 \nabla \times \vec{M} \quad (2.11)$$

For the problems without iron yoke, i.e. in the absence of the iron magnetization, Eq. (2.11) is reduced to the following Poisson equation:

$$\nabla^2 \vec{A} = -\mu_0 \vec{j}_s \quad (2.12)$$

For the current free regions, e.g. inside the aperture of the magnet, equation (2.12) is further reduced to the Laplace equation:

$$\nabla^2 \vec{A} = 0 \quad (2.13)$$

The analytical and numerical solution of these three equations in practical cases corresponding to the magnetostatic problems in superconducting accelerator magnets will be discussed in details later in this chapter.

2.2 Multipole Expansion of the Complex Magnetic Field

Let us define the complex magnetic field induction in a 2-D plane as follows:

$$\tilde{B}(z) = B_y(x, y) + iB_x(x, y) \quad (2.14)$$

The variable z is a complex number of the form $z = x + iy$, whereas B_x and B_y are real functions of x and y . $\tilde{B}(z)$ can be expressed in form of multipole magnetic field expansion only if it is an analytical function. Any analytical function can be represented in a form of power series expanded about a given point z . In order to fulfill this requirement the $\tilde{B}(z)$ has to be infinitely differentiable in a neighborhood of that point. If the first derivative of the function exists all of the higher order derivatives will exist as well. $\tilde{B}(z)$ defined in some neighborhood of point z is said to be differentiable if the derivative

$$\tilde{B}'(z) = \frac{d\tilde{B}}{dz} = \lim_{\zeta \rightarrow z} \frac{\tilde{B}(\zeta) - \tilde{B}(z)}{\zeta - z} \quad (2.15)$$

exists and if the limit (2.15) is unique, and therefore independent of how ζ approaches z . Let us express the denominator of the limit under question as $\zeta - z = \Delta x + i\Delta y$. Two cases are to be considered:

1. $\Delta x = 0, \Delta y \rightarrow 0$

$$\frac{d\tilde{B}}{dz} = \frac{\partial(B_y + iB_x)}{i\partial y} = -i \frac{\partial B_y}{\partial y} + \frac{\partial B_x}{\partial y}$$

2. $\Delta x \rightarrow 0, \Delta y = 0$

$$\frac{d\tilde{B}}{dz} = \frac{\partial(B_y + iB_x)}{\partial x} = \frac{\partial B_y}{\partial x} + i \frac{\partial B_x}{\partial x}$$

Both limits produce a unique result only and only if

$$\frac{\partial B_x}{\partial x} = -\frac{\partial B_y}{\partial y} \quad \text{and} \quad \frac{\partial B_y}{\partial x} = \frac{\partial B_x}{\partial y} \quad (2.16)$$

Equations in (2.16) are the **Cauchy-Riemann conditions** that have to be satisfied by the $\tilde{B}(z)$ function if it is an analytic function. $\tilde{B}(z)$ expressed using vector potential notation of (2.6) has the following form:

$$\tilde{B}(z) = B_y(x, y) + iB_x(x, y) = -\frac{\partial A_z}{\partial x} + i \frac{\partial A_z}{\partial y}$$

The first Cauchy-Riemann condition defined by Eqs. (2.16) is identical with the Maxwell equation (2.2) and thus it is satisfied automatically.

$$\frac{\partial B_x}{\partial x} = -\frac{\partial B_y}{\partial y} = \frac{\partial A_z}{\partial x \partial y}$$

From the second condition one obtains the Laplace equation (2.13) for iron-free magnetostatic problems

$$\frac{\partial^2 A_z}{\partial x^2} + \frac{\partial^2 A_z}{\partial y^2} = \nabla^2 A_z = 0$$

For the 2-D complex magnetic field as defined by Eq. (2.14) the Cauchy-Riemann conditions are identical with two of the Maxwell equations. Hence the complex magnetic field can be expanded in power series and the quality of the magnetic field in the magnet can be analyzed in terms of the multipoles of such an expansion. According to the design project of the LHC [6], the complex magnetic field induction is expanded as follows:

$$B_y + iB_x = \sum_{n=1}^{\infty} (\mathcal{B}_n + i\mathcal{A}_n) z^{n-1} \quad (2.17)$$

Coefficients \mathcal{B}_n indicate normal and \mathcal{A}_n skew field multipoles. Taking into account different representations of the complex number z ,

$$z = x + iy = re^{i\theta} = r(\cos \theta + i \sin \theta)$$

and the transformation of the magnetic field vector from the Cartesian to polar coordinates,

$$\begin{bmatrix} B_r \\ B_\theta \end{bmatrix} = \begin{bmatrix} \cos \theta & \sin \theta \\ -\sin \theta & \cos \theta \end{bmatrix} \cdot \begin{bmatrix} B_x \\ B_y \end{bmatrix} = \begin{bmatrix} B_x \cos \theta + B_y \sin \theta \\ -B_x \sin \theta + B_y \cos \theta \end{bmatrix} \Rightarrow B_\theta + iB_r = (B_y + iB_x) e^{i\theta} \quad (2.18)$$

the complex field expansion can be rewritten as:

$$B_\theta + iB_r = \sum_{n=1}^{\infty} (\mathcal{B}_n + i\mathcal{A}_n) r^{n-1} e^{i(n-1)\theta} e^{i\theta} \quad (2.19)$$

Hence the decomposition of the series into Cartesian and polar coordinates follows immediately.

$$B_x(r, \theta) = \sum_{n=1}^{\infty} r^{n-1} (\mathcal{B}_n \sin(n-1)\theta + \mathcal{A}_n \cos(n-1)\theta) \quad (2.20)$$

$$B_y(r, \theta) = \sum_{n=1}^{\infty} r^{n-1} (\mathcal{B}_n \cos(n-1)\theta - \mathcal{A}_n \sin(n-1)\theta)$$

$$B_r(r, \theta) = \sum_{n=1}^{\infty} r^{n-1} (\mathcal{B}_n \sin n\theta + \mathcal{A}_n \cos n\theta) \quad (2.21)$$

$$B_\theta(r, \theta) = \sum_{n=1}^{\infty} r^{n-1} (\mathcal{B}_n \cos n\theta - \mathcal{A}_n \sin n\theta)$$

One can introduce the radius dependent multipole coefficients as:

$$A_n(r) = \mathcal{A}_n r^{n-1} \quad B_n(r) = \mathcal{B}_n r^{n-1} \quad (2.22)$$

Using this notation B_r and B_θ evaluated at the reference radius r_0 can be expressed as:

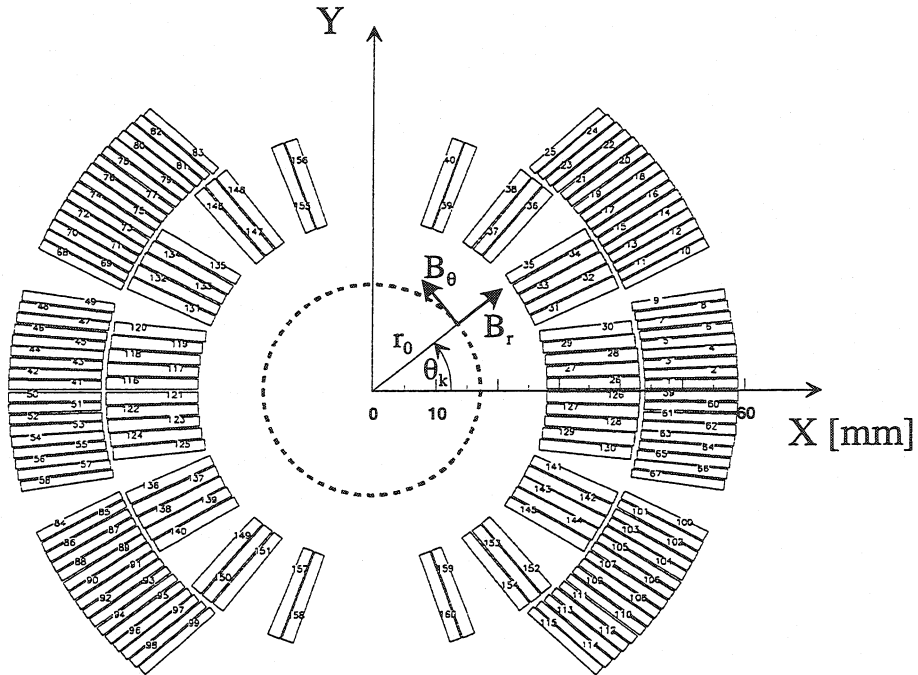
$$B_r(r_0, \theta) = \sum_{n=1}^{\infty} (B_n(r_0) \sin n\theta + A_n(r_0) \cos n\theta) \quad (2.23)$$

$$B_\theta(r_0, \theta) = \sum_{n=1}^{\infty} (B_n(r_0) \cos n\theta - A_n(r_0) \sin n\theta)$$

The coefficients $A_n(r)$ and $B_n(r)$ of the Fourier expansion, given in Tesla, can be calculated, e.g. from the radial component B_r , as follows:

$$A_n(r_0) = \frac{1}{\pi} \int_0^{2\pi} B_r(r_0, \theta) \cos n\theta \, d\theta \quad B_n(r_0) = \frac{1}{\pi} \int_0^{2\pi} B_r(r_0, \theta) \sin n\theta \, d\theta \quad (2.24)$$

In practice, for the harmonic analysis of the magnetic field the radial component of the magnetic field is calculated in discrete, equidistant points around the circle of radius r_0 as shown in Fig. 2.4 on the cross-section of the LHC dipole magnet.



Let N indicate the total number of the evaluation points covering the full cycle interval $[0, 2\pi]$ and located at discrete angles

$$\theta_k = k \frac{2\pi}{N} \quad \text{where } k = 0, 1, 2, \dots, N-1$$

Then the discrete Fourier transform yields:

$$A_n(r_0) \approx \frac{2}{N} \sum_{k=0}^{N-1} B_r(r_0, \theta_k) \cos n\theta_k \quad B_n(r_0) \approx \frac{2}{N} \sum_{k=0}^{N-1} B_r(r_0, \theta_k) \sin n\theta_k \quad (2.25)$$

The approximation error depends on the number of points and the magnitude of the higher order multipole errors in the magnetic field pattern. Experience shows that in general 80 evaluation points are sufficient for multipole calculations up to $n = 15$.

2.3 Normalized Multipole Coefficient Notation

By introducing a reference magnetic field, equal to the main dipole field B_1 , and the normal and skew multipole coefficients relative to the main field at a reference radius r_0 ,

$$b_n = \left. \frac{\mathcal{B}_n r^{n-1}}{B_1} \right|_{r=r_0} = \frac{B_n(r_0)}{B_1} \quad a_n = \left. \frac{\mathcal{A}_n r^{n-1}}{B_1} \right|_{r=r_0} = \frac{A_n(r_0)}{B_1} \quad (2.26)$$

the radial and azimuthal components of the magnetic field can be expressed as:

$$\begin{aligned} B_r(r, \theta) &= B_1 \sum_{n=1}^{\infty} \left(\frac{r}{r_0} \right)^{n-1} (b_n \sin n\theta + a_n \cos n\theta) \\ B_\theta(r, \theta) &= B_1 \sum_{n=1}^{\infty} \left(\frac{r}{r_0} \right)^{n-1} (b_n \cos n\theta - a_n \sin n\theta) \end{aligned} \quad (2.27)$$

With this choice of the reference field the main normal coefficient of the multipole expansion (b_1) is always normalized to 1. Higher coefficients express magnetic field errors relative to the main dipole B_1 , and are given in dimensionless units of 10^{-4} . The vector potential expressed in the normalized multipole coefficient notation has the following form:

$$A_z(r, \theta) = -B_1 r_0 \sum_{n=1}^{\infty} \frac{1}{n} \left(\frac{r}{r_0} \right)^n (b_n \cos n\theta - a_n \sin n\theta) \quad (2.28)$$

The normalized multipole coefficients obey very simple scaling rules. Knowing the value of the coefficients at a given radius r_0 one can easily calculate their value at a different radius r_1 according to the formulas given below:

$$b_n(r_1) = \left(\frac{r_1}{r_0}\right)^{n-1} b_n(r_0) \quad a_n(r_1) = \left(\frac{r_1}{r_0}\right)^{n-1} a_n(r_0) \quad (2.29)$$

For example, let us assume that the value of the normal sextupole b_3 measured at the reference radius of $r_0 = 10$ mm is $1.42 \cdot 10^{-4}$.

$$b_3(r_0) = \frac{B_3(r_0)}{B_1} = 1.42 \cdot 10^{-4}$$

Thus if the value of the main dipole field is e.g. $B_1 = 8.36$ T the absolute value of the sextupole component of the magnetic field at the distance of 10 mm from the center of the aperture will be about 12 Gauss ($1.42 \cdot 10^{-4} \cdot 8.36 \text{ T} = 11.8712 \cdot 10^{-4} \text{ T} \approx 12 \cdot 10^{-4} \text{ T}$). The value of b_3 is positive, which means that the sextupole component of the magnetic field has the same direction as the dipole field, and on the median plane of the magnet ($\theta = 0$) the value of the sextupole will add up to the value of the dipole*. According to (2.29) the value of b_3 at $r_1 = 17$ mm will be,

$$b_3(r_1) = \frac{B_3(r_1)}{B_1} = 1.7^2 \cdot 1.42 \cdot 10^{-4} = 4.1038 \cdot 10^{-4}$$

which means that at the radius of 17 mm the absolute value of the sextupole component will amount already to 34.3 Gauss. Higher field harmonics, e.g. decapole b_5 , will scale with the distance as the power of 4. One can see how important it is to minimize the magnetic field errors in the magnet. Higher multipole errors present in the magnetic field may introduce a substantial distortion to the orbit of the particle beam circulating in the accelerator.

Remarks

In American literature the sum in the multipole field expansion starts with the index $n = 0$. The expansion given by Eqs. (2.27) in American notation would look as follows:

* The vector field geometry of different magnetic field harmonics will be discussed later in details.

$$B_r(r, \theta) = B_0 \sum_{n=0}^{\infty} \left(\frac{r}{r_0} \right)^n (b_n \sin n\theta + a_n \cos n\theta)$$

$$B_\theta(r, \theta) = B_0 \sum_{n=0}^{\infty} \left(\frac{r}{r_0} \right)^n (b_n \cos n\theta - a_n \sin n\theta)$$

The main reference dipole field is denoted here as B_0 . The relative multipole coefficients b_0 , b_1 , b_2 , correspond to the dipole, quadrupole, sextupole fields respectively. In general a multipole b_n in European notation corresponds to the multipole b_{n-1} in American notation.

Also the sign conventions vary in the literature throughout the world. For example a definition of the vector potential taken as (compare with Eq. 2.28)

$$A_z(r, \theta) = -B_1 r_0 \sum_{n=1}^{\infty} \frac{1}{n} \left(\frac{r}{r_0} \right)^n (b_n \cos n\theta + a_n \sin n\theta)$$

reverses the signs of the skew multipoles a_n in the multipole expansion (2.27). In expansion given by the formulas (2.27) a positive skew multipole causes that the radial component of the magnetic field is positive on the positive half OX axis, which is not the case when the sign of a_n is changed.

The situation with the reversed signs as compared to the expansion (2.27) is often encountered in the literature (see for example ref. [3]). The sign conventions and the multipole expansions used throughout this work are fully compatible with the specifications for the field error naming conventions recommended for the LHC magnets [7]. They are a natural consequence of the complex field expansion defined by Eq. (2.14), and constructed especially in order to satisfy the Cauchy-Riemann conditions.

2.4 Solution of the Laplace Equation for the Vector Potential

Laplace equation for the vector potential in two dimensions has the form of Eq. (2.13). It is valid only for the regions free of currents and magnetizing materials, which are the practical conditions inside the aperture of accelerator magnets. As it was shown before, the vector potential of a 2-D magnetic field has only one component A_z , dependent only on the x and y coordinates. Thus Eq. (2.13) written in the cylindrical coordinates takes the following form:

$$\nabla^2 A_z(r, \theta) = \frac{1}{r} \frac{\partial}{\partial r} \left(r \frac{\partial A_z}{\partial r} \right) + \frac{1}{r^2} \frac{\partial^2 A_z}{\partial \theta^2} = 0 \quad (2.30)$$

This partial differential equation can be solved with the method of separation of variables. Let us assume that the vector potential can be represented as the product of two functions dependent only on separated variables r and θ respectively:

$$A_z(r, \theta) = R(r)F(\theta) \quad (2.31)$$

Replacing the vector potential function in Eq. (2.30) with the expression (2.31) one obtains the following differential equation:

$$F \frac{1}{r} \frac{d}{dr} \left(r \frac{dR}{dr} \right) + R \frac{1}{r^2} \frac{d^2 F}{d\theta^2} = 0 \quad (2.32)$$

After dividing this equation by the product of R and F and multiplying by r^2 it becomes:

$$\frac{r}{R} \frac{d}{dr} \left(r \frac{dR}{dr} \right) + \frac{1}{F} \frac{d^2 F}{d\theta^2} = 0 \quad (2.33)$$

The first term in Eq. (2.33) is independent of the variable θ . At the same time the equation must be satisfied for all arbitrary values of angle θ covering the full cycle of $[0, 2\pi]$. This condition can be fulfilled only if the radial term under question is constant,

$$\frac{r}{R} \frac{d}{dr} \left(r \frac{dR}{dr} \right) = n^2$$

where the separation constant is expressed by n^2 . After several basic transformations this equation becomes:

$$r^2 \frac{d^2 R}{dr^2} + r \frac{dR}{dr} - Rn^2 = 0 \quad (2.34)$$

Eq (2.34) is a second order linear ordinary differential equation with variable coefficients. It can be transformed into a differential equation with constant coefficients by defining the following substitution:

$$r = e^{\xi} \Rightarrow \xi = \ln r$$

Then the derivatives of ξ with respect to r yield:

$$\frac{d\xi}{dr} = \frac{1}{r} \quad \frac{d^2\xi}{dr^2} = -\frac{1}{r^2}$$

And the corresponding derivatives of R with respect to r become:

$$\begin{aligned} \frac{dR}{dr} &= \frac{dR}{d\xi} \frac{d\xi}{dr} = \frac{dR}{d\xi} \frac{1}{r} \\ \frac{d^2R}{dr^2} &= \frac{d}{dr} \left(\frac{dR}{d\xi} \frac{d\xi}{dr} \right) = \frac{d^2R}{d\xi^2} \left(\frac{d\xi}{dr} \right)^2 + \frac{dR}{d\xi} \frac{d^2\xi}{dr^2} = \frac{1}{r^2} \left(\frac{d^2R}{d\xi^2} - \frac{dR}{d\xi} \right) \end{aligned} \quad (2.35)$$

Replacing the derivatives in Eq. (2.34) with the results of (2.35) a differential equation with constant coefficients is obtained, in which R is expressed as a function of the new variable ξ .

$$\frac{d^2R}{d\xi^2} - Rn^2 = 0$$

The general solution of this equation is:

$$R(\xi) = C_1 e^{n\xi} + C_2 e^{-n\xi}$$

And expressed as a function of the original variable r :

$$R(r) = C_1 r^n + C_2 r^{-n} \quad (2.36)$$

Now, replacing the radial term in Eq. (2.33) with the separation constant n^2 leads to the following differential equation for the function F :

$$\frac{d^2F}{d\theta^2} + n^2 F = 0 \quad (2.37)$$

The vector potential A_z is single valued; measured around the circle of radius r_0 it is a periodical function of the angle, i.e. $A_z(r_0, 0) = A_z(r_0, 2\pi)$. As a consequence the separation constant n must be an integer. The general solution of the equation (2.37) is:

$$F(\theta) = D_1 \sin n\theta + D_2 \cos n\theta \quad (2.38)$$

Finally, the general solution of the Laplace equation is the sum of products of the solutions (2.36) and (2.38) over all values of n :

$$A_z(r, \theta) = \sum_{n=1}^{\infty} (C_{1,n} r^n + C_{2,n} r^{-n}) (D_{1,n} \sin n\theta + D_{2,n} \cos n\theta) \quad (2.39)$$

If the solution for the current free area confined by the coils of the magnet is considered, A_z has to be finite in the middle of the aperture (for $r = 0$). Hence all of the $C_{2,n}$ coefficients must vanish. By introducing two new constants,

$$C_n = C_{1,n} \cdot D_{1,n}$$

$$D_n = C_{1,n} \cdot D_{2,n}$$

the vector potential can be rewritten as:

$$A_z(r, \theta) = \sum_{n=1}^{\infty} r^n (C_n \sin n\theta + D_n \cos n\theta) \quad (2.40)$$

Then the magnetic field components according to (2.7) are

$$\begin{aligned} B_r(r, \theta) &= \frac{1}{r} \frac{\partial A_z}{\partial \theta} = \sum_{n=1}^{\infty} n r^{n-1} (C_n \cos n\theta - D_n \sin n\theta) \\ B_\theta(r, \theta) &= -\frac{\partial A_z}{\partial r} = -\sum_{n=1}^{\infty} n r^{n-1} (C_n \sin n\theta + D_n \cos n\theta) \end{aligned} \quad (2.41)$$

The relations between the multipole coefficients introduced in (2.22) and the coefficients C_n and D_n are as follows

$$A_n(r) = C_n n r^{n-1} \quad B_n(r) = -D_n n r^{n-1} \quad (2.42)$$

Taking them into account we obtain the formulas in (2.23) derived in the previous section for the values of the radial and azimuthal magnetic field components at the reference radius r_0 .

2.5 Magnetic Field Harmonics of a Single Current Line Conductor

Let us calculate the magnetic field due to the conductor located in the air, running along the OZ axis and carrying the current I as shown in Fig. 2.5.

The normal component of the curl of the field intensity vector H is by definition:

$$(\nabla \times \vec{H})_n = \lim_{S \rightarrow 0} \frac{\oint \vec{H} d\vec{l}}{S}$$

This leads directly to the Stoke's theorem:

$$\iint_S (\nabla \times \vec{H}) d\vec{S} = \oint \vec{H} d\vec{l}$$

Using equations (2.1) and (2.3) without magnetization one obtains the Ampere's law:

$$\mu_0 \iint_S \vec{j} d\vec{S} = \mu_0 I = \oint \vec{B} d\vec{l} \quad (2.43)$$

Hence the azimuthal component of the magnetic field at the radius r is:

$$B_\theta \cdot 2\pi r = \mu_0 I \Rightarrow B_\theta(r, \theta) = \frac{\mu_0 I}{2\pi r} \quad (2.44)$$

And the axial component of the vector potential is:

$$A_z = - \int B_\theta dr = - \frac{\mu_0 I}{2\pi} \ln\left(\frac{r}{a}\right) \quad (2.45)$$

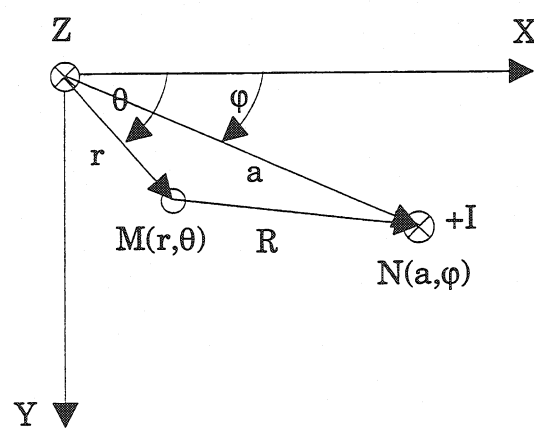


Figure 2.5 Single line conductor

The integration constant a is introduced into the natural logarithm in Eq. (2.45) to keep its argument dimensionless.

Next let us consider the magnetic field at point $M(r, \theta)$ due to the conductor with current I located at point $N(a, \varphi)$ (Fig. 2.6). From the cosine theorem:

$$R = \sqrt{r^2 + a^2 - 2ar \cos(\theta - \varphi)}$$

Figure 2.6 Single line conductor – general case

Then using Eqs. (2.44) and (2.45)

$$B_{\theta} = \frac{\mu_0 I}{2\pi R}$$

$$A_z(r, \theta) = -\frac{\mu_0 I}{2\pi} \ln\left(\frac{R}{a}\right) \quad (2.46)$$

Let us transform expression (2.46) using a multipole expansion to see which magnetic field harmonics are generated by a single current line. For the region $r < a$, using the Euler's equation,

$$e^{iz} = \cos z + i \sin z \Rightarrow \cos z = \frac{e^{iz} + e^{-iz}}{2}$$

it is convenient to express R in the following form:

$$\begin{aligned} R^2 &= a^2 + r^2 - 2ar \cos(\theta - \varphi) = a^2 + r^2 - ar(e^{i(\theta-\varphi)} + e^{-i(\theta-\varphi)}) = \\ &= a^2 \left(1 + \frac{r^2}{a^2} - \frac{r}{a} (e^{i(\theta-\varphi)} + e^{-i(\theta-\varphi)}) \right) = a^2 \left(1 - \frac{r}{a} e^{i(\theta-\varphi)} \right) \left(1 - \frac{r}{a} e^{-i(\theta-\varphi)} \right) \end{aligned}$$

Then

$$\ln \frac{R}{a} = \frac{1}{2} \left[\ln \left(1 - \frac{r}{a} e^{i(\theta-\varphi)} \right) + \ln \left(1 - \frac{r}{a} e^{-i(\theta-\varphi)} \right) \right]$$

The Taylor expansion of natural logarithm,

$$\ln(1-z) = -z - \frac{1}{2}z^2 - \frac{1}{3}z^3 - \dots - \frac{1}{n}z^n = -\sum_{n=1}^{\infty} \frac{z^n}{n}$$

is valid for $z \in \mathcal{C}$ and $|z| < 1$. Thus,

$$\ln \frac{R}{a} = -\frac{1}{2} \left[\sum_{n=1}^{\infty} \frac{\left(\frac{r}{a} e^{i(\theta-\varphi)} \right)^n}{n} + \sum_{n=1}^{\infty} \frac{\left(\frac{r}{a} e^{-i(\theta-\varphi)} \right)^n}{n} \right] = -\sum_{n=1}^{\infty} \frac{1}{n} \left(\frac{r}{a} \right)^n \cos n(\theta - \varphi)$$

The vector potential (2.46) becomes:

$$A_z(r, \theta) = \frac{\mu_0 I}{2\pi} \sum_{n=1}^{\infty} \frac{1}{n} \left(\frac{r}{a} \right)^n \cos n(\theta - \varphi) \quad (2.47)$$

And the magnetic field components are:

$$\begin{aligned}
B_r(r, \theta) &= \frac{1}{r} \frac{\partial A_z}{\partial \theta} = -\frac{\mu_0 I}{2\pi r} \sum_{n=1}^{\infty} \left(\frac{r}{a}\right)^n \sin n(\theta - \varphi) = -\frac{\mu_0 I}{2\pi a} \sum_{n=1}^{\infty} \left(\frac{r}{a}\right)^{n-1} \sin n(\theta - \varphi) \\
B_\theta(r, \theta) &= -\frac{\partial A_z}{\partial r} = -\frac{\mu_0 I}{2\pi a} \sum_{n=1}^{\infty} \left(\frac{r}{a}\right)^{n-1} \cos n(\theta - \varphi) \\
B_z(r, \theta) &= 0
\end{aligned} \tag{2.48}$$

For the magnetic field calculations in the region $r > a$ it is convenient to write down R in the following form:

$$\begin{aligned}
R^2 &= r^2 \left(1 - \frac{a}{r} e^{i(\theta - \varphi)}\right) \left(1 - \frac{a}{r} e^{-i(\theta - \varphi)}\right) \\
\ln R &= \ln r + \frac{1}{2} \left[\ln \left(1 - \frac{a}{r} e^{i(\theta - \varphi)}\right) + \ln \left(1 - \frac{a}{r} e^{-i(\theta - \varphi)}\right) \right] // + \ln \frac{1}{a} \\
\ln \frac{R}{a} &= \ln \frac{r}{a} + \frac{1}{2} \left[\ln \left(1 - \frac{a}{r} e^{i(\theta - \varphi)}\right) + \ln \left(1 - \frac{a}{r} e^{-i(\theta - \varphi)}\right) \right] = \ln \frac{r}{a} - \sum_{n=1}^{\infty} \frac{1}{n} \left(\frac{a}{r}\right)^n \cos n(\theta - \varphi)
\end{aligned}$$

Then

$$\begin{aligned}
A_z(r, \theta) &= -\frac{\mu_0 I}{2\pi} \ln \left(\frac{r}{a}\right) + \frac{\mu_0 I}{2\pi} \sum_{n=1}^{\infty} \frac{1}{n} \left(\frac{a}{r}\right)^n \cos n(\theta - \varphi) \\
B_r(r, \theta) &= -\frac{\mu_0 I}{2\pi r} \sum_{n=1}^{\infty} \left(\frac{a}{r}\right)^n \sin n(\theta - \varphi) = -\frac{\mu_0 I}{2\pi a} \sum_{n=1}^{\infty} \left(\frac{a}{r}\right)^{n+1} \sin n(\theta - \varphi) \\
B_\theta(r, \theta) &= \frac{\mu_0 I}{2\pi r} + \frac{\mu_0 I}{2\pi} \sum_{n=1}^{\infty} \frac{a^n}{r^{n+1}} \cos n(\theta - \varphi) = \frac{\mu_0 I}{2\pi r} + \frac{\mu_0 I}{2\pi a} \sum_{n=1}^{\infty} \left(\frac{a}{r}\right)^{n+1} \cos n(\theta - \varphi) \\
B_z(r, \theta) &= 0
\end{aligned} \tag{2.50}$$

In both regions all of the field harmonics are present in the magnetic field generated by a single current line.

2.6 Pure Multipole Field Generation

A single current line considered in the previous paragraph generates multipole fields of any order. To see how one can generate pure multipole fields by means of current distribution let us consider an arrangement of the current leads mounted around a cylinder of radius a (Fig. 2.7). Let us assume that the current flowing in the conductors in the direction of the axis OZ has the following distribution expressed as a function of the azimuthal angle φ : $I(\varphi) = I_0 \cos(m\varphi)$, where m is an integer.

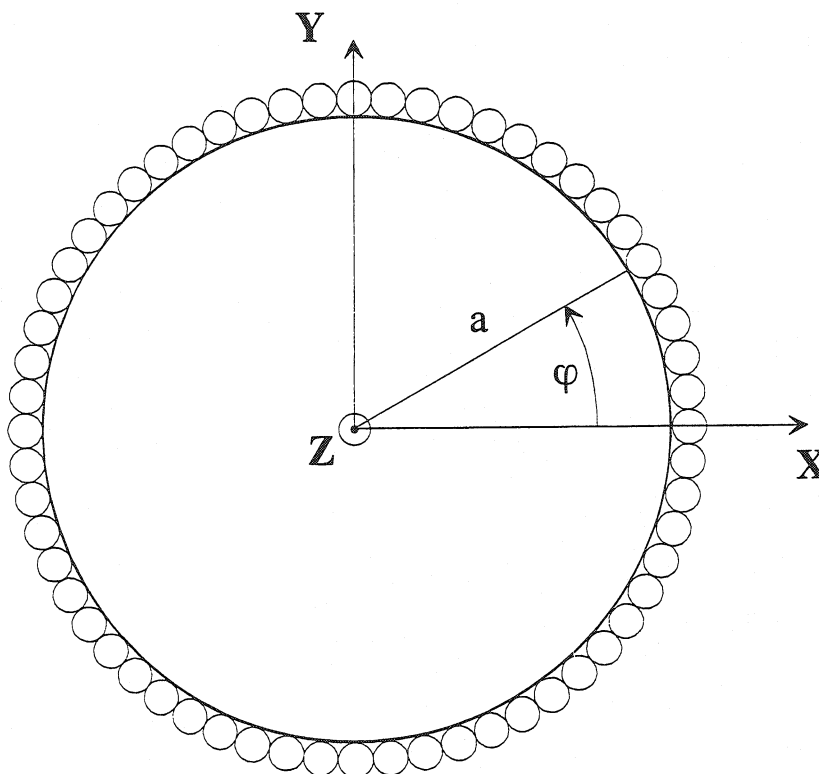


Figure 2.7 Single current lines mounted around the cylinder of radius a

The vector potential for the given current distribution (in the region $r < a$) is according to the formula (2.47):

$$A_z(r, \theta) = \frac{\mu_0 I_0}{2\pi} \sum_{n=1}^{\infty} \frac{1}{n} \left(\frac{r}{a} \right)^n \int_0^{2\pi} \cos m\varphi \cos n(\theta - \varphi) d\varphi$$

$$\int_0^{2\pi} \cos m\varphi \cos n(\theta - \varphi) d\varphi = \cos n\theta \int_0^{2\pi} \cos m\varphi \cos n\varphi d\varphi + \sin n\theta \int_0^{2\pi} \cos m\varphi \sin n\varphi d\varphi$$

Taking the orthogonality relations of the trigonometric functions into account,

$$\int_0^{2\pi} \cos m\varphi \cos n\varphi d\varphi = \pi \delta_{m,n}$$

$$\int_0^{2\pi} \cos m\varphi \sin n\varphi d\varphi = 0$$

A_z is reduced to:

$$A_z(r, \theta) = \frac{\mu_0 I_0}{2\pi} \frac{1}{m} \left(\frac{r}{a} \right)^m \pi \cos m\theta = \frac{\mu_0 I_0}{2} \frac{1}{m} \left(\frac{r}{a} \right)^m \cos m\theta \quad (2.51)$$

And the corresponding magnetic field components are:

$$B_\theta(r, \theta) = -\frac{\mu_0 I_0}{2a} \left(\frac{r}{a} \right)^{m-1} \cos m\theta$$

$$B_r(r, \theta) = -\frac{\mu_0 I_0}{2r} \left(\frac{r}{a} \right)^m \sin m\theta = -\frac{\mu_0 I_0}{2a} \left(\frac{r}{a} \right)^{m-1} \sin m\theta \quad (2.52)$$

One can see that the suggested $\cos(m\varphi)$ current distribution leads to the generation of a pure multipole component of the order $n = m$ only. All other multipole terms of the magnetic field vanish.

The transformation of the field components from the cylindrical to Cartesian coordinates is achieved with the following matrix:

$$\begin{bmatrix} B_x \\ B_y \end{bmatrix} = \begin{bmatrix} \cos \theta & -\sin \theta \\ \sin \theta & \cos \theta \end{bmatrix} \cdot \begin{bmatrix} B_r \\ B_\theta \end{bmatrix} = \begin{bmatrix} B_r \cos \theta - B_\theta \sin \theta \\ B_r \sin \theta + B_\theta \cos \theta \end{bmatrix} \quad (2.53)$$

1. For $m = 1$ the current distribution is $I(\varphi) = I_0 \cos \varphi$

According to Eqs. (2.52) and (2.53) the corresponding magnetic field components in Cartesian coordinate system are:

$$B_x = B_r \cos \theta - B_\theta \sin \theta = 0$$

$$B_y = B_r \sin \theta + B_\theta \cos \theta = -\frac{\mu_0 I_0}{2a} \sin^2 \theta - \frac{\mu_0 I_0}{2a} \cos^2 \theta = -\frac{\mu_0 I_0}{2a} = \text{const.}$$

Thus for $m = 1$ a constant magnetic field in OY direction is obtained, therefore $m = 1$ corresponds to a pure dipole field (Fig. 2.8).

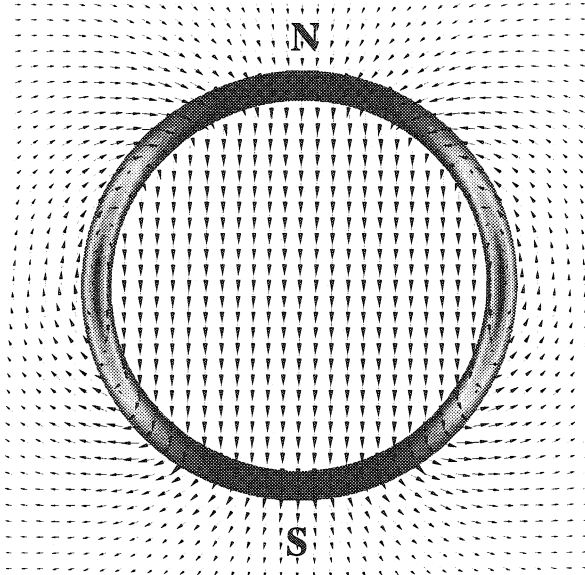


Figure 2.8 Pure normal dipole field (b₁)

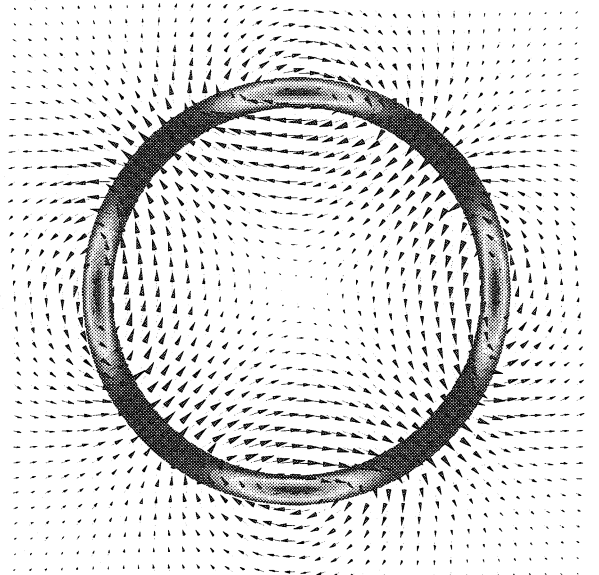


Figure 2.9 Pure normal quadrupole field (b₂)

2. For $m = 2$ the current distribution is $I(\varphi) = I_0 \cos 2\varphi$

$$B_r(r, \theta) = -\frac{\mu_0 I_0}{2a^2} r \sin 2\theta \quad B_\theta(r, \theta) = -\frac{\mu_0 I_0}{2a^2} r \cos 2\theta$$

The field gradient is: $g = \left. \frac{\partial B_r}{\partial r} \right|_{\theta=\frac{\pi}{4}} = -\frac{\mu_0 I_0}{2a^2}$

In Cartesian coordinates

$$B_x = gr \sin 2\theta \cos \theta - gr \cos 2\theta \sin \theta = gr(\sin 2\theta \cos \theta - \cos 2\theta \sin \theta) = gr \sin \theta = gy$$

$$B_y = gr(\sin 2\theta \sin \theta + \cos 2\theta \cos \theta) = gr \cos \theta = gx$$

The vector field specified by these two components is plotted in Fig. 2.9. It corresponds to a **pure quadrupole field**. In the median plane of the beam pipe, i.e. for $y = 0$ only the B_y component of the field exists. Moreover, it changes its sign while passing from the negative to the positive OX half-axis. This feature is characteristic for the vector field geometry of all of the normal even order field harmonics.

3. For $m = 3$ the current distribution is $I(\varphi) = I_0 \cos 3\varphi$

$$B_r(r, \theta) = -\frac{\mu_0 I_0}{2a^3} r^2 \sin 3\theta \quad B_\theta(r, \theta) = -\frac{\mu_0 I_0}{2a^3} r^2 \cos 3\theta$$

$$g = \left. \frac{\partial B_r}{\partial r} \right|_{\theta=\frac{\pi}{6}} = -\frac{\mu_0 I_0}{a^3} r = g'r \quad g' = -\frac{\mu_0 I_0}{a^3}$$

$$B_x = \frac{1}{2} g' r^2 \sin 3\theta \cos \theta - \frac{1}{2} g' r^2 \cos 3\theta \sin \theta = \frac{1}{2} g' r^2 (\sin 3\theta \cos \theta - \cos 3\theta \sin \theta) =$$

$$= \frac{1}{2} g' r^2 \sin 2\theta = g' r^2 \sin \theta \cos \theta = g' xy$$

$$B_y = \frac{1}{2} g' r^2 (\sin 3\theta \sin \theta + \cos 3\theta \cos \theta) = \frac{1}{2} g' r^2 \cos 2\theta = \frac{1}{2} g' r^2 (\cos^2 \theta - \sin^2 \theta) = \frac{1}{2} g' (x^2 - y^2)$$

For $m = 3$ a **pure sextupole field** is obtained (Fig. 2.10). In this case, as well as for all of the odd order normal multipoles, the B_y component of the magnetic field in the median plane (i.e. for $y = 0$) does not change its sign while passing from the negative to the positive OX half-axis.

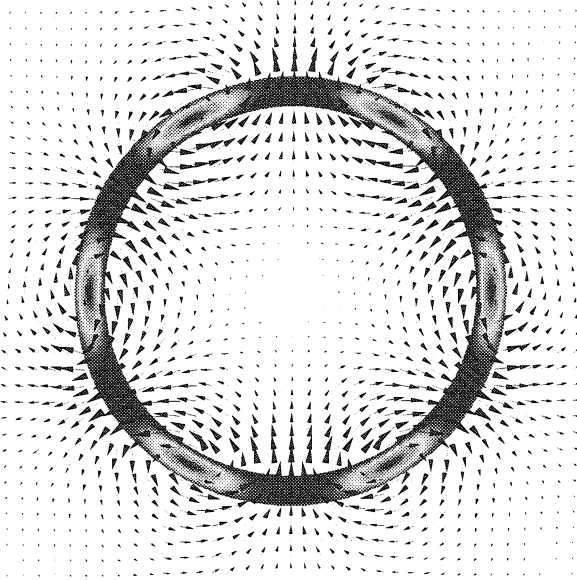


Figure 2.10 Pure normal sextupole field (b_3)

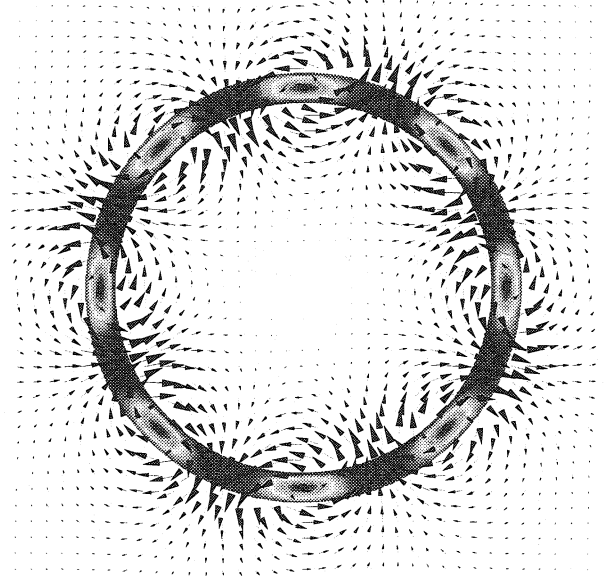


Figure 2.11 Pure normal octupole field (b_4)

4. For $m = 4$ the current distribution is $I(\varphi) = I_0 \cos 4\varphi$

$$B_r(r, \theta) = -\frac{\mu_0 I_0}{2a^4} r^3 \sin 4\theta \quad B_\theta(r, \theta) = -\frac{\mu_0 I_0}{2a^4} r^3 \cos 4\theta$$

$$g = \left. \frac{\partial B_r}{\partial r} \right|_{\theta=\frac{\pi}{8}} = -\frac{3}{2} \frac{\mu_0 I_0}{a^4} r^2 = g'' r^2 \quad g'' = -\frac{3}{2} \frac{\mu_0 I_0}{a^4}$$

$$B_x = \frac{1}{3} g'' r^3 \sin 4\theta \cos \theta - \frac{1}{3} g'' r^2 \cos 4\theta \sin \theta = \frac{1}{3} g'' r^3 (\sin 4\theta \cos \theta - \cos 4\theta \sin \theta) =$$

$$= \frac{1}{3} g'' r^3 \sin 3\theta = \frac{1}{3} g'' r^3 (3 \sin \theta \cos^2 \theta - \sin^3 \theta) = \frac{1}{3} g'' (3x^2 y - y^3)$$

$$\begin{aligned}
B_y &= \frac{1}{3} g'' r^3 (\sin 4\theta \sin \theta + \cos 4\theta \cos \theta) = \frac{1}{3} g'' r^3 \cos 3\theta = \\
&= \frac{1}{3} g'' r^3 (\cos^3 \theta - 3 \sin^2 \theta \cos \theta) = \frac{1}{3} g'' (x^3 - 3xy^2)
\end{aligned}$$

For $m = 4$ a pure octupole field is generated (Fig. 2.11). In a similar way for $m = 5$ a pure decapole field can be obtained, etc.

The notion of the normal and skew field multipoles was already introduced in section 2.2. In the formulas for the multipole expansion of the vector potential, e.g. in Eq. (2.28), the coefficients of $\cos(n\theta)$ terms denoted as b_n (or B_n depending on the fact if they are related or not to the reference magnetic field) always represent normal fields, whereas the coefficients of $\sin(n\theta)$ terms denoted as a_n (or A_n) correspond to skew fields. The same is valid for the vector potential expansion (2.47), which can be rewritten as:

$$\begin{aligned}
A_z(r, \theta) &= \frac{\mu_0 I}{2\pi} \sum_{n=1}^{\infty} \frac{1}{n} \left(\frac{r}{a} \right)^n \cos n(\theta - \varphi) = -\frac{\mu_0 I}{2\pi} \sum_{n=1}^{\infty} \frac{1}{n} \left(\frac{r}{a} \right)^n (-\cos n\theta \cos n\varphi - \sin n\theta \sin n\varphi) = \\
&= -\sum_{n=1}^{\infty} \frac{r^n}{n} (\mathcal{B}_n \cos n\theta - \mathcal{A}_n \sin n\theta) = -r \sum_{n=1}^{\infty} \frac{1}{n} (B_n(r) \cos n\theta + A_n(r) \sin n\theta) \quad (2.54)
\end{aligned}$$

In this way the multipole coefficients in Eq. (2.54) correspond exactly to the ones defined in section 2.2. All of the pure multipoles analyzed for the $I(\varphi) = I_0 \cos m\varphi$ current distribution are normal fields. If the current distribution around the cylinder in Fig. (2.7) is rotated by an angle of $\pi/2m$ a current distribution of $I(\varphi) = I_0 \sin m\varphi$, leading to the skew multipoles, is obtained. The vector potential is then proportional to $\sin(m\theta)$:

$$A_z(r, \theta) = \frac{\mu_0 I_0}{2\pi} \sum_{n=1}^{\infty} \frac{1}{n} \left(\frac{r}{a} \right)^n \int_0^{2\pi} \sin m\varphi \cos n(\theta - \varphi) d\varphi = \frac{\mu_0 I_0}{2} \frac{1}{m} \left(\frac{r}{a} \right)^m \sin m\theta \quad (2.55)$$

The field components are:

$$\begin{aligned}
B_r(r, \theta) &= \frac{\mu_0 I_0}{2a} \left(\frac{r}{a} \right)^{m-1} \cos m\theta \\
B_\theta(r, \theta) &= -\frac{\mu_0 I_0}{2a} \left(\frac{r}{a} \right)^{m-1} \sin m\theta
\end{aligned}$$

Let us calculate the case for a skew dipole ($m = 1$)

$$\begin{aligned}
B_r(r, \theta) &= \frac{\mu_0 I_0}{2a} \cos \theta & B_\theta(r, \theta) &= -\frac{\mu_0 I_0}{2a} \sin \theta
\end{aligned}$$

$$B_x = B_r \cos \theta - B_\theta \sin \theta = \frac{\mu_0 I_0}{2a} (\sin^2 \theta + \cos^2 \theta) = \frac{\mu_0 I_0}{2a} = \text{const.}$$

$$B_y = B_r \sin \theta + B_\theta \cos \theta = 0$$

A skew dipole generates a constant horizontal field (Fig. 2.12). Such magnets are used in particle accelerators as the corrector magnets adjusting the orbit of the particle beam in the vertical plane. The results for the pure normal and skew multipoles up to $n = 4$ are listed in Table 2.1.

Table 2.1 Cartesian field components of the pure multipoles

Multipoles	B_x	B_y
Normal dipole (b_1)	0	const.
Skew dipole (a_1)	- const.	0
Normal quadrupole (b_2)	gy	gx
Skew quadrupole (a_2)	$-gx$	gy
Normal sextupole (b_3)	$g'xy$	$\frac{1}{2}g'(x^2 - y^2)$
Skew sextupole (a_3)	$-\frac{1}{2}g'(x^2 - y^2)$	$g'xy$
Normal octupole (b_4)	$\frac{1}{3}g''(3x^2y - y^3)$	$\frac{1}{3}g''(x^3 - 3xy^2)$
Skew octupole (a_4)	$-\frac{1}{3}g''(x^3 - 3xy^2)$	$\frac{1}{3}g''(3x^2y - y^3)$

The remaining skew field patterns are shown in Figures 2.13-2.15. In the horizontal median plane only the B_x component of the skew multipoles is present. For all of the odd orders of the skew harmonics this component has the same sign along the OX axis. For all of the even orders of the skew multipoles B_x changes its sign in the middle of the median plane (at $x = 0$).

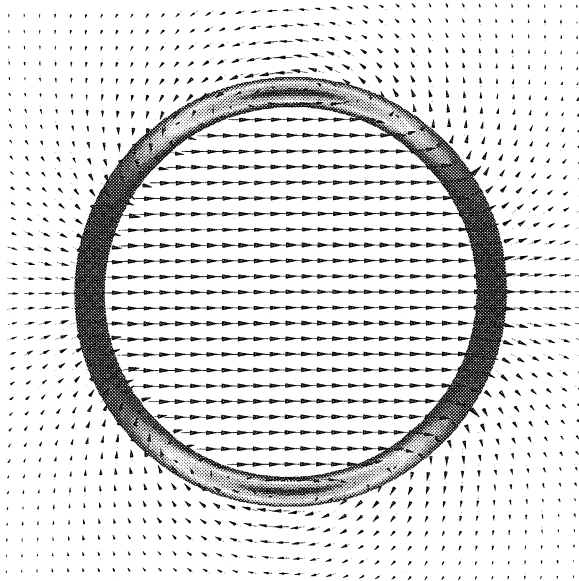


Figure 2.12 Pure skew dipole field (a_1)

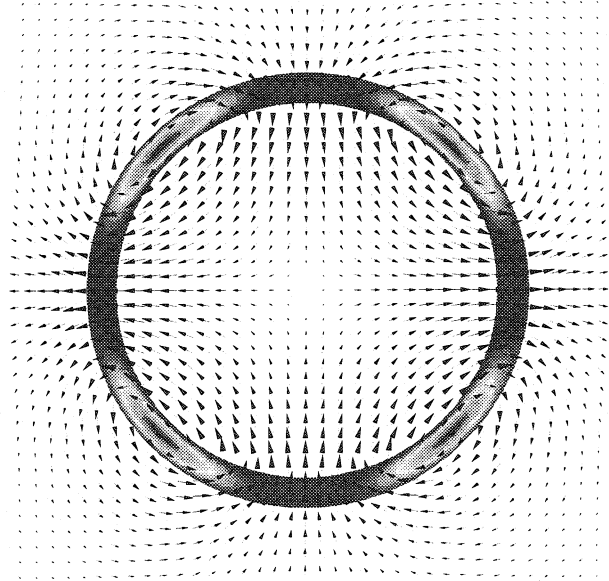


Figure 2.13 Pure skew quadrupole field (a_2)

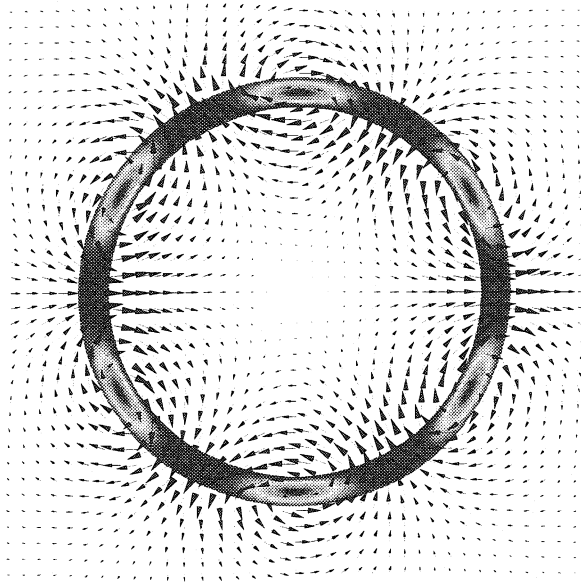


Figure 2.14 Pure skew sextupole field (a_3)

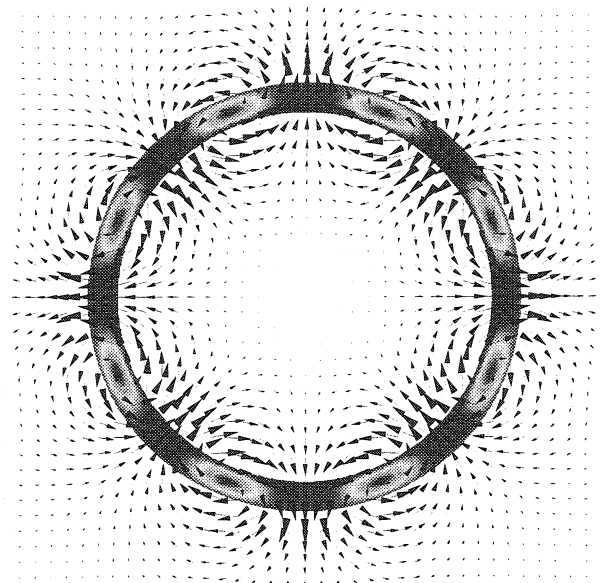


Figure 2.15 Pure skew octupole field (a_4)

2.7 Current Shell Approximation

In practice the ideal current distribution with cosine dependence can be approximated by an arrangement of current shells with uniform current density. The field at point $M(r, \theta)$ due to a symmetric $2m$ -pole magnet ($m = 1$ for a dipole magnet, $m = 2$ for a quadrupole magnet, $m = 3$ for a sextupole magnet, etc.) can be sufficiently approximated by current shells. In order to implement this model, the XY plane has to be divided into $2m$ regions (corresponding to $2m$ poles of the magnet) with the conductors located at points:

$$C_1(a, \varphi), C_2(a, \pi/m - \varphi), C_3(a, \pi/m + \varphi), C_4(a, 2\pi/m - \varphi), \\ C_5(a, 2\pi/m + \varphi), \dots, C_{4m}(a, 2m \cdot \pi/m - \varphi),$$

each of them carrying currents $+I, -I, -I, +I, +I, \dots, +I$, respectively (Fig. 2.16).

- The vector potential at the point $M(r, \theta)$ inside the aperture of the magnet ($r < a$) calculated using Eq. (2.47) is:

$$A_z(r, \theta) = \frac{\mu_0 I}{2\pi} \sum_{n=1}^{\infty} \frac{1}{n} \left(\frac{r}{a} \right)^n \sum_{k=0}^{2m-1} (-1)^k \left[\cos n \left(k \frac{\pi}{m} - \varphi - \theta \right) + \cos n \left(k \frac{\pi}{m} + \varphi - \theta \right) \right]$$

The sum of the two cosine terms in the brackets yields:

$$2 \cos n \left(k \frac{\pi}{m} - \theta \right) \cos n \varphi = 2 \cos n \varphi \left(\cos nk \frac{\pi}{m} \cos n \theta + \sin nk \frac{\pi}{m} \sin n \theta \right)$$

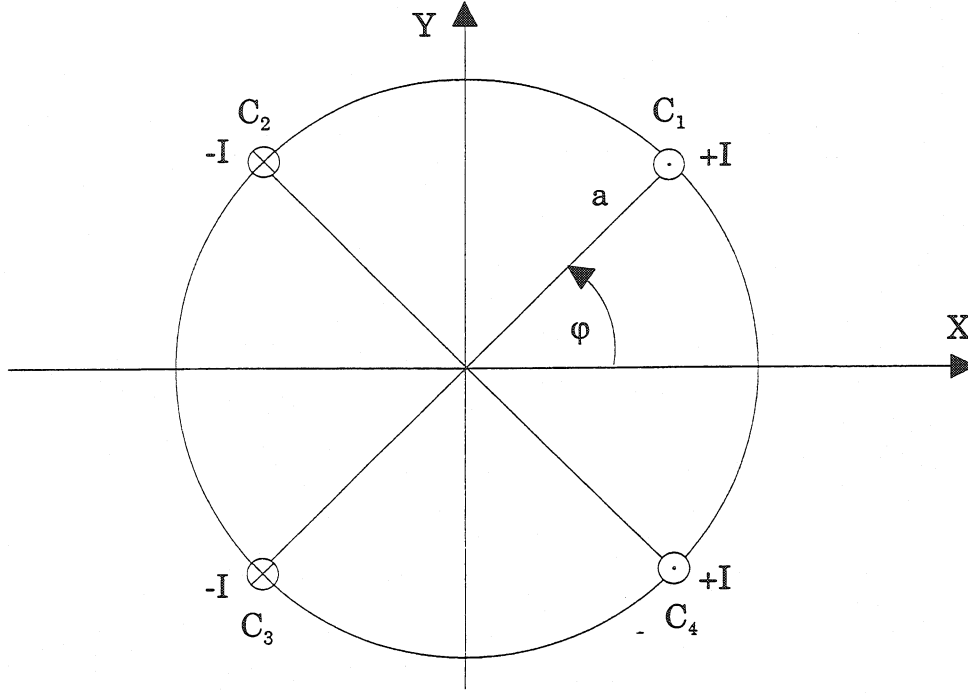


Figure 2.16 Position of the conductors in the approximation for dipole geometry

Thus

$$A_z(r, \theta) = \frac{\mu_0 I}{\pi} \sum_{n=1}^{\infty} \frac{1}{n} \left(\frac{r}{a} \right)^n \cos n\varphi \sum_{k=0}^{2m-1} (-1)^k \left(\cos nk \frac{\pi}{m} \cos n\theta + \sin nk \frac{\pi}{m} \sin n\theta \right)$$

For a dipole coil $m = 1$, and the sum over index k is simplified to:

$$\begin{cases} \sin nk\pi = 0 & \text{for } n \in \mathbb{N} \\ \sum_{k=0}^1 (-1)^k \cos nk\pi \cos n\theta = \begin{cases} 0 & \text{for } n = 2l & \text{where } l \in \mathbb{N} \\ 2 \cos n\theta & \text{for } n = 2l + 1 & \text{where } l \in \mathbb{N} \end{cases} \end{cases}$$

As a result A_z is reduced to:

$$A_z(r, \theta) = \frac{2\mu_0 I}{\pi} \sum_{n=2l+1} \frac{1}{n} \left(\frac{r}{a} \right)^n \cos n\varphi \cos n\theta \quad (2.55)$$

As one can see a coil with dipole symmetry generates only the multipoles proportional to the $\cos(n\theta)$ terms, i.e. normal multipoles only.. Moreover, the orders of the multipoles are odd numbers only. None of the even order harmonics are present in the expansion (2.55).

- The vector potential at point $M(r, \theta)$ outside the aperture of the magnet, calculated using Eq. (2.49) is:

$$A_z(r, \theta) = \frac{\mu_0 I}{2\pi} \sum_{n=1}^{\infty} \frac{1}{n} \left(\frac{a}{r} \right)^n \sum_{k=0}^{2m-1} (-1)^k \left[\cos n \left(k \frac{\pi}{m} - \varphi - \theta \right) + \cos n \left(k \frac{\pi}{m} + \varphi - \theta \right) \right]$$

The same calculation procedure applied for the region $r > a$ leads to the result:

$$A_z(r, \theta) = \frac{2\mu_0 I}{\pi} \sum_{n=2l+1}^{\infty} \frac{1}{n} \left(\frac{a}{r} \right)^n \cos n\varphi \cos n\theta \quad (2.56)$$

The simplest current shell arrangement for a dipole coil is shown in Fig. 2.17. Let us assume that the current density in the shell is constant ($J = J_0$). Then $dI = J_0 a \cdot da \cdot d\varphi$. An angle φ_1 is the limiting angle of the current shell, a_1 and a_2 indicate its inner and outer radii, respectively. The vector potential due to the coil with dipole geometry is then calculated by integrating A_z over the radial and angular extent of the current shell.

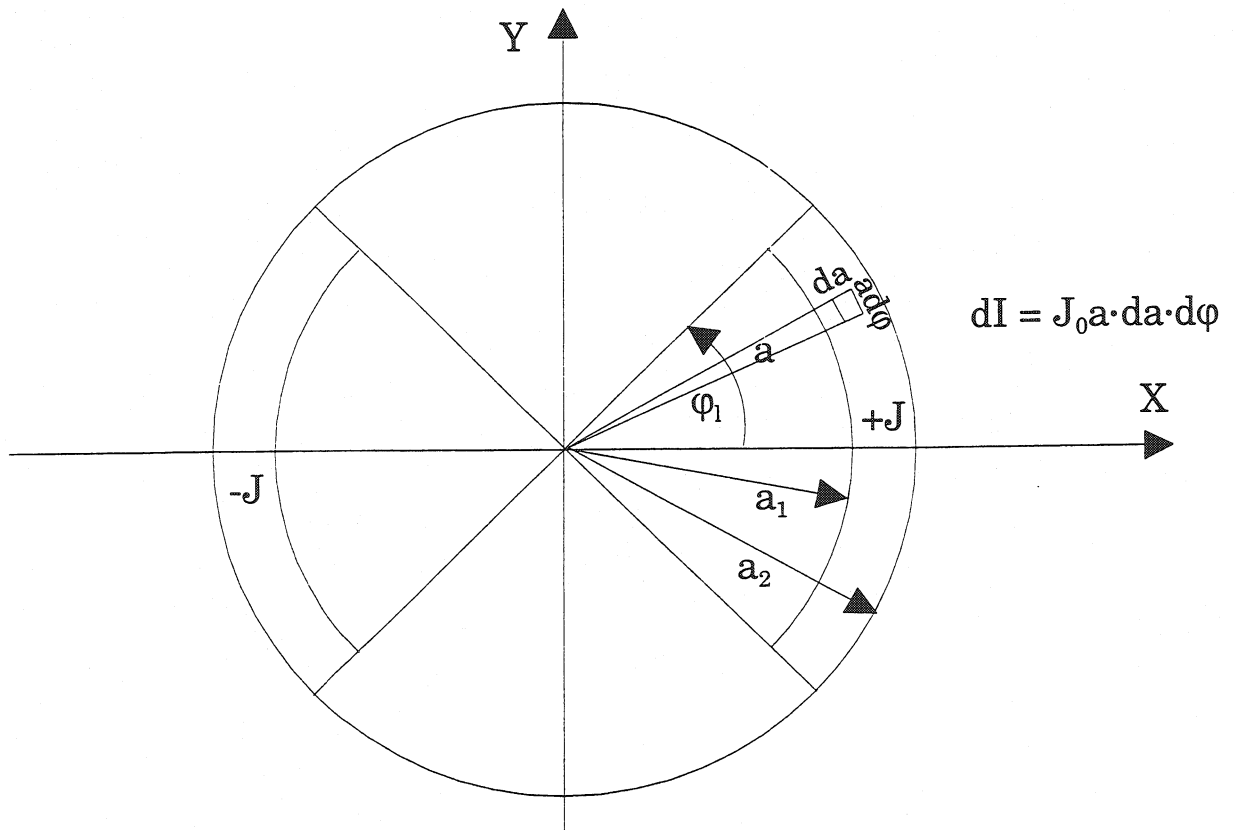


Figure 2.17 Current shell configuration for dipole geometry

- For the region inside the aperture ($r < a_1$)

$$\begin{aligned}
 A_z(r, \theta) &= \frac{2\mu_0 J_0}{\pi} \sum_{n=2l+1} \frac{1}{n} \cos n\theta \int_{a_1}^{a_2} \int_0^{\varphi_l} \left(\frac{r}{a}\right)^n a \cos n\varphi \, da \, d\varphi = \frac{2\mu_0 J_0}{\pi} \sum_{n=2l+1} \frac{r^n \cos n\theta}{n^2} \sin n\varphi_l \int_{a_1}^{a_2} \frac{da}{a^{n-1}} = \\
 &= \frac{2\mu_0 J_0}{\pi} \sum_{n=2l+1} \frac{r^n}{n^2(n-2)} \left(\frac{1}{a_1^{n-2}} - \frac{1}{a_2^{n-2}} \right) \cos n\theta \sin n\varphi_l
 \end{aligned} \quad (2.57)$$

The multipole components of the magnetic field are:

$$\begin{aligned}
 B_{r,n}(r, \theta) &= -\frac{2\mu_0 J_0}{\pi} \frac{r^{n-1}}{n(n-2)} \left(\frac{1}{a_1^{n-2}} - \frac{1}{a_2^{n-2}} \right) \sin n\theta \sin n\varphi_l \\
 B_{\theta,n}(r, \theta) &= -\frac{2\mu_0 J_0}{\pi} \frac{r^{n-1}}{n(n-2)} \left(\frac{1}{a_1^{n-2}} - \frac{1}{a_2^{n-2}} \right) \cos n\theta \sin n\varphi_l
 \end{aligned} \quad (2.58)$$

The magnitude of the B_n -th ($n = 1, 3, 5 \dots$) component of the magnetic field is:

$$B_n = \sqrt{B_{r,n}^2 + B_{\theta,n}^2} = \frac{2\mu_0 J_0}{\pi} \frac{r^{n-1}}{n(n-2)} \left(\frac{1}{a_1^{n-2}} - \frac{1}{a_2^{n-2}} \right) |\sin n\varphi_l| \quad (2.59)$$

On the median plane of the magnet ($\theta = 0$) the radial component becomes zero and B_n is obtained including its sign relative to the main dipole field B_l :

$$B_n = B_{\theta,n}(r, 0) = -\frac{2\mu_0 J_0}{\pi} \frac{r^{n-1}}{n(n-2)} \left(\frac{1}{a_1^{n-2}} - \frac{1}{a_2^{n-2}} \right) \sin n\varphi_l \quad (2.60)$$

- For the region outside the aperture ($r > a_2$)

$$\begin{aligned}
 A_z(r, \theta) &= \frac{2\mu_0 J_0}{\pi} \sum_{n=2l+1} \frac{1}{n} \cos n\theta \int_{a_1}^{a_2} \int_0^{\varphi_l} \left(\frac{a}{r}\right)^n a \cos n\varphi \, da \, d\varphi = \frac{2\mu_0 J_0}{\pi} \sum_{n=2l+1} \frac{\cos n\theta}{n^2 r^n} \sin n\varphi_l \int_{a_1}^{a_2} a^{n+1} da = \\
 &= \frac{2\mu_0 J_0}{\pi} \sum_{n=2l+1} \frac{1}{n^2(n+2)r^n} (a_2^{n+2} - a_1^{n+2}) \cos n\theta \sin n\varphi_l
 \end{aligned} \quad (2.61)$$

The multipole components are:

$$B_{r,n}(r, \theta) = -\frac{2\mu_0 J_0}{\pi} \frac{1}{n(n+2)r^{n+1}} (a_2^{n+2} - a_1^{n+2}) \sin n\theta \sin n\varphi_l$$

$$B_{\theta,n}(r,\theta) = \frac{2\mu_0 J_0}{\pi} \frac{1}{n(n+2)r^{n+1}} (a_2^{n+2} - a_1^{n+2}) \cos n\theta \sin n\varphi_l \quad (2.62)$$

- For the coil region inside the current shell ($a_1 \leq r \leq a_2$)

$$\begin{aligned} A_z(r,\theta) &= \frac{2\mu_0 J_0}{\pi} \sum_{n=2l+1} \frac{1}{n} \cos n\theta \int_{a_1}^r \int_0^{\varphi_l} \left(\frac{a}{r}\right)^n a \cos n\varphi \, da \, d\varphi + \\ &+ \frac{2\mu_0 J_0}{\pi} \sum_{n=2l+1} \frac{1}{n} \cos n\theta \int_r^{a_2} \int_0^{\varphi_l} \left(\frac{r}{a}\right)^n a \cos n\varphi \, da \, d\varphi = \\ &= \frac{2\mu_0 J_0}{\pi} \sum_{n=2l+1} \frac{\cos n\theta \sin n\varphi_l}{n^2} \left[\frac{1}{(n+2)r^{n+1}} (r^{n+2} - a_1^{n+2}) + \frac{r^n}{n-2} \left(\frac{1}{r^{n-2}} - \frac{1}{a_2^{n-2}} \right) \right] \end{aligned} \quad (2.63)$$

And the multipole components are:

$$\begin{aligned} B_{r,n}(r,\theta) &= -\frac{2\mu_0 J_0}{\pi} \frac{\sin n\theta \sin n\varphi_l}{n} \left[\frac{1}{(n+2)r^{n+1}} (r^{n+2} - a_1^{n+2}) + \frac{r^{n-1}}{n-2} \left(\frac{1}{r^{n-2}} - \frac{1}{a_2^{n-2}} \right) \right] \\ B_{\theta,n}(r,\theta) &= \frac{2\mu_0 J_0}{\pi} \frac{\cos n\theta \sin n\varphi_l}{n} \left[\frac{1}{(n+2)r^{n+1}} (r^{n+2} - a_1^{n+2}) - \frac{r^{n-1}}{n-2} \left(\frac{1}{r^{n-2}} - \frac{1}{a_2^{n-2}} \right) \right] \end{aligned} \quad (2.64)$$

Let us come back to the magnetic field in the aperture of the magnet. The dipole term B_l in a median plane is evaluated for $n = 1$ using formula (2.60)

$$B_l = B_{\theta,1}(r,0) = -\frac{2\mu_0 J_0}{\pi} (a_2 - a_1) \sin \varphi_l \quad (2.65)$$

The ratio of the n -th term of the multipole expansion to the dipole field component is:

$$\begin{aligned} \frac{B_n}{B_l} &= \frac{\frac{r^{n-1}}{n(n-2)} \left(\frac{1}{a_1^{n-2}} - \frac{1}{a_2^{n-2}} \right) \sin n\varphi_l}{(a_2 - a_1) \sin \varphi_l} = \frac{r^{n-1}}{n(n-2)(a_2 - a_1)} \left(\frac{a_2^{n-2} - a_1^{n-2}}{(a_1 a_2)^{n-2}} \right) \frac{\sin n\varphi_l}{\sin \varphi_l} = \\ &= \frac{r^{n-1} (a_2 - a_1)}{n(n-2)(a_2 - a_1)} \frac{\sum_{k=0}^{n-3} a_2^{n-3-k} a_1^k}{(a_1 a_2)^{n-2}} \frac{\sin n\varphi_l}{\sin \varphi_l} = \frac{r^{n-1}}{n(n-2)} \frac{1}{\sum_{k=0}^{n-3} a_2^{k+1} a_1^{n-2-k}} \frac{\sin n\varphi_l}{\sin \varphi_l} \end{aligned} \quad (2.66)$$

If the limiting angle of the current shell is chosen to be $\varphi = \pi/3$, the main dipole component becomes:

$$B_1 = B_{\theta,1}(r,0) = -\frac{\sqrt{3}\mu_0 J_0}{\pi} (a_2 - a_1)$$

At the same time **the sextupole term $n = 3$ vanishes ($B_3 = 0$)**. The next non-zero term in the expansion is the decapole $n = 5$.

$$B_5 = B_{\theta,5}(r,0) = \frac{\sqrt{3}\mu_0 J_0}{\pi} \frac{r^4}{15} \left(\frac{1}{a_1^3} - \frac{1}{a_2^3} \right)$$

$$\frac{B_5}{B_1} = -\frac{r^4}{15} \left(\frac{1}{a_2^3 a_1} + \frac{1}{a_2^2 a_1^2} + \frac{1}{a_2 a_1^3} \right)$$

Let us see how big is this ratio at the reference radius of $r_0 = 10$ mm for the inner radius of the shell equal to $a_1 = 28$ mm, and the outer one equal to $a_2 = 43.4$ mm. (These parameters correspond to the radii of the inner layer coil for the LHC dipole magnet.) If moreover the limiting angle of the shell is $\pi/3$ the following result is obtained:

$$b_5 = B_5/B_1 = -14.4 \cdot 10^{-4}$$

This is approximately one order higher than the upper limit of acceptable values for the higher multipole components in a good quality dipole magnet.

In order to improve the quality of the magnetic field, two layers of coils are used in the LHC dipole magnet. Moreover, to obtain optimal current distribution approximating the ideal cosine dependence, each layer is divided into sections by means of longitudinal wedge-shaped copper spacers inserted at certain angles between the blocks of superconducting cable. If $\alpha_1, \alpha_2, \dots, \alpha_k$ indicate the angles limiting the conductor blocks in the shell (Fig. 2.18) then the angular integral in the formulas (2.57), (2.61) and (2.63) for the vector potential have to be split into the following sum of integrals:

$$\int_0^{\varphi_l} \cos n\varphi \, d\varphi = \int_0^{\alpha_1} \cos n\varphi \, d\varphi + \int_{\alpha_2}^{\alpha_3} \cos n\varphi \, d\varphi + \dots + \int_{\alpha_k}^{\varphi_l} \cos n\varphi \, d\varphi =$$

$$= \frac{1}{n} (\sin n\alpha_1 - \sin n\alpha_2 + \sin n\alpha_3 - \dots - \sin n\alpha_k + \sin n\varphi_l) \quad (2.67)$$

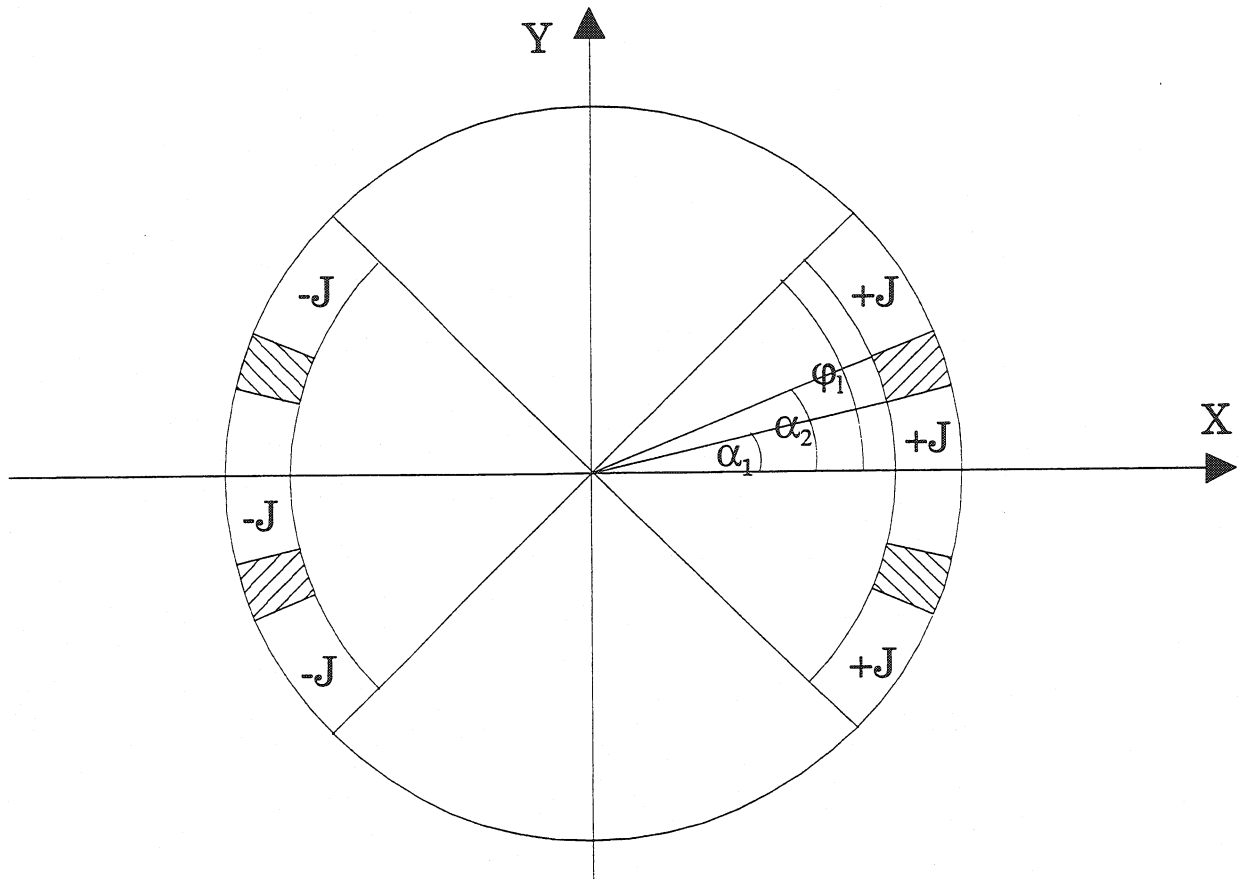


Figure 2.18 Current blocks arrangement

2.8 Approximate Magnetic Field Calculations for the LHC Dipole Coils

The quadrant cross-section of the LHC dipole coil and its approximation with ideal cylindrical current shells are shown in Fig. 2.19. Since the positioning of the superconducting cables in the layers is not radially concentric, the angular limits defining the location of the current shells have to be approximated. In the example below the angles are measured between the center of the aperture and the corresponding points on the mean radius of the layer (as demonstrated for the inner layer in Fig. 2.19). Under nominal operating conditions both layers of the coils connected in series are powered up with 11.5 kA (exactly 11530 A) direct current. To approximate these conditions in the current shell model the corresponding current densities must be calculated for the inner and outer layer. At the end the quality of this approximation will be compared with the precise analytical calculations taking into account an exact position of every cable in each layer. The multipoles are calculated up to $n = 9$.

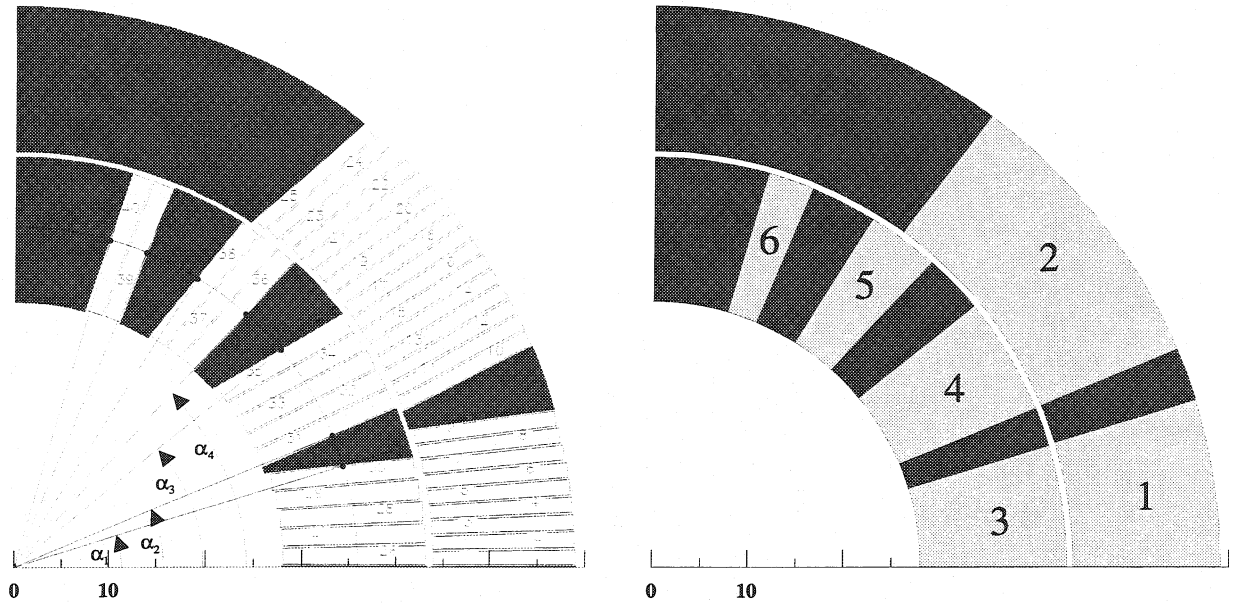


Figure 2.19 Transversal cross-section of the LHC dipole coil and its approximation with the current shells

2.8.1 Inner layer contribution to the field induction inside the aperture

Inner radius $a_1 = 28$ mm Outer radius $a_2 = 43.4$ mm Average radius $a_{avg} = 35.7$ mm

Reference radius $r_0 = 10$ mm corresponds to the maximum deviation of the particles guided by a dipole magnet from the beam axis. Angles defining positions of the current shells in the inner layer are:

$$\alpha_1 = 17^\circ \quad \alpha_2 = 23^\circ \quad \alpha_3 = 39.5^\circ \quad \alpha_4 = 48^\circ \quad \alpha_5 = 58^\circ \quad \alpha_6 = 67^\circ \quad \alpha_7 = 74^\circ$$

The angular factor in the formulas for the field induction has the form:

$$\sin(n\varphi_l) = \sin(n\alpha_1) - \sin(n\alpha_2) + \sin(n\alpha_3) - \sin(n\alpha_4) + \sin(n\alpha_5) - \sin(n\alpha_6) + \sin(n\alpha_7)$$

This gives the following results:

$$\begin{aligned} \text{for } n = 1: \sin(\varphi_l) &= 0.68 & \text{for } n = 3: \sin(3\varphi_l) &= -0.07 & \text{for } n = 5: \sin(5\varphi_l) &= 0.31 \\ \text{for } n = 7: \sin(7\varphi_l) &= 0.11 & \text{for } n = 9: \sin(9\varphi_l) &= 0.27 \end{aligned}$$

For the current density estimation in the inner layer shell, let us consider, e.g. the shell No. 4 (Fig. 2.19). Its angular extent is $\alpha_3 - \alpha_2 = 16.5^\circ$. The total surface of the sector is 158 mm^2 . This current shell represents 5 cables, thus the effective surface of one cable is 31.6 mm^2 (in reality a surface of the conductive area of the inner layer cable at room temperature is 28.69 mm^2). The current of 11.5 kA flowing in each cable results in the current density of $J_0 = 365$

A/mm². To simplify the calculations this value will be considered to be the current density in all of the inner layer current shells.

The contributions to the field induction in the median plane, at the reference radius r_0 , resulting from the inner layer are:

$$B_1 = B_{\theta,1}(r_0, 0) = -\frac{2.105 \mu_0 J_0}{\pi} \cdot 10^{-2} [T]$$

For $J_0 = 365 \text{ A/mm}^2$ $B_1 = -3.073 \text{ T}$. The remaining multipoles are:

$$B_3 = B_{\theta,3}(r_0, 0) = +\frac{6.05 \mu_0 J_0}{\pi} \cdot 10^{-5} [T] \quad B_5 = B_{\theta,5}(r_0, 0) = -\frac{1.385 \mu_0 J_0}{\pi} \cdot 10^{-5} [T]$$

$$B_7 = B_{\theta,7}(r_0, 0) = -\frac{3.26 \mu_0 J_0}{\pi} \cdot 10^{-7} [T] \quad B_9 = B_{\theta,9}(r_0, 0) = -\frac{6.05 \mu_0 J_0}{\pi} \cdot 10^{-8} [T]$$

2.8.2 Outer layer contribution to the field induction inside the aperture

Inner radius $a_1 = 43.9 \text{ mm}$ Outer radius $a_2 = 59.3 \text{ mm}$ Average radius $a_{avg} = 51.6 \text{ mm}$

Angles defining positions of the conductor blocks:

$$\alpha_1 = 17^\circ \quad \alpha_2 = 23^\circ \quad \alpha_3 = 54^\circ$$

The angular factor in the formulas for the field induction has the form:

$$\sin(n\phi_l) = \sin(n\alpha_1) - \sin(n\alpha_2) + \sin(n\alpha_3)$$

This gives the following results:

$$\text{for } n = 1: \sin(\phi_l) = 0.71 \text{ (almost the same as for the inner layer)} \quad \text{for } n = 3: \sin(3\phi_l) = 0.15$$

$$\text{for } n = 5: \sin(5\phi_l) = -0.91 \quad \text{for } n = 7: \sin(7\phi_l) = 0.86 \quad \text{for } n = 9: \sin(9\phi_l) = 1.72$$

For the current density estimation in the outer layer shells, let us consider, e.g. the shell No. 2 (Fig. 2.19). Its angular extent is $\alpha_3 - \alpha_2 = 31^\circ$. The total surface of the sector is 430 mm^2 . This current shell represents 16 cables, thus the effective surface of one cable is 26.9 mm^2 (in reality a surface of the conductive area of the inner layer cable at room temperature is 22.35 mm^2). The current of 11.5 kA flowing in each cable results in the current density of $J_1 = 429 \text{ A/mm}^2$. To simplify the calculations this value will be considered to be the current density in all of the outer layer current shells. For the multipole calculations the current density J_1 is expressed as a function of the current density in the internal layer ($J_1 = 1.175 J_0$).

The contributions to the field in the median plane, at the reference radius r_0 , resulting from the outer layer are:

$$B_1 = B_{\theta,1}(r_0, 0) = -\frac{2.19 \mu_0 J_1}{\pi} \cdot 10^{-2} = -\frac{2.57 \mu_0 J_0}{\pi} \cdot 10^{-2} [T]$$

For $J_0 = 365 \text{ A/mm}^2$ $B_1 = -3.752 \text{ T}$.

The remaining multipoles are:

$$B_3 = B_{\theta,3}(r_0, 0) = -\frac{7.07 \mu_0 J_0}{\pi} \cdot 10^{-5} [T]$$

$$B_5 = B_{\theta,5}(r_0, 0) = +\frac{1.00 \mu_0 J_0}{\pi} \cdot 10^{-5} [T]$$

$$B_7 = B_{\theta,7}(r_0, 0) = -\frac{6.58 \mu_0 J_0}{\pi} \cdot 10^{-7} [T]$$

$$B_9 = B_{\theta,9}(r_0, 0) = -\frac{8.89 \mu_0 J_0}{\pi} \cdot 10^{-8} [T]$$

2.8.3 Total field induction due to both layers

The total dipole field induction resulting from both layers becomes,

$$B_1 = B_{\theta,1}(r_0, 0) = -\frac{4.675 \mu_0 J_0}{\pi} \cdot 10^{-2} [T]$$

which amounts to -6.825 T . The sextupole contribution from the inner layer has a positive sign. The corresponding contribution from the outer layer enters the sum with a negative sign. Thus both terms tend to cancel each other out.

$$B_3 = B_{\theta,3}(r_0, 0) = -\frac{1.02 \mu_0 J_0}{\pi} \cdot 10^{-5} [T]$$

$$b_3 = \frac{B_3}{B_1} = 2.18 \cdot 10^{-4}$$

Also the decapole contributions from both layers tend to cancel each other out.

$$B_5 = B_{\theta,5}(r_0, 0) = -\frac{0.385 \mu_0 J_0}{\pi} \cdot 10^{-5} [T]$$

$$b_5 = \frac{B_5}{B_1} = 0.82 \cdot 10^{-4}$$

Total of B_7 yields

$$B_7 = B_{\theta,7}(r_0, 0) = -\frac{9.84 \mu_0 J_0}{\pi} \cdot 10^{-7} [T]$$

$$b_7 = \frac{B_7}{B_1} = 0.21 \cdot 10^{-4}$$

And the total of B_9 :

$$B_9 = B_{\theta,9}(r_0, 0) = -\frac{1.49 \mu_0 J_0}{\pi} \cdot 10^{-7} [T]$$

$$b_9 = \frac{B_9}{B_1} = 0.03 \cdot 10^{-4}$$

2.9 Comparison of the Current Shell Model with ROXIE Calculations

The ROXIE program mentioned already at the beginning of this chapter [5] was created at CERN for the integrated design of superconducting accelerator magnets. It allows a feature-based geometry modeling of the coil and the surrounding magnetic structure, i.e. the iron yoke, both in 2- and in 3-D, using a concise set of meaningful design data. These variables supplied to the program can be then addressed in the optimization problems, e.g. the optimization of the magnet geometry as a function of the desired magnetic field pattern. The mathematical details are given in reference [8].

In this section the results from the current shell model will be compared with the analytical ROXIE calculations. High accuracy of these calculations is obtained by representing each strand in the cable cross-section with a single current line. The conductors in the ROXIE model are subdivided into the regions corresponding to the actual number of

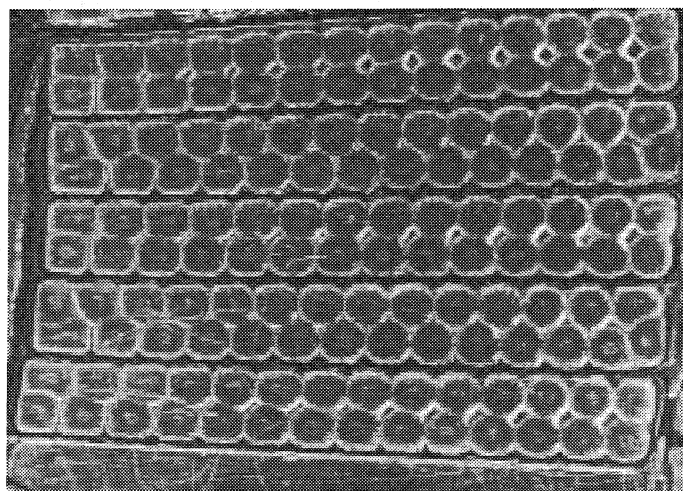


Figure 2.20 Keystoned shape of the cables

strands in the cables, i.e. 2 rows of 18 elements for the external layer cable, and 2 rows of 14 elements for the internal one. The current line representing the strand is located in the center of each region. The magnetic field resulting from the coils is calculated directly from the Biot-Savart law.

Two types of ROXIE cases are considered below. The first type takes into account the current grading resulting from the keystone (trapezoidal) shape of the cable's transversal cross-section (Fig. 2.20). As a consequence of this shape the strands near the inner perimeter of the cable are closer to each other than the ones near the outer edge. This results in grading of the current density throughout the conductor. The second type of cases assumes uniform current density in the conductors. Both types are considered under the cold and warm conditions. For the cold conditions (1.9 K) a temperature depended contraction of the cables is taken into account. In the cases denoted as *warm* the thermal contraction between ambient temperature and the operating temperature of 1.9 K is not considered. Fig. 2.21 shows the magnetic field due to the coils of the magnet. Table 2.2 compares the ROXIE results with the current shell model. The coils are powered up with 11.5 kA direct current.

Table 2.2 ROXIE calculations vs. Current Shell Model

$r_0 = 10 \text{ mm}$	$B_1 \text{ [T]}$	b_3	b_5	b_7	b_9
ROXIE (current grading, cold)	-6.90	1.355	-0.124	0.031	0.0018
ROXIE (current grading, warm)	-6.88	1.347	-0.123	0.030	0.0017
ROXIE (uniform current density, cold)	-6.87	1.952	-0.127	0.032	0.0020
ROXIE (uniform current density, warm)	-6.85	1.940	-0.126	0.032	0.0019
Current Shell Model	-6.83	2.180	0.820	0.210	0.0300

Looking at the ROXIE results one can immediately draw a conclusion that by neglecting the cold contraction the magnetic field pattern does not change in a substantial way. On the other hand the uniform density cases give about 0.6 units higher sextupole in comparison to the current grading cases (which reflect the real current distribution in the cables).

For a good quality superconducting magnet the ratios of the higher order field components to the main field should be less than one unit ($1 \text{ unit} = 10^{-4}$). The geometry of the LHC dipole coil was optimized to compensate the persistent current effects [9], therefore the sextupole b_3 is deliberately higher than one unit. As it was pointed out in the first chapter, when the particle beam is injected from the SPS high energy booster to the LHC ring, the magnetic field in the magnets is ramped at constant rate, in order to keep the accelerated particle beam on the same orbit. The ramping is finished when the beam reaches its maximum energy. At this point the magnets produce the maximal magnetic field intensity and are being operated with steady current. Nevertheless, during the ramping the superconducting cables are submitted to the variable magnetic field. In such conditions the eddy currents are generated. Since these eddy current loops flow in the superconducting material, they do not decay exponentially as standard eddy currents, but become persistent instead. This effect can create essential distortions in the nominal magnetic field and therefore must be compensated.

Relative multipole coefficients obtained during harmonic analysis of the magnetic field are of the order of 10^{-4} and their computation requires high accuracy. The validity of the results relies on the precise definition of the coil geometry and correct implementation of the current density distribution into the model. In this regard the current shell approximation gives a fast and reasonable estimate of the magnetic field generated by the coils. The decapole component according to the approximation is positive, which is not the case in reality as it is demonstrated with the ROXIE calculation. The conductor block consisting of cables 26-30 in the inner layer (Fig.2.19) is mostly responsible for the generation of the decapole field. The angular confinement of this block used to define the corresponding

current shell is too rough an approximation in comparison to the real stacking position of the cables, almost parallel to the median plane in this conductor block.

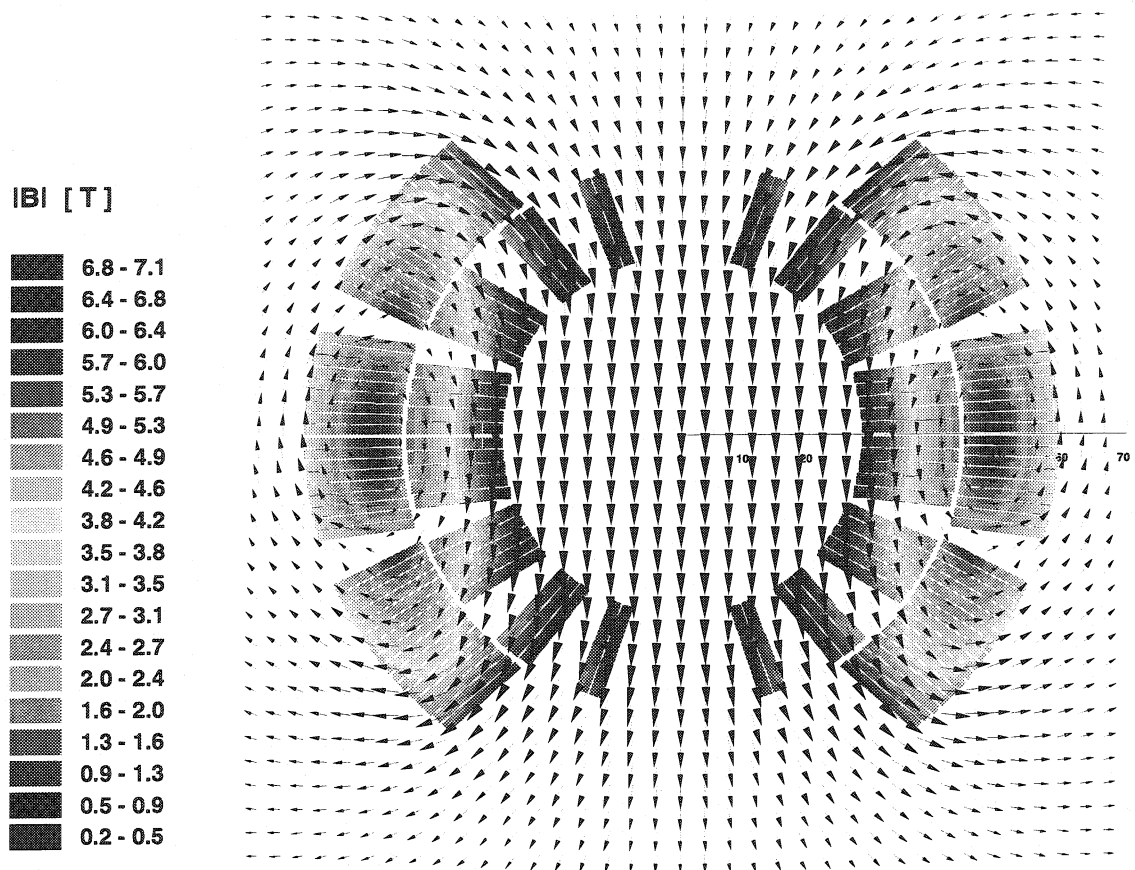


Figure 2.21 Magnetic field computed with ROXIE

2.10 Influence of the Nonsaturated Iron Yoke on the Magnetic Field within the Magnet

Not only the superconducting coils determine the magnetic field generated by the magnet. The iron yoke surrounding the coils has important effects on the magnetic field:

1. It increases the magnetic field induction inside the aperture of the magnet.
2. It reduces the total field energy.
3. It shields the fringing fields and provides convenient flux return paths for the magnetic field outside the magnet aperture.
4. It provides magnetic decoupling between two neighboring magnets installed in the accelerator.

2.10.1 Cylindrical air-iron boundary problem

Before this influence is analyzed in details we will address an elementary cylindrical air-iron boundary problem consisting of the calculation of the magnetic fields due to a single current line in a cylindrical cavity surrounded by iron. In order to do this let us consider again a single line conductor from section 2.5, embedded this time in a cylindrical air tunnel of radius $r = b$, cut out in an infinite mass of iron characterized by relative permeability μ (Fig. 2.22).

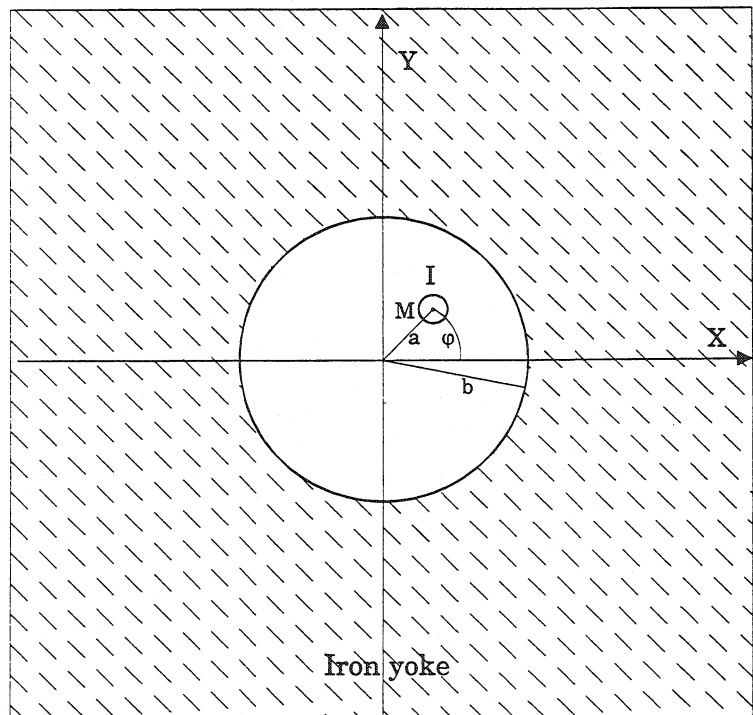


Figure 2.22 Cylindrical iron-air boundary problem

The conductor located at a given point $M(a, \varphi)$ runs parallel to the OZ axis of the cylinder. The flux lines of the magnetic field generated by the current line enter the iron at the boundary of the interface between both media. Two components of the magnetic field must be preserved across the interface in order to satisfy the boundary conditions. These are:

- normal component of the magnetic field induction B , and
- tangential component of the magnetic field intensity H .

As seen from the air region the lines of the magnetic field enter the surface of the surrounding iron, and thus the boundary surface appears to exhibit negative magnetization polarity. On the other hand, as seen from the iron side, the lines issue from the boundary surface into the medium, and for this region the surface seems to exhibit positive magnetization polarity. This polar magnetization of the boundary is merely apparent, nevertheless very useful in the implementation of the electromagnetic image methods. Two systems of electromagnetic images must be taken into account:

1. The influence of the iron yoke with relative permeability μ and inner bore radius $r = b$ on the field generated by a single line conductor carrying current I and located at point $M(a, \varphi)$, where $a < b$, can be represented by an image line traversed by current I_1 and located on the normal to the boundary, on the other side of the interface at point $N(a_1, \varphi)$ ($a_1 > b$). Image and original current lines should allow to ignore the existence of the boundary because their objective is to produce together the same magnetic effect on the field inside the cavity as the magnetization induced on the real boundary due to the presence of the iron yoke. Thus when both lines are in place the entire space is considered to be filled with air, but the magnetic field calculation is valid only for the air region inside the cavity ($r < b$).
2. The second image system is required to represent the magnetic field inside the iron yoke. It is assumed that this can be achieved by means of two current lines carrying currents I_2 and I_3 located at points $M(a, \varphi)$ and $O(0,0)$, respectively (Fig. 2.23). Again the objective is to ignore the existence of the boundary, with the restriction that the magnetic field pattern set up by both lines is valid only in the iron region ($r > b$), which spreads to infinity.

If the assumptions pointed out above are contradictory it will be impossible to satisfy the boundary conditions of the problem. The first condition to be fulfilled by the current lines is derived directly from the Ampere's law (2.43). The curl of the magnetic field intensity along the boundary in the air region (set up by lines I and I_1) must be equal to the same curl calculated along the boundary on the iron side (set up by the current lines I_2 and I_3).

$$\oint_{air} \vec{H} d\vec{l} = \oint_{iron} \vec{H} d\vec{l} \quad (2.68)$$

Hence it follows immediately that:

$$I = I_2 + I_3 \quad (2.69)$$

Let us consider the magnetic field at any point $P(r, \theta)$ close to the boundary.

- Contribution of the current line I at point P

The vector potential at point P resulting from this line is according to Eq. (2.46):

$$A_z(r, \theta) = -\frac{\mu_0 I}{2\pi} \ln\left(\frac{R}{a}\right) = -\frac{\mu_0 I}{2\pi} \ln\left(\frac{\sqrt{a^2 + r^2 - 2ar \cos(\theta - \varphi)}}{a}\right)$$

Then the field intensity components are:

$$H_r(r, \theta) = \frac{1}{\mu_0 r} \frac{\partial A_z}{\partial \theta} = -\frac{I}{2\pi} \frac{a \sin(\theta - \varphi)}{a^2 + r^2 - 2ar \cos(\theta - \varphi)}$$

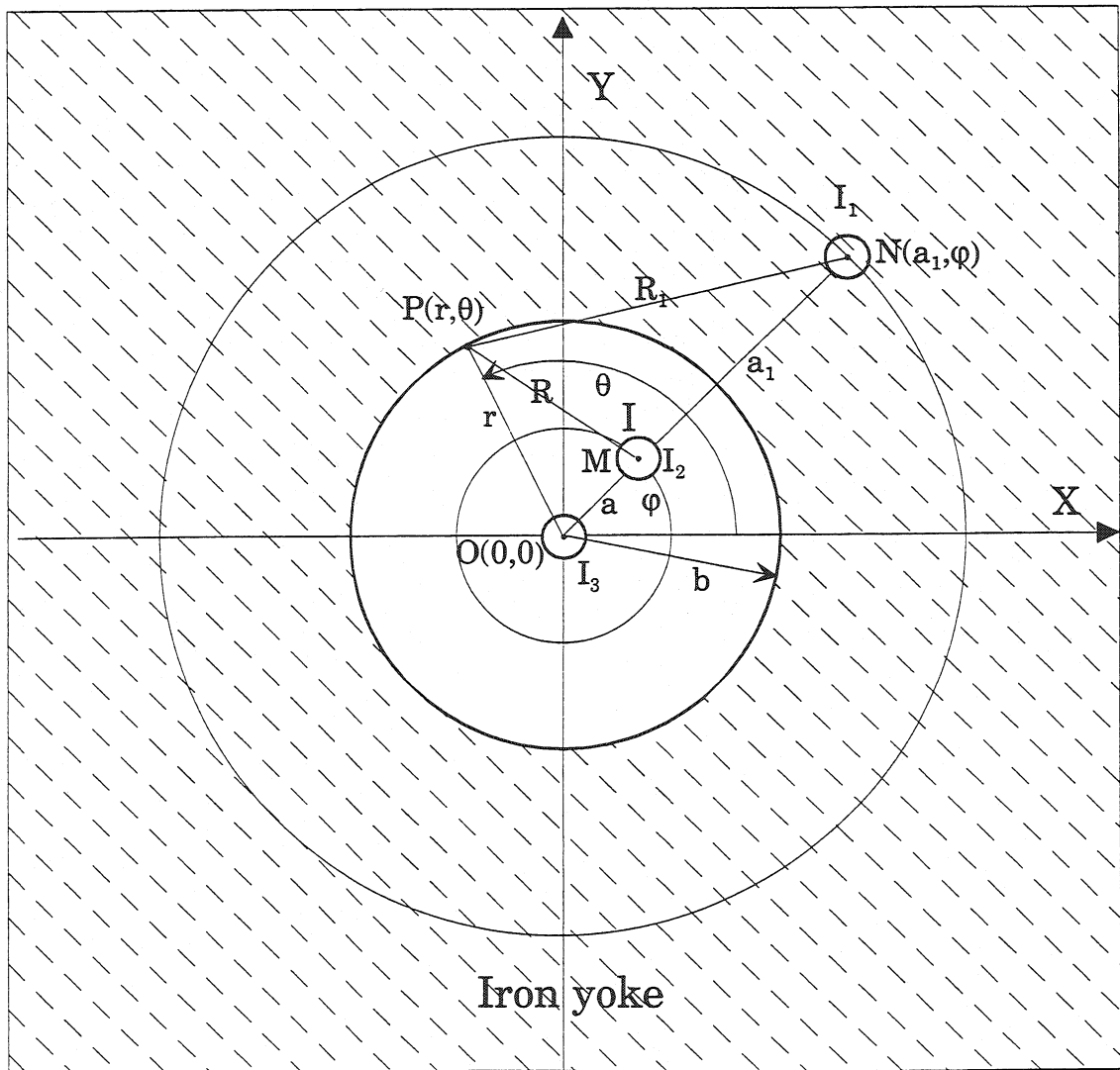


Figure 2.23 Conductor positions in electromagnetic image method

$$H_{\theta}(r, \theta) = -\frac{1}{\mu_0} \frac{\partial A_z}{\partial r} = \frac{I}{2\pi} \frac{r - a \cos(\theta - \varphi)}{a^2 + r^2 - 2ar \cos(\theta - \varphi)}$$

- Contribution of the current line I_1

$$H_{r,1}(r, \theta) = -\frac{I_1}{2\pi} \frac{a_1 \sin(\theta - \varphi)}{a_1^2 + r^2 - 2a_1 r \cos(\theta - \varphi)}$$

$$H_{\theta,1}(r, \theta) = \frac{I_1}{2\pi} \frac{r - a_1 \cos(\theta - \varphi)}{a_1^2 + r^2 - 2a_1 r \cos(\theta - \varphi)}$$

- Contribution of the current line I_2

$$H_{r,2}(r, \theta) = -\frac{I_2}{2\pi} \frac{a \sin(\theta - \varphi)}{a^2 + r^2 - 2ar \cos(\theta - \varphi)}$$

$$H_{\theta,2}(r, \theta) = \frac{I_2}{2\pi} \frac{r - a \cos(\theta - \varphi)}{a^2 + r^2 - 2ar \cos(\theta - \varphi)}$$

- Contribution of the current line I_3

$$H_{r,3}(r, \theta) = 0$$

$$H_{\theta,3}(r, \theta) = \frac{I_3}{2\pi r}$$

The normal component of the field induction across the boundary must be preserved, i.e. for $r = b$ the following equation should be satisfied,

$$\mu_0 H_r(b, \theta) + \mu_0 H_{r,1}(b, \theta) = \mu \mu_0 H_{r,2}(b, \theta) + \mu \mu_0 H_{r,3}(b, \theta) \quad (2.70)$$

which leads immediately to:

$$-\frac{\mu_0 I}{2\pi} \frac{a \sin(\theta - \varphi)}{a^2 + b^2 - 2ab \cos(\theta - \varphi)} - \frac{\mu_0 I_1}{2\pi} \frac{a_1 \sin(\theta - \varphi)}{a_1^2 + b^2 - 2a_1 b \cos(\theta - \varphi)} = -\frac{\mu \mu_0 I_2}{2\pi} \frac{a \sin(\theta - \varphi)}{a^2 + b^2 - 2ab \cos(\theta - \varphi)}$$

The condition has to be valid along the entire interface air-iron, and thus for all values of the angle θ . This can be satisfied only if the expressions in the denominators of the equation above are similar functions of θ , i.e. a_1 has to comply with the following relation:

$$\frac{b}{a} = \frac{a_1}{b} \quad (2.71)$$

Hence $aa_1 = b^2$, and it turns out that the point at which the image current I_1 has to be placed is an inversion image of the position of the original single line conductor with respect to the cylindrical boundary of radius $r = b$. With this additional constraint the second term on the left-hand side of the boundary condition (2.70) becomes:

$$\begin{aligned}
 & -\frac{\mu_0 I_1}{2\pi} \frac{a_1 \sin(\theta - \varphi)}{a_1^2 + b^2 - 2a_1 b \cos(\theta - \varphi)} = -\frac{\mu_0 I_1}{2\pi} \frac{a_1 \sin(\theta - \varphi)}{b^2 \left(\left(\frac{a_1}{b} \right)^2 + 1 - 2 \frac{a_1}{b} \cos(\theta - \varphi) \right)} = \\
 & = -\frac{\mu_0 I_1}{2\pi} \frac{a_1 \sin(\theta - \varphi)}{b^2 \left(\left(\frac{b}{a} \right)^2 + 1 - 2 \frac{b}{a} \cos(\theta - \varphi) \right)} = -\frac{\mu_0 I_1}{2\pi} \frac{\frac{b^2}{a} \sin(\theta - \varphi)}{\frac{b^2}{a^2} (b^2 + a^2 - 2ba \cos(\theta - \varphi))} = \\
 & = -\frac{\mu_0 I_1}{2\pi} \frac{a \sin(\theta - \varphi)}{a^2 + b^2 - 2ab \cos(\theta - \varphi)}
 \end{aligned}$$

And the boundary condition is reduced to:

$$I + I_1 = \mu I_2 \quad (2.72)$$

The boundary condition for the tangential component of the field intensity imposes that

$$H_\theta(b, \theta) + H_{\theta,1}(b, \theta) = H_{\theta,2}(b, \theta) + H_{\theta,3}(b, \theta) \quad (2.73)$$

Taking advantage of relation (2.71), after several transformations equation (2.73) can be brought to the following form:

$$(b - a \cos(\theta - \varphi))(I - I_2 - I_3) = \left(\frac{a^2}{b} - a \cos(\theta - \varphi) \right) (I_3 - I_1)$$

Hence, considering that the condition has to be satisfied for all values of θ , and taking Eq. (2.69) into account, it follows immediately that $I_1 = I_3$. Thus a set of three equations is available for the determination of the current values and directions in every conductor:

$$\begin{cases} I = I_2 + I_3 \\ I + I_1 = \mu I_2 \\ I_1 = I_3 \end{cases}$$

After solving it the following results are obtained:

$$\begin{cases} I_1 = I_3 = \frac{\mu - 1}{\mu + 1} I \\ I_2 = \frac{2I}{\mu + 1} \end{cases} \quad (2.74)$$

Fig. 2.24 shows a pattern of the magnetic flux lines plotted for the iron yoke with inner bore radius of 100 mm and a single conductor line placed 60 mm away from the axis of the cylindrical cavity. The calculation was carried out for the relative permeability coefficient $\mu = 7$.

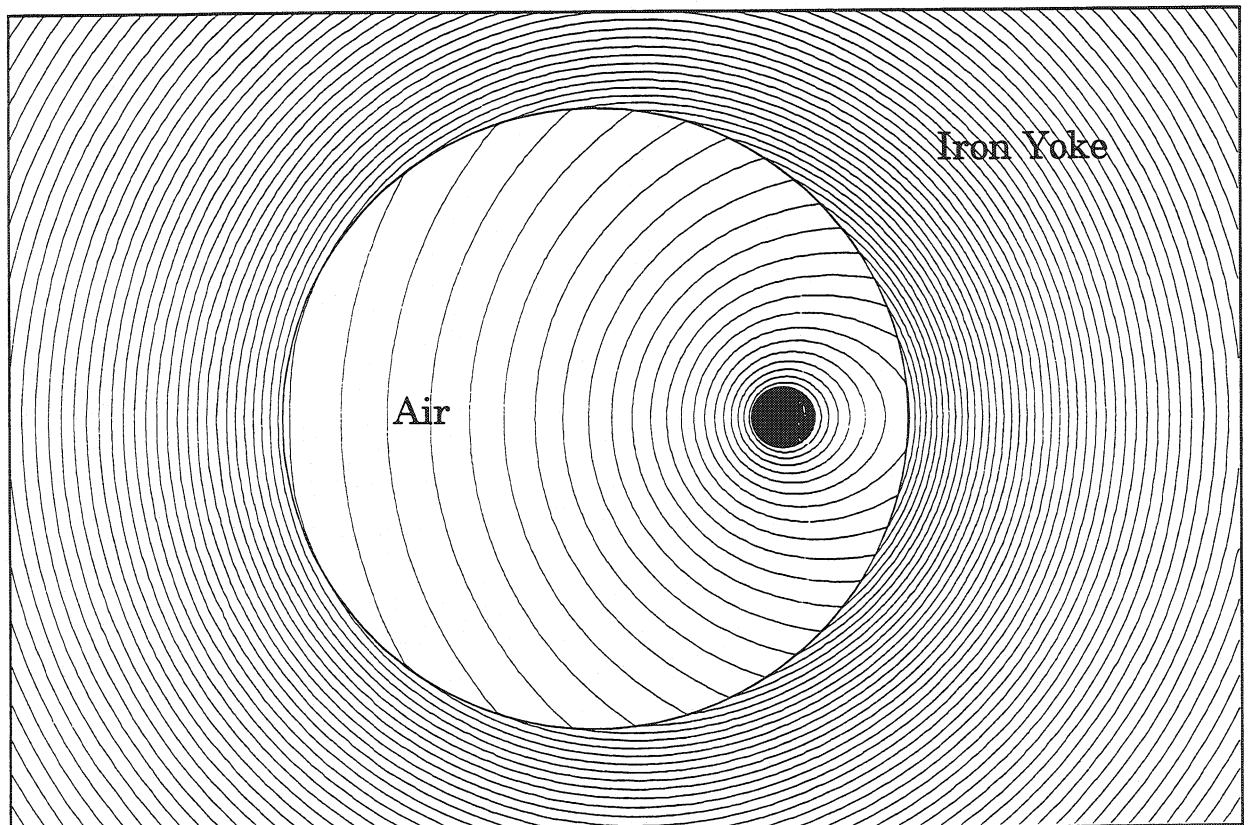


Figure 2.24 Flux pattern due to a single line conductor in a cylindrical air-iron boundary problem

Summary

In the problem considered, the magnetic field in a cylindrical air cavity can be represented by the original conductor carrying current I and its image current line at the position inverse to original with respect to the air-iron boundary, and carrying current $\frac{\mu - 1}{\mu + 1} I$. With both current lines in place the problem can be treated as if the boundary had not existed and the

entire space had been filled with air. The magnetic field in the iron yoke can be represented by the conductor transporting current $\frac{2I}{\mu + 1}$, located at the same point as the original current line, and a second current line with current $\frac{\mu - 1}{\mu + 1}I$ running along the central axis of the cylindrical air tunnel.

Remarks

The boundary problem addressed in this section is known as the Searle's problem of the second kind. Although it was solved by Searle already in 1898, the detailed calculations are rarely found in the literature. In reference [10], which is based on Searle's original works, the discussion of the problem is based on the geometrical properties of the inversion transformation. The boundary condition for the tangential component of the magnetic field intensity is treated alternatively by comparison of the difference of magnetic potential between two points as measured on both sides of the air-iron interface. In order to implement this approach the author analyses the work carried out by an imaginary unitary magnetic pole by moving it from one point to another. The work calculated in this way along the boundary must be then equal in both media.

The approach just presented in this section follows a strict mathematical treatment of the boundary conditions, which does not require the introduction of the unitary magnetic pole. Moreover, the position of the image current line, setting up the magnetic field in the air cavity due to the presence of the iron yoke, is not assumed in advance. The inversion transformation automatically becomes a necessity if the boundary conditions are to be satisfied.

2.10.2 Analytical Calculations for the Nonsaturated Iron Yoke

The image current method is valid only if the iron yoke is not saturated. Only then the permeability can be considered to be constant and independent of the position within the yoke. Taking advantage of the results obtained in the previous section we can calculate the influence of the iron yoke on the magnetic field within the magnet in such a case.

The position of the conductors in the approximation for dipole geometry magnet including the effect of the iron yoke is shown in Fig. 2.25. The point $C'_1(a', \varphi)$ is the inversion image of point $C_1(a, \varphi)$ with respect to the boundary of the air-iron interface at $r = b$, and μ is the permeability of the iron yoke. According to the properties of the inversion transformation $a' = b^2/a$.

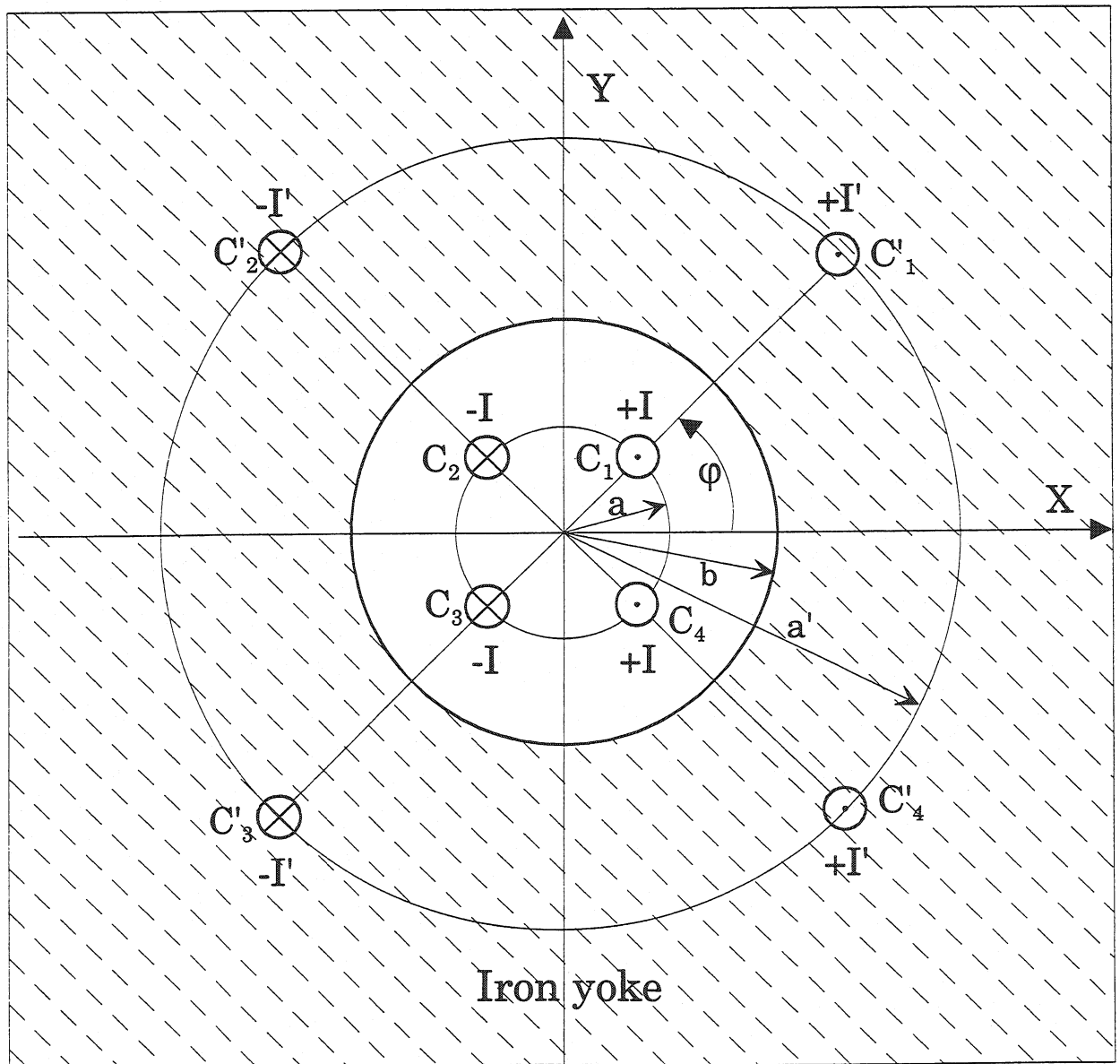


Figure 2.25 Effect of the iron yoke on the inner field of the single line conductors

- Magnetic field inside the magnet aperture ($r < a_1$)

The contribution to the vector potential from the conductors representing the current shell for $r < a$ is given by Eq. (2.55). The contribution from the image current lines accounting for the iron yoke effect is according to the same formula:

$$A'_z(r, \theta) = \frac{2\mu_0 I'}{\pi} \sum_{n=2l+1} \frac{1}{n} \left(\frac{r}{a'} \right)^n \cos n\varphi \cos n\theta = \frac{2\mu_0}{\pi} \left(\frac{\mu-1}{\mu+1} \right) I \sum_{n=2l+1} \frac{1}{n} \left(\frac{ra}{b^2} \right)^n \cos n\varphi \cos n\theta \quad (2.75)$$

The total of both terms is

$$A_z(r, \theta) = \frac{2\mu_0 I}{\pi} \sum_{n=2l+1} \frac{1}{n} \left(\frac{r}{a} \right)^n \left[1 + \left(\frac{\mu-1}{\mu+1} \right) \left(\frac{a}{b} \right)^{2n} \right] \cos n\varphi \cos n\theta \quad (2.76)$$

The current shell arrangement including the image shells representing the contribution of the iron yoke is shown in Fig. 2.26. If we assume that the current density in the shells

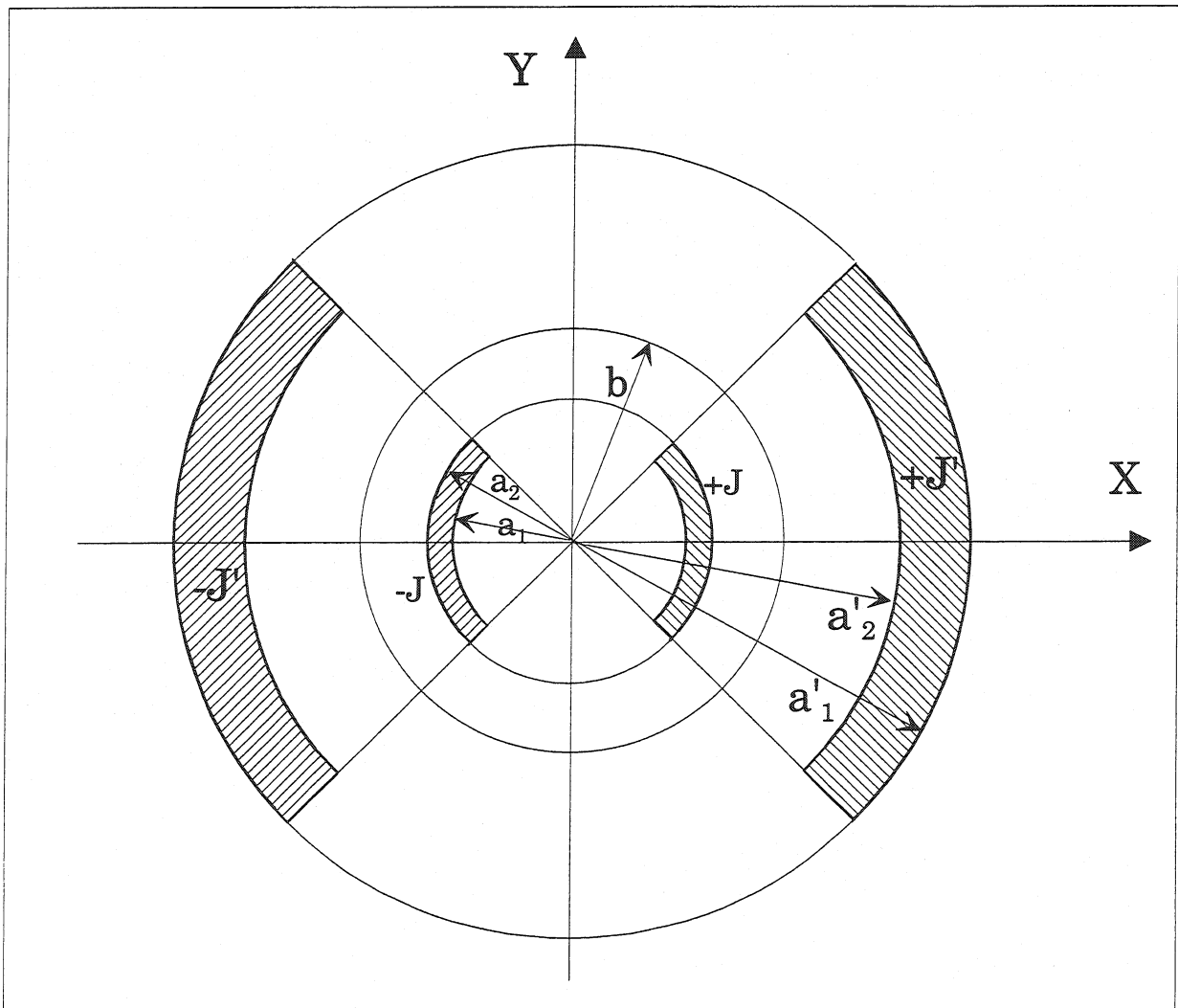


Figure 2.26 Effect of the iron yoke on the inner field of the current shell

representing the coil is constant ($J = J_0$) then $dI = J_0 a da d\varphi$. In order to calculate the vector potential due to the magnet it is sufficient to integrate A_z over the radial and angular extent of the coil (from a_1 to a_2 , and from 0 to φ_l). The contribution of the iron yoke will be automatically taken into account including the form of the image current and the fact that the current density in the image shells is smaller than in the coil shells due to the surface increase of the image shells after the inversion. The total vector potential is:

$$A_z(r, \theta) = \frac{2\mu_0 J_0}{\pi} \sum_{n=2l+1} \frac{r^n \cos n\theta}{n^2} \sin n\varphi_l \int_{a_1}^{a_2} \frac{\left[1 + \left(\frac{\mu-1}{\mu+1}\right)\left(\frac{a}{b}\right)^{2n}\right]}{a^n} a da = \quad (2.77)$$

$$= \frac{2\mu_0 J_0}{\pi} \sum_{n=2l+1} \frac{r^n}{n^2} \left\{ \frac{1}{n-2} \left(\frac{1}{a_1^{n-2}} - \frac{1}{a_2^{n-2}} \right) + \left(\frac{\mu-1}{\mu+1} \right) \frac{1}{b^{2n}(n+2)} (a_2^{n+2} - a_1^{n+2}) \right\} \cos n\theta \sin n\varphi_l$$

The first term in the sum between parentheses represents the coil contribution to the magnetic field and the second one corresponds to the contribution of the iron yoke. The multipole components of the magnetic field are:

$$B_{r,n}(r, \theta) = -\frac{2\mu_0 J_0}{\pi} \frac{r^{n-1}}{n} \sin n\theta \sin n\varphi_l \left\{ \frac{1}{n-2} \left(\frac{1}{a_1^{n-2}} - \frac{1}{a_2^{n-2}} \right) + \left(\frac{\mu-1}{\mu+1} \right) \frac{1}{b^{2n}(n+2)} (a_2^{n+2} - a_1^{n+2}) \right\}$$

$$B_{\theta,n}(r, \theta) = -\frac{2\mu_0 J_0}{\pi} \frac{r^{n-1}}{n} \cos n\theta \sin n\varphi_l \left\{ \frac{1}{n-2} \left(\frac{1}{a_1^{n-2}} - \frac{1}{a_2^{n-2}} \right) + \left(\frac{\mu-1}{\mu+1} \right) \frac{1}{b^{2n}(n+2)} (a_2^{n+2} - a_1^{n+2}) \right\} \quad (2.78)$$

- Magnetic field outside the coils but within the bore of the iron yoke ($a_2 < r < b$)

The contribution to the vector potential from the conductors representing the current shell for $r > a$ is given by Eq. (2.56). The contribution from the image current lines is the same as in the previous case and given by Eq. (2.75). The total of both terms is

$$A_z(r, \theta) = \frac{2\mu_0 I}{\pi} \sum_{n=2l+1} \frac{1}{n} \left(\frac{a}{r} \right)^n \left[1 + \left(\frac{\mu-1}{\mu+1} \right) \left(\frac{r}{b} \right)^{2n} \right] \cos n\varphi \cos n\theta \quad (2.79)$$

The integration over the extent of the current shell yields:

$$A_z(r, \theta) = \frac{2\mu_0 J_0}{\pi} \sum_{n=2l+1} \frac{\cos n\theta \sin n\varphi_l}{n^2 (n+2) r^n} \left[1 + \left(\frac{\mu-1}{\mu+1} \right) \left(\frac{r}{b} \right)^{2n} \right] (a_2^{n+2} - a_1^{n+2}) \quad (2.80)$$

The multipole components are:

$$\begin{aligned}
 B_{r,n}(r,\theta) &= -\frac{2\mu_0 J_0}{\pi} \frac{\sin n\theta \sin n\varphi_l}{n(n+2)r^{n+1}} \left[1 + \left(\frac{\mu-1}{\mu+1} \right) \left(\frac{r}{b} \right)^{2n} \right] (a_2^{n+2} - a_1^{n+2}) \\
 B_{\theta,n}(r,\theta) &= \frac{2\mu_0 J_0}{\pi} \frac{\cos n\theta \sin n\varphi_l}{n(n+2)r^{n+1}} \left[1 - \left(\frac{\mu-1}{\mu+1} \right) \left(\frac{r}{b} \right)^{2n} \right] (a_2^{n+2} - a_1^{n+2})
 \end{aligned}
 \tag{2.81}$$

- Magnetic field in the coil region of the magnet ($a_1 \leq r \leq a_2$)

The total vector potential for this case is a mixture of two previous cases. The integration over the extent of the current shell has to be executed in the following manner:

$$\begin{aligned}
 A_z(r,\theta) &= \frac{2\mu_0 J_0}{\pi} \sum_{n=2l+1} \frac{1}{n} \left[1 + \left(\frac{\mu-1}{\mu+1} \right) \left(\frac{r}{b} \right)^{2n} \right] \cos n\theta \int_0^{\varphi_l} \int_{a_1}^r \left(\frac{a}{r} \right)^n a \cos n\varphi \, da \, d\varphi + \\
 &+ \frac{2\mu_0 J_0}{\pi} \sum_{n=2l+1} \frac{1}{n} \cos n\theta \int_r^{a_2} \int_0^{\varphi_l} \left(\frac{r}{a} \right)^n \left[1 + \left(\frac{\mu-1}{\mu+1} \right) \left(\frac{a}{b} \right)^{2n} \right] a \cos n\varphi \, da \, d\varphi = \\
 &= \frac{2\mu_0 J_0}{\pi} \sum_{n=2l+1} \frac{\cos n\theta \sin n\varphi_l}{n^2} \left\{ \frac{1}{(n+2)r^n} \left[(r^{n+2} - a_1^{n+2}) + \left(\frac{\mu-1}{\mu+1} \right) \left(\frac{r}{b} \right)^{2n} (a_2^{n+2} - a_1^{n+2}) \right] + \right. \\
 &\quad \left. + \frac{r^n}{n-2} \left(\frac{1}{r^{n-2}} - \frac{1}{a_2^{n-2}} \right) \right\}
 \end{aligned}
 \tag{2.82}$$

The multipole field components are:

$$\begin{aligned}
 B_{r,n}(r,\theta) &= -\frac{2\mu_0 J_0}{\pi} \frac{\sin n\theta \sin n\varphi_l}{n} \left\{ \frac{1}{(n+2)r^{n+1}} \left[(r^{n+2} - a_1^{n+2}) + \left(\frac{\mu-1}{\mu+1} \right) \left(\frac{r}{b} \right)^{2n} (a_2^{n+2} - a_1^{n+2}) \right] + \right. \\
 &\quad \left. + \frac{r^{n-1}}{n-2} \left(\frac{1}{r^{n-2}} - \frac{1}{a_2^{n-2}} \right) \right\} \\
 B_{\theta,n}(r,\theta) &= \frac{2\mu_0 J_0}{\pi} \frac{\cos n\theta \sin n\varphi_l}{n} \left\{ \frac{1}{(n+2)r^{n+1}} \left[(r^{n+2} - a_1^{n+2}) - \left(\frac{\mu-1}{\mu+1} \right) \left(\frac{r}{b} \right)^{2n} (a_2^{n+2} - a_1^{n+2}) \right] + \right. \\
 &\quad \left. - \frac{r^{n-1}}{n-2} \left(\frac{1}{r^{n-2}} - \frac{1}{a_2^{n-2}} \right) \right\}
 \end{aligned}
 \tag{2.83}$$

- Magnetic field in the iron yoke ($r > b$)

As it was shown in the previous section the magnetic field in the nonsaturated iron yoke due to a single conductor line carrying current I and placed inside an air cylinder bored within the iron can be represented by a system of two image current lines. The first one with current $I_\alpha = \frac{2I}{\mu+1}$ should be placed in the same position as the original, and the second one carrying current $I_\beta = \frac{\mu-1}{\mu+1}I$ along the central axis of the aperture.

In the current shell model applied for the dipole geometry the conductor lines representing both coils carry currents in opposite directions, therefore the image lines at the center of the magnet's aperture cancel each other out. The contribution of the remaining image conductors to the vector potential is given by Eq. (2.56), which for the iron of permeability μ takes the following form:

$$A_z(r, \theta) = \frac{2\mu_0\mu I_\alpha}{\pi} \sum_{n=2l+1} \frac{1}{n} \left(\frac{a}{r}\right)^n \cos n\varphi \cos n\theta = \frac{4\mu_0\mu I}{(\mu+1)\pi} \sum_{n=2l+1} \frac{1}{n} \left(\frac{a}{r}\right)^n \cos n\varphi \cos n\theta \quad (2.84)$$

The integration over the radial and angular extent of the image shell (which has the same geometry as the original current shells) yields:

$$A_z(r, \theta) = \frac{4\mu_0\mu J_0}{(\mu+1)\pi} \sum_{n=2l+1} \frac{\cos n\theta \sin n\varphi_l}{n^2(n+2)r^n} (a_2^{n+2} - a_1^{n+2}) \quad (2.85)$$

The multipole components are:

$$B_{r,n}(r, \theta) = -\frac{4\mu_0\mu J_0}{(\mu+1)\pi} \frac{\sin n\theta \sin n\varphi_l}{n(n+2)r^{n+1}} (a_2^{n+2} - a_1^{n+2}) \quad (2.86)$$

$$B_{\theta,n}(r, \theta) = \frac{4\mu_0\mu J_0}{(\mu+1)\pi} \frac{\cos n\theta \sin n\varphi_l}{n(n+2)r^{n+1}} (a_2^{n+2} - a_1^{n+2})$$

Magnetic flux lines for the dipole geometry current shells characterized by inner radius $a_1 = 40$ mm, outer radius $a_2 = 60$ mm, and the limiting angle of $\varphi_l = \pi/3$, enveloped by the iron yoke with inner bore radius $b = 100$ mm are plotted in Fig. 2.27 for the relative permeability $\mu = 9$. Es an example, the magnetic flux lines for a variant of the twin aperture dipole magnet calculated with the Poisson program package [11] are shown in Fig. 2.28.

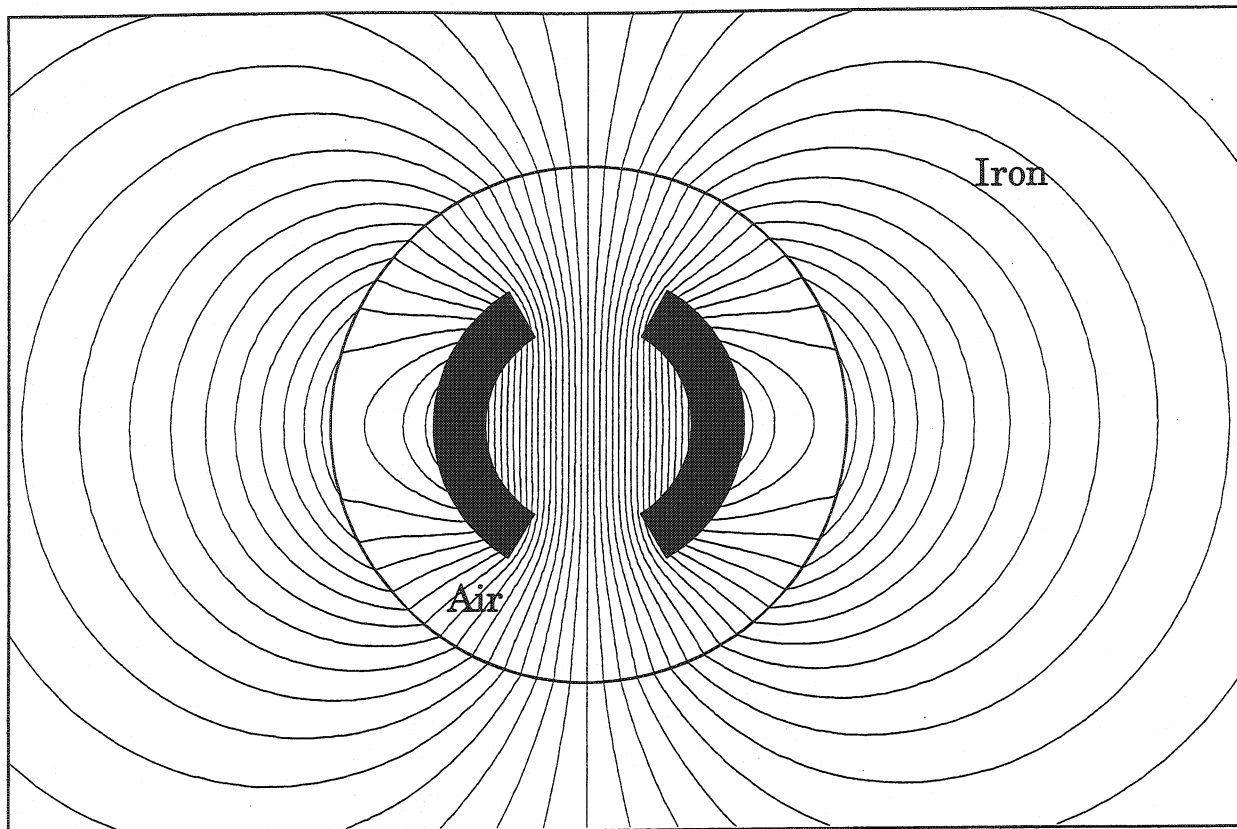


Figure 2.27 Magnetic flux lines generated by the dipole geometry current shells with nonsaturated iron yoke

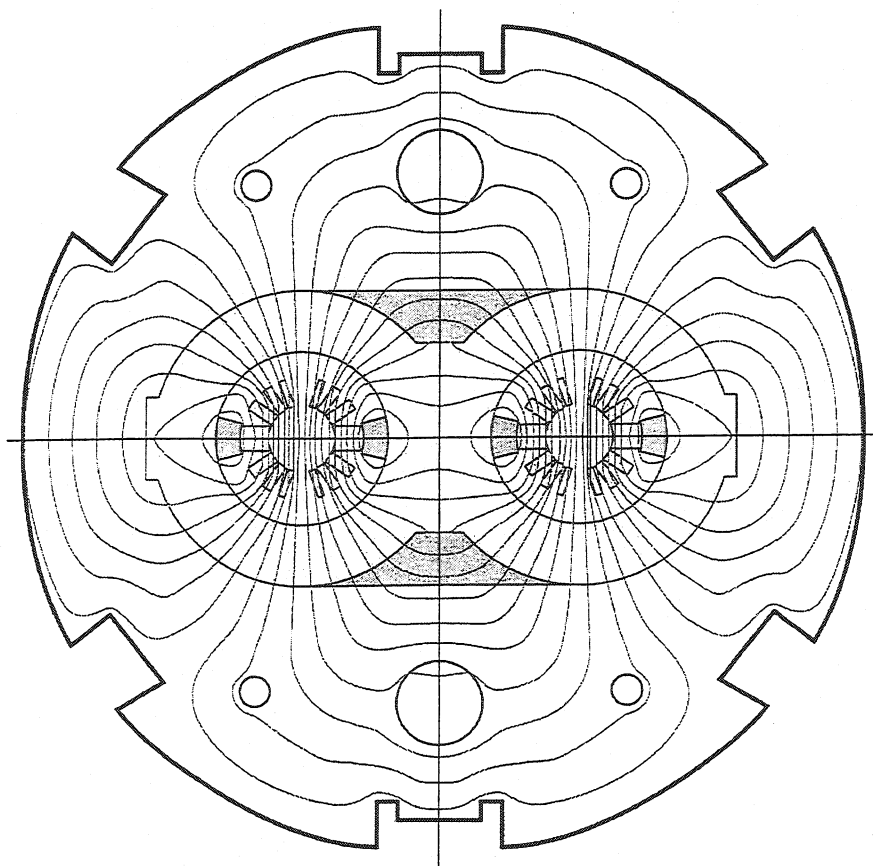


Figure 2.28 Magnetic flux lines generated by a twin aperture dipole magnet

2.10.3 Single Aperture LHC Dipole Magnet with Nonsaturated Iron Yoke

The quality of the field in the region where the particle beam is guided, i.e. inside the magnet's aperture is of special interest. In that region the field in the median plane of the magnet is:

$$B_n = B_{\theta,n}(r, 0) = -\frac{2\mu_0 J_0}{\pi} \frac{r^{n-1}}{n} \sin n\varphi_l \left\{ \frac{1}{n-2} \left(\frac{1}{a_1^{n-2}} - \frac{1}{a_2^{n-2}} \right) + \left(\frac{\mu-1}{\mu+1} \right) \frac{1}{b^{2n}(n+2)} (a_2^{n+2} - a_1^{n+2}) \right\} \quad (2.87)$$

The nonsaturated iron yoke does not produce any new multipoles in the magnet. For the dipole geometry coils the index n takes the values of odd numbers only as it was in the case of the bare coil arrangement. The ratio of the iron to coil contribution to the magnetic field induction is:

$$\frac{B_{n,iron}}{B_{n,coil}} = \frac{\left(\frac{\mu-1}{\mu+1} \right) \frac{1}{b^{2n}(n+2)} (a_2^{n+2} - a_1^{n+2})}{\frac{1}{n-2} \left(\frac{1}{a_1^{n-2}} - \frac{1}{a_2^{n-2}} \right)} = \left(\frac{\mu-1}{\mu+1} \right) \frac{n-2}{b^{2n}(n+2)} \frac{(a_1 a_2)^{n-2} (a_2^{n+2} - a_1^{n+2})}{a_2^{n-2} - a_1^{n-2}} \quad (2.88)$$

Taking into account that the permeability of the nonsaturated iron yoke of the LHC dipole magnet is $\mu = 4000$, the ratio $(\mu - 1)/(\mu + 1) \approx 1$ and the formula (2.88) is reduced to:

$$\frac{B_{n,iron}}{B_{n,coil}} = \frac{n-2}{b^{2n}(n+2)} \frac{(a_1 a_2)^{n-2} (a_2^{n+2} - a_1^{n+2})}{a_2^{n-2} - a_1^{n-2}} \quad (2.89)$$

The inner bore radius of the LHC iron yoke is $b = 98$ mm. For $n = 1$ the presence of the iron yoke enhances the magnetic field generated uniquely by the coils by 13.5 % in the case of the inner layer and by 27.9 % in the case of the outer one. Taking the approximated results of section 2.8 into account the total dipole field due to both layers enveloped by a nonsaturated iron yoke is,

$$B_{1,total} = B_{\theta,1}(r_0, 0) = -\frac{5.676 \mu_0 J_0}{\pi} \cdot 10^{-2} [T]$$

which amounts to -8.29 T, and means that the intensity of the dipole field in the aperture of the magnet is 21.4 % greater than the one generated only with the coils (see section 2.8).

Or in other words, the magnetic field due to the iron yoke constitutes 17.6 % of the total dipole field in the magnet:

$$\frac{B_{1,iron}}{B_{1,total}} = 0.176$$

Let us analyze how the iron yoke influences the values of the other multipole coefficients. For the sextupole ($n = 3$) there is a 0.2 % field enhancement due to the inner layer and 2.18 % due to the outer one. The total field sextupole field is:

$$B_3 = B_{\theta,3}(r_0, 0) = -\frac{1.16 \mu_0 J_0}{\pi} \cdot 10^{-5} [T]$$

And the relative multipole coefficient is:

$$b_3 = \frac{B_3}{B_{1,total}} = 2.04 \cdot 10^{-4}$$

With the presence of the iron yoke the sextupole component becomes slightly smaller for the current shell model analyzed in section 2.8. In practice the distribution of the material in the real iron yoke is shaped taking into account its influence on the value of b_3 . The decapole component ($n = 5$) due to both layers is almost not affected (inner layer by 0.004 %, outer by 0.17%.):

$$B_5 = B_{\theta,5}(r_0, 0) = -\frac{0.383 \mu_0 J_0}{\pi} \cdot 10^{-5} [T] \quad b_5 = \frac{B_5}{B_{1,total}} = 0.675 \cdot 10^{-4}$$

For $n = 7$ there is virtually no field change due to the iron yoke (0.0008% for inner layer, and 0.013% for the outer one.) The relative multipole coefficient is lower due to the important dipole field increase.

$$b_7 = \frac{B_7}{B_{1,total}} = 0.17 \cdot 10^{-4}$$

B_9 is also not affected by the presence of the iron yoke (by $1.3 \cdot 10^{-6}$ % for the inner, and by 0.001 % for the outer layer.)

$$b_9 = \frac{B_9}{B_{1,total}} = 0.026 \cdot 10^{-4}$$

The results for the current shell model without and with iron yoke are grouped in Table 2.3. Since the current shell model does not take into account the effect of thermal contraction it is compared with the results of the ROXIE calculations under warm conditions and without current grading in the conductors. (Table 2.4). The analytical calculations for the nonsaturated iron yoke in ROXIE are also based on the image method with the difference that an image current line is created for every superconducting strand in the cable cross-section. In this way a high precision analytical solution is obtained. Table 2.5 contains different variations of the ROXIE cases with the nonsaturated iron yoke. The percentage of the dipole field enhancement in comparison to the dipole field generated by the coils only is given in brackets next to the coefficient B_1 . Corresponding values of B_1 due to the coils were given in Table 2.2.

Table 2.3 Current Shell Model Results

$r_0 = 10$ mm	B_1 [T]	b_3	b_5	b_7	b_9
coils only	-6.83	2.18	0.82	0.21	0.030
coils with nonsaturated iron yoke	-8.29 (21.4 %)	2.04	0.68	0.17	0.026

Table 2.4 ROXIE Model Results

$r_0 = 10$ mm (uniform current dens., warm conditions)	B_1 [T]	b_3	b_5	b_7	b_9
coils only	-6.85	1.940	-0.126	0.032	0.0019
coils with nonsaturated iron yoke	-8.31 (21.3 %)	1.920	-0.106	0.026	0.0016

Table 2.5 Various ROXIE Cases for Nonsaturated Iron Yoke

$r_0 = 10$ mm	B_1 [T]	b_3	b_5	b_7	b_9
Current grading, cold conditions	-8.36 (21.2 %)	1.434	-0.106	0.026	0.0015
Current grading, warm conditions	-8.33 (21.1 %)	1.426	-0.104	0.025	0.0014
Uniform current density, cold	-8.33 (21.3 %)	1.932	-0.108	0.027	0.0016
Uniform current density, warm	-8.31 (21.3 %)	1.920	-0.106	0.026	0.0016

Analyzing the results in all tables the conclusions similar to the ones in section 2.9 can be drawn. The current shell model gives not only a good estimate of the main dipole field due to the coils but also a correct value of its enhancement caused by the nonsaturated iron yoke. Looking at the formula (2.87) it is clear that by bringing the boundary of the iron yoke closer to the coils one can obtain a dipole enhancement much more substantial than 20%. For example, if the inner bore radius of the iron yoke is changed from 98 to 80 mm, the dipole magnetic field in the ROXIE case in Table 2.4 will increase from 8.31 to 9.04 T giving thus a 32 % magnetic field enhancement due to the yoke. Unfortunately this may jeopardize the

stability of the magnet system. Bringing the yoke closer to the coils of the magnet imposes the decrease of the size of the collars. As a consequence this direct reinforcement structure of the coils may be not rigid enough to efficiently counteract the Lorentz forces exerted on the coils. On the other hand the closer the iron is to the coils the higher magnetic field penetrates into the yoke causing its faster saturation. Thus the iron yoke boundary cannot be simply brought as close as possible to the magnet coils.

The iron yoke does not significantly affect the higher order field harmonics. During the design process the field harmonics are usually at first optimized using the analytical approach with the nonsaturated yoke. In reality the yoke is not fully saturated only during the ramping of the magnet at low currents; when the magnetic field in the magnet is very low. The saturation effects on the magnetic field pattern, and especially on the lower order field harmonics are addressed in the next section.

2.11 Saturated Iron Yoke

During the operation of the magnet at its nominal field of 8.36 T the iron yoke is highly saturated. The permeability of the iron is not uniform – it depends on the position within the yoke. Eq. (2.3), which applies to this problem, can be alternatively written as,

$$\vec{B} = \mu(\vec{H})\vec{H} \quad (2.90)$$

where $\mu(H)$ is a field-dependent permeability of the saturated iron yoke. For isotropic soft magnetic materials μ can be considered to be a scalar mono-valued function of the magnetic field intensity. Taking under consideration that μ is a function it is more convenient to rewrite Eq. (2.11) for the magnetostatic problem as:

$$\nabla \times \frac{1}{\mu} \nabla \times \vec{A}_z = \vec{j}_z \quad (2.91)$$

The most efficient techniques of solving it numerically for the complex problem domains are based on the Finite Element Method (FEM). The term *finite element* appeared for the first time in the literature in 1960 [12]. The first comprehensive book introducing the numerical calculation procedure was written by Zienkiewicz [13]. Originally the method was used to handle the complex problems of structural mechanics. The earliest application of FEM to the electromagnetic problems dates back to 1967 [14]. The first paper that treated the finite element solution for the saturated magnetic materials was written in 1970 [15]. Nowadays many sophisticated software packages like ROXIE, ANSYS [16], OPERA [17] address electromagnetic problems for static, as well as for steady state and transient time-varying magnetic fields using FEM solvers.

The principle of FEM is based on the discretization of the problem domain into a number of small inter-connected sub-regions called elements. The network of the elements obtained after the division of the solution domain constitutes a mesh. An example of the mesh generated with triangular elements is shown in Fig. 2. 29. The objective of the method is to approximate the unknown vector potential in each element by a certain trial function, which interpolates the behavior of the unknown function within the element. With the application of weighted residuals method or by minimization of properly constructed functionals in variational principle, the partial differential equations defining the problem, are reduced to a sparse matrix equation. In this way an algebraic system of equations is obtained.

FEM can treat problems with high degree of complexity of the geometry and media distribution. The disadvantage of the method is that only a finite domain can be divided into

elementary sub-regions. As a consequence all of the open boundary problems that have to consider an infinite space must be approximated with far field boundaries, i.e. a large air region must be meshed around the effective model in order to validate the solution and minimize the approximation errors. Moreover, not only the iron yoke, but also the complicated coil region must be meshed. In Fig. 2.29 a part of the mesh in the coil region is shown. As one can see even the small air gaps between the conductive areas of the cable must be divided into finite elements. Sometimes this may pose major problems during the subdivision, because the length of the air gaps (15 mm) is unproportionally bigger than their width (250 μm).

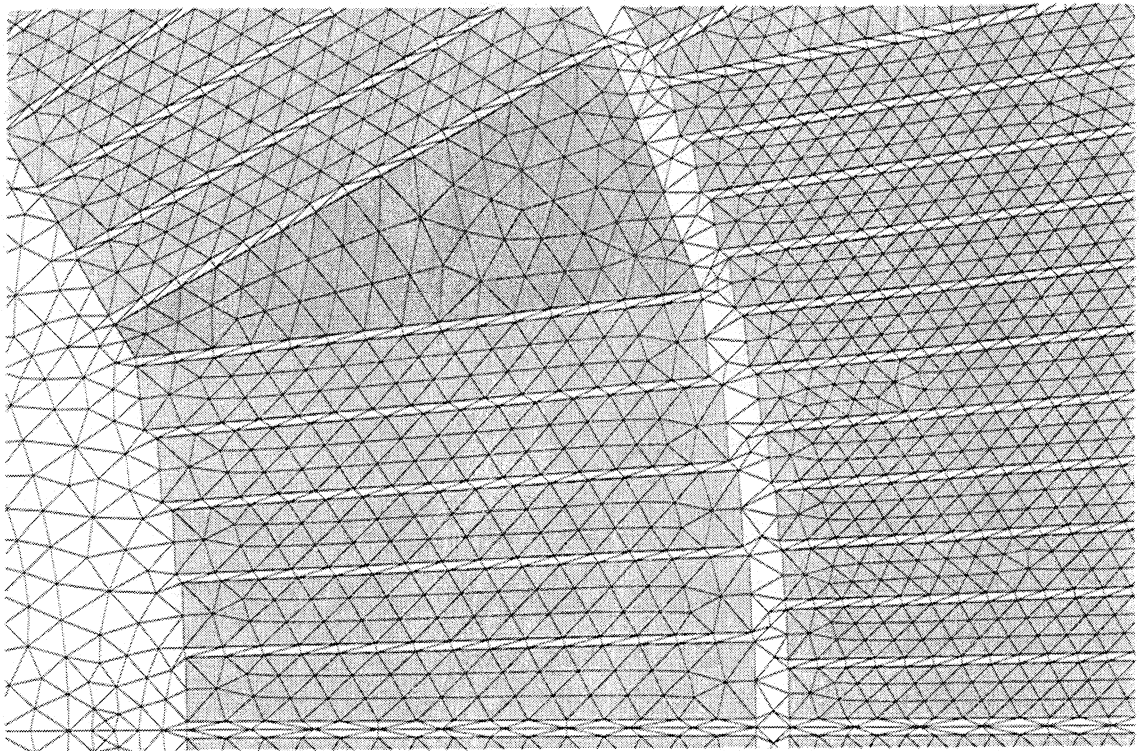


Figure 2.29 A fragment of the problem domain meshed with triangular elements

A high-precision analytical solution for the coil region can be obtained without resorting to FEM as it was demonstrated in the previous sections. The FEM solver incorporated in ROXIE [18] is based on a reformulation of the standard total vector potential representation of FEM by means of the reduced vector potential [19]. This approach does not require the meshing of the domain in the coil region and allows to combine the FEM solution for the saturated iron yoke with the analytical solution for the coils. Such an approach reduces also the calculation errors due to the far field boundary. The aperture of the magnet must still be meshed pro forma but the mesh does not have to represent the geometry of the coils. Although the benefits of this method are satisfactory in 2-D problems the approach becomes quite inconvenient in the 3-D calculations.

Further advantages can be achieved with a relatively young Boundary Element Method (BEM), which is based on the boundary integral equation and the principle of weighted residuals. The objective of BEM is to find the unknown function and its normal derivative along the boundary between the media. The first book entitled Boundary Elements was published in 1978 [20]. Since then the BEM approach addresses also nonlinear and time dependent problems. On the contrary to FEM, BEM is defined on an infinite domain and can address open boundary problems without approximation. Unfortunately, as compared to FEM, the consideration of nonhomogenous materials is much more difficult using BEM formalism.

Optimal results are obtained with the coupled BEM-FEM method. The idea was developed at the University of Stuttgart in Germany [21] and combines the FEM formalism for the magnetic media with the BEM description applied for the regions containing imposed source currents and for the air space surrounding the model [22]. This method gives also an essential reduction of the size of the system matrix describing the problem, which reflects substantially in the speed of the numerical calculations.

2.11.1 FEM Formulation for 2-D Numerical Analysis of the LHC Dipole Magnets with Saturated Iron Yoke

The FEM approach will be extensively used in chapter 3 for the analysis of the transient states of the magnetic field. The presentation of the method adapted specifically for the LHC magnets starts already here in the magnetostatic case.

An example of a problem domain for a single aperture dipole magnet is shown in Fig. 2.30. For the fully symmetric geometry it is entirely sufficient to consider only a quadrant of the domain with properly applied symmetry conditions. When the analysis comprises asymmetric current distributions or geometry, the entire domain must be modeled. The coils are confined in a fixed volume of the iron bore by the collars. Since the collars are made of nonmagnetic stainless steel they are not included in the static model. However, when the magnetic fields are time varying, also all of the nonmagnetic metallic materials must be taken under consideration, as it will turn out in chapter 4.

The entire solution domain Ω consists of two sub-domains representing the air Ω_{air} with permeability μ_0 and the iron Ω_{iron} with permeability μ . The air regions can contain a number of conductor sources with imposed currents, which do not intersect the air region. Let us remind that all of the imposed currents in any 2-D problem flow uniquely in the OZ

direction. The first step on the way to the FEM solution is to formulate the problem in terms of physical laws. The problem is described by the equation (2.91) valid in the entire domain $\Omega = \Omega_{\text{air}} \cup \Omega_{\text{iron}}$.

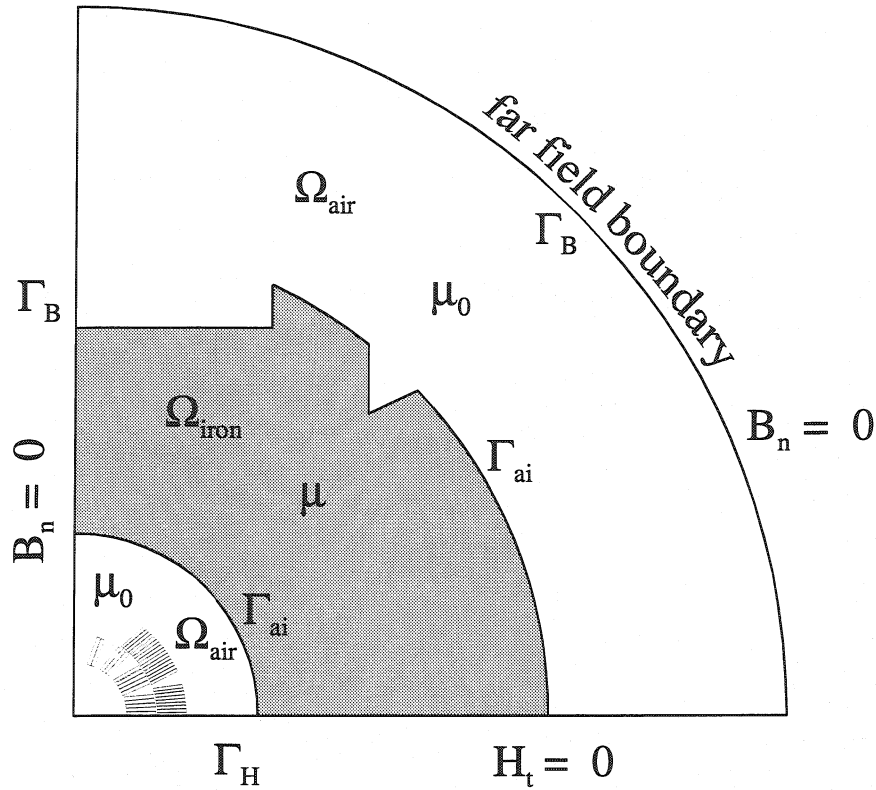


Figure 2.30 Elementary model for the numerical magnetic field calculation in a single aperture dipole magnet with the saturated iron yoke

Equation (2.91) is subject to the following boundary conditions,

- satisfied on the boundary Γ_B :

$$\vec{B} \cdot \vec{n} = (\nabla \times \vec{A}_z) \cdot \vec{n} = 0 \Rightarrow A_z = 0 \quad (2.92)$$

- satisfied on the boundary Γ_H

$$\vec{H} \times \vec{n} = \frac{1}{\mu} (\nabla \times \vec{A}_z) \times \vec{n} = 0 \Rightarrow \frac{\partial A_z}{\partial n} = 0 \quad (2.93)$$

These are homogenous Dirichlet and Neumann boundary conditions. A Dirichlet condition specifies a value of the unknown function, whereas a Neumann condition assigns a value of its normal derivative on the boundary. A combination of both kinds of the boundary conditions must be then

- satisfied on the interface air-iron Γ_{ai} :

$$(\vec{B}_i - \vec{B}_a) \cdot \vec{n} = 0 \Rightarrow A_{z,i} = A_{z,a} \quad (2.94)$$

$$(\vec{H}_i - \vec{H}_a) \times \vec{n} = \left(\frac{1}{\mu} (\nabla \times \vec{A}_{z,i}) - \frac{1}{\mu_0} (\nabla \times \vec{A}_{z,a}) \right) \times \vec{n} = 0 \Rightarrow \frac{1}{\mu} \frac{\partial A_{z,i}}{\partial n} = \frac{1}{\mu_0} \frac{\partial A_{z,a}}{\partial n} \quad (2.95)$$

The complete formulation of the 2-D problem is given by the differential equation (2.91) and its boundary value problem specified by the conditions (2.92- 2.95).

The second step is to subdivide the problem domain into a net of finite elements as demonstrated in Fig. (2.29.) This operation replaces the solution domain with infinite degrees of freedom by a meshed domain having finite number of degrees of freedom. In reality ROXIE uses quadrilateral elements, because they provide better interpolation of the vector potential within the elements and are easier to extrude in a 3-D case. However in order to simplify the discussion, simple 3-noded triangular elements, as shown in Fig. (2.29), will be used. Let us consider one of such elements denoted as e and drawn in Fig. (2.31).

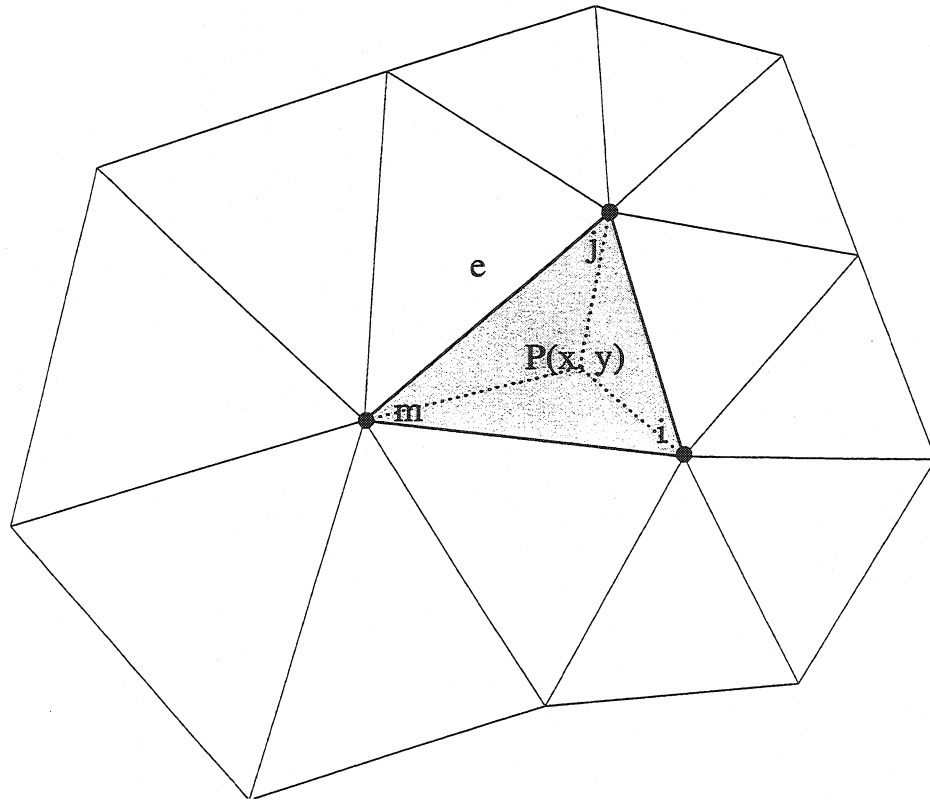


Figure 2.31 A finite element in a fragment of triangular mesh

The behavior of the unknown vector potential A_z is approximated within the element by a function A_e constructed as a linear polynomial:

$$A_z(x, y) \approx A_e(x, y) = \alpha_1 + \alpha_2 x + \alpha_3 y \quad (2.96)$$

The choice of the polynomial is dictated by the ease of its integration and differentiation, as well as by the fact that any function can be approximated by a polynomial containing enough terms. The unknown coefficients α are evaluated from the nodal values of approximation (2.96). The element contains three nodes and there are also three unknown coefficients α ; thus the representation (2.96) of the vector potential is said to be complete, because it contains all of the terms necessary to account for the linear variation of A_e within a triangular element. For quadrilateral elements a corresponding complete interpolation of A_z within the element would read:

$$A_z(x, y) \approx A_e(x, y) = \alpha_1 + \alpha_2 x + \alpha_3 y + \alpha_4 xy$$

Coming back to the triangular mesh, a following system of equations can be written for the nodes of the element e :

$$\begin{cases} A_i = \alpha_1 + \alpha_2 x_i + \alpha_3 y_i \\ A_j = \alpha_1 + \alpha_2 x_j + \alpha_3 y_j \\ A_m = \alpha_1 + \alpha_2 x_m + \alpha_3 y_m \end{cases} \quad (2.97)$$

Equation system (2.97) in matrix representation is:

$$\begin{bmatrix} A_i \\ A_j \\ A_m \end{bmatrix} = \begin{bmatrix} 1 & x_i & y_i \\ 1 & x_j & y_j \\ 1 & x_m & y_m \end{bmatrix} \begin{bmatrix} \alpha_1 \\ \alpha_2 \\ \alpha_3 \end{bmatrix} \quad (2.98)$$

The solution of matrix equation (2.98) is

$$\alpha_1 = \frac{1}{2S} \begin{vmatrix} A_i & x_i & y_i \\ A_j & x_j & y_j \\ A_m & x_m & y_m \end{vmatrix} \quad \alpha_2 = \frac{1}{2S} \begin{vmatrix} 1 & A_i & y_i \\ 1 & A_j & y_j \\ 1 & A_m & y_m \end{vmatrix} \quad \alpha_3 = \frac{1}{2S} \begin{vmatrix} 1 & x_i & A_i \\ 1 & x_j & A_j \\ 1 & x_m & A_m \end{vmatrix} \quad (2.99)$$

where S is the area of the element:

$$S = \frac{1}{2} \begin{vmatrix} 1 & x_i & y_i \\ 1 & x_j & y_j \\ 1 & x_m & y_m \end{vmatrix}$$

If auxiliary coefficients a_i, b_i, c_i , are defined as,

$$\begin{aligned} a_i &= \begin{vmatrix} x_j & y_j \\ x_m & y_m \end{vmatrix} = x_j y_m - y_j x_m \\ b_i &= - \begin{vmatrix} 1 & y_j \\ 1 & y_m \end{vmatrix} = y_j - y_m \\ c_i &= \begin{vmatrix} 1 & x_j \\ 1 & x_m \end{vmatrix} = x_m - x_j \end{aligned} \quad (2.100)$$

and the remaining coefficients $a_j, b_j, c_j, a_m, b_m, c_m$, are created by analogy, using cyclic permutation of indices, the solution (2.99) can be conveniently rewritten as,

$$\begin{cases} \alpha_1 = \frac{1}{2S} (a_i A_i + a_j A_j + a_m A_m) \\ \alpha_2 = \frac{1}{2S} (b_i A_i + b_j A_j + b_m A_m) \\ \alpha_3 = \frac{1}{2S} (c_i A_i + c_j A_j + c_m A_m) \end{cases} \quad (2.101)$$

with

$$S = \frac{1}{2} (a_k + b_k x_k + c_k y_k)$$

where $k = i, j, m$. Substituting the solution (2.101) into Eq. (2.96) gives the following result,

$$A_e(x, y) = \sum_k \frac{1}{2S} (a_k + b_k x + c_k y) A_k = \sum_k N_k^e A_k \quad (2.102)$$

which is valid locally in the domain Ω_e spawn by the element. The functions N_k given by,

$$N_k^e = \frac{1}{2S} (a_k + b_k x + c_k y) \quad (2.103)$$

are the local shape functions assigned to the element e . Thus the vector potential (2.102) interpolating the behavior of the field within the element is a linear combination of the shape functions and the nodal values of this element. Formula (2.103) transforms the Cartesian coordinates of the element into the area coordinates. For example the value of N_j at point $P(x_p, y_p)$, which lies within the element e (see Fig. 2.31),

$$N_j^e(x_p, y_p) = \frac{1}{2S} (a_j + b_j x_p + c_j y_p) \quad (2.104)$$

is a ratio of the surface of the triangle Δ_{miP} to the surface of the entire element.

Thus the shape functions specify the area coordinates of the point inside the element. The inverse transformation from the area to the Cartesian coordinates yields:

$$\begin{aligned}x_p &= N_i(P)x_i + N_j(P)x_j + N_m(P)x_m \\y_p &= N_i(P)y_i + N_j(P)y_j + N_m(P)y_m \\1 &= N_i(P) + N_j(P) + N_m(P)\end{aligned}\tag{2.104}$$

The third equation in (2.104) is an identity. It gives the ratio of the sum of all three internal sub-triangles, defined between the point P and the nodes of the element, to the surface of the entire element. It expresses the fact that only two area coordinates are independent – only two shape functions are the base functions of the area coordinate system. Summing up, the shape functions have the following properties:

- $N_k^e(x_l, y_l) = \delta_{k,l}$ where k and $l = i, j, m$ and δ symbol is a Kronecker's delta:

$$\delta_{k,l} = \begin{cases} 1 & \text{for } k = l \\ 0 & \text{for } k \neq l \end{cases}$$

Thus, e.g. $N_i = 1$ at node i and zero at all the remaining nodes of the element.

- $\sum_k N_k^e(P) = \begin{cases} 1 & \text{if point P is inside the element} \\ 0 & \text{if point P is outside the element} \end{cases}$

The solution for the vector potential within the element is not an exact solution of the problem equation (2.91), therefore when (2.102) is substituted into Eq. (2.91) a residual will be created inevitably.

$$\nabla \times \frac{1}{\mu_e} \nabla \times \sum_k N_k^e \vec{A}_k - \vec{j}_z = \vec{R}_e\tag{2.105}$$

The permeability in Eq. (2.105) in the iron region is considered to be constant in each element, although it may vary from one subdivision area to another. In the air region it is constant in all of the elements.

The next step for obtaining a system of algebraic equations for unknown A_k is to force the residuals R_e to zero in an average sense over the entire domain Ω . The entire problem domain consists of the sum of all of the sub-domains Ω_e defined by the finite elements.

$$\Omega = \sum_{e=1}^K \Omega_e$$

Index K indicates the total number of elements in the mesh. If the global residual tends to zero in the entire domain, the approximated vector potential can be considered as a good approximate solution of the problem. Forcing of the global residual to zero is done by means of an arbitrary weighting function w .

$$\int_{\Omega} \vec{w} \cdot \vec{R} d\Omega = \sum_{e=1}^K \int_{\Omega_e} \vec{w}_k \cdot \vec{R}_e d\Omega = 0 \quad (2.106)$$

In Eq. (2.105), which describes a single element the residual vector R_e has only a z component, because in the 2-D problem vector potential and imposed current sources have only this component. In this regard the vector weighting functions w_k must have only a z component as well.

$$\vec{w}_k = \begin{bmatrix} 0 \\ 0 \\ w_k \end{bmatrix}$$

Moreover, they must obey the homogeneous complementary boundary conditions:

$$\begin{aligned} \vec{w}_k \cdot \vec{n} &= 0 \quad \text{on the boundary } \Gamma_H \\ \vec{w}_k \times \vec{n} &= 0 \quad \text{on the boundary } \Gamma_B \end{aligned} \quad (2.107)$$

Forcing the residuals in Eq. (2.105) to zero for all of the elements in the problem domain yields:

$$\int_{\Omega} \vec{w} \cdot \vec{R} d\Omega = \sum_{e=1}^K \int_{\Omega_e} \vec{w}_k \cdot \vec{R}_e d\Omega = \sum_{e=1}^K \int_{\Omega_e} \vec{w}_k \cdot \left(\nabla \times \frac{1}{\mu_e} \nabla \times \vec{A}_e - \vec{j}_z \right) d\Omega = 0 \quad (2.108)$$

Hence

$$\sum_{e=1}^K \int_{\Omega_e} \vec{w}_k \cdot \left(\nabla \times \frac{1}{\mu_e} \nabla \times \vec{A}_e \right) d\Omega = \sum_{e=1}^K \int_{\Omega_e} \vec{w}_k \cdot \vec{j}_z d\Omega \quad (2.109)$$

Eq. (2.108) will hold only if all of the integrals on the left-hand side of Eq. (2.109) are finite. The definitions and the properties of the shape functions N_k assure this for all of the points inside the elements, nevertheless the property is not guaranteed while crossing the boundary between the adjacent elements due to the discontinuities resulting from the differentiation of the vector potential. To demonstrate it let us consider a simple 1-D example illustrated in Fig. 2.32. At the boundary between the elements the vector potential is by definition always forced to be continuous. Its first derivative is not continuous nevertheless it is finite. Yet it is clear that the second derivative will be neither continuous nor finite at the boundary between both elements. This level of continuity is known as C_0 . An equivalent type of the second order derivative in 2-D would cause a problem in Eq. (2.109). Therefore the equation under

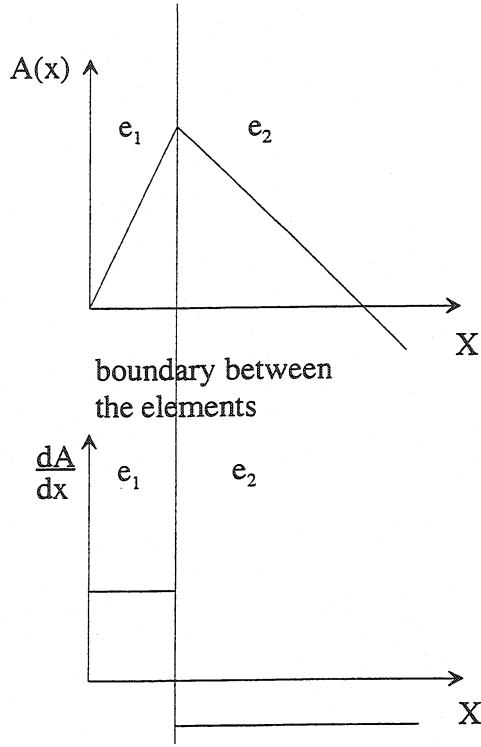


Figure 2.32 A C_0 continuity of a function

question should be transformed to the weak form, which does not contain the derivatives higher than the first order. One can get rid of the second order derivatives in Eq. (2.109) by using the vector form of the Green's theorem, according to which:

$$\begin{aligned} \int_{\Omega_e} \bar{w}_k \cdot \left(\nabla \times \frac{1}{\mu_e} \nabla \times \bar{A}_e \right) d\Omega &= \quad (2.110) \\ &= \int_{\Omega_e} \left(\frac{1}{\mu_e} \nabla \times \bar{A}_e \right) \cdot (\nabla \times \bar{w}_k) d\Omega - \oint_{\Gamma} \bar{w}_k \cdot \left(\frac{1}{\mu_e} \nabla \times \bar{A}_e \times \bar{n} \right) d\Gamma \end{aligned}$$

While transforming Eq. (2.109) the circular integral in identity (2.110) is evaluated step by step for all elements in turn and vanishes due to the interface condition requiring the continuity of the magnetic flux between them. For the elements, which are a part of the global problem boundaries Γ_H , Γ_B or Γ_{ai} the circular

integral vanishes there due to the boundary value problem specified by conditions (2.92 – 2.95) combined with the complementary boundary conditions (2.107) satisfied by the weighting functions. In this way Eq. (2.109) is reduced to:

$$\sum_e \int_{\Omega_e} \left(\frac{1}{\mu_e} \nabla \times \bar{A}_e \right) \cdot (\nabla \times \bar{w}_k) d\Omega = \sum_e \int_{\Omega_e} \bar{w}_k \cdot \bar{j}_z d\Omega \quad (2.111)$$

Thus the second order derivatives in Eq. (2.111) are already removed, and the continuity requirements for the vector potential across the element boundaries are reduced. However, the first derivatives of w_k appear in the equation, which implies that the transformation was done at the cost of increase of the continuity requirements put on the weighting functions. Both the vector potential and the weighting function in 2-D problems have only the z component while being independent of the z coordinate at the same time, therefore both can be represented as,

$$\begin{aligned} \nabla \times \bar{A}_e &= \nabla A_e \times \bar{e}_z \\ \nabla \times \bar{w}_k &= \nabla w_k \times \bar{e}_z \end{aligned}$$

which further simplifies Eq. (2.111) to

$$\sum_e \int_{\Omega_e} \frac{1}{\mu_e} (\nabla w_k) \cdot (\nabla A_e) d\Omega = \sum_e \int_{\Omega_e} \bar{w}_k \cdot \bar{j}_z d\Omega \quad (2.112)$$

The current density is present in Eq. (2.112), which enforces, as mentioned already before, that the coil region must be meshed reflecting the coil geometry of the magnet. In the next section it will be demonstrated how to avoid it.

The final step on the way to the FEM solution is to derive the matrix equation for the single element. Using the Galerkin's approach the choice of the weighting functions coincides with the shape functions. Thus

$$\vec{w}_k = \vec{N}_k^e = \begin{bmatrix} 0 \\ 0 \\ N_k^e \end{bmatrix}$$

Since the shape functions are C_0 continuous this choice does not violate the increased continuity requirements imposed on the weighting functions by equation (2.112). It was also shown [23] that apart from a few isolated cases this method gives the best results. In this regard the equation (2.112) rewritten for a single element becomes:

$$\int_{\Omega_e} \frac{1}{\mu_e} \left(\frac{\partial N_k^e}{\partial x} \frac{\partial A_e}{\partial x} + \frac{\partial N_k^e}{\partial y} \frac{\partial A_e}{\partial y} \right) d\Omega - \int_{\Omega_e} N_k^e j_z d\Omega = 0 \quad (2.113)$$

Partial derivatives of N_k and A_e with respect to x and y can be calculated directly from Eqs. (2.103) and (2.102). Hence,

$$\begin{aligned} \frac{\partial N_k^e}{\partial x} &= \frac{b_k}{2S} \\ \frac{\partial N_k^e}{\partial y} &= \frac{c_k}{2S} \\ \frac{\partial A_e}{\partial x} &= \sum_k \frac{b_k A_k}{2S} \\ \frac{\partial A_e}{\partial y} &= \sum_k \frac{c_k A_k}{2S} \end{aligned}$$

where $k = i, j, m$. As far as the second term in Eq. (2.113) is concerned the current density is constant in the elements representing the coils and can be taken out before the integral. In the remaining elements it is zero. The integral of N_k is executed over the surface of the triangular element:

$$\begin{aligned} \int_{\Omega_e} N_k^e dx dy &= \frac{a_k}{2S} \int_{\Omega_e} dx dy + \frac{b_k}{2S} \int_{\Omega_e} x dx dy + \frac{c_k}{2S} \int_{\Omega_e} y dx dy = \\ &= \frac{1}{2S} \left(a_k S + b_k S \cdot \frac{1}{3} \sum_k x_k + c_k S \cdot \frac{1}{3} \sum_k y_k \right) = \frac{1}{2} (a_k + b_k \bar{x} + c_k \bar{y}) = \frac{1}{2} \cdot \frac{2}{3} S = \frac{S}{3} \end{aligned}$$

Thus Eq. (2.113) evaluated at the node $k = i$ yields:

$$\frac{1}{\mu_e} \left(\frac{b_i}{2S} \sum_{k=i,j,m} \frac{b_k A_k}{2S} + \frac{c_i}{2S} \sum_{k=i,j,m} \frac{c_k A_k}{2S} \right) \cdot S - \frac{S}{3} j_z = 0 \quad (2.114)$$

After regrouping the terms, Eq. (2.114) is transformed to:

$$\frac{1}{4\mu_e S} ((b_i^2 + c_i^2) A_i + (b_i b_j + c_i c_j) A_j + (b_i b_m + c_i c_m) A_m) - \frac{S}{3} j_z = 0 \quad (2.115)$$

By repeating the same procedure for the remaining nodes the entire element matrix can be assembled:

$$\frac{1}{4\mu_e S} \begin{bmatrix} b_i^2 + c_i^2 & b_i b_j + c_i c_j & b_i b_m + c_i c_m \\ b_j b_i + c_j c_i & b_j^2 + c_j^2 & b_j b_m + c_j c_m \\ b_m b_i + c_m c_i & b_m b_j + c_m c_j & b_m^2 + c_m^2 \end{bmatrix} \cdot \begin{bmatrix} A_i \\ A_j \\ A_m \end{bmatrix} - \frac{S}{3} j_z \cdot \begin{bmatrix} 1 \\ 1 \\ 1 \end{bmatrix} = 0 \quad (2.116)$$

Matrix equation (2.116) can be rewritten in a convenient short form as:

$$\mathbf{K}_e \mathbf{A}^e + \mathbf{S}_e = 0 \quad (2.117)$$

The element matrix \mathbf{K}_e in Eq. (2.116) is a symmetric matrix of the order of 3 (corresponding to the number of nodes in the element) with positive elements on the diagonal. The vector \mathbf{A}^e contains unknown potentials whereas \mathbf{S}_e is the vector of the source currents.

The complete system matrix of the order N , where N is a total number of the nodes in the domain, is a combination of the matrices obtained for the single elements. The value of unknown potential at a given node is composed of the contributions of all of the values resulting from the elements connected to this node. In order to obtain the system matrix each element matrix must be expanded to the global matrix of the order N by adding zeros in the remaining locations. The coefficients of the element matrix are put in the global matrix at the row-column positions corresponding to the subscripts i, j, m present in the element matrix. During the assembly of the system matrix all of the element matrices must be added together. Thus the generic formula for the global matrix assembly is,

$$\mathbf{K} = \sum_{e=1}^L \mathbf{K}_e \quad (2.118)$$

where L is the total number of elements in the finite element mesh.

The system equation after the assembly of the global matrix has the following form corresponding to the form of the single element equation (2.117).

$$\mathbf{KA} + \mathbf{S} = 0 \quad (2.119)$$

The imposed current sources are present in matrix equation (2.119), which implies that the geometrically complicated coil region must be meshed in the finite element model. In the next section it will be demonstrated how to circumvent this inconvenient requirement by using a reduced vector potential representation.

2.11.2 Reduced vector potential representation

As it was pointed out in the previous section the total vector representation enforces that the geometrically complicated coil region must be modeled in the finite element mesh. Knowing that the source field resulting from the coils can be calculated by means of analytical methods with a good precision it would be of great advantage to fuse the analytical results for the coil region with the FE numerical calculations applied merely to the region of the saturated iron. The discussion in section 2.10.3 demonstrated that the field enhancement due to the nonsaturated iron yoke in the LHC dipole magnet is of the order of 20% in reference to the magnetic field generated by the coils. Thus it is obvious that the major part of the magnetic field in the magnet aperture is definitely attributed to the coil windings. If the precise analytical solution for this region is incorporated into the FEM model for the iron yoke, it will significantly reduce the errors due to the far field boundary in comparison to the total vector potential representation, where all regions must be included in the FE mesh.

These objectives can be achieved by splitting the total vector potential from the previous section into two parts:

$$\vec{A}_z = \vec{A}_s + \vec{A}_r \quad (2.120)$$

The first part, denoted as A_s , represents the vector potential corresponding to the source currents flowing in the coil of the magnet located in free space. The A_r part expresses the reduced vector potential describing uniquely the magnetic field induced by the saturated iron yoke, i.e. the part of the total magnetic field of the fully assembled magnet attributed only to the iron magnetization. The source magnetic field can be calculated from the coil geometry using either the Biot-Savart law or the vector potential integrals. The problem Eq. (2.91) using the new notation of Eq. (2.120) becomes:

$$\nabla \times \frac{1}{\mu} \nabla \times (\vec{A}_s + \vec{A}_r) = \vec{j}_z \quad (2.121)$$

Taking Eqs. (2.1), (2.3) for the air region and the material relationship (2.90) for the saturated iron into account, Eq. (2.121) can be transformed immediately to the following form,

$$\nabla \times \frac{1}{\mu} \nabla \times \vec{A}_r = \nabla \times \vec{H}_s - \nabla \times \frac{\mu_0}{\mu} \vec{H}_s \quad (2.122)$$

in which the vector potential A_r is an unknown function and H_s is the intensity of the magnetic field generated by the coils stripped of the iron. Eq (2.122) is valid in the entire problem domain Ω . The form of this equation is quite similar to the original problem Eq. (2.91), in which the total vector potential was an unknown function, with the exception that here the source current density does not appear explicitly on its right-hand side.

In this formulation the boundary conditions (2.92) and (2.93) become nonhomogeneous Dirichlet and Neumann conditions respectively:

$$(\nabla \times \vec{A}_r) \cdot \vec{n} = -\mu_0 \vec{H}_s \cdot \vec{n} \quad \text{on the boundary } \Gamma_B \quad (2.123)$$

$$\frac{1}{\mu} (\nabla \times \vec{A}_r) \times \vec{n} = -\frac{\mu_0}{\mu} \vec{H}_s \times \vec{n} \quad \text{on the boundary } \Gamma_H \quad (2.124)$$

The interface conditions on the boundary between the iron and the air regions for the reduced vector potential are corresponding to the ones expressed in Eqs. (2.94) and (2.95) for the total vector potential. The weak form of Eq. (2.122) can be obtained using identity (2.110) according to which the following equation is valid in the entire 2-D problem domain:

$$\begin{aligned} \int_{\Omega} \left(\frac{1}{\mu} \nabla \times \vec{A}_r \right) \cdot (\nabla \times \vec{w}_k) d\Omega - \oint_{\Gamma} \vec{w}_k \cdot \left(\frac{1}{\mu} \nabla \times \vec{A}_r \times \vec{n} \right) d\Gamma = \\ = \int_{\Omega} \left(\vec{H}_s - \frac{\mu_0}{\mu} \vec{H}_s \right) \cdot (\nabla \times \vec{w}_k) d\Omega - \oint_{\Gamma} \vec{w}_k \cdot \left(\vec{H}_s \times \vec{n} - \frac{\mu_0}{\mu} \vec{H}_s \times \vec{n} \right) d\Gamma \end{aligned} \quad (2.125)$$

Combining the fact that the tangential component of H_s is zero on the Γ_H boundary together with the boundary conditions of the problem and the complementary boundary conditions satisfied by the weighting functions w_k (see Eqs. (2.107)), the weak form given by Eq. (2.125) is reduced to:

$$\int_{\Omega} \left(\frac{1}{\mu} \nabla \times \vec{A}_r \right) \cdot (\nabla \times \vec{w}_k) d\Omega = \int_{\Omega} \left(\vec{H}_s - \frac{\mu_0}{\mu} \vec{H}_s \right) \cdot (\nabla \times \vec{w}_k) d\Omega \quad (2.126)$$

In the sub-domain Ω_{air} the right hand side of Eq. (2.126) vanishes because one has to substitute $\mu = \mu_0$ for the entire air region. As it was already mentioned before the current

density is not explicitly present in Eq. (2.126) allowing thus to calculate the magnetic field resulting from the coils using analytical methods without jeopardizing the consistency of the numerical solution in the iron region. Fig. 2.33 shows the reduced magnetic field resulting from the iron magnetization, whereas Fig. 2.34 illustrates the total magnetic field distribution resulting from the analytical calculations for the coil region combined with the FEM modeling of the saturated iron yoke. Table 2.6 contains the comparison of the cold condition ROXIE results for the nonsaturated iron yoke with the results obtained for its saturated variant. As indicated already in the previous sections the percentage of the dipole field enhancement in comparison to the dipole field generated by the coils is given in brackets next to the coefficient B_1 . Corresponding value of B_1 due to the coil geometry was given in Table 2.3.

Table 2.5 Nonsaturated vs. saturated iron yoke

$r_0 = 10$ mm	B_1 [T]	b_3	b_5	b_7	b_9
Coils with nonsaturated iron yoke	-8.36 (21.2 %)	1.434	-0.106	0.026	0.0015
Coils with saturated iron yoke	-8.28 (20.0 %)	1.874	-0.109	0.026	0.0015

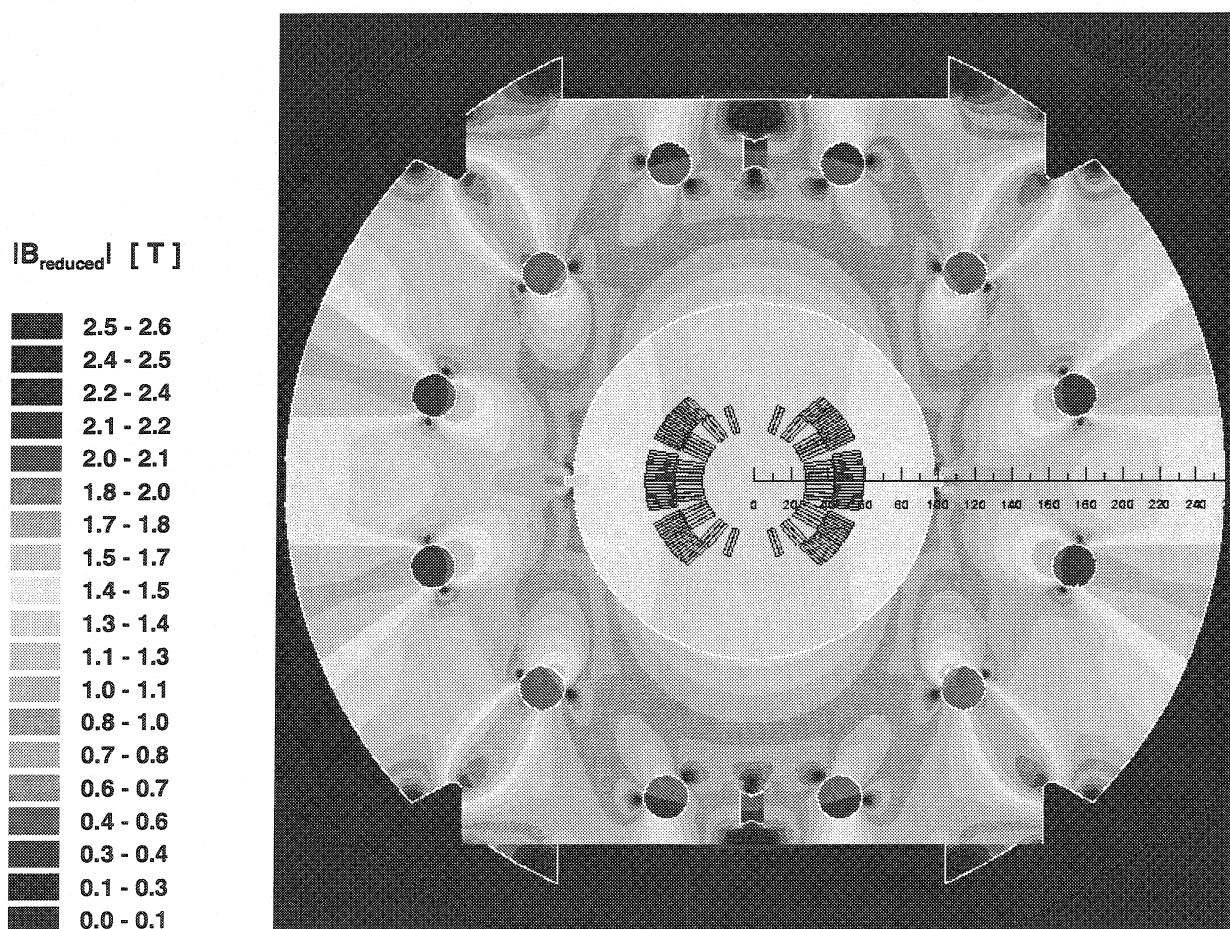


Figure 2.33 Distribution of the reduced magnetic field resulting from the iron magnetization

As expected after the analytical considerations, the iron yoke affects higher order field harmonics. Looking at the results in Table 2.5 one can remark smaller value of the main dipole field in comparison to the nonsaturated iron yoke. Also the value of the sextupole b_3 is increased by 0.44 units. The decapole b_5 changes only slightly, whereas the higher order multipoles remain unchanged. In this regard the very first stage of the design process of the accelerator magnets for the LHC comprises the optimization of the analytical solution as far as the higher order multipoles are concerned. The second stage addresses then the analysis of the influence of the iron saturation on the magnetic field harmonics of the lower orders and the optimization of the iron distribution around the coils.

The reduced vector potential method is a very useful adaptation of the FEM approach for the calculation of the magnetic field distribution in the LHC magnets, which by definition include large, highly saturated iron parts. The coil region of the magnet still must be meshed but the mesh does not have to reflect the complicated geometry of the coil windings. The hybrid combination of the analytical solution for the coil region with the FEM numerical treatment of the iron yoke gives the results with higher precision in comparison to the

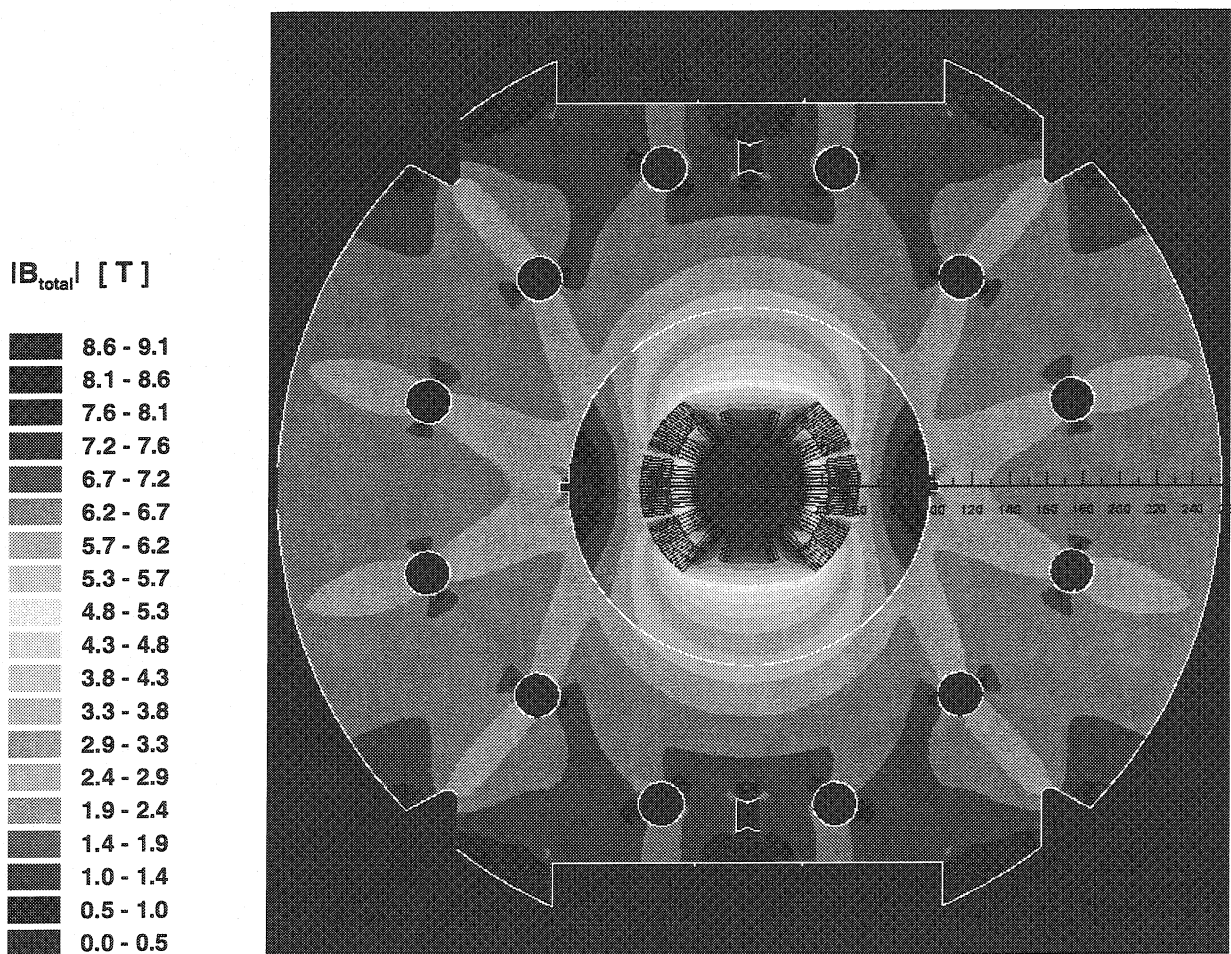


Figure 2.34 Distribution of the total magnetic field in the magnet

standard FEM approach applied to the entire problem domain. Since the FEM solution represents the iron induced magnetic field only, the errors imposed on the total field calculation due to the far field boundary are considerably reduced.

Concluding Remarks

This chapter presented the techniques of analysis of flawless superconducting magnets. The next chapter addresses the analysis of magnets with internal insulation defects in view of precise localization of the fault-affected area before the damaged magnet is disassembled for repair.

References for Chapter 2

- [1] Martin N. Wilson, Superconducting Magnets, Clarendon Press, Oxford 1983
- [2] Fred M. Asner, High Field Superconducting Magnets, Clarendon Press, Oxford 1999
- [3] K. H. Mess, P. Schmüser, S. Wolf, Superconducting Accelerator Magnets, World Scientific Publishing 1996
- [4] O. C. Zienkiewicz, The Finite Element Method, Maidenhead, Berkshire, England, McGraw Hill 1977
- [5] S. Russenschuck et al., Integrated Design of Superconducting Accelerator Magnets. A Case of Study of the Main Quadrupole, The European Physical Journal, Applied Physics, vol. 1, pp. 93-102, January 1998
- [6] The LHC Study Group. The Large Hadron Collider: Conceptual Design, CERN/AC/95-05, CERN, Geneva 1995
- [7] R. Wolf, Field Error Naming Conventions for LHC Magnets, LHC-MMS/ES/01, CERN, Geneva 1998
- [8] S. Russenschuck (editor), ROXIE: Routine for the Optimization of Magnet X-Sections, Inverse Field Calculation and Coil End Design, Proceedings of the First International ROXIE Users Meeting and Workshop, CERN 16-18 March 1998, CERN 99-01, Geneva 1999
- [9] R. Wolf, Persistent Current Effects in LHC Magnets, LHC Note 158, CERN, Geneva, September 1991
- [10] B. Hague, The Principles of Electromagnetism Applied to Electrical Machines, Dover Publications 1962
- [11] C. Iselin, The CERN Poisson Program Package, CERN, Geneva 1982
- [12] R. W. Clough, The Finite Element Method in Plane Stress Analysis, J. Struct. Div., ASCE, Proceedings of the 2nd Conference on Electronic Computation, pp. 345-378, 1960
- [13] O. C. Zienkiewicz, Y. K. Cheung, The Finite Element Method in Structural and Continuum Mechanics, McGraw Hill, London 1967
- [14] A. M. Winslow, Numerical Solution of the Quasilinear Poisson's Equation in a Nonuniform Triangular Mesh, Journal of Computational Physics, vol. 2, pp. 149-172, 1967

- [15] P. P. Silvester, M. V. K. Chari, Finite Element Solution of Saturable Magnetic Field Problem, IEEE Trans. on PAS-89, pp. 1642 – 1651, 1970
- [16] ANSYS, Engineering Analysis System, ver. 5.0, Swanson Analysis System Inc., 1998
- [17] OPERA, Software Environment for Electromagnetic Design, ver. 7.0, Vector Fields Ltd., Oxford 1998
- [18] K. Preis et al., Numerical Analysis of 3-D Magnetostatic Fields, IEEE Transactions on Magnetics, vol. 27, pp. 3798 – 3803, 1991
- [19] C. Paul, K. Preis, S. Russenschuck, 2-D Finite Element Calculation of Superconducting Magnets Applying a Reduced Vector Potential Formulation, Proceedings of the 7th International IGTE Symposium, pp. 30-36, Graz, Austria, 1996
- [20] C. A Brebbia, Boundary Element Method, Pentech Press, 1978
- [21] S. Kurz et al., An Improved Algorithm for the BEM-FEM Coupling Method Using Domain Decomposition, IEEE Transactions on Magnetics, vol. 31, pp. 1737-1740, May 1995
- [22] S. Kurz et al., A Novel Iterative Algorithm for the Nonlinear BEM-FEM Coupling Method, IEEE Transactions on Magnetics, vol. 33, pp. 1772-1775, March 1997
- [23] O. C. Zienkiewicz, K. Morgan, Finite Elements and Approximation Method, John Wiley and Sons, New York, 1983

Chapter 3

A Novel Method for the Inter-Turn Short-Circuit Localization in Superconducting Collared Coils

In the previous chapter it was shown that in a dipole magnet the symmetry defined by the coil geometry and the current distribution in the conductors generates only odd order magnetic field harmonics. The diagnostic method presented in this chapter is based on the analysis of the magnetic field effects created when this prerequisite geometry is broken due to a possible short-circuit between the turns of the coil windings.

To begin with, the problem is studied in the static case. Under such circumstances the detection of the longitudinal position of the defect is already possible providing that the resistance of the short-circuit is much lower than that of the cable turn affected by the fault. In most practical situations, however, the electrical defect requires to be triggered by a high voltage discharge. The presence of an intern-turn short circuit is then typically detected by observing the change of the coil inductance as compared to the flawless reference magnet. Thanks to the specific topology of the pancake winding used in the dipole coil, already at this stage some valuable conclusions can be drawn concerning the azimuthal position of the fault affected area. Nevertheless, the longitudinal localization of the problem still remains out of reach.

The measurement of the transient magnetic field harmonics generated in the magnet during the test discharge can successfully solve this problem. At first, the physical laws responsible for the transient phenomena taking place in the coils and their surrounding reinforcement structure are formulated and adapted to the specific case of the dipole magnet. Based on this study, a FEM transient model of the magnet, and the relevant physical parameters optimized with experimental measurements are presented and discussed. Thereafter, the design and fabrication of the instrumentation necessary for the

implementation of the detection method is described. The detection procedure is then thoroughly verified on a dedicated short (1-m long) dipole magnet model equipped with micro-relays capable of activating artificial inter-turn short-circuits in the internal layer of the coil. As predicted by the transient model, the method based on the analysis of the distortion of a pulsed magnetic field described in this chapter is successfully applied to fast and reliable localization of both the longitudinal and azimuthal positions of the fault-affected area with the precision of a few millimeters.

3.1 Static Analysis of an Inter-Turn Short-Circuit at Room Temperature

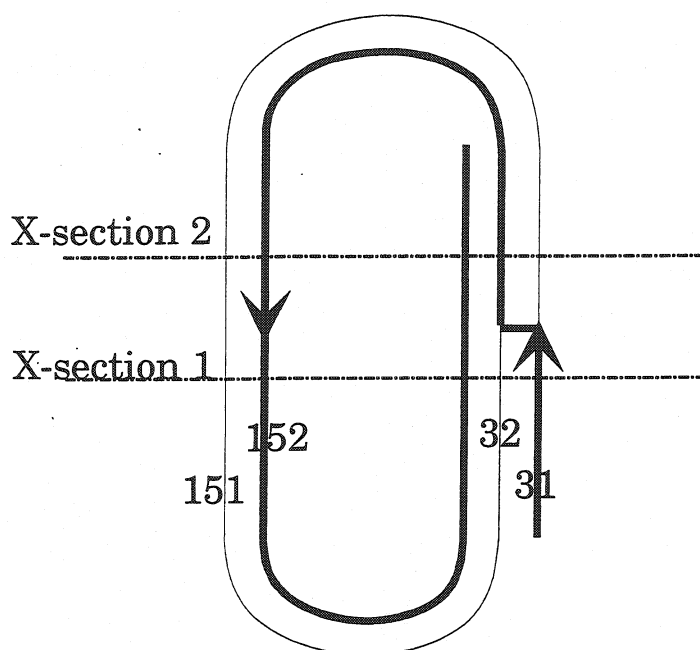


Figure 3.1 Schematic representation of an inter-turn short-circuit in the coil

In this section we will analyze theoretically an ideal low-ohmic inter-turn short circuit in the coils of the magnet. The numbering of the conductors in the 6-block coil is shown in Fig. 3.2. Let us assume that there exists an inter-turn short circuit between the cables number 31 and 32 (Fig. 3.1). Due to the electrical defect the current is redirected to the neighboring cable turn via the short-circuit path. On one side of the inter-turn short circuit the current distribution in the coil is asymmetric

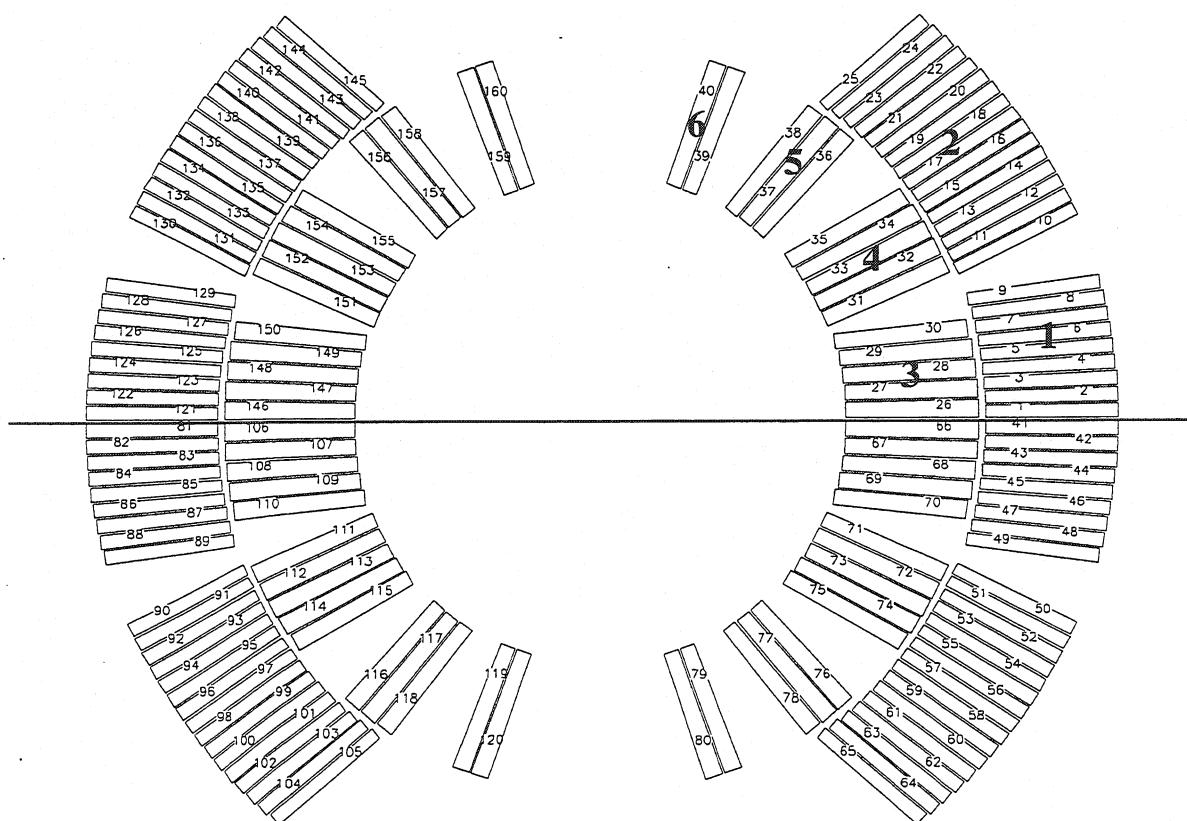


Figure 3.2 Numbering of the cables in the coil

(cross-section No. 1). In terms of 2-D analysis, in the cross-section preceding the position of the short-circuit the source current flows in conductor No. 31 but not in No. 32. It returns carried by conductor No. 152 only. The initial symmetry of the current distribution in the dipole coil is definitely broken in this way. On the other side of the defect (in cross-section No. 2) this symmetry is partially recovered; the current distribution becomes symmetric again with respect to the vertical symmetry axis of the coil. Nevertheless the current leads No. 31 and No. 151 are deprived of current, and the symmetry of the current distribution with respect to the median plane of the magnet (marked with the line in Fig. 3.2) still remains broken. Let us see what are the implications of this symmetry breaking in terms of magnetic field analysis.

Table 3.1 shows how the short circuit affects the normal multipoles of the magnetic field in comparison to the flawless magnet. The multipoles are listed in the units of $[\times 10^{-4}]$. The calculations performed with ROXIE include the effect of the nonsaturated iron yoke.

Table 3.1 Static analysis of the normal multipoles under inter-turn short-circuit conditions

Normal multipoles [$\times 10^{-4}$]	Flawless Coil (no fault)	X-section 1 (before the fault)	X-section 2 (behind the fault)
b_1	10000	10000	10000
b_2	0	2.29	0
b_3	1.43	-1.41	-2.65
b_4	0	0.49	0
b_5	-0.105	0.666	0.518
b_6	0	0.029	0
b_7	0.026	0.139	0.140
b_8	0	-0.004	0
b_9	0.0015	0.0080	0.0107
b_{10}	0	-0.0012	0
b_{11}	0.0030	0.0027	0.0031

In cross-section No. 1, where the current distribution is asymmetric, measurable multipoles of even orders, i.e. quadrupole, octupole, etc., are developed. As it was shown in chapter 2 these multipoles are not generated in a flawless dipole magnet. They are not present in the magnetic field pattern in the cross-section No. 2 either due to the fact that the current distribution is there symmetric again. In both cross-sections the signs of b_3 and b_5 are changed with respect to the reference flawless magnet. Multipoles b_7 and b_9 increase by one order of magnitude in comparison to the reference coil. Multipole b_{11} remains virtually unaffected.

Besides these changes in both cross-sections a development of skew multipoles is observed. The results for the skew multipoles are listed in Table 3.2 in units of $[\times 10^{-4}]$. In the

cross-section No. 2 only even orders of the skew multipoles are developed. The odd orders of the skew harmonics vanish from the magnetic field pattern in this region. On the contrary, all of the skew harmonics are present in the cross-section No. 1. It is remarkable that in both cross-sections the value of the skew quadrupole is quite high. In order to visualize the contribution of the short-circuit to the magnetic field of the magnet the graphs in Fig 3.3 are presented for both cross-sections in form of the negative contrast image, created by turning off the current in the entire coil except for the short-circuit current traversing the path modified by the point of fault.

Table 3.2 Static Analysis of the Skew Multipoles under Inter-turn Short-circuit Conditions

Skew multipoles [$\times 10^{-4}$]	Flawless Coil (no fault)	X-section 1 (before the fault)	X-section 2 (behind the fault)
a_1	0	4.94	0
a_2	0	36.94	35.17
a_3	0	0.26	0
a_4	0	3.90	4.03
a_5	0	-0.12	0
a_6	0	0.15	0.22
a_7	0	-0.026	0
a_8	0	-0.016	-0.008
a_9	0	-0.002	0
a_{10}	0	-0.003	-0.003
a_{11}	0	0.0001	0

Summing up the results of the analysis, measurable normal multipoles of even orders as well as the skew field harmonics with high skew quadrupole are developed in the region preceding the electrical defect. In the region behind the short-circuit even orders of the normal multipoles and odd orders of the skew harmonics vanish from the magnetic field pattern. Thus passing from one area towards the other a certain discontinuity in the magnetic field should be detected. This discontinuity effect could be used for the longitudinal localization of the electrical defect. However, an additional important question must be investigated if there are any clues resulting from the analysis of the magnetic field that would also pinpoint the azimuthal position of the fault-affected area within the specified block of conductors.

$|B|$ [T]

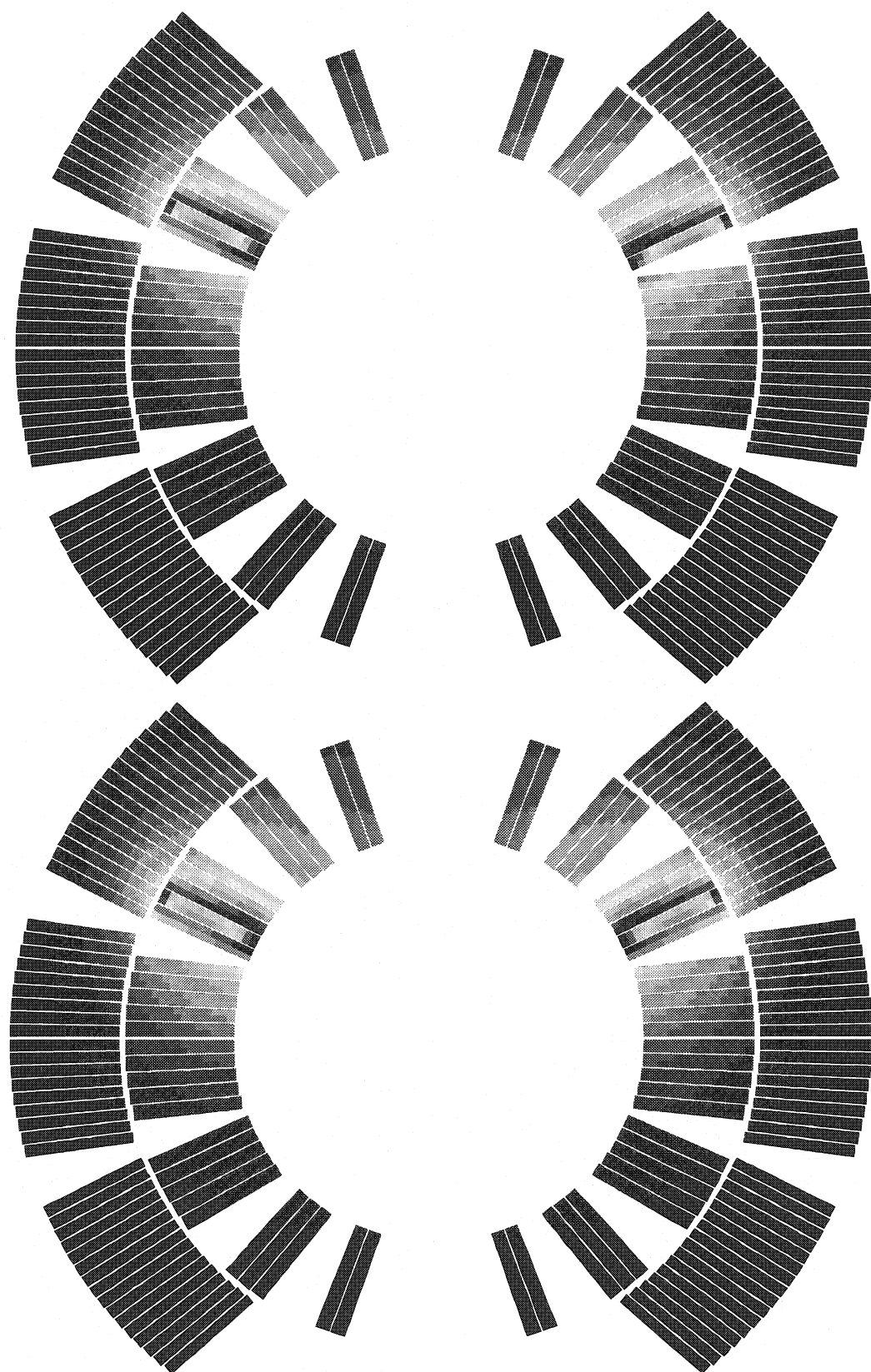
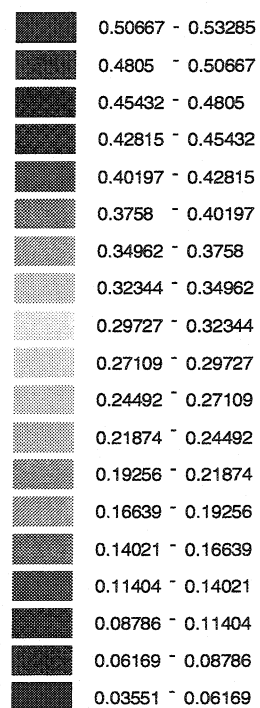


Figure 3.3 Contribution of the inter-turn short circuit to the magnetic field of the coil. (X-section no. 1 – top, X-section no. 2 – bottom)

3.2 Criteria for the Azimuthal Localization of the Fault-Affected Area

In the way demonstrated in the previous section the short-circuit analysis has been carried out for the faults located at different positions in the coil. Three parameters reflecting particularly well the changes in the field as a function of the short-circuit position were selected to summarize the results. These parameters are normal quadrupole (b_2), normal sextupole (b_3) and skew quadrupole (a_2). The results are gathered in the tables below.

- Reference – flawless coil

Reference template [$\times 10^{-4}$]	b_2	b_3	a_2
Flawless coil	0	1.43	0

- Internal layer – block No. 3 (see Fig. 3.2 for the block and conductor numbering convention)

Short-circuit 26-27 [$\times 10^{-4}$]	b_2	b_3	a_2
X-section before the fault	0.43	-11.84	6.10
X-section after the fault	0	-12.11	3.24

Short-circuit 27-28 [$\times 10^{-4}$]	b_2	b_3	a_2
X-section before the fault	0.76	-11.07	11.77
X-section after the fault	0	-11.57	8.97

Short-circuit 28-29 [$\times 10^{-4}$]	b_2	b_3	a_2
X-section before the fault	1.09	-9.88	17.25
X-section after the fault	0	-10.58	14.56

Short-circuit 29-30 [$\times 10^{-4}$]	b_2	b_3	a_2
X-section before the fault	1.42	-8.30	22.50
X-section after the fault	0	-9.18	19.94

The criteria for the localization of the fault-affected area within the conductor block No. 3 of the internal layer could be summarized in the following manner:

- ☞ normal quadrupole $0.4 \leq b_2 < 1.5$ (arithmetic progression with step 0.33)
- ☞ high negative normal sextupole $b_3 < 0$ & $8 < |b_3| < 12.5$
- ☞ remarkably high skew quadrupole $3 < a_2 < 23$

- internal layer – conductor block No. 4

Short-circuit 31-32 [$\times 10^{-4}$]	b_2	b_3	a_2
X-section before the fault	2.30	-1.41	36.94
X-section after the fault	0	-2.65	35.17

Short-circuit 32-33 [$\times 10^{-4}$]	b_2	b_3	a_2
X-section before the fault	2.50	1.10	40.14
X-section after the fault	0	-0.17	38.70

Short-circuit 33-34 [$\times 10^{-4}$]	b_2	b_3	a_2
X-section before the fault	2.65	3.61	42.72
X-section after the fault	0	2.37	41.58

Short-circuit 34-35 [$\times 10^{-4}$]	b_2	b_3	a_2
X-section before the fault	2.78	6.04	44.66
X-section after the fault	0	4.85	43.85

The criteria for the localization of the problem within block No. 4 of the internal layer are:

- ☞ *normal quadrupole* $2 < b_2 < 3$
- ☞ *normal sextupole* $-1.5 < b_3 < 6.5$
- ☞ *very high skew quadrupole* $35 < a_2 < 45$

- internal layer – conductor block No. 5

Short-circuit 36-37 [$\times 10^{-4}$]	b_2	b_3	a_2
X-section before the fault	2.80	13.56	45.60
X-section after the fault	0	13.03	46.28

Short-circuit 37-38 [$\times 10^{-4}$]	b_2	b_3	a_2
X-section before the fault	2.70	14.40	43.86
X-section after the fault	0	14.09	44.89

The criteria for the localization of the problem within block No. 5 of the internal layer are:

- ☞ *normal quadrupole:* $2.5 < b_2 < 3$
- ☞ *high positive normal sextupole:* $13 < b_3 < 15$
- ☞ *very high skew quadrupole:* $43 < a_2 < 45$

- internal layer – conductor block No. 6

Short-circuit 39-40 [$\times 10^{-4}$]	b_2	b_3	a_2
X-section before the fault	1.78	12.86	29.18
X-section after the fault	0	13.54	31.44

The criteria for the localization of the problem within block No. 6 of the internal layer are:

- ☞ *normal quadrupole:* $1.5 < b_2 < 2$
- ☞ *high positive normal sextupole:* $12.5 < b_3 < 14$
- ☞ *very high skew quadrupole:* $29 < a_2 < 32$

- external layer – conductor block No. 1 (selected short-circuit positions)

Short-circuit 01-02 [$\times 10^{-4}$]	b_2	b_3	a_2
X-section before the fault	0.06	-2.89	1.69
X-section after the fault	0	-2.92	0.90

Short-circuit 02-03 [$\times 10^{-4}$]	b_2	b_3	a_2
X-section before the fault	0.12	-2.81	3.26
X-section after the fault	0	-2.86	2.48

Short-circuit 05-06 [$\times 10^{-4}$]	b_2	b_3	a_2
X-section before the fault	0.27	-2.33	7.85
X-section after the fault	0	-2.44	7.11

Short-circuit 08-09 [$\times 10^{-4}$]	b_2	b_3	a_2
X-section before the fault	0.42	-1.50	12.13
X-section after the fault	0	-1.65	11.46

The criteria for the localization of the problem within block No. 1 of the external layer are:

- ☞ *normal quadrupole:* $0 < b_2 < 0.5$
- ☞ *negative normal sextupole:* $b_3 < 0$ & $1.5 \leq |b_3| < 3$
- ☞ *skew quadrupole:* $3 < a_2 < 12.5$

- external layer – block no. 2 (selected short-circuits)

Short-circuit 10-11 [$\times 10^{-4}$]	b_2	b_3	a_2
X-section before the fault	0.59	0.22	17.50
X-section after the fault	0	0.002	16.98

Short-circuit 12-13 [$\times 10^{-4}$]	b_2	b_3	a_2
X-section before the fault	0.66	1.09	19.41
X-section after the fault	0	0.87	18.97

Short-circuit 18-19 [$\times 10^{-4}$]	b_2	b_3	a_2
X-section before the fault	0.78	3.66	22.77
X-section after the fault	0	3.47	22.64

Short-circuit 24-25 [$\times 10^{-4}$]	b_2	b_3	a_2
X-section before the fault	0.78	5.41	22.37
X-section after the fault	0	5.32	22.56

The criteria for the localization of the problem within block No. 2 of the external layer are:

- ☞ *normal quadrupole:* $0.5 < b_2 < 0.8$
- ☞ *positive normal sextupole:* $0 < b_3 < 5.5$
- ☞ *skew quadrupole:* $17 < a_2 < 23$

The short-circuits located in the second quadrant of the coil cross-section produce the same results for the cross-section before the fault and different results for the one behind the defect due to the changed current distribution. Compare the results for the short-circuits 33-34 and 153-154 and notice the difference in the current redirection in Fig. 3.1 and Fig. 3.6 in section 3.4. In case of the defect in the first quadrant (33-34) the values of b_3 and a_2 in the second cross-section become smaller in comparison to the cross-section No. 1, whereas for the corresponding defect in the second quadrant (153-154) they increase.

Short-circuit 153-154 [$\times 10^{-4}$]	b_2	b_3	a_2
X-section before the fault	2.65	3.61	42.72
X-section after the fault	0	4.85	43.85

Short-circuits located in the third and fourth quadrants of the coil produce skew multipoles with reversed sign as referred to the first two quadrants. Compare previous table with the corresponding results for the short-circuit in the third quadrant of the coil listed below.

Short-circuit 113-114 [$\times 10^{-4}$]	b_2	b_3	a_2
X-section before the fault	2.65	3.61	-42.72
X-section after the fault	0	4.85	-43.85

Three conditions connected by logical AND constitute a criterion for the identification of the position of the short-circuit within the given block of conductors. All of these conditions are exclusive, which means that a set of three values for computed control parameters b_2 , b_3 and a_2 chosen at random describes unambiguous field pattern and thus allows the assignment of the fault location to the specific block of conductors. Moreover, a monotonous behavior of the parameters as a function of the short-circuit position gives the possibility to deduce the exact number of the coil turn affected by the fault. From the measured experimental values of the multipoles it should be possible to deduce the longitudinal and angular position of the short-circuit within the magnet by solving a properly imposed inverse magnetic field problem.

3.3 Limitations of DC Test and Analysis for Detection and Localization of Inter-Turn Short-Circuits

The effect generated by a short-circuit predicted for the static case is hypothetically measurable with the rotating pick-up coil system used for the quality assessment of the magnetic field in the magnets [1]. Unfortunately there are serious restrictions in using this system for the short-circuit analysis. During the measurements under room temperature conditions the magnet is resistive. The coils of the magnet operated with steady current overheat very fast under such circumstances jeopardizing the future performance of the entire magnet assembly. Therefore the intensity of the steady current must be kept very low and the testing time should be minimized to avoid a possible damage inflicted to the coils due to excessive heating. It is an opposing objective as far as the measurement procedure with the rotating coils is concerned. The measurement procedure requires certain lapse of time (the longer the better) for the stabilization of the signals resulting from the higher multipoles and for obtaining a high level of the measurement reliability and precision. Moreover, the real damages of the coils in the magnet are never perfect. Often a partial perforation of the insulating material produces a high-ohmic fault, which does not disturb the flow of the steady current in the magnet at all, creating thus a false impression that the magnet is intact. In this case a certain amount of energy must be released into the magnet within short time duration in order to identify a hidden fault and reveal its true nature. This is done by means of the high-voltage discharge measurements described in details in Appendix A at the end of this chapter and applied for the damaged dipole magnet in the section that follows.

3.4 Detection of the Insulation Failures with the High Voltage Discharge Test

Often inter-turn short-circuits are well detectable when the magnet is collared. The presence of the insulation failure in the magnet can be diagnosed by means of pulse propagation methods at room temperature. A current impulse is injected between the terminals of the magnet by a discharge generator. The coil response in form of voltage and current oscillations is then registered by the EDMA application program [2] and analyzed in terms of pseudo-period of the oscillations, inductance and effective resistance of the coils (see Appendix A). Figs. 3.4 and 3.5 show the discharge curves acquired on the collared magnet assembly during a test at 1 kV. In other words a pulsed current is supplied from a discharge generator by releasing the energy accumulated in a 1- μ F capacitor charged initially at 1 kV, into the test object.

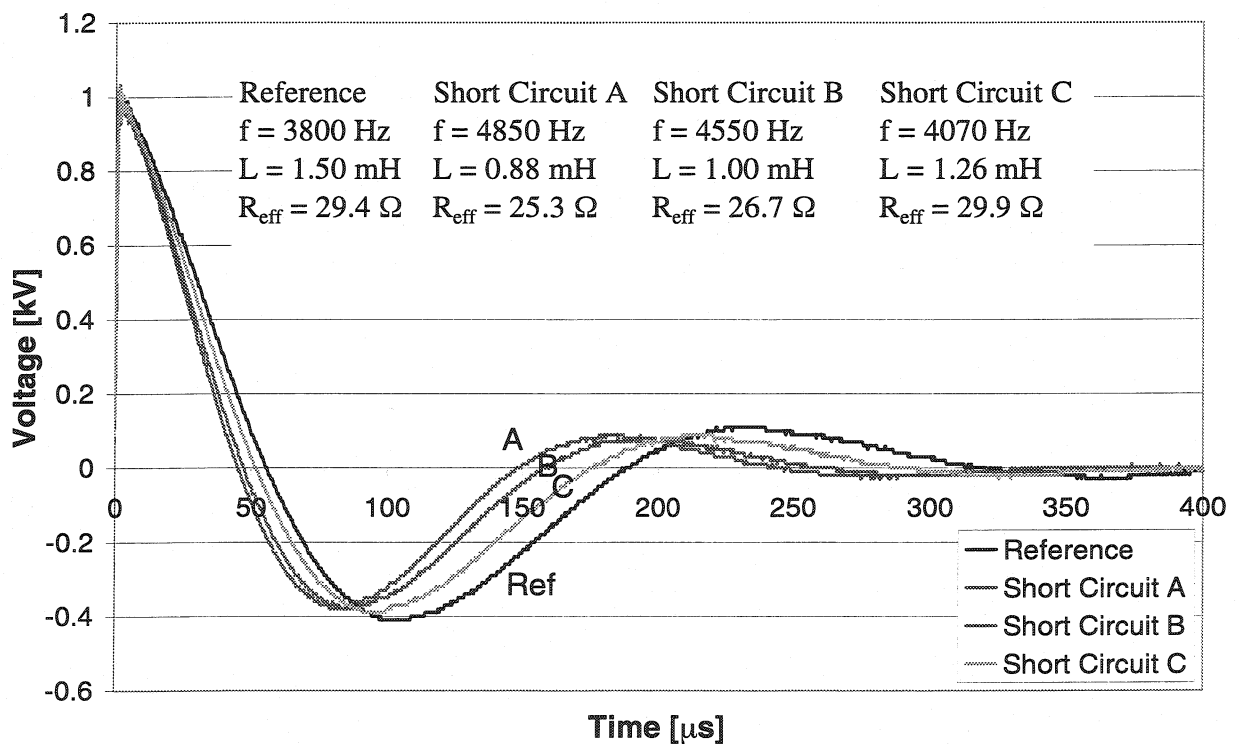


Figure 3.4 Voltage oscillation curves at 1-kV discharge test

Figure 3.4 shows the damped voltage oscillation curves for the reference flawless magnet and for several inter-turn short circuits located in the internal layer of the coils. The test was carried out on the older design of the 1-m long LHC dipole magnet model realized with the 5-block geometry coils (2 conductor blocks in the outer, and 3 in the inner layer of the

transversal cross-section of the coil quadrant). The positions of the short-circuits and the geometry of the 5-block coil are shown in Fig. 3.6 (compare with the current 6-block design of the coil geometry depicted in Fig. 3.2). Fig. 3.5 pictures the plots of the current oscillation

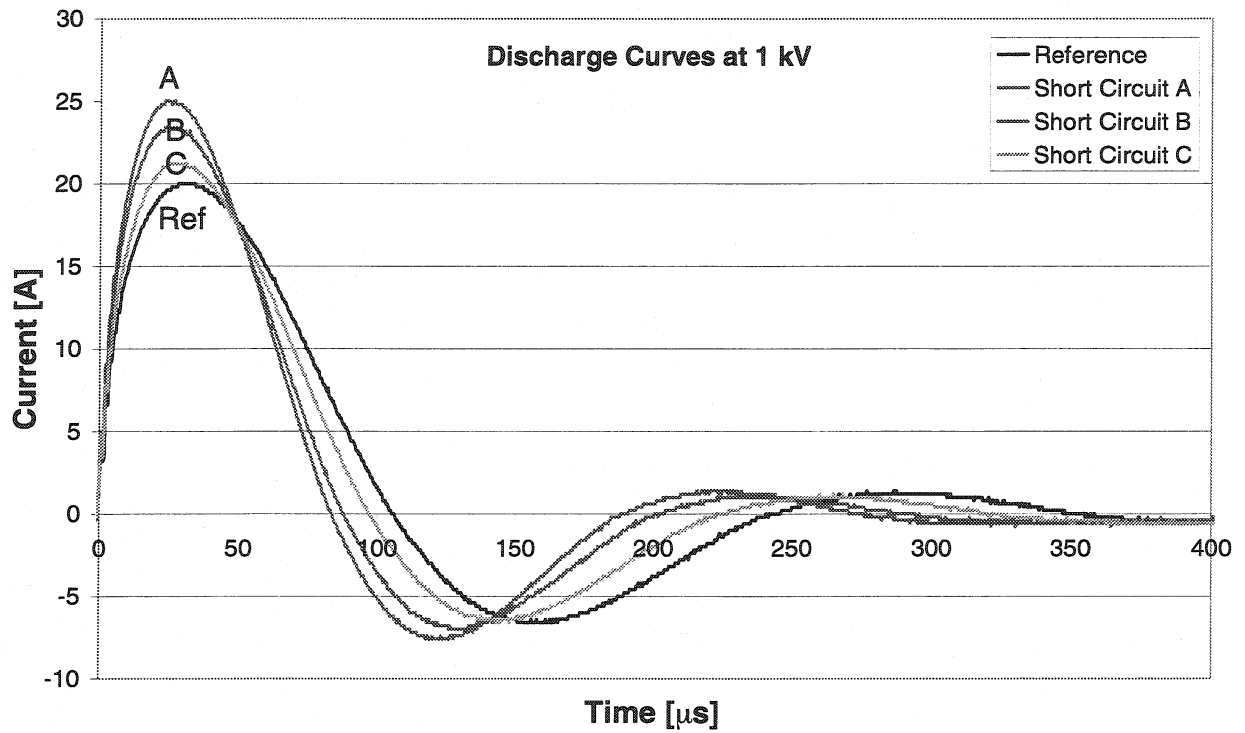


Figure 3.5 Current oscillation curves at 1-kV discharge test

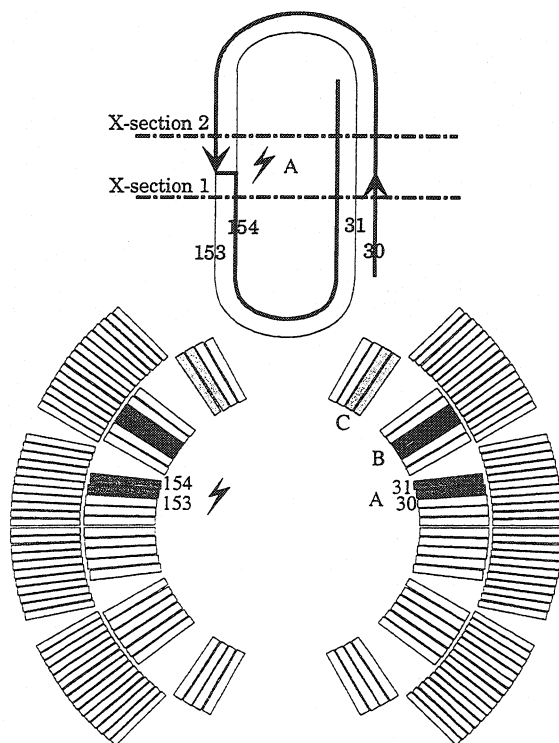


Figure 3.6 Short-circuit positions during the HV discharge tests

curves measured during the test at the input terminals of the magnet.

In case of an inter-turn short-circuit the source current supplied to the magnet is redirected to the neighboring cable turn through the short-circuit path. The energy released into the magnet is additionally dissipated at the point of fault. For the propagating impulse the coil appears to be shorter by a length of a cable turn affected by the electrical defect. This passive winding deprived of initially imposed source current is marked with a thin line in Fig. 3.6. During the discharge test a transient time-varying magnetic field is induced in the magnet. As

indicated on the time axis in Figs. 3.4 and 3.5 the entire measurement process is completed after approximately 400 μ s. The variable magnetic field generated in the aperture during this time will induce a high current in the passive winding deprived of the initially imposed transport current. The current curves shown in Fig. 3.5 do not have anything in common with the current induced in the passive loop. These curves correspond to the source current oscillation, which is measured at the input terminals of the magnet. The short-circuit current induced in the passive winding is much higher. Unfortunately, a direct access to the fault-affected area of the magnet and to its passive loop does not exist and the value of the secondary current induction in the failure region cannot be measured directly. However, as it will be demonstrated in the following sections, it can be evaluated from the model. The induced current will generate a magnetic field opposing the flux change in the area spawn by the fault-affected loop. This current has also an asymmetric distribution on one side of the short-circuit, and a symmetric one on the other side. Thus, despite additional physical processes taking place here in comparison to the static case, the effects predicted for the static case as far as the magnetic field analysis is concerned, should also take place. Exactly as for the static case one should observe the vanishing of the even orders of the normal field harmonics and of the odd orders of the skew field harmonics in the area of the magnet were the current distribution becomes symmetric. One can expect that this field discontinuity effect should be considerably amplified due to the transient nature of the discharge phenomena as well as due to the essential degradation of the magnetic field consistency caused by the secondary current flow in the passive winding.

As a consequence of the current redistribution imposed in the coil windings by the insulation failure the value of the magnet inductance decreases, whereas the damping factor and the frequency of the oscillations increase (see Figs. 3.4 and 3.5). The existence of the fault can be thus verified, nevertheless the method does not allow to localize the position of the short-circuit. Any intervention on the magnet assembly aiming to repair the malfunction requires dismounting of the collars. After the reinforcement structure of the magnet is removed the internal prestress in the coils is released and the short-circuit simply disappears. In order to reestablish and localize the failure the pressure must be locally increased over small sections of the coil using external press. This procedure simulates locally the forces exerted on the coils in the collared assembly. Each time the section of the coil is changed the discharge test must be repeated in order to check on the acquired oscillation curves if the short circuit is located in the region of the coil under increased pressure conditions. The zone

of the increased pressure moves in small overlapped steps along the entire magnet coils. The procedure may take from one to two weeks until the longitudinal position of the problem is localized in the 15-m long dipole magnet. Thus it becomes extremely unpleasant, time-consuming and expensive. It is also quite easy to miss the spot during the first complete pressure scan of the coil. Once the longitudinal position is localized, the traditional localization procedures based on resistance and voltage ratio measurements between the adjacent cable turns are employed for the azimuthal localization of the affected coil winding.

As far as the azimuthal position of the short-circuit is concerned the discharge test on the collared assembly gives already some valuable hints regarding the angular position of the defect in the block of conductors. The surface of the passive winding deprived of the source current is the main factor determining the magnitude of the self-inductance drop in the magnet. The bigger the surface, the higher the intensity of the current induced in the passive loop, and finally the bigger the inductance drop in comparison to the reference magnet. In case of the pan-cake topology of the coil winding used for the LHC dipole magnets the surface of the single coil turn is maximal in the median plane of the magnet and becomes smaller the further the cable is away from the median plane (see Fig. 3.6). Hence originates a valuable hint concerning the azimuthal position of the defect, i.e. the bigger the frequency change, and the greater the inductance drop, the closer the failure to the median plane of the magnet. Thus among the short circuits presented in Figs. 3.4 and 3.5 the one in position A (with the highest peak current measured at the terminals of the magnet (Fig. 3.5)) is the closest one with respect to the median plane and the one in position C the one furthest away. This conclusion is in total agreement with the actual positions of the short-circuits depicted in Fig. 3.6.

The discharge curves do not give any clue as to the longitudinal position of the defect, because inter-turn short circuits with the same azimuthal position affect the winding with the same surface no matter what the longitudinal position of the fault-affected area is. However the analysis of the current distribution symmetry that we have carried out so far suggests that the precise longitudinal localization of the problem should be possible with the dedicated system capable of detecting the discontinuity of the certain field harmonics in the magnet excited with a high voltage pulse. In this way the development of the idea approaches the domain of the time-varying magnetic fields.

3.5 Eddy Currents in Quasi-Static Time-Varying Magnetic Fields

Eddy currents are induced in any conductive medium submitted to the time-varying magnetic field. In this regard eddy currents can be generated due to the time-varying excitation current applied to the test object or by the relative motion of the conductive medium with respect to the source magnetic field. Only the first of these two cases will be considered here. In general two types of eddy current problems can be specified aiming to calculate either

- eddy currents induced in the conductive medium which does not carry any initially imposed source currents; this is a proximity effect induced by an external exciting source present in the neighborhood of the medium under question,
- or
- eddy currents induced in the source-driven current conductors; this kind of problem is called a skin effect problem and it leads to the redistribution of the total current density in an arbitrary system of the current carrying conductors.

Both of above-mentioned effects must be taken into account to analyze the development of the magnetic field during the high voltage discharge test performed on the LHC dipole magnets. All of the nonmagnetic but conducting parts of the magnet structure must be taken into account during the calculations. Eddy currents will be induced in the copper wedges inserted between the conductor blocks, in the 0.7-mm thick austenitic steel protection sheet surrounding the coils, and in the direct reinforcement structure of the coil: the collars, the collaring rods and the assembly pins. All of these elements of the magnet structure were thoroughly omitted in the calculation of the magnetostatic problems in the previous chapter, because all of them are nonmagnetic. On the contrary to chapter 2, all of the tests presented in this chapter are performed on the collared single aperture magnet assembly deprived of the iron yoke. Due to this fact the magnetic parts of the magnet structure will be neglected in the magnet modeling following in the next sections. However, during the test excitation of the magnet in the pulsed mode all of the nonmagnetic parts of the assembly will contribute to the final profile and harmonic contents of the time-varying magnetic field pattern generated in the aperture of the magnet. Also the current density redistribution in the coil conductors will also have to be taken under consideration.

The exact analytical solutions for eddy currents exist only for a certain group of problems with simple geometry containing only isotropic and linear conducting media [3]. All of the industrial, complex geometry problems including nonlinear or anisotropic materials must be treated with numerical methods, and even then the computation of eddy currents in a great number of 3-D problems is not satisfactory yet. Only 2-D considerations are presented consequently throughout this work.

3.5.1 Proximity Effects in the Copper Wedges and in the Coil Reinforcement Structure

During the discharge test performed on the collared magnet assembly the proximity effects will be observed in the copper wedges and in the entire coil reinforcement structure composed of the collaring shoe, the collars, the collaring rods and the assembly pins. In order to derive the field equations governing the eddy current flow in these media let us consider an elementary problem depicted in Fig. 3.7 and related to the LHC dipole magnet. Region Ω_c represents a conductive medium of the wedge-shaped longitudinal spacer inserted between the conductor blocks of the coil. The wedge is made of copper, thus it is nonmagnetic ($\mu = \mu_0$), homogeneous and isotropic. Eddy currents will be induced in this region during the discharge. Region Ω_s represents a single turn of the coil, which is also homogenous and

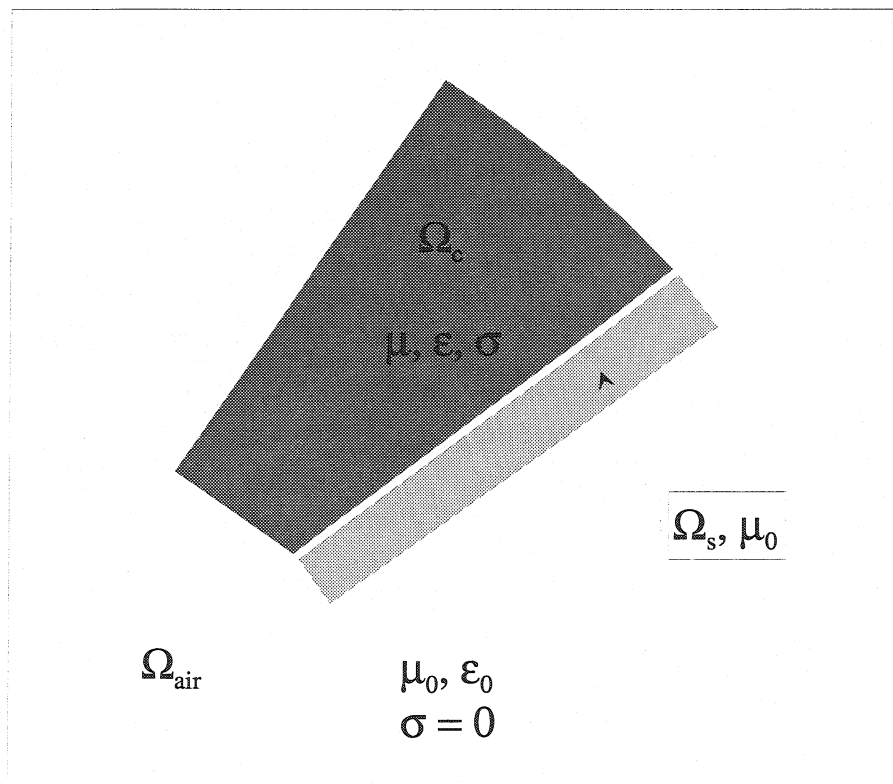


Figure 3.7 Elementary eddy current problem in the LHC dipole magnet during high voltage discharge test

isotropic; the conductivity and electrical permittivity of the medium are constant at every point and in every direction. Area denoted as Ω_{air} corresponds to the inner and outer space regions of the magnet, filled with air. For the time being let us assume that the skin effect in the source-driven conductor Ω_s does not have to be considered, and let us concentrate on the eddy currents induced in the area of the copper wedge Ω_c .

The current on the right-hand side of Eq. (2.1) has to be split into two terms: j_s describing the density of the source current supplied to the cable of the coil, and j_e corresponding to the density of the eddy currents induced in the copper wedge:

$$\nabla \times \vec{H} = \vec{j}_s + \vec{j}_e \quad (3.1)$$

The displacement current still remains neglected in Eq. (3.1) because its value is very small in comparison to the conduction current for the wave frequencies smaller than the optical spectrum frequencies. The problems in which the displacement current is neglected are called quasi-static problems. As a consequence of this assumption the charge distribution on the surface of the conducting media is not present. This is especially valid for the 2-D problems considered in this work.

Besides Eqs. (3.1), (2.2) and (2.3), the following Maxwell equations for the electric field must be considered while defining the problem,

$$\nabla \times \vec{E} = -\frac{\partial \vec{B}}{\partial t} \quad (3.2)$$

$$\nabla \vec{D} = \rho \quad (3.3)$$

$$\vec{D} = \epsilon \vec{E} \quad (3.4)$$

where E is the strength of the electric field, D is the electric field induction (electric displacement), ρ expresses free charge density, and ϵ electric permittivity. The density of the eddy currents induced in the copper wedge is related to the intensity of the electric field by means of Ohm's law

$$\vec{j}_e = \sigma \vec{E} \quad (3.5)$$

in which σ is the conductivity of the wedge given in [S/m]. By substituting the magnetic field induction (2.4) into Eq. (3.2) one obtains an electric field strength expressed in terms of the magnetic vector potential A with the precision characterized by the gradient of an arbitrary scalar field:

$$\vec{E} = -\frac{\partial \vec{A}}{\partial t} - \nabla V \quad (3.6)$$

Since in electrostatic problems, i.e. in absence of the time dependent terms in (3.6), the negative gradient of the scalar electric potential defines the strength of the electrostatic field it is quite natural to use the same potential in Eq. (3.6). Hence the density of the induced eddy currents can be expressed as:

$$\vec{j}_e = -\sigma \left(\frac{\partial \vec{A}}{\partial t} + \nabla V \right) \quad (3.7)$$

Substitution of the eddy current density from expression (3.7) into Eq. (3.1) leads to the following vector diffusion equation with the magnetic vector potential as an unknown variable:

$$\nabla \times \frac{1}{\mu} \nabla \times \vec{A} + \sigma \frac{\partial \vec{A}}{\partial t} + \sigma \nabla V = \vec{j}_s \quad (3.8)$$

Eq. (3.8) must be solved numerically for each region in which eddy currents will be induced. The position of the magnetic permeability in the equation is kept on purpose to address the most general case of the magnetic non-homogenous materials. In the analyzed case of the nonmagnetic copper wedges this permeability could be of course replaced with the constant permeability of air and taken out before the first nabla operator.

The eddy current density given by formula (3.7) cannot be calculated using the vector potential alone. Although the vector potential is just an auxiliary variable introduced to simplify the description of the problem a precise physical meaning is assigned to its integral. The magnetic flux traversing a given area can be expressed in terms of the closed contour integral of the vector potential calculated along the boundary of this area. In Eq. (3.8) the vector potential at a given point in the region of the copper wedge does not correspond directly to the amount of the interlinkage flux across the area between this point and the reference point of zero vector potential value. Thus the gradient of the scalar electrical potential in (3.8) expresses a corrector term acting as a modifier of the interlinkage flux of the conductive copper wedge region characterized by the vector potential. In 2-D problem domain Eq. (3.8) can be transformed to the following form

$$\nabla \times \frac{1}{\mu} (\nabla A_z \times \vec{e}_z) + \sigma \frac{\partial \vec{A}_z}{\partial t} + \sigma (\nabla V \cdot \vec{e}_z) = \vec{j}_s \quad (3.9)$$

which can be further simplified to:

$$-\nabla \frac{1}{\mu} \nabla A_z + \sigma \frac{\partial \vec{A}_z}{\partial t} + \sigma \frac{\partial V}{\partial z} = \vec{j}_s \quad (3.10)$$

In general case the gradient of the electric scalar potential should be considered as an additional unknown in Eq. (3.9). However if the model meets certain conditions this term can be entirely neglected during the calculations. Let us see under which circumstances this can be done. According to formula (3.7) the total current density on the right-hand side of Eq. (3.1) is:

$$\vec{j} = \vec{j}_s + \vec{j}_e = \vec{j}_s - \sigma \left(\frac{\partial \vec{A}_z}{\partial t} + \nabla V \right) \quad (3.11)$$

Hence the total current intensity in the entire problem domain can be obtained:

$$I = \int_{\Omega} \vec{j} d\Omega = \int_{\Omega} \vec{j}_s d\Omega - \int_{\Omega} \sigma \left(\frac{\partial \vec{A}_z}{\partial t} + \nabla V \right) d\Omega \quad (3.12)$$

On the other hand the induced eddy currents cannot generate any extra current in the average sense over the domain, therefore by definition the entire measurable current intensity is due to the imposed source currents:

$$I = \int_{\Omega_s} \vec{j}_s d\Omega \quad (3.13)$$

Hence taking into account Eqs. (3.12) and (3.13) it follows immediately that the total intensity of the eddy currents induced in the copper wedge must be limited to zero:

$$- \int_{\Omega_c} \sigma \left(\frac{\partial \vec{A}_z}{\partial t} + \nabla V \right) d\Omega = 0 \quad (3.14)$$

Eq. (3.14) reveals the physical meaning of the gradient of the electric scalar potential:

$$\nabla V = - \frac{1}{\Omega_c} \int_{\Omega_c} \frac{\partial \vec{A}_z}{\partial t} d\Omega \quad (3.15)$$

It expresses the mean value of the speed of variation of the vector potential in time in the region spawn by the conducting domain. The partial derivative of the vector potential with respect to time could be used to judge in which cases the gradient of the electric scalar potential becomes zero and can be neglected while solving problem equation (3.9). The integration area must contain all regions, which experience the flow of the same eddy currents. The entire eddy current loop must be included in the integration domain. For example, during the 2-D analysis of cross-section No. 2 in Fig. 3.6, cables No. 31 and 154 are deprived of the initially prescribed source current due to the insulation defect encountered at the point of fault. Both conductors are considered in the 2-D model to be parallel and infinitely long. However, they are connected together at the end in the head region of the coil,

and therefore the integration domain for the calculation of the eddy currents induced in the passive winding must include transversal cross-sections of both conductors affected by the short-circuit. In the case of the parallel conductors, which are not connected with each other at the end of the magnet, the integration region will include only a transversal cross-section surface of one such conductor at a time. This is exactly the case corresponding to the longitudinal copper wedges inserted between the cable blocks to optimize the current distribution in the coils of the magnet.

An attentive reader would ask immediately what happens if the current redistribution is to be recalculated in the source-driven conductors. Indeed all of the cables in the positive half-plane of the coil ($x > 0$) in Fig. 3.6, not only the ones affected by the inter-turn short-circuit, are connected with their corresponding return current conductors in the negative half-plane ($x < 0$). The source current must be prescribed to these conductors by specifying the direction of its flow; normally positive for the conductors in the positive half-plane and negative for the remaining ones. In this regard the imposed source current density has different polarity for the two halves of the coil defined by the vertical symmetry axis. Therefore all of the source-driven conductors must be considered as separate ones for the calculation of the total current density redistribution due to the skin effect.

Unfortunately, the corrector term expressed by the electric scalar potential cannot be calculated directly using formula (3.15) because the space distribution and time evolution of the vector potential are not known prior to the solution of Eq. (3.9). To circumvent this inconvenient impasse let us analyze an elementary eddy current loop illustrated in Fig. 3.8. The picture in Fig. 3.8 shows a 2-D case of the eddy current loop induced in a slab made of conducting medium. The illustration was extruded in the direction of the OZ axis only for better visualization of the problem. Let us assume that the eddy current loop has a unit length along the OZ axis and that the zero vector potential line of the 2-D model does not coincide with the symmetry axis of the eddy current loop. The eddy currents induced in the slab are due to the magnetic flux between points P_1 and P_2 .

$$E_1 - E_2 = - \frac{\partial \phi_{12}}{\partial t} \quad (3.16)$$

Thus the following relation defines the electric fields at both points:

$$E_1 = -E_2 = - \frac{\partial \left(\frac{\phi_{12}}{2} \right)}{\partial t} \quad (3.17)$$

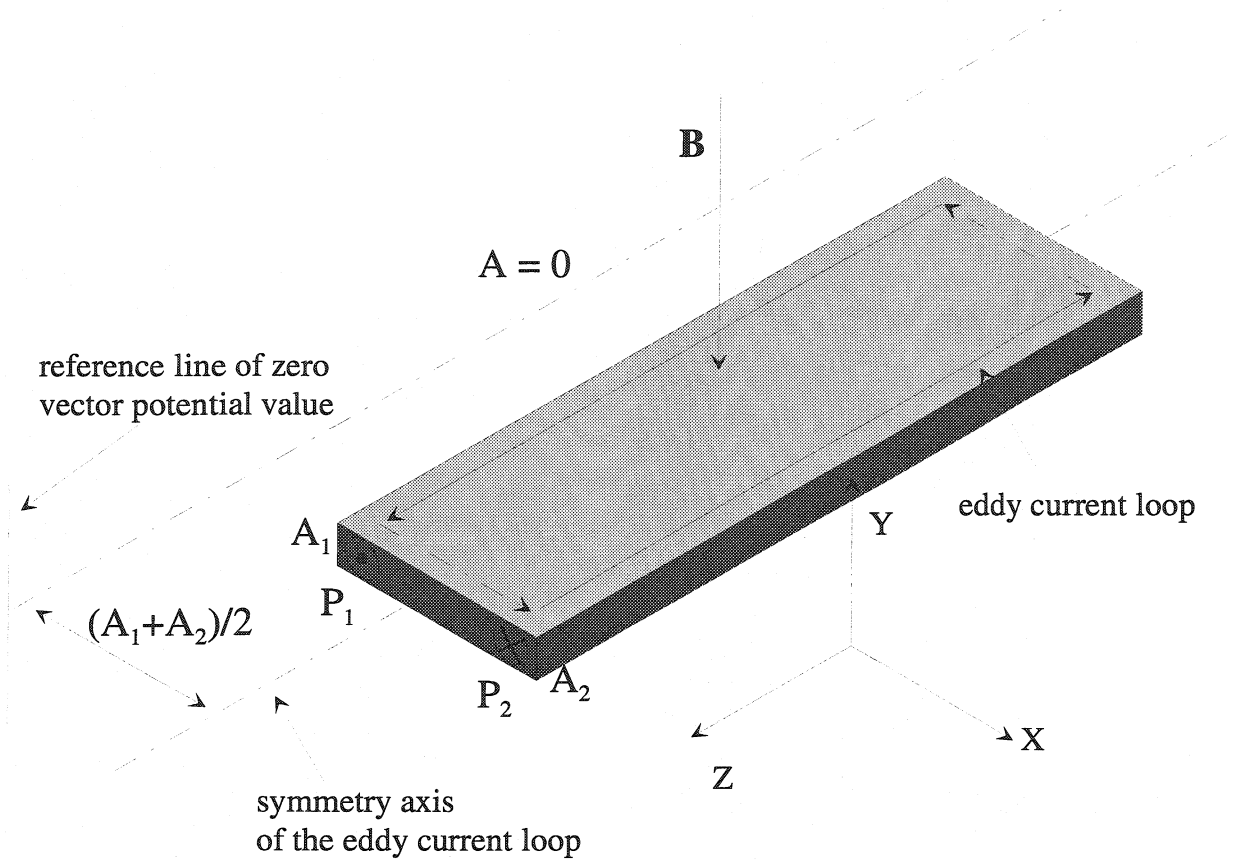


Figure 3.8 Elementary eddy current loop induced in a conducting slab

The magnetic flux traversing the eddy current loop can be expressed as the difference of the vector potentials between both points:

$$\phi_{12} = A_1 - A_2 \quad (3.18)$$

The value of A_1 corresponds to the magnetic flux crossing the area of unit length in the OZ direction, spawn between point P_1 and the reference line of zero vector potential value. By analogy the value of A_2 expresses the flux traversing a similar area defined between point P_2 and the reference line. Taking Eq. (3.6) into account the electric field strengths at both points are:

$$E_1 = -\frac{\partial \left(\frac{A_1 - A_2}{2} \right)}{\partial t} = -\frac{\partial A_1}{\partial t} + \frac{\partial}{\partial t} \left(\frac{A_1 + A_2}{2} \right) \quad (3.19)$$

$$E_2 = -\frac{\partial \left(\frac{A_1 - A_2}{2} \right)}{\partial t} = -\frac{\partial A_2}{\partial t} + \frac{\partial}{\partial t} \left(\frac{A_1 + A_2}{2} \right) \quad (3.20)$$

The first term in Eqs. (3.19) and (3.20) is related to the flux across the respective areas designated by the points P_1 and P_2 , and the reference line. The second term in both equations

is related to the magnetic flux in the area stretched between the symmetry axis of the analyzed eddy current loop and the zero vector potential line (see Fig. 3.8). Due to the fact that the zero vector potential line does not coincide with the symmetry axis of the eddy current loop the electric field strengths cannot be calculated directly from the values of the vector potential at points P_1 and P_2 . After the comparison of Eqs. (3.19) and (3.20) with Eq. (3.6) it turns out immediately that:

$$\nabla V = -\frac{\partial}{\partial t} \left(\frac{A_1 + A_2}{2} \right) \quad (3.21)$$

Thus the gradient of the electric scalar potential indeed plays a role of the correction term modifying the distribution of the eddy current density in the conducting medium in case if the symmetry axis of the induced eddy current loop does not coincide with the $A = 0$ reference line. Otherwise, if the reference line passes through the middle of the induced loop, $A_1 = -A_2$ and the correction term (3.21) becomes zero. Hence a very important conclusion can be drawn for the analysis of the eddy current distribution. If the central line of symmetry exists for the flux distribution resulting from the eddy current induction, the gradient of the electric scalar potential can be neglected in Eq. (3.9) providing that the vector potential along this line is set to zero. The validity of this fact was proven for the numerical treatment of eddy current problems by Nakata [4]. Under such conditions Eq. (3.9) is simplified to:

$$\nabla \times \frac{1}{\mu} (\nabla A_z \times \vec{e}_z) = \vec{j}_s - \sigma \frac{\partial \vec{A}_z}{\partial t} \quad (3.22)$$

In the case of the single aperture dipole magnet, the line of the zero vector potential runs along the vertical symmetry axis of the magnet (see Fig. 2.30). Thus the problem of the eddy current distribution in the entire reinforcement structure of the magnet will be indeed governed by Eq. (3.22). However for the analysis of the copper wedges the corrector term (3.21) must be taken into account.

3.5.2 Skin Effect in the Current-Driven Coil Conductors

In order to model the magnetic field pattern generated in the magnet aperture during the high voltage discharge test it will be necessary to analyze also the flow of eddy currents in the source current driven conductors of the coil. In Fig. 3.7 a single coil conductor is represented by the Ω_s region. The scalar potential gradient term in Eq. (3.9) cannot be neglected in this case. In the previous section the total current intensity resulting from the eddy currents induced in the collars was limited to zero (see Eq. 3.14). In the case of the region submitted to the flow of the prescribed source current, the total measurable current resulting from the redistribution of the current density in the cable due to the eddy currents must also be limited. This limit is specified by the current intensity resulting from the initially imposed source current:

$$-\int_{\Omega_s} \sigma \left(\frac{\partial \vec{A}_z}{\partial t} + \nabla V \right) d\Omega = \int_{\Omega_s} \vec{j}_s d\Omega \quad (3.23)$$

Since the electric scalar potential considered along the straight conductor of the magnet coil represents a gradient field, it must satisfy the Laplace equation:

$$\nabla^2 V = 0 \quad (3.24)$$

The equipotential surfaces in the cable are normal to the current flow, i.e. they correspond to the transversal cross-sections of the cable. Thus the solution of Eq. (3.24) can be expressed in the following manner

$$V(z) = \frac{V(d) - V(0)}{d} z + V(0) \quad (3.25)$$

where $V(0)$ and $V(d)$ are the electric potential values at the respective cross-sections $z = 0$ and $z = d$ in Fig. 3.9. In 2-D model the gradient of the scalar electric potential corresponds to the derivative of the potential with respect to the z coordinate. Hence, taking the form of the solution (3.25) into account it turns out that the gradient under question is a constant in 2-D problem domain:

$$\nabla V \cdot \vec{e}_z = \frac{\partial V}{\partial z} = \frac{V(d) - V(0)}{d} = \text{const.} \quad (3.26)$$

Thus the part of the eddy current distribution described by the scalar potential gradient in Eq. (3.23) results in a spatially uniform current density over the conductor. This uniform current density is given by

$$\vec{j}_v = -\sigma \nabla V \quad (3.27)$$

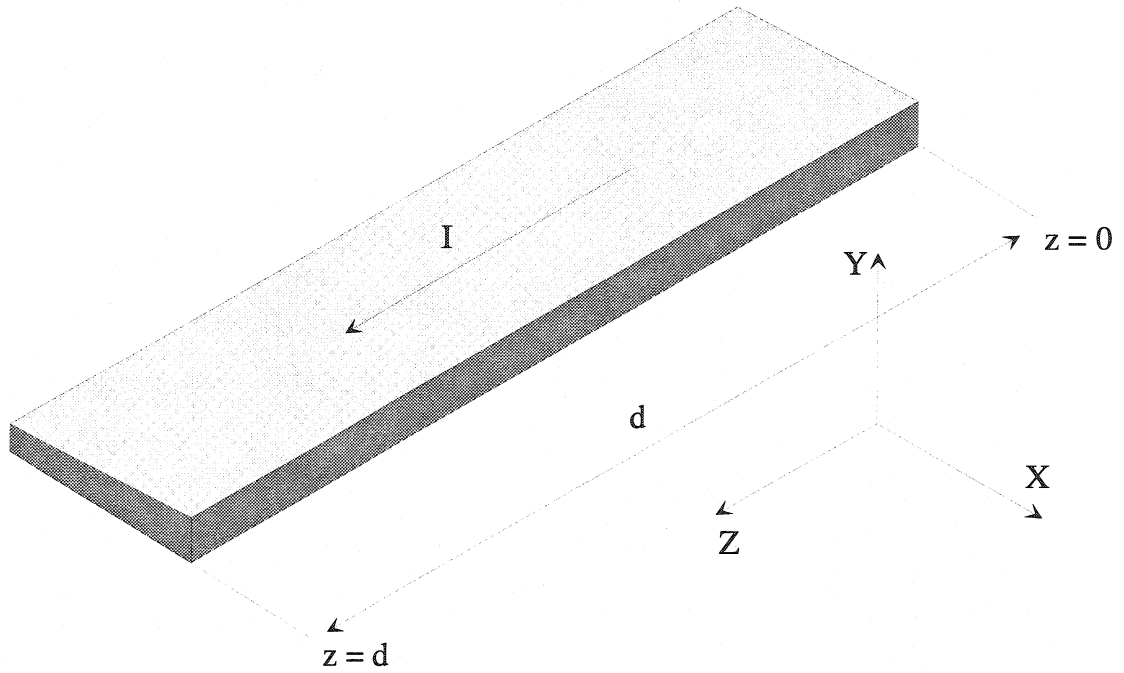


Figure 3.9 Current-driven key-stoned coil conductor

The equation for the skin effect problem must be solved along with the current constraint condition (3.23) for each conductor in the problem domain:

$$\begin{cases} \nabla \times \frac{1}{\mu} (\nabla A_z \times \vec{e}_z) = \vec{j}_v - \sigma \frac{\partial \vec{A}_z}{\partial t} \\ \int_{\Omega_s} \left(\vec{j}_v - \sigma \frac{\partial \vec{A}_z}{\partial t} \right) d\Omega = \int_{\Omega_s} \vec{j}_s d\Omega \end{cases} \quad (3.28)$$

The equation set (3.28) together with the boundary conditions for the vector potential define completely the skin effect problem in the current-driven conductors. If the source currents are sinusoidal functions of time the problem is classified as a steady state alternating current problem. The vector potential and the driving source currents can be represented as the real parts of the complex harmonic functions of time, e.g.

$$\begin{aligned} A_z &= \text{Re}\{A_c e^{i\omega t}\} \\ j_s &= \text{Re}\{j_c e^{i\omega t}\} \end{aligned} \quad (3.29)$$

Where, $\omega = 2\pi f$ is the circular frequency of the sinusoidal wave. The use of complex arithmetic in the equation system (3.28) definitely simplifies the search for the solution in this case. The calculation of time derivatives becomes straightforward. The equation system in phasor notation is simplified to:

$$\begin{cases} -\nabla \frac{1}{\mu} \nabla A_c = j_{vc} - i\omega\sigma A_c \\ \int_{\Omega_s} (j_{vc} - i\omega\sigma A_c) d\Omega = \int_{\Omega_s} j_c d\Omega \end{cases} \quad (3.30)$$

Unfortunately (3.30) is not valid for the transient case. During the discharge test performed on the magnet more than one frequency is present in the spectrum of the damped current oscillations. The discharge itself has a character of an instantaneous switching followed by a rapid release of the energy into the magnet. The magnet is definitely not in a steady state during the test. In order to better understand the meaning of the transient skin effect let us analyze a quasi 2-D problem of a slab excited with a current representing an arbitrary function of time.

3.5.3 Transient Skin Effect

Let us consider a metal plate of conductivity σ with infinite planar extent in the XZ plane (Fig. 3.10). The surface of the conductor is defined by the (0, 0, z) plane. Let us assume that the current density traversing the slab has only one component dependent only on the x

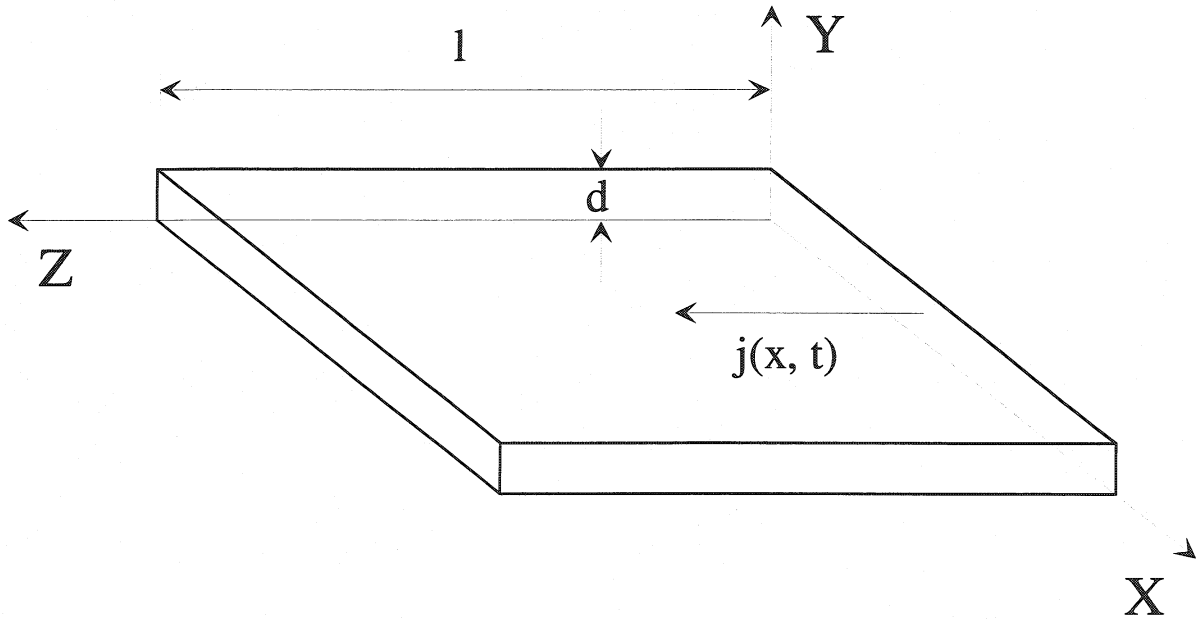


Figure 3.10 A conductor slab model for the quasi 2-D analysis of the transient skin effect coordinate and parallel to the OZ axis. In the analysis that follows this current density is the only term on the right-hand side of Eq. (3.1). Since the transient regime of the slab will be analyzed, it is convenient to apply the Laplace transform to the Maxwell equations:

$$\nabla \times \overline{H(s)} = \sigma \overline{E(s)} \quad (3.31)$$

$$\nabla \times \vec{E}(s) = -s\mu \vec{H}(s) \quad (3.32)$$

The curl of Eq. (3.32) yields in the absence of the free space charges:

$$\nabla \times \nabla \times \vec{E} = \nabla(\nabla \cdot \vec{E}) - \nabla^2 \vec{E} = -\nabla^2 \vec{E} = \nabla \times (-s\mu \vec{H}) = -s\mu \nabla \times \vec{H} = -s\mu \sigma \vec{E} \quad (3.33)$$

And thus

$$\nabla^2 \vec{E} - s\mu \sigma \vec{E} = 0 \quad (3.34)$$

The same equation is satisfied for the current density:

$$\nabla^2 \vec{j} - s\mu \sigma \vec{j} = 0 \quad (3.35)$$

In the case of the metal plate considered, equation (3.35) is reduced to:

$$\frac{d^2 j(x, s)}{dx^2} - s\mu \sigma j(x, s) = 0 \quad (3.36)$$

The characteristic equation of (3.36) has the form

$$\begin{aligned} r^2 - s\mu \sigma &= 0 \\ r_{1,2} &= \pm \sqrt{s\mu \sigma} \end{aligned} \quad (3.37)$$

The general solution of Eq. (3.36) is then

$$j(x, s) = A(s)e^{-\sqrt{s\mu \sigma} x} + B(s)e^{\sqrt{s\mu \sigma} x} \quad (3.38)$$

It has to comply with the following boundary condition:

$$\lim_{x \rightarrow \infty} j(x, s) = 0 \Rightarrow B(s) = 0 \quad (3.39)$$

Therefore,

$$j(x, s) = A(s)e^{-\sqrt{s\mu \sigma} x} \quad (3.40)$$

where $A(s) = J_0(s)$ is the current density at the surface of the conductor slab. The operational current flowing in the segment of width d (see Fig. 3.10) of the conductor integrated over its full planar extent is:

$$\begin{aligned} I(s) &= J_0(s) \int_0^{\infty} de^{-\sqrt{s\mu \sigma} x} dx \\ I(s) &= \frac{d}{\sqrt{s\mu \sigma}} J_0(s) \end{aligned} \quad (3.41)$$

Thus the current can be considered to be of the uniform density when flowing in a skin region of thickness expressed by the operational skin depth:

$$\delta_0(s) = \frac{1}{\sqrt{s\mu \sigma}} \quad (3.42)$$

Any uniform density $J(s)$ can be assumed in a skin of thickness

$$\delta(s) = \frac{1}{\sqrt{s\mu\sigma}} \frac{J_0(s)}{J(s)} \quad (3.43)$$

In the transient regime the current of density $J(s)$ will flow in the region specified by operational skin depth (3.42) as measured from the surface ($x = 0$) of the conductor. In order to calculate the effective resistance of the conductor under such circumstances one would have to analyze the power dissipation in the skin region. Unfortunately Joule's law cannot be applied in the transient case because of its nonlinearity. As a consequence, $W(s) \neq R(s)I^2(s)$, even for the constant $R(s)$ operator.

$$RI^2(s) = R \left[\int_0^\infty e^{-st} i(t) dt \right]^2 \neq \int_0^\infty e^{-st} Ri^2(t) dt$$

To establish $R(s)$ per unit length as a function of the skin depth one has to consider the voltage drop across the conductor section of length l (see Fig. 3.10)

$$V(s) = R(s) \cdot l \cdot I(s) \quad (3.44)$$

$R(s)$ is the resistance of the conductor submitted to the flow of current $I(s)$ distributed uniformly with the density $J(s)$ in the area $d \cdot \delta(s)$.

In the time domain

$$\begin{aligned} R &= \frac{l}{\sigma S} = \frac{l}{\sigma d \cdot \delta} \\ V(t) &= \frac{l}{\sigma d \cdot \delta} i(t) \\ i(t) &= j(t) d \cdot \delta \\ V(t) &= \frac{l}{\sigma} j(t) \end{aligned} \quad (3.45)$$

Taking (3.41) into account, the Laplace transform of the last equation in (3.45) yields:

$$V(s) = \frac{l}{\sigma} j(s) = \frac{l}{\sigma} \frac{J(s)}{J_0(s)} J_0(s) = \frac{l}{\sigma} \frac{J(s)}{J_0(s)} \frac{\sqrt{s\mu\sigma}}{d} I(s) \quad (3.46)$$

Then the operational effective resistance is:

$$R(s) = \frac{1}{\sigma} \frac{J(s)}{J_0(s)} \frac{\sqrt{s\mu\sigma}}{d} = \frac{1}{\sigma d \delta(s)} \quad (3.47)$$

Each value of $J(s)/J_0(s)$ in Eq. (3.47) is characterized by a different operational skin depth $\delta(s)$. The operational skin depth relates the Laplace transforms of the current $I(s)$ and the

current density $J(s)$. The average current density characterized by $J = J_0$ results in the following skin depth:

$$\delta(s) = \frac{1}{\sqrt{s\mu\sigma}} \quad (3.48)$$

If the average current density in the slab is assumed to be $J = \frac{J_0}{\sqrt{2}}$ the skin depth is,

$$\delta(s) = \sqrt{\frac{2}{s\mu\sigma}} \quad (3.49)$$

which corresponds to the real skin depth of the sinusoidal AC steady state:

$$\delta(f) = \sqrt{\frac{2}{\omega\mu\sigma}} = \frac{1}{\sqrt{\pi f\mu\sigma}} \quad (3.50)$$

3.6 FEM Formulation of the Transient Electromagnetic Problem for the Numerical Analysis of the Magnetic Field During the High Voltage Discharge Test

The FEM formulation for the analysis of the transient magnetic field during the high voltage discharge test performed on the collared assembly of the magnet is very similar to the procedure discussed in details for the magnetostatic case in chapter 2 (see §2.11.1). The redistribution of the total current density in the coil conductors must be taken into account here, therefore the convenient reduced vector potential formulation cannot be efficiently incorporated into the solution of the problem (see §2.11.2). As a consequence the entire coil region must be thoroughly meshed reflecting the complicated geometry of the magnet coils in details. Galerkin's method applied to the weak forms of the equations (3.28) and (3.9) leads to the time-dependent matrix equation of the form

$$\mathbf{K}\mathbf{A} + \mathbf{M}\frac{\partial\mathbf{A}}{\partial t} + \mathbf{S} = 0 \quad (3.51)$$

where \mathbf{K} is the system matrix assembled from the single element matrices, the term \mathbf{M} in front of the time derivative also represents a matrix, \mathbf{A} is a time-dependent vector of the unknown vector potentials, and \mathbf{S} is a time-dependent vector of the driving source currents (compare Eq. (3.51) with Eq. (2.119) obtained for the magnetostatic case).

The time dependent solution of the matrix equation (3.51) is also based on the Galerkin's procedure. Vectors \mathbf{A} and \mathbf{S} are discretized in the time domain by means of the first order function of time $\tau(t)$,

$$\mathbf{A}(t) = (1 - \tau) \cdot \mathbf{A}_n + \tau \cdot \mathbf{A}_{n+1} \quad (3.52)$$

$$\mathbf{S}(t) = (1 - \tau) \cdot \mathbf{S}_n + \tau \cdot \mathbf{S}_{n+1} \quad (3.53)$$

which has the following form:

$$\tau(t) = \frac{t - t_n}{t_{n+1} - t_n} \quad (3.54)$$

The vectors \mathbf{A}_n and \mathbf{S}_n are the values of vectors \mathbf{A} and \mathbf{S} at the time step t_n , which can be easily verified by substituting $t = t_n$ in formulas (3.52) and (3.53). Application of (3.54) as the weighting function in the residual solution of the matrix equation (3.51) results in a recurrence formula establishing a relationship between the vector potential solution at the time t_{n+1} and at the preceding time step t_n :

$$\left(\xi \cdot \mathbf{K} - \frac{\mathbf{M}}{t_{n+1} - t_n} \right) \cdot \mathbf{A}_n + \left((1 - \xi) \cdot \mathbf{K} + \frac{\mathbf{M}}{t_{n+1} - t_n} \right) \cdot \mathbf{A}_{n+1} + \xi \cdot \mathbf{S}_n + (1 - \xi) \cdot \mathbf{S}_{n+1} = 0 \quad (3.55)$$

If the linear elements are used to discretize the problem domain the constant factor appearing in the recursive formula (3.55) equals $\xi = \frac{1}{3}$.

The mathematical apparatus for the treatment of the transient electromagnetic problem is now complete. The damped current oscillation curve (see Fig. 3.5) must be introduced into the model as the driving-current supplied to the coils of the magnet during the high voltage discharge test. At this stage a transient model corresponding to the discharge test performed on the collared assembly of the single aperture LHC dipole magnet can be created and optimized. Once it is done, we will be able to simulate the test procedure, calculate the time-development of the transient magnetic field pattern in the aperture of the magnet, analyze its harmonic contents, and study the feasibility of the observed processes for the precise localization of the inter-turn short-circuits.

3.7 Modeling of the Collared Magnet Assembly

Both static and transient models of the 5-block collared dipole magnet without iron yoke were developed and analyzed using two different CAD environments. The magnet modeling process, initiated with the static case and developed towards final transient model, is schematically depicted on the flow diagram in Fig. 3.11.

3.7.1 Evolution from the Static Towards the Transient Model

In the static model created with ROXIE the conductors are excited with a 20 A direct current. Data concerning the characteristic properties of the superconducting cable used for winding of the external and internal layer of the coil are taken directly from the internal ROXIE database. In this way the geometry of the model corresponds to the actual geometry of the magnet used for testing. Since the collars of the magnet are nonmagnetic the calculation of the magnetic field harmonics in the static case is based uniquely on the geometry of the coils and on the current distribution in the conductors. The results of the harmonic analysis of the radial magnetic field component at $r_0 = 10$ mm are given in Table 3.3. (Refer to chapter 2 §2.9 for the explanation concerning the current grading option.)

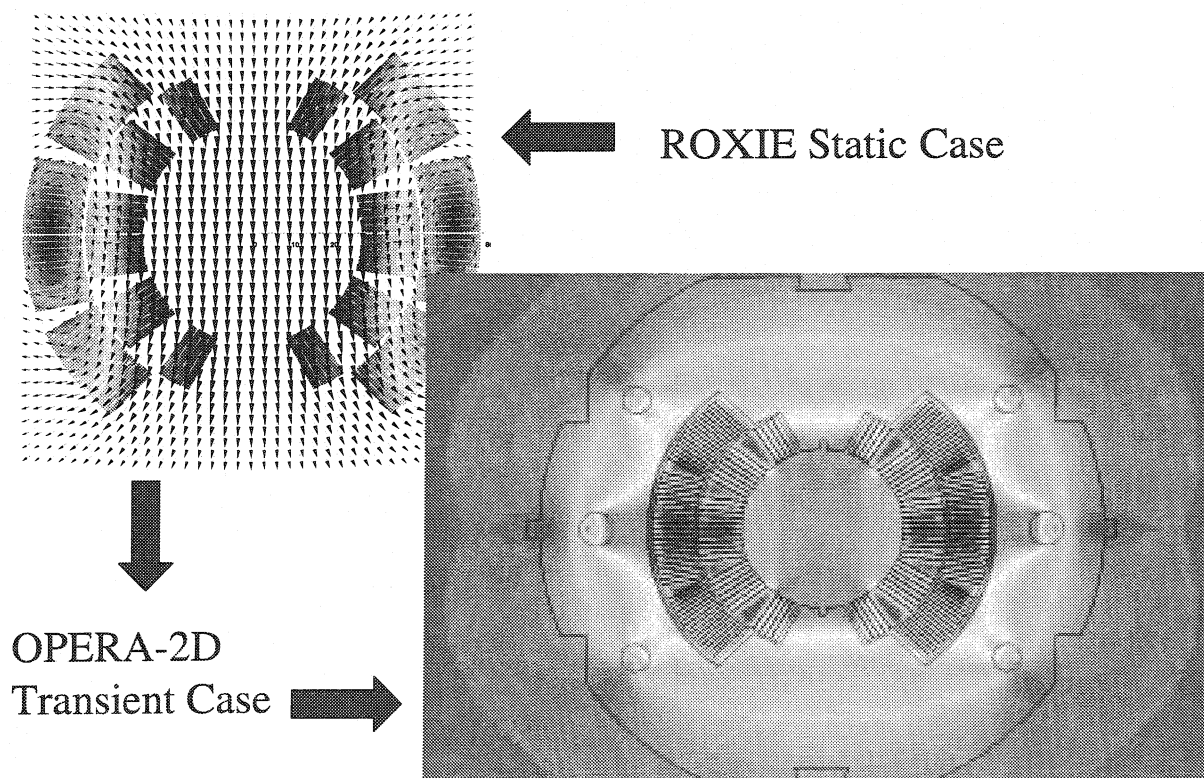


Figure 3.11 Modeling process of the collared magnet assembly

Table 3.3 Harmonic analysis of the magnetic field in the ROXIE static model

Current grading	B_1 [$\cdot 10^{-4}$ T]	b_3	b_5	b_7	b_9	b_{11}	b_{13}	b_{15}
On	-122.8	-0.96	0.032	0.008	-0.0001	0.0114	-0.0005	-0.0001
Off	-122.2	-0.52	0.017	0.013	0.0002	0.0109	-0.0005	-0.0001

Due to the dipole symmetry of the coils neither skew multipole terms nor even orders of the normal multipoles are present in the field expansion. Grading of the current gives a difference of 0.44 units for the sextupole in comparison to the uniform current density case. All of the normalized coefficients are less than 1 unit ($1 \cdot 10^{-4}$), which indicates high quality dipole field with minimized influence of higher harmonics.

The geometry of the coils defined in ROXIE served as a reference for the transient model implemented in OPERA-2D [5]. Relative multipole coefficients are of the order of 10^{-4} and their computation requires very high precision and accuracy. The validity of the results is highly dependent on the proper geometry transfer between both CAD environments, as well as on the correct implementation of the current density distribution into the new model. Therefore the model implemented in OPERA-2D was cross-checked in the static case to verify if the results computed with ROXIE can be reproduced. To assure the same notation and sign convention for the multipole expansion, the harmonic analysis of the field pattern was carried out outside the OPERA-2D environment. The B_x and B_y components of the magnetic field were extracted from the OPERA-2D results for 360 points (1 point per degree) located around the reference radius of $r_0 = 10$ mm measured from the center of the aperture. The extracted values were reassembled afterwards into the radial component B_r , which was then analyzed harmonically by means of Discrete Fast Fourier Transform algorithms. In order to complete the task a special program incorporating Advanced Analysis Library functions was written in LabVIEW graphical programming environment [4]. Table 3.4 contains a geometry transfer cross-check between ROXIE and OPERA-2D.

Table 3.4 Comparison of static models at $r_0 = 10$ mm

Static Case	B_1 [$\cdot 10^{-4}$ T]	b_3	b_5	b_7	b_9	b_{11}
ROXIE (no grading)	-122.2	-0.52	0.017	0.013	0.0002	0.011
Opera-2D	-119.3	-0.55	0.020	0.013	-0.001	0.013

The comparison shows that the model implemented in Opera-2D and analyzed in the static case corresponds to the static case analyzed in ROXIE without current grading in the conductors. Current grading implementation would essentially complicate the mesh division of the already complicated coil region in OPERA-2D. Besides, during the tests at room

temperature the current supplied to the coils is carried by the copper matrix of the cable, because the superconducting Nb-Ti filaments are a very bad conductor unless they are in a superconducting state. Due to this fact the static current density distribution at room temperature is closer to the uniform distribution than to the current-graded case.

3.7.2 Optimization of the Transient Model

The transient model uses FEM approach to simulate the behavior of the magnet during a 1-kV pulsed discharge in which the peak current reaches a value of 20 A (see the reference current curve in Fig. 3.5). In this case the voltage-current decay and the eddy current effects in the conductors, copper wedges, collaring shoe, collars, collaring rods and assembly pins, are taken into account. The elements of the model are presented in Fig. (3.12). A 2-D model of the collared magnet assembly implemented in the XY plane has certain essential discrepancies in comparison to reality. These limitations of the 2-D modeling must be taken very thoroughly under consideration if the model is to reflect an actual real-life experiment. The most important discrepancy between the 2-D simulation and the 3-D reality is posed by the collars. In reality the coil reinforcement structure is composed of 0.3-mm thick laminated collars, which means that two adjacent slices of collars instead of being in direct electrical

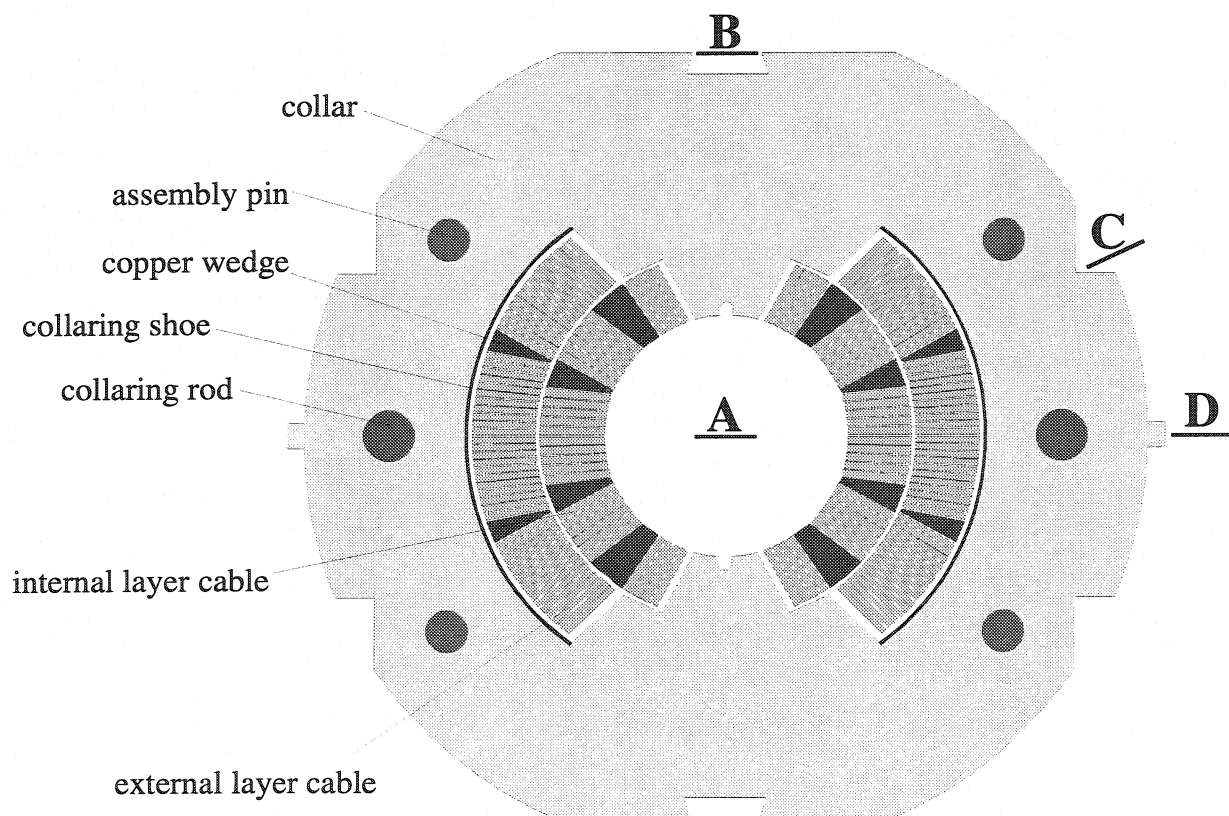


Figure 3.12 Elements of the model and the check-point positions for the model optimization

contact with each other, actually are separated by a 0.1-mm wide air gap. The lamination of the collars results in the conductivity anisotropy between the XY plane and the Z direction. Small thickness of a single collar becomes an obstacle limiting the induction of the eddy currents in the Z direction. On the contrary, in the model the collar region is considered to be a bulk continuous material spreading out to infinity in the *OZ* direction. The effect of the limited eddy current induction can be introduced into the model only in terms of the effective conductivity different than the actual conductivity value corresponding to the material used in the collars. The effective conductivity of the collars was adjusted in the model in order to fine-tune the computational results to the experimental data acquired by measuring the peak field induction inside the aperture and in several locations around the collars. Four test points are indicated in Fig. 3.12 with letters A, B, C and D. Position of the pick-up coil used to carry out the measurements at the respective locations is schematically marked with a black thick line.

Despite the laminations the collars are not electrically isolated. They are in contact with each other due to the two collaring rods running along the entire reinforcement structure of the magnet. The assembly pins also provide the contact path between the collars, but on the contrary to the collaring rods they do not run along the entire magnet length. They cover the 9 cm-long sections of the collaring blocks (one block is a set of 29 aluminum collars). To express the lower contact coupling factor of the assembly pins the effective conductivity must be used as well. Test point C is in a good location to verify the effective conductivity of the pins. The collaring shoe layer is also in direct contact with the collars along the entire length of the magnet. All of the elements of the model in touch with the collars are electrically connected with each other forming thus loops in which the induced currents will flow. On the other hand, the longitudinal wedge-shaped spacers inserted between the blocks of coil conductors are separate, i.e. there is no electrical contact between any two of them. The results of the optimization are listed in Table 3.5.

Table 3.5 Results of the model optimization: main and fringe field adjustment

Field induction [$\cdot 10^{-4}$ T]	Position A	Position B	Position C	Position D
Experiment	-81.8	-13.3	10.8	4.6
Model	-82.0	-13.1	11.0	4.9

If the collaring rods and assembly pins were not taken into account the absolute value of the fringe field in the model in locations B, C, and D would be the same. The following conductivity values were used in the model for the coil reinforcement structure:

- collaring shoe (nonmagnetic stainless steel inox) $0.13 \cdot 10^7$ S/m real value
- collaring rods (nonmagnetic stainless steel inox) $0.13 \cdot 10^7$ S/m real value
- collaring pins (nonmagnetic stainless steel inox) $0.06 \cdot 10^7$ S/m effective value
- collars (aluminium) 10 S/m effective value

Thus the best matching was obtained for an extremely low value of the conductivity of collars (real conductivity of aluminum is $3.65 \cdot 10^7$ S/m) virtually restricting the induction of the eddy currents in the collars to zero. It turns out the remaining parts of the coil reinforcement structure are almost entirely responsible for the shape of the fringe fields around the magnet. The matching between the experiment and the simulation is very good as it is demonstrated for the detailed measurements in the proximity of the checkpoint *B* (Fig. 3.

13) carried out as a function of the distance from the top of the collars (Table 3.6).

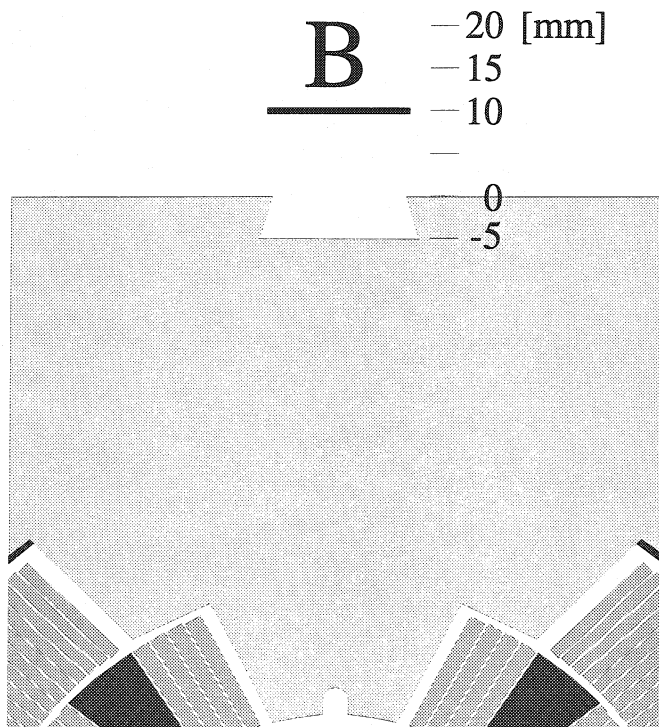


Figure 3.13 Fringe field measurements as a function of the distance from the collars

Table 3.6 Fringe field measurement vs. model computation

Distance [mm]	B [$\cdot 10^{-4}$ T]	
	Experiment	Simulation
-5	-15.7	-15.2
0	-13.3	-13.1
10	-10.8	-10.4
15	-9.5	-9.3
20	-8.5	-8.2

For setting the correct value of the conductivity of the cables an additional test was carried out to evaluate the magnitude of the eddy current effects. For this purpose separate layers of the coils were excited one at a

time to analyze the screening effects. The measurement was done at the checkpoint *A*. The discharge voltages were adjusted to retain the 20 A of peak current during the test. The corresponding current oscillation curves for separate layers of the magnet coils are shown in Fig. 3.14. The peak current of 20 A is reached in the inner layer at the charging test voltage of 275 V. For the outer (external) layer this voltage amounts to 600 V.

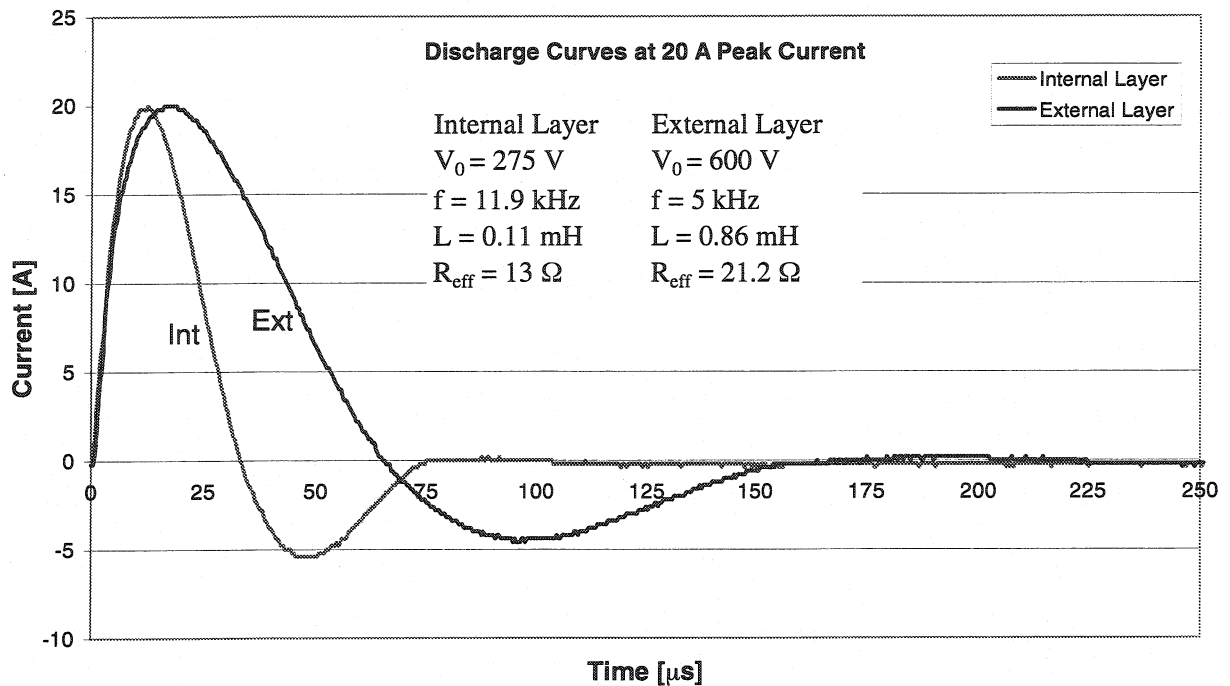


Figure 3.14 Current oscillation curves for the separate layers of the collared magnet assembly

A close match between the model and the experiment was achieved by assigning to the conductors the conductivity values measured with 1 A direct current. The peak field values measured during the experiment and calculated from the model are listed in Table 3.7.

Table 3.7 Separate layer tests

Layer of the Coil	B [$\cdot 10^{-4}$ T]	
	Experiment	Simulation
Internal	21.4	22.5
External	39.5	40.3

The conductivity of the coil components in the model were set to the following values:

- inner layer cable $3.64 \cdot 10^7 \text{ S/m}$ 1 Amp DC measured value
- outer layer cable $3.23 \cdot 10^7 \text{ S/m}$ 1 Amp DC measured value
- copper wedges $5.88 \cdot 10^7 \text{ S/m}$ real value

The results of the optimization are satisfactory and imply the conclusion that the created model is a good theoretical equivalent of the real collared magnet assembly. It would be the time to use this model for the numerical analysis of the distortions introduced by the inter-turn short-circuits in the pattern of the magnetic field during a pulsed discharge.

3.8 Transient Magnetic Field in Presence of the Inter-Turn Short-Circuit

In previous section the parameters of the model have been optimized until the simulated magnetic field map inside and outside the magnet matched the experimental results. In this part the optimized transient model implemented in OPERA-2D will be used to analyze the magnetic field pattern generated in the aperture of the magnet during the discharge.

3.8.1 The Reference Field Pattern

For the calculation of the reference field pattern a standard behavior of the flawless magnet during a discharge test at 1 kV is simulated. The current excitation curve corresponds to the reference curve from Fig. 3.5. The results of the harmonic analysis of the peak field around the reference radius of $r_0 = 10$ and $r_1 = 17$ mm are given in Table 3.8.

Table 3.8 Peak field analysis at 10 and 17 mm

Transient model	$B_1 [\cdot 10^{-4} \text{ T}]$	b_3	b_5	b_7	b_9	b_{11}
analysis at $r_0 = 10$ mm	-82.2	-156.4	9.8	0.3	-0.4	0.01
analysis at $r_1 = 17$ mm	-82.2	-452.0	81.9	7.2	-27.9	2.02

The eddy current effects induced in the model components deteriorate significantly the quality of the magnetic field in comparison to the static case (see Table 3.3). Main dipole field is attenuated by approximately 33 %. The development of a large sextupole is remarkable; at 17 mm it scales already to – 452 units relative to the main dipole field. Higher order field errors cannot be neglected either. Despite the transient nature of the generated magnetic field neither the even orders of normal multipoles nor the skew harmonics are present in the field pattern. Only the harmonics characteristic to the dipole geometry are induced in the magnet.

3.8.2 Magnetic Field Distortions Induced by Short-Circuits

Due to the transient effects accompanying the discharge, the effect of the field discontinuity in presence of the inter-turn short-circuit should be amplified in comparison to the theoretical predictions made for the static case in §3.1 and §3.2 at the very beginning of this chapter. Indeed, it is the case. Table 3.9 lists the computed multipole values for the short-circuit in position denoted as A (see Fig. 3.6) in comparison to the pulsed magnetic field generated in the flawless magnet (Table 3.8).

As it was already explained before, in case of short-circuit the transport current follows a path different from the nominal one (see Fig. 3.6). On one side of the inter-turn short-circuit the current distribution in the coil windings is asymmetric (cross-section No. 1). On the other side it becomes symmetric again despite the additional short-circuit-related transient current induced in the passive winding affected by the electrical defect. In terms of the magnetic field quality this symmetry change in the current distribution corresponds to the vanishing of even-order harmonics of the normal field and of odd orders of the skew multipoles in the area where the current distribution is symmetric. Remarkable amplification

Table 3.9 Short-circuit analysis at $r_0 = 10$ mm

Normal	Reference	X-section 1	X-section 2
B_1	$-82.2 \cdot 10^{-4}$ T	$-60.9 \cdot 10^{-4}$ T	$-61.4 \cdot 10^{-4}$ T
b_2	0.0	113.2	0.0
b_3	-156.4	-768.4	-697.0
b_4	0.0	31.6	0.0
b_5	9.8	-9.9	2.82
b_6	0.0	5.2	0.0
b_7	0.3	1.4	3.1
b_8	0.0	0.5	0.0
b_9	-0.4	-0.9	-0.6
b_{10}	0.0	0.1	0.0
b_{11}	0.01	-0.03	0.01

Skew	Reference	X-section 1	X-section 2
a_1	0.0	271.5	0.0
a_2	0.0	1320.9	1455.7
a_3	0.0	45.8	0.0
a_4	0.0	195.0	204.5
a_5	0.0	1.0	0
a_6	0.0	23.5	22.7
a_7	0.0	-0.7	0.0
a_8	0.0	1.9	1.5
a_9	0.0	-0.4	0.0
a_{10}	0.0	-0.1	-0.3
a_{11}	0.0	-0.07	0.0

of the effect predicted for the static case is observed. The skew quadrupole is of the order of 1400 units instead of the max. 40 units obtained for the static case. The intensity of the current induced in the passive winding, deprived of the initially imposed source current, reaches during the discharge a peak value of 510 A for the analyzed position of the short-circuit. This transient current generates a parasite magnetic field opposing the original magnetic field induced in the magnet by the electrically intact part of the coil. The effect is mostly responsible for the essential deterioration of the magnetic field quality in presence of

the inter-turn short-circuit. High values of the even-order normal multipoles and odd-order skew multipoles in the cross-section No. 1 indicate an increased magnitude of the field discontinuity effect to be measured while passing by the point of electrical fault towards cross-section No. 2 (see Fig. 3.6). Thus the transient regime promises a good feasibility of the analysis of the magnetic field distortions for the precise localization of the insulation failure.

Right now we know exactly what we would like to measure in order to detect and localize the fault-affected area. The physical effect acting in our favor is there. The last question remains unanswered: 'What would be the best approach to put it to work and measure it?'

3.9 Detection Method

The development of the field harmonics during a pulsed discharge can be detected with a system of pick-up coils (Fig. 3.15) aligned on the median plane of the magnet. The schematic position of the individual pick-up coils inside the aperture is shown in Fig. 3.16. In order to visualize and explain the detection method the pure normal and skew quadrupoles in Fig. 3.16 were chosen as the representatives of the even-order field harmonics, and the pure normal and skew sextupoles as the representatives of the odd-order multipoles. For the detailed description of the vector field geometry corresponding to different normal and skew multipoles refer to § 2.6.

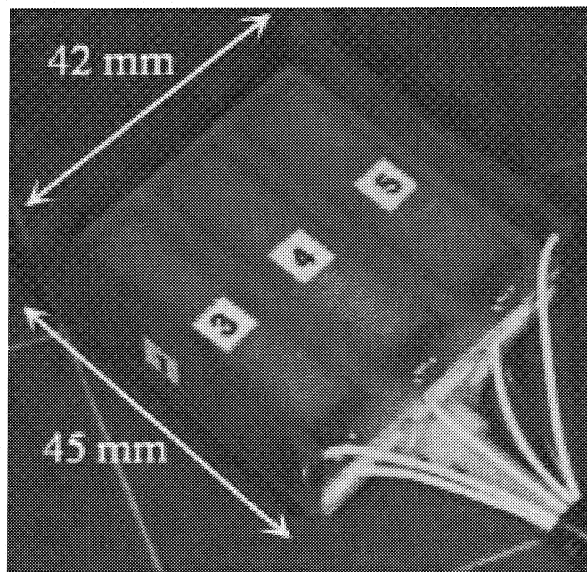


Fig. 3.15 Multi-layer printed circuit pick-up coils

If the pick-up platform is aligned exactly in the median plane of the magnet aperture, the coils C3, C4, C5 do not pick up any flux resulting from the skew field harmonics. The skew flux is detected by the coils C1 and C2. On the other hand the contribution of the normal multipoles to the flux picked up by the coils C1 and C2 is virtually zero as well. Let us denote the sum of all of the contributions of the normal and skew even-order field components by E_n and E_s respectively, and the corresponding sum of the odd-order multipoles by O_n and O_s .

- **Normal multipole detection**

If the even orders of the normal multipoles are present in the pulsed magnetic field pattern the coil C3 will pick up a signal $+E_n - O_n$, whereas the coil C5 the signal $-E_n - O_n$. The magnetic flux resulting from the normal harmonics of even orders crosses both coils in opposite directions (see Fig. 3.16). Thus the difference in the voltage induction between the two coils will be observed and it will correspond to two times the sum of all of the normal even-order multipoles. As soon as the E_n components vanish from the field pattern the induction difference on both coils will disappear. The contribution of the even-order field harmonics in the central coil C4 cancels out. Since the

higher order multipoles are negligible close to the center of the aperture, coil C4 picks up mainly the dipole field.

- **Skew multipole detection**

If the odd-order skew multipoles are present in the pulsed magnetic field pattern the coil C1 will pick-up a signal $-E_s + O_s$, whereas the coil C2 the signal $+E_s + O_s$. In this case the magnetic flux resulting from the skew harmonics of the odd-orders traverses coils C1 and C2 in opposite directions (Fig. 3.16). Thus the sum of the voltage induction on the two coils corresponds to two times the total of all of the skew odd-order multipoles. If the O_s components are not present in the magnetic field pattern this sum will drop down to zero.

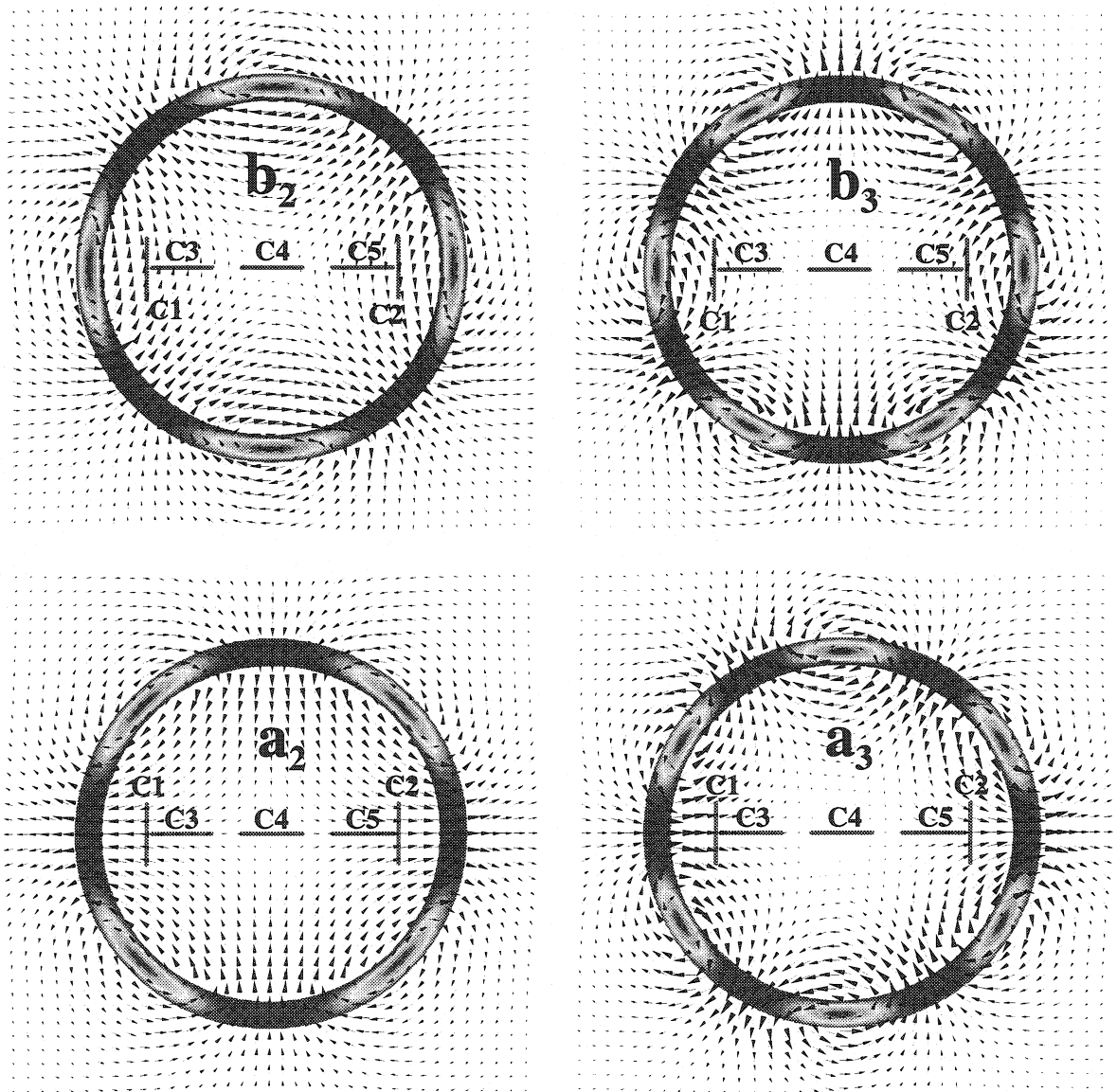


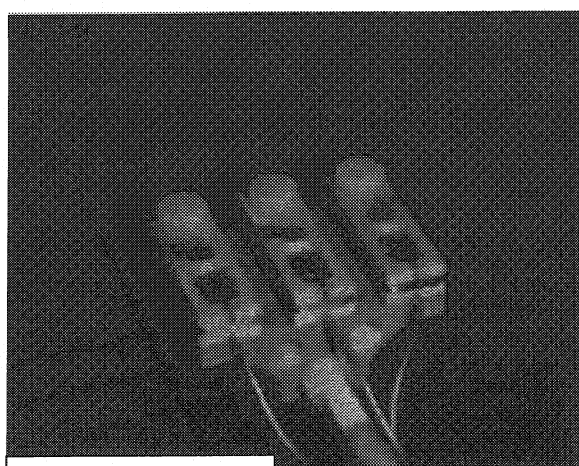
Fig. 3.16 Schematic representation of the detection method

3.10 Design and Fabrication of the Pick-Up Coils

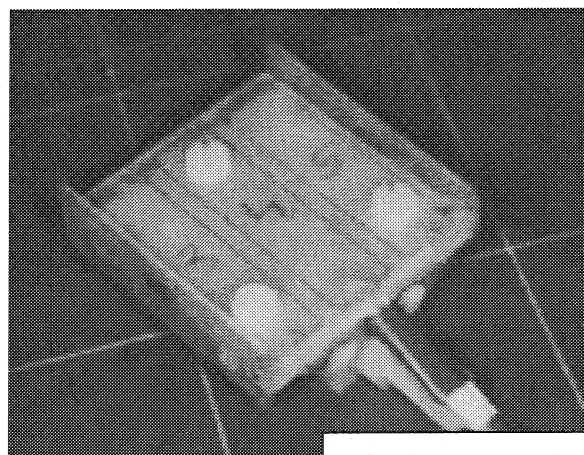
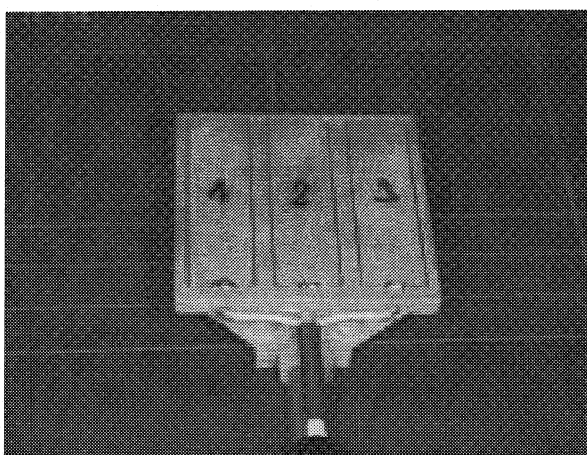
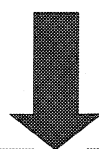
Although the magnitude of the effects to be measured is remarkably increased due to the transient regime of the test, precise and reliable measurement of the pulsed magnetic field remains still the most important prerequisite of a successful experiment. The detection method described in the previous section is based on the measurement of the voltages induced in an exotic pick-up coil. Due to the relatively short duration of the pulse the recorded signal will contain high frequency components. Originally, the precision of such a measurement was put under question. Fortunately for the method, very sophisticated comparisons of the pulsed magnetic field measurements by means of pick-up coils with the results of Faraday [7] and Zeeman effects [8] proved the contrary. A detailed analysis of the phenomena demonstrated that the approach may result in the surprisingly high measurement accuracy of $\pm 1\%$ if the proper precautions are taken both for the design and manufacture of the pick-up coils and for the adequate implementation of the transient data recording techniques and signal processing.

3.10.1 Evolution of the Design Process in Search for the Optimal Solution

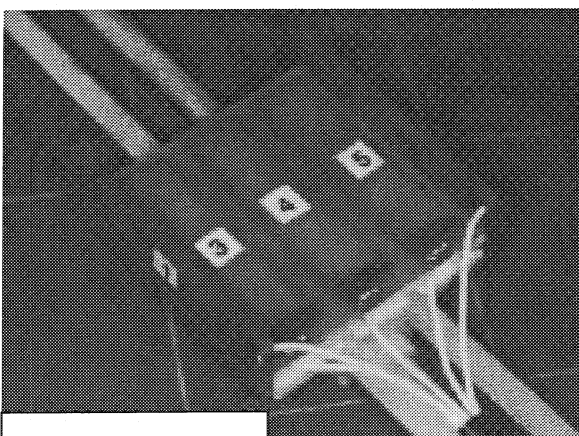
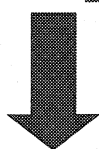
The evolution of the design of the pick-up coils for the localization of the inter-turn short-circuits is shown on the flow diagram in Fig. 3.17. In the first approach (Stage 1) each of three coils contains 650 turns wound with fine thin wire. The coil windings are potted in an epoxy resin for stabilization. Each coil is 3 cm long and 1 cm wide. The triplet is selected from a larger lot of the coils manufactured according to the same design. All of the coils are installed on a vibrating sample holder and calibrated in a constant 1 T field. The criterion is to select the three with the same total surface. For the three coils in Fig. 3.17 (Stage 1) the surface measured during the calibration process varied between 2006 and 2007 cm². In the entire lot of 18 manufactured coils the measured surface varied from 1981 to 2025 cm². Since the coils are made with a thin wire their total resistance is very high. For the three selected coils it varied within the range of 1.4 to 1.5 k Ω . After the winding it turns out that the coils with the same surface are not necessarily obliged to have the same resistance at the same time, which becomes a big disadvantage. The coaxial cabling of the coil should be terminated with the characteristic impedance, especially if the cables are long and the applied excitation pulse is short. The exact impedance match of the pick-up system with such a high resistive load during the discharge is virtually impossible. Even if the pick-up platform is terminated



Stage 1



Stage 2



Stage 3

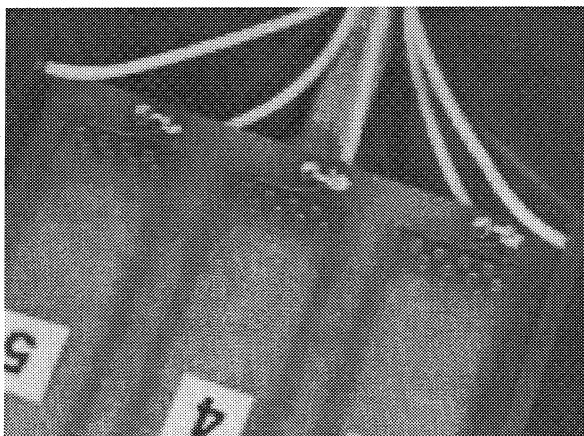


Figure 3.17 Evolution of the pick-up coil design

with 1 M Ω by the read-out oscilloscope, the dynamic behavior and effective resistance of the coils must be taken into account in the calculation of the voltage division between the terminating resistance and the combined resistance of the pick-up platform and its cabling. One simply cannot ignore the resistance of 1.5 k Ω in comparison to 1 M Ω termination. This introduces already some relevant errors while recalculating the voltage induction. The errors are magnified even more while integrating the signal for the calculation of the magnetic flux. Moreover, due to the large amount of cable used for winding, the coils are quite vulnerable to the thermal expansion effects.

To circumvent all of these problems it is much better to use pick-up coils with a very small resistance in comparison to the characteristic impedance of the cable used for the connection of the pick-up probe with the oscilloscope. In addition all of the coils on the pick-up probe should have exactly the same resistance and the same surface. All of these objectives are achieved in Stage 2 of the design in form of the single turn printed circuit pick-up coils realized with chemical surface etching techniques. Each single-turn coil is 4 cm long and 1 cm wide resulting in the surface of 4 cm². Each of them has a very low resistance of 0.4 Ω . The alignment of the coils is controlled already at the production level. This pick-up probe gives already very good results during the measurement of the transient magnetic field, but the level of the induced signal is quite low. At this stage also the idea of the simultaneous analysis of both normal and skew harmonics of the magnetic field was conceived and implemented in the pick-up probe.

To improve the level of the induced voltages the final design is realized using the procedure normally employed for the design and manufacture of the multi-layer printed circuit electronic boards (Stage 3). Each pick-up coil on the platform is composed of 8 layers of printed circuit windings (1 x 4 cm each) stacked above each other to create an 8-turn miniature coil with the total surface of 32 cm². Two additional protective layers close the entire sandwich from both sides. Each turn has a resistance of 0.4 Ω . Together with the contact resistance between the layers the total resistance of a single pick-up coil amounts to 3.5 Ω . After the connection of the coaxial cables to the terminals of each pick-up coil the calibration measurement with the vibrating sample holder in the static reference magnetic field of 1 T confirms the effective surface of 32.1 cm² for all of them. The conductive copper path, acting as a wire in a standard coil, has a rectangular cross-section 35 μ m high and 150 μ m wide. The thickness of the entire 10-layer assembly is 1.4 mm \pm 0.2 mm. The total height of the active coil part composed of 8 internal layers does not exceed 1 mm.

3.10.2 Assembly of the Multilayer Printed Circuit Pick-Up Probe.

All of the pick-up coils; the triplet responsible for the detection of the normal multipoles (coils C3, C4, and C5 in Fig. 3.15) and the remaining side-winger coils responsible for the detection of the skew harmonics (C1 and C2) are produced together. The general rules and definitions of terms concerning the design and the end product specification for rigid multilayer printed boards are given in the standard specification IPC-ML-910 A [9]. Nevertheless, as far as the specific solution is concerned the freedom of realization of the project is left to the designer alone. The layout of the single pick-up coil decomposed into separate slices explaining the interconnection scheme between the adjacent layers is shown in Fig. 3.18. The interconnection points are designed in this way that the surface of a single turn

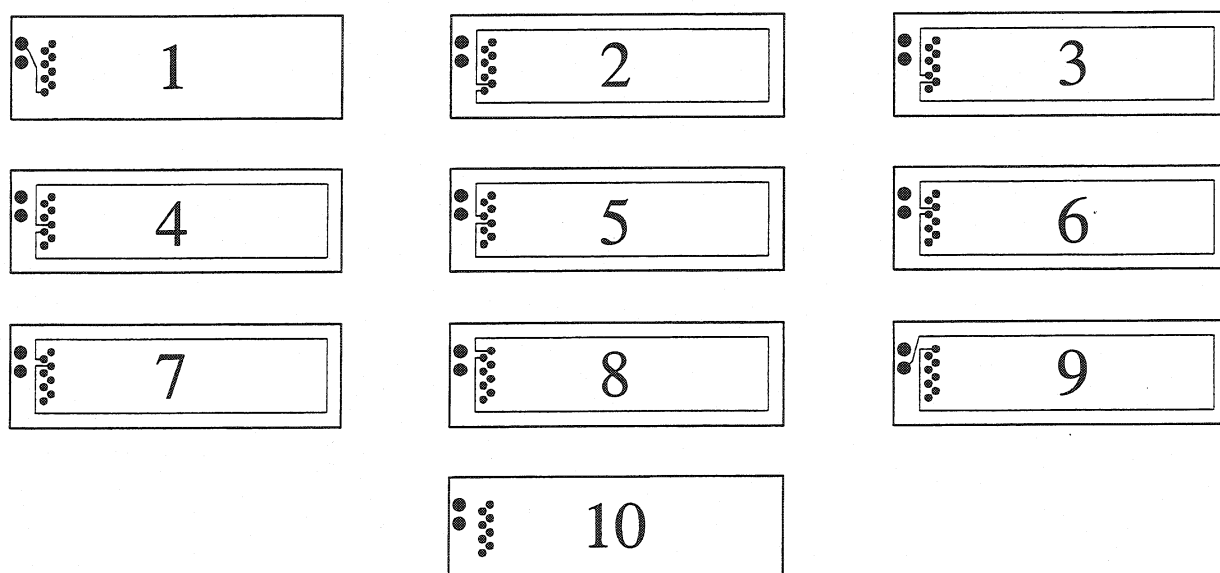


Figure 3.18 Circuit winding and inter-connections between the layers of the pick-up coil

in each layer is exactly the same. The continuous winding from a given layer to its neighbor located one level below follows a unique direction, which assures that the fully assembled printed circuit board behaves like a standard 8-turn pick-up coil wound with traditional wire.

The assembly of the 5 double-sided printed circuit boards follows the multilayer technology. Each double-sided board (2 layers) is composed of 0.1-mm thick fiberglass epoxy base covered on both sides with 35 μm of conductive copper layer. The outermost layers of the entire assembly are covered only with 5 μm of copper (see Fig. 3.19 for the dimensions of the layers and the thickness of the copper deposit). The process starts with the drilling of the positioning reference holes for the precise alignment of the layers. Then the circuit images prepared on the photosensitive films are transferred to the internal layers (No. 2 to No. 9) in the following steps:

- The 35- μm thick deposit of copper initially present on the layers is covered with the photoresistive dry film.
- The negatives with the images of the printed circuits are placed on the dry film surface.
- The parts of the dry film exposed to the UV radiation are polymerized.
- After the development of the dry film in the 1% solution of NaOH base, at the temperature of 30 – 35 $^{\circ}\text{C}$, the circuit paths are efficiently masked with the blue polymerized residue of the dry film.
- The layers prepared in this way are submitted to the chemical etching process in a bath of FeCl_3 with 3-5 % of HCl acid for approximately 2 minutes. During this period of time the parts of copper film, which are not covered by the mask, are chemically attacked and thoroughly removed from the surface of the layer.

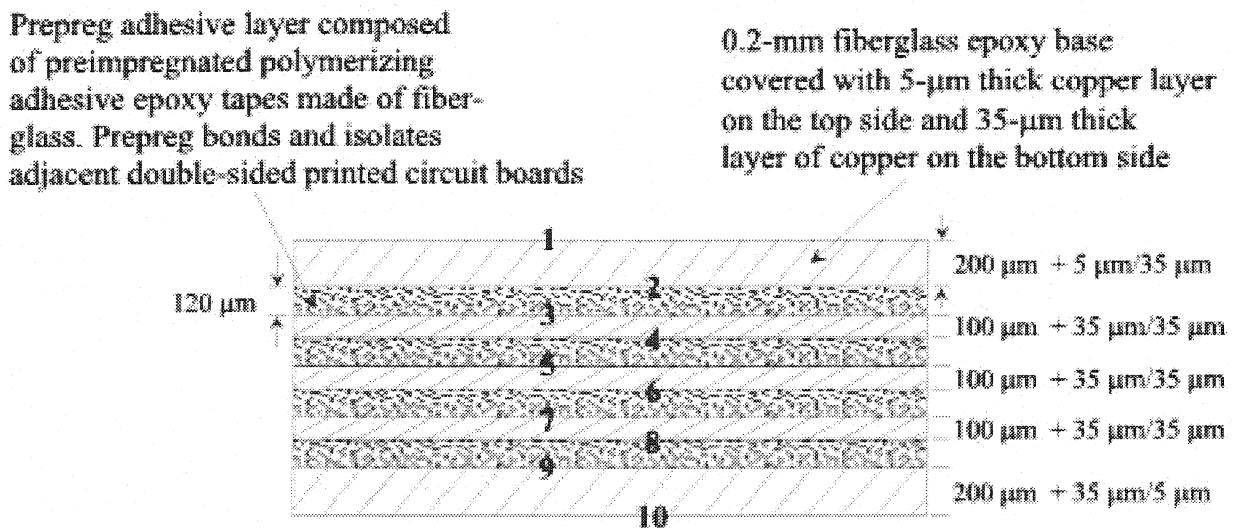


Figure 3.19 Schematic representation of the multi-layer stacking configuration

- After etching, the dry film mask still covering the circuit paths is stripped off in a 6% solution of KOH base at the temperature of 45 $^{\circ}\text{C}$.
- Stripping is followed by the final chemical surface treatment preventing the copper paths from oxidation. In a chemical bath a 3-5 μm layer of nickel and a 0.02 μm layer of gold are deposited on the surface.

Once the internal layers are prepared, they are interlaced with the 120- μm thick layers of pre-impregnated low-flow fiberglass, which form an epoxy adhesive tape. The entire sandwich is aligned with help of the positioning reference holes and glued under the press. The bonding of the adjacent layers takes place in the vacuum chamber under pressure of 15-18 bars at the

temperature of 180 °C. At this temperature the fiberglass from the adhesive tape starts flowing and filling the gaps between the copper circuit paths outstanding from the surface of the layer. At the same time the heat treatment triggers the polymerization of the adhesive material and the layers of the assembly are bound together. The entire process takes 40 minutes. At this stage the two outermost layers of the multilayer assembly are still entirely covered with the initial 5 μm of copper.

After the cooling of the sample the interconnection holes (8 small round connection terminals in Fig. 3.18) and the coil connection terminals (2 large round holes) are drilled across the entire multilayer assembly. Next step involves a two-stage metalization of the drilled interconnection terminals with the conductive layer. In the first stage of the chemical line treatment the interior of the holes is covered with a preliminary thin layer of copper. Once the very first thin conductive connection exists inside the openings, a galvanic copper deposition stage is launched. In the galvanic acid bath the interior of the holes and the outermost layers of the assembly are covered with 20- μm thick layer of copper. At this point the adjacent internal layers are electrically connected with each other forming the circuit of the pick-up coil.

Only now the image transfer of the circuit access paths is performed for the external layers (No. 1 and 10). During the chemical etching the terminal holes are masked to preserve the results of the metalization. After the stripping and the final surface treatment the outer layers are covered with the 50- μm of the protective solder mask (another sort of dry film), and the completed coils are ready to be detached from the motherboard material. The detailed technical specifications of the circuit design along with the films containing the images of the circuit paths and interconnections between the layers are stored in the archives of the Printed Circuit Design Department at CERN [10].

3.11 Experimental Set-Up

One of the short dipole magnets was equipped with micro-relays soldered on the internal layers of the coils in two clusters; one centered around the cross section in the middle of the magnet and the other close to the end region of the coil (Figs. 3.20 and 3.21). The relays, excited externally with direct current one at a time, create short circuits between adjacent cable turns in well-defined positions depicted in Fig. 3.22. A pulsed current is supplied from a discharge generator by releasing the energy accumulated in a $1\ \mu\text{F}$ capacitor, charged at 1 kV, into the magnet. The voltage induced in the pick-up coils is measured during the discharge and integrated thereafter to obtain the time evolution of the magnetic field induction.

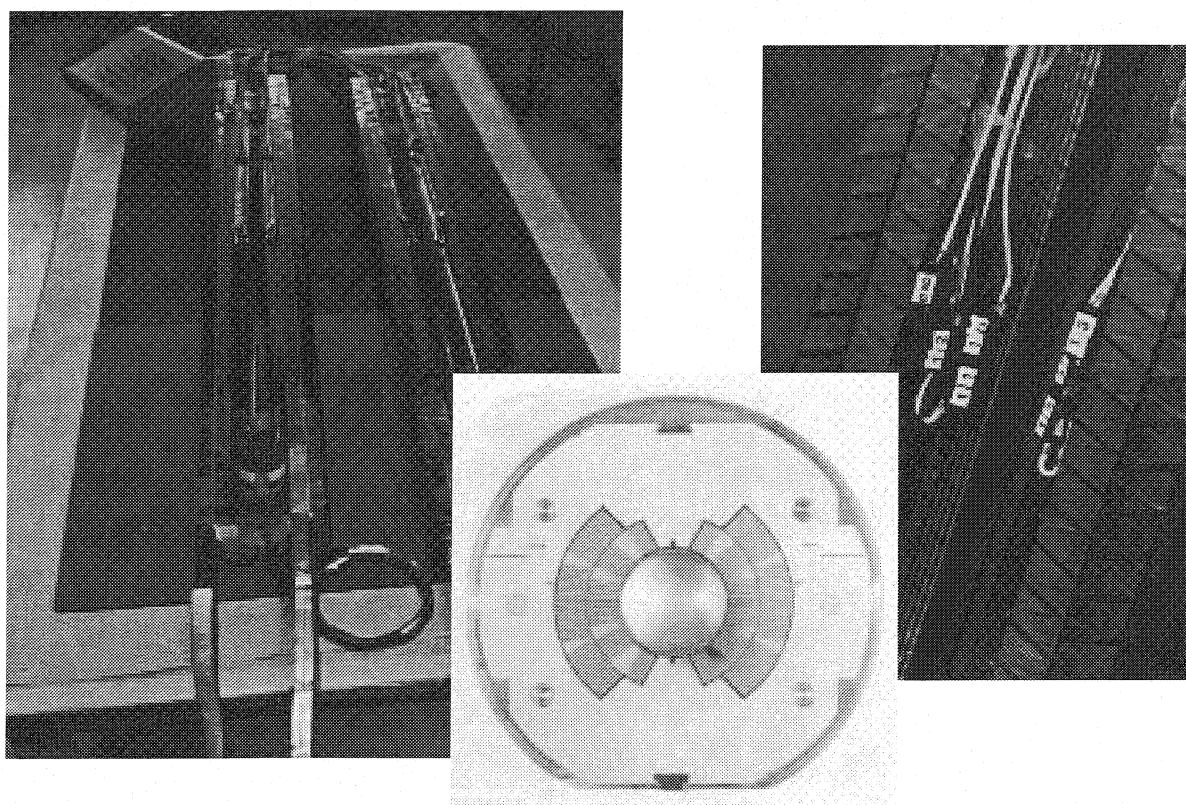


Figure 3.20 Magnet coils equipped with micro-relays

The pick-up probe configuration shown in Fig. 3.15 is mounted on the vetronite (G-11) support. Entire platform slides longitudinally on two vetronite rods aligned inside the aperture of the magnet (Fig. 3.17 Stage 3). The longitudinal tensile stress is applied to the rods by the bolted endplates mounted at both extremities of the collared assembly. Fixed targets installed as an extension to the endplates allow precise micrometric control of the platform position inside the aperture. The solution adapted for the long magnets will be discussed later.

The size and the shape of the support drawn schematically in Fig. 3.23 are the results of the compromise between the positions of the micro-relays soldered on the superconducting cable and the free space left inside the aperture of the magnet for the longitudinal displacement of the pick-up probe.

The precision soldering of the low-noise high-screen coaxial connection cable to the individual pick-up coils is done with all of the necessary precautions aiming to avoid the creation of any additional artificial loops at the connection terminal. Since the probe operates in time-varying magnetic fields, there are no metallic parts on the detection platform or in its vicinity

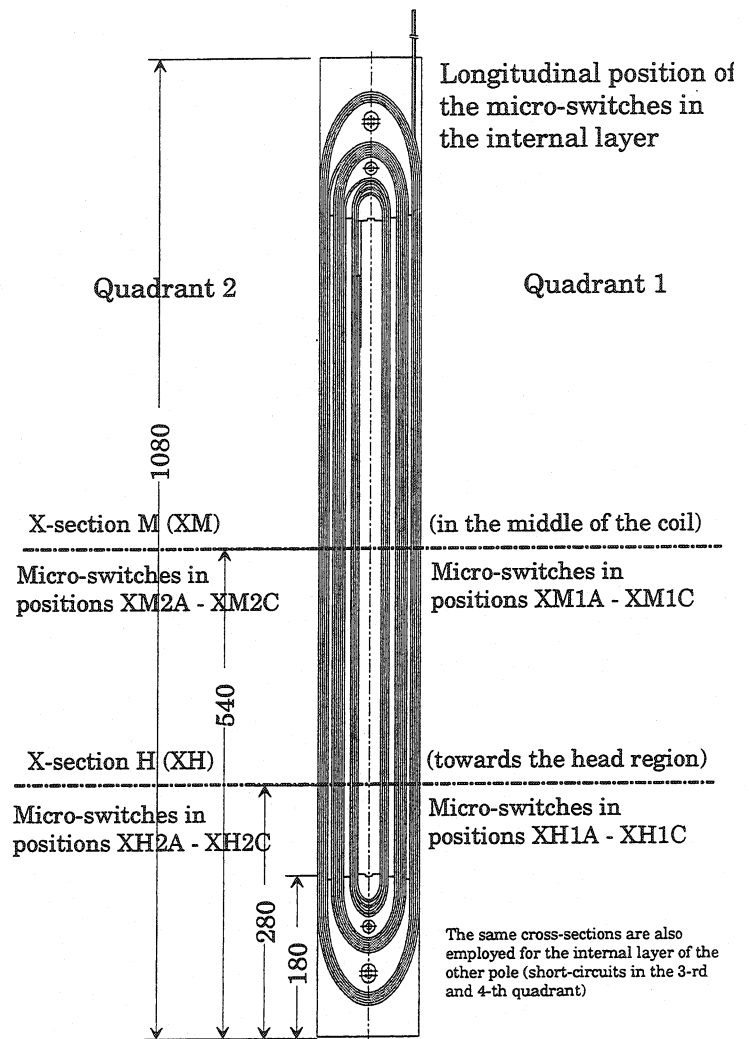


Figure 3.21 Longitudinal positions of two micro-relay clusters

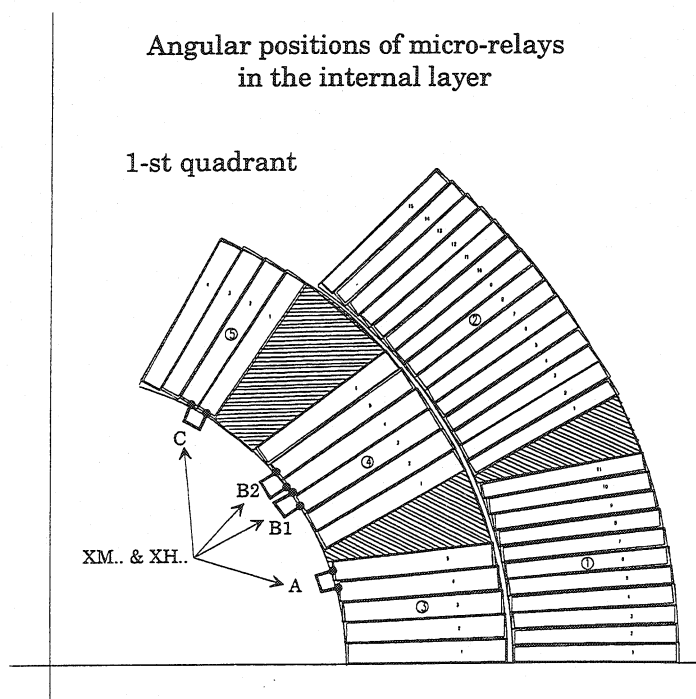


Figure 3.22 Azimuthal position of the micro-relays

that would distort the signal picked up by the coils. The only conducting media on the pick-up coils are the printed circuit paths, and their dimensions are much smaller than the skin depth at the main frequency of the discharge. (The skin depth value for the copper at the frequency of 4 kHz is approx. 1 mm).

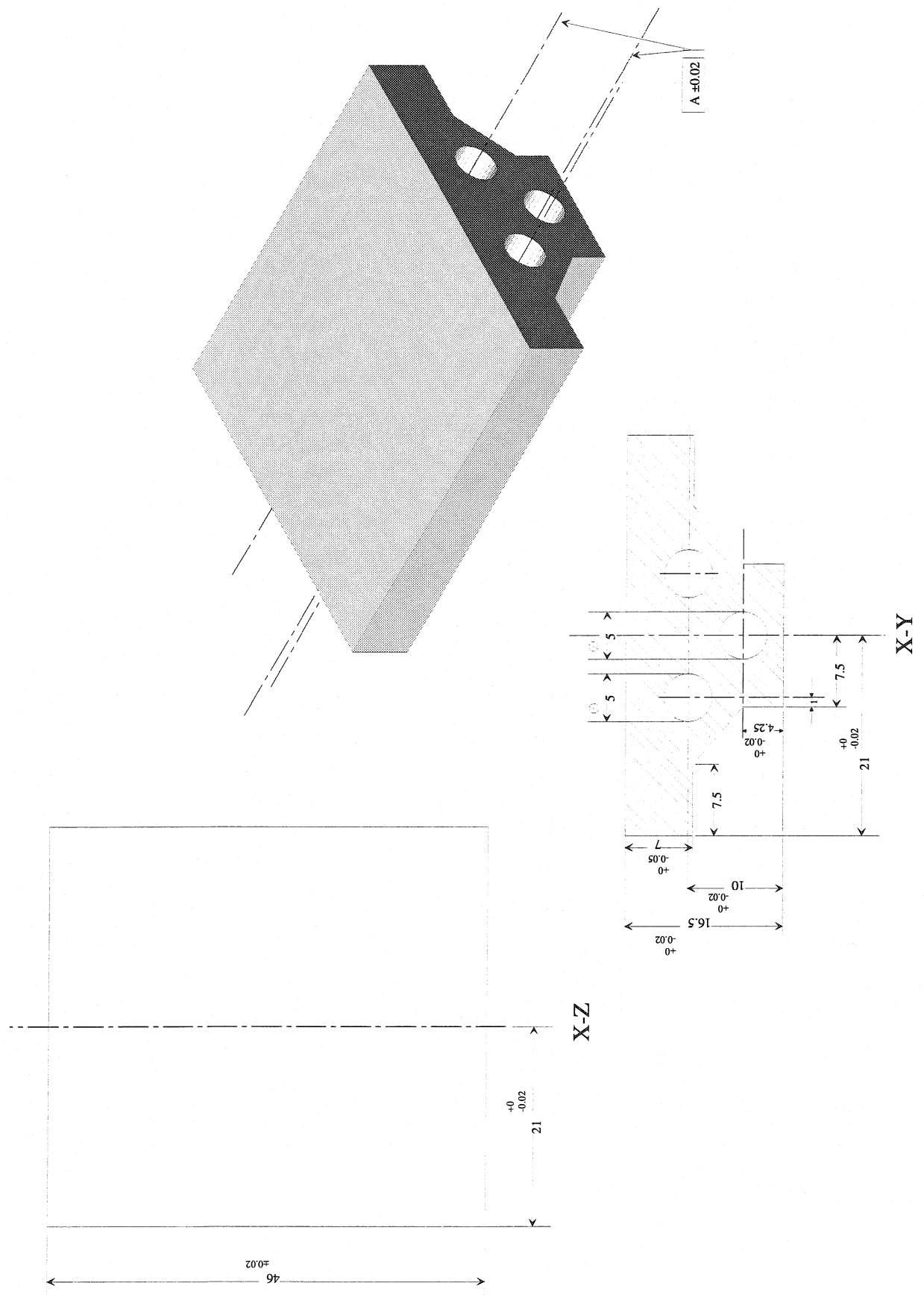


Figure 3.23 Vetronite support for the pick-up probe

3.12 Test Results

The test results confirm the computational analysis demonstrated in section § 3.8. The signals registered by the five pick-up coils of Fig. 3.15 allowed to identify the longitudinal position of all triggered faults and also gave an indication of the azimuthal position of the short-circuits. Before we come to the analysis of these results let us explain the measurement process using an example of the reference field pattern.

3.12.1 Reference Magnetic Field

The reference magnetic field is measured on the flawless magnet, with no short-circuits engaged. Figure 3.24 shows the raw signal induced on the central pick-up coil C4.

With modern digital oscilloscopes it is very easy to over-sample the signal, which is an evident case for the voltage induction curve shown in Fig. 3.24. The sampling rate of the digital oscilloscope can be much higher than the rate required for the actual bandwidth of the signal being analyzed. This effect can be used to efficiently enhance the resolution of the recorded data by an online application of the Finite Impulse Response (FIR) filters [11].

The original signal is noticeably covered with white noise and also with a certain dose of ringing resulting from the impedance mismatch. We are interested in a high precision of

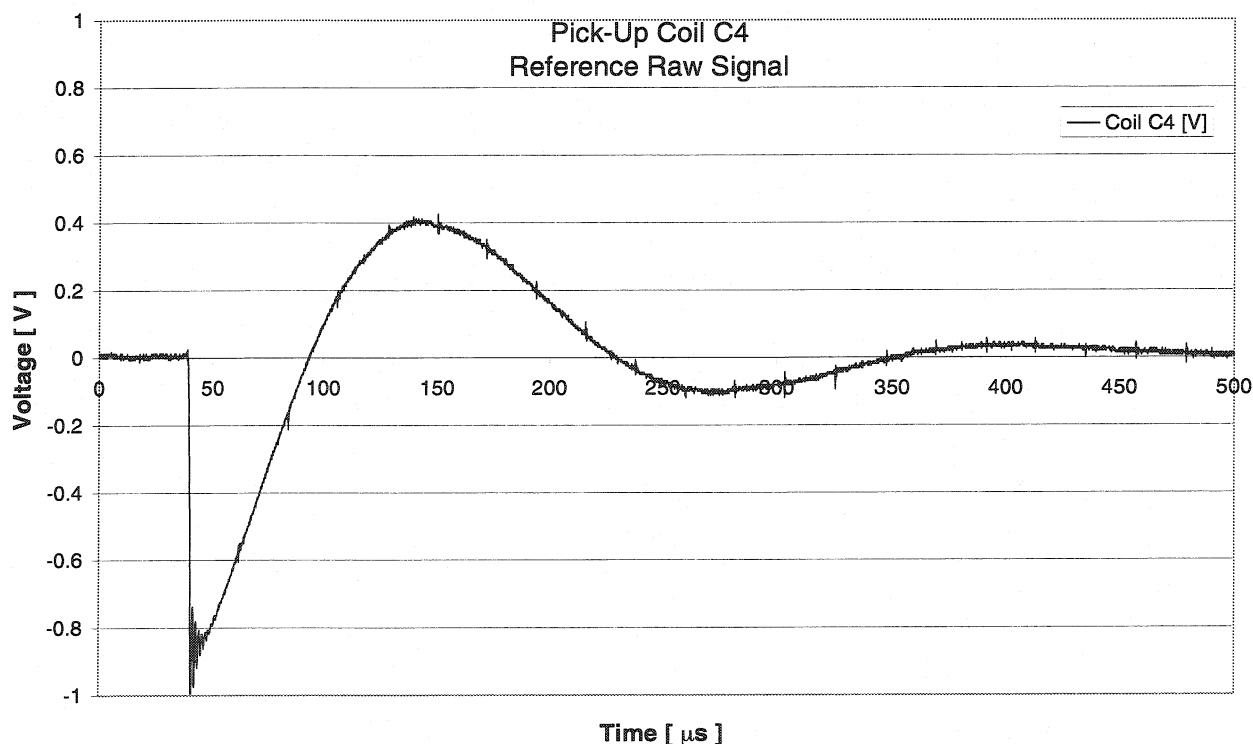


Figure 3.24 Raw signal induced on the pick-up coil C4

the waveform measurement and in this concern the FIR filter will not only increase the capability to distinguish closely spaced voltage levels on the data curve but it will also eliminate undesirable noise from the signal. The nature of the discharge test enforces a single-shot data acquisition mode; therefore it is not possible to average multiple traces of the same waveform. Digital treatment of the single-shot signal with the FIR filter is similar to smoothing of the acquired data by means of the moving average algorithm, with the exception that the FIR filter has much better passband characteristics.

A very interesting feature of the FIR filter is its finite magnitude response resulting in the guaranteed stability of the filter. Moreover, FIR filter has a constant, zero phase response; there is no phase shift in the filtered signal in comparison to the original data, i.e. the data filtered by the FIR filter is FFT-ready. The relative position of different time events in the original waveform is not distorted by the filtering process even if the frequency content of these events after filtering is different.

The original signal picked up by the coil C4 after the 3-bit resolution enhancement realized with a low-pass FIR filter is shown in Fig. 3.25. The noise in the original waveform is evenly distributed across the frequency spectrum, therefore the improvement in the signal to noise ratio (SNR) corresponds to the significant improvement of the actual resolution of the filtered signal. Had the noise spectrum been shifted towards high frequencies the SNR

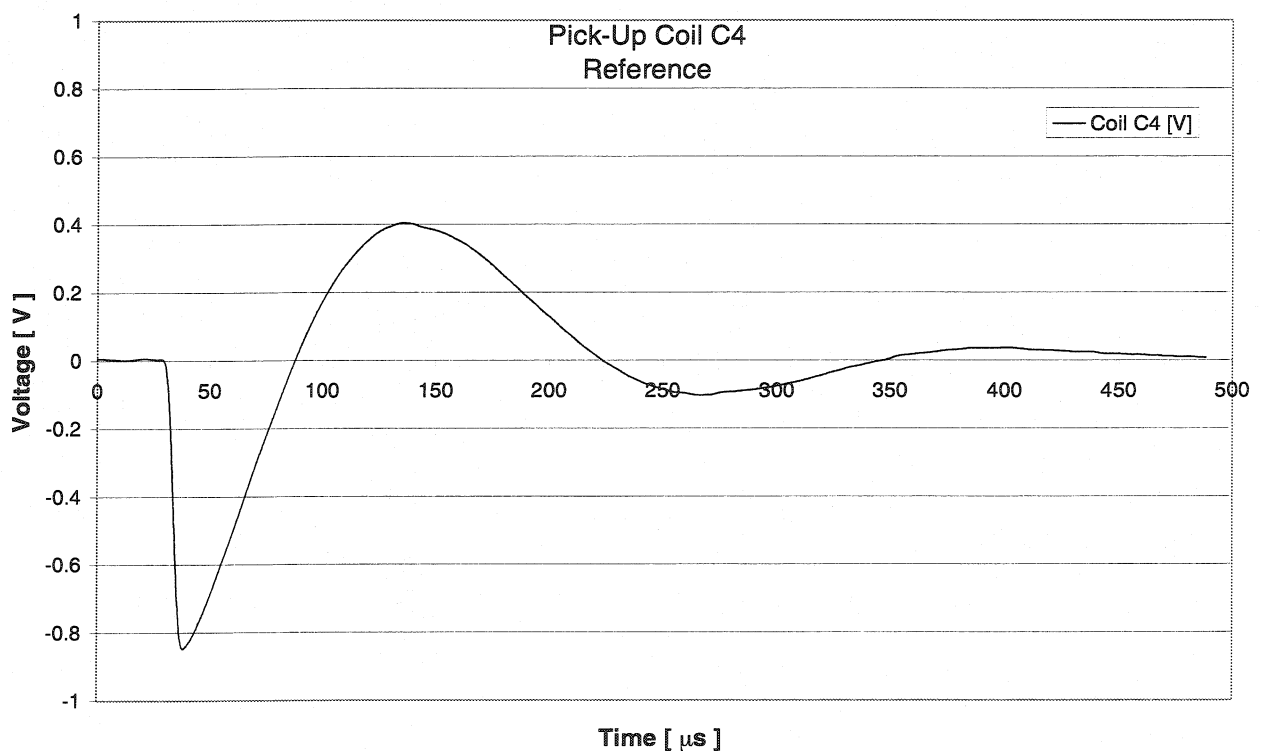


Figure 3.25 Signal resolution enhancement by means of the low-pass FIR filter

would have been better than the resolution enhancement, whereas in the opposite case the resolution improvement would have been more interesting than the actual gain in terms of SNR.

With the online FIR filter applied during the measurements the resolution enhancement between 0.5 and 3 bits can be realized with the steps of 0.5 bits [12]. Each step corresponds to the reduction of the original frequency bandwidth by the factor of 2. According to the sampling theorem one can reconstruct a continuous time signal from discrete, equally spaced samples if the sampling frequency of the digital system is at least twice that of the highest frequency in the original signal. If this prerequisite is not satisfied the aliasing between the consecutive digital samples will occur and the acquisition procedure will result in the complete loss of the features of the original waveform.

The original raw signal in Fig. 3.24 is sampled at equally spaced time intervals of $\Delta t = 100$ ns without losing any information in the process. The sampling frequency is thus:

$$f_s = \frac{1}{\Delta t} = 10 \text{ MHz}$$

The highest frequency of the original waveform that the digital read-out system can cope with is called the Nyquist frequency. According to the sampling theorem this frequency amounts to:

$$f_{Nyq} = \frac{f_s}{2} = 5 \text{ MHz}$$

The 3-bit resolution enhancement constitutes the sixth step in the available range of the bandwidth vs. resolution trade-off. Thus the bandwidth of the low-pass FIR filter applied to the signal is:

$$f_{FIR} = \frac{f_{Nyq}}{2^6} \approx 0.016 \cdot 5 \text{ MHz} = 80 \text{ kHz}$$

All of the signal components with the harmonic frequencies higher than 80 kHz are cut off from the original data during the filtering process. The main harmonic frequency of the voltage induction curve in Fig. 3.24 is $f_0 = 3.8$ kHz. Thus due to the fact that the original signal is highly over-sampled the bandwidth resulting from the 3-bit resolution enhancement is still wide enough not to produce any distortions in the filtered waveform. The 3-bit resolution enhancement was applied to all of the signals acquired in the measurements. The smoothing effects of the FIR filter are illustrated in the zoomed windows in Fig. 3.26.

The next step in the signal processing is to integrate the voltage induction curve in order to obtain the total flux density and eventually the time evolution of the magnetic field induction. In order to minimize the errors, the integration of the FIR-filtered signal is performed simultaneously with the data acquisition by an internal digital integrator embedded

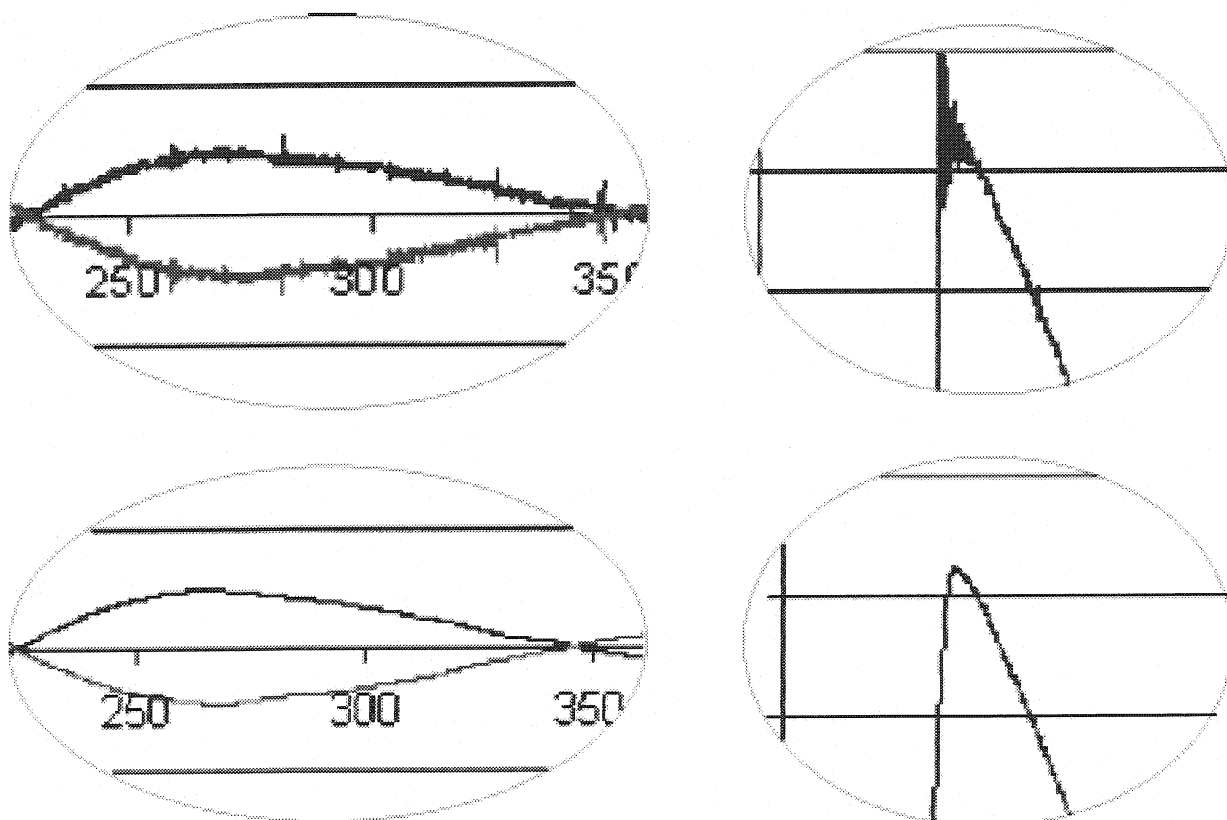


Figure 3.26 FIR filtering effects

directly in the read-out oscilloscope. The digital on-line integration eliminates many of the restrictions put on the integration techniques realized with analog devices, e.g. the finite integration time of the analog RC integrator and its disturbance by the input resistance and capacitance of the recording instrument do not have to be taken into account.

In our case the resistance of the single pick-up coil (3.5Ω) is very small in comparison to the $1\text{-M}\Omega$ termination of the oscilloscope. In this way the entire induced voltage is read by the oscilloscope, and the voltage division between the terminating resistor and the combined resistance of the pick-up coil and its cabling does not have to be considered either. The only disadvantage of this approach is that the signal from the pick-up coil reaching the input channel of the oscilloscope gets reflected there as if it has reached an open circuit termination, which results in a certain amount of ringing observed in the original signal. Nevertheless, as already demonstrated, this effect can be entirely canceled out by an appropriate application of the FIR filter. The integration itself acts as a filter, because the irregularities of the signal are smoothed out in the process. Actually the integration of the original waveform and of its 3-bit enhanced resolution version gives the same results. Sometimes the unique measurement of the integrated signal can be deceptive, because the

anomalies, which may appear in the induced voltage due to the malfunction of the experimental setup or spurious voltages coupled into the pick-up coil circuit, are automatically smoothed out. Therefore the measurement of the induced voltages must be always run in parallel.

The integrated magnetic field induction corresponding to the signal picked-up by the coil C4 is shown in Fig. 3.27. The peak value of the magnetic field induction reaches -81.8 Gauss (-82 Gauss predicted by the model).

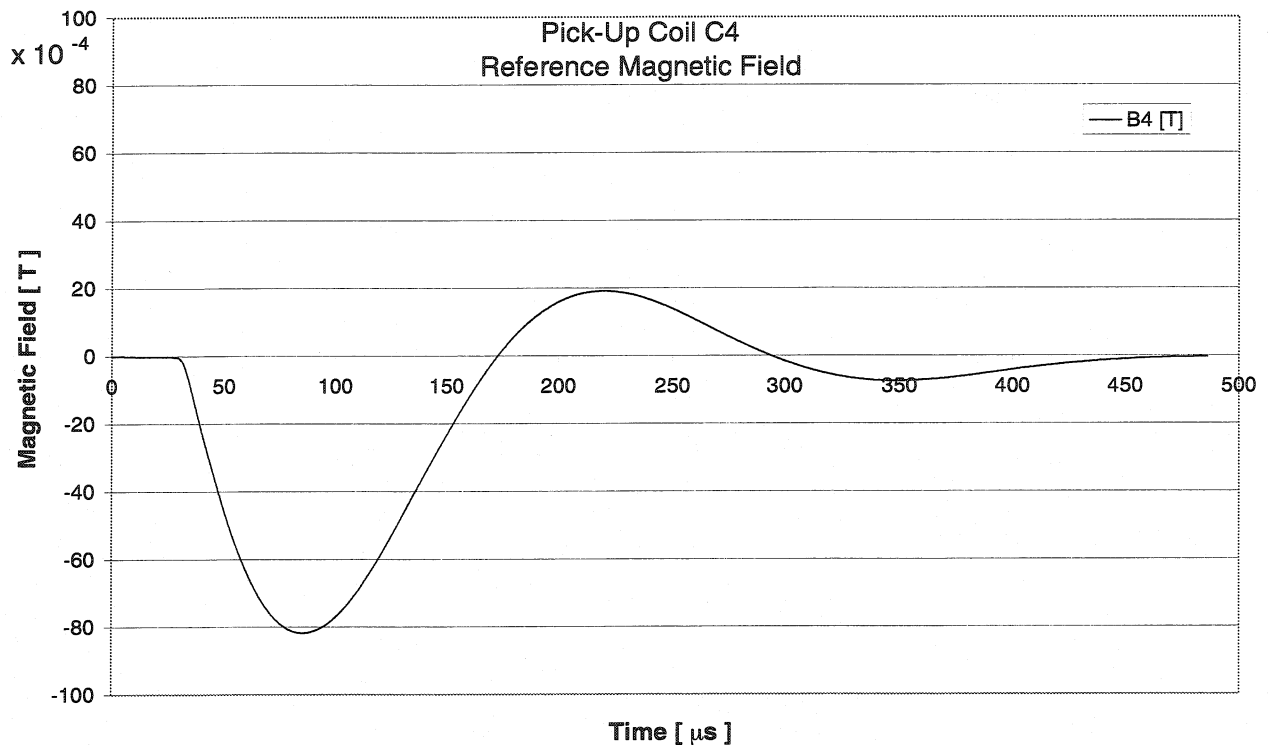


Figure 3.27 Time evolution of the magnetic field induction recorded by the pick-up coil C4

The voltages induced on the pick-up coils C3 and C5 are shown in Fig. 3.28. In reality the signals on these coils are of the same negative polarity. To avoid overlapping of the waveforms on the graph both curves are plotted using the opposite polarity representation for the reader's convenience. The corresponding plots of the magnetic field induction are drawn in Fig. 3.29. The peak field values registered by both coils are the same and equal to -80 Gauss (-80.2 Gauss predicted by the model).

In the case of the flawless magnet with no activated inter-turn short circuits virtually no signal is picked-up by the coils C1 and C2. Only the voltage induction curves are shown for these two coils in Fig. 3.30. The diagram in Fig. 3.31 compares the experimental data with the results obtained from the model. As one can see the transient model yields the values equivalent to the ones obtained during the experiment.

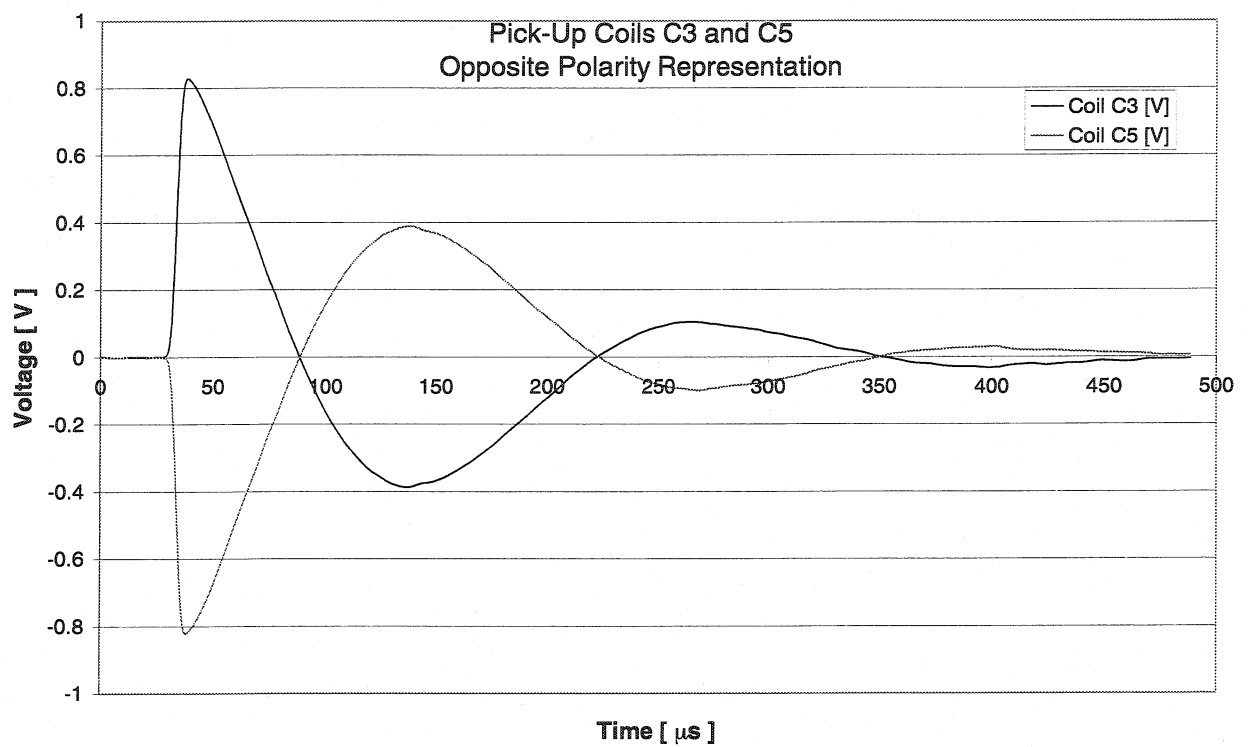


Figure 3.28 Voltages induced on the pick-up coils C3 and C5. In reality both signals have negative polarity.

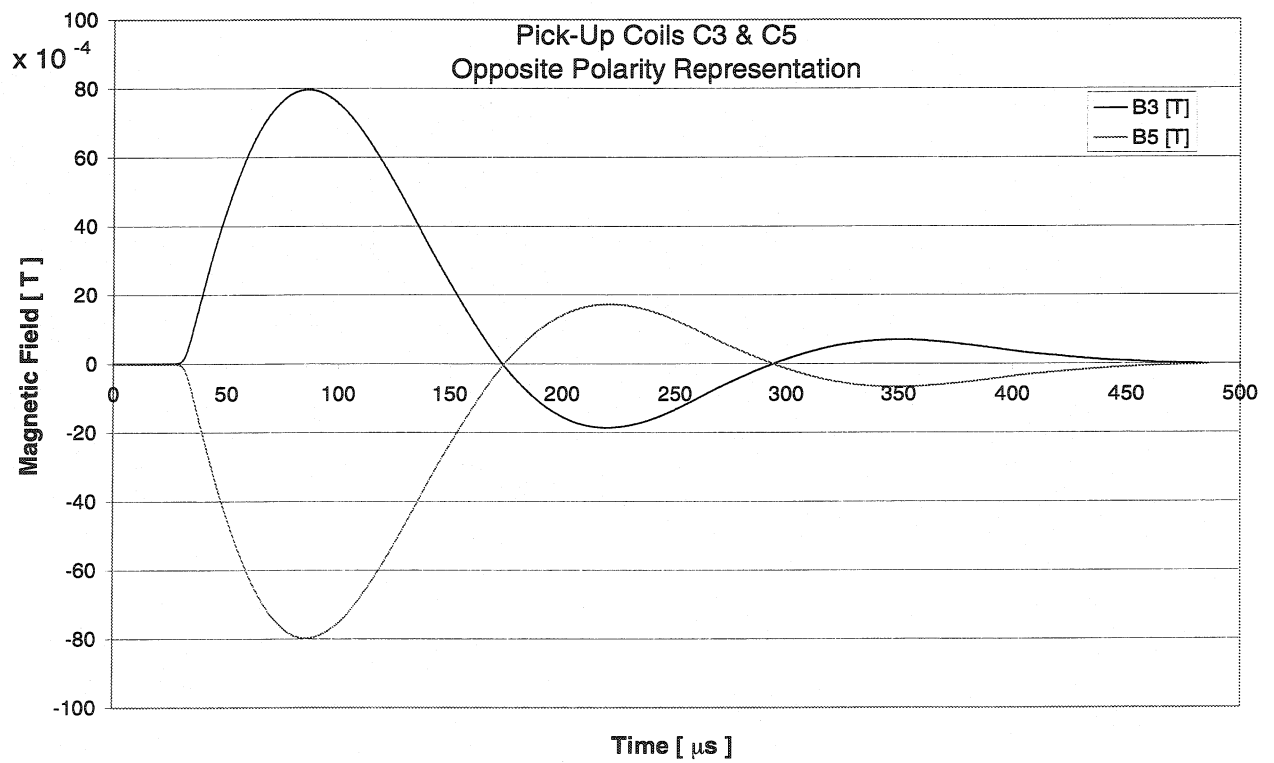


Figure 3.29 Time evolution of the magnetic field induction on pick-up coils C3 and C5. In reality both curves have negative polarity.

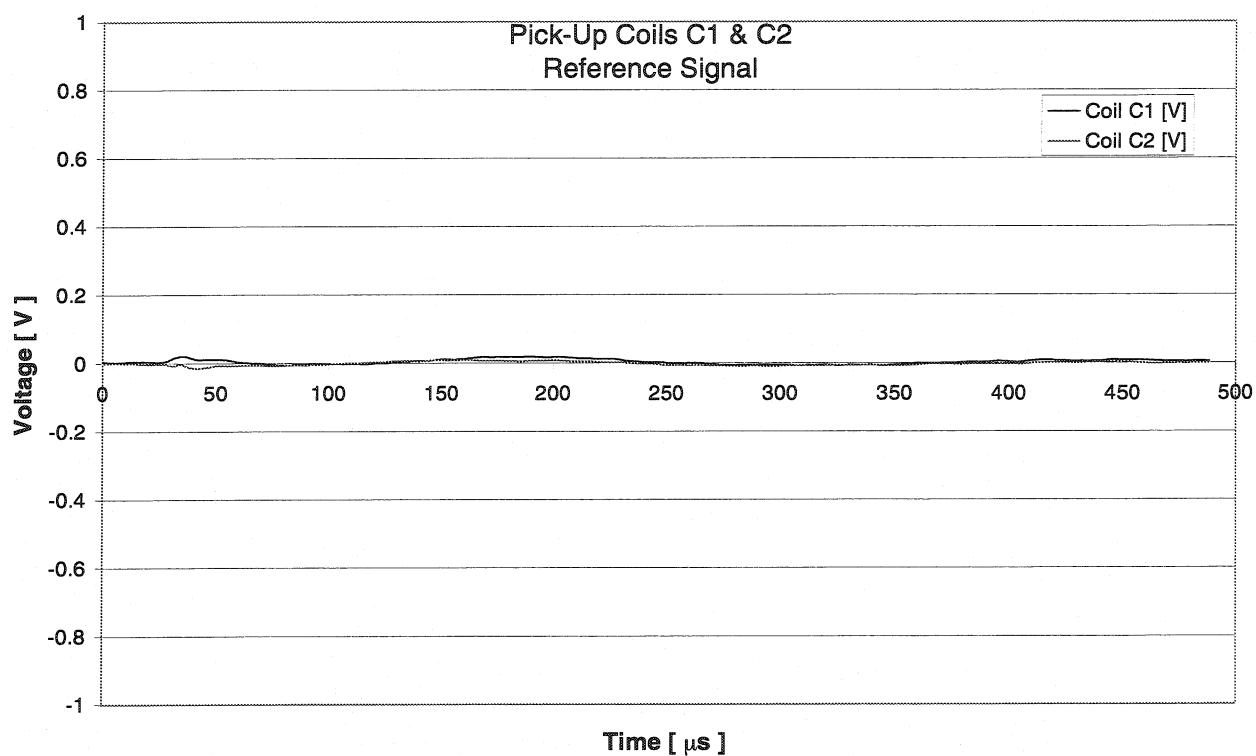


Figure 3.30 Voltages induced on the pick-up coils C1 and C2.

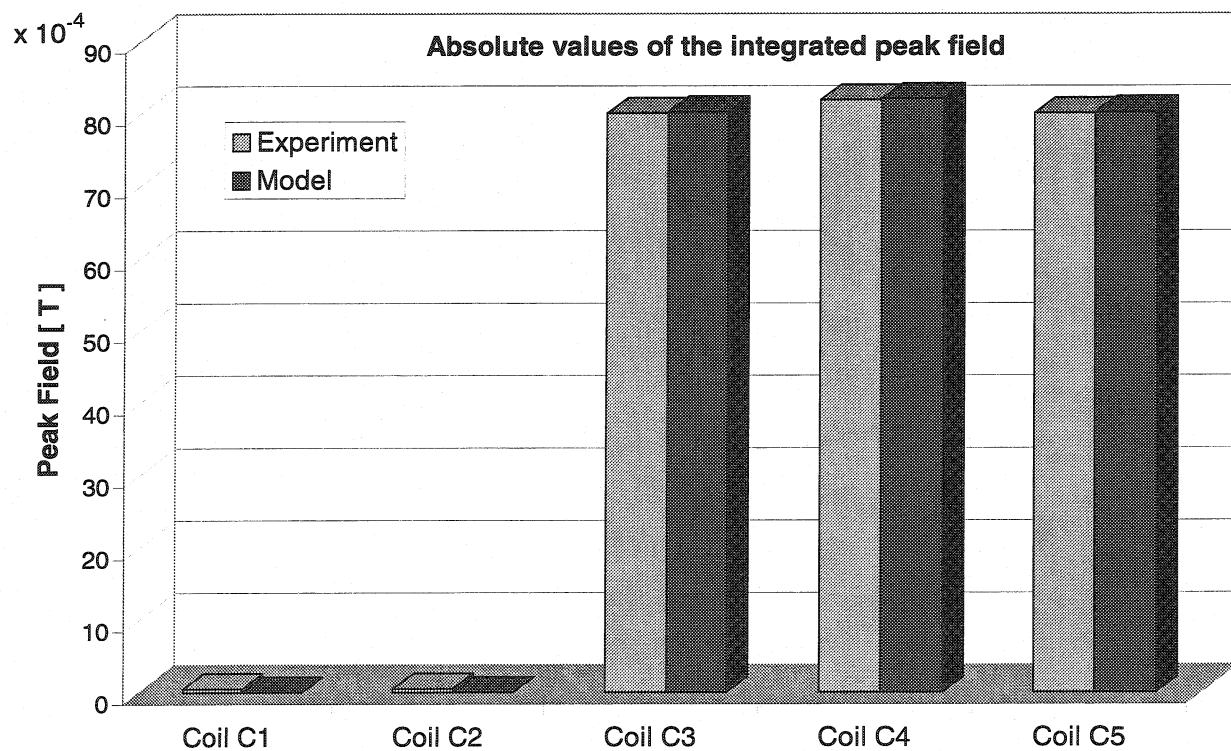


Figure 3.31 Pick-up coil indications in the flawless magnet

3.12.2 Activation of the Inter-Turn Short-circuits and Analysis of the Damaged Magnet

As an example of the analysis of the magnet with an active inter-turn short circuit, typical results of the measurements are given below for the short-circuit engaged in position denoted as A (see Fig. 3.6). Under the fault conditions skew multipoles of remarkable magnitude are generated in the aperture of the magnet. High amplitudes of the voltages induced on the coils C1 and C2 reflect the presence of the insulation failure. Let us recall that in the flawless magnet the residual signal picked-up by both coils was close to nothing (Fig. 3.30). The radical change of situation under the fault conditions occurs because of the redirection and redistribution of the source current in the electrically intact part of the coil, and also due to

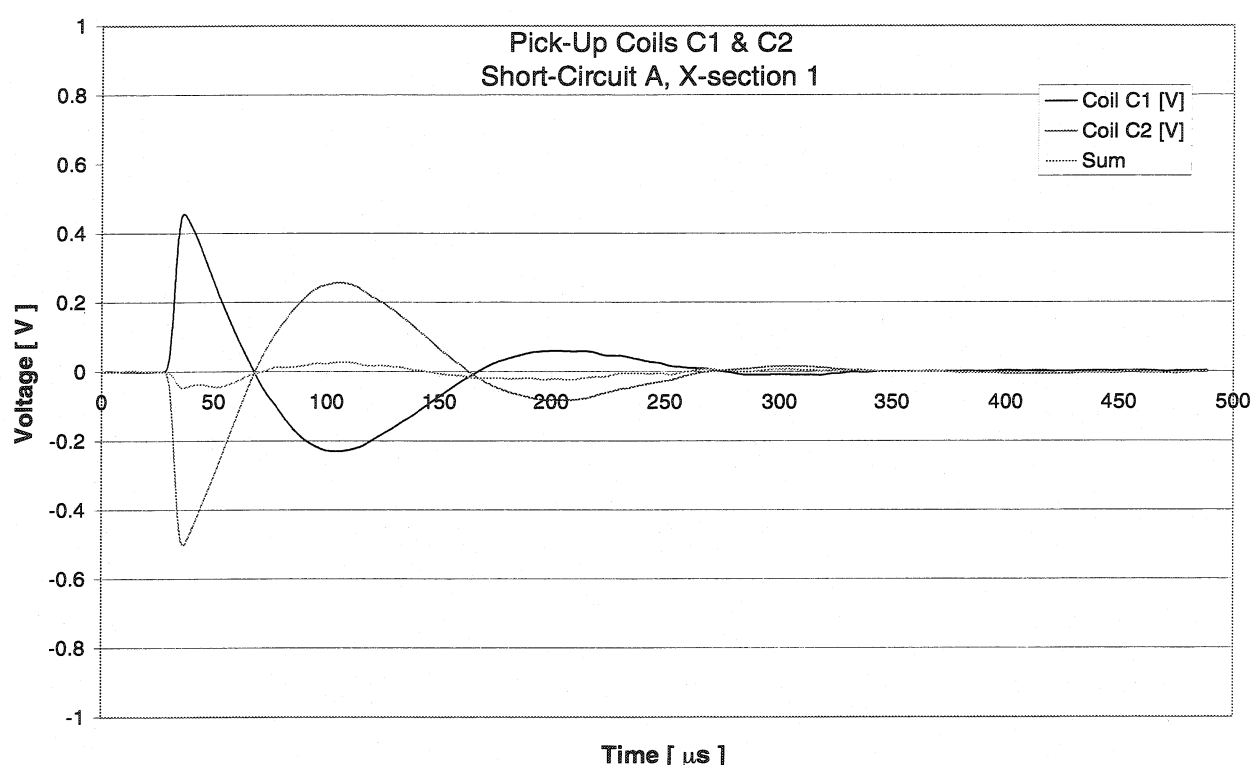


Figure 3.32 Voltages induced on pick-up coils C1 and C2 in the area preceding the point of short-circuit

the transient short-circuit current induced in the passive winding loop deprived of the initially imposed transport current. The model predictions for the analyzed position of the inter-turn short circuit indicate that the transient current in the passive winding reaches the maximum peak value of 510 A.

As expected, the signals on the coils C1 and C2 as well as on the coils C3 and C5 are unbalanced in the region preceding the point of fault (cross-section No. 1). One observes a measurable difference between the voltage induction indicated by the coils C3 and C5 (Fig. 3.32), as well as the measurable sum of the signals induced on the coils C1, C2 (Fig. 3.33).

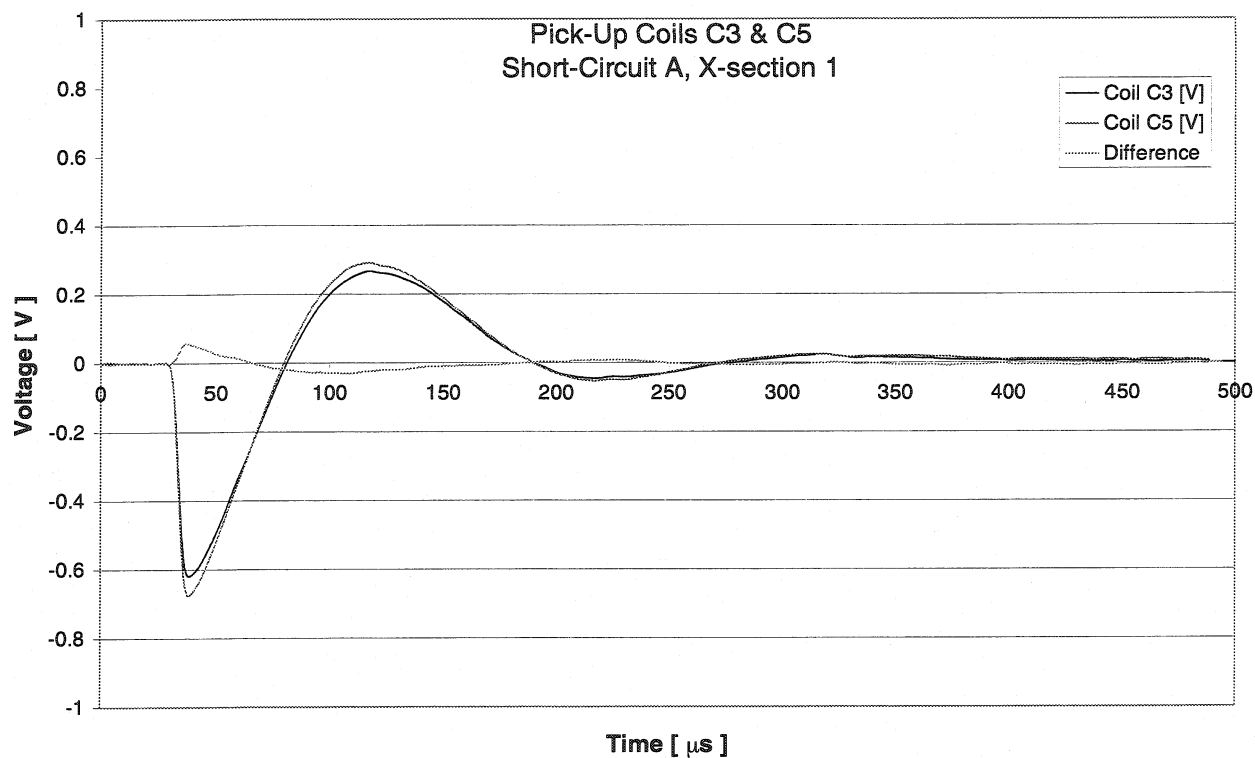


Figure 3.33 Voltages induced on pick-up coils C3 and C5 in the area preceding the point of short-circuit. The third curve shows the difference C3-C5.

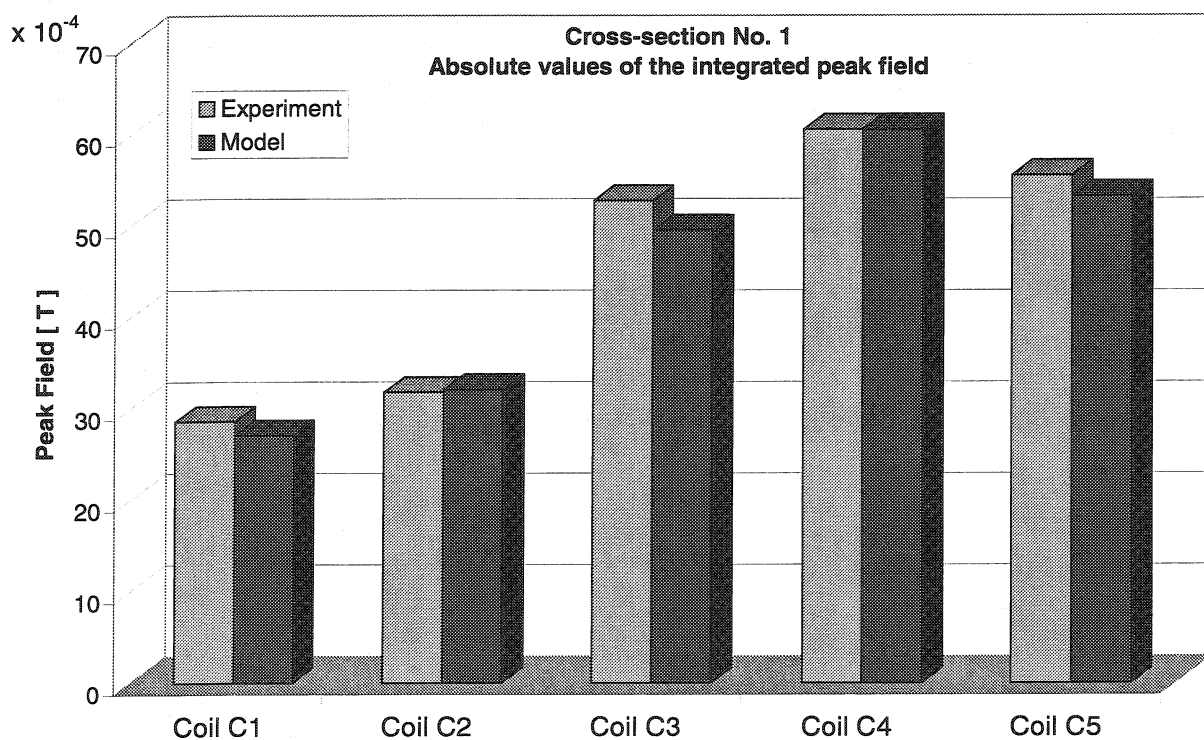


Figure 3.34 Test results for short-circuit A in the area preceding the position of the insulation failure. In reality the signals picked-up by the coils C1 and C2 are of opposite polarity.

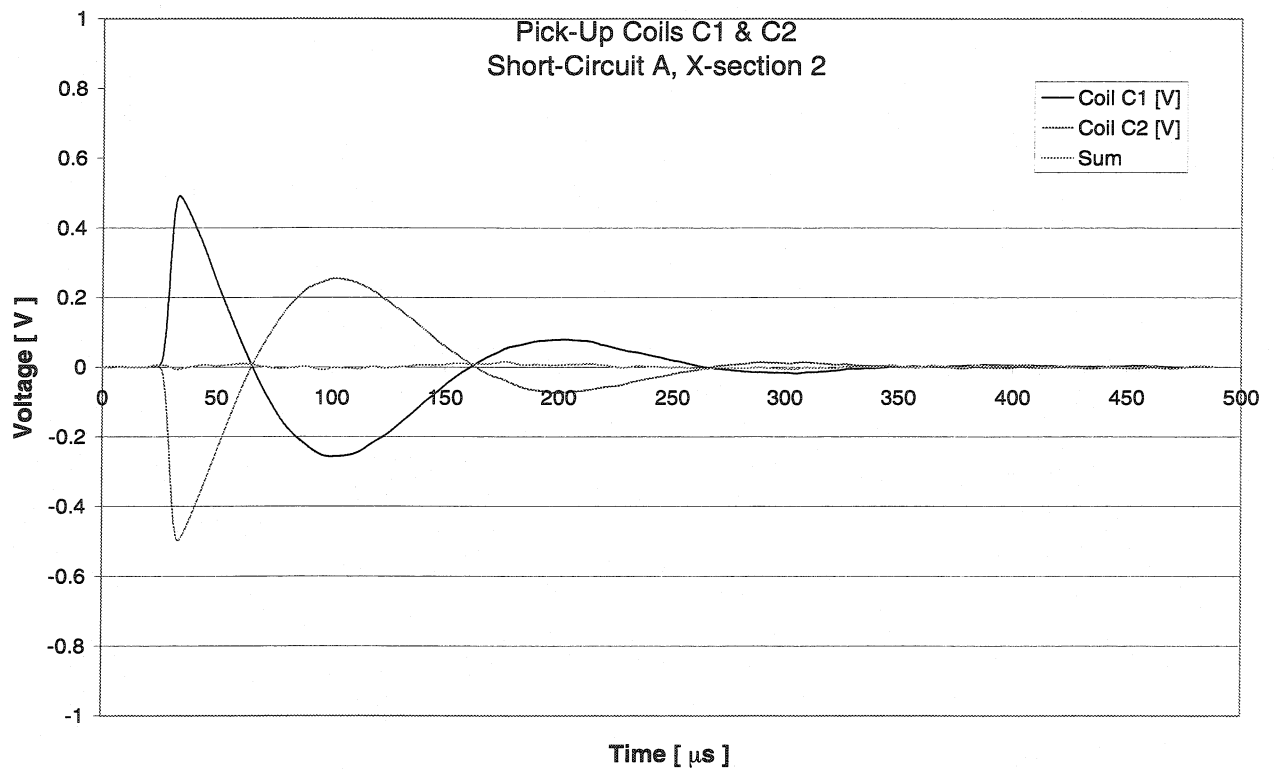


Figure 3.35 Voltages induced on pick-up coils C1 and C2 in the area behind the point of fault

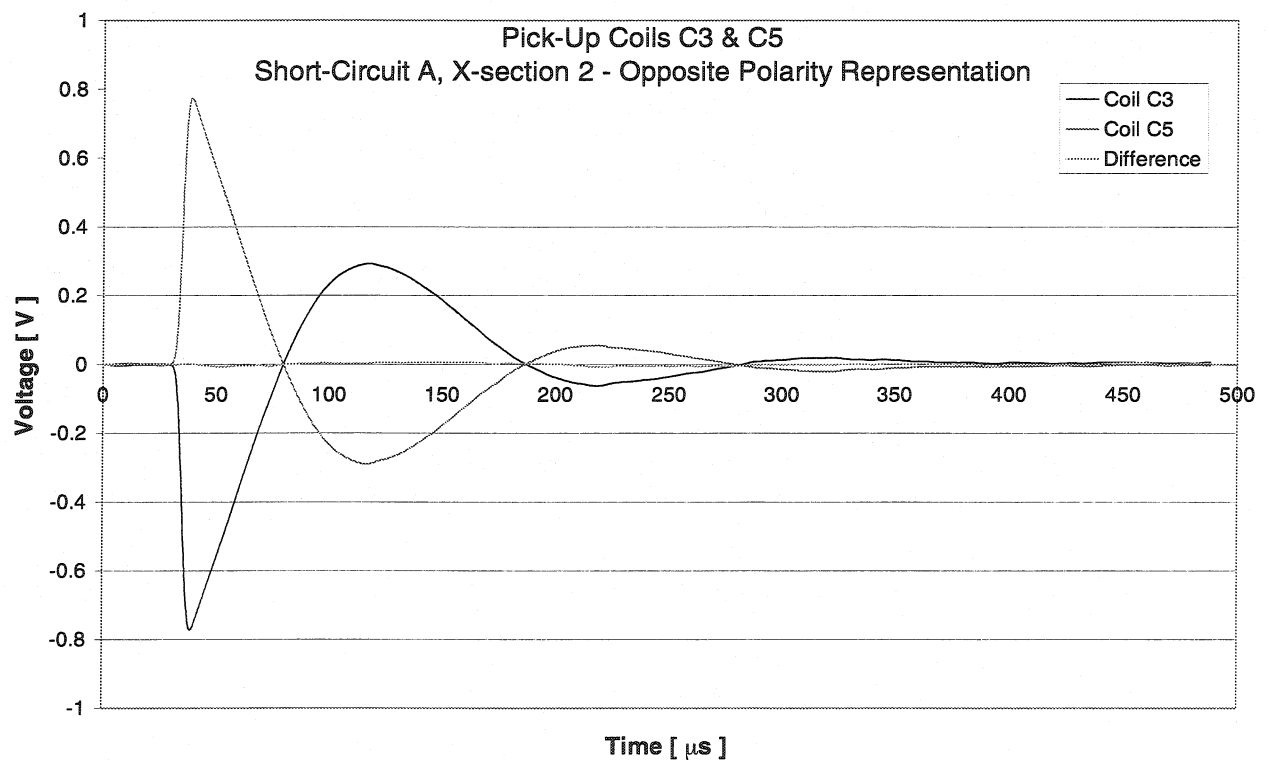


Figure 3.36 Voltages induced on pick-up coils C3 and C5 in the area behind the point of fault. In reality both waveforms are of the same negative polarity. The third curve shows the difference C3-C5 between the original signals.

The absolute values of the experimental integrated peak field are compared for all pick-up coils with the transient model results in Fig. 3.34. Further attenuation of the main dipole field registered by the coil C4 under fault conditions (see Fig. 3.31 for comparison) reflects the magnitude of the parasite magnetic field generated in the aperture due to the presence of the electrical failure.

As soon as the pick-up platform passes behind the point of fault and finds itself entirely in the region designated as cross-section No. 2, i.e. in the area where the current distribution becomes symmetric with respect to the vertical symmetry axis of the magnet, the differences in the voltage induction on the coils C1 and C2 (Fig. 3.35), as well as C3 and C5 disappear (Fig. 3.36). In this way the operator of the experiment knows that the pick-up probe has just passed by the point of electrical failure. The longitudinal location of the inter-turn short-circuit can be established in this way with the precision of a few millimeters. The absolute values of the peak field induction on all pick-up coils in cross-section No. 2 compared with the transient model results are shown on the diagram in Fig. 3.37.

The amplitude of the signal picked up by the coils C1 and C2 is directly linked to the magnitude of the parasite magnetic field generated in the magnet. According to the analysis of the FEM model, high values of the skew multipoles appearing in the magnetic field pattern under fault conditions are mostly due to the transient current induced in the passive winding

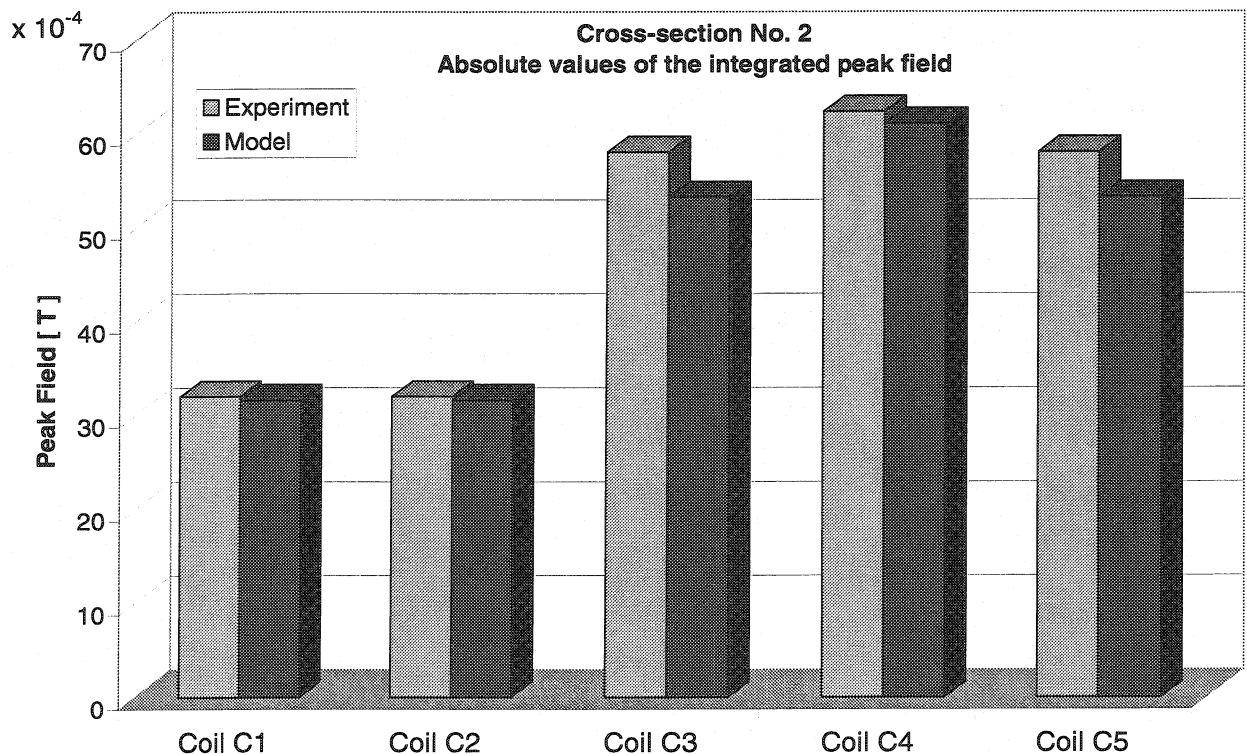


Figure 3.37 Test results for short-circuit A in the area behind the position of the insulation failure

of the coil. Since the surface of the passive winding changes with the azimuthal position of the insulation failure the amplitude of the signal picked up by the coils C1 and C2 must be indeed very sensitive to the azimuthal position of the inter-turn short-circuit. However the effect cannot be linear because with the change of the azimuthal position the passive winding is traversed by a different initial magnetic flux generated by the magnet. The peak value of the transient current intensity induced in the passive winding will depend on this initial flux crossing the dead loop of the winding as well as on the surface of the winding itself. Depending on these two factors imposed by the azimuthal position of the defect different magnitudes of parasite multipoles will be generated, and they will have different net effect influencing the total magnetic field experienced by the pick-up probe on the median plane of the magnet. The experiment confirms the predictions of the transient model also in this matter.

Fig. 3.38 shows the peak field indications of the pick-up coil C1 in cross-section No. 2 as a function of the azimuthal position of the inter-turn short-circuit. An essential difference in the coil indication is visible even for the two neighboring inter-turn short circuits denoted as B1 and B2 (see Fig. 3.22) between the two consecutive cable turns. In general case, the higher the signal on one of the skew pick-up coils is (C1 or C2), the smaller is the magnitude of the dipole field registered by the coil C4, and the closer to the median

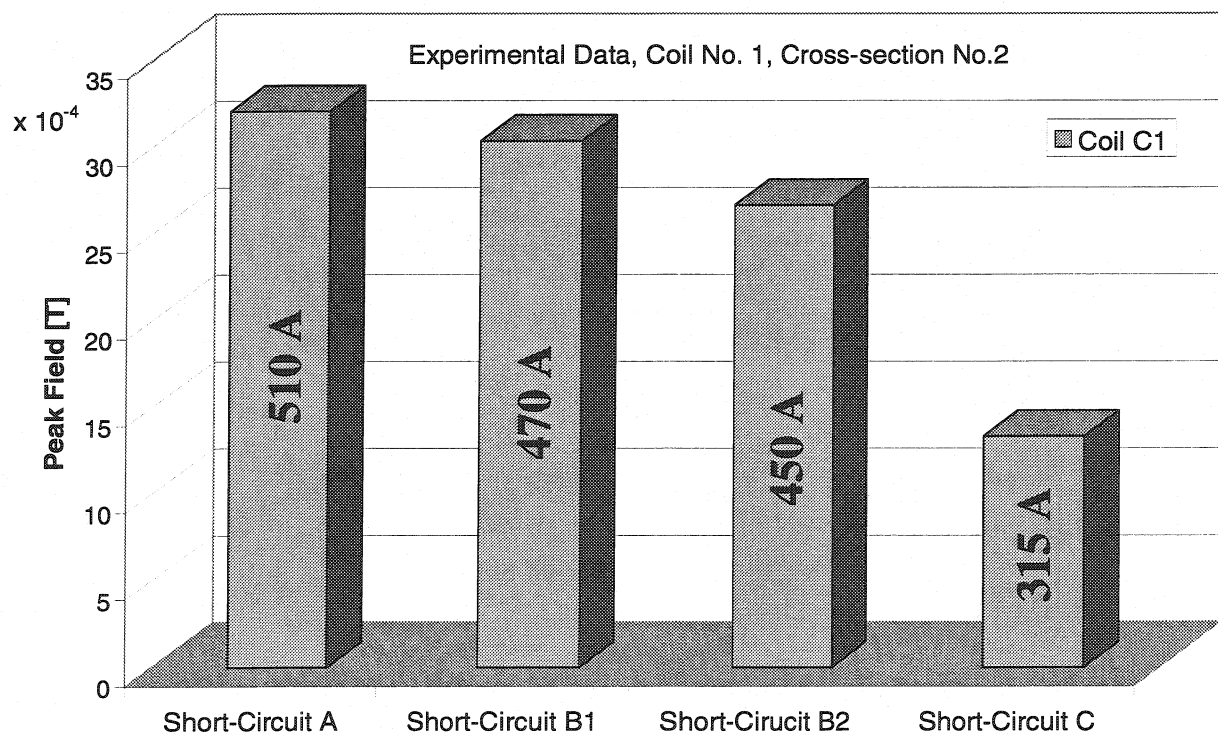


Figure 3.38 Indications of the coil C1 as a function of the azimuthal position of the short-circuit

plane can the defect be found. The figures indicated on the diagram bars correspond to the peak current induced in the passive winding calculated from the model.

The longitudinal position of the inter-turn short-circuits was successfully established for all of the micro-relays installed in the magnet using the same procedure. The effects predicted for the static case, e.g. the reversal of the sign of the induced skew multipoles for the inter-turn short circuits located in the coils below the median plane of the magnet with respect to the defects triggered in the coils above the median plane, were verified experimentally. The longitudinal displacement of both clusters of micro-relays allowed to verify that the insulation failures with the same azimuthal position affected the same passive winding deprived of the initially imposed transport current. Thus the inter-turn short circuit located at a specific azimuthal position in the conductor block generated the same magnetic field distortions in the corresponding regions before and behind the point of fault independently of its longitudinal position. The study of the signals induced on the pick-up coils, and especially the analysis of the skew field, gave also the indication of the azimuthal position of the defects.

The integration of the acquired signals is necessary for the comparison with the transient model simulations. As far as the detection method is concerned the integration is used only for convenience. The original voltage induction signal boosted with the properly applied FIR filter is entirely sufficient for the successful application of the method.

3.12.3 Probe Misalignment Analysis

The results of the misalignment analysis are presented for the short-circuit in position A located above the median plane of the magnet (Figs. 3.39 and 3.40) for both cross-sections (Tables 3.10 and 3.11). The peak field on each coil is given in Gauss ($1 \text{ Gauss} = 10^{-4} \text{ T}$). The misalignment cases include horizontal and vertical displacements of the entire pick-up probe by $\pm 1 \text{ mm}$ and the angular rotation by $\pm 2 \text{ degrees}$.

Table 3.10 Misalignment analysis in cross-section No. 1

X-section 1	C1	C2	C3	C4	C5	C1+C2	C3-C5
dx=0, dy=0	27.1	-32.1	-49.5	-60.5	-53.2	-5	3.7
dx=0, dy = +1mm	24.6	-30.9	-47.6	-59.7	-51.2	-6.3	3.6
dx=0, dy = -1mm	29.0	-32.9	-51.5	-61.4	-55.3	-3.9	3.8
dx =+1mm, dy = 0	23.7	-36.0	-51.0	-60.5	-52.3	-12.3	1.3
dx = -1mm, dy = 0	31.1	-28.7	-48.0	-60.4	-54.2	2.4	6.2
Phi = 2 deg.	27.0	-32.7	-51.1	-60.4	-51.5	-5.7	0.4
Phi = -2 deg.	26.7	-31.0	-48.0	-60.5	-54.9	-4.3	6.9
Experiment	28.6	-31.8	-52.7	-60.5	-55.5	-3.2	2.8

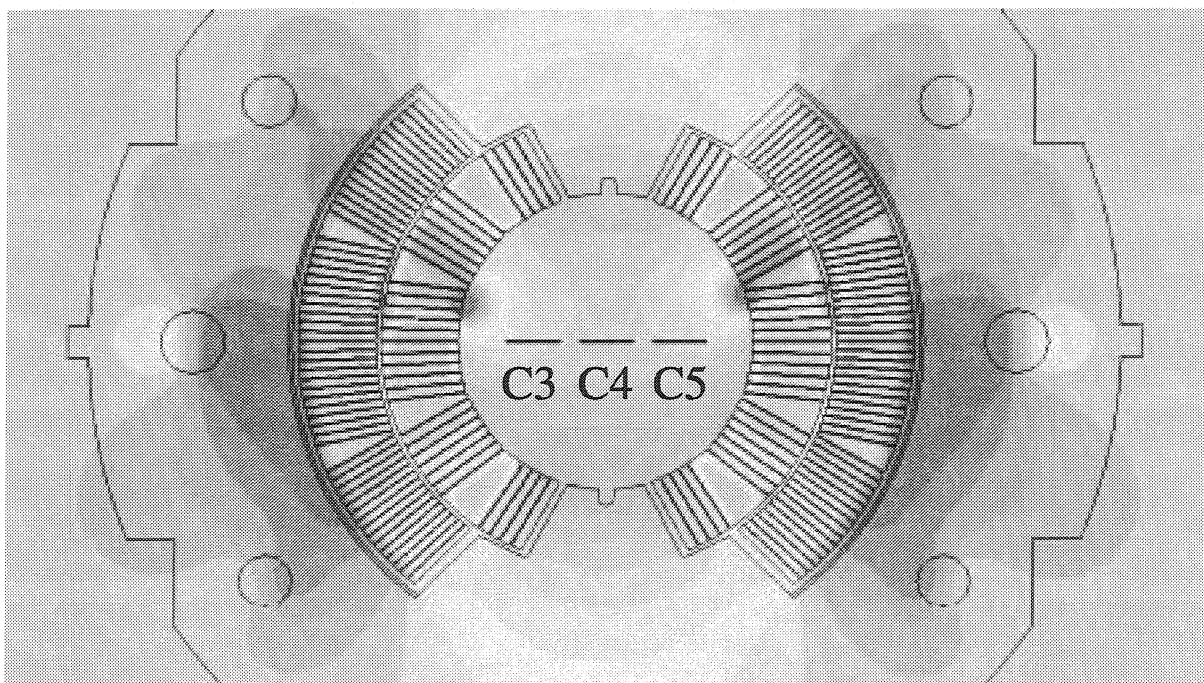


Figure 3.39 Cross-section No. 1, inter-turn short-circuit A: position of the normal pick-up coils on the background of the B_y component of the magnetic field

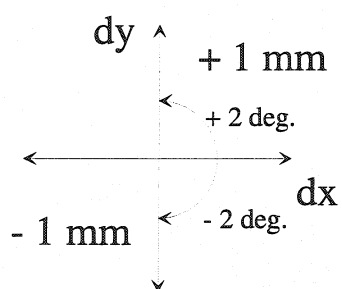


Figure 3.40 Cross-section No. 1, short-circuit A: position of the skew pick-up coils on the background of the B_x component of the magnetic field

Table 3.11 Misalignment analysis in cross-section No. 2

X-section 2	C1	C2	C3	C4	C5	C1+C2	C3-C5
dx=0, dy=0	31.6	-31.6	-53.2	-61.0	-53.2	0	0
dx=0, dy = +1mm	30.3	-30.3	-51.2	-60.2	-51.2	0	0
dx=0, dy = -1mm	32.3	-32.3	-55.3	-62.0	-55.3	0	0
dx =+1mm, dy = 0	28.1	-35.4	-54.2	-61.0	-52.3	-7.3	-1.9
dx = -1mm, dy = 0	35.4	-28.1	-52.3	-61.0	-54.2	7.3	1.9
Phi = 2 deg.	30.5	-32.2	-54.9	-61.0	-51.5	-1.7	-3.4
Phi = -2 deg.	32.2	-30.5	-51.5	-61.0	-54.9	1.7	3.4
Experiment	32.0	-32.0	-58.0	-62.3	-58.0	0	0

Vertical displacements do not affect the results of the detection. By comparison of the experimental results with the misalignment analysis it turns out immediately that during the measurements presented in the previous section apparently the pick-up probe was not ideally aligned on the median plane, but found itself slightly vertically displaced below the actual horizontal symmetry axis of the magnet.

On the other hand horizontal misalignment of the pick-up probe as well as an angular error of the rotational type can be disastrous. The character of the original effect used by the detection method is seriously distorted. Nevertheless the discontinuity of the even-order normal field harmonics and of the odd-order skew multipoles is still reflected by the pick-up coils while the probe passes the point of electrical fault, providing that the same misalignment error is maintained during the experiment.

For example, let us have a closer look at the angular misalignment of the pick-up platform by +2 degrees. All of the pick-up coils experience in this case a mixture of magnetic flux resulting from both skew and normal multipoles. In cross-section No. 1 the sum of signals on the pick-up coils C1 and C2 gives an easily detectable value of -5.7 Gauss, whereas the small difference between the signals induced on coils C3 and C5 (0.4 Gauss) would suggest that the probe is already in the cross-section No. 2, which is of course not the case yet.

As soon as the probe actually reaches cross-section No. 2 the sum of the peak field induction on coils C1 and C2 jumps to -1.7 Gauss, whereas the difference between the coils C3 and C5 changes from close to zero in cross-section No. 1 to remarkable value of -3.4 Gauss. Thus the discontinuity of the magnetic field is still detected while passing the point of the electrical defect, assuming that the same rotational error of 2 degrees is kept during the entire measurement.

Nevertheless to avoid any confusing situations certain precautions were taken into account while preparing the prototype of the detection system for the 15-m long LHC dipole

magnets. The pick-up probe is embedded in the middle of the cylindrical support. The cylinder fits exactly into the beam-pipe of the magnet. It slides on three points; two fixed, and one acting as a suspension canceling the small ovalization errors of the beam pipe. In this way the pick-up platform is always in the middle of the aperture no matter how it is rotated. To control the rotation and provide an ideal horizontal position of the pick-up platform in the aperture an electrolytic tilt resistor is mounted behind the support cylinder. Whenever the pick-up probe is not aligned on the median plane of the magnet the tilt resistor transmits an electrical signal proportional to the angular error to the operator outside the magnet. The signal is processed by a special signal conditioner and the horizontal alignment of the probe is corrected. The system will be introduced as a diagnostic tool to the serial production of the LHC magnets at the beginning of the year 2000.

The detection method described in this chapter was presented on the 16th International Conference on Magnet Technology, which took place at the end of September in Ponte Vedra Beach in USA. The résumé of the entire concept was accepted for publication in the IEEE Transactions on Applied Superconductivity, and will appear in print early in the year 2000 [13].

Appendix A. High Voltage Discharge Measurements; Test Procedures and Analysis of the Results

The high voltage discharge test allows to detect the presence of the possible perforation in the insulating material, but the precise localization of the problem remains beyond the scope of the method. The experimental part of the work described in this thesis has begun with the implementation of this test method for the general diagnosis of the LHC dipole magnets. A measurement system capable of simultaneous recording of the voltage and current response of the coil during the discharge has been designed, set up and tested.

A.1 Description of the Experimental Set-Up

The layout of the experimental set-up illustrating the principle of the test is presented in Fig. A.1. A pulsed current is supplied from a high voltage discharge generator (max. charging voltage of 6 kV) by releasing the energy accumulated in a $1\ \mu\text{F}$ capacitor into the coil of the magnet. Apart from the generator, shown in the top part of Fig. A.1, the system contains a high voltage divider present on the schematics as two parallel pairs of resistors and

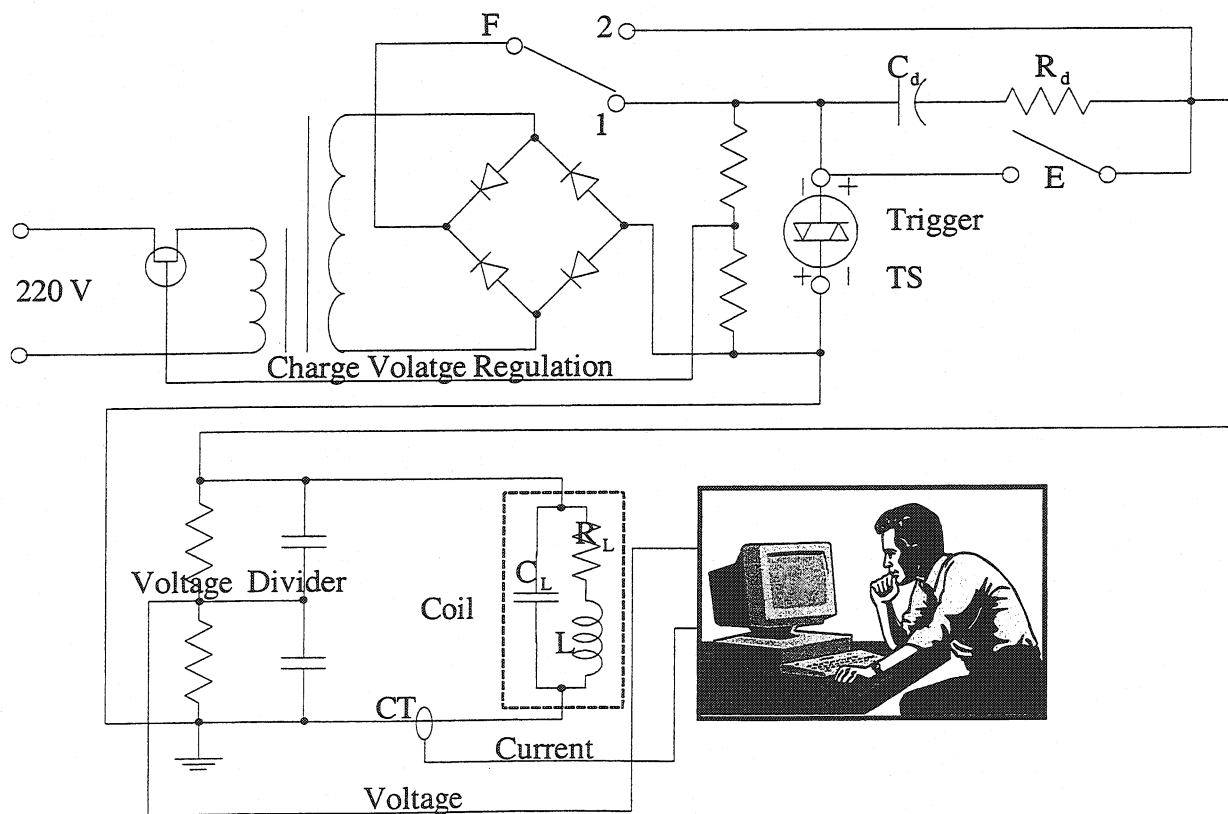


Figure A.1 Schematic layout of the HV discharge test

capacitors, and a desktop PC controller console with a PC-scope card installed inside. The coil under test is represented by three lumped parameters: its self-inductance L , its effective resistance R_L , and its total capacitance to ground C_L . The test is carried out at room temperature. When the system is triggered, the energy accumulated in the capacitor C_d , charged at the testing voltage, is released through the resistance R_d into the coil under test via the thyristor TS. The current transformer ring CT mounted directly around one of the input terminals gives an output response of 0.5 V per 1 A of the current flowing in the coil. Two individual input channels of the scope card installed in the PC control unit simultaneously read the signals from the voltage divider and from the current monitor. After the test the remaining charge of the capacitor C_d is neutralized by means of the switch E.

In order to provide an efficient and convenient management of the data acquisition as well as to control the oscilloscope card and to take advantage of its advanced features the software called Electrical Discharge Measurements Application (EDMA) [2] has been developed in the LabVIEW programming environment. EDMA combines the control of the data flow with the analysis of the general condition of the superconducting coils for the LHC dipole magnets. Acquired data are analyzed on-line in terms of pseudo period of the oscillations, inductance and effective resistance of the coils, and then compared with the oscillation curves corresponding to the flawless reference magnet. The program communicates with the high voltage pulse generator via an opto-coupled RS-232 interface. The application has been designed to conform to the maximum safety requirements;

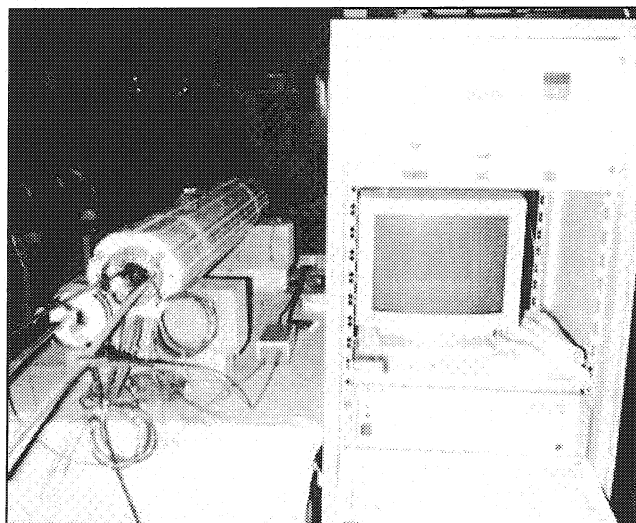


Figure A.2 Experimental set-up

missing connections, manual interventions of the user are immediately detected and acknowledged on the screen. The set-up provides all the necessary real time information to perform a preliminary diagnosis of the inter-turn cable insulation integrity. A photograph of the complete experimental set-up is shown in Fig. A.2. The screenshots of the EDMA application are presented in Fig. A.3. The entire test system has been assembled in several units and shipped to the external companies in order to carry out the impulse tests for the series production of the LHC dipole magnets. Currently it is being used at Noell in Germany, Jeumont in France and Ansaldo in Italy.

A.2 Discharge Circuit Modeling

The objective of the discharge circuit modeling is to find a set of parameters which would allow to characterize the experimental data acquired during the discharge test in view to distinguish between the flawless reference magnet and the damaged magnet affected by an inter-turn short-circuit. Since the test results are the damped current and voltage oscillations it seems natural to classify the test object in terms of the oscillation frequency and the damping factor of the current/voltage decay. In order to do this the coil of the magnet is represented in a simplified way by a set of lumped parameters describing its self-inductance L , effective resistance R and the total capacitance to ground C_1 (Fig. A.4). The energy stored in the capacitor C_0 charged with the testing voltage V_0 is released into the coil under test via the resistance R_0 . This transient situation corresponds exactly to the experimental set-up discussed in the previous section. Thus before the discharge is triggered or the switch in Fig. A.4 closed the initial voltage on the discharge capacitor equals V_0 . There are no initial currents flowing in the coil, and the initial voltage across the capacitor representing the total capacitance of the coil to the ground is assumed to be zero.

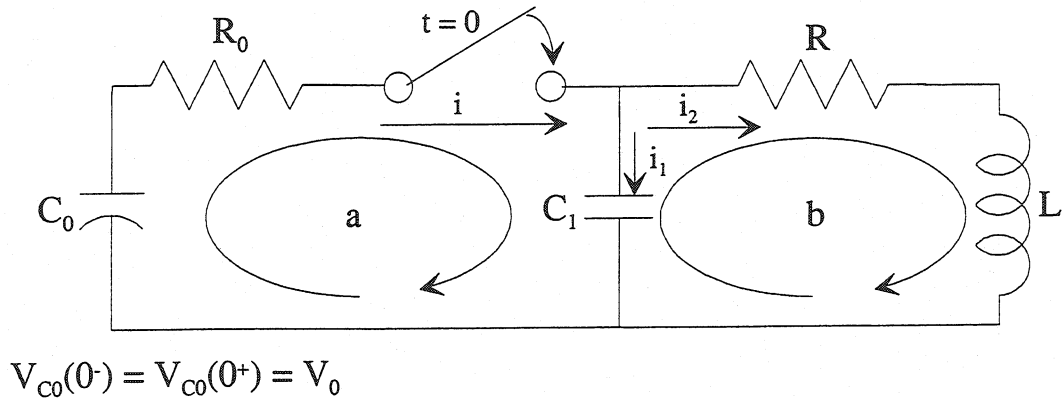


Figure A.4 Lumped discharge circuit

The circuit equations are as follows:

$$\left\{ \begin{array}{l} V_0 - \frac{1}{C_0} \int_0^t i \, dt - iR_0 - \frac{1}{C_1} \int_0^t i_1 \, dt = 0 \\ \frac{1}{C_1} \int_0^t i_1 \, dt - i_2 R - L \frac{di_2}{dt} = 0 \\ i = i_1 + i_2 \end{array} \right. \quad (A.1)$$

From the second equation in the system (A.1) it follows that:

$$i_1(t) = RC_1 \frac{di_2}{dt} + LC_1 \frac{d^2 i_2}{dt^2} \quad (A.2)$$

The first equation in the system (A.1) can be rewritten as:

$$V_0 - \frac{C_0 + C_1}{C_0 C_1} \int_0^t i_1 dt - \frac{1}{C_0} \int_0^t i_2 dt - i_1 R_0 - i_2 R_0 = 0 \quad (\text{A.3})$$

After substitution of the formula (A.2) and differentiation of Eq. (A.3) with respect to time, the following linear differential equation of the third order is obtained:

$$R_0 L C_1 \frac{d^3 i_2}{dt^3} + \left(\frac{C_0 + C_1}{C_0} L + R_0 R C_1 \right) \frac{d^2 i_2}{dt^2} + \left(R_0 + \frac{C_0 + C_1}{C_0} R \right) \frac{d i_2}{dt} + \frac{i_2}{C_0} = 0 \quad (\text{A.4})$$

Its characteristic equation has the form

$$s^3 + a s^2 + b s + c = 0 \quad (\text{A.5})$$

where

$$\begin{aligned} a &= \frac{C_0 + C_1}{R_0 C_0 C_1} + \frac{R}{L} \\ b &= \frac{1}{L C_1} + \frac{C_0 + C_1}{R_0 L C_0 C_1} R \\ c &= \frac{1}{R_0 L C_0 C_1} \end{aligned} \quad (\text{A.6})$$

Eq. (A.5) is a third order polynomial equation. All of the coefficients are positive. In the oscillatory case considered it will always have one negative real root and two complex roots with negative real parts. This results from the stability considerations of the passive RLC circuit. Analyzing the general solution of the third order polynomial equation [14], it can be proven that the linear term can be factored out according to the following procedure.

We introduce two auxiliary variables q and r , as indicated by:

$$\begin{aligned} q &= \frac{a^2 - 3b}{9} = \frac{1}{9} a^2 - \frac{1}{3} b \\ r &= \frac{2a^3 - 9ab + 27c}{54} = \frac{1}{27} a^3 - \frac{1}{6} ab + \frac{1}{2} c \end{aligned} \quad (\text{A.7})$$

If $r^2 < q^3$ the cubic equation has three real roots. It will never be the case for the RLC oscillatory passive circuit. Otherwise, if $r^2 \geq q^3$ two more auxiliary factors d and d' must be calculated according to the formulas:

$$\begin{aligned} d &= -\text{sgn}(r) \sqrt[3]{|r| + \sqrt{r^2 - q^3}} \\ d' &= \begin{cases} \frac{q}{d} & \text{if } d \neq 0 \\ 0 & \text{if } d = 0 \end{cases} \end{aligned} \quad (\text{A.8})$$

The real root (s_0) of the cubic equation equals then:

$$s_0 = (d + d') - \frac{a}{3} \quad (\text{A.9})$$

Now the characteristic equation (A.5) can be factored in the following manner:

$$\begin{aligned} (s - s_0)(s^2 + Es + F) &= 0 \\ s^3 + (E - s_0)s^2 + (F - s_0E)s - s_0F &= 0 \end{aligned} \quad (\text{A.10})$$

where

$$\begin{aligned} E &= a + s_0 \\ F &= b + Es_0 = b + as_0 + s_0^2 = -\frac{c}{s_0} \end{aligned} \quad (\text{A.11})$$

After having determined the coefficients of the quadratic equation in (A.10) the remaining roots can be found. They are

$$\begin{aligned} s_1 &= \frac{-E - i\sqrt{\delta}}{2} \\ s_2 &= \frac{-E + i\sqrt{\delta}}{2} \end{aligned} \quad (\text{A.12})$$

where $\delta = 4F - E^2$ is always greater than zero in the transient oscillatory problem considered. For notational convenience two auxiliary coefficients are introduced

$$\begin{aligned} \beta &= \frac{E}{2} \\ \gamma &= \frac{\sqrt{\delta}}{2} \end{aligned} \quad (\text{A.13})$$

With the use of these coefficients the roots s_1 and s_2 become

$$\begin{aligned} s_1 &= -\beta - i\gamma \\ s_2 &= -\beta + i\gamma \end{aligned} \quad (\text{A.14})$$

and the general form of the solution of Eq. (A.4) is

$$i_2(t) = Ae^{s_0 t} + C'e^{s_1 t} + D'e^{s_2 t}$$

As it was pointed out before, the root s_0 is always negative. Let us introduce a new coefficient $\alpha = |s_0|$. Then

$$i_2(t) = Ae^{-\alpha t} + C'e^{(-\beta - i\gamma)t} + D'e^{(-\beta + i\gamma)t} = Ae^{-\alpha t} + e^{-\beta t}(C \cos(\gamma t) + D \sin(\gamma t)) \quad (\text{A.15})$$

One can see that if the roots of the cubic equation (A.5) had positive real parts, the exponential factor in the solution (A.15) would increase with time without bound. This would mean that the analyzed system is unstable. The response of such a system always tends to

infinity no matter what excitation input is applied. Any passive RLC circuit could never behave in this way. Our particular RLC circuit is excited only with one initial voltage on the discharge capacitor. The oscillations are always present during the discharge. During each cycle of the oscillations the energy is exchanged between the capacitors and the inductor but dissipated in the resistances. Hence, the oscillations will be gradually damped down until the system reaches its condition of rest. This implies that all the roots of the characteristic equation (A.5) must be found in the left ($\text{Re}(s) < 0$) complex half-plane.

According to the initial conditions of the circuit the commutation rule for the inductor states that $i_2(0^-) = i_2(0^+) = 0$. Hence

$$A + C = 0 \quad (\text{A.16})$$

The commutation rules for the capacitor representing the total capacitance of the coil to ground impose that $V_{C1}(0^-) = V_{C1}(0^+) = 0$. The change of voltage on the capacitor C_1 is described by the second equation in the system (A.1) of the circuit equations. Hence

$$(A + C)R + (D\gamma - C\beta - A\alpha)L = 0$$

Taking (A.16) into account the condition is simplified to:

$$D\gamma - C\beta - A\alpha = 0 \quad (\text{A.17})$$

The third relation binding the constants in the solution (A.15) is obtained from the commutation rules for the discharge capacitor $V_{C0}(0^-) = V_{C0}(0^+) = V_0$. This condition is:

$$\frac{(A + C)RC_1 + (D\gamma - C\beta - A\alpha)LC_1}{C_0} - \frac{2}{C_0} \left(\frac{D\gamma}{\beta^2 + \gamma^2} + \frac{C\beta}{\beta^2 + \gamma^2} + \frac{A}{\alpha} \right) = V_0$$

Taking into account two previous conditions it is simplified to:

$$\frac{D\gamma}{\beta^2 + \gamma^2} + \frac{C\beta}{\beta^2 + \gamma^2} + \frac{A}{\alpha} = -\frac{V_0 C}{2} \quad (\text{A.18})$$

From the set of three equations (A.16), (A.17) and (A.18) the constants A, C, and D can be calculated

$$\begin{bmatrix} A \\ C \\ D \end{bmatrix} = \begin{bmatrix} -\frac{1}{2}V_0C_0\alpha \frac{\beta^2 + \gamma^2}{(\alpha - \beta)^2 + \gamma^2} \\ \frac{1}{2}V_0C_0\alpha \frac{\beta^2 + \gamma^2}{(\alpha - \beta)^2 + \gamma^2} \\ \frac{\beta - \alpha}{2\gamma}V_0C_0\alpha \frac{\beta^2 + \gamma^2}{(\alpha - \beta)^2 + \gamma^2} \end{bmatrix} \quad (\text{A.19})$$

The resistance $R_0 = 100 \text{ m}\Omega$ of the discharge generator introduces but a small correction to the model. If this resistance is neglected the model will still reflect the oscillatory character of the voltage/current decay in the coil, at the same time it will be essentially simplified. In order to introduce this simplification it would be enough to substitute $R_0 = 0$ in the Eq. (A.4). However the final result can be obtained even faster if the Laplace transform is used.

By substituting $R_0 = 0$ the following equation can be obtained from the equation system (A.1)

$$V_0 \frac{C_0}{C_0 + C_1} - \frac{1}{C_0 + C_1} \int_0^t i_2 dt - i_2 R - L \frac{di_2}{dt} = 0 \quad (\text{A.20})$$

Denoting $V_i = \frac{V_0 C_0}{C_0 + C_1}$ and $C = C_0 + C_1$ Eq. (A.20) is transformed to the form corresponding to the equivalent circuit represented in Fig. A.5.

$$V_i - \frac{1}{C} \int_0^t i_2 dt - i_2 R - L \frac{di_2}{dt} = 0 \quad (\text{A.21})$$

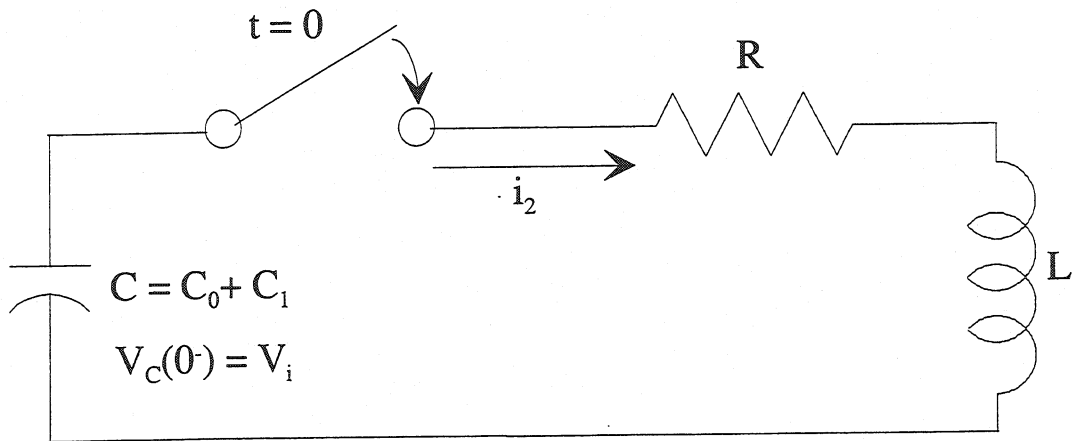


Figure A.5 Equivalent circuit described by Eq. (A.21)

In the Laplace transform domain the impedance of this circuit equals:

$$Z(s) = \frac{1}{Cs} + Ls + R = \frac{LCs^2 + RCs + 1}{Cs} \quad (\text{A.22})$$

And the transfer function is:

$$G(s) = \frac{1}{Z(s)} = \frac{Cs}{LCs^2 + RCs + 1} \quad (\text{A.23})$$

The current response is given by $I(s) = G(s)V(s)$ and hence

$$I(s) = \frac{V_i}{s} \frac{Cs}{LCs^2 + RCs + 1} = \frac{V_i C}{LCs^2 + RCs + 1} \quad (\text{A.24})$$

For convenience two auxiliary factors ω and ξ are introduced

$$\begin{aligned} \omega^2 &= \frac{1}{LC} \\ \xi\omega &= \frac{R}{2L} \Rightarrow \xi = \frac{R}{2} \sqrt{\frac{C}{L}} \end{aligned} \quad (\text{A.25})$$

Taking them into account, the expression (A.24) takes form

$$\begin{aligned} I(s) &= \frac{V_i}{LC} \frac{C}{s^2 + \frac{R}{L}s + \frac{1}{LC}} = \frac{V_i}{L} \frac{1}{s^2 + 2\xi\omega s + \omega^2} = \\ &= \frac{V_i}{L} \frac{1}{(s + \omega\xi)^2 - (\omega\xi)^2 + \omega^2} = \frac{V_i}{L} \frac{1}{(s + \omega\xi)^2 + \omega^2(1 - \xi^2)} \end{aligned} \quad (\text{A.26})$$

The second order polynomial in the denominator of formula (A.26) can have 0, 1 or 2 real roots depending on the value of ξ . The oscillatory case equivalent to the situation of the HV discharge test corresponds to the case when both roots are complex, i.e. when $\xi < 1$. From the properties of the Laplace transform it is well known that:

$$\mathcal{L}^{-1}\left(\frac{1}{(s+a)^2 + k^2}\right) = e^{-at} \frac{\sin kt}{k}$$

Hence the inverse Laplace transform of formula (A.26) yields immediately:

$$\begin{aligned} i_2(t) &= \frac{V_i}{L} e^{-\omega\xi t} \frac{\sin(\omega t \sqrt{1 - \xi^2})}{\omega \sqrt{1 - \xi^2}} = \frac{V_i}{\sqrt{\frac{L}{C}} \sqrt{1 - \xi^2}} e^{-\omega\xi t} \sin(\omega t \sqrt{1 - \xi^2}) = \\ &= \frac{2V_i \xi}{R \sqrt{1 - \xi^2}} e^{-\omega\xi t} \sin(\omega t \sqrt{1 - \xi^2}) \end{aligned} \quad (\text{A.27})$$

From the first and the third equation in equation system (A.1) (for $R_0 = 0$) it follows that

$$\int_0^t i_1(t) dt = \frac{C_0 C_1}{C_0 + C_1} V_0 - \frac{C_1}{C_0 + C_1} \int_0^t i_2(t) dt \Rightarrow i_1(t) = -\frac{C_1}{C_0 + C_1} i_2(t) \quad (\text{A.28})$$

Thus the total current flowing through the coil of the magnet (represented by the ensemble of three parameters R, L and C_1 in Fig. A.4) is

$$i(t) = \frac{C_0}{C_0 + C_1} i_2(t) = \frac{2V_i^2 \xi}{R V_0 \sqrt{1 - \xi^2}} e^{-\omega\xi t} \sin(\omega t \sqrt{1 - \xi^2}) \quad (\text{A.29})$$

The voltage oscillation in the coil of the magnet is equivalent to the voltage change across the capacitor C_1 . Thus

$$\begin{aligned}
 V_{C1}(t) &= \frac{1}{C_1} \int_0^t i_1(t) dt = -\frac{1}{C} \int_0^t i_2(t) dt = \\
 &= \frac{1}{C\omega} \cdot \frac{2V_i\xi}{R\sqrt{1-\xi^2}} e^{-\omega\xi t} (\sqrt{1-\xi^2} \cos(\omega t \sqrt{1-\xi^2}) + \xi \sin(\omega t \sqrt{1-\xi^2})) - \frac{2V_i\xi}{C\omega R} = \\
 &= \frac{V_i}{\sqrt{1-\xi^2}} e^{-\omega\xi t} \cos(\omega t \sqrt{1-\xi^2} - \varphi) - V_i
 \end{aligned} \tag{A.30}$$

where $\cos \varphi = \sqrt{1-\xi^2}$ and $\sin \varphi = \xi$. The voltage oscillation in the experimental set-up is read from the capacitive voltage divider (see Fig. A.1). Moreover the scope card acquiring the data works in the AC coupling mode. Therefore in reality the DC offset present in formula (A.30) is canceled, which results in the voltage variation of the following form:

$$V(t) = \frac{V_0 C_0}{(C_0 + C_1) \sqrt{1-\xi^2}} e^{-\omega\xi t} \cos(\omega t \sqrt{1-\xi^2} - \varphi) \tag{A.31}$$

The auxiliary parameters introduced in (A.25) represent quantities with well-defined physical meaning. The term $\omega\sqrt{1-\xi^2}$ corresponds to the angular frequency of the oscillations, whereas the product of ω and ξ is the damping factor responsible for the decay of the voltage/current oscillations in the coil of the magnet. In other words $\omega\xi = \frac{1}{\tau}$ where τ is the time constant of the system. After the lapse of time characterized by τ the initial amplitude of the oscillations is damped e times, where e is the base of the natural logarithm. The pseudo-period of the oscillations equals

$$T = \frac{2\pi}{\omega\sqrt{1-\xi^2}} = \frac{2\pi\sqrt{L(C_0 + C_1)}}{\sqrt{1 - \frac{R^2(C_0 + C_1)}{4L}}} \tag{A.32}$$

A.3 Procedure Applied for the Analysis of the Experimental Data

The analysis of the experimental data is explained in Fig. A.6 on the example of the data set acquired during a discharge test performed on a single pole of a short dipole model before the assembly of the magnet. As a first step the extrema are found in the analyzed signal. Afterwards the maximum and the minimum envelope is fitted to the exponential model $f(t) = Ae^{Bt}$ where A and B are the parameters of the fit. The fitting is performed using the least square method after taking the natural logarithm of the experimental data: $\ln f(t) = \ln A + Bt$. The model transformed in this way corresponds to the straight line with slope B and intercept $\ln A$.

The results of the linear regression are used as the initial vector for the general nonlinear exponential fit based on the Levenberg-Marquardt method. The fitted model becomes then $f(t) = Ae^{Bt} + C$. Zero is used as the initial value for the C parameter. In this way the amplitude, the damping factor, and the constant shift of the upper and lower envelope of the oscillations is calculated, along with the mean squared error,

$$S_x = \frac{1}{N} \sum_{i=0}^{N-1} (f_i - y_i)^2 \quad (\text{A.33})$$

where N is the total number of the data points, f_i represents the series of the best fit sequence and y_i the experimental data.

The final stage of the data fitting comprises full nonlinear regression of the damped oscillation curves. The model describing the current oscillation data is

$$f(t) = Ae^{Bt} \sin(2\pi ft) + D \quad (\text{A.34})$$

and the corresponding function for the voltage oscillations is

$$f(t) = Ae^{Bt} \cos(2\pi ft - \varphi) + D \quad (\text{A.35})$$

The initial values for the parameters A , B and the voltage phase shift φ are derived from the previous stage of the regression analysis. The initial value of the oscillation frequency is taken from the auto power spectrum analysis of the signal. The initial value of the constant offset parameter D is assumed to be zero.

The auto power spectrum of the analyzed signal is calculated as the FFT of the signal multiplied by its complex conjugate FFT and divided by the squared number of the data samples in the input sequence. The results are displayed in root mean squared kV^2 or A^2 depending on the nature of the analyzed signal (voltage or current response). Auto power spectrum is used to find the base frequency of the oscillations.

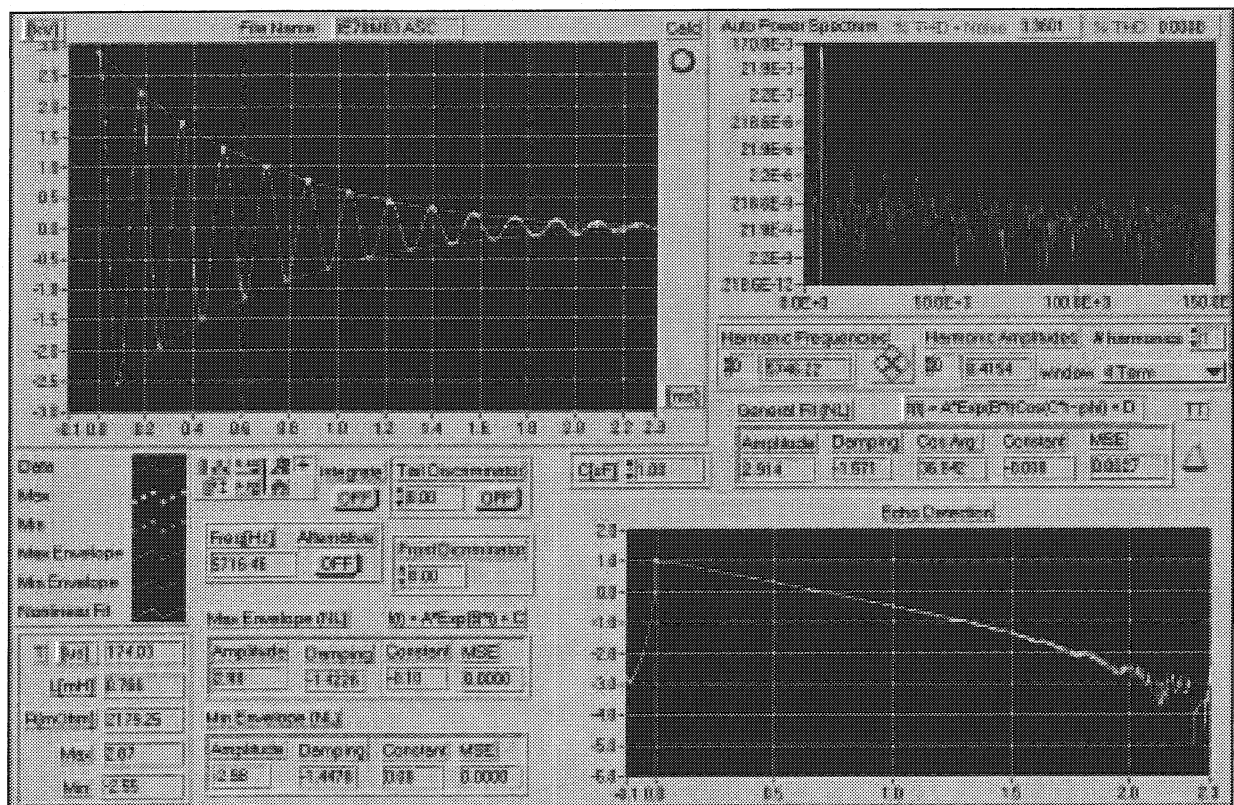


Figure A.6 Analysis procedure

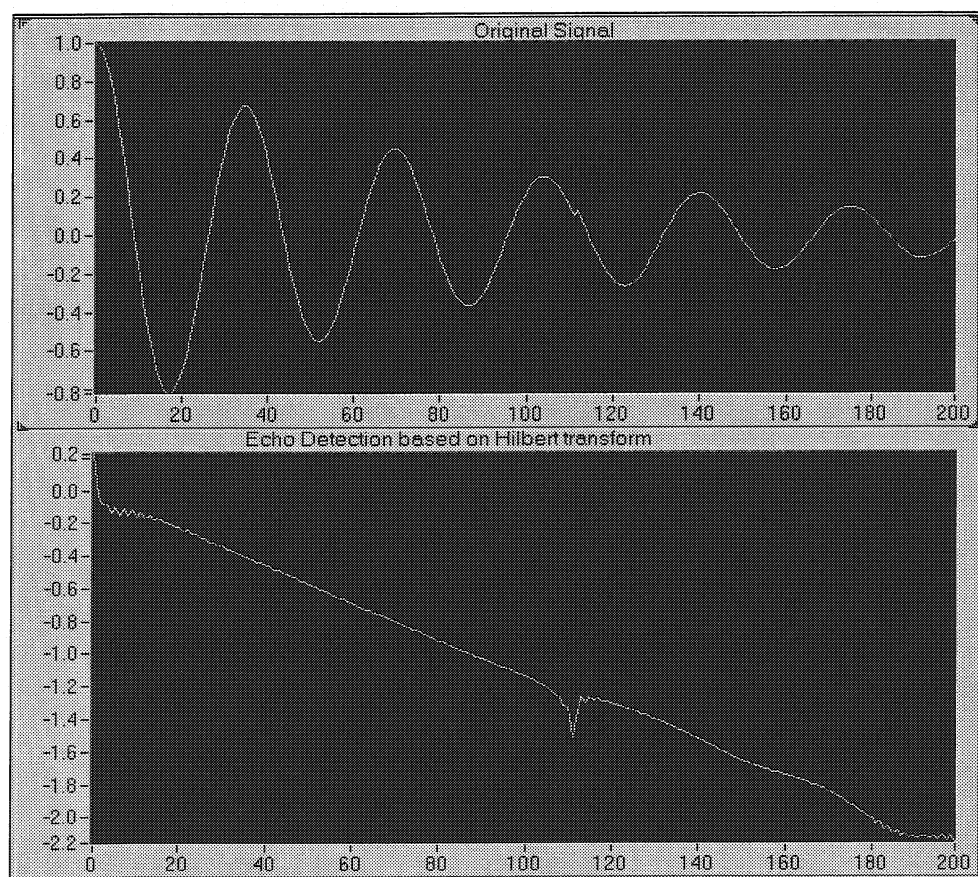


Figure A.7 Idealized echo detection based on the Hilbert transform

The pseudo-period of the oscillations is evaluated directly from the frequency and verified by analyzing the zeros of the oscillation curve. The parameter B in functions (A.34) and (A.35) is always negative. By comparison with the analysis of the discharge circuit in the previous section $B = -\omega\xi = -\frac{1}{\tau} = -\frac{R}{2L}$ and thus it is responsible for the attenuation of the signal. Incorporating B into the calculations, the formula (A.32) for the pseudo-period of the oscillations can be rewritten as

$$T = \frac{2\pi\sqrt{L(C_0 + C_1)}}{\sqrt{1 - B^2L(C_0 + C_1)}} \quad (\text{A.36})$$

The capacitance of the coil to the ground expressed by parameter C_1 is of the order of 10 nF and can be neglected in comparison to the capacity of the discharge capacitor C_0 adjustable in the discharge generator unit within the range of 1 – 3 μF with the step of 0.5 μF . From (A.36) a formula for the self-inductance of the coil can be derived:

$$L = \frac{1}{C_0 \left[\left(\frac{2\pi}{T} \right)^2 + B^2 \right]} \quad (\text{A.37})$$

This formula is used to evaluate the inductance of the magnet coils during the discharge test. An effective resistance of the coil is calculated then as:

$$R_{\text{eff}} = 2L|B| \quad (\text{A.38})$$

The time constant of the oscillations (τ) can also be extracted by applying the Hilbert transformation to the experimental data. Moreover, this kind of approach can also be helpful as far as echo detection in the signal is concerned. The Hilbert transform of the function $f(t)$ is defined as:

$$\mathcal{H}[f(t)] = -\frac{1}{\pi} \int_{-\infty}^{\infty} \frac{x(\zeta)}{t - \zeta} d\zeta \quad (\text{A.39})$$

This transform is especially useful in the analysis of the oscillating signals. It can be applied to extract an instantaneous phase information, to determine the envelopes of the oscillation, as well as to magnify the echoes. One can show that the Fourier transform of the Hilbert transform of a given function is directly related to the Fourier transform of this function [15]

$$\mathcal{F}[\mathcal{H}[f(t)]] = -i \operatorname{sgn}(\omega) F(i\omega) \quad (\text{A.40})$$

where

$$F(i\omega) = \mathcal{F}[f(t)] = \int_{-\infty}^{\infty} f(t) e^{-i\omega t} dt \quad (\text{A.41})$$

is the Fourier transform of the function $f(t)$. Thus the fast Hilbert transform of the sampled digital data can be obtained from its FFT spectrum.

The amplitude part of the signals modeled with functions (A.34) and (A.35) can be expressed as:

$$f_A(t) = Ae^{Bt} \quad (\text{A.42})$$

Its natural logarithm can be written as

$$\ln|f_A(t)| = \ln|f(t) + i\mathcal{H}[f(t)]| = -\frac{t}{\tau} + \ln A \quad (\text{A.43})$$

The slope of the line described by formula (A.43) equals the reciprocal of the time constant of the oscillations. If there is an echo in the response signal, it is extremely hard to locate it simply by analyzing the original data. The amplitudes of echoes are minor in comparison to the amplitude of the original signal, and their time delays are usually much shorter than the time constant of the oscillating system. The procedure described by the formula (A.43) serves to amplify them. In the first step the analytic complex signal of the form $g(it) = f(t) + i\mathcal{H}[f(t)]$ is generated from the original sampled data $f(t)$ using the fast Hilbert transform. Then the magnitude of the signal $g(it)$ is found. Finally the natural logarithm of this magnitude is computed for the echo detection. The entire echo detection procedure is shown in the idealized simulation illustrated in Fig. A.7. The complete post-processor for the HV discharge test analysis was implemented in the LabVIEW programming environment [16].

References for Chapter 3

- [1] L. Walckiers, The Harmonic Coil Method, Proceedings of the CERN Accelerator School on Magnetic Measurement and Alignment, Hyatt Conf. Center, 16-20 March 1992, Montreaux, Switzerland, pp. 138-166
- [2] P. Komorowski, EDMA User's Guide – Electrical Discharge Measurements Application, LHC-MMS 97-08, CERN, Geneva, September 1997
- [3] J. A. Tegopoulos, E. E. Kriezis, Eddy Currents in Linear Conducting Media, Studies in Electrical and Electronic Engineering, Vol. 16, Elsevier Science Publishers B. V., Amsterdam 1985

- [4] T. Nakata et al., Physical Meaning of $\nabla\phi$ in Eddy Current Analysis Using Magnetic Vector Potential, IEEE Transactions on Magnetics, Vol. 24, No. 1, pp. 178-181, January 1988
- [5] OPERA-2D, Software Environment for 2-D Electromagnetic Design, ver. 7.0, Vector Fields Ltd., Oxford 1998
- [6] LabVIEW Analysis VI Reference Manual, Part No. 320538B-01, National Instruments Corporation, September 1994
- [7] H. Rohrer, Journal of Applied Physics, Vol. 40, p. 1472, 1969
- [8] W. B. Garn et al., Review of Scientific Instrumentation, Vol. 37, p. 762, 1966
- [9] Standard Specification IPC-ML-910A, Design and End Production Specification for Rigid Multilayer Printed Boards, Institute of Printed Circuits, Evanston, Illinois, August 1976
- [10] P. Komorowski, W. Billereau, Proj. Ref. No. LHC 680-2042-200, Multilayer Printed Circuit Pick-Up Coils for the Detection and Localization of the Inter-Turn Short-Circuits in Superconducting Collared Coils, Bureau d'études de circuits imprimés, ECP-PES-LT, CERN, December 1998
- [11] T. W. Parks, C. S. Burrus, Digital Filter Design, John Wiley and Sons, Inc., New York 1987
- [12] LeCroy Digital Oscilloscopes, Operator's Manual: 9350/54 Series, LeCroy, February 1996
- [13] P. Komorowski, D. Tommasini, Localization of Electrical Insulation Failures in Superconducting Collared Coils by Analysis of the Distortion of a Pulsed Magnetic Field, accepted for publishing in IEEE Transactions on Applied Superconductivity early in the year 2000
- [14] Carl E. Pearson (editor), Handbook of Applied Mathematics, Selected Results and Methods, Van Nostrand Reinhold, New York 1990
- [15] J. E. Maisel, Hilbert Transform Works with Fourier Transforms to Dramatically Lower Sampling Rates, Personal Engineering and Instrumentation News, PEIN-7, February 1990
- [16] LabVIEW Graphical Programming for Instrumentation, National Instruments Inc., 1995, 1999

Chapter 4

Advanced TDR Techniques for the Signal Integrity Analysis in the Instrumentation of the LHC Magnets

Time Domain Reflectometry (TDR) is one of the most powerful methods used to analyze the integrity of the signal propagating in a transmission line. The method is based on the principle that the wave propagating in the line is reflected at the locations where the impedance of the line changes. The fault points, joints, branches, junctions, abrupt cross-section changes, etc., cause such reflections. The reflectometry technique involves the excitation of the circuit under test with either a fast edge step function or a well-defined impulse confined in time and frequency domains, and thereafter detection of the amplitude and time of the reflections [1]. TDR techniques have a very wide range of applications [2] covering among others: analysis of the signal integrity and transfer functions in microstrip, wafer, and hybrid structures, printed circuits, PC-boards and backplanes, connector interfaces and cables. In this chapter both variants of the method are successfully applied to localize electrical faults in the voltage tap connections, pressure transducers, and temperature sensing carbon gage circuits of the LHC dipole and quadrupole magnets.

In the first part of this chapter basic concepts of TDR techniques are addressed along with the types of faults encountered in the tested circuits. In the next step the transient losses in the line and the frequency dependent waveform deformation are analyzed in view of choosing the correct input signal for a specific test. As an attempt the TDR technique is used to localize inter-turn short-circuits in a 30-m long solenoidal dummy coil wound with the superconducting Rutherford cable. The discussion of the problem and the analysis of the experimental results give clear explanation why the TDR approach fails and cannot be used for the detection and localization of electrical failures in the superconducting coils of the LHC magnets.

Nevertheless, the TDR techniques can be quite efficiently adapted for the analysis of the signal integrity in the auxiliary instrumentation circuits of the LHC magnets. These circuits, installed in order to monitor vital status information of the magnet and of its cryogenic environment, are realized with standard copper non-coaxial cables. The instrumentation cables constitute rather short transmission lines, in general not exceeding the length of 10 m, and they are not wound in form of the coils.

In the experimental part of the chapter both variants of the TDR are applied for the identification, detection and localization of electrical faults in the instrumentation circuits of the LHC String Magnets [3]. The shape and the magnitude of the TDR reflections bear important information concerning the type (inductive, capacitive, resistive), the nature (shunt or series loss) and the parameters (characteristic impedance, time constant, excess inductance, excess capacitance) of the faults, transitions, or discontinuities encountered in the line under study. In order to allow a correct interpretation of the results obtained with pulse reflection methods, the calculation techniques of the responses to different complex loads and discontinuities are demonstrated in appendices at the end of the chapter. The reader will also find there some details concerning the operational calculus approach to the distributed line problem, which is generally used as a convenient mathematical formalism throughout this chapter.

4.1 General Remarks on the Measurement Method

The measurement is carried out according to the following procedure. An impulse of a well-defined shape and duration is sent into the circuit under test. The reflected signal is registered and displayed on the screen of an oscilloscope. Knowing the time elapsed between sending of the input impulse and the arrival of the reflected signal, as well as the velocity of the propagation of the wave in the cable of the circuit, the distance to the fault can be calculated. In the case of a fast step excitation the voltage waves reflected at the points of impedance mismatch appear on the screen of the scope as an algebraic sum with the initial incident wave. The time separation between the incident step and the reflected wave allows to identify the reflection and the distance to the mismatch. The velocity of the propagation of the signal in the cable immersed in a medium depends on the relative dielectric constant of the medium and the velocity of light according to the formula,

$$v = \frac{c}{\sqrt{\epsilon_p}} \quad (4.1)$$

The value of v can be estimated without knowledge of the conductor material or of its cross-section, by measuring the travel time of the wave in a sample of the cable of the same type. The successful application of reflectometry is limited to the faults producing a visible deflection of the propagating wave.

4.2 Types of Electrical Faults Encountered in the Circuits

The faults encountered in the circuits can be divided into three main groups:

1. *Inductive faults* - produce reflections without the change of polarity of the incident signal.
The faults in this group are: open circuit, inter-turn short circuit (in the systems with wound cables), inductive discontinuity in the cable (caused by an inlet of the cable with the cross-section smaller than the rest of the line or a corresponding damage e.g. a cable kink)
2. *Capacitive faults* - produce reflections with the change of polarity of the incident signal.
The faults in this group are: short circuit at the end of the line, ground fault, stray capacitance to the ground, capacitive discontinuity (caused by an inlet of the cable with the cross-section larger than the rest of the line or a corresponding damage inflicted to the line e.g. cable pop-up.)

3. *Resistive faults* – caused by purely resistive loads, produce reflections with or without the change of polarity depending on the value of the mismatched load in comparison to the characteristic impedance of the line under test. Open and short circuit of the line, classified above as extreme cases of inductive and capacitive faults can also be classified as extreme cases of resistive faults with resistance of the load tending to infinity and to zero, respectively.

4.3 Transient Losses in the Line and the Choice of the Input Signal

The ideal lossless lines, which do not distort the waveform of the propagating signal, do not exist. Any realistic transmission line causes that the original waveform of the input signal is deformed and its magnitude diminished. Once the instrumentation of the magnet is installed the only access point to the circuit exists via the input flange of the magnet. Therefore in the pulse reflection measurements it is essential to choose the right input signal capable of reaching the end of the line under test and of coming back again to the monitoring point at the input of the line.

4.3.1 Transient Skin Effect in a Pulse-Excited Cable

Let us analyze the magnitude of the deformation experienced by a fast voltage step propagating in the line represented schematically in Fig. 4.1. The amount of the deformation will be inevitably influenced by the magnitude of the skin effect in the transient regime of the excited line. At $t = 0$ a voltage step is applied to the line

$$e(t) = \begin{cases} E & \text{for } t \geq 0 \\ 0 & \text{for } t < 0 \end{cases}$$

Thus $e(t) = Eu_{-1}(t)$ where $u_{-1}(t)$ is a unit step function. The Laplace transform of such a source is: $\mathcal{L}(e(t)) = \frac{E}{s}$

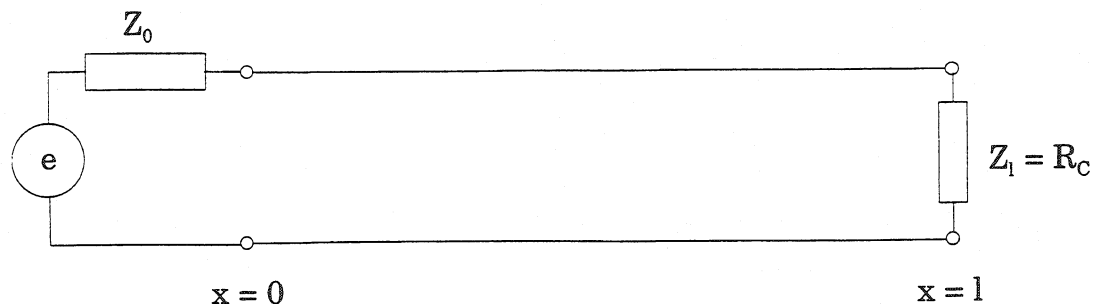


Figure 4.1 Schematic representation of the pulse-excited transmission line

The general solution for the operational voltage in the transmission line has the following form*,

$$\mathcal{V}(x, s) = \mathcal{E}(s) \frac{Z_c}{Z_0 + Z_c} \frac{e^{-\gamma x} + r_e e^{-\gamma(2l-x)}}{1 - r_i r_e e^{-2\gamma l}} \quad (4.2)$$

Where γ is the operational propagation function defined as:

$$\gamma = \sqrt{(R + Ls)(G + Cs)} \quad (4.3)$$

The resistance, conductance, self-inductance and capacitance in formula (4.3) are the parameters given per unit length of the line.

If the input impedance of the circuit in Fig. 4.1 is $Z_0 = 0$ and the line is terminated with its characteristic impedance $Z_l = R_c$, where R_c is the real characteristic impedance in the lossless line approximation, then the reflection coefficients at the input and at the end of the line are $r_i = -1$ and $r_e = 0$, respectively. According to formula (4.2) the operational voltage at the end of the line ($x = l$) becomes:

$$\mathcal{V}(l, s) = \frac{E}{s} e^{-\gamma(s)l} \quad (4.4)$$

At the beginning of the transient regime the shunt losses can be neglected in comparison to the skin effect losses. This means that the shunt losses are much lower than the losses due to the inductance and the capacitance of the line. The line is in the transient regime during the time:

$$0 \leq t_{trans} \leq t_{end} = \min \left\{ \frac{L}{R}, \frac{C}{G} \right\} \quad (4.5)$$

The conditions expressed by inequality (4.5) transformed from the time domain into the Laplace transform domain take the following form:

$$\begin{aligned} R &\ll Ls \\ G &\ll Cs \end{aligned} \quad (4.6)$$

At this point it will be convenient to use the results of the transient skin effect analysis from chapter 3. For the operational skin depth (3.49) the operational effective resistance (3.47) becomes:

$$R(s) = \frac{1}{\sigma d} \sqrt{\frac{s\mu\sigma}{2}} = \kappa\sqrt{s} \quad (4.7)$$

* Refer to Appendix A at the end of this chapter for the details.

The entire part of resistance (4.7) independent of the variable s was replaced by the constant factor κ expressed in $[\Omega s^{1/2}/m]$. As one can see, κ characterizes the geometric and electromagnetic properties of the cable.

According to the assumption that the losses in the line at the beginning of the transient regime occur mostly due to the skin effect one has to replace the resistance R in the propagation function (4.3) with the expression (4.7) and the conductivity with $G = 0$. The propagation factor γ becomes then:

$$\gamma(s) = \sqrt{(\kappa\sqrt{s} + Ls) Cs} = s\sqrt{LC} \sqrt{1 + \frac{\kappa}{L\sqrt{s}}} \quad (4.8)$$

In absence of shunt losses ($G = 0$) the time constant expressed by the ratio of C/G in the condition (4.5) tends to infinity and the smaller of the two terms is expressed by the ratio of L/R . Thus only the first condition in (4.6) has to be considered. It takes the following form:

$$\frac{\kappa}{L\sqrt{s}} \ll 1 \quad (4.9)$$

If the condition (4.9) is fulfilled then the second expression under the square root in (4.8) can be approximated as:

$$\sqrt{1 + \frac{\kappa}{L\sqrt{s}}} \approx 1 + \frac{1}{2} \frac{\kappa}{L\sqrt{s}} \quad (4.10)$$

Then the propagation function can be split into two separate terms,

$$\gamma(s) = s\sqrt{LC} + \frac{\kappa}{2R_c} \sqrt{s} = s\beta_0 + \frac{\kappa}{2R_c} \sqrt{s} \quad (4.11)$$

where $\beta_0 = \sqrt{LC}$ and $R_c = \sqrt{\frac{L}{C}}$ are respectively the propagation constant and the real characteristic impedance in the lossless line approximation. Taking propagation function (4.11) into account the operational voltage (4.4) at the end of the line becomes,

$$\mathcal{V}(l, s) = \frac{E}{s} e^{-\left(s\beta_0 + \frac{\kappa}{2R_c} \sqrt{s}\right)l} = E e^{-s\tau} \frac{e^{-\frac{\kappa\sqrt{s}}{2R_c}l}}{s} \quad (4.12)$$

where $\tau = \beta_0 l$ is the total delay of the line (the time needed by the signal to pass through the entire cable length).

Knowing that

$$\mathcal{L}^{-1}\left(\frac{e^{-k\sqrt{s}}}{s}\right) = 1 - \operatorname{erf}\left(\frac{k}{2\sqrt{t}}\right) \quad (4.13)$$

where $k \geq 0$ and $\text{erf}(z) = \frac{2}{\sqrt{\pi}} \int_0^z e^{-\zeta^2} d\zeta$ is an error function, the inverse transform of (4.12) yields:

$$V(l, t) = E \left[1 - \text{erf} \left(\frac{\frac{\kappa l}{2R_c}}{2\sqrt{t-\tau}} \right) \right] u_{-1}(t-\tau) = E \left[1 - \text{erf} \left(\frac{1}{2} \sqrt{\frac{\tau_{0.5}}{t-\tau}} \right) \right] u_{-1}(t-\tau) \quad (4.14)$$

The term $\tau_{0.5}$ in Eq. (4.14)

$$\tau_{0.5} = \frac{\kappa^2 l^2}{4R_c^2} \quad (4.15)$$

has the dimension of time and represents a fixed constant for a given length of a given cable. Taking the advantage of the properties of the error function it turns out immediately that,

$$V(l, \tau + \tau_{0.5}) = E \left[1 - \text{erf} \left(\frac{1}{2} \right) \right] \approx \frac{E}{2} \quad (4.16)$$

which implies that $\tau_{0.5}$ specifies the time after which the amplitude of the voltage at the end of the line reaches half of the value of the excitation voltage at the input.

To establish the magnitude of the losses we will consider the sinusoidal steady state. In order to do so the variable s must be replaced with complex $i\omega$, where ω is the angular frequency of the sinusoidal waveform. In this case the propagation function (4.11) takes the following form:

$$\begin{aligned} \gamma(i\omega) &= i\omega\beta_0 + \frac{\kappa}{2R_c} \sqrt{i\omega} = i\omega\beta_0 + \frac{\kappa}{2R_c} \sqrt{\omega} \left(\frac{\sqrt{2}}{2} + i \frac{\sqrt{2}}{2} \right) = \\ &= \frac{\kappa}{2R_c} \sqrt{\frac{\omega}{2}} + i \left(\omega\beta_0 + \frac{\kappa}{2R_c} \sqrt{\frac{\omega}{2}} \right) \end{aligned} \quad (4.17)$$

The following identity was used in the transformations executed in (4.17)

$$\sqrt{i} = e^{i\frac{\pi}{4}} = \frac{\sqrt{2}}{2} (1+i)$$

The real part of the propagation function γ always represents attenuation, i.e. it determines the rate at which the signal decays as it travels along the line. For the lossless line $\text{Re}(\gamma)$ automatically becomes zero. In the transient case considered, taking (4.17) into account, attenuation per unit length of the line is:

$$\alpha = \frac{\kappa}{2R_c} \sqrt{\frac{\omega}{2}} = \frac{\kappa}{2R_c} \sqrt{\pi f} \quad (4.18)$$

The attenuation factor α is expressed in nepers per meter [Np/m]. Neper is a dimensionless quantity indicating a neperian, i.e. a natural logarithm.

If single-shot pulses are applied to the circuit under test (e.g. a monocycle sine), the frequency close to the highest frequency in the spectrum of the pulse should be used for the loss evaluation using formula (4.18). In case of input signal in the form of the fast step function discussed here, a reciprocal of the rise time is used as the value of the frequency in question. For example if the applied step voltage has the rise time of 20 ns, the frequency of 50 MHz should be used to estimate the attenuation of the line.

The total attenuation measured experimentally for the line of length l expressed in decibels is given by the following formula,

$$\alpha_{dB} \cdot l = 20 \log \frac{A_i}{A_e} \quad (4.19)$$

where A_i and A_e indicate amplitude of the injected pulse and its respective amplitude at the end of the line. The unit conversion between the α factor in (4.18) and the attenuation per unit length expressed in decibels is as follows:

$$\alpha_{dB} [\text{dB/m}] = \frac{20\alpha}{\ln 10} \approx 8.686\alpha [\text{Np/m}] \quad (4.20)$$

4.3.2 Distortion of the Rectangular Pulse

The attenuation factor (4.18) is frequency dependent, therefore different harmonic components of the test pulse propagating along the line are attenuated with different magnitude, and as a result an essential distortion and smearing of the original signal is observed. Let us see how this distortion looks like for a rectangular pulse.

A rectangular pulse of finite width t_n can be easily constructed by superimposing two step functions of opposite polarity in the following manner:

$$e(t) = E(u_{-1}(t) - u_{-1}(t - t_n)) \quad (4.21)$$

The resulting source signal has the required properties of an ideal rectangular pulse confined in the time domain and characterized by the amplitude E :

$$e(t) = \begin{cases} E & \text{for } 0 \leq t \leq t_n \\ 0 & \text{for } t > t_n \end{cases}$$

The response of the line to the unit step function is given by (4.14). According to the properties of the Laplace transform and the superposition theorem for linear systems, the

response of the circuit to the rectangular pulse can be obtained by adding the separate responses to the individual step voltages defining this pulse. The response to the second step voltage in the source signal (4.21) is obtained immediately by negating the response (4.14) and shifting it in time by t_n . If we neglect the delay τ of the line and shift the time origin to the very moment at which the wave front is read out at the end of the cable the total response to the excitation with the ideal rectangular pulse will read:

$$V(l, t) = E \left[1 - \operatorname{erf} \left(\frac{1}{2} \sqrt{\frac{\tau_{0.5}}{t}} \right) \right] u_{-1}(t) - E \left[1 - \operatorname{erf} \left(\frac{1}{2} \sqrt{\frac{\tau_{0.5}}{t - t_n}} \right) \right] u_{-1}(t - t_n) \quad (4.22)$$

Fig. 4.2 shows the shape of the waveform arriving at the end of the line for a couple of different ratios defined by factor $\xi = \frac{t_n}{\tau_{0.5}}$.

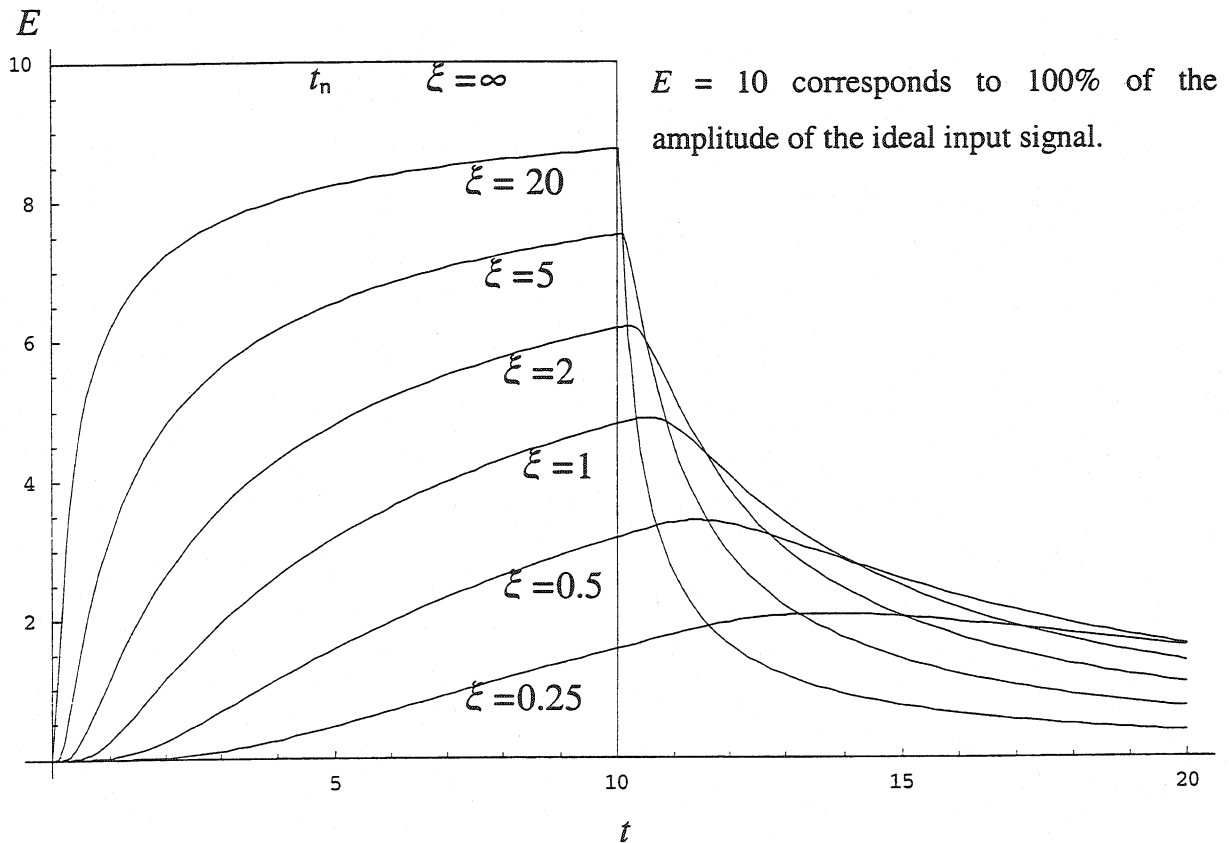


Figure 4.2 Distortion of an ideal rectangular pulse in a lossy cable

Both the amplitude and the shape of the input signal deteriorate and degrade as a result of the distortion introduced by the line. Sharp edges of the rectangular pulse are softened. Rise time and fall time of the pulse become longer. The centroid of the pulse is displaced to the right and a characteristic trailing tail is developed. At a certain degree of distortion the waveform arriving at the end of the cable is so smeared that it does not resemble the input signal in any of its original features.

4.3.3 Distortion of the Haversine Pulse

Since attenuation is a function of frequency, an input signal should be confined within a narrow frequency bandwidth. Obviously rectangular pulse is rather a bad example of such a confinement. The best choice of the input waveform for the impulse reflection measurements is therefore based on the sinusoidal family of functions.

Before the measurement starts the information regarding the characteristics of the tested circuit is required. The knowledge of the transfer functions and of the delay times of the cables used as components of the line is essential for the calibration of the detection equipment and for the analysis and interpretation of the results. Also the information about the location of the inter-connectors and of the cable configuration and routing allows to draw maximum of advantages from the measurement. For example, a system with wound cables, and in particular a coil, is the system with confined bandwidth as far as its response in the frequency domain is concerned. It has been established that wound cables exhibit very low damping for all frequencies below the natural resonant frequency of the coil [4]. To take advantage of this fact, the input stimulation in the form of the sinusoidal single-shot impulse should be used. The spectral decomposition of such a signal shows that the pulse is formed mainly by the base frequency component. If moreover the frequency of the impulse is chosen to be exactly a half of the base frequency of the coil's oscillations, all of the higher harmonics are already in the bandwidth of the coil response, and therefore are effectively attenuated. The only component in the low attenuation bandwidth region is the first harmonic of the sine pulse. Useful pulse shapes are illustrated schematically in Fig. 4.3

Knowing the unit step response of the line $V_{-1}(t)$ expressed by formula (4.14) we can calculate the response of the cable excited with an arbitrary waveform $V_{in}(t)$, e.g. a haversine

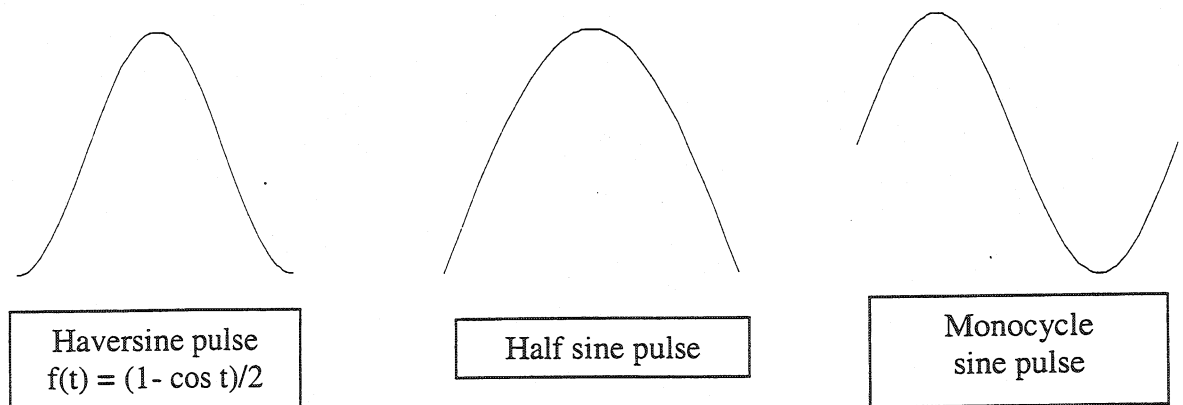


Figure 4.3 Useful pulse shapes for finite impulse reflection measurements

function, using the convolution theorem. The shape of the waveform at the end of the line can be calculated according to the following convolution integral:

$$V_{out}(t) = \int_0^t \frac{dV_{in}(\zeta)}{d\zeta} \cdot V_{-1}(t - \zeta) d\zeta \quad (4.23)$$

Unfortunately the convolution (4.23) would involve the integration of the error function resulting in an indefinite implicit integral. The final result can be obtained a little bit easier if the impulse response $V_\delta(t)$ of the circuit under test is known. In this case one has to analyze the voltage at the end of the line excited with the Dirac's delta function stimulus $\delta(t)$. Dirac's delta function is a distribution and its Laplace transform equals unity:

$$\mathcal{L}(\delta(t)) = 1 \quad (4.24)$$

Thus starting again from Eq. (4.2) as a result of the discussion similar to the one carried out in details for the voltage step function, the operational voltage at the end of the line excited with the $\delta(t)$ impulse is:

$$\mathcal{V}_\delta(l, s) = e^{-s\tau} \cdot e^{-\sqrt{\tau_{0.5}} \cdot \sqrt{s}} \quad (4.25)$$

Knowing that,

$$\mathcal{L}^{-1}\left(e^{-k\sqrt{s}}\right) = \frac{k}{2\sqrt{\pi}t^3} e^{-\frac{k^2}{4t}} \quad (4.26)$$

where $k > 0$, the inverse transform of (4.25) yields:

$$V_\delta(l, t) = \frac{1}{2\sqrt{\pi}} \sqrt{\frac{\tau_{0.5}}{(t-\tau)^3}} \cdot e^{-\frac{\tau_{0.5}}{4(t-\tau)}} \cdot u_{-1}(t-\tau) \quad (4.27)$$

Or, if the time origin is shifted to the very moment of the arrival of the wave front at the end of the line:

$$V_\delta(l, t) = \frac{1}{2\sqrt{\pi}} \sqrt{\frac{\tau_{0.5}}{t^3}} \cdot e^{-\frac{\tau_{0.5}}{4t}} \cdot u_{-1}(t) \quad (4.28)$$

Then according to the convolution theorem the response of the line to the excitation signal $V_{in}(t)$ is given by:

$$V_{out}(t) = V_{in}(t) * V_\delta(t) = \int_0^t V_{in}(\zeta) \cdot V_\delta(t - \zeta) d\zeta = \int_0^t V_{in}(t - \zeta) \cdot V_\delta(\zeta) d\zeta \quad (4.29)$$

Unfortunately the analytical closed form solution of the convolution (4.29) can be rarely

found and the problem must be treated numerically. The advantage of (4.29) in comparison to the convolution (4.23) is that both functions under the integral are explicit functions of time.

A single haversine pulse shown in Fig. 4.4 can be extracted from the continuous, harmonic haversine signal of the angular frequency ω and amplitude E by applying a rectangular window:

$$V_{in}(t) = E \left(\frac{1 - \cos \omega t}{2} \right) \cdot \left(u_{-1}(t) - u_{-1} \left(t - \frac{2\pi}{\omega} \right) \right) \quad (4.30)$$

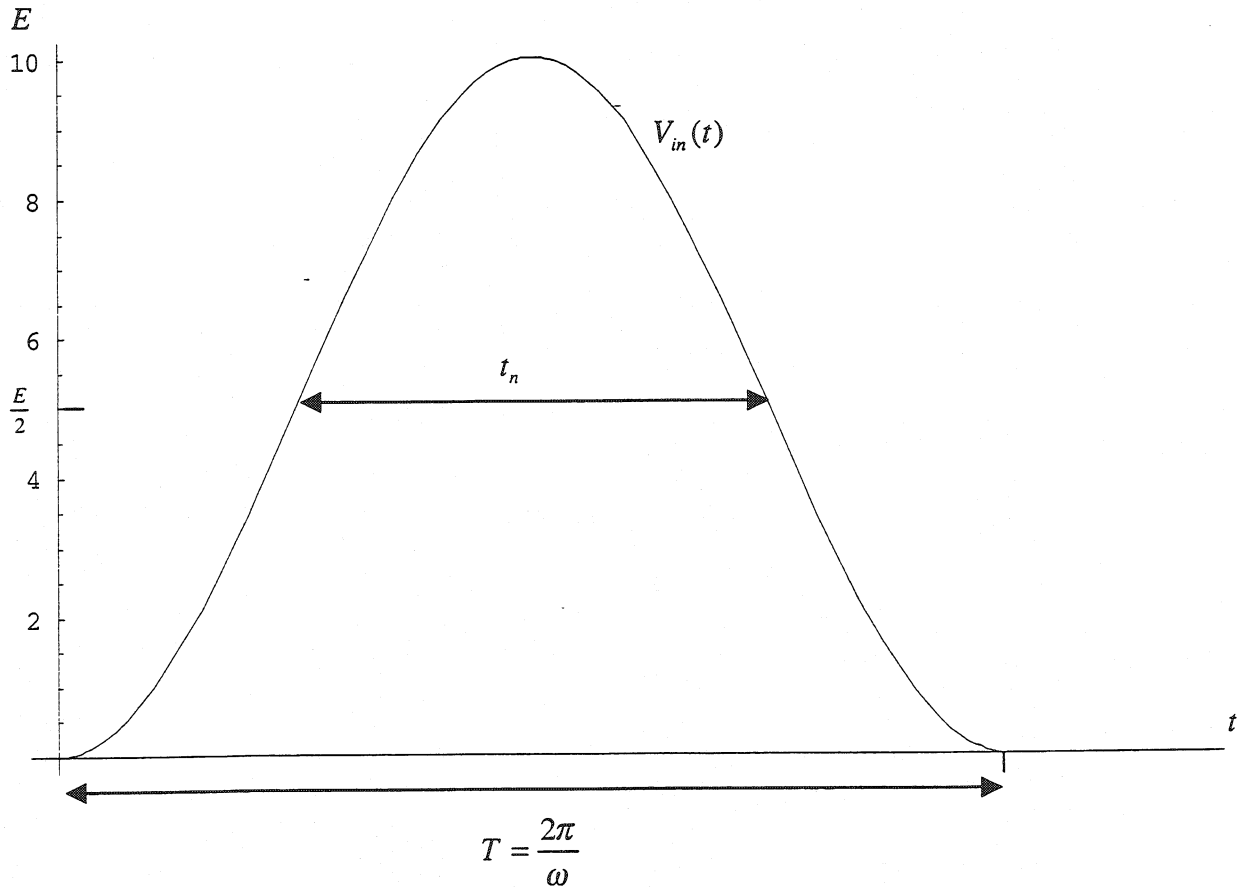


Figure 4.4 Single haversine pulse. $E = 10$ is the amplitude of the pulse.

In order to compute numerically the shape of the waveform at the end of the cable, both the input signal $V_{in}(t)$ and the impulse response $V_{\delta}(t)$ must be represented as discrete signals sampled with the same fixed time interval Δt . The convolution integral (4.29) is then replaced with the following sum:

$$V_{out}(n) = V_{in}(n) * V_{\delta}(n) = \sum_m V_{in}(m) \cdot V_{\delta}(n - m) \cdot \Delta t \quad (4.31)$$

The value of the n -th sample in the output signal corresponds to the time $n \cdot \Delta t$ and is obtained as a result of discrete convolution of the digitized input signal and impulse response.

Index m covers the range defined by the total number of time samples in the convoluted functions. The entire process is demonstrated step-by-step in Figs. 4.5 to 4.7 for the ratio $\xi = \frac{t_n}{\tau_{0.5}} = 0.5$. The term $t_n = \frac{\pi}{\omega}$ indicates the half-width of the input pulse, i.e. the width of the pulse measured at 50% of its amplitude (see Fig. 4.4). Fig. 4.5 shows the input function of Fig. (4.4) sampled at equally spaced time intervals. Index n on the OX axis enumerates the samples. Fig. 4.6 shows the digitized impulse response function (4.28) plotted for the factor $\tau_{0.5}$ imposed by the coefficient $\xi = 0.5$. The result of the discrete convolution of both sampled

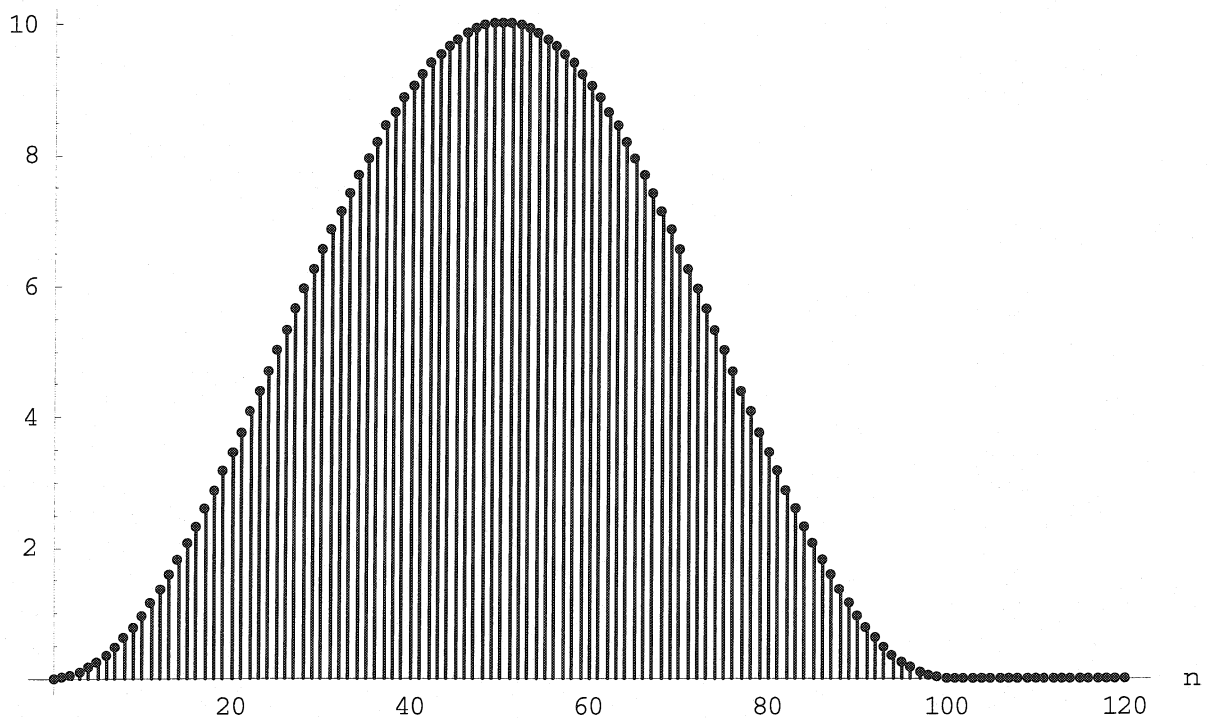


Figure 4.5 Discretized haversine pulse

data sets is illustrated in Fig. 4.7. Fig. 4.8 gathers several output waveforms computed for different values of ξ . All of the plots were generated using the discrete signal processing functions of the Signals and Systems add-on package available for *Mathematica* [5].

Comparing the plots in Fig. 4.8 with the distorted rectangular waveforms in Fig 4.2 one can draw the conclusion that with the lowering value of the coefficient ξ the shape of the initial input signal is preserved much better for the haversine. The coefficient ξ was used in the discussion as a sort of the pulse quality factor. Decreasing value of ξ , considered for the same input pulse, indicates increased degradation of the pulse arriving at the end of the line.

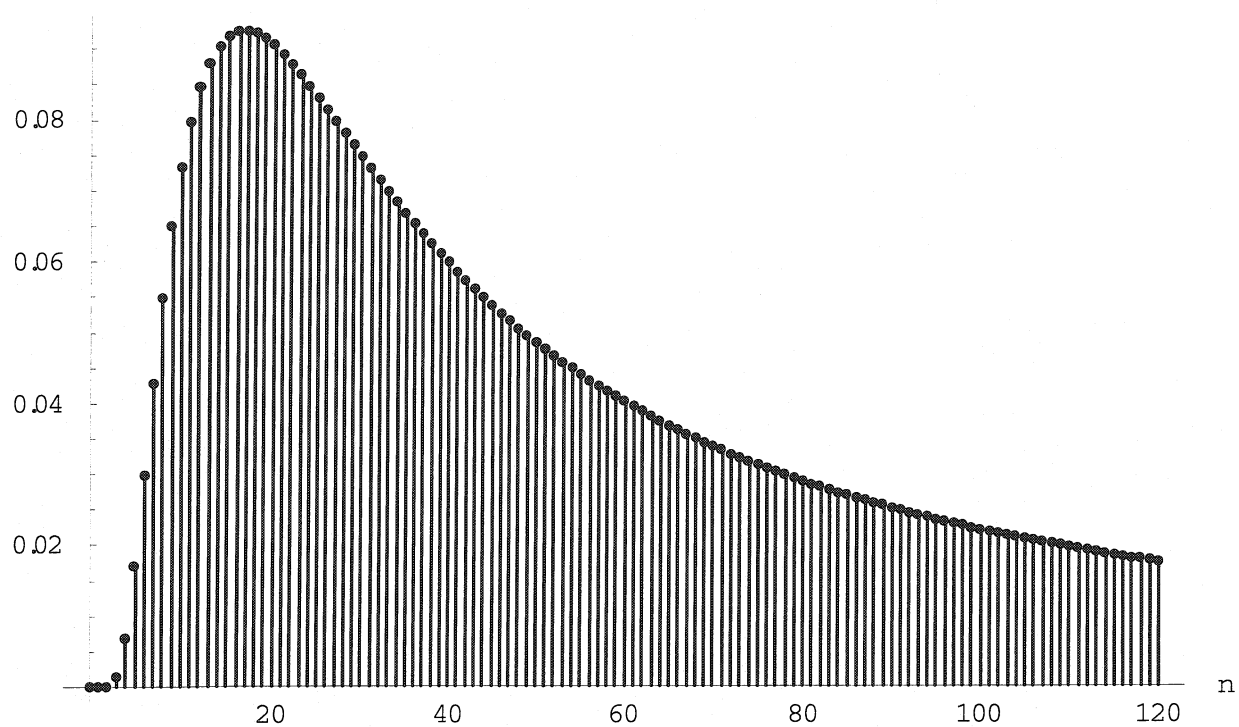


Figure 4.6 Discretized impulse response function $V_{\delta}(n)$ plotted for $\xi = 0.5$

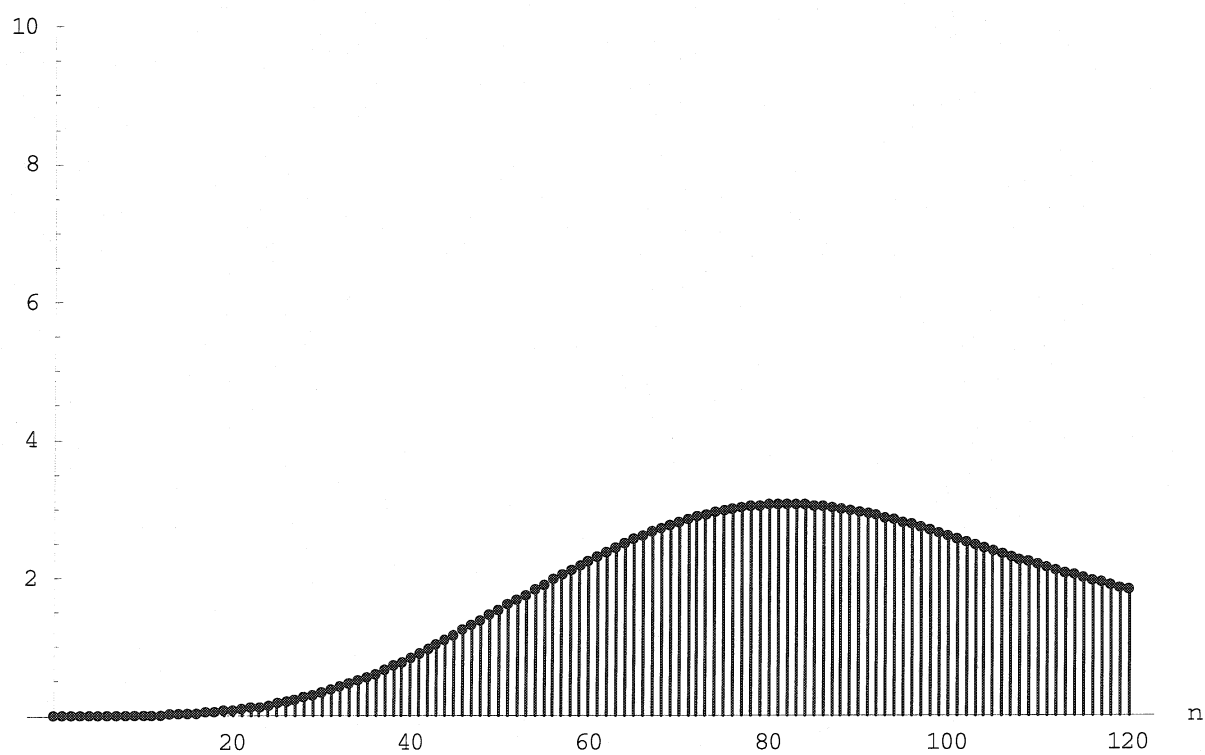


Figure 4.7 Result of the discrete convolution – waveform at the output of the cable for $\xi = 0.5$

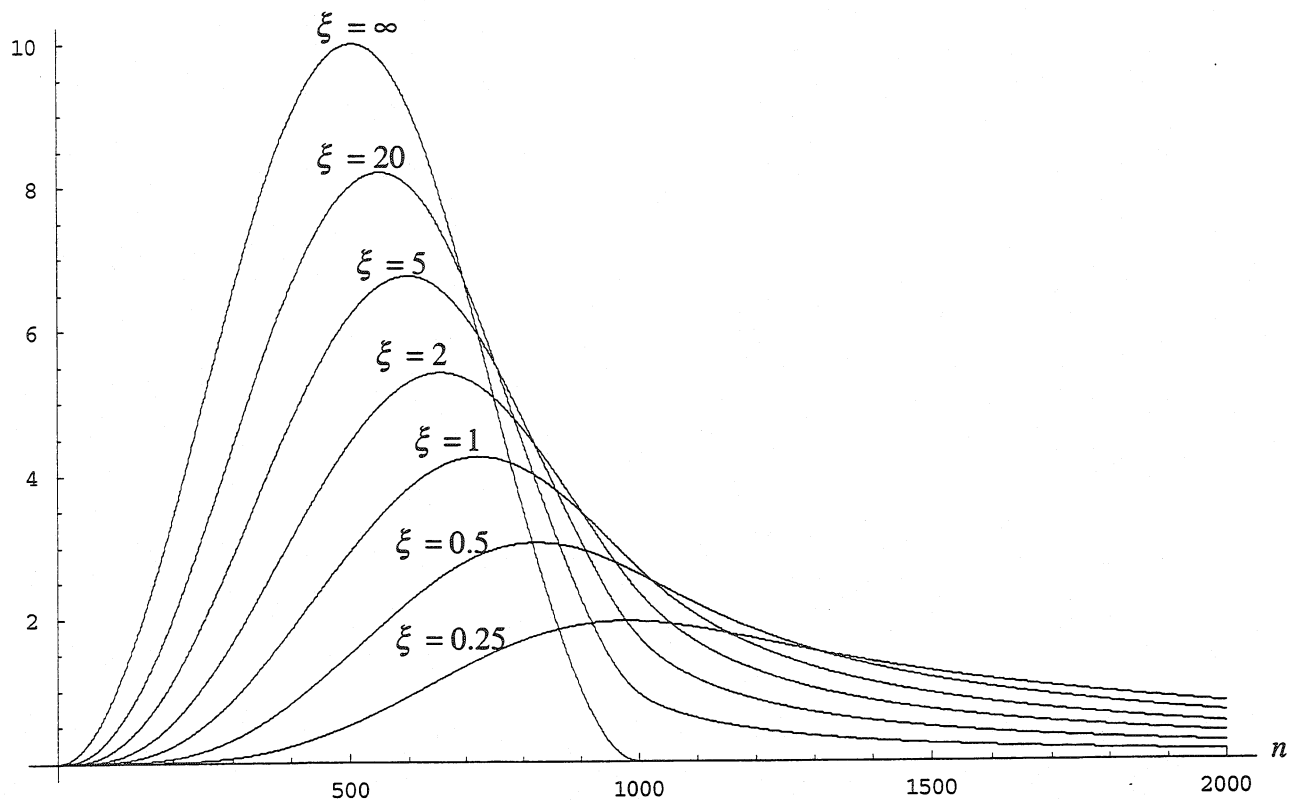


Figure 4.8 Distortion of the original haversine pulse ($\xi = \infty$) for different values of coefficient ξ

Regarding the definition of the ratio specified by coefficient ξ , such situation is equivalent to increase of $\tau_{0.5}$, which for the same cable type corresponds simply to increase of the cable length.

Not only the frequency spectrum of the pulse decides about its feasibility in the measurements. The other important factor is the confinement of the input signal in the time domain. It determines the width of the dead zone. If the pulse is too wide and the electrical fault is too close to the beginning of the line the reflection from the fault will be overlapped by the input signal, and thus impossible to detect.

On the other hand if the signal is too fast and the fault is at the end of the long line, the input pulse will be attenuated completely before it even reaches the fault. Therefore fast, narrow pulses should be used to detect the problems on short transmission lines and close to the input, and slow, wide pulses to localize the faults on the long lines far away from the beginning of the circuit.

4.3.4 Time Duration of the Transient Regime

The attenuation factor (4.18) cannot be used for the estimation of the losses in the line at high frequencies because it completely neglects the effect of leakage across the dielectric of the cable. This type of loss introduces a second term linearly dependent on frequency into the attenuation factor α . For the commonly used dielectrics like polyethylene these losses remain very small up to the frequency of several hundred MHz. Although they are small they may be very important and should be considered especially in the analysis of fast pulses containing high frequency harmonics and propagating in short transmission lines. At the frequency of approximately 1GHz the dielectric leakage becomes predominant in comparison to the skin effect losses. Above that limit the attenuation increases quickly with the frequency, the main transversal electromagnetic mode of the signal propagation in the cable is dominated by different modes and eventually the cable cannot be used for the signal transmission any more.

The use of attenuation factor (4.18) with its only term dependent on the square root of the frequency is constrained only to the time period covering the beginning of the transient regime. As it was explained in section 4.3.1 at the beginning of the transient regime the shunt losses can be neglected in comparison to the skin effect losses. The factor $\tau_{0.5}$ expressed as the function of losses becomes

$$\tau_{0.5} = \frac{\alpha^2 l^2}{\pi f} \quad (4.32)$$

and it can be established experimentally by measuring the attenuation in the line. To evaluate the duration of the beginning of the transient regime, and thus to specify the validity region for the attenuation factor in formula (4.18), the condition (4.9) has to be transformed back into time domain. This can be done after having rewritten it in the form

$$\frac{\kappa}{Ls} \ll \frac{\sqrt{s}}{s} \quad (4.33)$$

where s is assumed to be positive and real. Inverse transform yields then

$$\frac{\kappa}{L} \ll \frac{1}{\sqrt{\pi t}} \Rightarrow t \ll \frac{L^2}{\pi \kappa^2} \quad (4.34)$$

If the term κ^2 from formula (4.15) is substituted here, the condition transforms to

$$t \ll \frac{L^2 l^2}{4\pi \tau_{0.5} R_c^2} \quad (4.35)$$

Hence, taking into account that $R_c^2 = \frac{L}{C}$ and $\tau = l\sqrt{LC}$ the condition for the beginning of the transient region becomes

$$t \ll \frac{\tau^2}{4\pi \tau_{0.5}} \quad (4.36)$$

Thus the term $\tau_{0.5}$ given by formula (4.32) is a good parameter describing the influence of the skin effect on the shape of the pulse propagating in the line if the reflectometry measurement is contained within the period of time which complies with the condition (4.36).

4.4 TDR for the Localization of Inter-Turn Short-Circuits in the Coiled Systems Wound with Superconducting Rutherford Cable

In this section we will test the feasibility of the TDR techniques for the detection and localization of the inter-turn short circuits in the coil-like test objects wound with Rutherford cable. Before we come to the experimental measurements and their discussion it will be convenient to derive the pattern of the expected reflection image imposed by the fault.

4.4.1 Reflection Image of the Inter-Turn Short-Circuit in the System with Wound Cables

It is extremely difficult to efficiently match the coil with its characteristic impedance during the reflectometry measurement. In order to provide the match at the beginning of the transient regime of the line a complex load termination would have to be composed of the real characteristic impedance connected in parallel with the capacitor representing a well established capacitance. Even then the perfect match cannot be realized, as the value of the terminating capacitance changes in time, i.e. the line matched at the beginning of the transient regime will not be matched as the time evolves. The case presented here will be analyzed in details for the line with an open end.

An inter-turn short-circuit in a system with wound cables can be represented by introducing a lumped parameter R_f , characterizing the resistance of the fault, into the line (Fig. 4.9). The input haversine pulse is applied between the core of the cable and the ground. The reflection image resulting from the simple resistive loads can be analyzed without resorting to the Laplace transform methods. The general idea of the expected image pattern can be obtained almost instantaneously by applying the method of traveling waves. In order to do this we split the line in front of the fault as shown in Fig. 4.9.

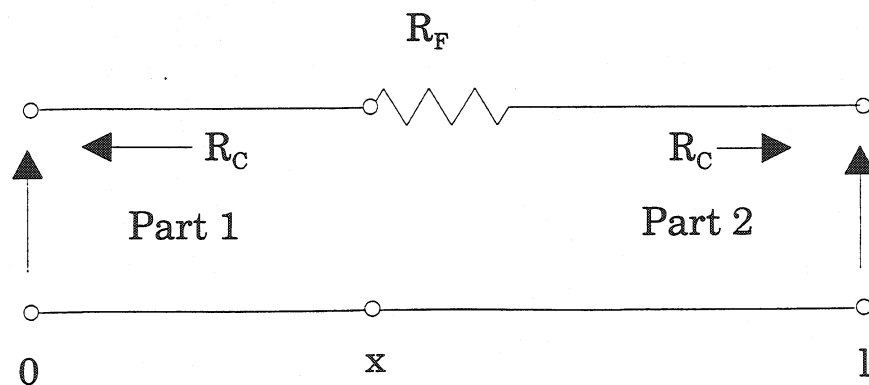


Figure 4.9 Inter-turn short circuit in the coiled line with an open end

The following indices will be used consequently for the voltage and current notation:

- i for incident voltage and current
- r for reflected voltage and current
- t for transmitted voltage and current

The positive direction for the voltages is indicated in Fig. 4.9 with the vertical arrows across the line. The positive direction for the currents is assumed to be from left to right. The size of the fault is considered to be negligible in comparison to the total length of the coil. Therefore the resistance of the fault is treated as a lumped parameter introduced into the line, and the fault itself is regarded as pointwise. According to these assumptions, the following relations are fulfilled:

- for the incident wave traveling towards the point of fault:

$$\frac{V_i}{i_i} = R_C \quad (4.37)$$

- for the wave reflected at the point of fault and traveling back towards the input of the line:

$$\frac{V_r}{i_r} = -R_C \quad (4.38)$$

- for the wave transmitted at the point of fault and traveling towards the end of the coil:

$$\frac{V_t}{i_t} = R_C + R_F \quad (4.39)$$

The following laws are satisfied at the junction between the two parts of the line (point of fault):

- Kirchhoff's equation for the currents

$$i_i + i_r = i_t \quad (4.40)$$

- equality of the voltages across both parts of the line

$$V_i + V_r = V_t \quad (4.41)$$

Eq. (4.40) rewritten using Eqs. (4.37 – 4.39) leads to the following relation

$$\frac{V_i}{R_C} - \frac{V_r}{R_C} = \frac{V_t}{R_C + R_F} = \frac{V_i + V_r}{R_C + R_F} \quad (4.42)$$

Transforming Eq. (4.42) one can calculate the voltage reflection coefficient for the waves traveling from *Part 1* to *Part 2* of the line:

$$\frac{V_r}{V_i} = \frac{R_F}{2R_C + R_F} = r_x \quad (4.43)$$

The law of the conservation of energy for the junction is:

$$V_i i_i = V_t i_t + |V_r i_r| \quad (4.44)$$

The absolute value of the reflection part must be taken because the energy is always positive. Using Eqs. (4.37 – 4.40) Eq. (4.44) can be transformed to:

$$\begin{aligned} \frac{V_i^2}{R_c} &= V_t (i_i + i_r) + \frac{V_r^2}{R_c} \\ \frac{V_i^2}{R_c} &= V_t \left(\frac{V_i}{R_c} - \frac{V_r}{R_c} \right) + \frac{V_r^2}{R_c} \\ V_i^2 - V_r^2 &= V_t (V_i - V_r) \Rightarrow V_i + V_r = V_t \end{aligned} \quad (4.45)$$

Thus the conservation of the energy implies condition (4.41). It means that this condition and the Kirchhoff's law (4.40) express together the conservation of the energy at the point of fault.

Dividing (4.41) by V_i and taking into account reflection coefficient (4.43), the formula for the voltage transmission coefficient for the waves traveling from *Part 1* to *Part 2* of the line is obtained:

$$\frac{V_t}{V_i} = 1 + r_x = t_x \quad (4.46)$$

If the reflection coefficient r_x is positive (and it is the case here), the amplitude of the transmitted wave will be greater than the amplitude of the incident wave. And thus the signal read at the end of the line will have higher amplitude than the injected one unless the frequency dependent attenuation of the line and the magnitude of the skin effect make it otherwise. In the experiments with the fault localization, the signals are read at the input of the line; the excitation pulse travels to the end of the line, is reflected there, and appears back at the beginning of the cable. In the case considered (with the open end of the line) a haversine pulse of amplitude V_i is applied to the line. At the point of fault a small part of this pulse is reflected and travels back towards the input. The amplitude of this pulse is given by:

$$V_r = r_x V_i \quad (4.47)$$

This reflection will appear at the input after time $t_f = 2x/v_p$, where x indicates the distance to the fault and v_p the velocity of wave propagation in the cable. The other part of the wave will be transmitted towards the end of the coil. The amplitude of this part is given by:

$$V_t = (1 + r_x) V_i \quad (4.48)$$

It will reach the end of the coil after the time $(l - l_0)/v_p$ where l is the total length of the coil,

and l_t is the length of the single turn of the coil. With the inter-turn short circuit the coil appears to the traveling signal to be shorter by the length of a single turn affected by the electrical defect as compared to the whole length.

At the open end of the cable the wave gets reflected with the reflection coefficient $r = 1$. At this moment the wave travels back from *Part 2* towards *Part 1* of the line. On its way it will encounter again the point of fault.

The ensemble of the discussion presented for the waves traveling from *Part 1* towards *Part 2* must be adjusted for the waves traversing the line in the opposite direction. For the new incident wave $V_i' = (1 + r_x)V_i$ coming back from the end of the coil towards the point of fault (from *Part 2* to *Part 1*) the following relations hold:

- for the new incident wave traveling towards the point of fault:

$$\frac{V_i'}{i_i'} = -(R_F + R_C) \quad (4.49)$$

- for the wave reflected at the point of fault and traveling back towards the end of the line:

$$\frac{V_r'}{i_r'} = R_F + R_C \quad (4.50)$$

- for the wave transmitted at the point of fault and traveling towards the input of the coil:

$$\frac{V_t'}{i_t'} = -R_C \quad (4.51)$$

The following laws are satisfied at the junction between the two parts of the line (point of fault)

- Kirchhoff's equation for the currents

$$i_i' + i_r' = i_t' \quad (4.52)$$

- equality of the voltages across both parts of the line

$$V_i' + V_r' = V_t' \quad (4.53)$$

Eq. (4.52) rewritten using Eqs. (4.49 – 4.51) leads to the following relation

$$\frac{-V_i'}{R_F + R_C} + \frac{V_r'}{R_F + R_C} = \frac{-V_t'}{R_C} = -\frac{V_i' + V_r'}{R_C} \quad (4.54)$$

Transforming Eq. (4.54) one can calculate the voltage reflection coefficient for the waves traveling from *Part 2* to *Part 1* of the line:

$$\frac{V_r'}{V_i'} = -\frac{R_F}{2R_C + R_F} = -r_x \quad (4.55)$$

A part of the wave coming back from the end of the line will be reflected at point x back towards the end with change of polarity. This part is not interesting because its image will not appear at the input within the time period of $[0, 2(l - l_t)/v_p]$ (the time period needed by the injected test pulse to reappear at the input of the coil).

Dividing (4.53) by V_i' and taking (4.55) into account, the formula for the voltage transmission coefficient for the waves traveling from *Part 2* to *Part 1* of the line is obtained:

$$\frac{V_t'}{V_i'} = 1 - r_x = t_x' \quad (4.56)$$

Thus the wave transmitted back to the input of the line after the time $2(l - l_t)/v_p$ will have the amplitude:

$$V_{final} = (1 - r_x)V_i' = (1 - r_x)(1 + r_x)V_i = (1 - r_x^2)V_i \quad (4.57)$$

The entire measurement process is schematically presented in Fig. 4.10.

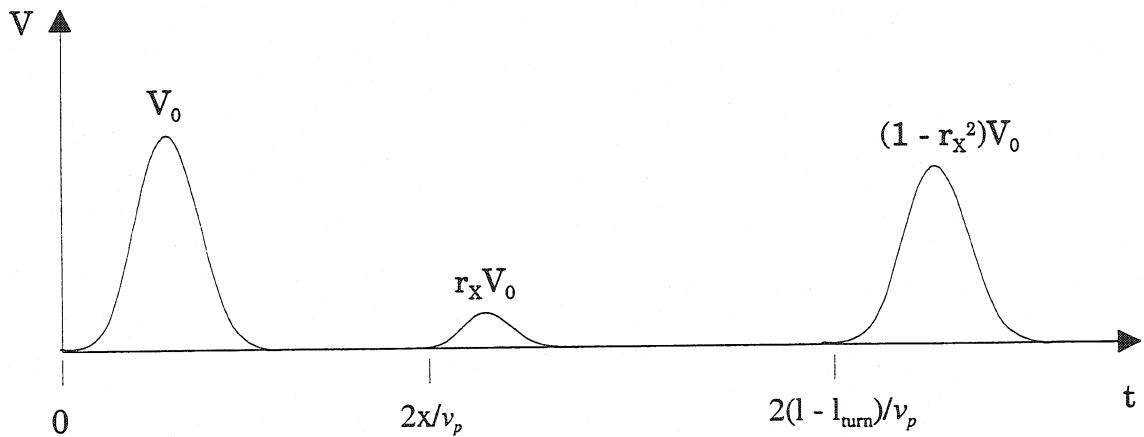


Figure 4.10. Detection of the inter-turn short circuit by means of pulse reflection

4.4.2 Pulse Reflection Measurements in the Coils Wound with Superconducting Cable

The test object is a solenoidal dummy coil composed of 60 turns wound using 30 meters of the untreated raw superconducting cable (the cable that has not been submitted to the heat treatment) around a plastic tube of 7.5-cm radius. The superconducting cable is exactly the same as the one used for winding of the LHC dipole magnets.

In the configuration adapted for the reflectometry measurements the solenoidal dummy coil is wrapped in a stainless steel foil, which simulates serves as a ground electrode. The gap in the foil provides the access to the cable necessary for the short-circuit simulation. The short circuits are created using the same tool as in the case of the HV discharge test (see. Fig. 2.5). The measuring system and the test object are presented in Fig. 4.11 and 4.12. The excitation pulse is sent from the function generator and applied between the core of the dummy coil cable and the stainless steel foil surrounding the solenoid. The oscilloscope is synchronized with the pulse sent from the function generator. The feedback signal is read between the same points where the excitation pulse was applied. The series of measurements was carried out with the 5 MHz haversine pulse (the highest available frequency for the single shot pulse of this shape and the instrument used). The other end of the coil remained open.

Fig. 4.12 shows the response of the dummy coil without any faults. Both injected and reflected pulses are clearly visible on the plot. The reflection image of the entire cable length is contained between the beginning of the injection (marked with the square) and the beginning of the reflection (marked with the circle.) The injected haversine pulse traverses the dummy coil to its end and back to the input in the time $2\tau = 528$ ns. Hence the total delay of the line is $\tau = 264$ ns. For the total cable length of $l = 30$ m this corresponds to the delay of 8.8 ns/m. The velocity of the wave propagation is $v = 1.1(36) \cdot 10^8$ m/s.

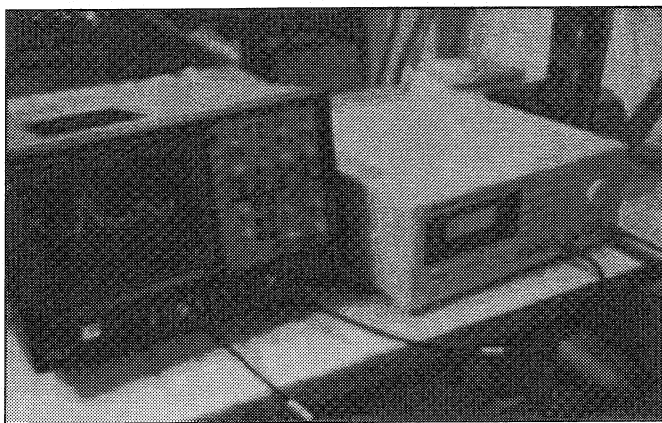


Figure 4.11 The measurement system

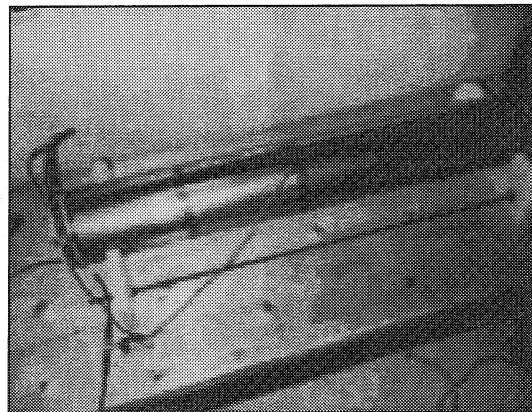


Figure 4.12 Dummy coil under test

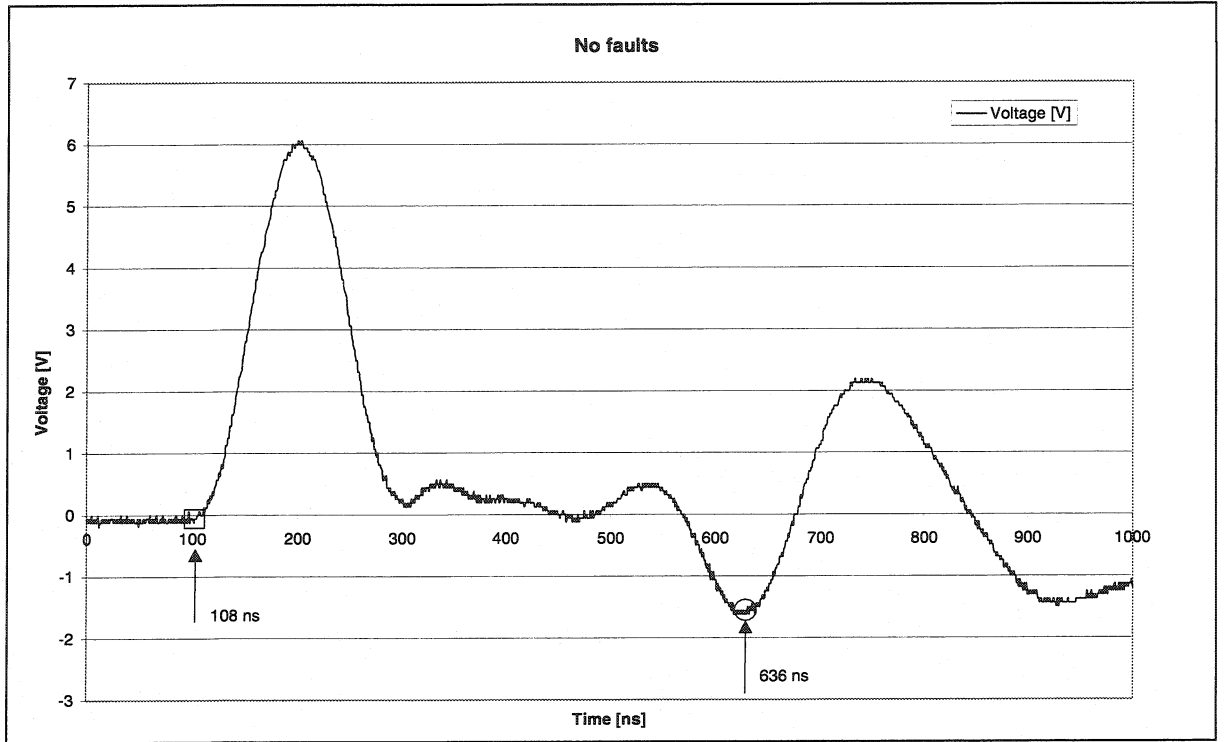


Figure 4.13 The reflection image of the dummy coil

The amplitude of the injected pulse is $A_{in} = 6$ V. The pulse reflected at the end shows an amplitude defect visible in form of the large undershoot of -1.5 V. The relative amplitude of the reflected pulse is $A_{2\tau} = 3.6$ V. Hence the attenuation of the 5 MHz haversine pulse by the dummy coil over the distance of 60 m ($2l$) equals 4.44 dB, which results in the attenuation factor of:

$$\alpha_{dB} = 0.074 \text{ dB/m}$$

and in nepers

$$\alpha = 8.52 \text{ mNp/m}$$

$$\alpha l = 0.256 \text{ Np}$$

The factor $\tau_{0.5}$ of the dummy coil at the frequency of 5 MHz is

$$\tau_{0.5} = 4.2 \text{ ns}$$

The condition (4.36) for the beginning of the transient regime yields $t \ll 1.32 \mu\text{s}$. Thus the condition is fulfilled and we are in the transient region during the entire pulse reflection measurement.

For comparison purposes the reflection image obtained with the 5 MHz haversine pulse injected into 100-m wound coaxial cable of characteristic impedance $R_C = 75 \Omega$ is shown in Fig. 4.14. The signal traverses the cable to the end and back again in the time $2\tau = 830$ ns. Hence the total delay of the line ($l = 100$ m) equals $\tau = 415$ ns what gives the

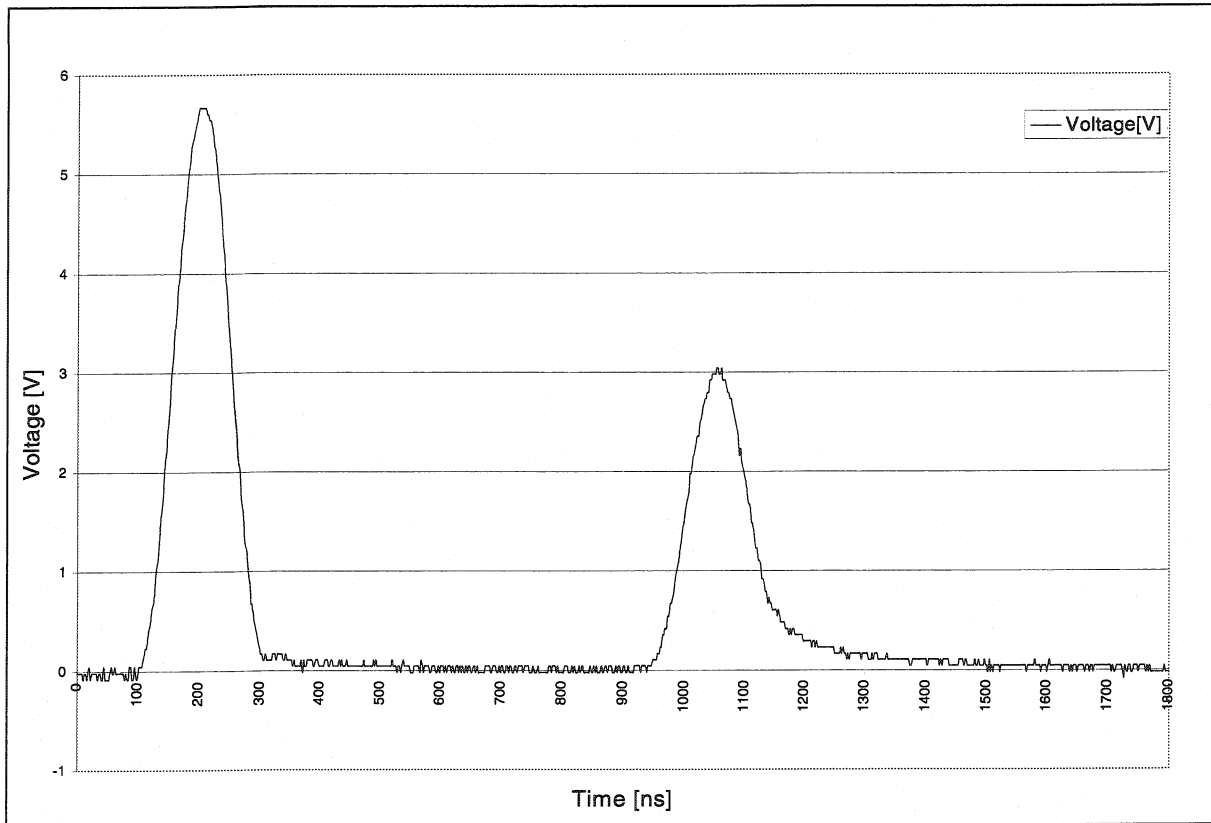


Figure 4.14 Reflection of the 5 MHz haversine pulse at the open end of the cable

delay of 4.15 ns per meter. The velocity of the propagation of the wave in the line is $v = 2.4096 \cdot 10^8$ m/s*. The amplitude of the injected pulse is $A_{in} = 5.7$ V, and of the reflected one that appears back at the beginning of the line is $A_{2\tau} = 3$ V. Hence, the attenuation of the haversine pulse at the frequency of 5 MHz and over the distance of 200 m equals 5.58 dB, which results in the attenuation factor:

$$\alpha_{dB} = 0.02788 \text{ dB/m}$$

and in nepers

$$\alpha = 3.2 \text{ mNp/m}$$

$$\alpha l = 0.32 \text{ Np}$$

The factor $\tau_{0.5}$ at $f = 5$ MHz for the haversine pulse is

$$\tau_{0.5} = 6.52 \text{ ns}$$

The condition (4.36) for the beginning of the transient region gives $t \ll 2.1 \mu\text{s}$.

* A simple cross-check of this result using formula (4.1) for the insulating material of $\epsilon_r = 1.5$ yields the velocity of the propagation of $2.4478 \cdot 10^8$ m/s which corresponds to the delay of 4.09 ns per meter.

The dummy coil behaves like a delay line in comparison to the wound coaxial cable; the electromagnetic wave propagates more than two times slower in the raw Rutherford cable in comparison to the coaxial line under test. The total attenuation over the length of 30 m of the solenoid is comparable to the total attenuation measured at 5 MHz over 100 m of the coaxial cable. At the same time the value of $\tau_{0.5}$ for the more than three times shorter superconducting line is only 35% lower than the corresponding value for the coaxial line under test. Also the quality of the reflection image is much worse. The pulse reflected at the open end of the coil is much wider than the injected one due to the anomalous development of the trailing tail. Moreover, as it was already pointed out before, an offset shift of -1.5 V is observed in the signal reflected at the end of the coil. The image region between both pulses is not a flat line. All this is a consequence of the sophisticated compound structure of the superconducting cable, which creates and magnifies all possible kinds of distortions and losses at ambient temperature. On the other hand the inductance of the solenoid increases the time constant of the wound system and causes the significant distortion of its impulse response. Another factor influencing the distorted reflection image is the low efficiency of the ground electrode. The stainless steel foil enveloping the solenoid is an example of a bulk electrode which, despite being grounded to the common ground of the measurement system, can be hardly considered as an equipotential surface. The quality of the reflection image is also related to the distance between the foil and the cable of the coil. If the foil is not tightly wrapped around the coil windings the signal will be remarkably deteriorated.

The fact that the image region between the injected and reflected pulses is not a flat line implies that the reflection image of the coil under the fault conditions can be interpreted only with respect to the reference image of the flawless coil. Fig. 4.15 illustrates such comparison for the inter turn short-circuit created in the middle of the coil between the turns No. 31 and 32. The beginning of the reflection caused by the short-circuit between these turns is visible on the plot at $t = 372$ ns and marked with the circle. The criterion for the identification of the reflection caused by the inter-turn short circuit is as follows:

The image region behind the falling slope of the injected pulse is scanned in search for the first reflection with the positive peak as compared to the reflection image of the flawless coil.

$$2t_f = 304 - 108 \text{ ns} = 264 \text{ ns}$$

The time of the wave propagation to the point of fault is then

$$t_f = 132 \text{ ns}$$

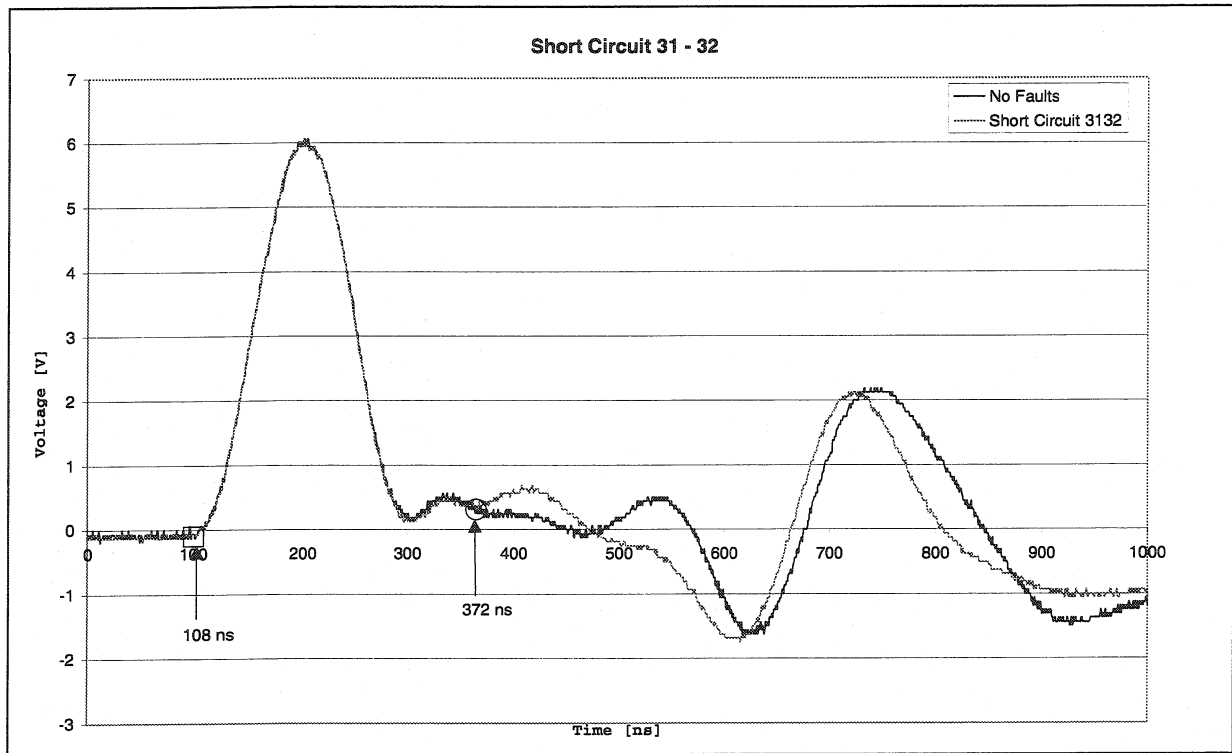


Figure 4.15 Reflection image of the short circuit between turns No. 31 and 32

Knowing the velocity of the wave propagation in the dummy coil we can calculate the distance to the point of fault:

$$l_f = 15 \text{ m from the beginning of the coil,}$$

which already indicates exactly the middle of the coil. The coil is wound around the tube with the radius of $r = 7.5 \text{ cm}$, therefore one turn is 47 cm long. The calculated distance to the fault thus corresponds to the turn number

$$N = 15 / 0.47 = 31.9$$

which results in the successful fault localization. As predicted during the discussion in section 4.4.1, the reflection at the open end of the coil takes place a little bit earlier as compared to the time of the corresponding reflection in the flawless coil. The coil with inter-turn short circuit is shorter for the propagating signal than the flawless coil by the length of the single turn winding. This shift was clearly visible for each simulated inter-turn short circuit. The magnitude of the shift can be used to estimate how many simultaneous inter-turn short circuits are present in the coil. Despite rather weak reflections caused by the inflicted inter-turn short-circuits all of the faults within the range of turns between numbers 23 to 45 were successfully localized with a good precision. Another example of the detection is shown in Fig. 4.16. As illustrated there for the turn No. 39 and 40, sometimes it was not straightforward to determine the actual beginning of the studied reflection in comparison to

the flawless reflection image. Errors in the estimation of the beginning of the reflection induce errors in the final localization of the problem.

The highest frequency of the haversine pulse produced by the function generator used in the measurements was limited to 5 MHz. This means that the width of the excitation pulse (200 ns) was comparable with the delay of the dummy coil ($\tau = 264$ ns). Such situation did not allow to detect the faults near the ends of the coil. Close to the input terminal of the solenoid, i.e. for turns No. 1 to 22, the reflection from the fault was covered with the image of the excitation pulse. Close to the end, i.e. for turns No. 46 to 60, the successful detection was not possible either, because the reflection at the end of the cable was too distorted, and thus too sensitive and too responsive to the signal changes taking place right before it.

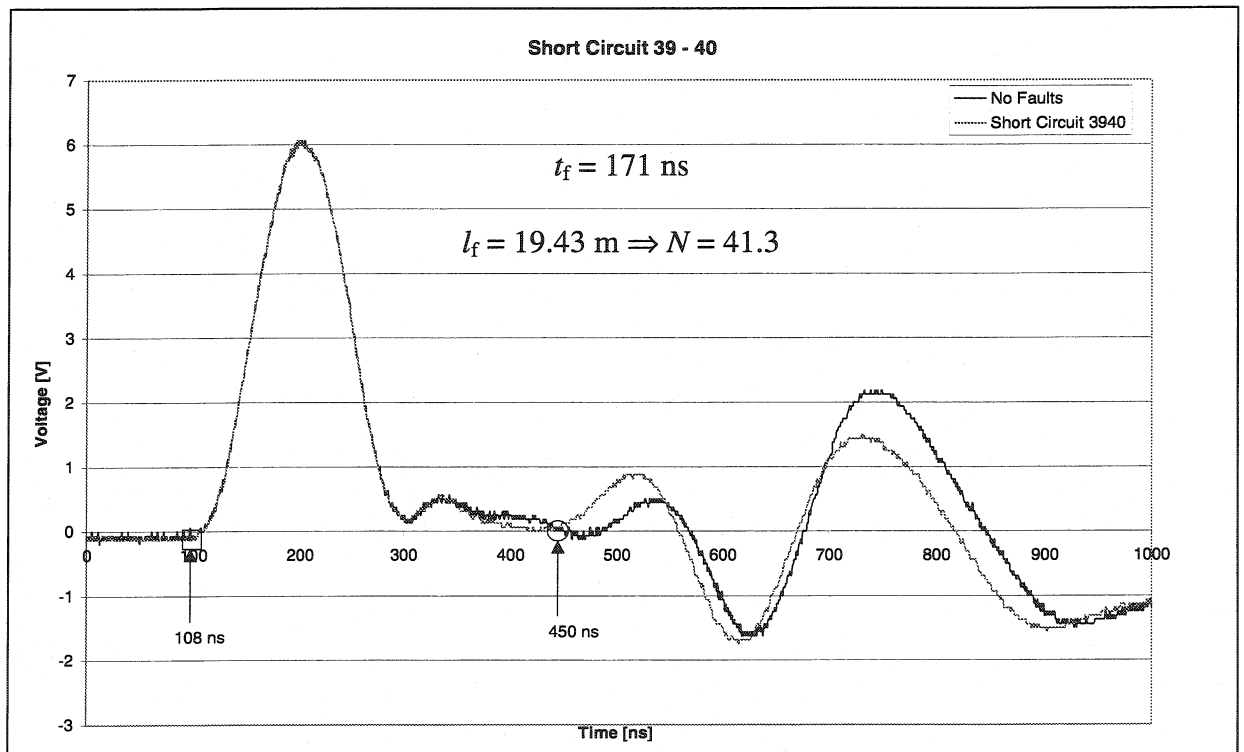


Figure 4.16 Reflection image of the short circuit between turns No. 39 and 40

The results of the test on the dummy coil clearly indicate that the method cannot be used for the detection of the inter-turn short-circuits in the real LHC magnets for the following reasons:

- Apart from the different than solenoidal topology of the coils the superconducting cable in the LHC dipole magnet is much longer. In a 1-m long model of the dipole magnet the total cable length is 176 m (in a single aperture). Thus the signal would have to be transmitted through the length of 352 m before arriving back at the input of the coil. This

would correspond to the total attenuation of some 26 dB as far as the amplitude of the signal reflected at the end of the coil is concerned. No need to remark that at such a high attenuation the reflections resulting from the electrical defects would remain beyond the capabilities of detection. In reality the injected signal does not even reach the end of the magnet winding, not only due to the high attenuation and distortion of the traveling wave front, but also due to the high inductance of the magnet. It is quite obvious that the method must fail in case of the real scale 15 m-long LHC dipole magnet in which the total length of the cable is approx. 2.4 km (in a single aperture).

- Distributed high self-inductance of the magnet causes that the system excited with an impulse does not produce the impulse response any more. An attempt was made for example to use TDR techniques for the signal integrity analysis in the sector of the compact small superconducting corrector magnets connected in series and separated by the 30 m-long straight sections of plain single-conductor superconducting cable. Whereas the rectangular pulse experienced big distortions while propagating in the short part of the cable between the two consecutive corrector magnets, very satisfactory results were achieved with the haversine pulses. Nevertheless if the signal was injected in front of the magnet, the waveform simply did not manage to successfully pass the magnet winding. The time constant of the 20 cm-long corrector magnet was simply too high in comparison to the rise-time of applicable test pulses in order to produce the response in form of an impulse.
- During the reflection measurements the signal must be injected between the core of the cable and the ground electrode. This does not pose any problems for the coaxial cables. For the noncoaxial cables a selection of the good ground electrode is a vital point for the successful test. Another approach addressing noncoaxial cables uses differential injection of the pulse into two parallel lines running close to each other. In the case of the magnet at any of its assembly stages the available ground electrodes are constituted either by the collars, the iron yoke or the cryostat. In each case the bulk material can be hardly regarded as an equipotential electrode, which seriously affects the quality of the reflection measurements.

4.5 Localization of Electrical Faults in the Instrumentation Circuits of the LHC Magnets

The auxiliary instrumentation circuits of the LHC magnets are used to monitor the vital status information concerning the magnet and its cryogenic environment. Their routing is realized with standard copper noncoaxial cables and therefore TDR techniques can be successfully adapted for the identification and localization of the possible circuit malfunction.

4.5.1 Voltage Tap Circuit

The experimental setup used for the detection and localization of the broken voltage tap connections in the LHC String Magnets is shown in Fig. 4.15. A pulse generator sends the signal into the circuit under test. Signal injection and the following reflections are registered on the screen of the oscilloscope. The pulse enters the voltage tap circuit of the magnet through a 16 ns-delay coaxial cable. The approximate geometry of the circuit in the dipole magnet was known prior to the measurements. The first part of the circuit is made of a capillary resin-impregnated guide about 4 m long. The cables used in this part are unshielded copper cables with the cross-section of 0.089 mm^2 . At the end of the capillary there is an inter-connector through which the cables enter the cold mass of the magnet and reach the

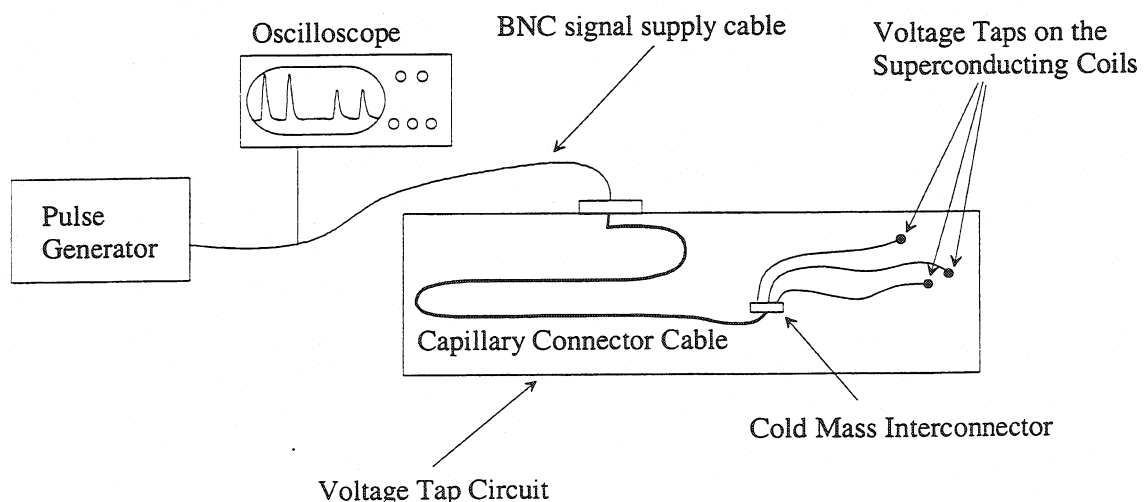


Figure 4.15 Experimental setup

electric potential checkpoints at well-defined positions on the superconducting coils of the magnet. The cables in the cold mass are not longer than 2 m depending on the exact position of the corresponding voltage taps, and their cross section after the inter-connector increases to 0.14 mm^2 . The geometry of the voltage tap circuit in the short straight section quadrupole

magnet was not known. In both cases the transfer functions of the cable components of the circuit were not available either. The total length of the circuit under test is rather short (6 m maximum for the dipole magnet) therefore fast pulses had to be applied for the detection of the faults. The input signal was a rectangular pulse 3-ns wide with the leading and trailing edges of 2 ns each. The pulse generator used in the system was not capable of producing other than rectangular functions.

Time Domain Reflectometry Tests
Thursday, December 10, 1998

BNC 16 ns signal supply cable

Input pulse characteristics:
Width: 3 ns
Leading and Trailing Edge: 2 ns each

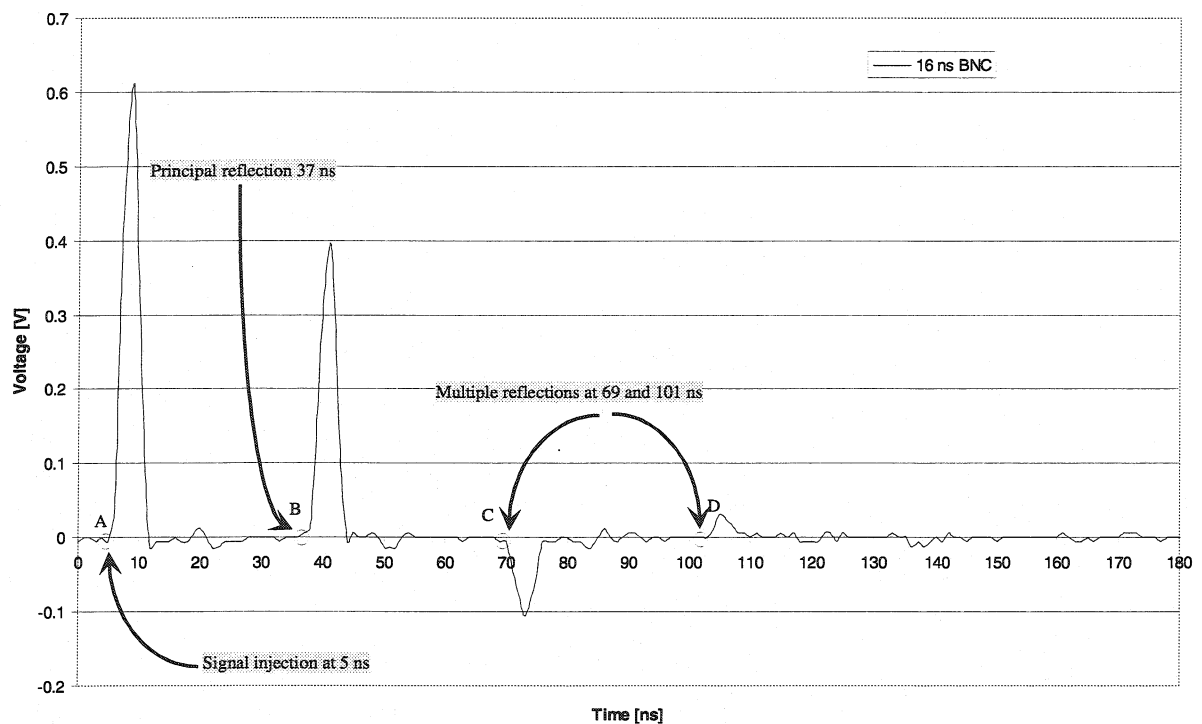


Figure 4.16 Reflection image of the coaxial 16 ns-delay cable

Fig. 4.16 shows the preliminary measurement on the coaxial signal-supply cable separated from the rest of the test circuit. Point A indicates an injection of the signal into the cable occurring at 5 ns. Point B denotes the principal reflection at the end of the cable at 37 ns. Thus the injected signal travels to the open end of the cable, gets reflected there and reappears at the input after 32 ns (there and back again time). This result verifies the delay of the cable to be 16 ns. At the beginning of the line the signal is not fully absorbed. Due to a small mismatch between the 50 Ω coaxial conductor and the load at the input of the system, the wave is reflected with the change of polarity. These multiple reflections appearing in regular consecutive intervals of 32 ns constitute a parasite background that will be present throughout the measurements.

Dipole Magnet MB2

Schematic drawing of the voltage tap layout on the LHC String Dipole Magnet is shown in Fig. 4.17. A broken voltage tap circuit is indicated with a dashed line. Fig. 4.18 shows the results of the reflection measurements performed for the operational voltage tap RAMS8 No. 8 in the proximity of the broken voltage tap RBMS8 No. 1. Reflections at points A, B and C

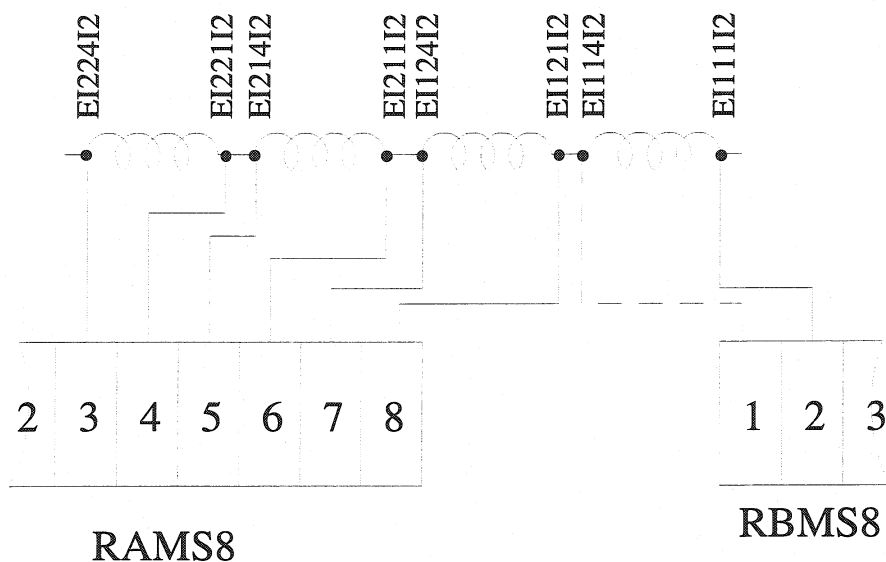


Figure 4.17 Voltage taps on the MB2 dipole magnet

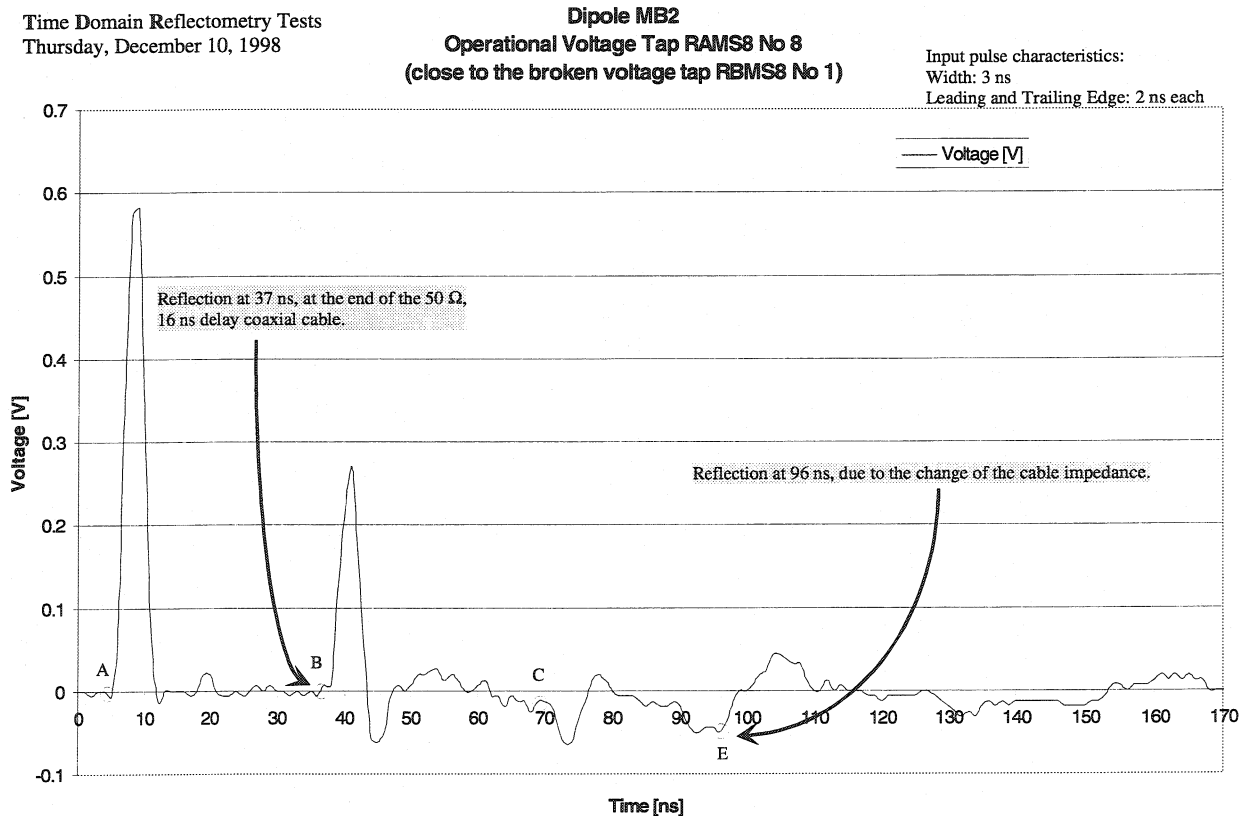


Figure 4.18 Reflection image of the RAMS8-8 voltage tap circuit

correspond to the ones identified before in Fig. 4.16. Reflection denoted as E occurring at 96 ns appears most probably due to the change of the cable impedance at the point where the voltage tap reaches the superconducting coil of the magnet. It takes place 29.5 ns away from point B on the time scale (59 ns there and back again propagation time). The exact delay times for the cables used in the voltage tap circuits due to the cable material and geometry as well as due to the dielectric properties of the media traversed by the cable are not known. To better visualize the analyzed data an average delay of 5.5 ns per meter* of the cable used in the circuits under test is assumed here for the distance calculations. Taking this assumption and the geometry of the circuit into account the distance from point B to the electrical

Time Domain Reflectometry Tests
Thursday, December 10, 1998

Dipole MB2
Broken Voltage Tap RBMS8 No 1

Input pulse characteristics:
Width: 3 ns
Leading and Trailing Edge: 2 ns each

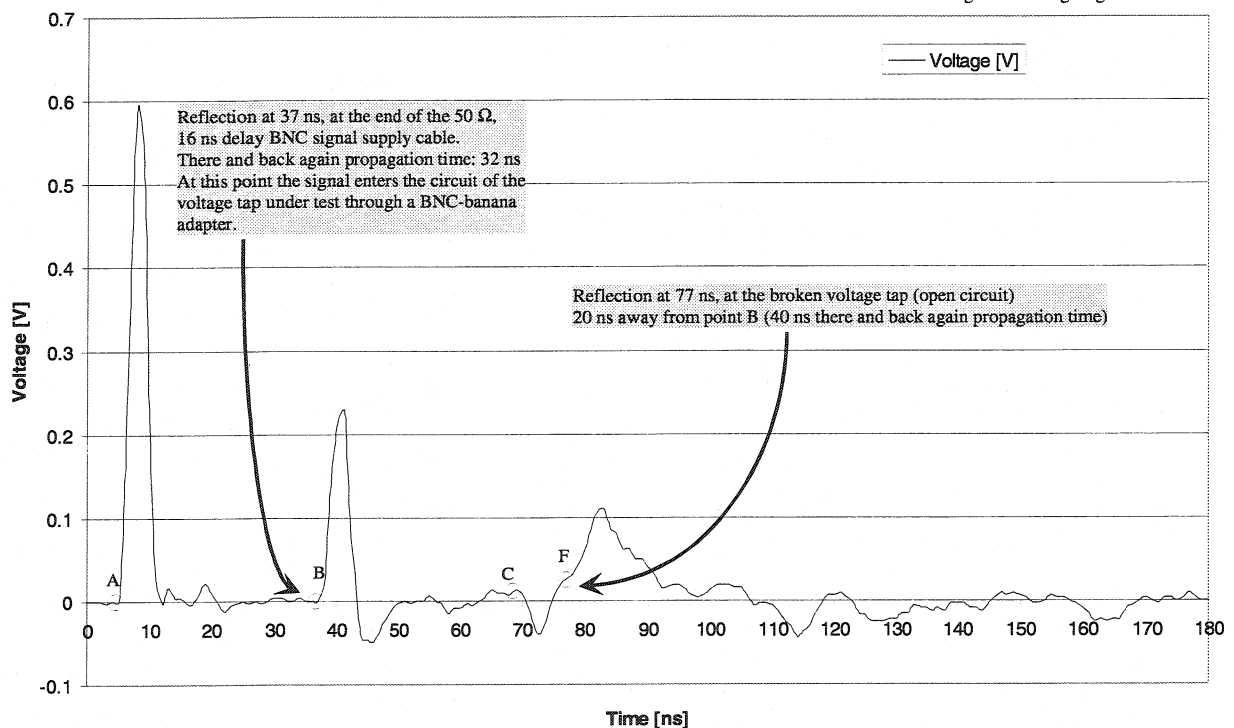


Figure 4.19 Reflection image of the RBMS8-1 voltage tap circuit

potential check-point on the superconducting coil would correspond to about 5.4 m, which indicates the length of about 1.4 m of the cable traversing the cold mass.

Fig. 4.19 shows the reflection image of the broken voltage tap circuit. Reflection due to the open circuit on the broken voltage tap appears at 77 ns (point F), i.e. 20 ns away from point B (40 ns there and back again propagation time). This corresponds to about 3.64 m

*Result of the impulse response test carried out on the 3 m of unshielded copper cable similar to the one used in the capillary

away from the input connector, which indicates an open circuit near the end of the capillary guide close to the inter-connector entering the cold mass of the magnet. Fig. 4.20 is a comparative plot of all curves. The plot corresponding to the broken voltage tap circuit is marked with a dashed line.

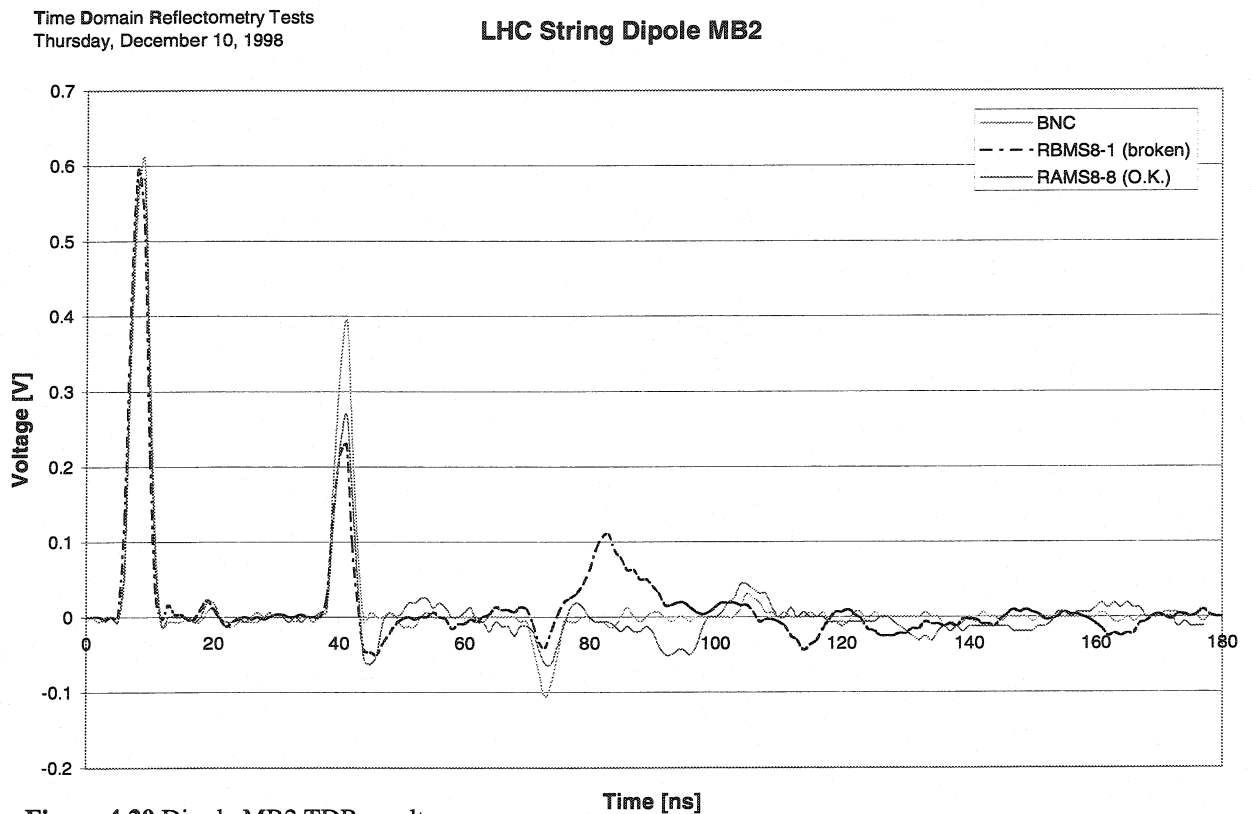


Figure 4.20 Dipole MB2 TDR results

Short Straight Section Quadrupole

Schematic layout of the voltage taps on the LHC String Short Straight Section Quadrupole is shown in Fig. 4.21. In this case there was no signal on the entire RBMS8 connector indicated with a dashed line.

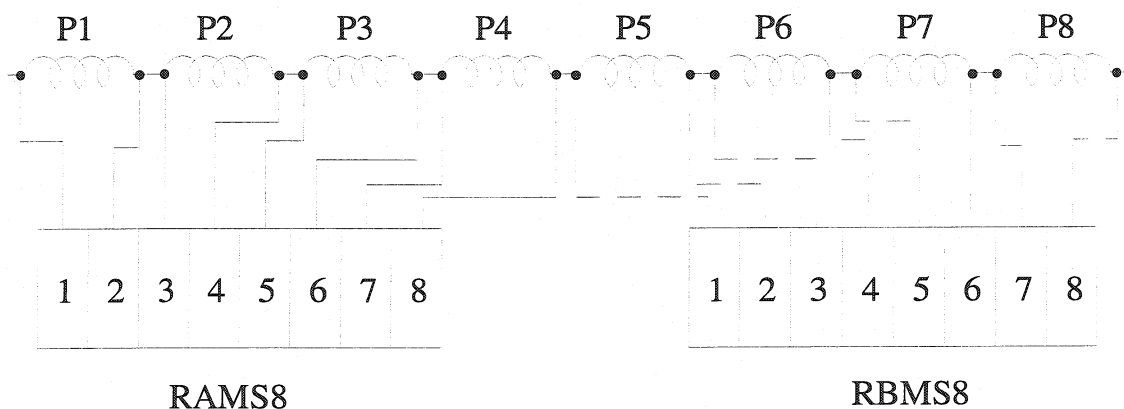


Figure 4.21 Voltage taps on the SSS quadrupole magnet

The reflection images of the circuits on the RAMS8 were the same for all available circuits (pins No. 1-8). One of them is presented in Fig. 4.22. The signal inversion at 100 ns could be due to the change of the cable impedance caused by its varying cross-section on both sides of the common inter-connector. Since the exact geometry of the circuit was not known prior to measurements the interpretation of this feature on the reflection image cannot be explicit.

Time Domain Reflectometry Tests
Thursday, December 10, 1998

**Short Straight Section Quadrupole
Operational Voltage Taps RAMS8 No 1-8**

Input pulse characteristics:
Width: 3 ns
Leading and Trailing Edge: 2 ns each

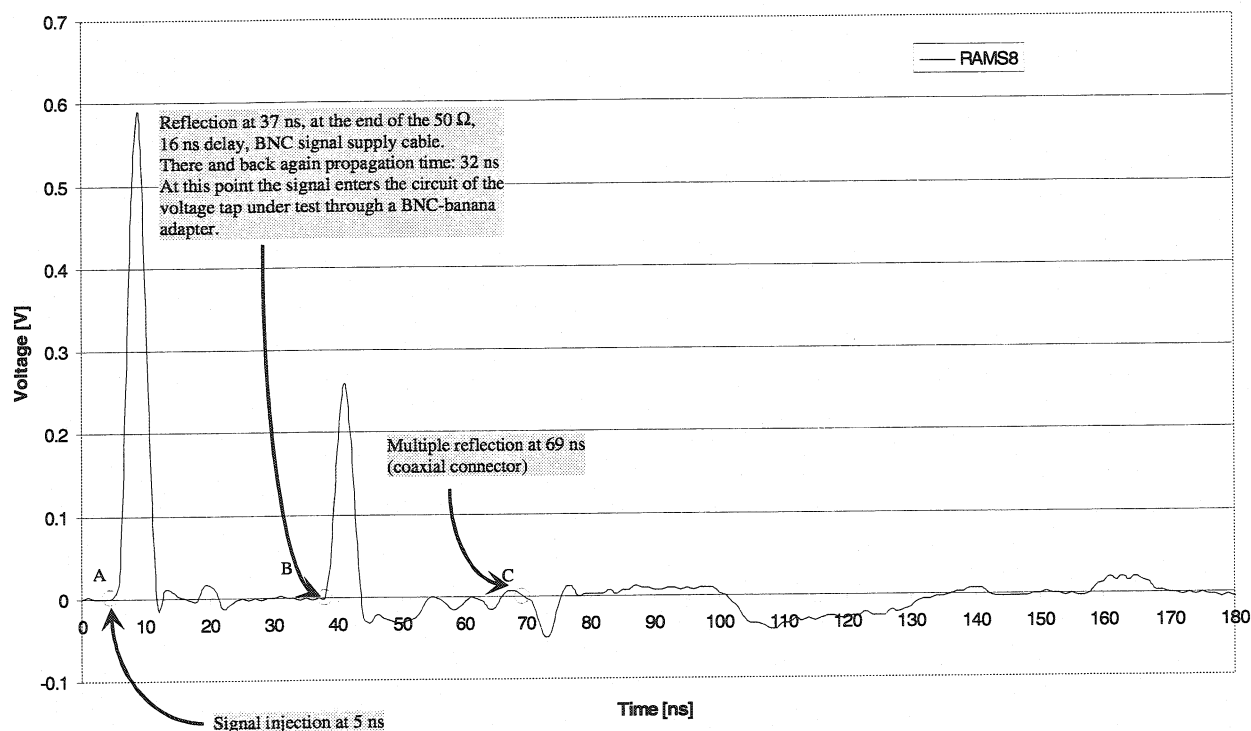


Figure 4.22 Reflection image of the circuits on the RAMS8 connector

Fig. 4.23 shows the reflection image for the circuits on the broken connector RBMS8 with the characteristic reflection from the point of fault at 94 ns (point F). The circuit is thus opened 28.5 ns away from point B on the time scale (57 ns there and back again signal propagation time). With the same assumption concerning an average delay of the cables as for the dipole MB2, the distance from point B to the fault corresponds to about 5.2 m. The reflection appears at the same time for all of the voltage tap circuits on the faulty connector. This implies that the entire inter-connector outlet common to all of the voltage taps in question is broken. Fig. 4.24 is a comparative plot of both curves with the coaxial cable background.

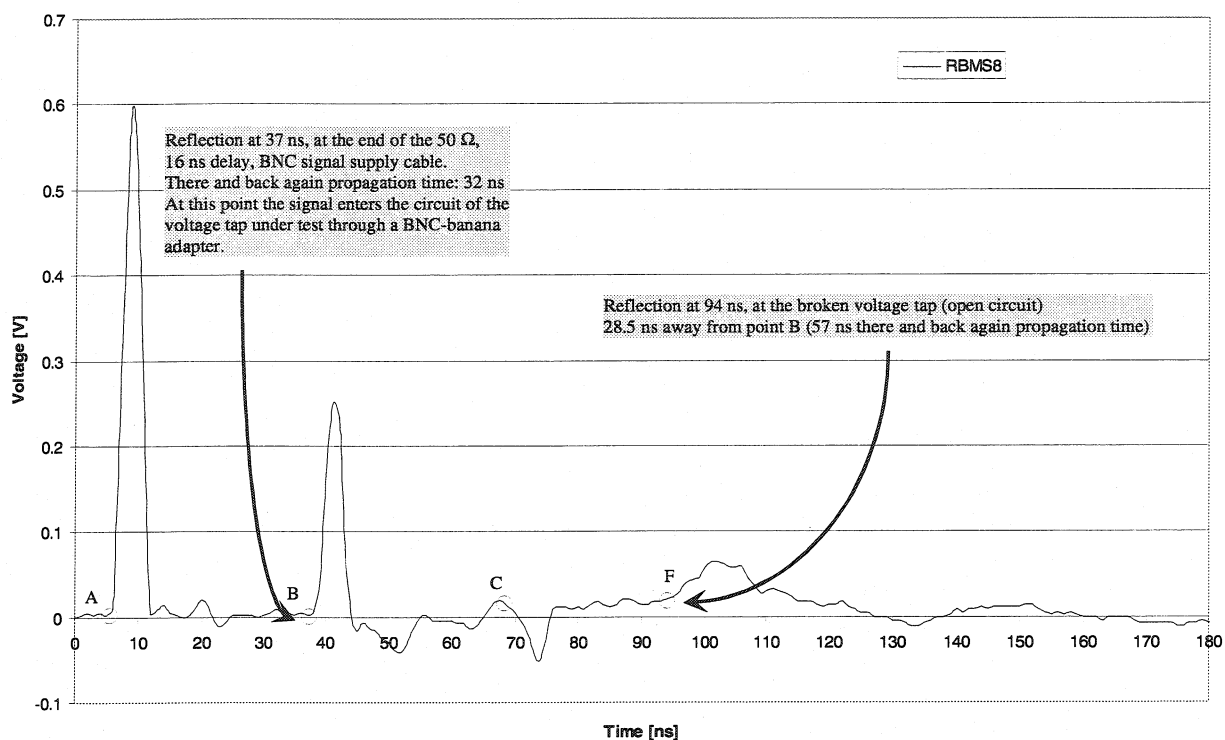


Figure 4.23 Reflection image of the circuits on the RBMS8 connector

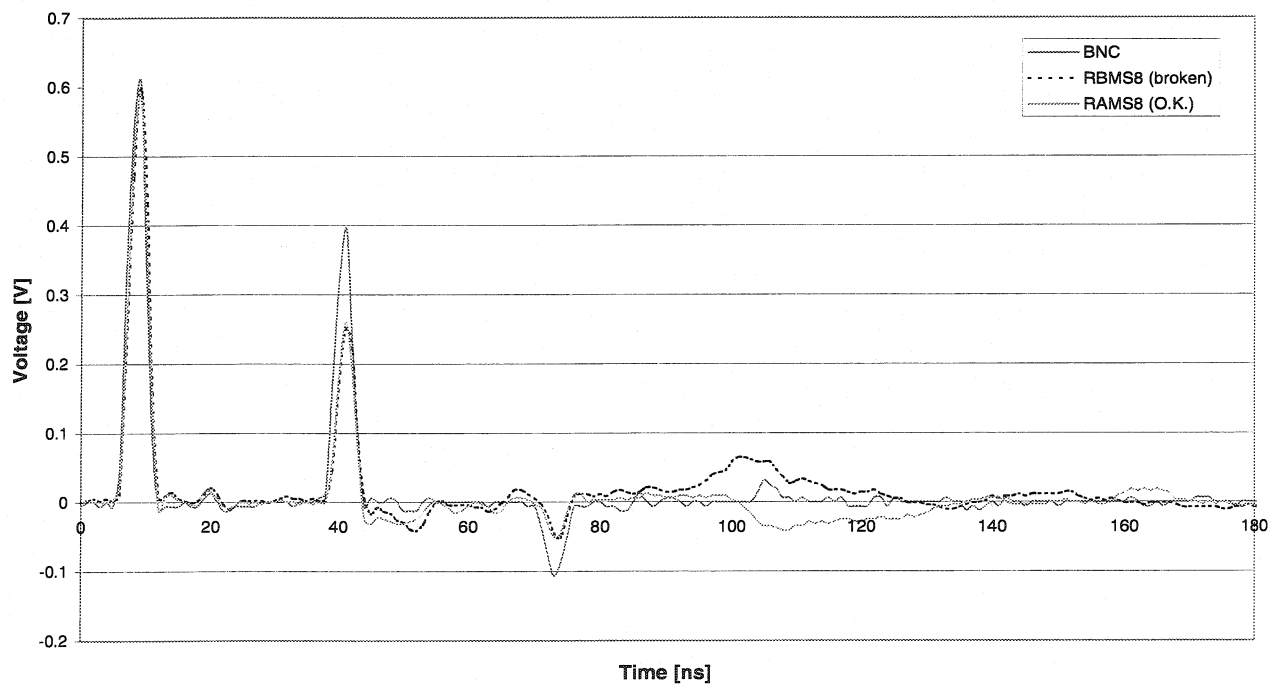


Figure 4.24 SSS Quadrupole TDR results

4.5.2 Temperature Transducer Circuit

The experimental setup used for the detection and localization of the broken connections in the temperature and pressure transducer circuits of the MB2 dipole magnet is shown in Fig. 4.25. The main difference in comparison to the setup presented in Fig. 4.15 is a 3.1-m long Fischer adapter cable inserted before the Fischer connector on the input flange of the magnet.

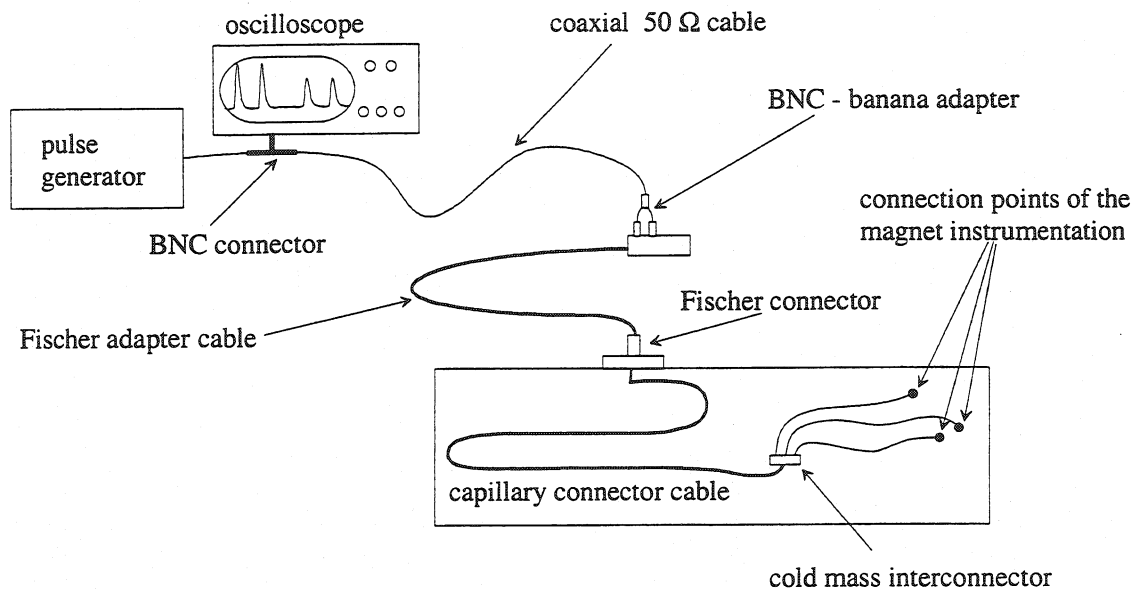


Figure 4.25 Experimental setup for detection of faults in the temperature and pressure transducers

The adapter cable provides convenient mapping of the input outlet pins to the corresponding pin numbers on the Fischer connector. For the finite impulse method a coaxial cable of 4 ns delay was used as the signal supply part of the circuit preceding the Fischer adapter cable. For the fast step TDR a 16 ns delay cable was applied in this place and the pulse generator was replaced by an analog time domain reflectometer. The transition between the coaxial cable and the Fischer adapter cable is done with a BNC-banana adapter. The geometry of the capillary guide described already in the previous section does not change for the temperature and pressure transducers. The background reflection images of the signal supply cables separated from the test circuit are shown in Fig. 4.26-4.31.

In fast step TDR an initial step of less than 1 ns rise time was applied to the cables. Fig. 4.26 and 4.27 show the open and short circuit images of the coaxial cable. The marker points on the plots are underlined to indicate that they do not correspond to the points marked with the same letters as in the voltage tap measurements plots. Point A denotes the injection of the incident 300 mV voltage step at 12 ns. Point B corresponds to the end of the 16 ns delay coaxial cable. In Fig. 4.27 a short-circuit termination was realized by connecting

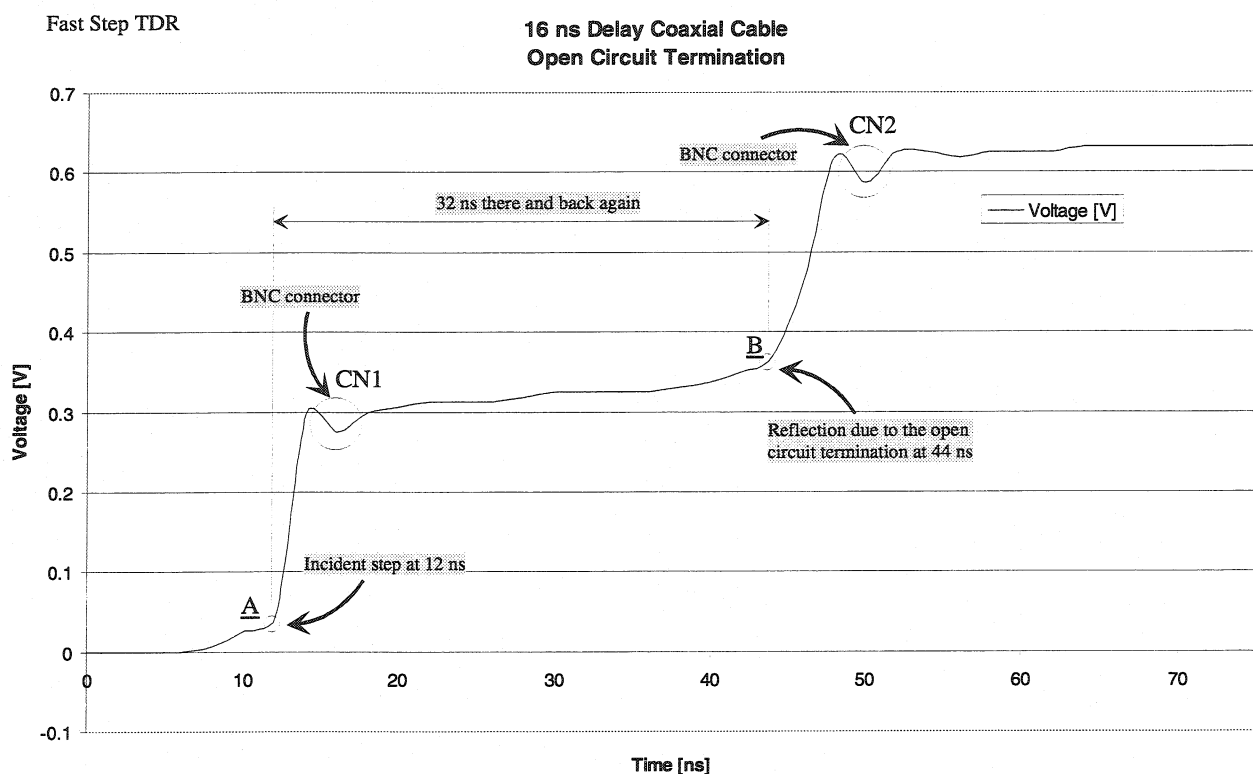


Figure 4.26 Fast step TDR reflection image of the coaxial cable with open circuit termination

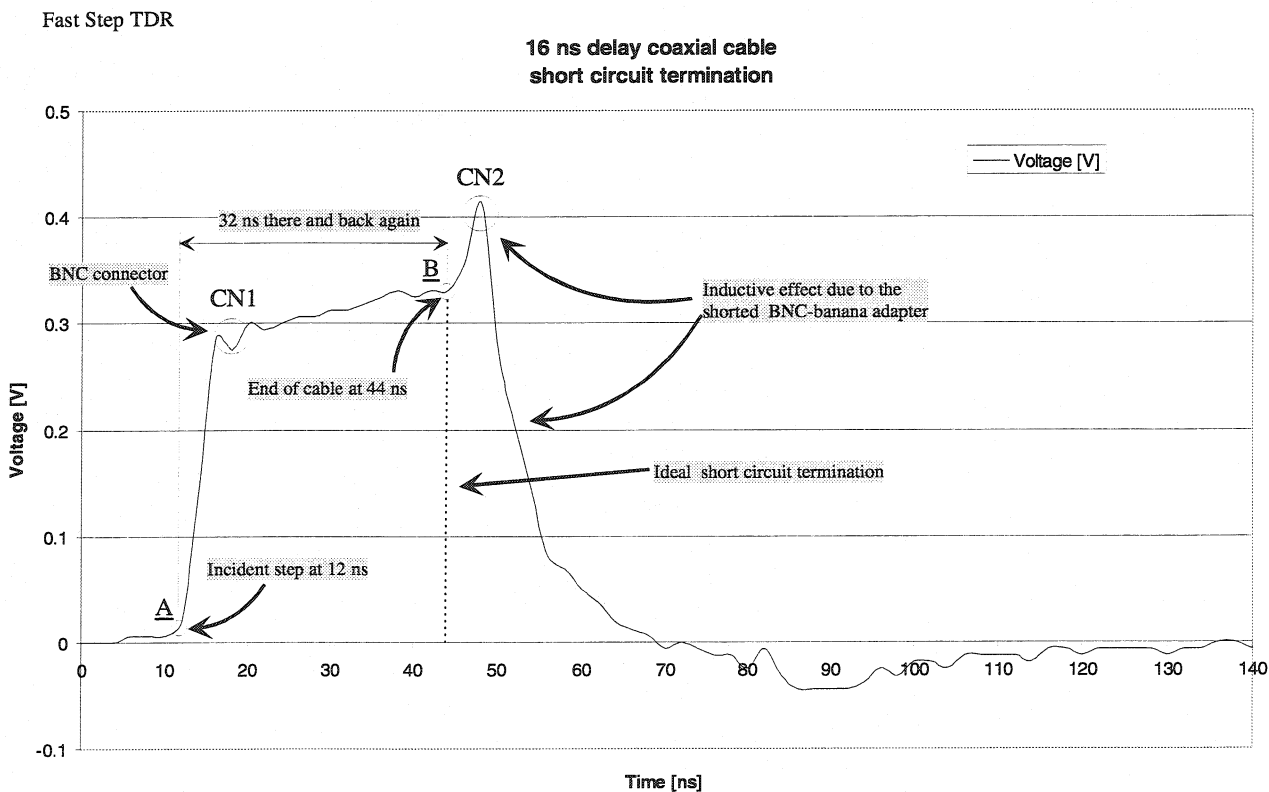


Figure 4.27 Fast step TDR reflection image of the coaxial cable with short-circuit termination

both cable ends of the BNC-banana connector. This created an inductive reflection, described in details in Appendix C at the end of this chapter, characteristic to the termination of the line with a small inductor. An ideal short circuit pattern is marked with a dashed line.

Fig. 4.28 and 4.29 show the reflection images of the coaxial and Fischer adapter cables connected together. At the junction at 44 ns (point B) a transition from a matched coaxial line to a non-coaxial line with different characteristic impedance takes place. The reflection at this point is positive – the reflected wave has the same polarity as the incident step. This implies that the Fischer adapter cable has higher characteristic impedance than the coaxial cable. The reflection coefficient read out from the plot is about 0.3. Knowing the impedance of the coaxial cable used ($50\ \Omega$) one can calculate approximate value of characteristic impedance of the Fischer adapter line. It amounts approximately to $93\ \Omega$. The formal treatment of the transitions between two different transmission lines is presented in Appendix D. The reflection at 78 ns (point C) indicates the end of the 3.1 m long Fischer adapter cable. The voltage wave travels from the BNC-banana adapter (point B) to the end of the Fischer adapter cable (point C) and back again in 34 ns. Thus it takes 17 ns for the wave to pass through the entire cable. This results in a delay of 5.5 ns per meter. Since the cable used in the Fischer adapter line is similar to the cable used in the instrumentation circuits inside the magnet this value is used for the distance calculations throughout this paper. The short circuit at the end of the Fischer adapter line was realized by shorting directly the pins on the Fischer connector, and the inductive effect visible for the BNC-banana connector in Fig. 4.27 is not present on the plot in Fig. 4.29. Due to the mismatch between the Fischer line and the coaxial cable the multiple reflections are visible on the plots. A returning wave reflected at the end of the Fischer line is partially reflected on its way back at the junction with the coaxial cable and redirected again towards the end of the Fischer line. As it is seen in Figs. 4.28 and 4.29 after a couple of such oscillations the magnitude of the multiple reflections approaches zero. The ideal responses of the system if the Fischer line were matched with the coaxial cable are plotted with a dashed line.

The equivalent plots are shown for the finite impulse method in Figs. 4.30 - 4.31. The marker points for these series of plots are in italics. The input signal is 300 mV rectangular pulse 2 ns wide with 1 ns leading and trailing edges. Fig. 4.30 shows the reflection image of the 4 ns-delay coaxial cable with an open-end termination. The injection of the signal takes place at 4 ns (point *A*) and the principal reflection at 12 ns (point *B*). This verifies the delay of the cable to be 4 ns. Points *C* and *D* denote multiple reflections.

Fast Step TDR

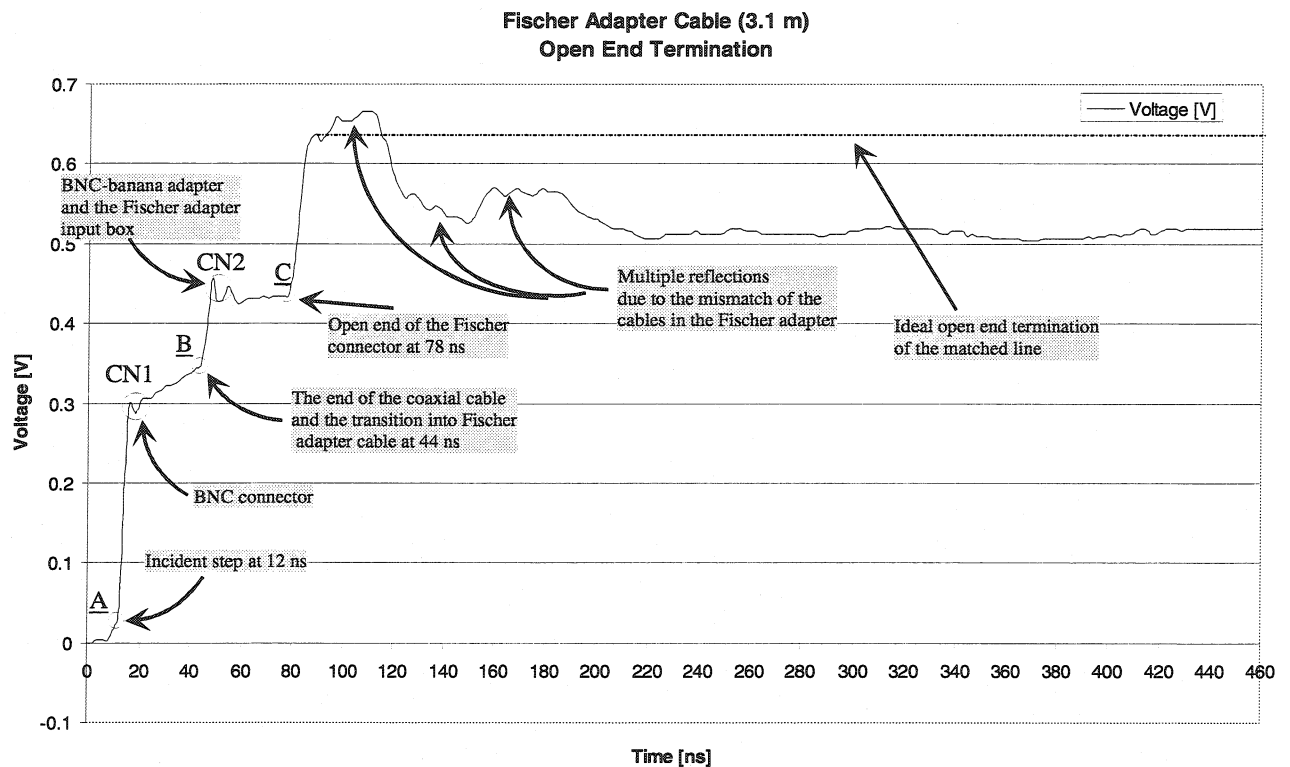


Figure 4.28 Open-end termination of the Fischer adapter cable

Fast Step TDR

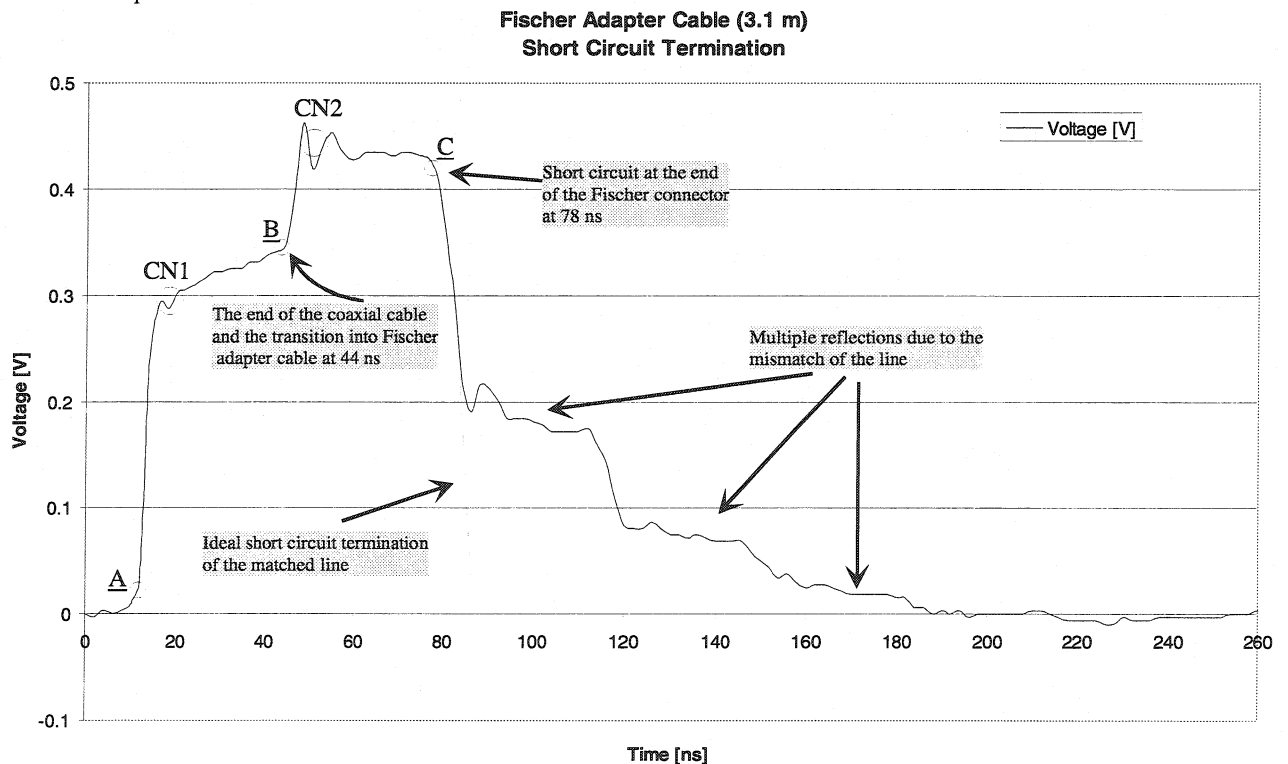


Figure 4.29 Short-circuit termination of the Fischer adapter cable

The reflection images of this cable connected with the Fischer adapter cable, both for open and short circuit terminations, are plotted in Figs. 4.31 and 4.32. Point *E* at 46 ns corresponds to the end of the Fischer line. The method cross checks the result of the fast step TDR as far as the delay of the Fischer adapter cable is concerned.

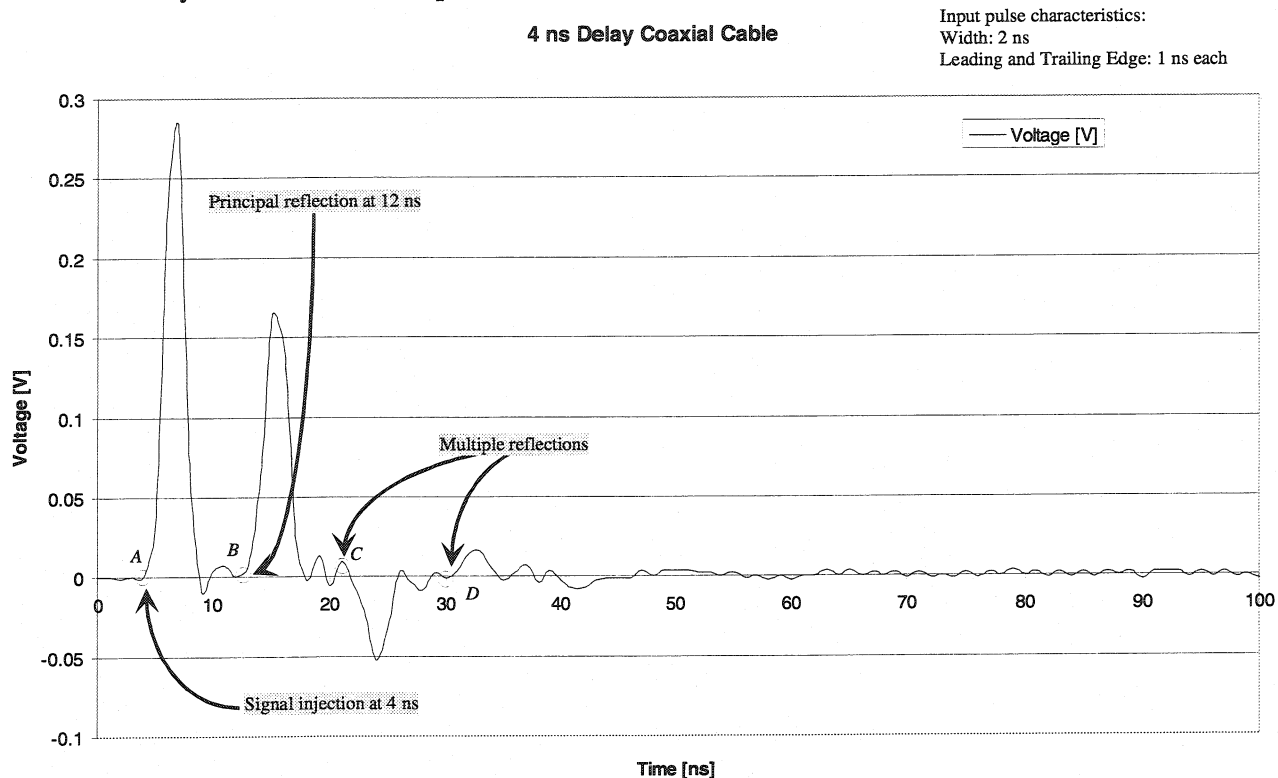


Figure 4.30 Open-end termination of the 4 ns-delay coaxial cable

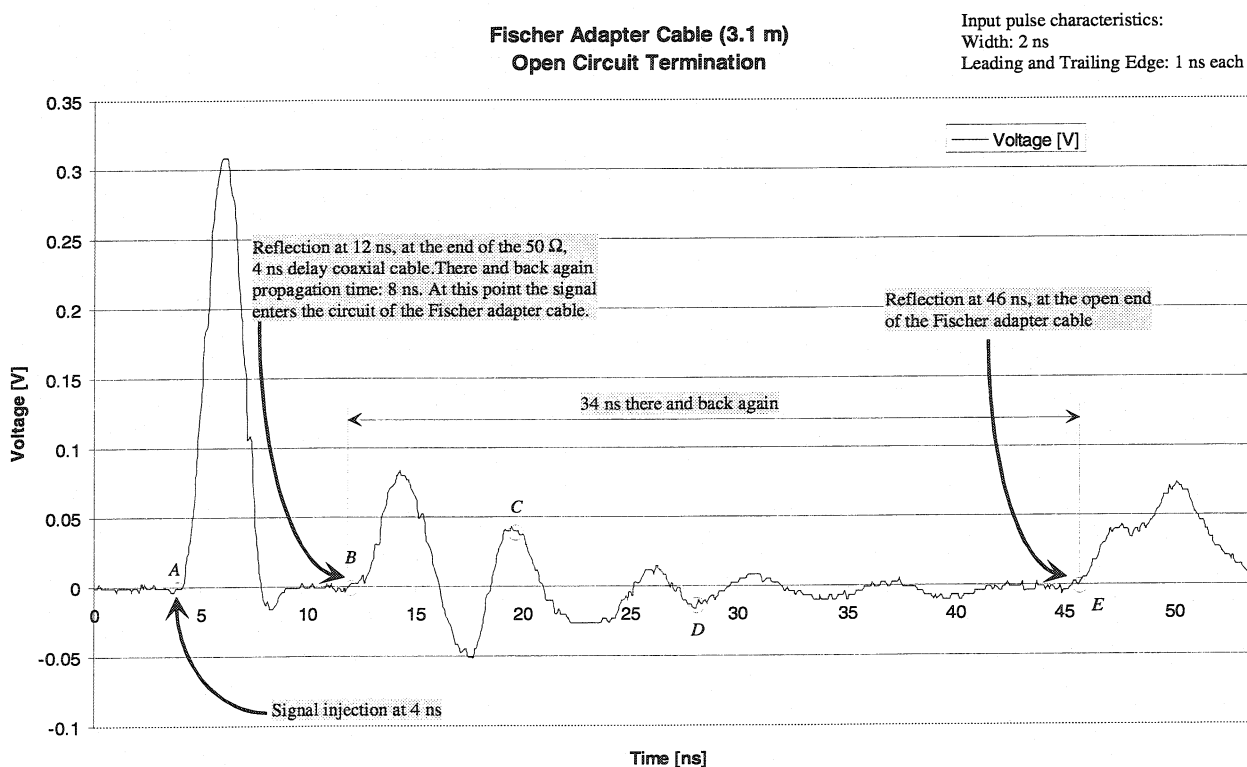


Figure 4.31 Open-end termination of the Fischer adapter cable

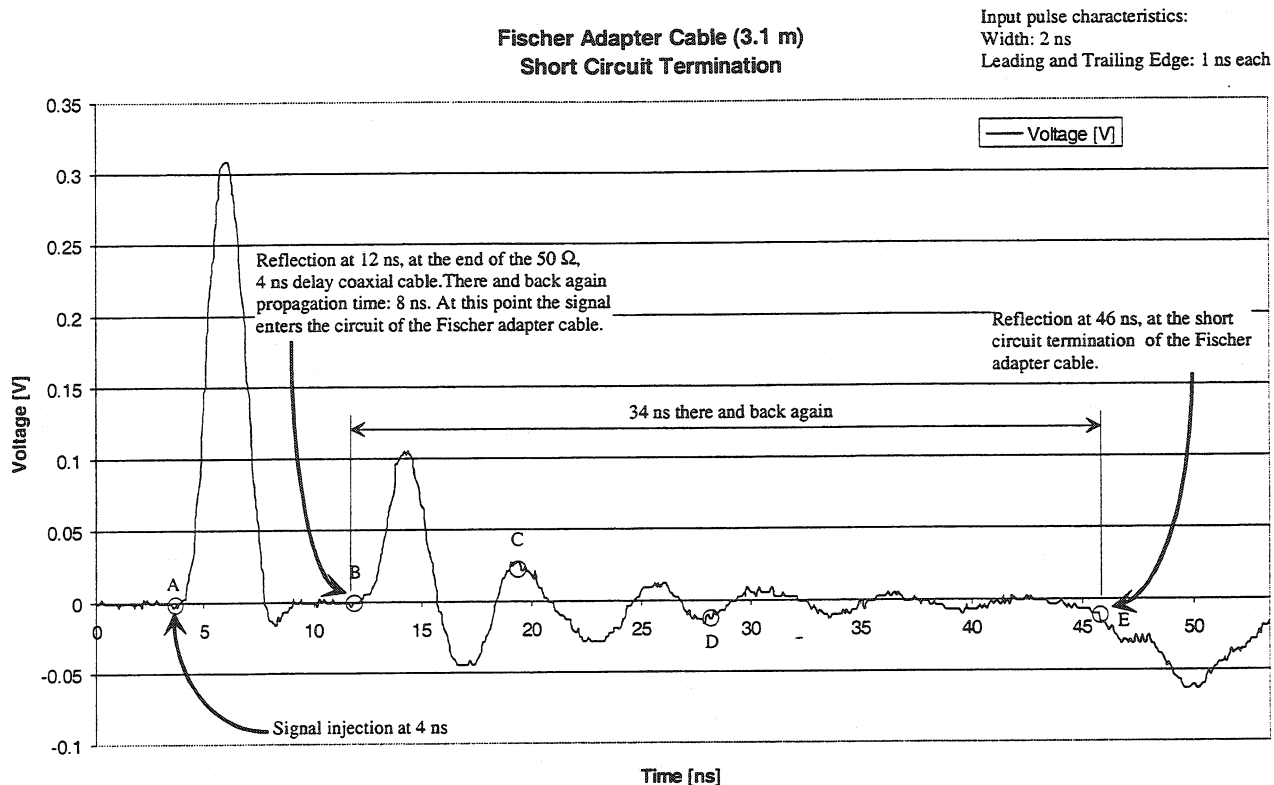
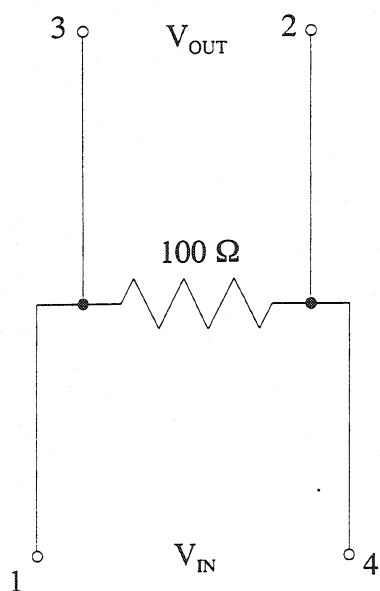


Figure 4.32 Short circuit termination of the Fischer adapter cable

A schematic layout of the temperature sensing carbon resistor is shown in Fig. 4.33. The sensor is located on the RAMS40 Fischer connector between pins 1-4. Pins 1 and 4 are used



for the power supply, and pins 2 and 3 for the temperature readout. The resistance of the sensor is 100 Ω. Preliminary resistance verification performed with a digital voltmeter gave the following results:

Pin No.	Resistance [Ω]
1-2	Open circuit
2-3	102
3-4	102
2-4	2.7
1-3	Open circuit
1-4	Open circuit

Figure 4.33 Temperature transducer

The resistance between pins 1-2 and 1-4 should normally indicate 102 Ω whereas pins 1 and 3 should be in low-ohmic contact. The preliminary measurement implies that the loss of contact appears somewhere along the cable connected to pin 1.

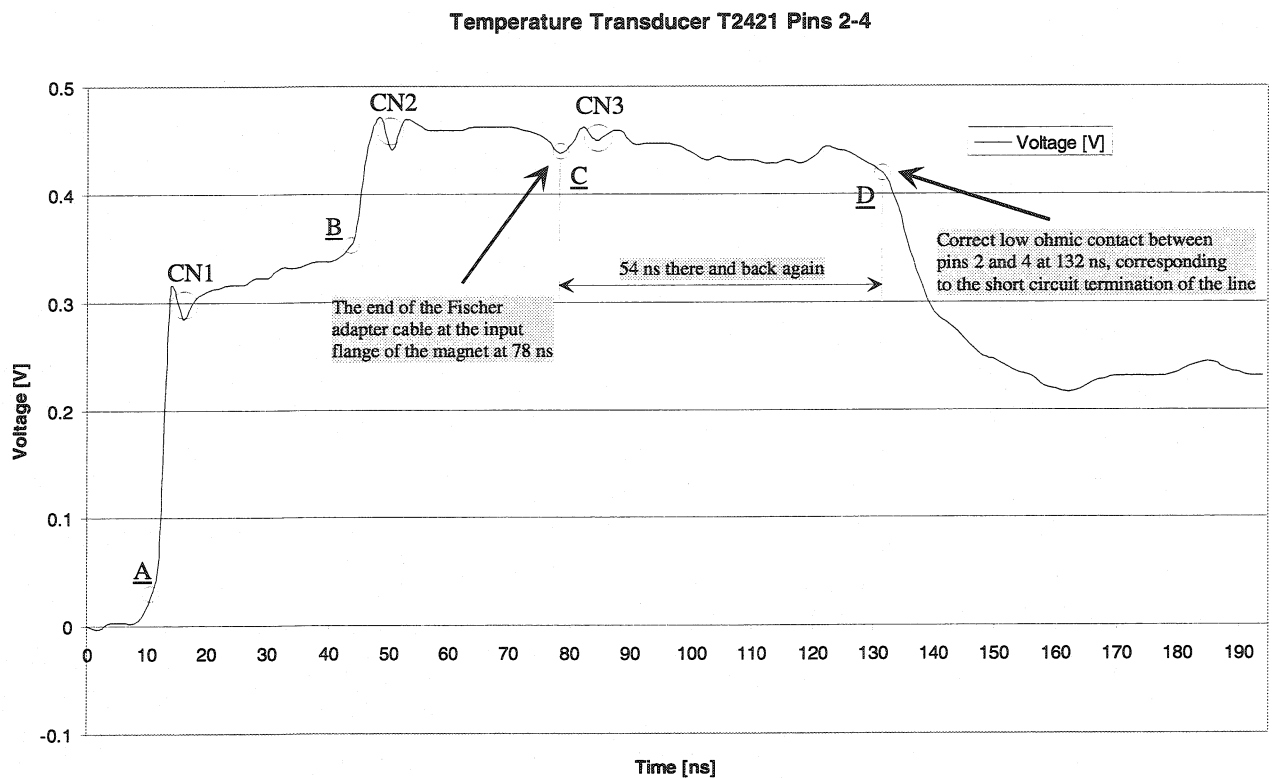


Figure 4.34 TDR image of the temperature sensing carbon resistor circuit – pins 2 - 4

Fig. 4.34 shows a correct fast step response of the circuit between pins 2 and 4. Since both pins are in contact the reflection image resembles the one of the short-circuit termination of the line. The reflection with the change of polarity occurs at point D, i.e. 27 ns away from the

Fast Step TDR

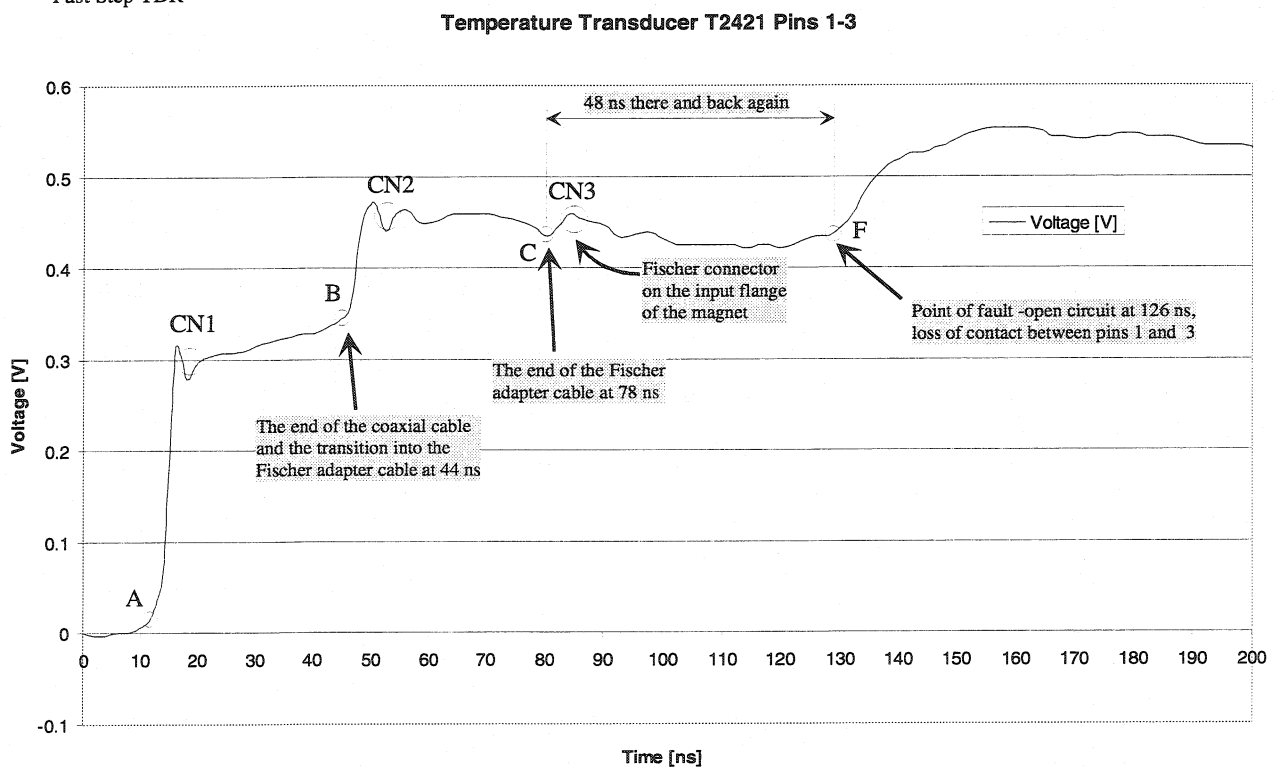


Figure 4.35 Fault detection in the circuit of temperature sensing carbon resistor – pins 1- 3

input flange of the magnet (point C) on the time scale (54 ns there and back again propagation time). This corresponds to a distance of about 4.9 m as measured from the Fischer connector at the input plug of the magnet. The reflection from the Fischer connector is denoted as CN3. On both sides of the connector the level of the signal remains virtually the same, which indicates that the transition takes place between two lines with almost the same characteristic impedance.

The same measurement carried out for the incident step launched between pins 1 and 3 gives the result presented in Fig. 4.36. Instead of a negative reflection a positive one occurs at 126 ns (point E) 24 ns away from point C (48 ns there and back again propagation time). This corresponds to 4.36 m distance measured from the input flange of the magnet and implies that the fault occurs at the inter-connector at the transition to the cold mass of the magnet. The results of the measurements with the finite impulse are gathered in Fig. 4.37 and 4.38. In Fig. 4.38 the input connector of the magnet (point E) and the point of fault (F) are separated by 24.5 ns (49 ns there and back again propagation time) which corresponds to the distance of 4.45 m. Half a nanosecond difference between the fast step TDR and finite pulse approach results in 9 cm difference in distance between both methods.

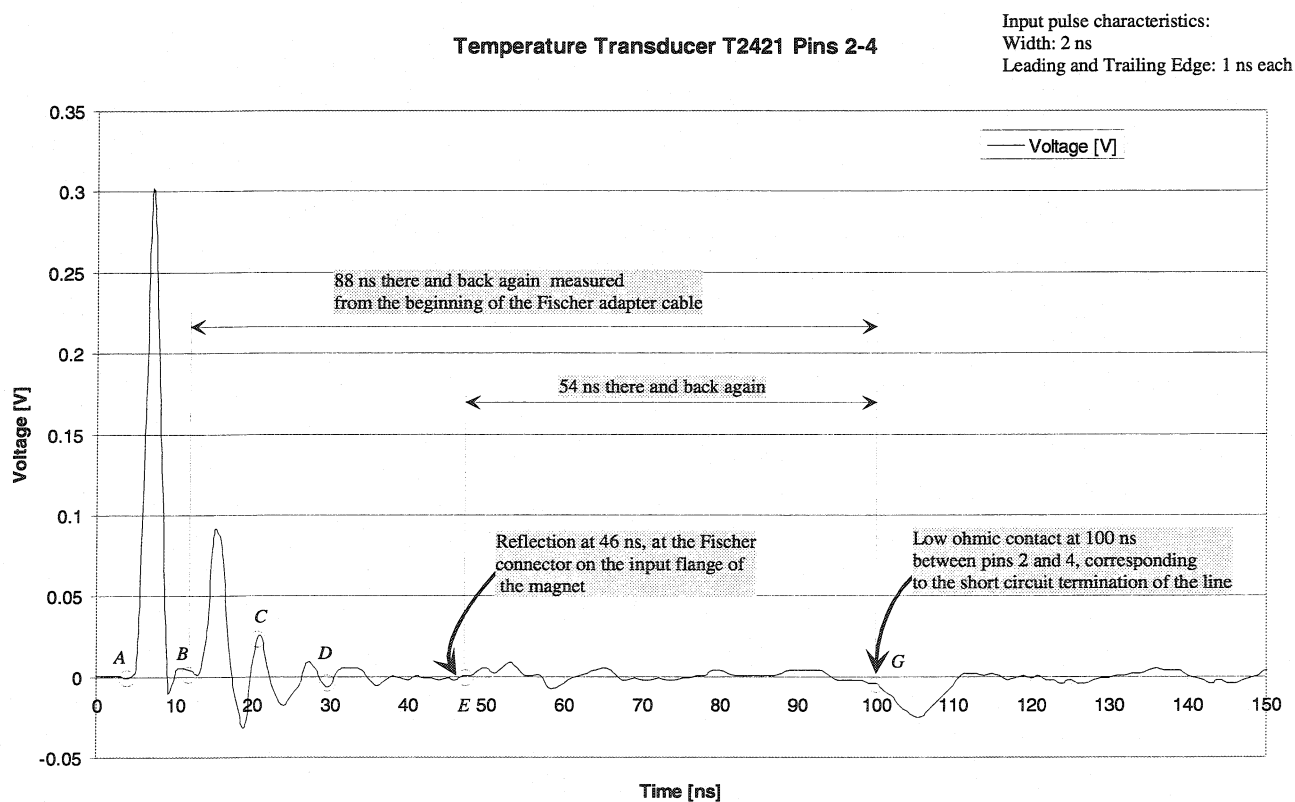


Figure 4.37 Low ohmic contact between pins 2 and 4

Temperature Transducer T2421 Pins 1-3

Input pulse characteristics:
Width: 2 ns
Leading and Trailing Edge: 1 ns each

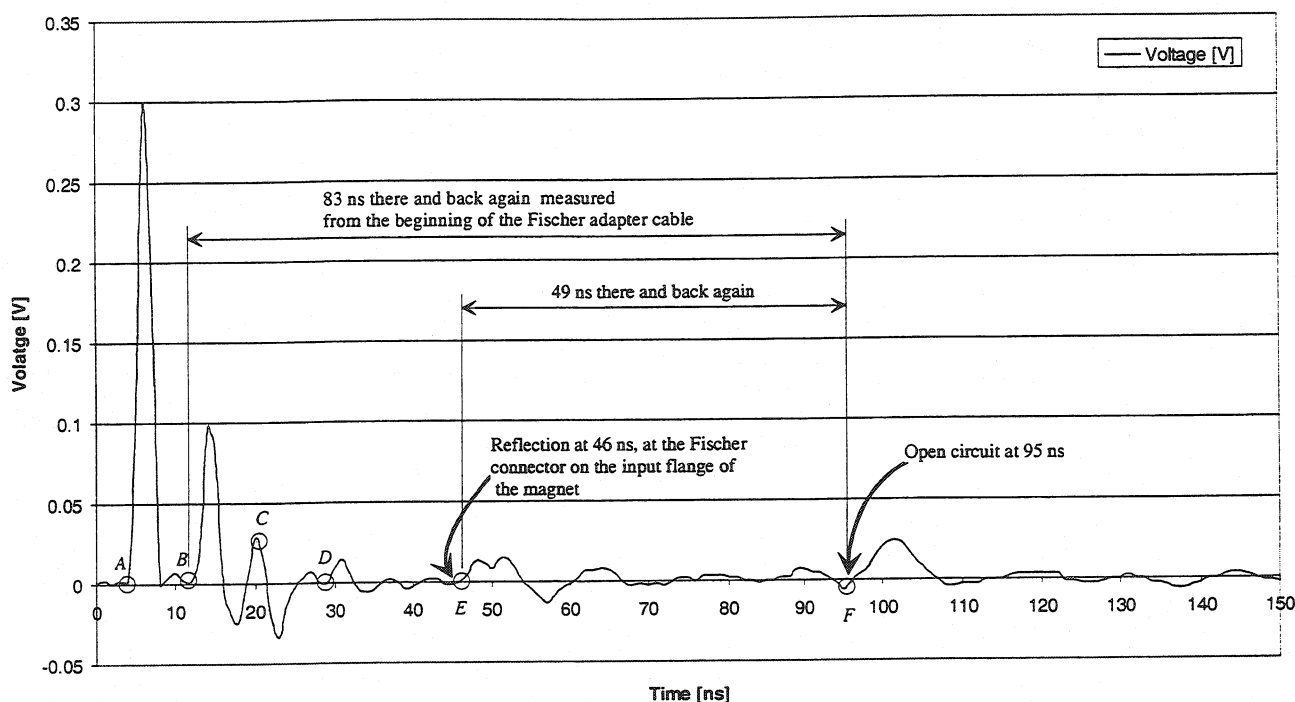


Figure 4.38 Loss of contact between pins 1 and 3

4.5.3 Pressure Transducer Circuit

A schematic layout of the pressure transducer bridge installed in the magnet is shown in Fig. 4.39. The sensor is located on the RAMS40 Fischer connector between pins 17-20. Power

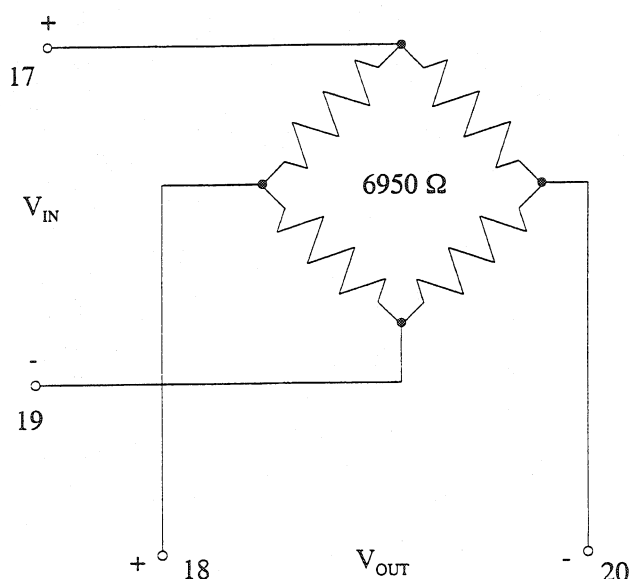


Figure 4.39 Pressure transducer

supply circuit is located between pins 17 and 19. Pins 18 and 20 are used for the pressure readout. The resistance of the operational bridge measured between pins 18 and 20 should read 6950 Ω. Preliminary resistance checks performed with a digital voltmeter indicated open circuit between any two pins of the circuit, which implies a complete loss of contact between the input pins and the resistors of the bridge. The results of the TDR measurements are shown in Fig. 4.40 and 4.41.

Pressure Transducer P2411 Pins 18-20

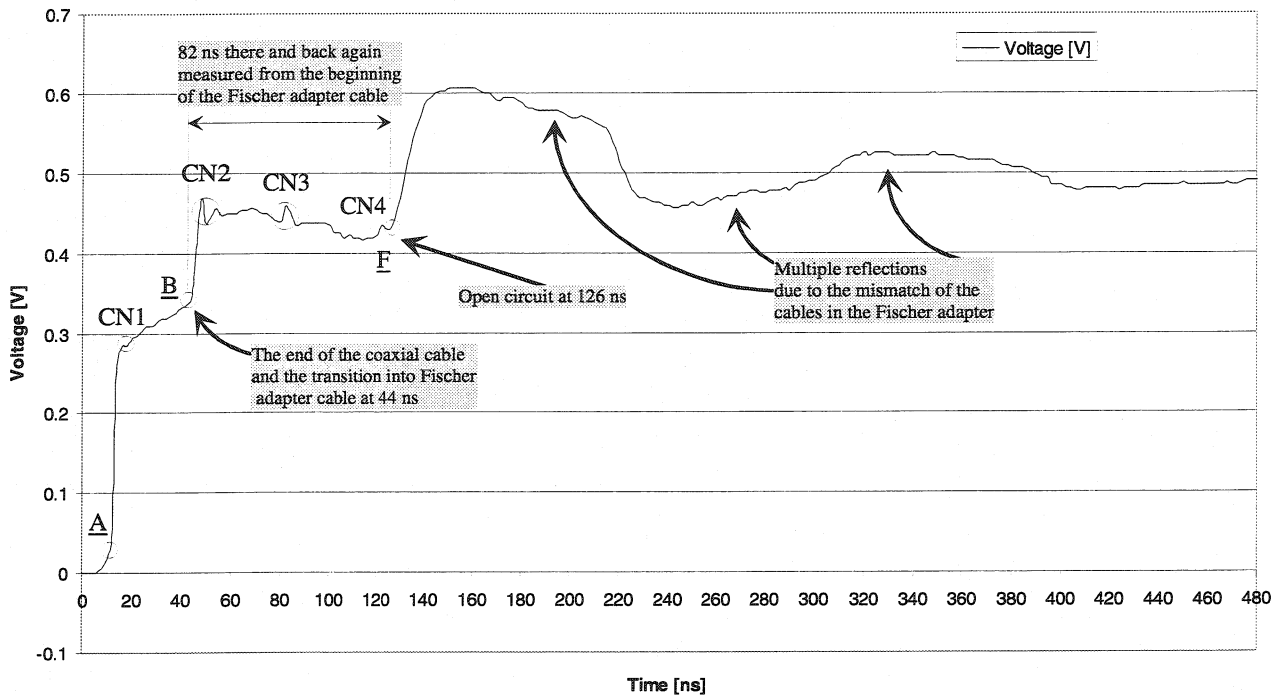


Figure 4.40 Loss of contact in the pressure transducer circuit

Pressure Transducer P2411 Pins 17-18, 19-20

Input pulse characteristics:
Width: 2 ns
Leading and Trailing Edge: 1 ns each

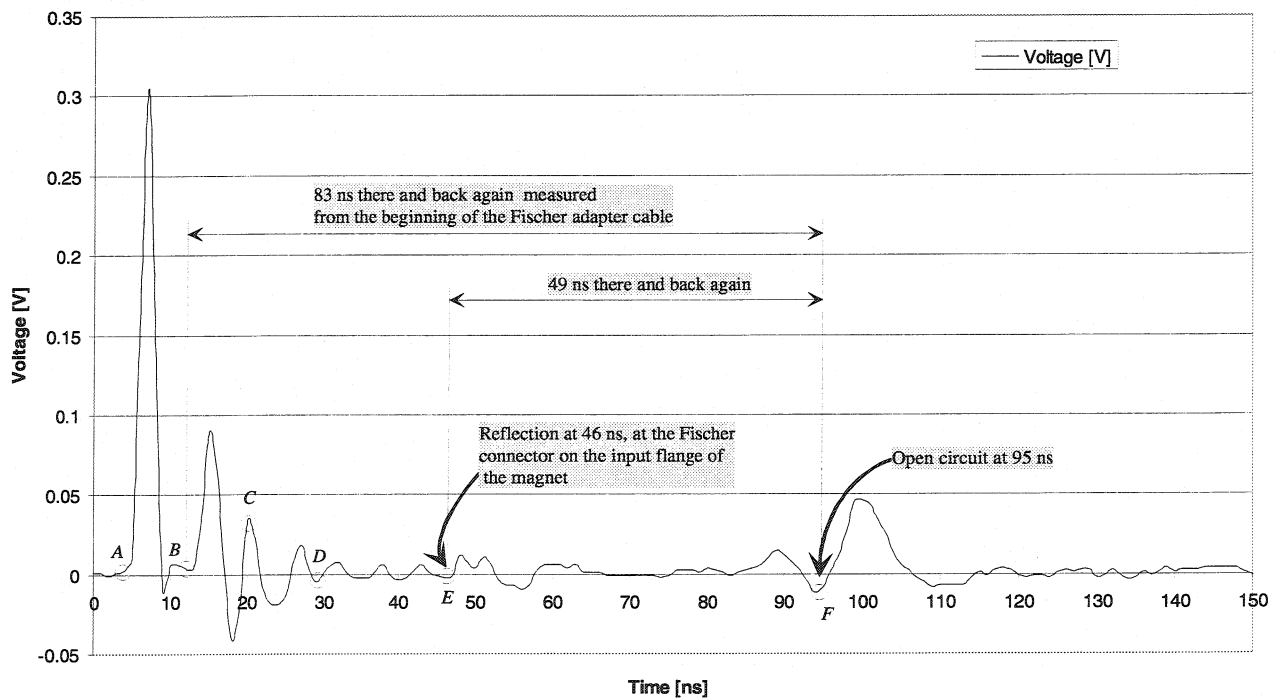


Figure 4.41 Loss of contact in the pressure transducer circuit

An open circuit occurs here exactly at the same distance as in the case of the fault localized on the temperature transducer, i.e. most probably on the inter-connector at the end of the capillary guide.

4.5.4 Conclusions

The localization of the electrical faults in the instrumentation of the LHC dipole magnets can be successfully carried out with TDR techniques. Both fast step and finite impulse methods gave convergent results and lead to the identification and localization of the fault in the circuits under study. The fast step TDR allows with higher precision to trace the position of the connectors and plugs along the line as well as to identify the transitions between the lines with different characteristic impedance. The effect of the parasite background signal from the coaxial cable can be circumvented either by using a time domain reflectometer capable of sending and registering the signal on the same channel, or by minimizing the length of the auxiliary coaxial cables in the system solution realized with individual pulse generator and oscilloscope. The second option enforces that the detection equipment should be placed as close as possible to the instrumentation circuit plugs.

The knowledge of the transfer functions and the delay times of the cables used as components of the instrumentation circuits is essential for the calibration of the detection equipment and for the analysis and interpretation of the results. These data can be obtained before installation of the instrumentation components in the magnet.

The information concerning the geometry of the circuit inside the magnet, i.e., the layouts and descriptions of: corresponding cable lengths, types, and cross-sections, positions of inter-connectors, common plugs and outlets, characterization of the media being traversed by the cables (resin, vacuum, proximity to magnetic and non-magnetic materials), exact location of the cable connections and routing in the cold mass of the magnet (along the section beginning with the inter-connector at the end of the capillary up to the taps on the superconducting coils.) would essentially facilitate the identification of the features on the reflection images.

Sometimes this knowledge is essential in order to avoid misinterpretation of the results. For example sending a signal between pins 2 and 4 of the temperature transducer circuit results virtually in no reflections observed at the end of the line. It turns out that the characteristic impedance of the thermocouple circuit is close to $100\ \Omega$ and coincides with the resistance of the temperature gage. Thus the differential injection of the input signal between

both pins gives an effect of impedance matching at the end of the line terminated with the temperature sensing carbon resistance. Thus ignoring the parameters of the circuit under test may cause a deviation from the correct diagnosis.

To additionally improve the quality of signal launching into single line unshielded copper cables the voltage tap lines running in the capillary could be clustered within a common shielded multi strand cable.

The résumé of the work discussed in this chapter was presented and published as an LHC Project Note [6].

Appendix A. Operational Calculus Approach to the Distributed Line Problem

Since in the pulse reflection methods the device under test is excited either with the impulse or with the fast step it is necessary to analyze the transient states of the line. Therefore it is convenient to apply the operational calculus. The basics of the distributed line theory in the Laplace transform formalism are introduced below. A comprehensive coverage of the Laplace transform properties and operational calculus can be found, e.g. in the references [7] and [8].

• Distributed line and the Laplace transform

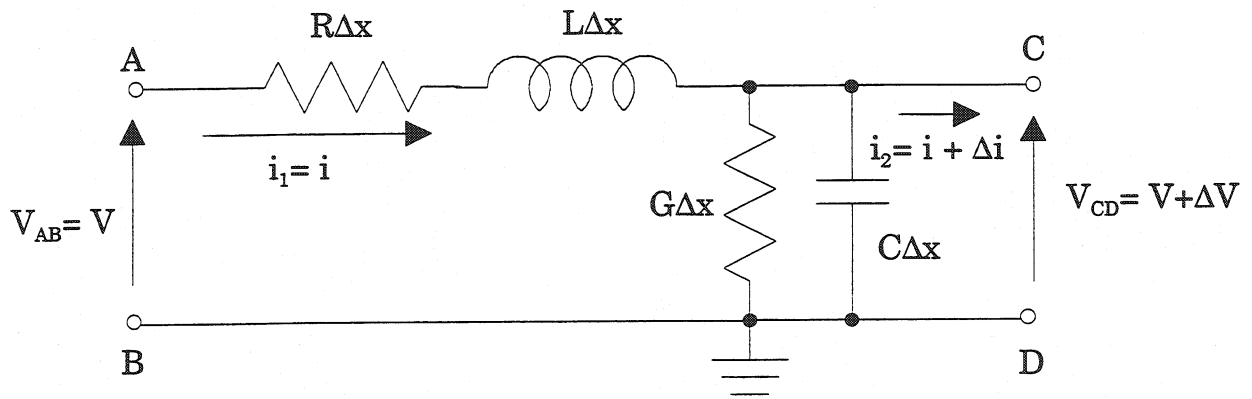


Figure A.1. A segment of a distributed line

The Kirchhoff's equations for the element of the network presented in Fig. A.1 are as follows:

- for the voltages

$$V_{AB} - R\Delta x i - L\Delta x \frac{\partial i}{\partial t} = V_{CD}$$

$$\Delta V = V_{CD} - V_{AB} = -R\Delta x i - L\Delta x \frac{\partial i}{\partial t} \quad (\text{A.1})$$

- for the currents

$$i_1 - G\Delta x V_{CD} - C\Delta x \frac{\partial V_{CD}}{\partial t} = i_2$$

$$\Delta i = i_2 - i_1 = -G\Delta x (V + \Delta V) - C\Delta x \frac{\partial (V + \Delta V)}{\partial t} \quad (\text{A.2})$$

In the limit for $\Delta x \rightarrow 0$ a set of two partial differential equations is obtained from Eqs. (A.1) and (A.2).

$$\lim_{\Delta x \rightarrow 0} \frac{\Delta V}{\Delta x} = \frac{\partial V}{\partial x} = -Ri - L \frac{\partial i}{\partial t} \quad (\text{A.3})$$

$$\lim_{\Delta x \rightarrow 0} \frac{\Delta i}{\Delta x} = \frac{\partial i}{\partial x} = -GV - C \frac{\partial V}{\partial t} \quad (\text{A.4})$$

The resistance, conductance, self-inductance and capacitance are the parameters given per unit length of the line. The Laplace transforms of the quantities present in Eqs. (A.3) and (A.4) for the zero initial conditions are listed below:

$$\mathcal{L}(V(x, t)) = \mathcal{V}(x, s) = \int_0^{\infty} e^{-st} V(x, t) dt$$

$$\mathcal{L}\left(\frac{\partial V(x, t)}{\partial t}\right) = s\mathcal{V}(x, s)$$

$$\mathcal{L}\left(\frac{\partial V(x, t)}{\partial x}\right) = \int_0^{\infty} e^{-st} \frac{\partial V(x, t)}{\partial x} dt = \frac{\partial}{\partial x} \int_0^{\infty} e^{-st} V(x, t) dt = \frac{\partial}{\partial x} \mathcal{V}(x, s)$$

By analogy the same applies to the corresponding transforms for the current. The form of the line equations in the operational representation is then

$$\frac{\partial \mathcal{V}}{\partial x} = (-R - Ls)I \quad (\text{A.5})$$

$$\frac{\partial I}{\partial x} = (-G - Cs)\mathcal{V} \quad (\text{A.6})$$

After the substitution of Eq. (A.6) into Eq. (A.5) differentiated with respect to x , the following second order partial differential equation is obtained:

$$\frac{\partial^2 \mathcal{V}}{\partial x^2} = (-R - Ls) \frac{\partial I}{\partial x} = (R + Ls)(G + Cs)\mathcal{V} \quad (\text{A.7})$$

The entire term in front of the voltage operator in this equation is denoted as the propagation function:

$$\gamma = \sqrt{(R + Ls)(G + Cs)} \quad (\text{A.8})$$

Then the equation (A.8) can be rewritten in the form,

$$\frac{\partial^2 \mathcal{V}}{\partial x^2} - \gamma^2 \mathcal{V} = 0 \quad (\text{A.9})$$

which is the equation of the voltage wave propagation in the line. In the same way a similar equation can be derived for the current operator. The general solution of the differential equation for the voltage is

$$\mathcal{V}(x, s) = \mathcal{V}_1(s)e^{-\gamma x} + \mathcal{V}_2(s)e^{\gamma x} \quad (\text{A.10})$$

Its first derivative with respect to x is

$$\frac{\partial \mathcal{V}}{\partial x} = -\gamma(\mathcal{V}_1(s)e^{-\gamma x} - \mathcal{V}_2(s)e^{\gamma x}) \quad (\text{A.11})$$

After the substitution of this derivative into Eq. (A.5) the formula for current is obtained.

$$I(x, s) = \frac{\gamma}{R + Ls} (\mathcal{V}_1(s)e^{-\gamma x} - \mathcal{V}_2(s)e^{\gamma x}) = \sqrt{\frac{G + Cs}{R + Ls}} (\mathcal{V}_1(s)e^{-\gamma x} - \mathcal{V}_2(s)e^{\gamma x}) \quad (\text{A.12})$$

$Z_C(s)$ defined as,

$$Z_C(s) = \sqrt{\frac{R + Ls}{G + Cs}} \quad (\text{A.13})$$

is a characteristic impedance of the line.

In order to determine the functions \mathcal{V}_1 and \mathcal{V}_2 the conditions at the beginning and at the end of the line must be considered (Fig. A.1)

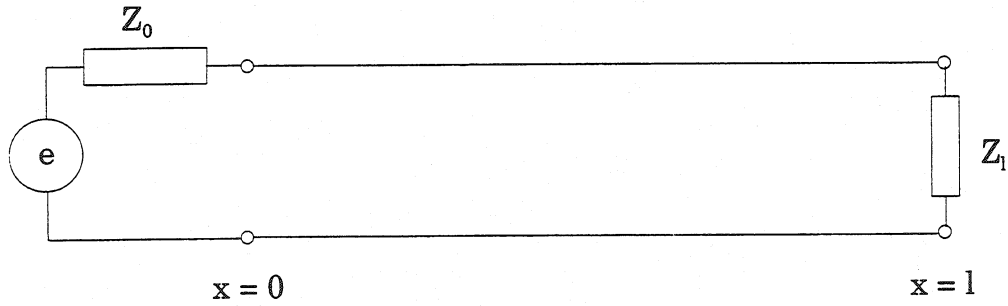


Figure A.1 Line excited by the voltage generator

Let us assume that the line is excited with the voltage generator producing the electromotive force $e(t)$. Then for the beginning of the line (for $x = 0$) the following Kirchhoff relation holds:

$$\mathcal{E}(s) - Z_0 I(0, s) - \mathcal{V}(0, s) = 0 \quad (\text{A.14})$$

Using the relations (A.10) and (A.12) the equation (A.14) becomes

$$\mathcal{E}(s) = Z_0 \frac{1}{Z} (\mathcal{V}_1 - \mathcal{V}_2) + (\mathcal{V}_1 + \mathcal{V}_2)$$

which after several transformations can be expressed conveniently expressed as

$$\mathcal{V}_1 - r_i \mathcal{V}_2 = \frac{Z_C}{Z_0 + Z_C} \mathcal{E}(s) \quad (\text{A.15})$$

where

$$r_i = \frac{Z_0 - Z_C}{Z_0 + Z_C} \quad (\text{A.16})$$

is the voltage reflection coefficient at the input of the line. At the end of the line of length l the following relation is satisfied:

$$Z_l = \frac{V(l, s)}{I(l, s)} = Z_c \frac{V_1 e^{-\gamma l} + V_2 e^{\gamma l}}{V_1 e^{-\gamma l} - V_2 e^{\gamma l}} \quad (\text{A.17})$$

After several transformations it can be rewritten as,

$$V_1 e^{-\gamma l} r_e = V_2 e^{\gamma l} \quad (\text{A.18})$$

where,

$$r_e = \frac{Z_l - Z_c}{Z_l + Z_c} \quad (\text{A.19})$$

is the voltage reflection coefficient at the end of the line.

From the two conditions for the beginning (A.15) and for the end of the line (A.18) the form of the functions V_1 and V_2 can be calculated.

$$V_1 = \mathcal{E}(s) \frac{Z_c}{Z_0 + Z_c} \frac{1}{1 - r_i r_e e^{-2\gamma l}} \quad (\text{A.20})$$

$$V_2 = \mathcal{E}(s) \frac{Z_c}{Z_0 + Z_c} \frac{r_e e^{-2\gamma l}}{1 - r_i r_e e^{-2\gamma l}} \quad (\text{A.21})$$

Thus the final solutions are:

$$V(x, s) = \mathcal{E}(s) \frac{Z_c}{Z_0 + Z_c} \frac{e^{-\gamma x} + r_e e^{-\gamma(2l-x)}}{1 - r_i r_e e^{-2\gamma l}} \quad (\text{A.22})$$

$$I(x, s) = \mathcal{E}(s) \frac{1}{Z_0 + Z_c} \frac{e^{-\gamma x} - r_e e^{-\gamma(2l-x)}}{1 - r_i r_e e^{-2\gamma l}} \quad (\text{A.23})$$

In order to obtain the inverse Laplace transform of the solution it is convenient to notice that the absolute value of the reflection coefficients is always contained between 0 and 1, and therefore the denominator part of the solutions can be expressed as a geometric series expansion:

$$\frac{1}{1 - r_i r_e e^{-2\gamma l}} = \sum_{n=0}^{\infty} r_i^n r_e^n e^{-2n\gamma l} \quad (\text{A.24})$$

Using this series expansion the final solutions can be rewritten as:

$$V(x, s) = \mathcal{E}(s) \frac{Z_c}{Z_0 + Z_c} (e^{-\gamma x} + r_e e^{-\gamma(2l-x)}) \sum_{n=0}^{\infty} r_i^n r_e^n e^{-2n\gamma l} \quad (\text{A.25})$$

$$I(x, s) = \mathcal{E}(s) \frac{1}{Z_0 + Z_c} (e^{-\gamma x} - r_e e^{-\gamma(2l-x)}) \sum_{n=0}^{\infty} r_i^n r_e^n e^{-2n\gamma l} \quad (\text{A.26})$$

When the line is matched with its characteristic impedance, i.e. when it is terminated with the lumped impedance corresponding to Z_C ($Z_l = Z_C$), then $r_e = 0$ and the formulas (A.25) and (A.26) become

$$\begin{aligned}\mathcal{V}(x, s) &= \mathcal{E}(s) \frac{Z_C}{Z_0 + Z_C} e^{-\gamma x} \\ I(x, s) &= \mathcal{E}(s) \frac{1}{Z_0 + Z_C} e^{-\gamma x}\end{aligned}\quad (\text{A.27})$$

One can see that in this case $\frac{\mathcal{V}(x, s)}{I(x, s)} = Z_C$ at each instant t , and at any point x along the line.

- **Approximation of the lossless line**

The line is considered to be lossless when $R = 0$ and $G = 0$. Under these conditions the propagation factor (A.8) becomes

$$\gamma = s\sqrt{LC} = s\beta_0 \quad (\text{A.28})$$

where $\beta_0 = \sqrt{LC}$ is the propagation constant. The characteristic impedance reduces to a real resistance equal to

$$R_C = \sqrt{\frac{L}{C}} \quad (\text{A.29})$$

The equations for the voltage and current become respectively:

$$\mathcal{V}(x, s) = \mathcal{E}(s) \frac{R_C}{Z_0 + R_C} (e^{-s\beta_0 x} + r_e e^{-s\beta_0(2l-x)}) \sum_{n=0}^{\infty} r_i^n r_e^n e^{-2ns\beta_0 l} \quad (\text{A.30})$$

$$I(x, s) = \mathcal{E}(s) \frac{1}{Z_0 + R_C} (e^{-s\beta_0 x} - r_e e^{-s\beta_0(2l-x)}) \sum_{n=0}^{\infty} r_i^n r_e^n e^{-2ns\beta_0 l} \quad (\text{A.31})$$

For the matched lossless line ($Z_l = R_C$) the voltage reflection coefficient at the end of the line $r_e = 0$ and the equations (A.30) and (A.31) simplify to

$$\begin{aligned}\mathcal{V}(x, s) &= \mathcal{E}(s) \frac{R_C}{Z_0 + R_C} e^{-s\beta_0 x} \\ I(x, s) &= \mathcal{E}(s) \frac{1}{Z_0 + R_C} e^{-s\beta_0 x}\end{aligned}\quad (\text{A.32})$$

The inverse Laplace transform for the voltage yields immediately

$$V(x, t) = V(0, t - \beta_0 x) \cdot u_{-1}(t - \beta_0 x) \quad (\text{A.33})$$

where $V(0, t) = \frac{e(t) \cdot R_c}{Z_0 + R_c}$ is the voltage at the input to the line and $u_{-1}(t)$ is the unit step function. Thus the voltage at any time t and point x along the line corresponds to the voltage at the input of the line ($x = 0$) at time $t - \beta_0 x$. This clearly implies that the wave applied at the input propagates along the line to any point x within the time $\beta_0 x$. Thus $1/\beta_0$ corresponds to the velocity of the propagation of the wave in the line.

$$v = \frac{1}{\beta_0} = \frac{1}{\sqrt{LC}} \quad (\text{A.34})$$

If the dielectric medium of the line is characterized by a relative dielectric constant ϵ_r , the wave propagates along the line with the same velocity as the electromagnetic waves in the medium

$$v = \frac{1}{\beta_0} = \frac{1}{\sqrt{LC}} = \frac{c}{\sqrt{\epsilon_r}} \quad (\text{A.35})$$

where c is the speed of light in vacuum. The per unit length parameters of the line L and C expressed as the functions of β_0 are as follows:

$$\begin{aligned} L &= R_c \beta_0 \\ C &= \frac{\beta_0}{R_c} \end{aligned} \quad (\text{A.36})$$

The total delay, inductance, and capacitance of the line of length l are:

$$\begin{aligned} \tau &= \beta_0 l \\ L_{tot} &= Ll = R_c \tau \\ C_{tot} &= Cl = \frac{\tau}{R_c} \end{aligned} \quad (\text{A.37})$$

Appendix B. Calculation of the Ideal Step Response to Complex Loads and Line Transitions

The fast step TDR techniques can provide very high resolution as far as the features on the reflection images of the tested system are concerned. The method allows to trace even the connections between different parts of the line. Correct interpretation of the measurements can determine

- whether the deflection of the input waveform was caused by an inductive, capacitive or resistive discontinuity encountered in the line,
- whether the defect causing the reflection represents the series or rather the shunt type of loss
- what are the characteristic parameters and the time constant of the defect which causes the distortion on the image of the propagating wave

In order to facilitate the correct recognition and interpretation of the reflection images, and to allow the extraction of the vital parameters characterizing the system under test, some examples of the calculation techniques addressing the voltage step response of the circuit to complex loads and line transitions are presented in this appendix. In all cases, unless stated otherwise, the line is excited with the step voltage.

$$e(t) = \begin{cases} E & \text{for } t \geq 0 \\ 0 & \text{for } t < 0 \end{cases}$$

Thus $e(t) = Eu_{-1}(t)$ and the Laplace transform of such a source is simply

$$\mathcal{L}(e(t)) = \frac{E}{s}$$

- **Example 1. Line matched at the input and terminated with shunt R-L load (Fig. B.1)**

The reflection coefficient at the input of the line is $r_i = 0$. The reflection coefficient at the end of the line:

$$r_e = \frac{\frac{RLs}{R + Ls} - R_c}{\frac{RLs}{R + Ls} + R_c} = \frac{Ls(R - R_c) - RR_c}{Ls(R + R_c) + RR_c}$$

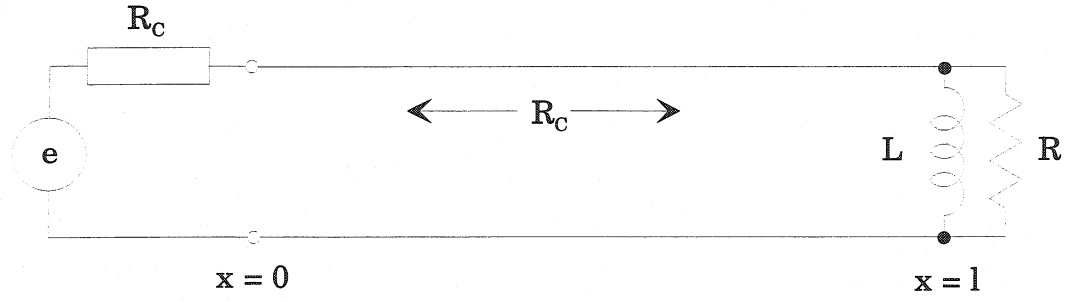


Figure B.1 Shunt R - L termination of the line

According to Eq. (A.22) the voltage at the input of the line is

$$\mathcal{V}(0, s) = \frac{E}{2s} \left(1 + \frac{Ls(R - R_c) - RR_c}{Ls(R + R_c) + RR_c} e^{-\frac{2ls}{v_p}} \right) \quad (\text{B.1})$$

$T = l/v_p$ is the time of the propagation of the incident wave from the input to the end of the line. In order to perform the inverse Laplace transform it is convenient to express the second term of (B.1) in form of the partial factorial expansion:

$$\frac{E}{2s} \frac{Ls(R - R_c) - RR_c}{Ls(R + R_c) + RR_c} e^{-2Ts} = \left(-\frac{E}{2s} + \frac{ELR}{Ls(R + R_c) + RR_c} \right) e^{-2Ts}$$

Then (B.1) takes the following form

$$\mathcal{V}(0, s) = \frac{E}{2s} + \left(-\frac{E}{2s} + \frac{\frac{ER}{R + R_c}}{\frac{RR_c}{(R + R_c)L} + s} \right) e^{-2Ts}$$

Hence, the inverse Laplace transform yields immediately,

$$V(0, t) = \mathcal{L}^{-1}(\mathcal{V}(0, s)) = \frac{E}{2} u_{-1}(t) + \left(-\frac{E}{2} + \frac{ER}{R + R_c} e^{-\frac{t-2T}{\tau}} \right) u_{-1}(t - 2T)$$

where the time constant of the exponential decay is

$$\tau = \frac{(R + R_c)L}{RR_c}$$

The voltage at the termination of the line ($x = l$) is

$$\mathcal{V}(l, s) = \frac{E}{2s} \left(e^{-Ts} + \frac{Ls(R - R_c) - RR_c}{Ls(R + R_c) + RR_c} e^{-Ts} \right)$$

From the inverse Laplace transform one obtains

$$V(l, s) = \mathcal{L}^{-1}(\mathcal{V}(l, s)) = \frac{ER}{R + R_c} e^{-\frac{t-T}{\tau}} u_{-1}(t-T)$$

Both signals are plotted in Fig. B.2. The signal read at the output of the line is marked with a dashed line. The incident wave V_i propagating from the input of the line has half of the amplitude of the incident step produced in reality by the step generator of the reflectometer.

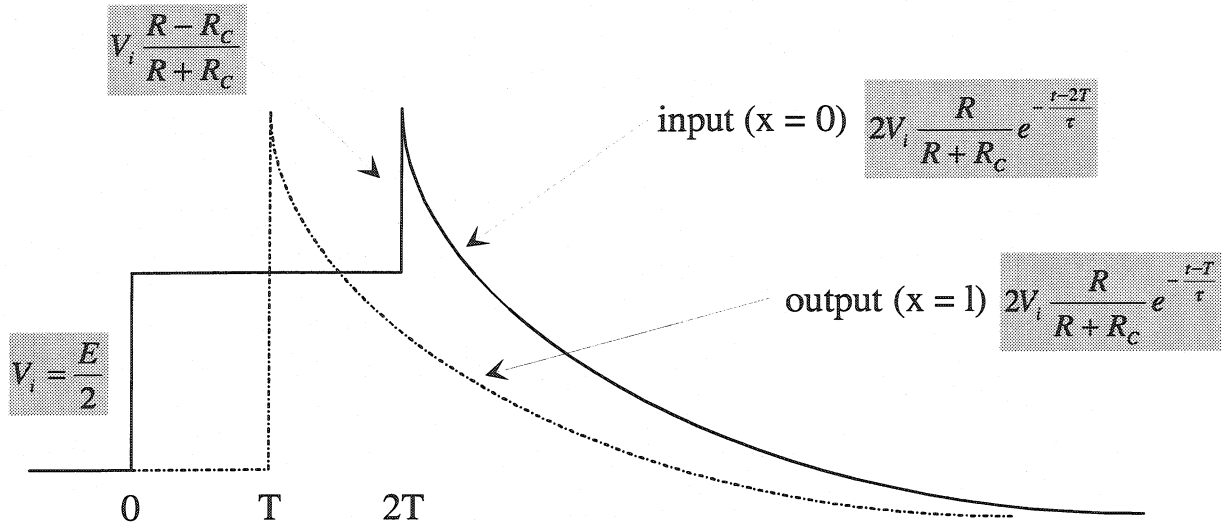


Figure B.2 Ideal step response to the shunt R - L termination of the line

All types of R - C , R - L shunt and series terminations can be treated in the same way. The results are listed below and shown in Figures B.3, B.4 and B.5.

- **Shunt R - C termination**

$$V(0, t) = \mathcal{L}^{-1}(\mathcal{V}(0, s)) = \frac{E}{2} u_{-1}(t) + \left(\frac{E}{2} \frac{R - R_c}{R + R_c} - \frac{ER}{R + R_c} e^{-\frac{t-2T}{\tau}} \right) u_{-1}(t-2T)$$

$$V(l, s) = \mathcal{L}^{-1}(\mathcal{V}(l, s)) = \frac{ER}{R + R_c} \left(1 - e^{-\frac{t-T}{\tau}} \right) u_{-1}(t-T)$$

$$\tau = \frac{CRR_c}{R + R_c}$$

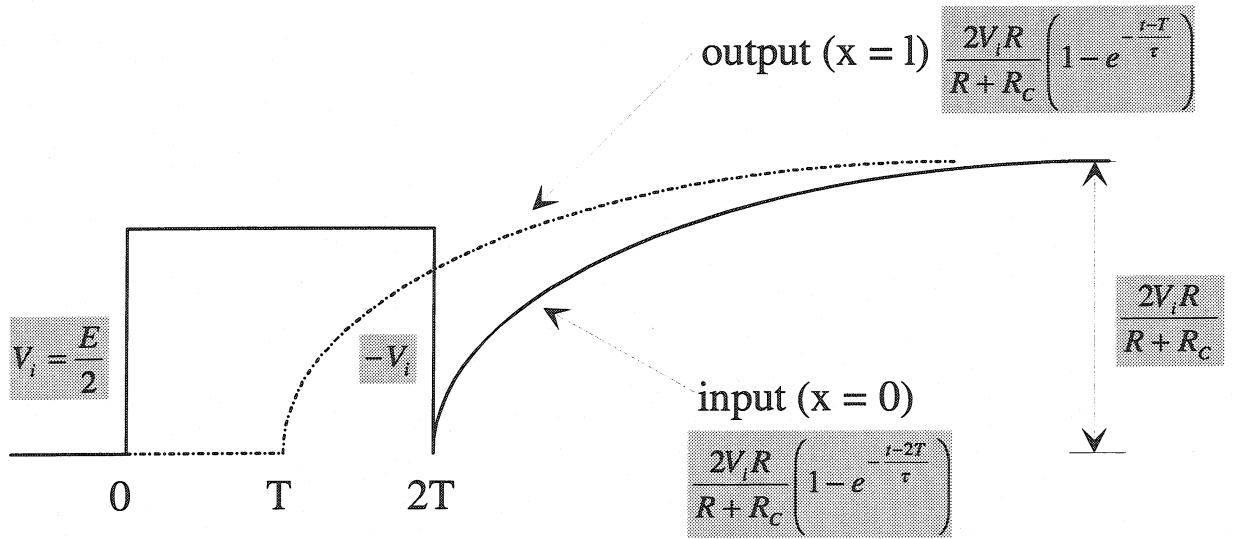


Figure B.3. Ideal step response to the shunt R - C termination of the line

- **Series R - L termination**

$$V(0, t) = \mathcal{L}^{-1}(\mathcal{V}(0, s)) = \frac{E}{2} u_{-1}(t) + \left(\frac{E R - R_c}{2 R + R_c} + \frac{E R_c}{R + R_c} e^{-\frac{t-2T}{\tau}} \right) u_{-1}(t - 2T)$$

$$V(l, s) = \mathcal{L}^{-1}(\mathcal{V}(l, s)) = \left(\frac{E R}{R + R_c} + \frac{E R_c}{R + R_c} e^{-\frac{t-T}{\tau}} \right) u_{-1}(t - T)$$

$$\tau = \frac{L}{R + R_c}$$

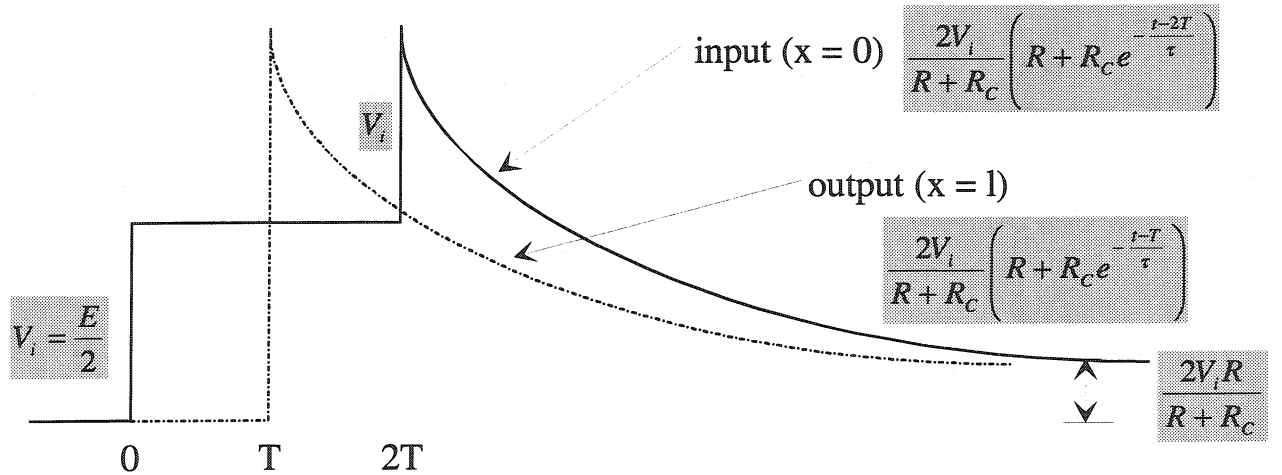


Figure B.4. Ideal step response to the series R - L termination of the line

- **Series R - C termination**

$$V(0, t) = \mathcal{L}^{-1}(\mathcal{V}(0, s)) = \frac{E}{2} u_{-1}(t) + \left(\frac{E}{2} - \frac{E R_c}{R + R_c} e^{-\frac{t-2T}{\tau}} \right) u_{-1}(t - 2T)$$

$$V(l, s) = \mathcal{L}^{-1}(\mathcal{V}(l, s)) = E \left(1 - \frac{R_c}{R + R_c} e^{-\frac{t-T}{\tau}} \right) u_{-1}(t-T)$$

$$\tau = C(R + R_c)$$

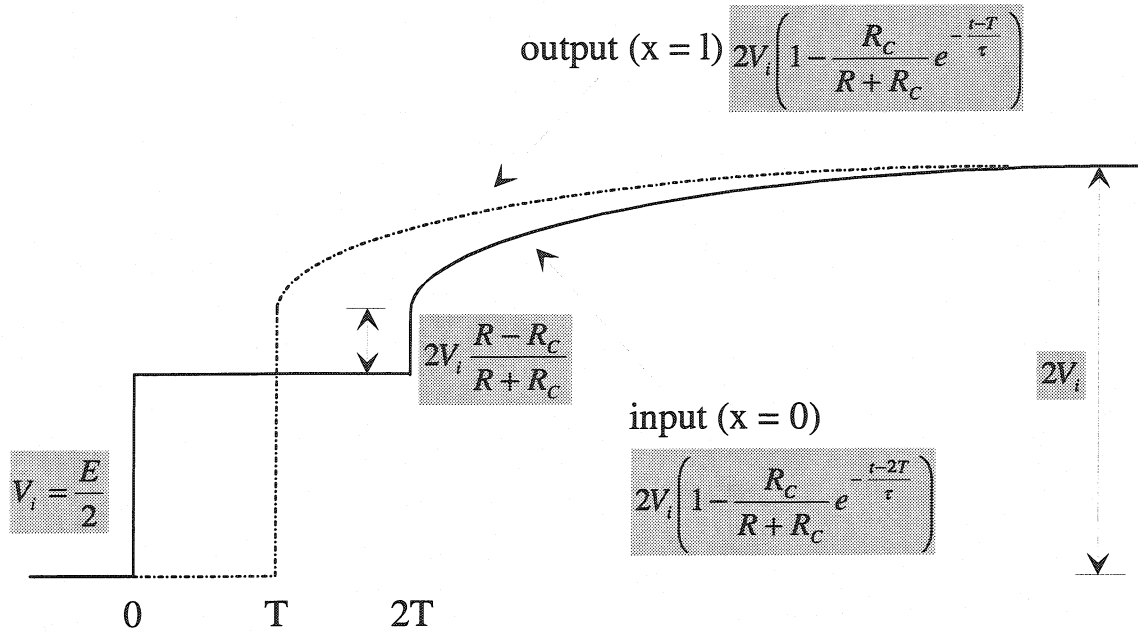


Figure B.5. Ideal step response to the series R - C termination of the line

• **Example 2. A connector between two cables of the same characteristic impedance**

The situation considered is presented in Fig. B.6. The second line is terminated with the load corresponding to its characteristic impedance. The effect of the connector on the junction between both lines can be modeled by introducing a lump inductor in series with the line at the connection point. An echo resulting from such a connector will be analyzed in this example.

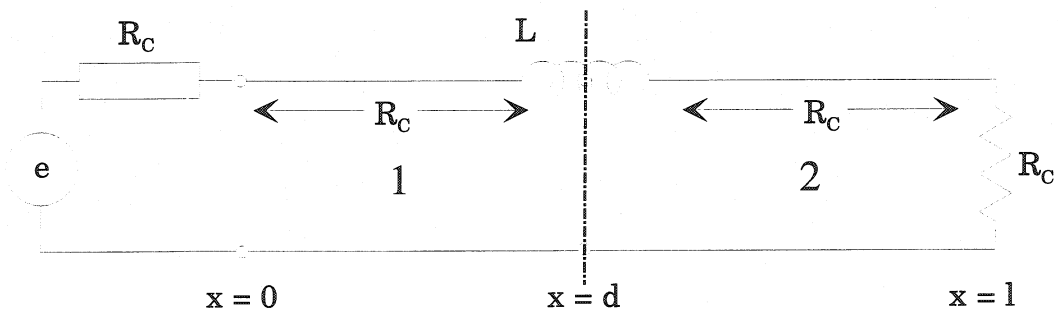


Figure B.6 A connector between two lines with the same characteristic impedance

The reflection coefficient at the input of the line is $r_i = 0$.

From the point of view of the connector located at point d the termination at the end of line 2 seems to be connected in series with the inductor L . Thus the reflection coefficient at the junction between two lines is

$$r_d = \frac{Ls}{Ls + 2R_C}$$

The operational voltage at the input of the line is:

$$\mathcal{V}(0, s) = \frac{E}{2s} \left(1 + \frac{Ls}{Ls + 2R_C} e^{-2T_1 s} \right) = \frac{E}{2s} + \frac{E}{2} \frac{1}{s + \frac{2R_C}{L}} e^{-2T_1 s}$$

$T_1 = d/v_p$ is the time of the propagation of the incident wave from the input of the first line to the junction with the second line.

$$V(0, t) = \mathcal{L}^{-1}(\mathcal{V}(0, s)) = \frac{E}{2} u_{-1}(t) + \frac{E}{2} e^{-\frac{t-T_1}{\tau}} u_{-1}(t - T_1)$$

The time constant of the exponential decay is

$$\tau = \frac{L}{2R_C}$$

The signal read at the input of the line is shown in Fig. B.7.

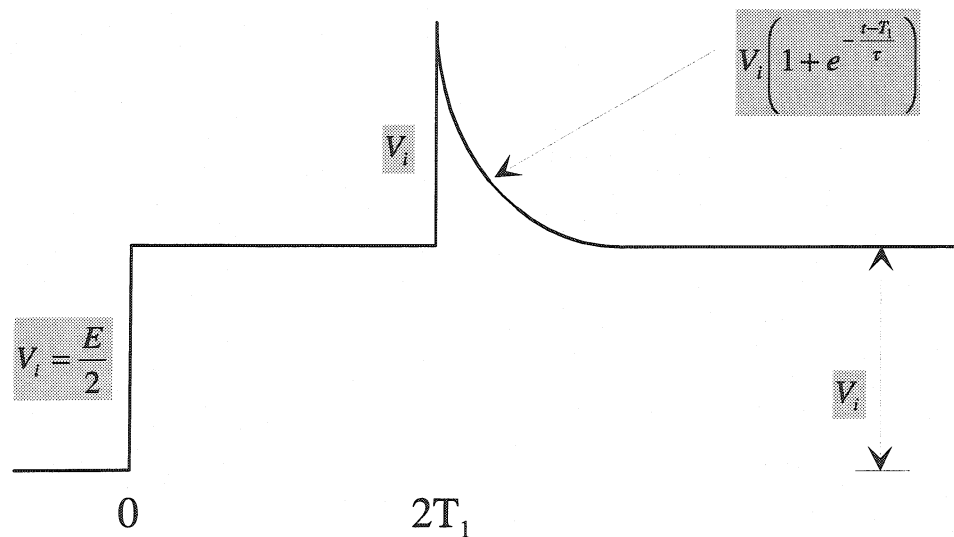


Figure B.7 The effect of the connector between two transmission lines of equal R_C

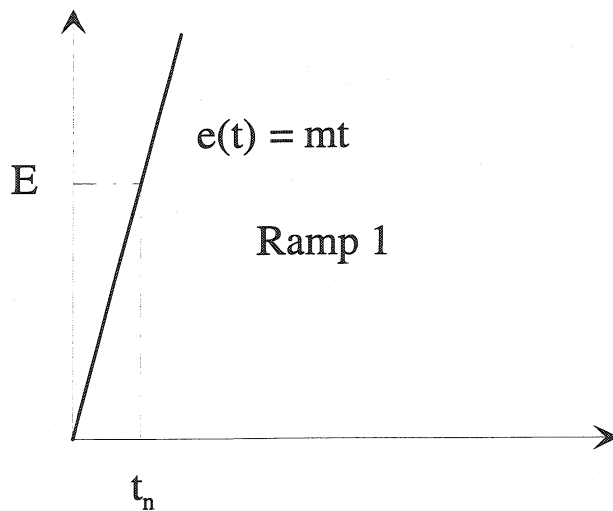


Figure B.8 Ramp signal

In reality the step produced by the pulse generator of the time domain reflectometer has a finite rise time greater than zero. In order to see how it affects the response of the circuit one has to analyze the response of the system to a ramp excitation shown in Fig. B.8. The signal is defined as $e(t) = mt$ for $t \geq 0$, where m is given in V/s. Let us additionally assume that $e(t_n) = E$. The Laplace transform of such a voltage source

$$\text{is } \mathcal{L}(e(t)) = \frac{m}{s^2}.$$

The operational voltage at the input of the line is then:

$$\mathcal{V}_1(0, s) = \frac{m}{2s^2} \left(1 + \frac{Ls}{Ls + 2R_c} e^{-2T_1 s} \right) = \frac{m}{2s^2} + \frac{m}{2s \left(s + \frac{1}{\tau} \right)} e^{-2T_1 s}$$

The partial factorial expansion of the second term in the above equation yields:

$$\frac{m}{2s \left(s + \frac{1}{\tau} \right)} e^{-2T_1 s} = \left(\frac{m\tau}{2s} - \frac{\frac{m\tau}{2}}{s + \frac{1}{\tau}} \right) e^{-2T_1 s}$$

Hence the inverse Laplace transform of the operational voltage gives the following result:

$$V_1(0, t) = \mathcal{L}^{-1}(\mathcal{V}(0, s)) = \frac{mt}{2} + \frac{m\tau}{2} \left(1 - e^{-\frac{t-2T_1}{\tau}} \right) u_{-1}(t - 2T_1)$$

An input step with nonzero rise time can be constructed by adding two ramps together as it is shown in Fig. B.9.

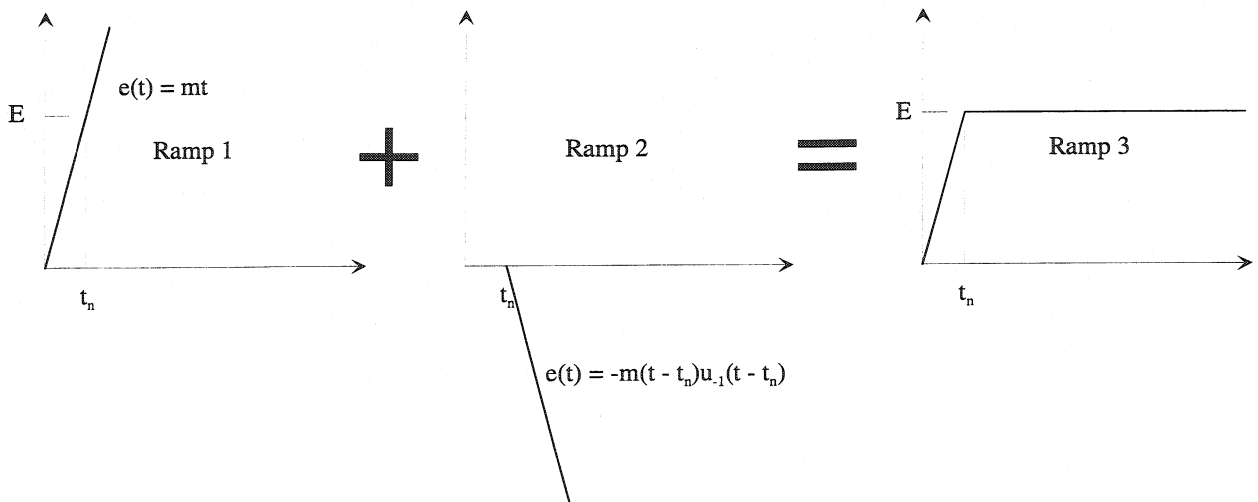


Figure B.9 Finite rise time step function as a sum of two ramp signals

According to the superposition theorem for linear systems the response of the connector to the finite rise time step function can be obtained by adding the responses to the individual ramps. The response to the second ramp is obtained immediately by negating the response to the first one and by displacing it by t_n :

$$V_2(0, t) = -\frac{m(t - t_n)}{2} u_{-1}(t - t_n) - \frac{m\tau}{2} \left(1 - e^{-\frac{t - t_n - 2T_1}{\tau}} \right) u_{-1}(t - t_n - 2T_1)$$

The sum of both responses is shown in Fig. B.10.

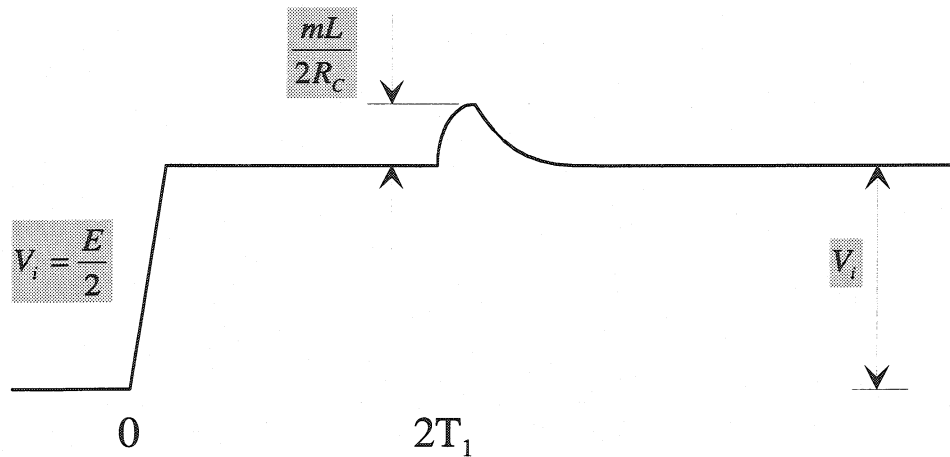


Figure B.10 Connector response to a finite rise time step function

In a similar way a response of any linear system can be calculated as a sum of responses to the individual ramps. Finite rise and fall time rectangular pulses can also be composed of multiple ramp functions.

In the fast step TDR a finite rise time of the initial step function enforces a bandwidth limitation on the measurements. If the discontinuity encountered in the transmission line has the time constant which is much lower than the rise time of the initial signal launched by the reflectometer the ideal response will be changed into an impulse response as it was demonstrated above in Figs. B.9 and B.10. If both time constants are similar the response of the system will not be an impulse any more, and the extraction of the circuit parameters will not be possible without numerical modeling. If two consecutive faults in the line are separated by the distance corresponding to half of the TDR rise time, the reflections resulting from these faults will merge as one, and the measurement will not be able to resolve them.

- **Example 3. Transition between the lines with different characteristic impedance**

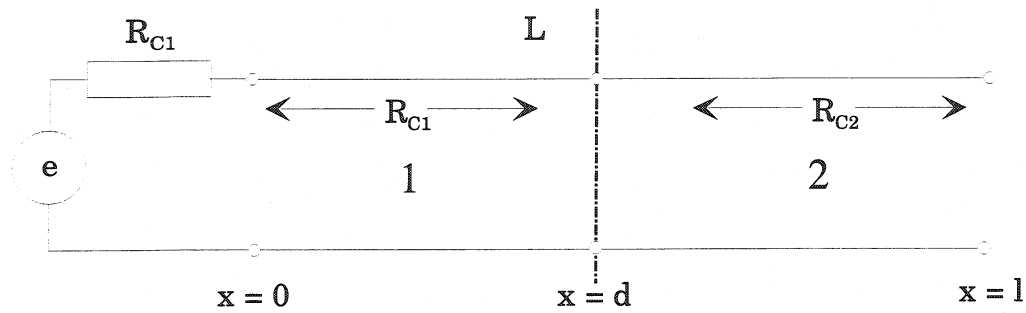


Figure B.11 Two transmission lines of different characteristic impedance

The same analysis as in the previous case can be applied for the transition between two lines with different characteristic impedance (Fig. B.11). Let us assume that $R_{C2} < R_{C1}$.

The corresponding reflection and transmission coefficients are:

- at the input

$$r_0 = 0$$

- at the junction between the lines

from line 1 to line 2

$$r_{1,2} = (R_{C2} - R_{C1}) / (R_{C2} + R_{C1})$$

$$t_{1,2} = 1 + r_{1,2}$$

from line 2 to line 1

$$r_{2,1} = -r_{1,2}$$

$$t_{2,1} = 1 + r_{2,1} = 1 - r_{1,2}$$

- at the end of line 2

$$r_e = 1$$

The response of the system to the step voltage is shown in Fig. B.12. The multiple reflections resulting from the returning wave partially reflected at the junction and traveling back towards the open end of line 2 are not shown on the plot.

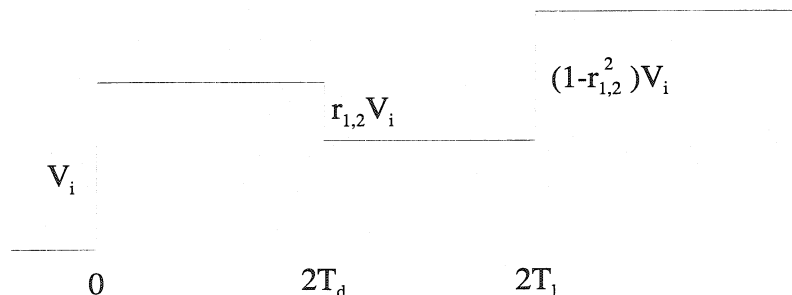


Figure B.12 Transition between two lines with different characteristic impedance

References for Chapter 4

- [1] L. Heinhold, R. Stubbe, Power Cables and Their Applications, Part 1, Siemens Aktiengesellschaft 1990
- [2] Hewlett Packard Application Note 62-3, Advanced TDR Techniques, May 1990
- [3] A. Bzagnet et al., The LHC Test String: First Operational Experience, Proceedings of EPAC'96 Sitges, Barcelona, Spain, 10-14 June 1996, pp. 358-360
- [4] E. Sinemus, Fehlerortungstechnik in Energie- und Nachrichtenkabeln, Expert Verlag 1981, Kontakt und Studium, Band 75
- [5] Mathematica ver. 4.0, A System for Doing Mathematics by Computer, Wolfram Reasearch, Inc., 1999
- [6] P. A. Komorowski, Time Domain Reflectometry for the Localization of Electrical Faults in the Instrumentation of the LHC String Magnets: A Study Case of Voltage Tap, Temperature, and Pressure Transducer Circuits, LHC Project Note 181, CERN, Geneva, February 1999
- [7] G. Lago, L. M. Benningfield, Circuit and System Theory, John Wiley & Sons, Inc., 1979
- [8] S. Goldman, Laplace Transform Theory and Electrical Transients, Dover Publications, Inc., New York, 1966

Chapter 5

Partial Discharge Analysis for the Overall Quality Assessment of the Ground Insulation in Superconducting Magnets

Partial discharges (PDs) are pulsed shaped high frequency currents, which may occur between the conductive area of the cable and its insulation or along the surface of the insulation under the conditions of the voltage stress. The results of the PD measurements, i.e. the number, the magnitude of the PDs and their phase angle, may lead to the detection of possible imperfections and defects, or of the ongoing degradation of the insulation system even if the HV tests, e.g. the measurements of leakage current, are successfully passed.

In general case the application of the high-amplitude AC voltage across the insulating material results either in a complete or partial breakdown of the insulator. During the complete breakdown the insulation collapses completely under the voltage stress bridging thus the insulated electrodes with a low-ohmic resistance. On the contrary, during the partial breakdown only a part of the insulation collapses, while the remaining part of the insulating system is still capable of withstanding the voltage stress. This kind of breakdown is referred to as a partial discharge by analogy to the discharges observed in ionized gaseous dielectrics.

During the partial discharge test the excitation AC high voltage with the frequency of 50 Hz is applied between the core of the cable and the ground, causing thus a development of a high electric stress voltage stress across the solid insulating material isolating both electrodes. In this case the defects present in the insulating material or on its interfaces are especially vulnerable for the generation of PDs. Most commonly encountered defects in the insulating systems are voids. Several types of possible void configurations can be identified as:

- a gas-filled cavity (e.g. an air bubble) present in the insulating material,

- surface void caused by the partial detachment of the insulating material from the surface of the cable,
- uniform or nonuniform continuous air-gap between the surface of the insulating material and the surface of the cable,
- uniform or nonuniform air-gap inside the insulating material.

These kinds of void defects lead to the generation of the PDs between the metal electrode and the insulation, between the insulation and insulation, along the surface of the metallic electrode or along the surface of the insulation.

Another type of the defect can be characterized by presence of the strange body in the dielectric, e.g. a metallic pin embedded in the bulk of the insulator material. This kind of defect leads to the severe local enhancement of the electric field around the metallic intruder and results in the destruction of the insulating material in the vicinity of the pin. As a part of the experimental approach aiming at the analysis of the breakdown and pre-breakdown phenomena in solids the metallic pin is introduced into the insulating materials under test on purpose.

The theory of the PDs, as well as the pre-breakdown and breakdown phenomena in solids are not fully understood yet. Currently used models range from the purely phenomenological and statistical formulations to purely quantum mechanical descriptions of the observed effects [1], [2]. Although the PD techniques were and are being more or less successfully applied for the analysis of the power cables [3], motor and generator stator windings [4], transformers [5] and other electrical machines, still in many cases the interpretation of the results of the measurements may be ambiguous. The analysis of the results is also approached with a wide variety of theories and procedures ranging from microwaves [6] and acoustics [7], through neural networks [8] and wavelet analysis [9] to deterministic chaos [10].

The challenge of applying this method in the framework of the superconducting magnets is posed already by the complex structure of the Rutherford superconducting cable. The insulation of the cable does not adhere ideally to the rough surface of the multi-stranded conductor, creating thus a nonuniform air-gap running along the entire surface of the cable. The winding configuration of the multiple insulation layers also imposes presence of the air gap between the consecutive sheets of insulating material. Moreover, in the case of the LHC magnets there are also the intentional 2 mm-wide equally spaced gaps between consecutive cable turns, which are designed for penetration of the cryogen between the coil windings.

This also creates a set of regularly spaced voids between the outer layer of the coil and the ground insulation. The ground insulation of the LHC dipoles is composed of further four separate layers of polyimide foil. Thus the air-gaps are omnipresent in the insulation system of the magnet, and they will create an omnipresent PD pattern. The most interesting question to be studied is whether a signal induced by the imperfections in the insulation system can be distinguished from this PD background signal.

One can imagine a fabrication error inadvertently introduced by locally missing layers of ground insulation. Although the coil is definitely weaker in the fault-affected area the magnet still successfully passes all of the standard tests and behaves like a perfect flawless magnet. Nevertheless the defect, although hidden beyond the detection capabilities of the standard HV tests, is still there. It might manifest itself later on during the magnet operation or during the training quenches.

Even locally missing insulation layer introduces the distortion into the standard geometry of the magnet, i.e. the air-gap between the insulation is increased beyond the norms of technical specifications. Can such a hidden defect be recognized with PD analysis? The following chapter brings the preliminary answer to this question.

Since the PD technique has never been used at CERN so far, the measurements presented in this chapter were carried out at the PD facilities in the Laboratory of Components, Materials and Electrical Technologies at the University of Genoa in Italy.

5.1 Partial Discharge Detection

The techniques of PD detection may suffer from a significant degradation and deterioration of the signal due to the cable length and noise. Therefore a detection system must be designed according to the recommendations for the implementation of low level signal measurements in order to successfully recover the PD signals from noise. In addition the measurement area should be decoupled from any external electromagnetic fields. E.g., the PD measurement facility at the Genoa University is installed in a shielded room allowing thus to reach the sensitivity of 1 pC as far as the magnitude of the detected PD is concerned. A standard non-shielded environment decreases the measurement resolution to 100 pC even if the precautions are taken for a thorough internal and external radio frequency noise rejection.

The principle of the measurement and the block diagram of the detection circuit are presented in Fig. 5.1 for a sample of cable used as a test object. An alternating 50 Hz voltage source provides an input excitation, which is applied across the insulation of the cable under test until the electric stress in the insulation reaches the threshold of the inception level. When

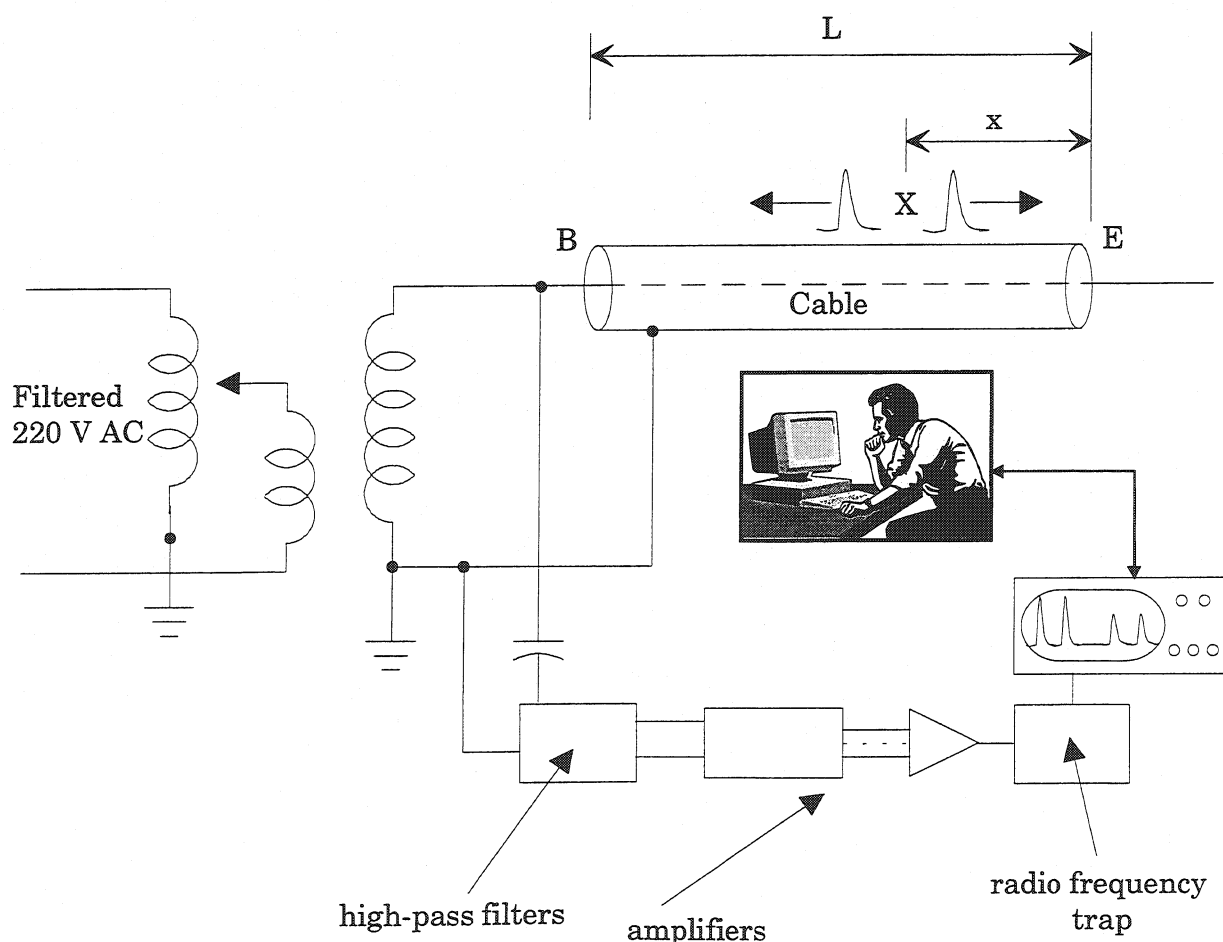


Figure 5.1 Partial discharges detection system

this happens, PDs occur at the point X of the insulation. A PD short duration pulse starts traveling towards the beginning of the cable (the input terminal where the excitation voltage was applied – point B on the diagram), at the same time the other pulse travels towards the end of the cable (point E) where it gets reflected and starts returning back towards point B . The signal detection system registers both the direct and reflected pulses. Both pulses are separated in time by twice the period required for the second pulse to travel from the PD's point of origin (X) to the end of the cable (E) and back to the point of origin. Both signals are reflected at the beginning of the cable, then at its end, and finally are recorded again upon their arrival at point B . The simplified form of the signals recorded by the detection circuit is presented in Fig. 5.2.

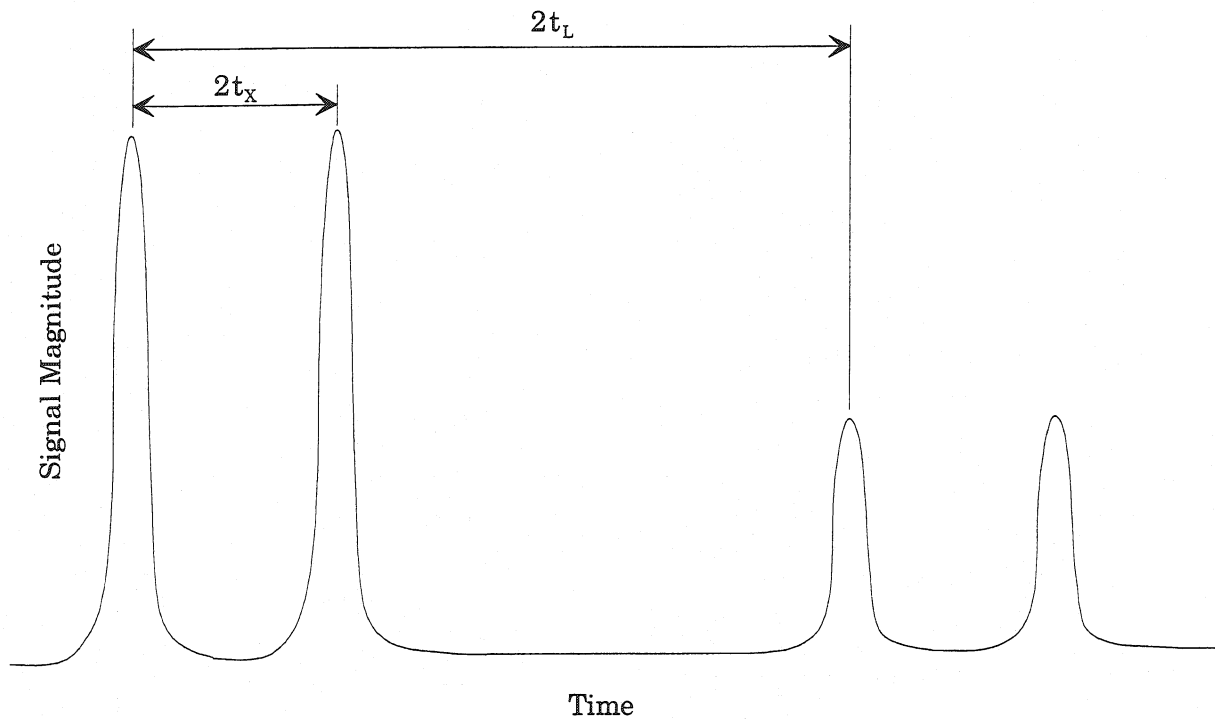


Figure 5.2 Schematic representation of partial discharges signals

If t_X denotes the travel time of the pulse from the PD's point of origin (X) to the end of the cable (E), and t_L a total travel time of the pulse along the entire cable length L , the localization of the source of the partial discharge X is calculated according to the following

ratio:
$$\frac{x}{L} = \frac{t_X}{t_L}.$$

In reality, due to the continuous AC excitation of the test object and the multiple, statistical character of the partial discharges, as well as the frequency dependence of the PD propagation velocity, the registration of the reflected PDs and the localization of the source of

the partial discharges cannot be established for an arbitrary test object. Direct PD current pulses can be filtered at the terminals of the test object. They appear in pulse trains of opposite polarity. In general case the number of discharges increases with the increase of the excitation voltage, whereas their amplitude remains virtually the same.

The detection system operating at the University of Genoa is voltage coupled. The main components of the voltage coupled system are:

- adjustable, precise resistive, capacitive and inductive components used to assure the RLC-type circuit response and to increase the input impedance of the system in order to limit the current flow in the device under test,
- RC high pass broadband filters,
- low-noise broadband operational amplifiers,
- RF traps for the rejection of radio interference,
- digital oscilloscope for the direct signal registration,
- PC system for the digital data acquisition and statistical analysis,
- a pulse height discriminator for acquiring statistical information concerning the number and the magnitude of the PD signals,
- an excitation voltage magnitude discriminator for the discrimination of the coherent noise covering parts of the excitation voltage cycle,
- phase shift analyzer,
- 3D digital matrix memory for enumerating the PD pulses displayed by the oscilloscope and storing the relevant magnitude – phase shift information characterizing them.

The digital acquisition system registers the PD pulses and sorts them with respect to their intensity and their phase angle. The measurement process is shown in Fig. 5.3. During a given period of time the data concerning all of the detected partial discharges are registered for further analysis. The results are displayed in form of the color map, on which the frequency of the PD occurrence is encoded by specific colors. Apart from the PD rate the graph shows the magnitude and the phase shift of the registered pulses. The phase shift is calculated in reference to the phase of the input AC excitation signal. Thus a colored dot indicates e.g. that more than 256 partial discharges having a magnitude of 150 pC and a phase shift of 135 degrees have occurred during the measurement process. After the data acquisition is finished a detailed statistical analysis of the measurement can be performed. An example of the information extracted from the acquired data is presented in Fig. 5.4.

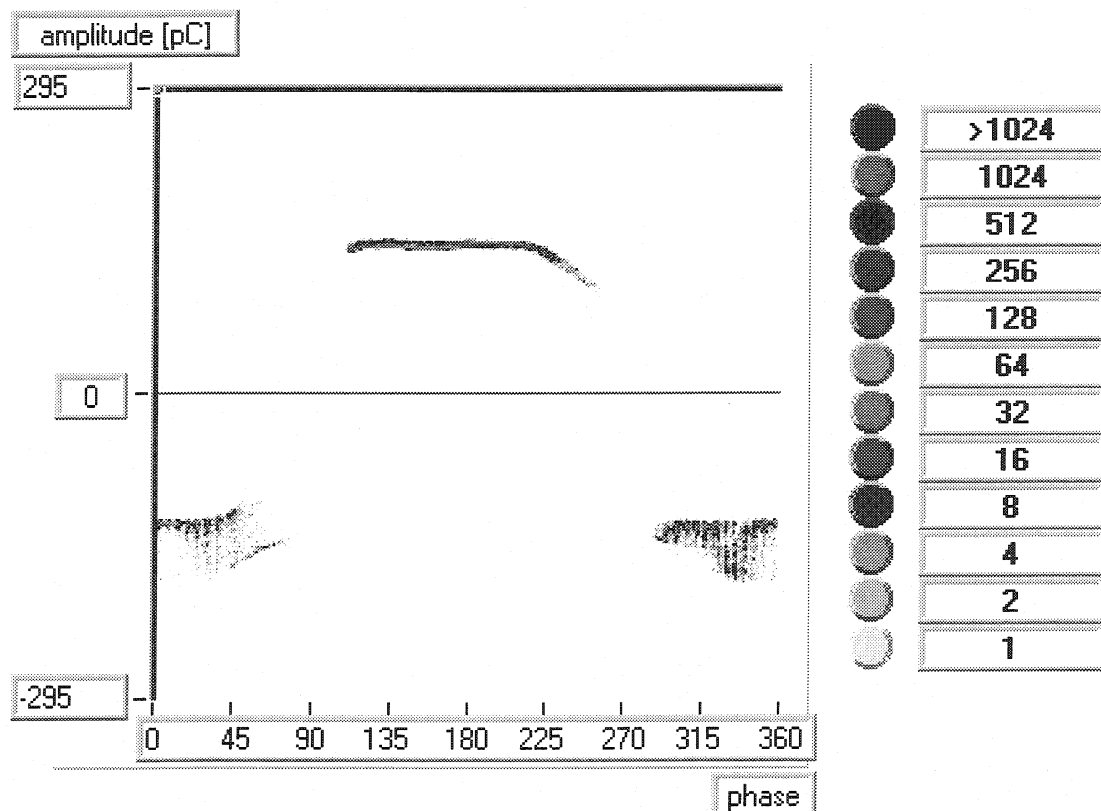


Figure 5.3 Statistical data acquired during the measurement

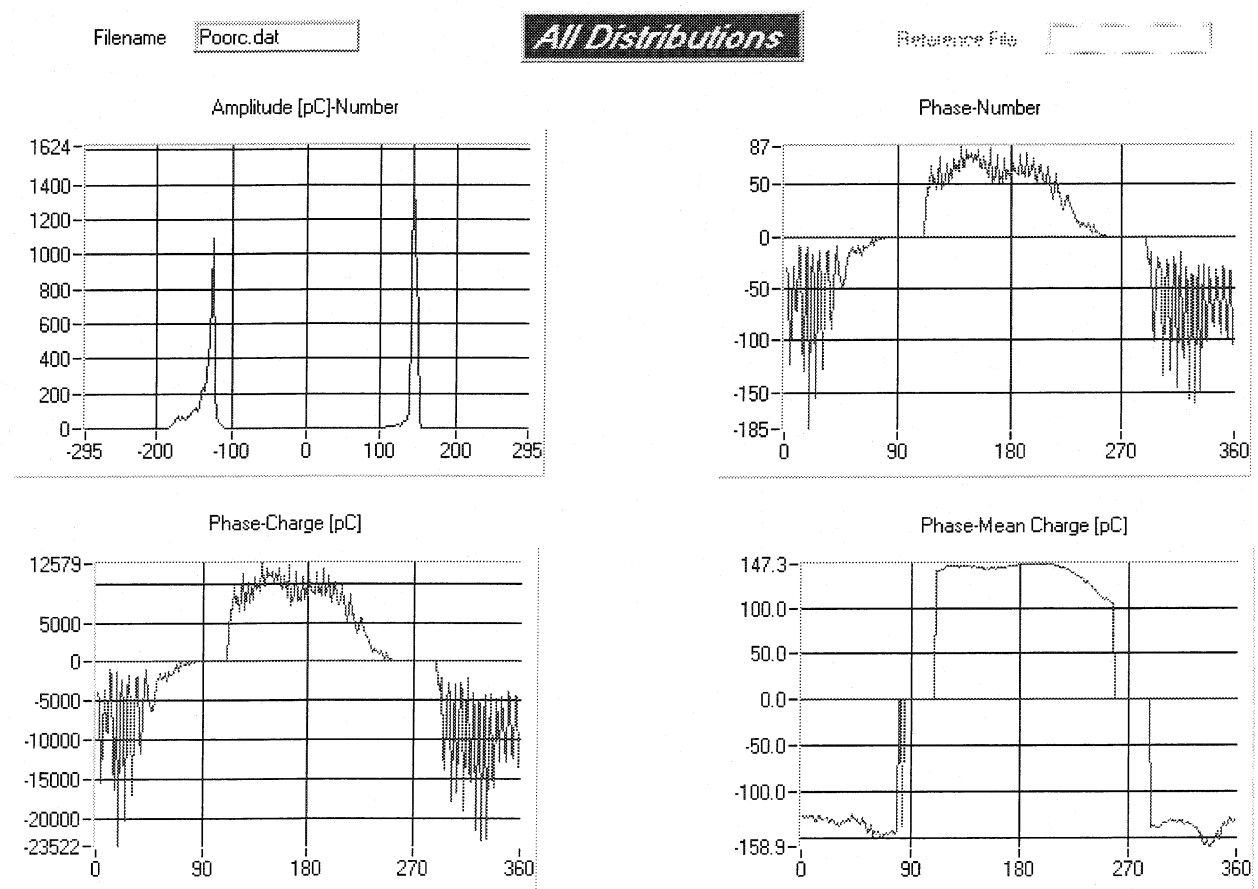


Figure 5.4 Comprehensive data analysis

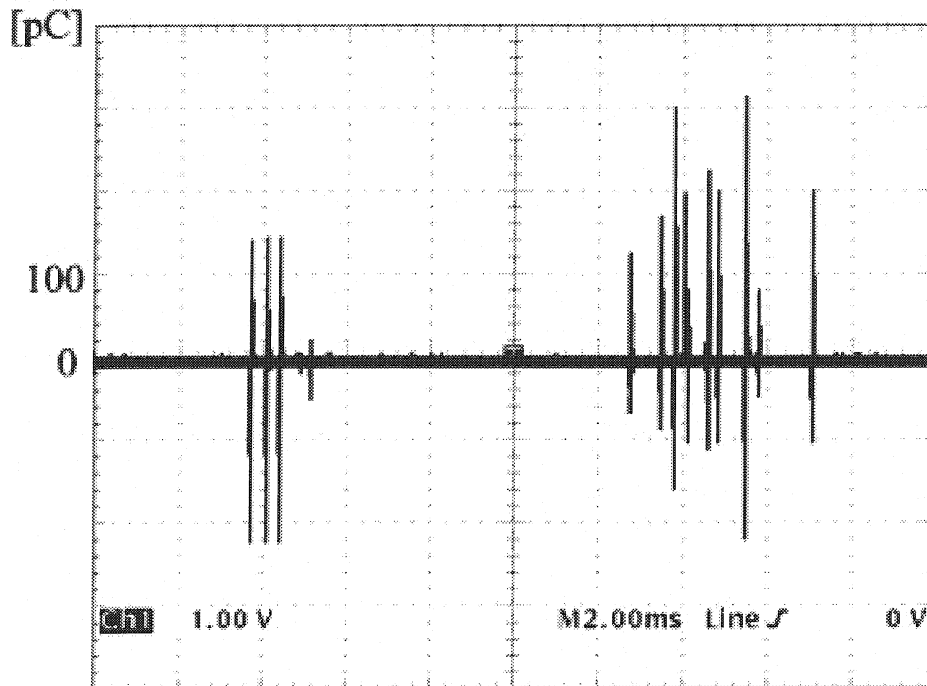


Figure 5.5 PDs between the insulation and the core of the superconducting cable

The original three-dimensional information (number, magnitude, phase shift) is dispatched into separate distributions; i.e. quantity of the observed partial discharges vs. their magnitude, magnitude vs. phase, quantity vs. phase, etc. The characteristic pattern related to the test object or its defect can be revealed in this way.

Fig. 5.5 shows a single oscilloscope screen shot of the PD test performed on a short sample of the outer layer cable used for the winding of the coils for the LHC dipole magnets. Prior to measurement the cable was wrapped in three sheets of polyimide foil simulating the ground insulation of the coil, and surrounded with the bulk metallic electrode simulating the collars. The input AC voltage was applied between the conducting core of the cable and the metallic electrode. The partial discharge pattern appeared when the amplitude of the voltage source reached 1500 V (inception voltage). The maximum magnitude of the partial discharges registered amounted to 300 pC. Despite the continuous excitation with the AC source there was no heating in the sample, because the current flow was very close to zero due to the high input impedance of the system.

The screenshot in Fig. 5.5 shows the distribution of the PD on the positive and negative AC half cycle. The discharge pattern where the first cluster of the discharges has lower amplitude than the second one is enforced by the insulation of the cable. It implies that the partial discharges appear between the surface of the cable and the insulation. As it was

already mentioned, due to the braided structure of the superconducting cable the first layer of the insulation cannot be ideally wrapped around the core of the conductor leaving thus the air gaps between both components. PDs start occurring when the excitation voltage reaches a certain inception level. At this moment the intensity of the electric field is high enough for the PD to appear, but still the first electron must be incepted in order to trigger the avalanche and create the discharge. When during the AC cycle the core of the cable is at the negative potential with respect to the insulation the discharge path will run from the metal towards the insulation. In this case it is quite easy to incept electrons from the metal surface and generate the discharge. Therefore these discharges occur very close to the inception voltage and result in lower amplitude of the apparent charge.

On the other hand, during the second part of the AC cycle the insulation is at negative potential with respect to the conductor. Even if the inception threshold was already reached the precursor electrons necessary to trigger the discharge are not available instantaneously. It is much harder to obtain a free electron from the surface of the dielectric. Therefore the local intensity of the electric field in the void must still be increased. At a certain moment the air in the gap is ionized. Eventually, when the excitation voltage is much higher than the actual inception level, the avalanche initiated from the insulation and running towards the surface of the cable occurs. Of course the amplitude of the PD is correspondingly higher in comparison to the discharges arcing in the opposite direction.

When the amplitudes of the apparent charge on both half cycles are equal, the PDs generally occur between insulation and insulation.

5.2 Test Magnets for the PD Analysis of the Ground Insulation Quality

Two 5-block single aperture short dipole models were prepared for the partial discharge measurements. One of the magnets was in perfect condition. In a flawless magnet there are 4 layers of ground insulation between the external layer of the coil and the collaring shoe. The first layer of the ground insulation, which is directly adjacent to the external layer of the coil, contains 25- μm thick quench heater strips sandwiched inside two 125- μm sheets of polyimide. Each of the remaining three layers is also made of 125- μm thick polyimide film.

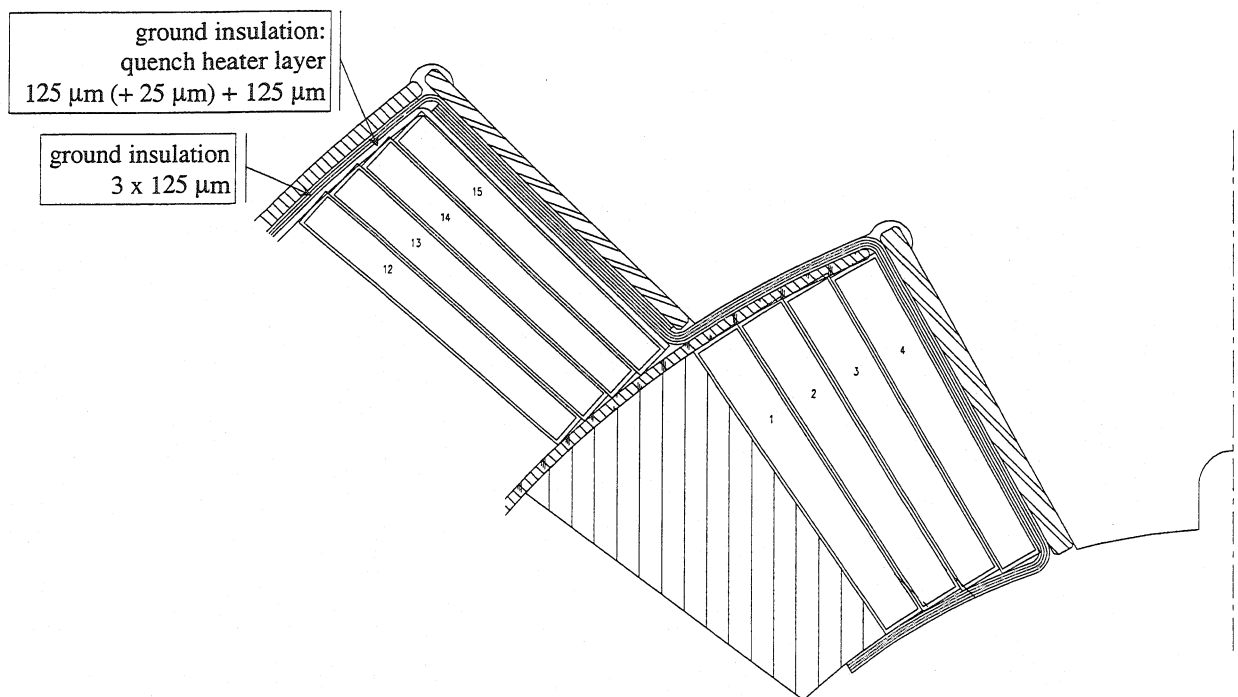


Figure 5.6 Structure of the ground insulation in the magnet

Quench heaters are 15 mm wide metallic strips running along the entire length of the external layer of the coil in positions illustrated in Fig. 5.7. The strips labeled with the same identifier (QH1 – QH4) are electrically connected with each other at the end of the magnet. During the PD measurements the quench heaters, the coils, and the collars are used as the electrodes characterizing different test configurations.

In reality the quench heaters are a part of the quench protection system of the magnet. In order to explain their role let us consider a schematic layout of the connection between the coils of the magnet drawn in Fig. 5.8. Both poles are defined by the median plane of the magnet aperture. When the magnet works in the superconducting state the voltage measured between the terminals of the separate poles is less than 40 mV. If this limit is exceeded it implies that a resistive voltage starts building up in one of the poles, which means the

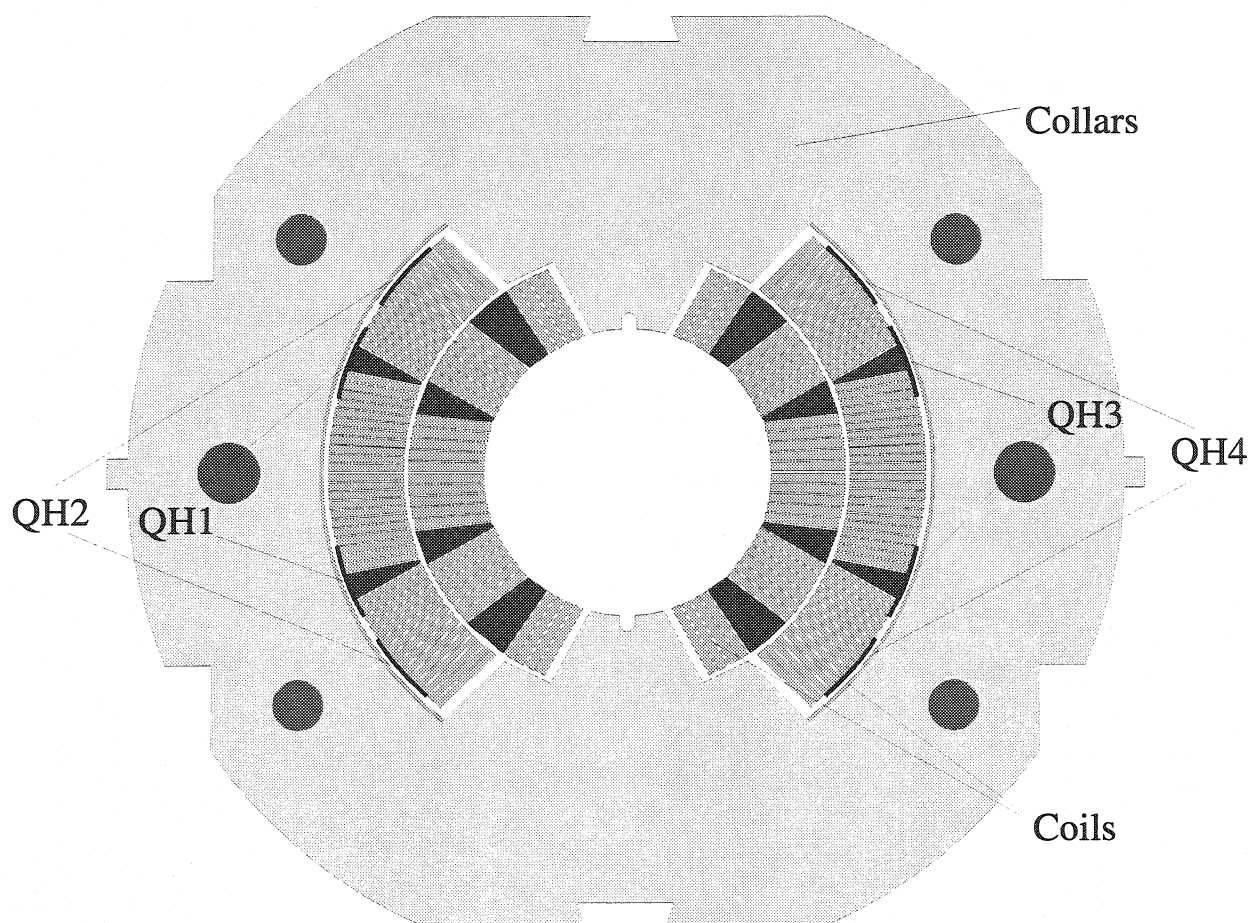


Figure 5.7 Electrodes for the PD measurements. Positions of the quench heaters are labeled with the respective QH indicators.

beginning of the quench, i.e. the violent resistive transition of the magnet from the superconducting to the normal state. The propagation of the quench starts from a single hot spot, where the temperature is higher than the critical temperature of the superconductor operating at a given location in a given local magnetic field. As soon as the quench is detected and confirmed the quench heaters are triggered to heat up the coils in order to speed

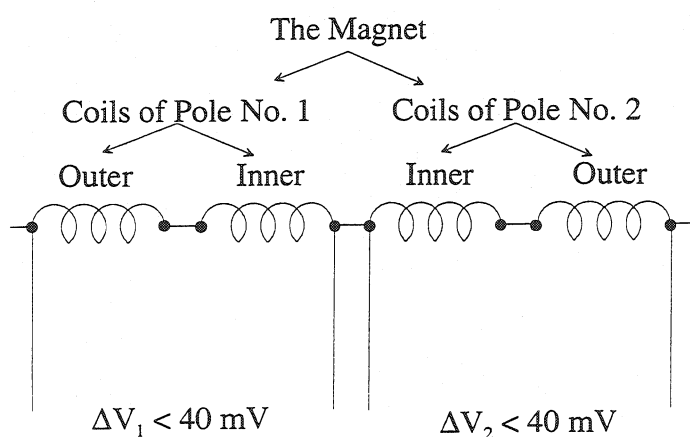


Figure 5.8 Serial connection of the separate coils in the magnet

up and improve the propagation of the normal zone throughout the magnet. In this way the entire energy initially stored in the superconducting magnet is uniformly distributed in the now resistive coil, and eventually it can be released into the special dump resistor via a diode, preventing thus the destruction of the coils. In some rare situations it may happen that two

quenches start propagating in the same pole of the magnet from two different locations in the opposite directions. In this way the voltage readout at the terminals of the pole will still indicate the potential difference lower than 40 mV. In order to prevent such situation, the secondary quench detection systems (QD2, and QD3) monitor the potential difference between the inner and outer layer of each pole. The details of the quench detection systems used for the protection of the LHC magnets can be found in ref. [5]. As far as the PD measurements are concerned quench heaters are reduced to the role of convenient electrodes located between the coils of the magnet and the collars.

Coming back to the preparation of the test objects, on the other magnet a square of 6 x 8 cm was cut off and removed from the two outermost layers of the ground insulation in location indicated by a white square in Fig. 5.9. In this way the ground insulation on one side of the coils was locally damaged. After this small surgery the magnet was collared according to the standard assembly procedure.

After the assembly both magnets have successfully passed HV discharge and leakage tests. During the leakage test the dielectric rigidity of the magnets to ground was examined. DC high voltage of 5 kV was applied between the coils of the magnet and the collars for a period of 180 s. The leakage current flowing across the dielectric insulation of the magnet was in both cases lower than 50 μ A, which fully complied with the test requirements.

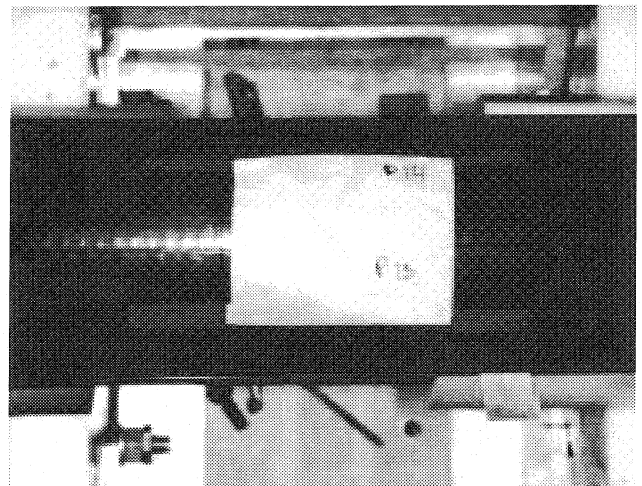


Figure 5.9 Locally missing two layers of the ground insulation

Both assemblies behaved like perfect magnets manufactured with highest precautions as far as the technical specification of the magnet assembly is concerned. The hidden damage intentionally inflicted to the ground insulation of one of them remained completely invisible within the scope of the employed standard testing methods.

An essential question remains to be answered if there is a way, apart from the human intuition, that would nevertheless lead to the recognition of the existing problem. The following section shows what answers are brought by the PD technique in this matter.

5.3 PD Measurements Performed on the Dipole Magnets

A comprehensive PD measurement session was carried out on both magnets. The electrodes available for the application of the excitation voltage are: the coils of the magnet, the collars, and the quench heaters (QH). Depending on the potentials applied to these electrodes different test configurations were analyzed.

- **Test No. 1 – General test of insulation between the quench heaters and the collars**

During this test the active potential electrode of the excitation source is connected to the coils of the tested magnet and to all of the quench heaters at the same time, whereas the ground electrode is connected to the collars. The excitation is 50 Hz AC sinusoidal waveform with the amplitude of 2.5 kV. The configuration minimizes the number of the partial discharges between the quench heaters and the coil since both of these electrodes are at the same potential and thus there is no electrical stress applied across the insulation between them. For the same reason there will be no PDs between the consecutive turns of the coil either. This arrangement serves for general analysis of the partial discharges across the insulation layers located between the quench heaters and the collars of the magnet.

Fig. 5.10 shows the comparison of the PD patterns for both magnets. Apart from the fact that certain amount of PDs observed in the damaged magnet showed higher amplitudes, and the PD map had to be rescaled in order to contain the entire signal, both patterns look very similar.

However when a thorough statistical analysis of the patterns is carried out essential

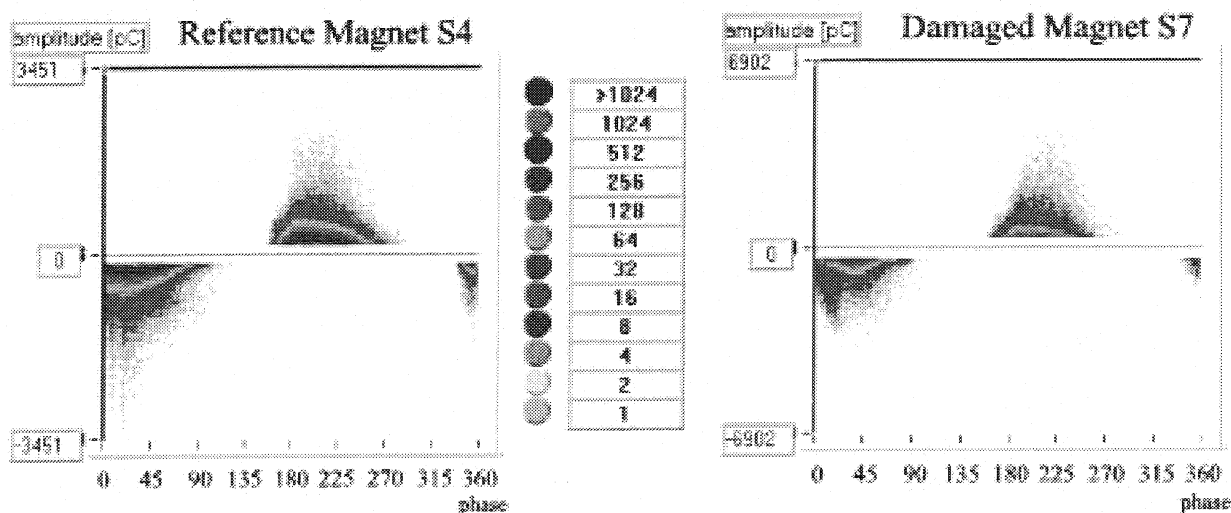


Figure 5.10 Test No. 1 – Comparison of PD patterns

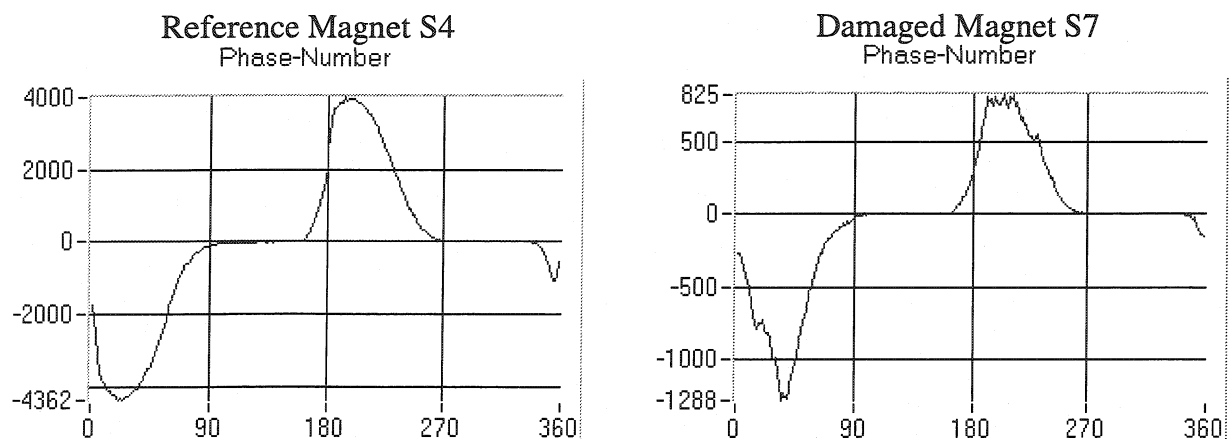


Figure 5.11 Test No. 1 – Phase vs. PD Number distribution

differences between both test objects become clearly visible. Fig. 5.11 shows the comparison of the Phase vs. Number distribution for both magnets. The plots display the total number of the PDs registered with the same phase shift in reference to the phase of the excitation voltage. During all of the measurements the acquisition time was set to 45 s. The shape of the extrema in the plot for the reference magnet is quite smooth, whereas for the damaged magnet both minimum and maximum become jittery, and small local extrema with lower amplitudes are separated from the global wide peaks. The differences in the scales between both plots express higher PD activity on the reference magnet.

Substantial differences in shape of the curves are also visible on the plots of Phase vs. Charge, where the total apparent charge of all of the registered PDs is summed together for the discharges with the same phase shift (Fig. 5.12). Again, higher values of the total charge for the reference magnet reflect higher number of PDs. However when the same plot is drawn for the average charge, i.e. the total charge divided by the number of PDs experiencing the same phase shift, it turns out immediately that the discharges observed on the damaged magnet

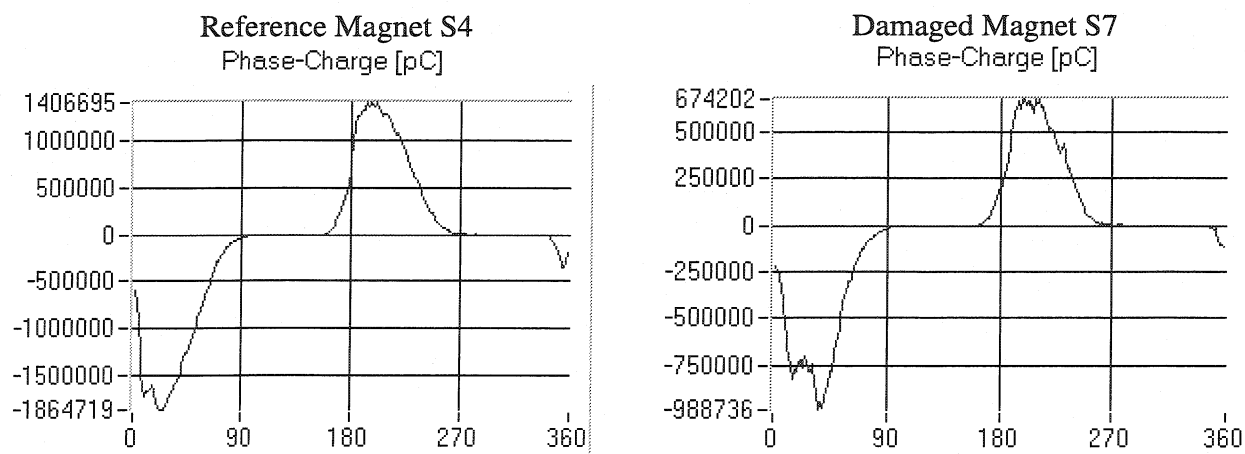


Figure 5.12 Test No. 1 – Phase vs. Total Apparent Charge distribution

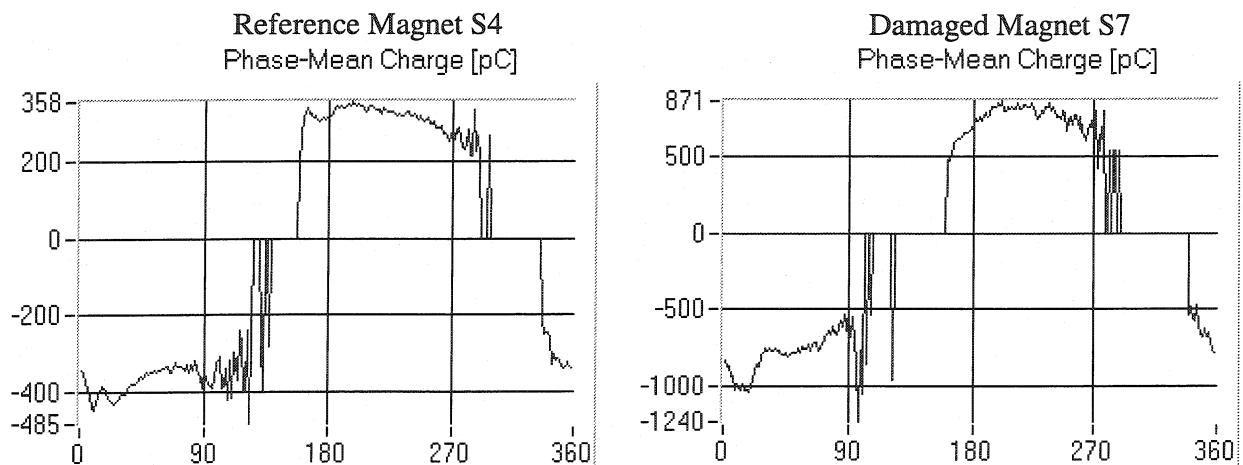


Figure 5.13 Test No. 1 – Phase vs. Average Charge distribution

magnet have higher amplitudes (Fig. 5.13). This situation may correspond to the discharges with the activation voltage much higher than the inception voltage, which would correspond to the discharges within the insulation (i.e. between the insulation and insulation). The following tests investigate this problem in a more detailed way.

- **Test No. 2 – Simultaneous test of insulation between the quench heaters and the coil and between the quench heaters and the collars**

During this test the active potential electrode of the excitation is connected only to all of the quench heaters, whereas the coils of the magnet and the collars are connected to the ground. The amplitude of the AC input signal is 2 kV. In this configuration the electrical stress is applied across the insulation between the quench heaters and the coils as well as across the insulation between the quench heaters and the collars. The PD pattern will reflect in this case the discharge activity in the entire ground insulation. Fig. 5.14 shows the comparison of the

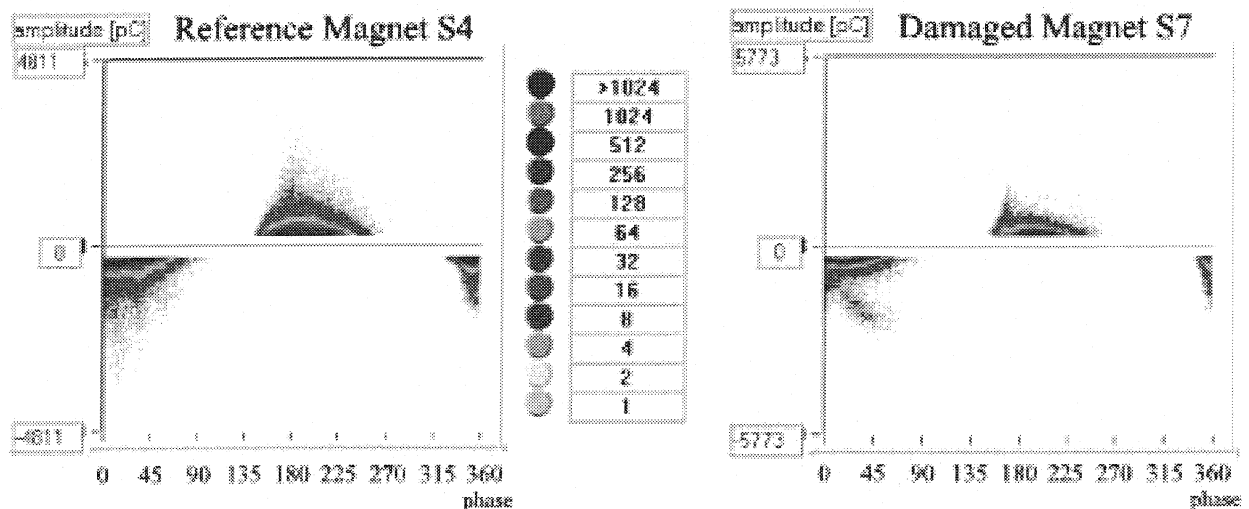


Figure 5.14 Test No. 2 – Comparison of PD patterns

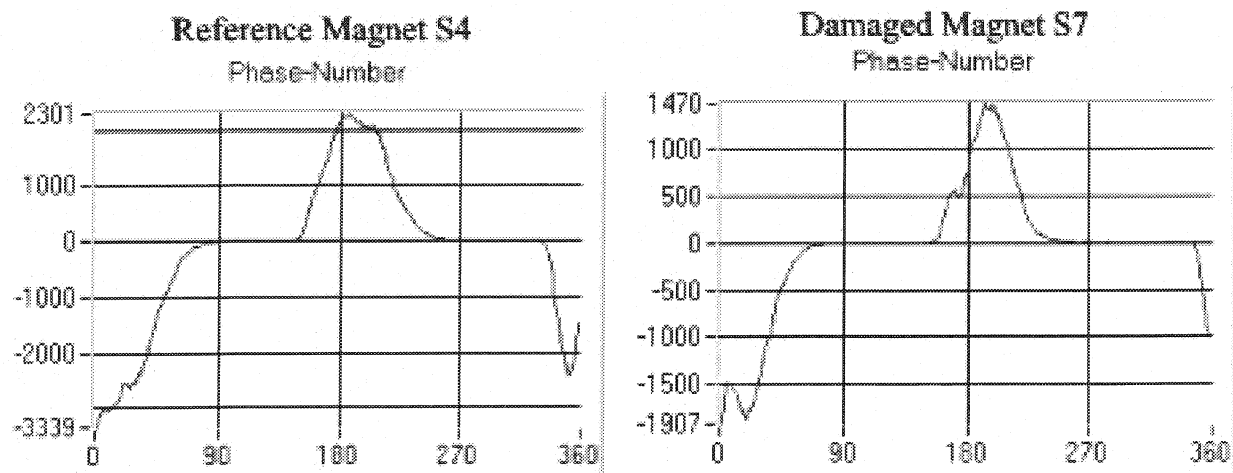


Figure 5.15 Test No. 2 – Phase vs. Number distribution

PD patterns acquired for both magnets. The tail visible on the PD pattern of the damaged magnet is a characteristic feature for an excessive void with the activation voltage much higher than the inception level. This feature is not present in the regular PD pattern of the reference magnet. The remaining statistical distributions are compared in Figs. 5.15 – 5.17. The defect visible already in Figs. 5.10 and 5.11 as a small local maximum split off the main positive peak is more pronounced on the plots in Figs. 5.15 and 5.16 for a different phase. The phase shift may result in the change of the electrode configuration. Also the distribution of the mean charge differs a lot from the one acquired for the reference magnet (Fig. 5.17).

There is definitely something wrong with the insulation of the magnet S7. Could we possibly diagnose which side of the magnet is affected by the problem?

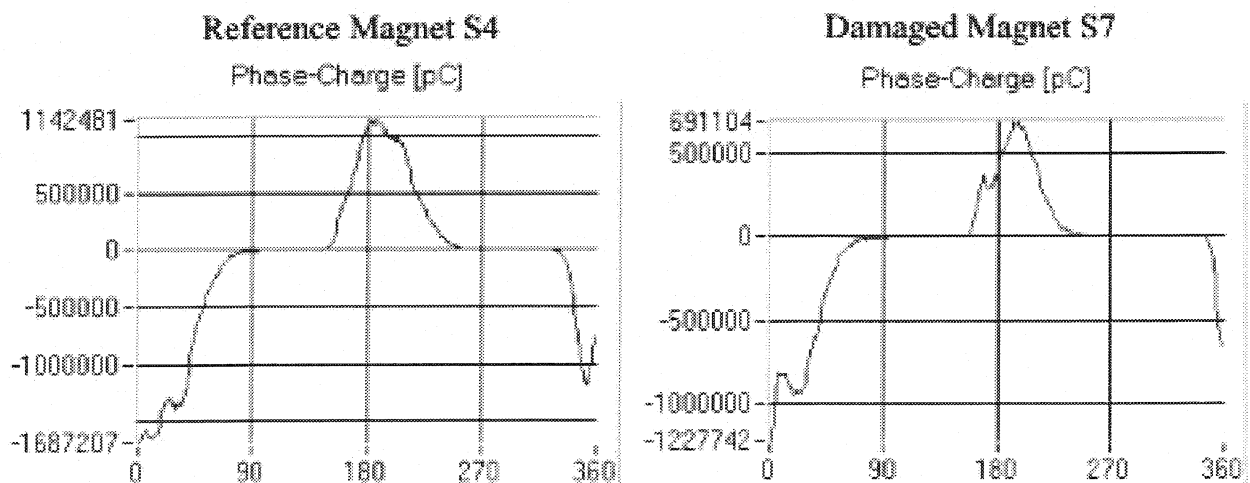


Figure 5.16 Test No. 2 – Phase vs. Total Apparent Charge distribution

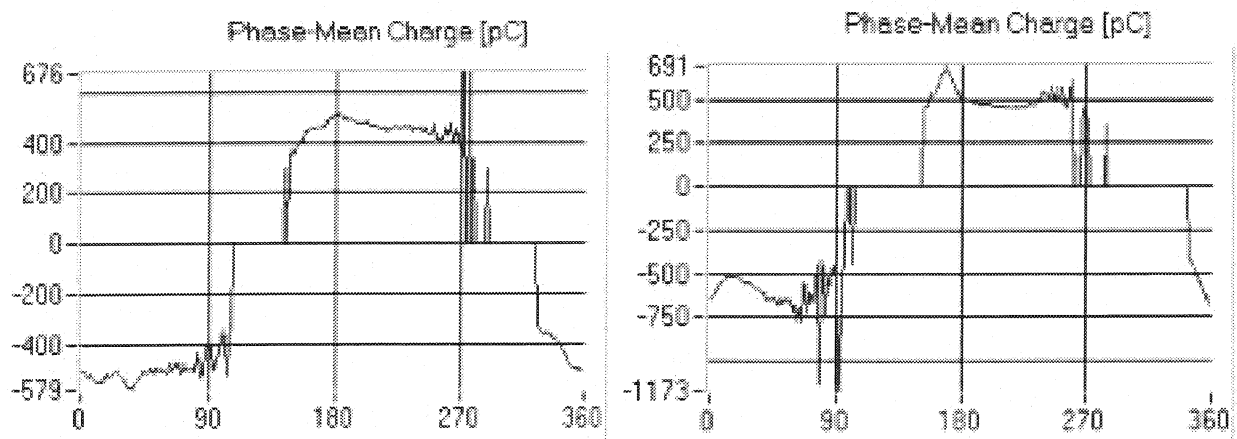


Figure 5.17 Test No. 2 – Phase vs. Average Charge distribution

- **Test No. 3a – Sidewise test of the ground insulation (QH1 & QH2)**

During this test the active potential electrode of the excitation source is connected uniquely to the quench heaters No. 1 and No. 2 (see Fig. 5.7), whereas the coils, the collars and the remaining quench heaters (QH3 & QH4) are connected to the ground. The excitation voltage is 50 Hz AC sinusoidal waveform with the amplitude of 2 kV. The configuration emphasizes the voltage stress across the ground insulation on one side of the magnet only. If the defected side of the damaged magnet is tested the PD pattern should be different there in comparison to the pattern acquired on the reference magnet. On the other hand if the intact side of the damaged magnet is analyzed both PD patterns should be quite similar.

The comparison between the PD patterns is shown in Fig. 5.18. Definitely both patterns are different. The pronounced arc-like feature corresponding to an excessive void is visible on the first AC half-cycle in the damaged magnet. There is also a double peak present

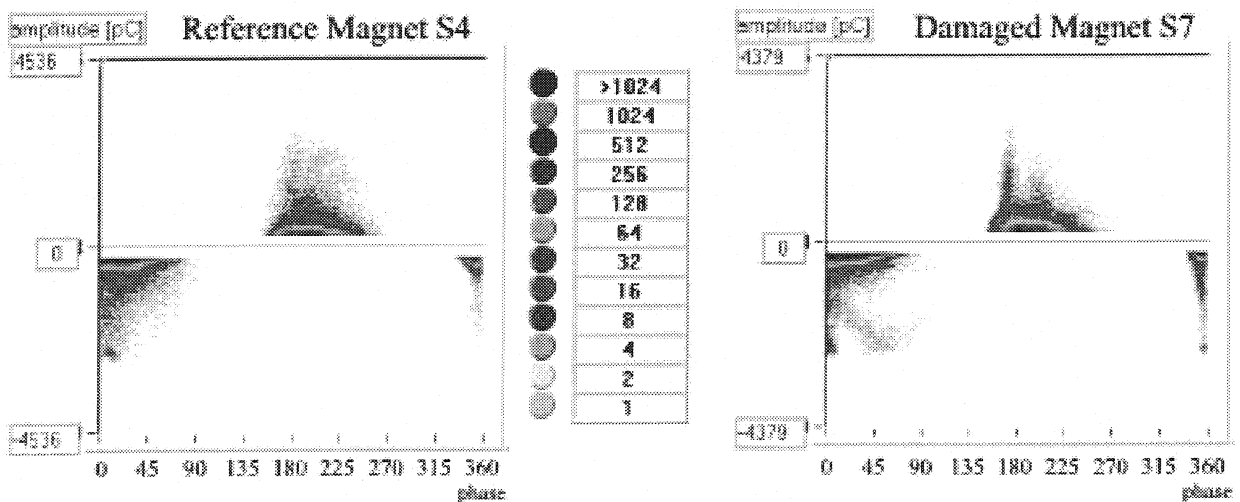


Figure 5.18 Test No. 3a – Comparison of PD patterns

on the pattern covering the second AC half-cycle. In general the PD pattern of the damaged magnet is not symmetric. Not all of the features present on one half-cycle are also visible on the other one. This expresses an increased discharge activity between the quench heaters and the ground insulation. The features present in the PD pattern of the damaged magnet cannot be identified in the corresponding pattern acquired on the reference magnet either.

- **Test No. 3b – Sidewise test of the ground insulation (QH3 & QH4)**

By analogy to the Test No. 3a the following configuration serves to analyze the PD pattern when the voltage stress is applied across the ground insulation on the opposite side of the magnet. This time during the test the active potential electrode of the excitation source is connected uniquely to the quench heaters No. 3 and No. 4, whereas the coils, the collars and the quench heaters No. 1 and No. 2 are connected to the ground. The excitation voltage is exactly the same as in the previous case. The comparison between the PD patterns is shown in Fig. 5.19. It turns out that, on the contrary to the results of the previous test, the PD patterns on this side of the magnet are quite similar in both cases.

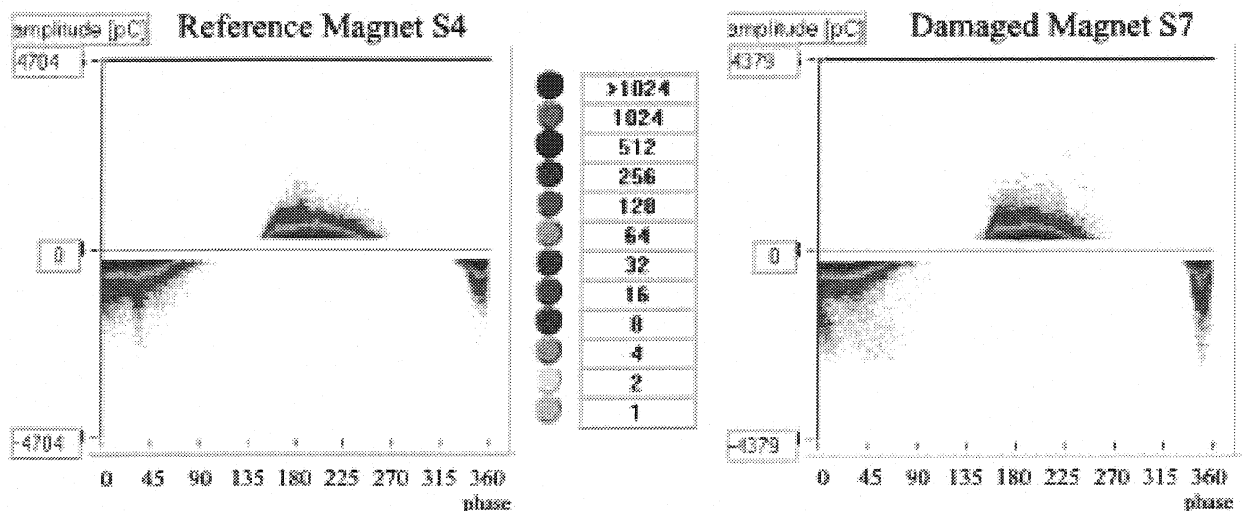


Figure 5.19 Test No. 3b – Comparison of PD patterns

In this regard the final conclusion can be drawn that the damaged ground insulation zone is located on the side of the magnet where the quench heaters No. 1 and 2 are. This diagnosis indeed corresponds to the side of the magnet where the damage was inflicted.

Thus the PD measurements enabled to identify the presence of the fault which was beyond the detection capabilities of the standard tests. This very first and preliminary demonstration of the PD techniques in the context of the LHC dipole magnets triggered a wave of growing interest concerning the possibility of successful detection of hidden

manufacturing errors. A thorough investigation of the measurement method performed on different magnet configurations has been planned for the year 2000.

References for Chapter 5

- [1] J. J. O'Dwyer, Breakdown in Solids, IEEE Transactions on Electrical Insulation, Vol. EI-17, No. 6, December 1982
- [2] Paul P. Budenstein, On the Mechanism of Dielectric Breakdown of Solids, IEEE Transactions on Electrical Insulation, Vol. EI-15, No. 3, June 1980
- [3] D. Peier, H. Schwarz, The location of Partial Discharges in High Voltage Cables by Calculation of the Transient Impulse Phenomena, Proceedings of the 5th International Symposium on High Voltage Engineering, Braunschweig, Germany, 24-28 August 1987
- [4] G. C. Stone et al., Application of Partial Discharge Testing to Motor and generator Stator Winding Maintenance, IEEE Transactions on Industry Applications, Vol. 32, Iss. 2, March-April 1996, pp. 459-464
- [5] D. Wenzel, E. Gockenbach, Pulse shaped noise reduction and partial discharge localization on transformers using the Karhunen-Loeve Transform, Proceedings of the 9th International Symposium on High Voltage Engineering, Graz , Austria, 28 August – 1 September 1995, Vol. 5, pp. 5623 - 5626
- [6] K. Tokura, I. Okada, Verification of the Detection of Partial Discharges by Microwaves, M. Kawada, et al., Proceedings of the 1995 International Symposium on Electrical Insulating Materials, Tokyo, Japan, 17-20 September 1995
- [7] M. Beyer, et al., Some Aspects About Possibilities and Limitations of Acoustic Partial Discharge Measurements in Insulating Fluids, Proceedings of the 5th International Symposium on High Voltage Engineering, Braunschweig, Germany, 24-28 August 1987
- [8] Yon Han Yoon et al., A Neural Network Approach for On-Line Estimation of Partial Discharge Location in Power Transformer Using Advanced Correlation Technique, Proceedings of ISAP' 96 – International Conference on Intelligent Applications to Power Systems, Orlando, Jan. – Feb. 1996

- [9] M. Mukai et al., Study on Degradation Diagnosis of Partial Discharge in a Void by Wavelet Analysis, 1995 International Symposium on Electrical Insulating Materials, Tokyo, September 1995
- [10] S. J. Dodd, J. V. Champion, Evidence for Deterministic Chaos in Partial Discharge Rate Measurements, IEE Colloquium on PD Display Systems and Analytical Software, London, February 1996

Conclusions

The work presented in this thesis was focused on the detection and localization of different possible defects in the electrical insulation system and in the instrumentation circuits of the superconducting accelerator magnets for the Large Hadron Collider. This kind of investigation was required by the preparation for the series production of the large number of technologically challenging 15-m long superconducting dipole magnets responsible for the deflection of the proton beam in the arc sections of the accelerator.

Initially the problem of the detection and localization of inter-turn short circuits in defective magnets was addressed. A manifestation of such a fault in the superconducting coils encountered during a resistive transition of the magnet from the superconducting to the normal state (triggered either as a part of the test and training of the magnet or caused inadvertently in a natural way by a thermal perturbation of the magnet system) causes an inevitable pointwise burnout of the superconducting cable, and thus an irreversible damage inflicted to the coils of the magnet.

In the beginning a complete experimental set-up integrated with data acquisition and analysis system was designed and implemented for the preliminary high voltage test of the inter-turn insulation in the magnet coil. This system has been already commissioned and delivered to three companies in France, Germany and Italy, contracted for the series production of the LHC magnets. The preliminary diagnosis performed with this kind of test enables to detect the presence of the defect in the magnet, nevertheless the location of the problem cannot be established. In most cases when the magnet is disassembled for repair the inter-turn short-circuit disappears due to the release of the internal prestress in the coils. Only

the development of a novel method reaching far beyond the diagnostic capabilities of the relatively standard high voltage discharge test would overcome these difficulties.

An elegant and efficient solution was brought by the analysis of the distortion of a pulsed magnetic field generated in the aperture of the magnet during the high voltage discharge test. The detection method was based on the study of the magnetic field harmonics induced by the current redistribution in the magnet coils. Such redistribution occurs in the magnet due to the breaking of the initial current distribution symmetry enforced by the presence of the inter-turn short circuit. The designed experimental procedure has been simulated with OPERA-2D and tested on a dedicated dipole magnet equipped with micro-relays capable of activating short-circuits in the internal layers of the coils. The longitudinal and azimuthal position of the short-circuits was successfully established for all of the installed micro-switches with a precision of a few millimeters. This new technique has been presented on the 16th International Conference of Magnet Technology in USA at the end of September 1999. The résumé of the entire concept has been accepted for publication in IEEE Transactions for Applied Superconductivity and it will appear in print early in the year 2000. At the moment I am writing these words the method undergoes its adaptation for the 15-m long LHC dipole magnets. It can be also easily adapted for the different types of accelerator magnets, e.g. quadrupoles.

In addition to inter-turn defects another kinds of faults have also been addressed in this study. Advanced time domain reflectometry techniques (TDR) have been successfully adapted for the analysis of the signal integrity in the auxiliary instrumentation circuits of the LHC magnets. The instrumentation circuits are responsible for transmitting the vital status information of the magnet and its cryogenic environment. Different TDR techniques were tested in the real-life situation on the voltage tap, temperature and pressure transducer circuits of the string of full-scale LHC magnets simulating the behavior of the standard half-cell of the LHC arc section. The results and conclusion of these tests were officially presented as a separate LHC project.

Finally, for the first time, partial discharge techniques were applied for the detection of hidden defects in the ground insulation of superconducting magnets. These types of human errors can be introduced inadvertently into the insulation system of the magnet during its assembly. They are beyond detection capabilities of any standard tests carried out on the magnet. The experiments gave very promising indications implying that the partial discharge analysis can be a powerful tool for the detection of such defects.